Crystallography Reports, Vol. 48, No. 3, 2003, pp. 347–350. Translated from Kristallografiya, Vol. 48, No. 3, 2003, pp. 391–394.
Original Russian Text Copyright © 2003 by Talis.

THEORY OF CRYSTAL STRUCTURES

Structural Characteristics of Gas Hydrates within the Framework of Generalized Crystallography

A. L. Talis
Russian Institute of Synthesis of Mineral Raw Materials, Aleksandrov, Vladimir oblast, 601650 Russia
e-mail: stm@vniisims.elcom.ru

Received September 16, 2002

Abstract—It is shown that the symmetry of the {5, 3, 3} polytope (four-dimensional dodecahedron) embedded into E^4 enables one to derive all the polyhedra–cavities that make up gas hydrates from the {5, 3} dodecahedron. Consideration is given to the allomorphic embedding of the {5, 3} subgraph into the incidence graph of the Desargues configuration 10_3, which determines the mechanism of incorporation of guest molecules into the polyhedra–cavities of gas hydrates and their escape from these polyhedra at the symmetry level. The relationships obtained may be considered as a basis for an *a priori* derivation of the determined (periodic and aperiodic) structures of gas hydrates. © *2003 MAIK “Nauka/Interperiodica”.*

The impossibility of dividing the three-dimensional Euclidean space E^3 into regular tetrahedra determines the structural characteristics of tetrahedrally coordinated aqueous frameworks of gas hydrates that cannot be adequately reflected within the framework of classical crystallography. For example, the polyhedra–cavities D, T, P, and H (dodecahedron, tetra-, penta-, and hexadecahedra), the constituent fragments of the structures of gas hydrates, are determined as dual to the $Z12$, $Z14$, $Z15$, and $Z16$ polyhedra (icosahedron and Frank–Kasper polyhedra) [1, 2]; the D' and E polyhedra–cavities (Fig. 1) have not been determined as yet [3]. The symmetry basis of the structural mechanism of the incorporation of guest molecules into polyhedra–cavities and their escape from these cavities is also unknown. Below, we show that the specific structural features of gas hydrates can be adequately described only within the framework of the generalized crystallography [4–7].

The division into regular tetrahedra that are impossible in E^3 can be made in a four-dimensional icosahedron–polytope {3, 3, 5} whose 120 vertices belong to the three-dimensional sphere S^3 embedded into E^4. The {3, 3, 5} polytope and the dual {5, 3, 3} polytope (four-dimensional dodecahedron) are mapped onto themselves by the group $Y' \times Y'$ of order 14 400. If group Y of icosahedron rotation consists of 60 $g(\mathbf{n}, \varphi)$ elements, where $\mathbf{n}$ is the unit vector directed along the icosahedron axis around which the rotation by an angle φ takes place, then group Y' consists of 120 $y(\mathbf{n}, \varphi)$ and $y(\mathbf{n}, \varphi + 2\pi) = -y(\mathbf{n}, \varphi)$ elements uniquely corresponding to $\pm\varphi$ disclinations introduced into the icosahedron along the vector $\mathbf{n}$. For example, the element $y\left(\mathbf{n}, -\frac{2\pi}{5}\right)$ corresponds to the disclination $-\frac{2\pi}{5}$, which transforms the pentagonal “cap” of the icosahedron into a hexagonal one (if a wedge with an angle $\frac{2\pi}{5}$ is inserted), with the disclination interactions being determined by the product of the corresponding elements of group Y'. The introduction of two, three, and four $-\frac{2\pi}{5}$ disclinations into an icosahedron along its fivefold axes results in the formation of the $Z14$, $Z15$, and $Z16$ polyhedra [2].

The introduction of a disclination quadruplet (consisting of two $-\frac{2\pi}{5}$ and two $\frac{2\pi}{5}$ disclinations) into the vertices of a “rhombus” built by two neighboring triangular faces of the icosahedron results in the flipping of the diagonal in this rhombus (Fig. 1). To the quadruplet q or the disclination 2π there corresponds the element $y(\mathbf{n}, 2\pi) = -1$ of group Y' and the rotation by 2π along the Möbius band [6]. Thus, introducing three 2π disclinations into the icosahedron (which preserve the subgroup C_3 of its group Y_h) and demanding the maximum point symmetry, we arrive at the twelve-vertex polyhedron $Z12^{3q}/D_{3h} = [4^3, 5^6, 6^3]$ with the symmetry group D_{3h} and twenty triangular faces. In this case, four edges meet at three vertices $Z12^{3q}/D_{3h}$, five edges at six vertices, and six edges at three vertices; a polyhedron dual to this polyhedron is the polyhedron–cavity D' (Fig. 1). Along each of the three straight lines connecting pairs of the vertices of the upper and lower hexagonal caps in $Z14 = Z12^{2d}/D_{6d} = [5^{12}, 6^2]$, one may introduce two $-\frac{2\pi}{5}$. 2π disclinations rearrange the diagonals of three tetragons consisting of halves of the triangular faces. As a result, a 20-vertex polyhedron $Z14^{6d, 3q}/D_{6h} = (Z12^{2d})^{6d, 3q}/D_{6h} = [5^{12}, 6^8]$ is formed, to which the polyhedron–cavity E is dual (Fig. 1).

1063-7745/03/4803-0347$24.00 © 2003 MAIK “Nauka/Interperiodica”

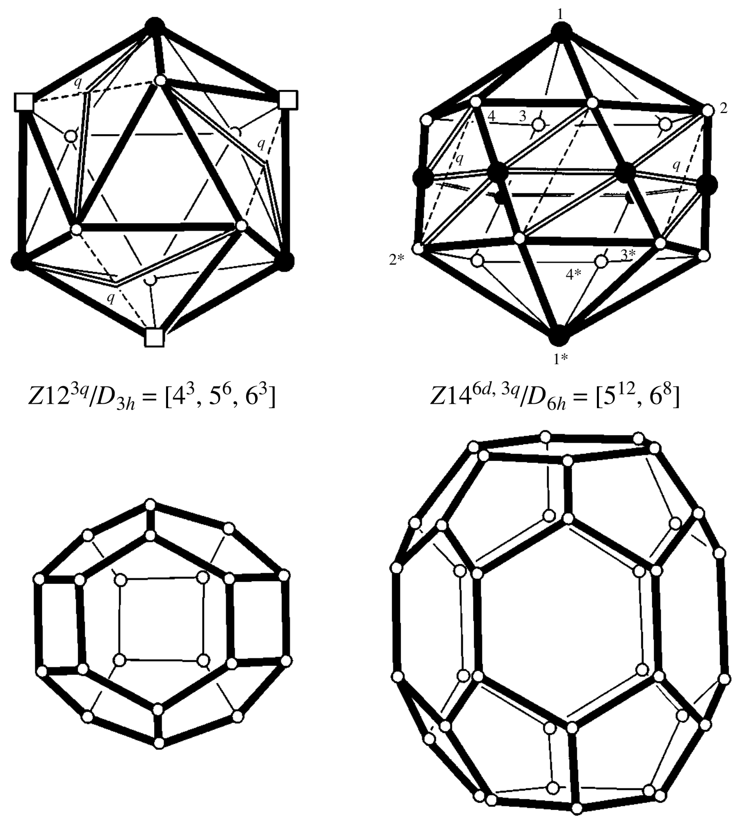

$Z12^{3q}/D_{3h} = [4^3, 5^6, 6^3]$ $Z14^{6d,\,3q}/D_{6h} = [5^{12}, 6^8]$

D' *E*

Fig. 1. Graphs of the $Z12^{3q}/D_{3h}$ and $Z14^{6d,\,3q}/D_{6h}$ polyhedra and the dual polyhedra–cavities *D*' and *E*. The vertices where six edges meet are indicated by filled circles; the vertices where four edges meet, by open squares; the 2π disclination is denoted by letter *q* in the center of a tetragon, where this disclination can reject and introduce edges shown by dashed and double lines, respectively. Some of the "back lines" in $Z14^{6d,\,3q}/D_{6h}$ are not shown, the filled vertices in its "equatorial belt" arise due to the introduction of $-\frac{2\pi}{5}$ disclinations along the straight lines 22*, 33*, and 44* in *Z*14.

In fact, the polyhedron symbols $Z12^{3q}/D_{3h} = [4^3, 5^6, 6^3]$ and $(Z12^{2d})^{6d,\,3q}/D_{6h} = [5^{12}, 6^8]$ set the disclinations and the corresponding elements of group *Y*', which determine the derivation of these polyhedra from the icosahedron. The symmetry of the dual polyhedron is the same as the symmetry of the initial one, and, therefore, all the polyhedra–cavities *D*', *T*, *P*, *H*, and *E* can be derived from the dodecahedron *D* (with the symmetry group Y_h) using the $-\frac{2\pi}{5}$ and 2π disclinations, whose interaction is determined by the products of the corresponding elements of *Y*'.

It is possible to consider as an energetically favorable transformation such a transformation of the cluster that would keep the maximum subgraph containing all its vertices, with all the other conditions being the same. Since the polyhedra–cavities are derived from the dodecahedron, the symmetry basis of the structural mechanism of incorporation of guest molecules into a polyhedron–cavity (and escape from it) can be determined from the transformation of the dodecahedron into a tetrahedrally coordinated 20-vertex cluster with equal edges that leaves no space for a guest molecule.

A dodecahedron is a $\{5, 3\}$ map on a sphere (at each vertex, three pentagons meet); its Petrie polygon is a decacycle—the sequence of edges in which each two (and not three) edges belong to one face [7]. Six such decacycles contain all 30 edges and 20 vertices of the dodecahedron and are isomorphous to the $\{10, 3\}_5$ map on the nonoriented surface (at each vertex, three decacycles meet, the vertices separated by five edges of Petrie's polygon are considered to be equivalent) [8]. The $\{10, 3\}_5$ map also contains pentacycles, which are its minimum cycles (Fig. 2a).

The $\{10, 3\}_5$ map is allomorphic to the $\{10, 3\}'_5$ map (Fig. 2b) and differs from the latter only in its minimum cycles—hexacycles [8]. The transition from $\{10, 3\}_5$ to $\{10, 3\}'_5$ and back is provided by 2π disclinations. Thus, if, for example, in the decacycle 13'65'21'36'74' (the primed figures numerate black vertices) divided into four pentacycles the edge 8'10 is

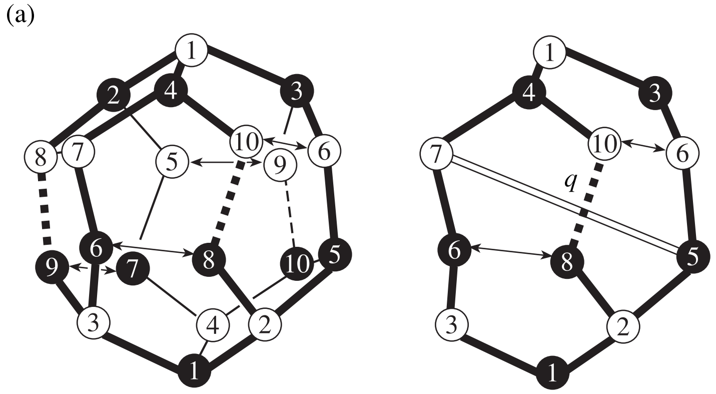

{5, 3}

	1	2	3	4	5	6	7	8	9	10
1		●	●	●						
2	●				●			●		
3	●					●			●	
4	●						●			●
5		●				●	◎			
6			●		◎		●			
7				●	●	◎				
8		●							○	◉
9			●					◉		○
10				●				○	◉	

Table of incidence {5, 3}

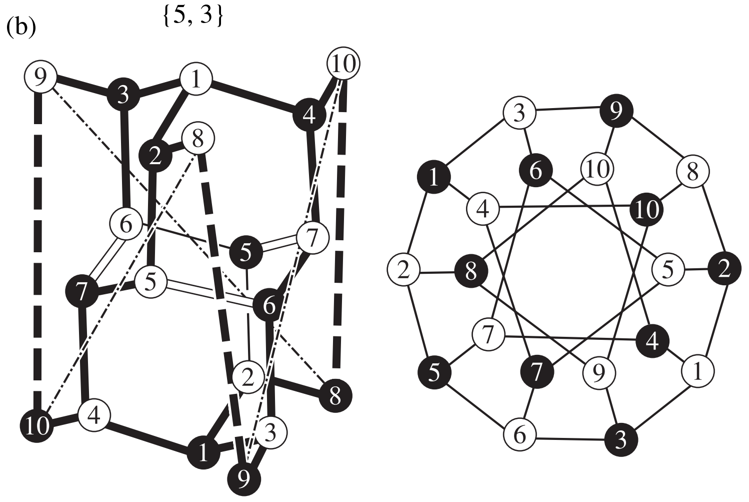

$\{10_3\}^6$ $\{10\} + \{10/3\}$

	1	2	3	4	5	6	7	8	9	10
1		●	●	●						
2	●				●			●		
3	●					●			●	
4	●						●			●
5		●				●	◉			
6			●		◉		●			
7				●	●	◉				
8		●							○	◎
9			●					◎		○
10				●				○	◎	

Table of incidence $\{10_3\}^6$

Fig. 2. Dodecahedron and the allomorphic twenty-vertex diamond cluster, their incidence graphs and corresponding incidence tables: (a) in the bichromatic {5, 3} graph of the dodecahedron, six arrows connect the vertices of the same color; the flipping of the edges by a 2π disclination *q* results in the appearance of a hexacycle in the decacycle; the incidence table of the {5, 3} graph coincides with the incidence table of the Desargues configuration 10_3 if six arrows are rejected; (b) a twenty-vertex diamond cluster whose bichromatic graph is embedded into the bichromatic graphs {10} + {10/3} set by the incidence table of the Desargues configuration 10_3. The nondiamond bonds are shown by dashed and dash-dotted lines. The filled circles in the incidence tables correspond to the cluster edges; the empty circles correspond to the bonds that are not edges. The incidence tables differ only in arrows and pairs of double-circle triads.

replaced by the edge 5'7, then, in addition to four pentacycles (two old ones and two new ones), the decacycle is also divided into two hexacycles, 13'65'74' and 76'31'25' (Fig. 2a). The $\{10, 3\}_5^{'}$ map is embedded into the graph {10} + {10/3}, which coincides (if the vertices are painted by two colors and the edges connect only differently colored vertices) with the bichromatic graph $\Gamma(10_3)$, the incidence graph of the Desargues configuration 10_3 (Fig. 2b). Thus, it becomes possible to embed the subgraph of the dodecahedron {5, 3} into the incidence graph of the Desargues configuration, the basic construction of the projective geometry [9].

The graph $\Gamma(10_3)$ is set by its incidence table, in which a line corresponds to a black vertex and a column, to a white vertex, whereas the incidence sign in the cell *i*, *j* corresponds to the edge between the *i*th black and the *j*th white vertices. The subtable of the incidence table 10_3 consisting of 24 filled circles determines a 20-vertex diamond cluster, $\{10_3\}^6$ [4]. The exchange in this table of the triads of double circles leads to the incidence table of a diamond cluster with the graph $\{d\} = \{10_3\}_d^6$ in which the bonds 56', 67', and 75' are broken and the bonds 89', (9, 10'), and (10, 8') are formed (Fig. 2b). Coloring the dodecahedron vertices two different colors, we set its incidence graph by the incidence table {5, 3}, where the elimination of six arrows corresponding to the edges connecting the vertices of one color also leads to the incidence table {*d*}, which determines the subgraph of the dodecahedron $\{d\} = \{5, 3\}^6$ (Fig. 2a). The mutual transformations of tetrahedrally coordinated clusters $\{5, 3\}^6$ and $\{10_3\}^6$ are performed in accordance with allomorphism by introducing three 2π disclinations, which preserve the symmetry D_3 of these clusters and change three edges of graph

$\{5, 3\}^6$ to three edges of graph $\{10_3\}^6$. As a result, mutual transformations of the clusters may occur under pressure applied to two vertices lying on the threefold axis, which gives rise to a synchronous screw-type motion of all the vertices implemented via hinge twisting of the edges [10, 11]. Thus, if the break of nine bonds (arrows and dashed lines in Fig. 2a) in the dodecahedral aqueous framework of the gas hydrate allows a guest molecule to escape from the cavity, then the remaining framework untwists into a diamond-like ice cluster until three new bonds of the same length (double lines in Fig. 2b) are formed. And vice versa, if three bonds in a 20-vertex diamond-like ice cluster break (double lines in Fig. 2b), then the remaining framework twists until the formation of nondiamond bonds with lengths equal to the lengths of diamond bonds (dashed lines in Fig. 2a), and the cavity thus formed can incorporate a guest molecule. Similar transformations seem to be possible not only for individual clusters but also for rods formed by such clusters.

The relationships obtained in this work can be considered as the necessary (symmetry) conditions for modeling the determined structures of gas hydrates. The results obtained lead to the following conclusions.

—All the polyhedra–cavities forming gas hydrates can be derived from the {5, 3} dodecahedron with the aid of the 2π and $-\frac{2\pi}{5}$ disclinations corresponding to the elements of the subgroup Y' of the group $Y' \times Y'$ of the {5, 3, 3} polytope.

—At the symmetry level, the mechanism of incorporation of guest molecules into the polyhedra–cavities of gas hydrates and escape from these cavities is determined by allomorphic embedding of the subgraph of the {5, 3} dodecahedron into the incidence graph of the Desargues configuration 10_3, which contains the graph of a 20-vertex atomic cluster of diamond-like ice.

ACKNOWLEDGMENTS

The author is grateful to V.A. Koptsik. I.A. Ronova, M.I. Samoilovich, L.I. Tsinober, and V.E. Dmitrienko for fruitful discussions.

REFERENCES

1. J. F. Sadoc and J. Charvolin, J. Phys. I **2**, 845 (1992).
2. D. R. Nelson, Phys. Rev. B **28** (10), 5515 (1983).
3. F. Liebau, *Structural Chemistry of Silicates: Structure, Bonding, and Classification* (Springer, Berlin, 1985; Mir, Moscow, 1988).
4. A. L. Talis, Kristallografiya **47** (4), 583 (2002) [Crystallogr. Rep. **47**, 527 (2002)].
5. A. L. Talis, Kristallografiya **47** (5), 788 (2002) [Crystallogr. Rep. **47**, 709 (2002)].
6. J. F. Sadoc and N. Rivier, Philos. Mag. B **55** (5), 537 (1987).
7. H. S. M. Coxeter, *Regular Polytopes* (Dover, New York, 1973).
8. H. S. M. Coxeter, Bull. Am. Math. Soc. **56**, 413 (1950).
9. F. Karteszi, *Introduction to Finite Geometries* (Akademiai Kiado, Budapest, 1976; Nauka, Moscow, 1980).
10. A. L. Talis, in *Proceedings of IV International Conference on Crystals: Growth, Properties, Real Structure, and Application* (VNIISIMS, Aleksandrov, 1999), p. 219.
11. A. L. Talis, *Synthesis of Minerals* (VNIISIMS, Aleksandrov, 2000), Vol. 3, p. 321.

Translated by L. Man

Crystallography Reports, Vol. 48, No. 3, 2003, pp. 351–354. Translated from Kristallografiya, Vol. 48, No. 3, 2003, pp. 395–398.
Original Russian Text Copyright © 2003 by Zorkiĭ, Obodovskaya, Panina.

THEORY OF CRYSTAL STRUCTURES

A Necessary Condition for the Formation of a Bisystem Molecular Crystal

P. M. Zorkiĭ, A. E. Obodovskaya, and N. G. Panina
Department of Chemistry, Moscow State University, Vorob'evy gory, Moscow, 119992 Russia

Received June 17, 2002

Abstract—A hypothesis is formulated which states that the necessary condition for the existence of a bisystem molecular crystal is the approximate equality of the total energies of the interactions of two symmetrically independent molecules N and N' with their environment in the crystal structure (U_Σ). The hypothesis was tested on four crystalline organic compounds of the structure class $P2_1/c$, $Z = 8(1, 1)$. The computations in the atom–atom approximation demonstrated that the energies $U_\Sigma(N)$ and $U_\Sigma(N')$ have very close values despite the different coordination numbers of the molecules and a difference in the structures of the molecular agglomerates that include the molecules N and N'. *© 2003 MAIK "Nauka/Interperiodica".*

Statistical studies of the distribution of organic crystals over structural classes [1, 2] show that ~90% of the homomolecular crystals, i.e., crystals consisting of chemically identical molecules, are monosystem crystals. We note once again that monosystem crystals are molecular crystals in which all the molecules occupy one system of equivalent positions (one orbit) in the space group. Consequently, all the molecules adopt the same conformation and have the same environment in the crystal. Evidently, this is true for ideal crystal structures that are infinite in three directions.

At the same time, about 11% of all organic homomolecular crystals with known structures (more than 8000 crystal structures[1]) are polysystem crystals. In other words, two or more orbits in these crystals are occupied by molecules ($k \geq 2$, where k is the number of occupied orbits). Bisystem crystals account for ~9% of polysystem crystals (more than 7300 structures). In these crystals, molecules that occupy different orbits are not related to each other by the symmetry operations of the space group. These molecules can adopt different conformations (the phenomenon of contact conformery [4]) and are virtually always surrounded by the neighboring molecules in different ways.

In many respects, the reasons for the formation of polysystem crystals and, in particular, bisystem crystals is still unclear. Actually, it seems more natural that, in the crystal structures of completely ordered systems of identical molecules at rather low temperature (when a further decrease in the temperature can hardly lead to a phase transformation), the molecules would occupy fully equivalent positions.

In previous studies [5–7], we made an attempt to answer the question under what conditions and on what occasions can bisystem crystals be formed. Most of these crystals (almost all of them) are characterized by the presence of supersymmetry, which can manifest itself in two ways—as a local pseudosymmetry of molecular subsystems (e.g., some triclinic crystals can have chains of molecules related by local screw axes 2_1 or gliding planes c) [5, 6] or as a hypersymmetry, which manifests itself in the presence of specific symmetry operations such as $2q$ or m_p that transform the molecules that are nonequivalent with respect to the space group into one another. Earlier [7], we considered the crystal structure of *L*, *D*-methylsuccinic acid and demonstrated how a system of hypersymmetry operations and, consequently, the bisystem crystal structure can be determined by the network of intermolecular hydrogen bonds.

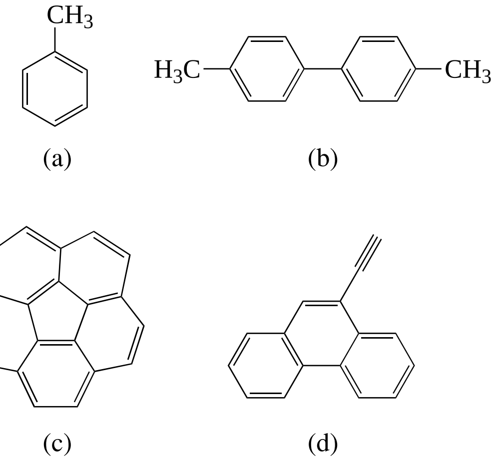

(a) (b) (c) (d)

Fig. 1. Structural formulas of (a) toluene, (b), 4,4'-dimethylbiphenyl, (c) corannulene, and (d) 9-ethylphenanthrene.

---

[1] The April 2002 version of the Cambridge Structural Database (CSD) contains 257 thousand entries. According to the relations reported in [3], this value approximately corresponds to the above-mentioned number of polysystem homomolecular organic crystals.

1063-7745/03/4803-0351$24.00 © 2003 MAIK "Nauka/Interperiodica"

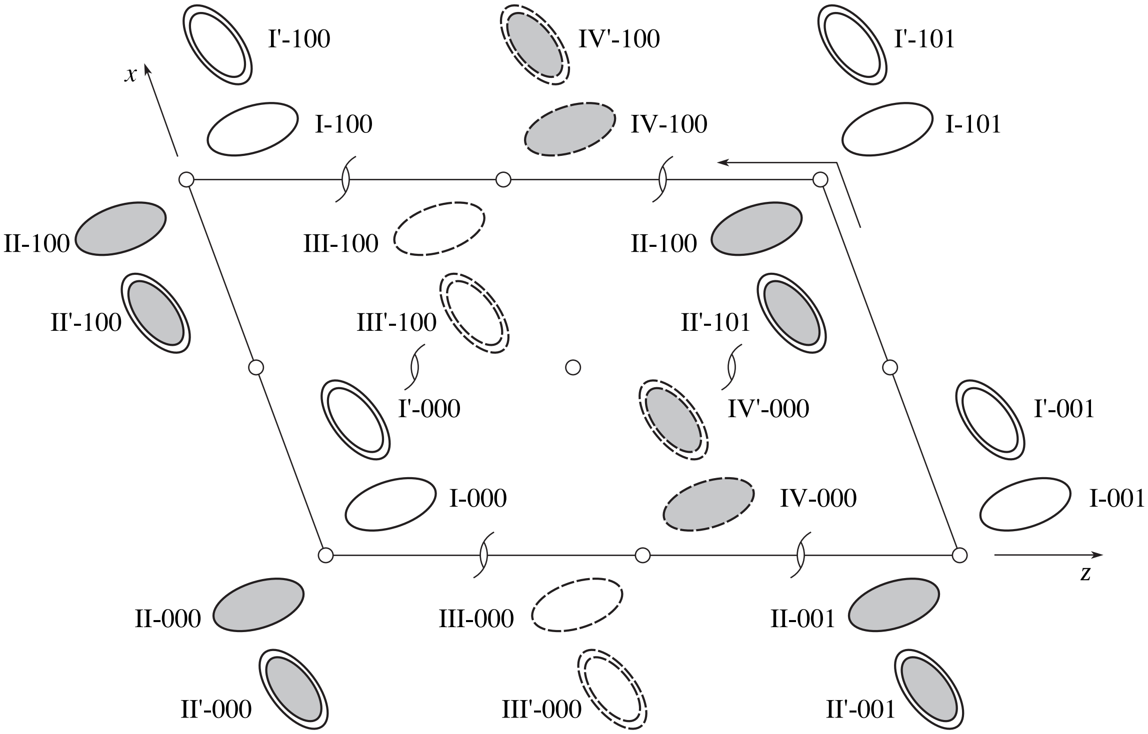

Fig. 2. Schematic representation of the arrangement of molecules in the structural class $P2_1/c$, $Z = 8(1, 1)$; the unit cell is projected onto the *xz* plane. The molecules depicted by solid and dashed contours are located at the heights $z = z_0$ and $z = z_0 + 1/2$, respectively. The shaded molecules are seen from the back (these molecules are turned over). The molecules of the first (*N*) and second (*N*') systems are depicted by single and double contours, respectively. In the general case, the molecules are denoted as *N-HKL*, where *N* is a Roman numeral indicating the molecule orientation, and *H*, *K*, and *L* are the integers signifying the translation shifts along the three crystallographic axes.

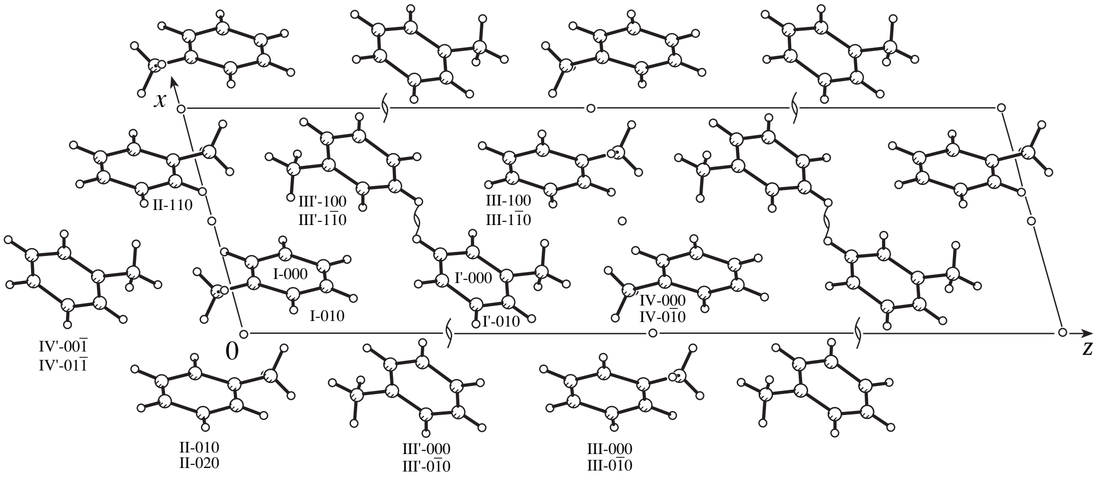

Fig. 3. Toluene crystal structure projected onto the *xz* plane.

In the present study, we considered the four compounds indicated in Table 1 together with their refcodes (CSD entry identifiers) in the Cambridge Structural Database, which was used as a source of the X-ray structural information. The structural formulas of these compounds are shown in Fig. 1.

All these crystals belong to the structural class $P2_1/c$, $Z = 8(1, 1)$.[2] This is the most widespread class of

---

[2] The symbol of the structural class includes the space group, the number of the molecules in the unit cell, and the notation of the orbits occupied by the molecules (in the form of the point groups characterizing the symmetry of the positions).

Table 1. Calculated energies of interactions between the molecules and their environment (kcal/mol)

Compound	Refcode	$K(N)$ $K(N')$	$-U_s(N)$ $-U_s(N')$	$-U_\Sigma(N)$ $-U_\Sigma(N')$	$-U_s/U_\Sigma(N)$ $-U_s/U_\Sigma(N')$	$-U_\Sigma$	References
Toluene	TOLUEN	12	11.08	12.86	0.86	12.85	[8]
		13	11.07	12.65	0.88		
4,4'-Dimethylbiphenyl	BTOLYL	14	20.78	23.37	0.89	23.60	[9]
		13	20.87	23.64	0.88		
Corannulene	CORANN 01	13	26.90	29.88	0.90	29.79	[10]
		13	26.34	29.52	0.89		
9-Ethylphenanthrene	NAMZOQ	14	23.97	26.60	0.90	26.48	[11]
		14	23.61	26.19	0.90		

bisystem crystals, which includes 30% of the total number of such crystals. The scheme of the arrangement of the molecules in the structural class $P2_1/c$, $Z = 8(1, 1)$ is shown in Fig. 2.

The energies of intermolecular interactions were calculated in the atom–atom approximation using an original program developed in the Laboratory of Crystal Chemistry at the Faculty of Chemistry of the Moscow State University. We calculated the energies of interactions of the initial molecule denoted as I-000 with the *N-HKL* molecules of its nearest environment:

$$U_{MM} = \sum_{i,j}(\varphi_{ij} + \psi_{ij}),$$

where i and j are the subscripts indicating the atoms of different molecules.

The computations were performed based on the atom–atom potentials 6-exp and the parameters obtained by Gavezzotti and Filippini [12]. Unlike the computational scheme that became very popular after the publication of the classical work by Williams [13], the procedure developed by Gavezzotti and Filippini does not take into account the effective atomic charges and Coulomb interactions. Gavezzotti and Filippini believe that appropriately chosen parameters of the 6–exp potentials ensure the correct computation of the energies of intermolecular interactions even without allowance for atomic charges. In fact, this signifies that, instead of the atom–atom potential

$$\varphi_{ij} + \psi_{ij} = -Ar_{ij}^{-6} + B\exp(-\alpha r_{ij}) + q_i q_j / r_{ij},$$

they use the potential containing only the first two of the three terms. In these two variants of the computations, the parameters A, B, and α have different values, but the shapes of the curves $\varphi_{ij} + \psi_{ij}$ are similar.

Table 1 gives the total energies of the interactions between the independent molecules and the molecules surrounding the former ones, $U_\Sigma(N)$ and $U_\Sigma(N')$, along with the energies of the interactions with the nearest environment, $U_s(N)$ and $U_s(N')$, and the ratios of these values. Table 1 also lists U_Σ corresponding to the total potential energies of the crystal structures. The energies $U_\Sigma(N)$ and $U_\Sigma(N')$ were calculated by summing up the energies of pair interactions U_{MM}, i.e., as the energies of the escape of the initial molecules from the crystal structure (per mole of the compound). The multiplicities of the contacts between the I-000 and *N-HKL* molecules were also taken into account. The computations were performed with due regard for the molecules located at distances not exceeding 20 Å from the origin of the coordinate system (the molecule closest to the origin of the coordinate system was chosen to be the initial molecule I-000). This ensures a negligible error (not higher than 1%), caused by the series termination upon the summation. The energies of the intermolecular interactions U_{MM} with the molecules of the first coordination spheres around both independent molecules in the crystal structure of toluene (Fig. 3) are given in Table 2 (w is the contact multiplicity). The final value of U_Σ of the bisystem crystal was obtained by averaging $U_\Sigma(N)$ and $U_\Sigma(N')$.

Table 2. Calculated energies of intermolecular interactions in toluene crystals (kcal/mol)

M–M contacts	w	$-U_{\mathrm{MM}}$	*M–M* contacts	w	$-U_{\mathrm{MM}}$
I-000 II-010	1	2.032	I'-000 III'-000	2	1.231
II-110	1	1.027	I'-010	2	0.939
I-010	2	0.960	III'-100	2	0.616
II-020	1	0.598	III-110	1	1.325
III'-100	1	1.325	III-100	1	1.260
III'-1$\bar{1}$0	1	1.260	III-010	1	0.692
III-000	1	0.692	III-000	1	0.599
III'-0$\bar{1}$0	1	0.599	I-000	1	0.587
I'-000	1	0.587	IV-010	1	0.537
IV'-01$\bar{1}$	1	0.537	VI- 000	1	0.500
IV'-00$\bar{1}$	1	0.500			

As can be seen from Table 1, $U_s(N)$ and $U_s(N')$, as well as $U_\Sigma(N)$ and $U_\Sigma(N')$, have close values, which confirms the above-formulated hypothesis. The energy equivalence of the molecules N and N' manifests itself in both the nearest and total environments of the molecules in the crystal; the $U_s(N)$-to-$U_\Sigma(N)$ ratio is almost constant and ranges within 0.86–0.90.

Therefore, it can be assumed that a bisystem crystal is characterized by very close energies of the environments around symmetrically nonequivalent molecules, even if the molecules have different coordination numbers, i.e., $K(N)$ and $K(N')$, and, as will be shown in the next publication, take part in different molecular agglomerates in the crystals.

ACKNOWLEDGMENTS

We are grateful to A.V. Kamchatkin for his help in preparing this paper.

This study was supported by the Russian Foundation for Basic Research, project no. 00-15-97346.

REFERENCES

1. V. K. Belsky, O. N. Zorkaya, and P. M. Zorky, Acta Crystallogr. A **51**, 473 (1995).
2. P. M. Zorky, J. Mol. Struct. **374**, 9 (1996).
3. P. M. Zorkiĭ and P. N. Oleĭnikov, Zh. Fiz. Khim. **74** (11), 1944 (2000).
4. P. M. Zorkiĭ and A. E. Razumaeva, Zh. Strukt. Khim. **20** (3), 463 (1979).
5. P. M. Zorkiĭ, A. E. Obodovskaya, and A. N. Kolyshev, Zh. Strukt. Khim. **39** (3), 369 (1998).
6. P. M. Zorkiĭ, A. E. Obodovskaya, and R. Yu. Muĭdinov, Vestn. Mosk. Univ., Ser. 2: Khim. **41** (3), 166 (2000).
7. P. M. Zorkiĭ, A. E. Obodovskaya, and R. Yu. Muĭdinov, Kristallografiya **44** (4), 581 (1999) [Crystallogr. Rep. **44**, 535 (1999)].
8. M. Anderson, L. Sodio, J. Bruneaux-Paulle, and R. Fourme, J. Chim. Phys. Phys.–Chim. Biol. **74**, 68 (1977).
9. G. Casalone, C. Mariani, A. Mugnoli, and M. Simonetta, Acta Crystallogr. B **25**, 1741 (1969).
10. J. C. Hanson and C. E. Nordmare, Acta Crystallogr. B **32**, 1147 (1976).
11. J. T. Mague, M. Foroozesh, N. E. Hopkins, *et al.*, J. Chem. Crystallogr. **27**, 183 (1997).
12. G. Filippini and A. Gavezzotti, Acta Crystallogr. B **49** (5), 868 (1993).
13. D. E. Williams, Acta Crystallogr. A **30** (1), 71 (1974).

Translated by T. Safonova

Crystallography Reports, Vol. 48, No. 3, 2003, pp. 355–358. Translated from Kristallografiya, Vol. 48, No. 3, 2003, pp. 399–402.

EXAFS Study of the Structure of Borate–Germanate Glasses Based on an $La_3Gd_{10}Eu(BO_3)_6(GeO_4)_2O_8$ Solid Solution

D. I. Kochubeĭ*, B. N. Novgorodov*, V. A. Krut'ko, G. V. Lysanova**, and K. K. Palkina****

* Boreskov Institute of Catalysis, Siberian Division, Russian Academy of Sciences,
pr. Akademika Lavrent'eva 5, Novosibirsk, 630090 Russia
e-mail: kroutko@igic.ras.ru
** Kurnakov Institute of General and Inorganic Chemistry, Russian Academy of Sciences,
Leninskiĭ pr. 31, Moscow, 119991 Russia

Received October 4, 2002

Abstract—The nearest environment of europium atoms in borate–germanate glass of composition $La_3Gd_{10}Eu(BO_3)_6(GeO_4)_2O_8$ was studied by EXAFS spectroscopy, and the Eu–O distances were determined. The structural data on the isostructural compound $Gd_{14}(BO_3)_6(GeO_4)_2O_8$ of similar composition were used for the construction of models. It was established that a europium atom is surrounded by eight oxygen atoms, and the Eu–O distance in the glass was equal to ~2.45 Å. These characteristics are close to the values in the crystals of the corresponding solid solutions. *© 2003 MAIK "Nauka/Interperiodica".*

INTRODUCTION

Earlier [1], crystalline solid solutions of composition $La_{14-x-y}Gd_xEu_y(BO_3)_6(GeO_4)_2O_8$ (x = 1–11, y = 1–3) isotypic to the borate–germanate compounds $Ln_{14}(BO_3)_6(GeO_4)_2O_8$, where Ln = Pr–Gd, were obtained by solid-phase synthesis. The structure of the latter compounds (trigonal system, sp. gr. $P3_1$), studied on Nd-, Sm-, or Gd-containing single crystals [2, 3], is built by 14 LnO_N polyhedra, with one of them being disordered over two positions. It was found that sharp cooling of melts results in the formation of solid solutions in the form of colored thermally stable glasses with a high content of rare earth oxide (~60 mol %). Crystalline and glassy rare-earth borate germanates with the above-mentioned composition are of interest because they exhibit bright luminescence in the range 500–650 nm.

The possible synthesis of such glasses and the fact that the glass-forming ability of acid oxides in glasses is reduced to zero because of the absence of É–O–É bonds allowed the authors of [4] to advance the hypothesis that rare-earth elements play the role of glass-forming agents in borate–germanate glasses of complex compositions. Comparative analysis of the luminescence spectra of crystalline and glassy solid solutions of the same composition [1] led to the conclusion that the nearest environment around the rare-earth ions in glasses is analogous to such an environment in crystalline samples of the same composition.

Unfortunately, the possibilities of applying traditional methods to studying the structures of such complex glasses containing a large number of various cations and anions are rather limited. In this connection, the EXAFS (extended X-ray absorption fine structure) method [5] in which the synchrotron radiation is used as an X-ray source, is of great interest for elucidation of glass structure.

EXAFS allows one to study the structures of the nearest coordination spheres of atoms of particular elements in a compound irrespective of its aggregation state. This method is based on analysis of the oscillating fine structure of X-ray spectra near the absorption edge of an element. These oscillations are caused by the scattering of photoelectrons from the nearest environment of an absorbing atom. The analytical expression for the oscillating behavior of the X-ray absorption coefficient can be derived using the Fourier transform.

In the present study, EXAFS spectroscopy was used to determine the coordination of an Eu atom and estimate Eu–O bond lengths in the borate–germanate glass of composition $La_3Gd_{10}Eu(BO_3)_6(GeO_4)_2O_8$. The experimental procedure and the method of analysis of the spectra are described elsewhere [6].

SAMPLE PREPARATION

A crystalline solid solution of the above-mentioned composition was preliminarily synthesized from freshly calcined La_2O_3, Gd_2O_3, Eu_2O_3, and GeO_2 (hexagonal modification) oxides and boric acid taken in stoichiometric amounts. The mixture was subjected to multistep annealing that was started at room temperature and carried out up to 1250°C with repeated transient grinding procedures. The annealing duration at the final temperature was 15 h. Rare-earth oxides (purity of at least 99.95%), GeO_2 (99.99%), and H_3BO_3 (reagent grade) were used. The samples were annealed in platinum crucibles in a silicon carbide furnace. The

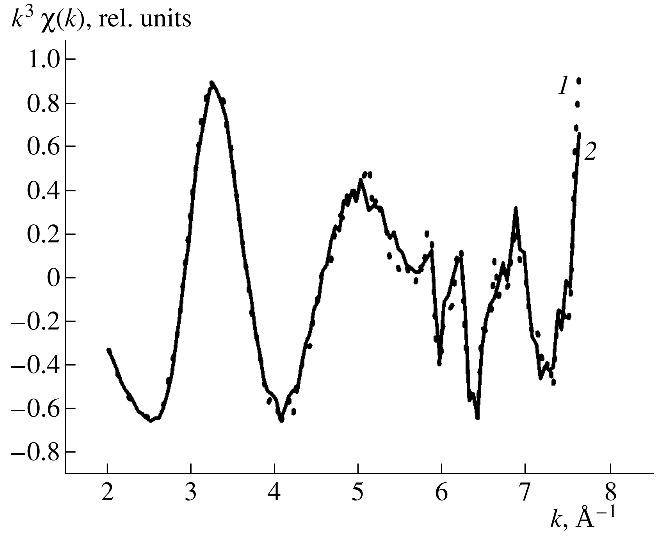

Fig. 1. Oscillating fine structure of the X-ray absorption band for the $La_3Gd_{10}Eu(BO_3)_6(GeO_4)_2O_8$ glasses prepared on (*1*) graphite and (*2*) platinum substrates.

phase composition of the annealing products was examined by powder X-ray diffraction on a DRON-2 diffractometer. The thermal characteristics were measured on a Paulik-Paulik-Erdey Q-1500D derivatograph in platinum crucibles with an accuracy of ±15°C. To prepare glasses, the samples annealed at 1250°C were heated in platinum crucibles to 1500–1550°C. After 30–40 min-storage at this temperature, the melts were taken away from the furnace and poured into either a graphite mold or onto a platinum plate. As a result, we obtained turquoise-colored transparent glasses.

EXAFS STUDY OF STRUCTURAL CHARACTERISTICS OF GLASSES

The experimental EXAFS data were collected in the Siberian Center of Synchrotron Radiation of the Siberian Division of the Russian Academy of Sciences. The absorption spectra of europium L_3-edge of borate–germanate glasses, which had the same $La_3Gd_{10}Eu(BO_3)_6(GeO_4)_2O_8$ composition but were prepared on different substrates, were recorded in the fluorescence mode up to the gadolinium L_2-absorption edge (7243 eV). The oscillating regions of the glass spectra (they are identical) are shown in Fig. 1.

The spectra could not be analyzed by standard techniques for two reasons. On the one hand, the small extension of the spectra limits the information on the coordination environment about an Eu atom from its L_3-absorption edge (6977 eV), because its energy is close to the L_2-absorption edge of gadolinium (7243 eV). This does not allow one to record the fine structure of the spectrum in the conventional energy range. On the other hand, compounds of this class are characterized by rather complicated structures in which the Ln–O distances (with the participation of rare-earth atoms including Eu) have different values depending on the coordination of the Ln atom.

Therefore, we compared the experimental spectra with the calculated model spectra without parameter fitting. The models were constructed based on the data [3] on the isostructural compound $Gd_{14}(BO_3)_6(GeO_4)_2O_8$ of similar composition. This compound contains a set of GdO_N polyhedra (where N ranges from 6 to 10). For the compound under study, the polyhedra for each N were constructed with the use of the Eu–O distances determined for the compound $Gd_{14}(BO_3)_6(GeO_4)_2O_8$ by X-ray diffraction analysis. For each polyhedron thus constructed, the theoretical oscillating portion of the absorption spectrum $\chi(k)$ was calculated, and the Fourier transform of the function $k^2\chi(k)$ was taken in the range of the wavenumbers k from 2.0 to 7.6 Å^{-1} using the program FEFF-7. As a result, the curves of Fourier-transform amplitudes were constructed. These curves correspond to the atomic radial-distribution functions (RDFs) about the Eu atom and have similar shapes for all the polyhedra. Due to the very short spectral range and the fact that the environment of a europium atom is characterized by different distances, the spectra have only one broad maximum. The only exception from the general rule is a europium atom with c.n. 8. The atomic RDF constructed for the model EuO_8 polyhedron has

Positions of the maxima R (Å) (without correction for the phase shift σ [5]) and their amplitudes (rel. units) for the moduli of Fourier transforms for the model EuO_N coordination polyhedra and the experimental EXAFS spectra

Coordination number (N) of Eu	6	7	8*	9	10	Experiment 1	Experiment 2
Amplitude	1.85	2.01	1.06	1.51	1.62	0.91	0.94
			0.40			~0.48	0.64
R	1.85	1.84	1.57	1.83	1.81	1.66	1.64
			2.39			~2.4	~2.4

Note: Experiments 1 and 2 were made with the use of glasses prepared on graphite and platinum substrates, respectively.
* Separation into the “nearest” and “next-nearest” coordination spheres (see Fig. 2).

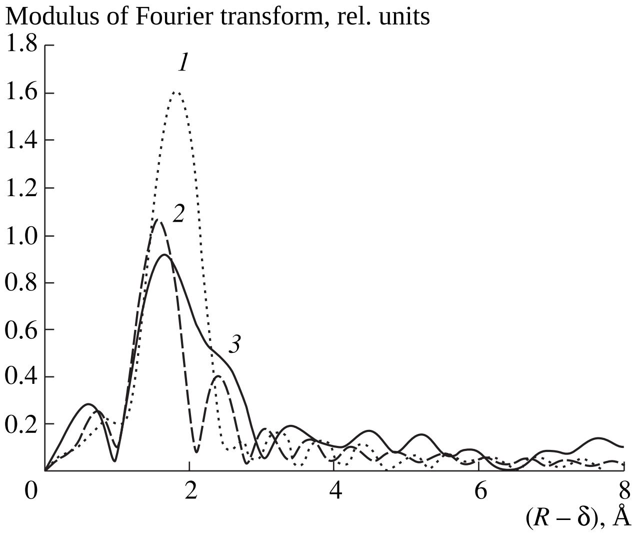

Fig. 2. Modulus of the Fourier transform of the radial-distribution function for the model (*1*) EuO_{10} and (*2*) EuO_8 coordination polyhedra and (*3*) the experimental spectra.

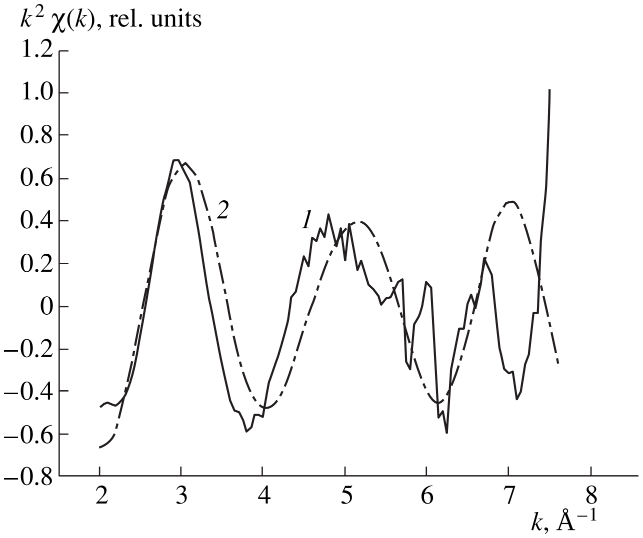

Fig. 3. Comparison of (*1*) the oscillating fine structure of the X-ray spectrum of the glass $La_3Gd_{10}Eu(BO_3)_6(GeO_4)_2O_8$ with (*2*) the oscillating fine structure calculated for the model EuO_8 coordination polyhedron.

two maxima, because, according to the structure data, the Eu–O interatomic distances can be divided into two different groups (2.248, 2.37, 2.375, 2.380, 2.397, and 2.430 Å in one group and 2.57 and 2.878 Å in the other).

Figure 2 shows the RDFs for an EuO_{10} polyhedron, with a shape that is characteristic of all EuO_N polyhedra (where N ranges from 6 to 10, except for 8); RDFs for EuO_8; and the functions calculated from the experimental EXAFS spectra of the samples studied. It can be seen that the RDF of a europium atom with c.n. = 8 is best fitted to the experimental data.

The coordinates of the maxima R on the RDFs (without a correction for the phase shift) and the amplitudes of these maxima for the Fourier-transform moduli of the model EuO_N coordination polyhedra are given in the table together with the corresponding data obtained from the experimental absorption spectra of europium in the glass $La_3Gd_{10}Eu(BO_3)_6(GeO_4)_2O_8$.

As can be seen from Fig. 3, the model (for an EuO_8 polyhedron) oscillating portion of the Eu L_3-edge absorption spectrum agrees well with the experimental data. Slight discrepancies are associated with the difference in the zero points of the energy scales E_0 used for the experimental and theoretical spectra and the high level of noise in the experimental data.

RESULTS AND DISCUSSION

In spite of the high level of noise and the small extent of the spectrum, one can reliably state that a europium atom in the glass based on an $La_3Gd_{10}Eu(BO_3)_6(GeO_4)_2O_8$ solid solution (molecular formula $La_3Gd_{10}EuGe_2B_6O_{34}$) is surrounded by eight oxygen atoms. This is consistent with the results of X-ray diffraction analysis for the isotypic $Nd_{4.3}Sm_{4.8}Eu_{4.9}Ge_2B_6O_{34}$ (**I**) and $Nd_{3.33}Sm_{3.71}Eu_{3.33} \times Gd_{3.63}Ge_2B_6O_{34}$ (**II**) [7, 8] solid solutions in which an Eu atom has a c.n. of 7 or 8. In the columns of the table that list the experimental data, R = 1.66 and 2.4 Å and R = 1.64 and 2.4 Å (experiments 1 and 2, respectively) correspond to the positions of the maxima R on the RDFs. Taking into consideration the correction for the phase shift (σ), which can reach 0.8 Å in this experiment, the Eu–O interatomic distances within the first coordination sphere around Eu in the glass under study are 2.46 and 2.44 Å; $(Eu–O)_{av}$ = 2.45 Å.

Taking into account all the Eu–O distances in crystalline compounds **I** and **II**, the average bond distances $(Eu–O)_{av}$ are equal to 2.39 Å. Hence, the coordination of europium and the $(Eu–O)_{av}$ bond lengths in the glasses are consistent with analogous data for the crystals of solid solutions (involving europium) with the structure $Ln_{14}(BO_3)_6(GeO_4)_2O_8$. Consequently, the structure of glasses of this type can be studied by considering the structures of solid solutions of the same composition.

To summarize, the nearest environment of europium in the glass prepared based on the $La_3Gd_{10}Eu(GeO_4)_2(BO_3)_6O_8$ solid solution is independent of the procedure of glass preparation (platinum or graphite substrates).

ACKNOWLEDGMENTS

We are grateful to Yu.L. Slovokhotov, G.A. Bandurkin, I.P. Stolyarov, and M.N. Vargaftik for helpful discussions and valuable advice.

This study was supported by the Russian Foundation for Basic Research, project no. 00-03-32587.

REFERENCES

1. G. V. Lysanova, V. A. Krut'ko, M. G. Komova, *et al.*, Neorg. Mater. **38** (11), 1 (2002).
2. A. B. Ilyukhin and B. F. Dzhurinskiĭ, Zh. Neorg. Khim. **39** (4), 556 (1994).
3. B. F. Dzhurinskiĭ and A. B. Ilyukhin, Zh. Neorg. Khim. **45** (1), 5 (2000).
4. A. B. Pobedina, M. G. Komova, and B. F. Dzhurinskiĭ, Zh. Neorg. Khim. **45** (7), 1134 (2000).
5. D. I. Kochubeĭ, Yu. A. Babanov, K. I. Zamaraev, *et al.*, *X-ray Spectral Method for Studying Structures of Amorphous Bodies* (Nauka, Novosibirsk, 1988).
6. I. V. Malakhov, S. G. Nikitenko, E. R. Savinova, *et al.*, J. Phys. Chem. B **106**, 1670 (2002).
7. K. K. Palkina, N. E. Kuz'mina, B. F. Dzhurinskiĭ, and A. B. Pobedina, Zh. Neorg. Khim. **44** (11), 1914 (1999).
8. K. K. Palkina, N. E. Kuz'mina, and A. B. Pobedina, Zh. Neorg. Khim. **45** (11), 1781 (2000).

Translated by T. Safonova

Crystallography Reports, Vol. 48, No. 3, 2003, pp. 359–362. Translated from Kristallografiya, Vol. 48, No. 3, 2003, pp. 403–406.
Original Russian Text Copyright © 2003 by Geguzina, Shuvayev, Shuvayeva, Gakh.

CRYSTAL CHEMISTRY

Substitution of Atoms in the Lattice of $A_{m-1}Bi_2B_mO_{3m+3}$ Phases and a Search for New Ferroelectrics[1]

G. A. Geguzina, A. T. Shuvayev, E. T. Shuvayeva, and S. G. Gakh
Institute of Physics, Rostov State University, pr. Stachki 194, Rostov-on-Don, 344090 Russia
e-mail: denis@ip.rsu.ru

Received November 18, 2002

Abstract—New complex oxides with phase transitions of a ferroelectric nature are found and synthesized by atomic replacement in the composition of known $A_{m-1}Bi_2B_mO_{3m+3}$-type phases with due regard for the systematization of their compositions and the conditions of existence of layered perovskite-like structures. © *2003 MAIK "Nauka/Interperiodica".*

Over more than five decades, about 60 Bi-containing layered perovskite-like oxides have been described [1–10]. These compounds are analogues of the Aurivillius phases traditionally described by the general formula

$$A_{m-1}Bi_2B_mO_{3m+3}, \quad (1)$$

where m = 1, 1.5, 2, 2.5, 3, 3.5, 4, 5, 6, 7, 8, and 10. Their chemical compositions do not exhaust all the possible atomic combinations in the A and B positions that can be imagined based on their systematics [11].

The unit cell of a Bi-containing perovskite-like oxide consists of alternating stacks of perovskite-like $[A_{m-1}B_mO_{3m+1}]^{2-}$ and bismuth–oxygen $[Bi_2O_2]^{2+}$ layers located between these stacks. The parallel layers are normal to the c axis. Almost all the members of a small family of Bi-containing layered perovskite-like oxides of the new composition are ferroelectrics with rather high phase-transition temperatures [5–10]. Preparation of each new Bi-containing layered perovskite-like oxide is a rather rare because it violates several principles of formation of these layered structures [4–6, 8, 9], on the one hand, and because it presents certain technological difficulties, on the other. All these facts determine the interest in the family of Bi-containing layered perovskite-like oxides and stimulate the search for new compounds. The search for new representatives of the family of Bi-containing layered perovskite-like oxides was the main aim of the present study. We also tried to refine the conditions of existence of these oxides.

Formula (1) can be written in a more general form demonstrating all the atoms occupying A^i and B^i positions in the lattice of complex Bi-containing layered perovskite-like oxide:

$$Bi_2(A^1_{\alpha_1}\ldots A^i_{\alpha_i}\ldots A^p_{\alpha_p})(B^1_{\beta_1}\ldots B^j_{\beta_j}\ldots B^q_{\beta_q})O_{3m+3}, \quad (2)$$

where $\sum_{i=1}^{p}\alpha_i = m-1$ and $\sum_{j=1}^{q}\beta_j = m$ and α_i and β_i are the fractions of A^i and B^j atoms, respectively. The search for new compounds was made based on the systematics of Bi-containing layered perovskite-like oxides [11] and the known conditions of their existence [8] using a partial or complete substitution of atoms in the A and B positions in some basic structures by a certain number of other atoms of appropriate valence.

We selected as the basic structures the simple Bi-containing layered perovskite-like oxides with high Curie temperatures [5, 8], namely: Bi_2WO_6 with $m = 1$ (T_C = 1233 K), $Bi_5Nb_3O_{15}$ with $m = 1.5$ (T_C = 720 K) [14], Bi_3TiNbO_9 with $m = 2$ (T_C = 1233 K), $Bi_7Ti_4Nb_{3.5}O_{21}$ with $m = 2.5$ (T_C = 1073 K), $Bi_4Ti_3O_{12}$ with $m = 3$ (T_C = 948 K), $Na_{0.5}Bi_{8.5}Ti_3O_{27}$ with $m = 3.5$ (T_C = 893 K), $Bi_5FeTi_3O_{15}$ with $m = 4$ (T_C = 1023 K), and $Bi_6Ti_3Fe_2O_{18}$ with $m = 5$ (T_C is unknown). For each group of the structures selected for synthesis of hypothetical Bi-containing layered perovskite-like oxides with different m values, the schemes of atomic substitutions in the corresponding basic structures were constructed. The schemes of substitutions of A and B atoms in the basic structures with m = 1.5, 2, and 3 are shown in Figs. 1 and 2.

On the left, the sets of atoms that can substitute only Bi^{III} in the A positions are shown; on the right, Nb^V, Ti^{IV}–Nb^V, or Ti^{IV} in the B positions. The two columns in the middle of the scheme indicate combined substitutions in both A (left column) and B (right column) positions. The replacing atoms are written by large bold letters if they are single phase materials; smaller bold letters indicate substitutions in known Bi-containing layered perovskite-like oxides. The substituting atoms are indicated in quotation marks if we failed to prepare the compound of corresponding composition. Inside groups, the compositions are indicated in the order of a decrease in the content of Bi^{III} in positions A and an increase of the number of another replacing atom. The

---

[1] This study was submitted to the Symposium "Phase Transitions in Solid Solutions and Alloys" (OMA), Sochi, 2002.

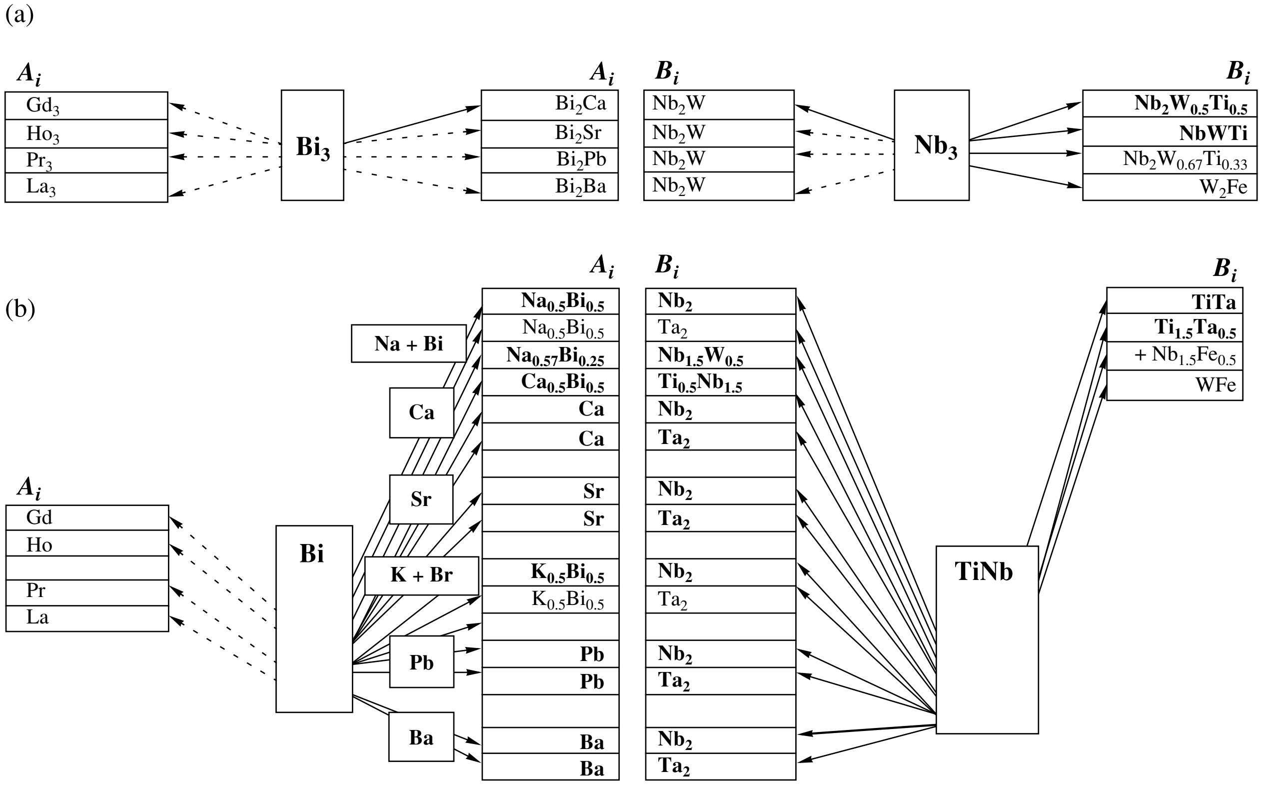

Fig. 1. Schemes of substitutions of (a) Bi (in *A* positions) and Nb (in *B* positions) atoms in $Bi_5Nb_3O_{15}$ with $m = 1.5$ and (b) Bi (in *A* positions) and TiNb (in *B* positions) atoms in Bi_3TiNbO_9 with $m = 2$. Compounds written in bold were prepared by the authors. The atoms substituting Bi^{III} atoms are framed in the A^i column.

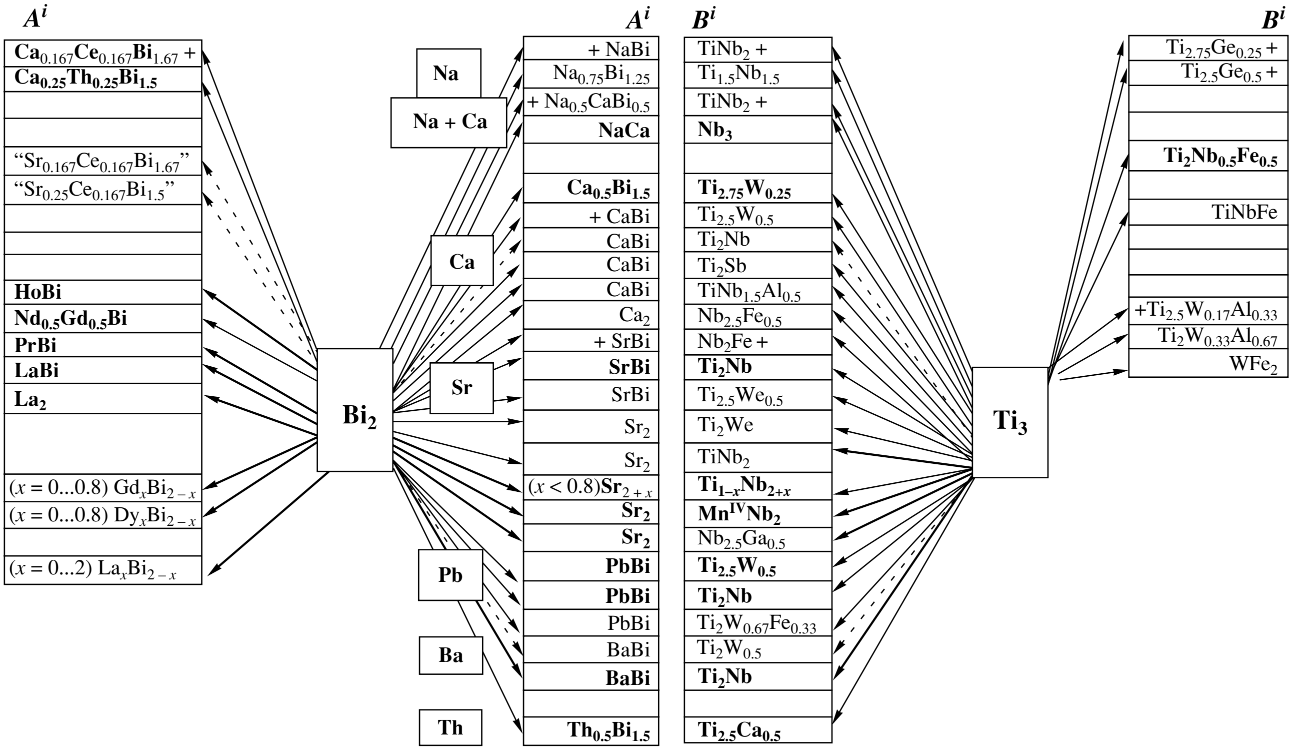

Fig. 2. Scheme of substitution of Bi (in *A* positions) and Ti (in *B* positions) atoms in $Bi_4Ti_3O_{12}$ with $m = 3$. For notation see Fig. 1.

Chemical compositions and calculated (a_{calcd} and c_{calcd}) and measured (a_t and c_t) parameters of the tetragonal (or pseudotetragonal $\bar{a}_{pt}$ for the orthorhombic phases) unit cells (Å) and the Curie temperatures T_{calcd} (K) for newly synthesized Bi-containing layered perovskite-like oxides

Chemical composition	Calculated unit-cell parameters		Measured unit-cell parameters, the difference between measured and calculated parameters				
	a_{calcd}	c_{calcd}	a_t ($\bar{a}_{pt}$)	δ_a	c_t	δ_{calcd}	T_{calcd}
m = 1.5							
$\mathbf{Bi}_5\mathbf{Nb}_3O_{15}$	3.884	20.97	3.850*	0.88	20.90*	0.35	720 [12]
$\mathbf{Bi}_5Nb_2Ti_{0.5}W_{0.5}O_{15}$	3.854	20.81	3.853	0.26	21.02	1.0	670 [12]
$\mathbf{Bi}_5NbTiWO_{15}$	3.825	20.66	3.832	0.18	20.97	1.3	720 [12]
m = 2							
$\mathbf{Bi}_3Ti_{1.5}W_{0.5}O_9$	3.817	24.73	3.810	0.19	24.95	0.89	~800
$Na_{0.75}Bi_{2.25}Nb_{1.5}W_{0.5}O_9$	3.852	24.96	3.872	0.52	24.78	0.73	
$Ca_{0.5}Bi_{2.5}Ti_{0.5}Nb_{1.5}O_9$	3.874	25.10	3.843	0.81	24.98	0.49	
m = 3							
$\mathbf{Bi}_4Ti_2Nb_{0.5}Fe_{0.5}O_{12}$	3.856	33.32	3.854	0.05	33.08	0.73	
$NaCaBi_2Nb_3O_{12}$	3.892	33.63	3.868	0.62	32.76	2.4	~800
$Ca_{0.25}Th_{0.25}Bi_{3.5}\mathbf{Ti}_3O_{12}$	3.829	33.09	3.826	0.08	32.82	0.82	
$Ca_{0.5}Bi_{3.5}Ti_{2.75}W_{0.25}O_{12}$	3.832	33.11	3.830	0.05	32.85	0.79	
$SrBi_3Ti_2NbO_{12}$	3.878	33.49	3.850*	0.73	33.21*	0.84	441 [14]
$PbBi_3Ti_{2.5}W_{0.5}O_{12}$	3.853	33.29	3.839	0.36	33.42	0.39	523 [15]
$PbBi_3Ti_2NbO_{12}$	3.890	33.61	3.865*	0.65	33.52*	0.27	570 [14]
$Nd_{0.5}Gd_{0.5}Bi_3\mathbf{Ti}_3O_{12}$	3.836	33.15	3.816	0.52	32.81	1.0	
$Th_{0.5}Bi_{3.5}Ti_{2.5}Ga_{0.5}O_{12}$	3.822	33.02	3.826	0.10	32.96	0.18	

Note: The stable atoms of basic oxides are indicated by semibold letters.
* Parameters of ceramics obtained by hot pressing.

same is also true for atoms in positions *B*. If the structure of the corresponding composition is formed, but the X-ray pattern shows some impurity peaks, the substitution is marked with a plus sign. The substitutions indicated by dashed arrows are as yet only planned.

Powdered Bi-containing layered perovskite-like oxides were synthesized in two or three stages by high-temperature solid phase reactions in a conventional muffle furnace at relatively low temperatures (from 1070 to 1370 K) [12–16]. Different sintering modes were tried to establish the optimum modes. The sintering of some new ceramic Bi-containing layered perovskite-like oxides was done by the hot pressing method on a hot pressing setup similar to that described in [17]. The crystal structure and single phase composition of prepared the Bi-containing layered perovskite-like oxides was checked by X-ray phase analysis. We also determined the parameters of the orthorhombic and tetragonal unit cells of the Bi-containing layered perovskite-like oxides obtained.

The phase transitions were revealed in six new Bi-containing layered perovskite-like oxides, their Curie temperatures were determined (see table), and the dielectric properties were studied. For $SrBi_3Ti_2NbO_{12}$ and $PbBi_3Ti_2NbO_{12}$, hysteresis loops characteristic of ferroelectrics are obtained [14]. Bi-containing layered perovskite-like oxides synthesized in [16] require better technology to prepare high-quality ceramics that would enable us to determine the T_C values and measure their electrophysical properties. The preliminary measurements of dielectric properties show that $NaCaBi_2Nb_3O_{12}$ and $Bi_3Ti_{1.5}W_{0.5}O_9$ (see table) undergo phase transitions in the vicinity of 800 K. The piezoelectric modulus of $Bi_3Ti_{1.5}W_{0.5}O_9$ was determined as $d_{33} \sim 9$ pC/N at room temperature.

The $\bar{a}_{pt}$ and c_{pt} parameters of the pseudotetragonal unit cells of orthorhombic Bi-containing layered perovskite-like oxides ($\bar{a}_{pt} = (a_{rhomb} + + b_{rhomb})/2\sqrt{2}$; $c_{pt} = c_{rhomb}$) and the tetragonal unit cells of Bi-containing layered perovskite-like oxide (see table) differ by not more that 1% from the parameters calculated based on their hypothetical compositions by the method proposed in [8], which indicates that the oxides obtained correspond to the set compositions. Note that none of the chosen substitutions of atoms in the *A* or *B* positions of the basic Bi-containing layered perovskite-like oxides with *m* = 4 and 5 and also *m* = 2.5, 3.5, and 4.5 were synthesized.

The atomic substitutions in the basic oxides with different *m* allowed one to synthesize 15 new single phase polycrystalline Bi-containing layered perovskite-like orthorhombic and tetragonal oxides with *m* = 1.5, 2, and 3. As a result, the relatively small family of Bi-containing layered perovskite-like oxides has been increased by almost 25%. Six new Bi-containing layered perovskite-like oxides undergo phase transitions of a ferroelectric nature.

ACKNOWLEDGMENTS

This study was supported by the Ministry of Education of the Russian Federation, project no. E00-3.4-560.

REFERENCES

1. B. Aurivillius, Ark. Kemi **1**, 449 (1950).
2. B. Aurivillius, Ark. Kemi **1**, 463 (1950).
3. B. Aurivillius, Ark. Kemi **2**, 510 (1951).
4. E. C. Subbarao, J. Phys. Chem. Solids **23**, 665 (1962).
5. *Physics of Ferroelectric Phenomena*, Ed. by G. A. Smolenskiĭ (Nauka, Leningrad, 1985).
6. T. Kikuchi, Mater. Res. Bull. **14**, 1561 (1979).
7. V. A. Isupov, Neorg. Mater. **33**, 1106 (1997).
8. G. A. Geguzina, E. G. Fesenko, and E. T. Shuvaeva, Ferroelectrics **167**, 311 (1995).
9. V. A. Isupov, Ferroelectrics **189**, 211 (1996).
10. L. A. Reznichenko, O. N. Razumovskaya, L. A. Shilkina, and N. V. Dergunova, Neorg. Mater. **32**, 474 (1996).
11. G. A. Geguzina, Kristallografiya **47** (6), 983 (2002) [Crystallogr. Rep. **47**, 913 (2002)].
12. E. G. Fesenko, V. G. Smotrakov, G. A. Geguzina, *et al.*, Neorg. Mater. **30**, 1446 (1994).
13. E. G. Fesenko, A. T. Shuvaev, V. G. Smotrakov, *et al.*, Neorg. Mater. **30**, 1057 (1994).
14. I. A. Trifonov, G. A. Geguzina, E. S. Gagarina, *et al.*, Neorg. Mater. **36**, 237 (2000).
15. I. A. Trifonov, G. A. Geguzina, A. T. Shuvaev, *et al.*, Neorg. Mater. **36**, 1358 (2000).
16. G. A. Geguzina, A. T. Shuvaev, E. T. Shuvaeva, *et al.*, in *Proceedings of International Symposium on Phase Transitions in Solid Solutions and Alloys (OMA)*, Sochi (2002), p. 56.
17. E. G. Fesenko, *Perovskite Family and Ferroelectricity* (Atomizdat, Moscow, 1972).

Translated by T. Dmitrieva

Crystallography Reports, Vol. 48, No. 3, 2003, pp. 363–369. Translated from Kristallografiya, Vol. 48, No. 3, 2003, pp. 407–413.
Original Russian Text Copyright © 2003 by Pecherskaya, Mikhaĭlov, Demina, Bogdanova, Belozerova.

CRYSTAL CHEMISTRY

Symmetry and Ordering of Compounds with a Beryl-Type Structure in the Mg-Enriched Part of the Beryllium Indialite–Cordierite–Beryl System[1]

S. G. Pecherskaya, M. A. Mikhaĭlov, T. V. Demina, L. A. Bogdanova, and O. Yu. Belozerova

Vinogradov Institute of Geochemistry, Siberian Division, Russian Academy of Sciences,
ul. Favorskogo 1a, Irkutsk, 664033 Russia
e-mail: svelta@igc.irk.ru

Received December 3, 2002

Abstract—The boundaries of the regions of solid solutions with beryl-type structures and different symmetry and degree of order obtained by solid-phase synthesis have been refined in the beryllium indialite–cordierite–beryl system. The change in the compositions of real crystals in the course of synthesis and the character of the dependence of the melting point on the composition are taken into account. *© 2003 MAIK “Nauka/Interperiodica”.*

INTRODUCTION

At present, there are only a small number of minerals and synthetic compounds with the beryl-type structure described by the general formula $O_2T'_3T''_6X_{18}$ [1] (Fig. 1). These are beryl ($Al_2Be_3Si_6O_{18}$) itself [2], bazzite ($Sc_2Be_3Si_6O_{18}$) [2], cordierite and indialite ($Mg_2Al_4Si_5O_{18}$) [2], stoppaniite ($Fe_2Be_3Si_6O_{18}$) [3], sekaninaite ($Fe_2Al_4Si_5O_{18}$) [2], Mn-cordierite ($Mn_2Al_4Si_5O_{18}$) [2], and beryllium indialite ($Mg_2BeAl_2Si_6O_{18}$) [4–6]. Among these compounds, only cordierite and sekaninaite are orthorhombic (*Cccm*), whereas the remaining minerals of this structure type (including beryllium indialite) are hexagonal (*P*6/*mcc*). In addition, solid solutions of the $Mg_2Al_4Si_5O_{18}$–$Mg_3Al_2Si_6O_{18}$ series have also been synthesized (implementation of the $Mg^{2+} + Si^{4+} = 2Al^{3+}$ isomorphism scheme) [7]. Solid solutions of the $Mg_2Al_4Si_5O_{18}$–$Mg_2BeAl_2Si_6O_{18}$ series were prepared based on beryllium indialite (according to the scheme Be + Si = 2Al) [4, 5] with the participation of the minal beryl (with the participation of schemes isomorphous replacements Be + Si = 2Al, $Al \longrightarrow Si$, and $Al_{IV} + Mg_{VI} \longrightarrow Be_{IV} + Al_{VI}$) [6]. It should be noted that some researchers consider the solid solutions of the $Mg_2Al_4Si_5O_{18}$–$Mg_3Al_2Si_6O_{18}$ series as metastable phases [8, 9], whereas $Mg_3Al_2Si_6O_{18}$ (so-called Mg-beryl [7]) has not been synthesized as yet.

beryllium indialites grown hydrothermally [5] or from melts [10] crystallize into hexagonal system (sp. gr. *P*6/*mcc*). However, variations in the compositions of the starting mixtures and the use of different methods of their synthesis (from flux, from melts, or by solid-phase reactions) made it possible not only to reveal a wide field of existence of solid solutions [6] but also to single out three regions of their existence [11], namely, region I of hexagonal beryllium indialites, region II of orthorhombic beryllium indialites, and region III of orthorhombic beryllium cordierites. These regions were separated based on the values of the parameter Δ, which reflects the degree of orthorhombicity of the structure and the values of the angle 2*V*, a crystallooptical characteristic related to crystal symmetry. Here, the parameter Δ coincides, in fact, with Δ_w proposed in [12] for the determination of the degree of orthorhombicity of cordierites (based on the distortion index Δ [13] and $W_{1/3}$ [14]). In cordierites, the index Δ (according to

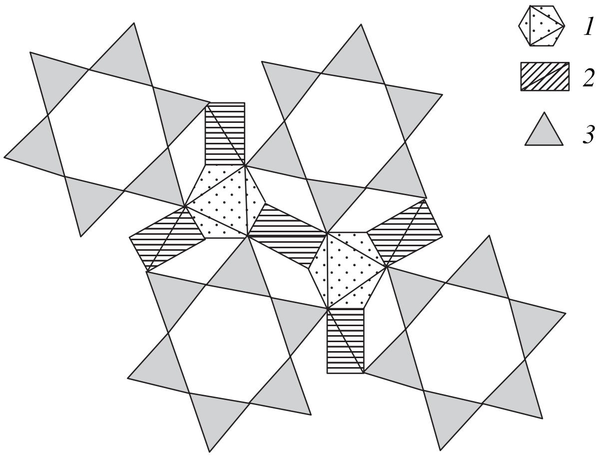

Fig. 1. Polyhedron linkage in the beryl structure type projected onto the (0001) plane; (*1*) an octahedron (O); (*2*) a tetrahedron not involved in the ring (*T*'); (*3*) a tetrahedron of the ring (*T*'').

---

[1] This work was presented at the symposium “Phase Transformations in Solid Solutions” (OMA), Sochi, 2002.

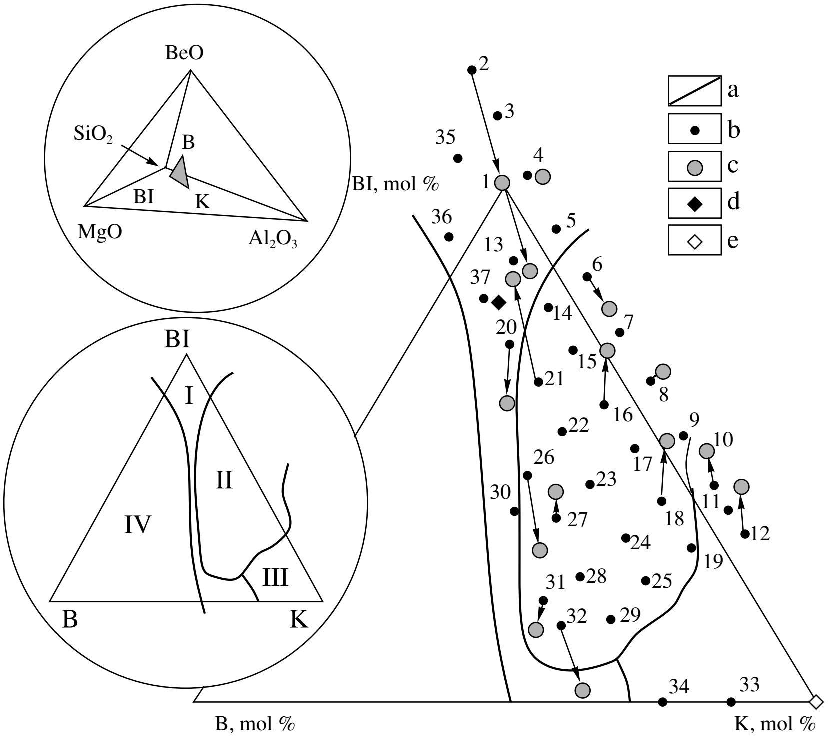

Fig. 2. (a) Boundaries between the regions of formation of (I) disordered hexagonal beryllium indialites, (II) poorly ordered (presumably, orthorhombic) beryllium indialites, and (III) ordered orthorhombic beryllium cordierites obtained by solid-phase synthesis; (IV) unstudied compositions; (b) the composition of the starting charge; (c) the final composition of the solid solution; (d) and (e) reference samples of hexagonal beryllium indialite and indialite (grown from flux [19]); BI is beryllium indialite, K is cordierite, and B is beryl; 1–37 are the ordinal numbers of the samples.

[2, 13, 15]) also characterizes the degree of order of Si and Al atoms and some of the Mg and Fe atoms in the mineral structure. The orthorhombic varieties of cordierite are ordered ($0.00° < \Delta < 0.30°$ or higher), whereas the hexagonal varieties of cordierite, are disordered ($\Delta = 0.00°$) [12–14] and are known as indialites. It was demonstrated [16] that hexagonal ($2V = 0°$) and orthorhombic ($0° < 2V < 20°$) varieties of beryllium indialites have disordered ($\Delta = 0.00°$) and poorly ordered ($0.00° < \Delta \leq 0.14°$) structures, respectively, whereas beryllium cordierites ($20° < 2V < 60°$) are characterized by an ordered state ($0.14° < \Delta \leq 0.26°$).

However, the boundaries of the above three regions in the field of the solid solutions in the beryllium indialite–cordierite–beryl system proposed in [11] should be considered as preliminary because the authors studied compositions that substantially differed from each other, there was no response on the melting-point curve on going from region II to region III, and because the samples studied were obtained by different methods.

The aim of the present study was to refine the boundaries between the regions of the solid solutions based on beryllium indialite and cordierite synthesized by the same method (solid-phase reactions of the components).

EXPERIMENTAL

The main approach used in this study was to estimate the boundaries in the field of solid solutions in terms of the indices Δ and the real compositions of crystals formed under the same conditions. As an additional characteristic, a plot of the melting temperature vs. composition was used.

When calculating the component ratios in the charge, we assumed that the direction and degree of the shift of the compositions of real crystals in the course of the synthesis relative to the starting compositions would be analogous to those found for a stoichiometric mixture of beryllium indialite under the same conditions [17]. This assumption required the use of compositions lying outside the beryllium indialite–cordierite–beryl triangle in the four-component BeO–MgO–Al_2O_3–SiO_2 system. For convenience, the compositions of the starting mixtures are given as formulas reduced to 18 oxygen atoms (table). These formulas not only allow one to compare the compositions of the starting charges and final products but also to indicate the ratios between Be, Mg, Al, and Si at any point inside and outside the beryllium indialite–cordierite–beryl triangle (Fig. 2).

Chemical compositions of the starting mixtures and characteristics of the solid solutions formed (real compositions and distortion indices)

Sample	Composition, mol %		Δ, deg
	starting charge*	final crystals	
1	$Mg_{2.04}Be_{1.00}Al_{2.00}Si_{6.00}O_{18}$	$Mg_{2.04}Cr_{0.20}Be_{0.99}Al_{2.03}Si_{5.81}O_{18}$	0.00
2	$Mg_{2.19}Be_{1.00}Al_{1.73}Si_{6.11}O_{18}$	$Mg_{2.0}Cr_{0.06}Be_{0.97}Al_{1.96}Si_{6.0}O_{18}$	0.00
3	$Mg_{2.19}Be_{0.90}Al_{1.90}Si_{6.01}O_{18}$	–	0.00
4	$Mg_{2.19}Be_{0.80}Al_{2.08}Si_{5.90}O_{18}$	$Mg_{2.04}Cr_{0.03}Be_{0.78}Al_{2.20}Si_{5.92}O_{18}$	0.04
5	$Mg_{2.19}Be_{0.70}Al_{2.25}Si_{5.80}O_{18}$	–	0.01
6	$Mg_{2.19}Be_{0.60}Al_{2.42}Si_{5.70}O_{18}$	$Mg_{1.98}Cr_{0.05}Be_{0.59}Al_{2.64}Si_{5.70}O_{18}$	0.05
7	$Mg_{2.19}Be_{0.50}Al_{2.60}Si_{5.60}O_{18}$	–	0.04
8	$Mg_{2.19}Be_{0.40}Al_{2.77}Si_{5.50}O_{18}$	$Mg_{2.06}Cr_{0.03}Be_{0.40}Al_{2.95}Si_{5.54}O_{18}$	0.03
9	$Mg_{2.19}Be_{0.30}Al_{2.94}Si_{5.40}O_{18}$	–	0.07
10	$Mg_{2.19}Be_{0.25}Al_{3.03}Si_{5.35}O_{18}$	$Mg_{2.12}Cr_{0.01}Be_{0.25}Al_{3.24}Si_{5.38}O_{18}$	0.14
11	$Mg_{2.19}Be_{0.20}Al_{3.11}Si_{5.29}O_{18}$	–	0.24
12	$Mg_{2.19}Be_{0.15}Al_{3.20}Si_{5.24}O_{18}$	$Mg_{2.10}Be_{0.15}Al_{3.43}Si_{5.30}O_{18}$	0.24
13	$Mg_{1.97}Be_{1.00}Al_{2.08}Si_{5.90}O_{18}$	–	0.05
14	$Mg_{1.97}Be_{0.90}Al_{2.25}Si_{5.80}O_{18}$	–	0.04
15	$Mg_{1.97}Be_{0.80}Al_{2.42}Si_{5.70}O_{18}$	–	0.03
16	$Mg_{1.97}Be_{0.70}Al_{2.60}Si_{5.60}O_{18}$	$Mg_{1.90}Cr_{0.07}Be_{0.69}Al_{2.63}Si_{5.68}O_{18}$	0.04
17	$Mg_{1.97}Be_{0.60}Al_{2.77}Si_{5.50}O_{18}$	–	0.03
18	$Mg_{1.97}Be_{0.50}Al_{2.94}Si_{5.40}O_{18}$	$Mg_{1.93}Cr_{0.03}Be_{0.49}Al_{3.03}Si_{5.50}O_{18}$	0.05
19	$Mg_{1.97}Be_{0.40}Al_{3.11}Si_{5.29}O_{18}$	–	0.01
20	$Mg_{1.75}Be_{1.20}Al_{2.08}Si_{5.90}O_{18}$	$Mg_{1.89}Cr_{0.08}Be_{1.18}Al_{2.15}Si_{5.80}O_{18}$	0.01
21	$Mg_{1.75}Be_{1.10}Al_{2.25}Si_{5.80}O_{18}$	$Mg_{1.81}Cr_{0.05}Be_{1.08}Al_{2.11}Si_{5.93}O_{18}$	0.06
22	$Mg_{1.75}Be_{1.00}Al_{2.42}Si_{5.70}O_{18}$	–	0.08
23	$Mg_{1.75}Be_{0.90}Al_{2.60}Si_{5.60}O_{18}$	–	0.06
24	$Mg_{1.75}Be_{0.80}Al_{2.77}Si_{5.50}O_{18}$	–	0.09
25	$Mg_{1.75}Be_{0.70}Al_{2.94}Si_{5.40}O_{18}$	–	0.04
26	$Mg_{1.53}Be_{1.30}Al_{2.25}Si_{5.80}O_{18}$	$Mg_{1.94}Cr_{0.01}Be_{1.28}Al_{2.23}Si_{5.71}O_{18}$	0.03
27	$Mg_{1.53}Be_{1.20}Al_{2.42}Si_{5.70}O_{18}$	$Mg_{1.88}Cr_{0.05}Be_{1.19}Al_{2.29}Si_{5.71}O_{18}$	0.06
28	$Mg_{1.53}Be_{1.10}Al_{2.60}Si_{5.60}O_{18}$	–	0.06
29	$Mg_{1.53}Be_{1.00}Al_{2.77}Si_{5.50}O_{18}$	–	0.00
30	$Mg_{1.46}Be_{1.33}Al_{2.31}Si_{5.77}O_{18}$	–	0.05
31	$Mg_{1.31}Be_{1.40}Al_{2.42}Si_{5.70}O_{18}$	$Mg_{1.76}Cr_{0.06}Be_{1.39}Al_{2.35}Si_{5.62}O_{18}$	0.02
32	$Mg_{1.31}Be_{1.30}Al_{2.60}Si_{5.60}O_{18}$	$Mg_{1.56}Cr_{0.10}Be_{1.29}Al_{2.63}Si_{5.53}O_{18}$	0.00
33	$Mg_{1.80}Be_{0.30}Al_{3.80}Si_{5.10}O_{18}$	–	
34	$Mg_{1.50}Be_{0.75}Al_{3.50}Si_{5.25}O_{18}$	–	0.33
35	$Mg_{1.97}Be_{1.20}Al_{1.73}Si_{6.11}O_{18}$	–	0.00
36	$Mg_{1.75}Be_{1.40}Al_{1.73}Si_{6.11}O_{18}$	–	0.00
37	$Mg_{1.75}Be_{1.90}Al_{1.90}Si_{6.01}O_{18}$	–	0.00

* Without added Cr_2O_3 (mol %).

Dry X-ray amorphous BeO (high-purity grade), MgO (analytical grade), Al_2O_3 (high-purity grade), SiO_2 (special-purity grade), and Cr_2O_3 (analytical grade) were used to prepare 37 mixtures; Cr_2O_3 (3 wt %) was added as a chromophore. The reagent mixtures were ground in an agate mortar in the presence of ethanol and then dried in air, which ensured a decrease in the amount of adsorption water in the samples (<0.01%) [18].

The charge was sintered in alundum crucibles. The temperature and time of the solid-phase synthesis were determined taking into account the known data [17]. Thus, the synthesis involved one-day storage of the charge at 300°C (to remove remaining adsorption water), heating to the calculated temperature of solid-phase synthesis at a rate of ~570°C/h, and three successive steps of isothermal steadiness at 1290 (for 5 days), 1310 (for 5 days), and 1340°C (for 15 days) with the aim of monitoring the degree of completeness of the solid-phase reactions by crystallooptical and powder X-ray diffraction analysis of the samples with different and intermediate compositions. For all compositions, the total time of the synthesis was 25 days, which, according to [17], considerably exceeded the time necessary for the attainment of equilibrium. In our case, the criterion for the attainment of equilibrium (the commonly accepted statement that the phase ratio remains constant against the background of 100% crystallized material) was supplemented by the condition that the maximum content of the compound with a beryl structure be attained.

The samples were studied by the methods of X-ray diffraction, crystal optics, X-ray microanalysis, and high-temperature microscopy on DRON-3, MIN-8, Superprobe-733, and MNO-2 instruments, respectively.

It should be emphasized that the starting mixtures were sintered in the course of the synthesis (so that they flaked away from the crucible walls). The samples for the analysis were selected from the regions that do not contact the crucible walls and bottom and, therefore, are not enriched with the crucible material.

X-ray diffraction patterns were measured with the use of Cu radiation (Ni filter without a monochromator). X-ray diffraction patterns in the scan range $8° < 2\theta < 60°$ were measured at a scan rate of 1 deg/min; the intensity scale was 400 pulses/min. These X-ray patterns were used to determine the phase compositions and characteristic features of the solid solutions prepared from starting materials of different compositions.

The phase compositions of the materials were also estimated by the method of crystal optics, including study of their morphological and optical characteristics. The symmetry of the compounds was determined by studying cross sections perpendicular to the *c* axis. These sections are isotropic for hexagonal crystals and anisotropic for crystals of lower symmetries. In addition, the diagnostics included the study of the characteristic feature of cordierite—its propensity to sectorial trilling [2].

To determine the Δ values, the reflections from the samples were collected in the 2θ scan region from 29° to 31° with a scan rate of 0.1 deg/min and an intensity scale of 400 pulses/min. The Δ value was determined as the difference between the peak width of the sample $W_{1/3}^{\text{sample}}$ and the calculated reference value $W_{1/3}^{\text{ref}}$ (according to the equation $\Delta = W_{1/3}^{\text{sample}} - W_{1/3}^{\text{ref}}$ [12]). The $W_{1/3}^{\text{ref}}$ parameter was determined using a calibration curve constructed from $W_{1/3}$ values corresponding to preliminarily synthesized indialite [19] ($W_{1/3} = 0.37°$) and hexagonal beryllium indialite ($W_{1/3} = 0.30°$).

The homogeneity of the region of the samples studied by X-ray microanalysis was attained as follows. The changes in the chemical composition of samples were estimated from the scan profile, and regions were selected where the concentrations of the main components (Mg, Al, and Si) remained unchanged. The chemical compositions of the samples were determined in the homogeneous region located at a distance of at least 20 μm from its boundary. The errors in the determination of the amounts of the main components (wt %, in different samples) were as follows: ±0.05–0.08, ±0.11–0.27, and ±0.18–0.22 for Mg, Al, and Si, respectively. The crystallochemical formulas of the samples were calculated (according to the standard procedure) for 18 oxygen atoms [1, 6] based on the concentrations of BeO in the starting mixtures.

The temperature at which the sample completely transformed into a drop that did not spread during isothermal heating (this temperature was calculated as the average of three samples) was taken to be the melting point of the sample. The accuracy of its determination was 5°C.

RESULTS AND DISCUSSION

We synthesized 37 solid solutions in the magnesium-enriched region in the beryllium indialite–cordierite–beryl system and outside it (Fig. 2). In total crystallization, the final products differed in their degrees of sintering. Thus, the samples closest to cordierite (e.g., samples 33 and 34) were loose materials, whereas all the other samples were synthesized as rather dense ingots. In all samples, a high percentage of the phase with a beryl structure (up to 95%) was detected by the method of crystal optics. The crystal dimension of this phase reached 2 mm. The main simple crystal forms of the indivuduals with a beryl structure were a hexagonal prism and a pinacoid. The fact that the cross sections perpendicular to the *c* axis were isotropic and the presence of a hexagonal prism in the crystal faceting of the solid solutions formed indicate a hexagonal system, pronounced anisotropy, and the existence of trillings (Fig. 3), i.e., the formation of orthorhombic individuals

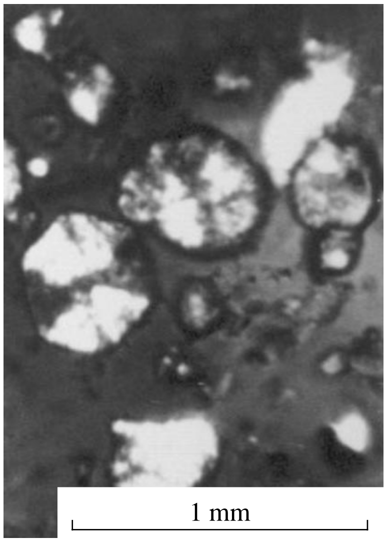

Fig. 3. Trilling of beryllium cordierite exhibiting a characteristic sectorial extinction (sample 34).

(beryllium cordierite). Most of the samples were characterized by weak anisotropy in the sections studied and were related to phases with a beryl structure of lower symmetry (presumably, the orthorhombic system). It should be noted that the interference colors gradually changed from dark gray to white with the shift of the starting composition from beryllium indialite to cordierite. Thus, at the stage of crystallooptical study the samples containing hexagonal individuals (presumably, beryllium indialites), orthorhombic beryllium cordierites, and intermediate varieties were found, and the boundaries between the regions of their formation were estimated.

According to the peak profiles in the 2θ region from 29° to 31° (Fig. 4) and the distortion indices Δ, all the samples were divided into three groups. As can be seen from Fig. 4, a single peak indexed as the (211) reflection in [5] is characteristic of all beryllium indialites, both disordered (Fig. 4b) and poorly ordered (Fig. 4c). The X-ray diffraction patterns from beryllium cordierites (Fig. 4d) show a slightly split peak consisting of reflections with unidentified indices. It should be noted that the (511), (421), and (131) reflections typical of orthorhombic cordierite were clearly seen, e.g., in Ti-cordierite grown from flux (Fig. 4f). beryllium indialites differed from each other in the width of their (211) peaks and were divided, according to the above-described classification, into disordered and poorly ordered samples. The boundaries of three crystallization fields of solid solutions characterized by different degrees of order and prepared by solid-phase reactions in the system under consideration were refined based on the indices Δ for all the samples and the final compositions of some of these samples (see Fig. 2). The solid solutions, which could, tentatively, contain (in minals) beryllium indialite (0–100%), cordierite (0–70%), and beryl (0–40%) were assigned to region I, which encloses disordered (hexagonal) beryllium indialites (Δ = 0). Poorly ordered (presumably, orthorhombic) crystals of beryllium indialites ($0.00 < \Delta < 0.14$) including beryllium indialites (10–80%), cordierite (20–70%), and beryl (0–40%) were assigned to region II. Ordered (orthorhombic) beryllium cordierites ($\Delta > 0.14$) containing beryllium indialite (0–30%), cordierite (70–100%), and beryl (0–30%) were assigned to region III. It should be noted that the field of poorly ordered beryllium indialites seemed to be much wider than was reported earlier [16]. The sample most similar to beryl in region II corresponds to the following composition (in minals): 16% of beryllium indialite, 47% of cordierite, and 37% of beryl (sample 31).

The component ratios in the crystals grown differed from those in the starting mixtures (Fig. 2, the directions from the starting compositions to the real crystals are indicated by arrows). These shifts of the composi-

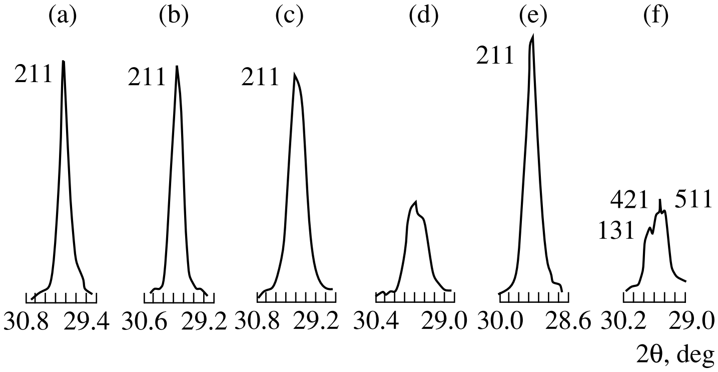

Fig. 4. Characteristic peaks of solid solutions of a beryl-type structure in the region 2θ = 29°–31°; (a) and (e) peaks from the reference samples of hexagonal beryllium indialite and indialite, respectively (grown from flux [19]); (b) peak from hexagonal beryllium indialite (sample 2); (c) peak from poorly ordered (presumably, orthorhombic) beryllium indialite (sample 23); (d) peak from ordered orthorhombic beryllium cordierite (sample 12); (f) peak from orthorhombic cordierite (grown from flux [19]).

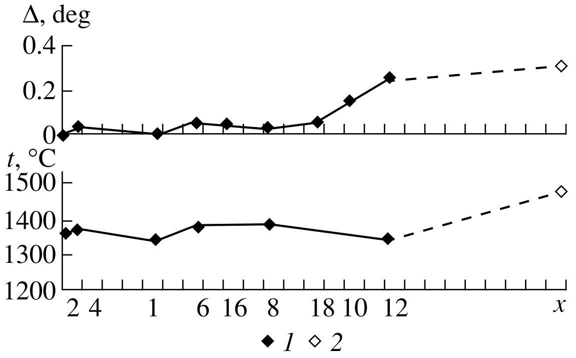

Fig. 5. Distortion index (Δ) and melting point (*t*) vs. real composition of the solid solution; *x* is the ordinal number of the sample; (*1*) our experimental data; (*2*) data for cordierite from [16].

tions of the solid solutions in the course of their synthesis occurred due to crystallization of the associated phases with tridymite and cristobalite structures. At least two such directions were found, which are associated either with depletion in the beryllium indialite minal (in a way similar to its stoichiometric mixture [17]) or enrichment in this minal. It should be noted that samples 21 and 32 synthesized from the starting compositions corresponding to region II contained disordered hexagonal solid solutions related to region I because of the shifts of the composition in different directions. Consideration of the total set of the samples demonstrated that the final compositions of most of these samples did not go outside the beryllium indialite–cordierite–beryl system, whereas a few samples did go outside it. It should be noted that the shift of the composition of only one of the solid solutions (sample 2) initially located outside the beryllium indialite–cordierite–beryl triangle fully corresponded to its calculated value. In this case, we managed to synthesize for the first time beryllium indialite with a composition close to the ideal formula, $Mg_{2.00}Cr_{0.06}Be_{0.97}Al_{1.96}Si_{6.00}O_{18}$. In the course of synthesis, all the other mixtures were transformed into solid solutions whose real compositions could not be described by the sum of the beryllium indialite, cordierite, and beryl minals (samples 4, 6, 8, 10, and 12). Hence, knowledge of the real compositions of the solid solutions allowed us to substantially refine the boundaries between regions I, II, and III (Fig. 2).

The boundaries between these regions determined from the indices Δ and the real compositions were also confirmed by the character of the changes in the melting points of the samples (Fig. 5). It can be seen that the inflection points in the plot of the melting point vs. solid-solution composition correspond to these boundaries and correlate with the dependence of the distortion index.

In conclusion, we note some characteristic features of the results obtained. First, the mutual location of the three regions attracts one's attention (Fig. 2). In the case of beryllium indialites enriched with aluminum (i.e., in the narrow region in the vicinity of the cordierite–beryl line), the transformation from region I to region III (from point 32 to point 34) takes place without the formation of "buffer" region II corresponding to gradual ordering of beryllium indialite. By contrast, the transformations of all the other compositions studied to orthorhombic cordierites requires the formation of region II. Second, the existence of a wide field of beryllium indialites and beryllium cordierites indicates that not only aluminum and silicon but also beryllium are involved in the ordering process in the structure of the solid solutions studied. Third, the changes revealed in the symmetry of the solid solutions observed with the shift of their compositions to beryl clarify the fine mechanism of separation of "sample-forming" components among structurally similar compounds (beryllium indialite, cordierite, and beryl) [20]. This mechanism leads to the formation of both hexagonal matrices (of beryl and disordered beryllium indialite) at low Mg/Be ratios and individuals with lower symmetry (beryllium cordierite and ordered beryllium indialite) at high Mg/Be ratios.

CONCLUSIONS

We managed to refine the boundaries between the three crystallization fields formed in the course of solid-phase synthesis in the beryllium indialite–cordierite–beryl system and in the vicinity of this system. These fields include disordered (hexagonal) beryllian indialites, poorly ordered (with lower symmetry) beryllium indialites, and ordered (orthorhombic) beryllium cordierites, respectively. The boundaries determined between these regions are confirmed by the character of the changes in the melting point depending on the composition of the solid solution.

It is established that, depending on the starting ratio of the components, the compositions of the solid solutions are shifted at least along two directions in the course of solid-phase synthesis.

The existence of a wide field of existence of beryllium indialites and beryllium cordierites indicates that not only aluminum and silicon but also beryllium participate in the structural ordering of these solid solutions.

REFERENCES

1. V. V. Bakakin, G. M. Rylov, and N. V. Belov, Geokhimiya, No. 11, 1302 (1970).
2. *Minerals: Handbook*, Ed. by F. V. Chukhrov (Nauka, Moscow, 1981), Vol. 3, No. 2.
3. G. Ferraris, M. Prencipe, and P. Rossi, Eur. J. Mineral. **10**, 491 (1998).
4. N. Kh. Valeev, Candidate's Dissertation in Chemistry (Sverdlovsk, 1977).
5. A. Holscher and W. Schreyer, Eur. J. Mineral. **1**, 21 (1989).

6. M. A. Mikhaĭlov and T. V. Demina, Zap. Vses. Mineral. O–va, No. 3, 22 (1998).
7. *Phase Diagrams of Silicate Systems*, 2nd ed., Ed. by V. P. Barzakovskiĭ (Nauka, Leningrad, 1972), No. 3.
8. W. Schreyer and J. F. Schairer, J. Petrol. **2** (3), 324 (1961).
9. N. A. Toropov and V. P. Barzakovskiĭ, *High-Temperature Chemistry of Silicate and Other Oxide Systems* (Akad. Nauk SSSR, Moscow, 1963).
10. Yu. I. Smolin, Yu. F. Shepelev, M. A. Mikhaĭlov, *et al.*, Kristallografiya **44** (3), 454 (1999) [Crystallogr. Rep. **44**, 414 (1999)].
11. T. V. Demina, M. A. Mikhaĭlov, L. A. Bogdanova, and O. Yu. Belozerova, in *Abstracts of XIV Russian Workshop on Experimental Mineralogy* (Chernogolovka, 2001), p. 92.
12. G. G. Afonina, V. V. Bezdelkin, A. A. Bobr-Sergeev, and L. A. Bogdanova, *1973 Yearbook* (Nauka, Novosibirsk, 1974), p. 315.
13. A. Miyashiro, Am. J. Sci. **255**, 43 (1957).
14. K. Langer and W. Schreyer, Am. Mineral. **54**, 1442 (1969).
15. J. H. Stout, Am. Mineral. **60** (3–4), 229 (1975).
16. M. A. Mikhaĭlov and T. V. Demina, in *Proceedings of International Simposium on Phase Transformations in Solid Solutions and Alloys*, *Sochi* (2002), Part 2, p. 22.
17. T. V. Demina and M. A. Mikhaĭlov, Mineral. Zh., No. 1, 61 (1993).
18. M. A. Mikhaĭlov, D. S. Glyuk, and T. V. Demina, *Geochemical Search Methods. Methods of Analysis* (Inst. Geokhim. Analit. Khim. Akad. Nauk SSSR, Irkutsk, 1979), p. 163.
19. T. V. Demina and M. A. Mikhaĭlov, in *Proceedings of XII All-Union Meeting on Experimental Mineralogy: Experiment in Mineralogy* (Chernogolovka, 1993), Vol. 2, p. 154.
20. T. V. Demina and M. A. Mikhaĭlov, Zap. Vses. Mineral. O–va, No. 2, 97 (2000).

Translated by T. Safonova

Crystallography Reports, Vol. 48, No. 3, 2003, pp. 370–373. Translated from Kristallografiya, Vol. 48, No. 3, 2003, pp. 414–417.
Original Russian Text Copyright © 2003 by Bikkulova, Danilkin, Fuess, Yadrovskiĭ, Beskrovnyĭ, Skomorokhov, Yagafarova, Asylguzhina.

DIFFRACTION AND SCATTERING OF IONIZING RADIATIONS

Crystal Structure of Non-Stoichiometric Copper Selenides Studied by Neutron Scattering and X-ray Diffraction

N. N. Bikkulova*, S. A. Danilkin, H. Fuess***, E. L. Yadrovskiĭ****, A. I. Beskrovnyĭ*****, A. N. Skomorokhov***, Z. A. Yagafarova*, and G. N. Asylguzhina***

** Sterlitamak State Pedagogical Institute, Sterlitamak, pr. Lenina 49, 453103 Bashkortostan, Russia*
e-mail: bickulova@mail.rb.ru
*** Hahn-Meitner-Institut, SF2, Glienicker Str. 100, Berlin, D-14109 Germany*
**** Technische Universität Darmstadt, Petersenstr. 23, Darmstadt, D-64287 Germany*
***** State Research Center Physicoenergetical Institute, Obninsk*
****** Frank Laboratory of Neutron Physics, Joint Institute for Nuclear Research,*
ul. Joliot-Curie, Dubna, Moscow oblast, 141980 Russia

Received January 10, 2002; in final form, September 30, 2002

Abstract—Structural characteristics of non-stoichiometric copper selenides were studied by the elastic neutron and X-ray scattering techniques. Rietveld analysis was used to refine the structure of the high-temperature β-phase of the $Cu_{1.75}Se$, $Cu_{1.78}Se$, and $Cu_{1.83}Se$ samples. The homogeneity ranges of the cubic phase were determined. The modification of the crystal structure accompanying the β–α phase transition was studied for $Cu_{1.75}Se$ and $Cu_{1.98}Se$ compounds within the 443–10 K temperature range. It was shown that the phase transition is accompanied by distortions of the fcc lattice and the ordering of copper ions. © *2003 MAIK "Nauka/Interperiodica".*

INTRODUCTION

Copper selenide is a superionic conductor with mixed electronic–ionic conductivity. Dynamic disordering in the cation sublattice is usually considered as the main mechanism underlying the formation of the superionic phase [1]. At the same time, there is no reliable data on the structure and character of disordering in copper selenides. This hinders our understanding of the processes accompanying the formation of the superionic state and the ionic transport phenomena and, in the final analysis, impedes the development of novel materials with advanced electrical and physical characteristics.

It is well known that superionic transition in copper selenide is accompanied by changes in its crystal structure [2]. It is also established that there are two copper selenide modifications: the low-temperature α phase and the high-temperature β phase. At temperatures exceeding 379–413 K, the latter phase has ionic conductivity, whose fraction does not exceed 10% of the total conductivity.

The crystal structure of the non-superionic low-temperature α phase of copper selenide is not clearly understood. Some publications state that the low-temperature phase is cubic or pseudocubic; some others, that it is tetragonal, rhombohedral, or even monoclinic [3–8]. The present study was undertaken to refine the phase diagram and the structure of copper selenide $Cu_{2-x}Se$ by X-ray and neutron diffraction methods on polycrystalline samples with different deviations from the stoichiometry ($0 < x < 0.25$).

EXPERIMENTAL

The samples with different deviations from the stoichiometry were synthesized by the direct sintering of the components in Pyrex ampoules with subsequent homogenization for a week at 723 K. The starting materials were selenium of ultrahigh purity (grade 17-4) and copper of 99.99% purity. The sample composition was

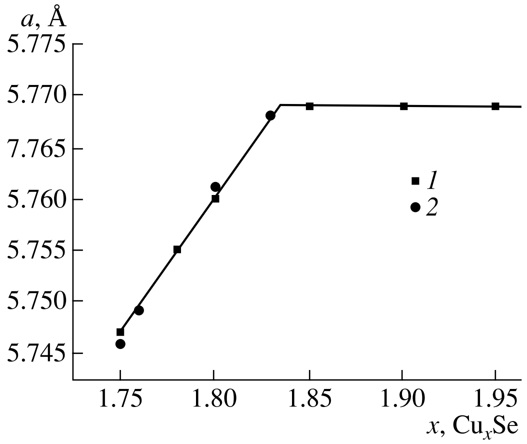

Fig. 1. Lattice parameter *a* of Cu_xSe ($1.75 < x < 2$) versus composition at 300 K; (*1*) experimental data, (*2*) data from [10].

1063-7745/03/4803-0370$24.00 © 2003 MAIK "Nauka/Interperiodica"

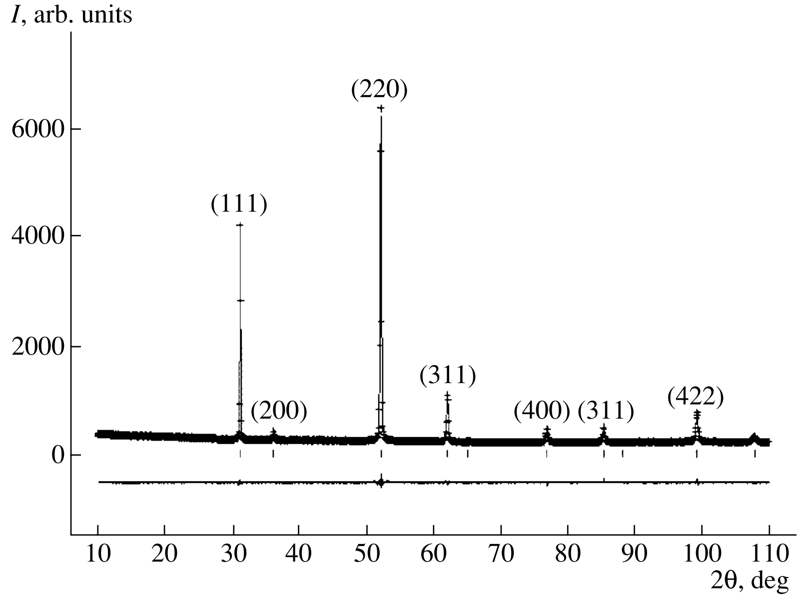

Fig. 2. Observed and calculated X-ray diffraction patterns and the difference curve for $Cu_{1.78}Se$ (λ = 1.7889 Å).

specified by the weights of the components during synthesis and then was controlled by coulometric titration for the compositions $Cu_{1.85}Se$, $Cu_{1.90}Se$, $Cu_{1.95}Se$, and Cu_2Se by measuring the unit-cell parameters (for cubic phases $Cu_{1.75}Se$ and $Cu_{1.8}Se$), as well as by chemical methods.

X-ray diffraction studies of polycrystalline samples were performed on a STOE diffractometer at room temperature ($CoK_{\alpha 1}$ radiation) at the Technical University of Darmstadt, Germany. The neutron diffraction studies were performed on a DN-2 diffractometer at the Joint Institute for Nuclear Research, Dubna, Russia.

RESULTS AND DISCUSSION

Analysis of the X-ray diffraction patterns demonstrated that the $Cu_{1.75}Se$ and $Cu_{1.78}Se$ samples are cubic and have the lattice constants a = 5.74(7) and 5.75(5) Å, respectively, whereas the $Cu_{1.85}Se$, $Cu_{1.90}Se$, and $Cu_{1.95}Se$ samples are a mixture of the high-temperature β phase with the lattice constant a = 5.76(9) Å (corre-

Atomic positions and factors of atomic thermal vibrations for $Cu_{1.75}Se$, $Cu_{1.78}Se$, and $Cu_{1.83}Se$ samples

Type	$Cu_{1.75}Se$ (a = 5.74(7) Å) Cubic system, *Fm*3*m*			Occupancy	Thermal parameter (U_{ISO})	Position multiplicity	*Rp*, %
	x	*y*	*z*				
Se	0	0	0	1	0.0439	4	7.41
Cu	0.2182	0.2182	0.2182	0.19895	0.0114	32	
Cu	0.4095	0.4095	0.4095	0.0198	0.00877	32	
	$Cu_{1.78}Se$ (a = 5.75(5) Å) Cubic system, *Fm*3*m*						
Se	0	0	0	1	0.03602	4	6.22
Cu	0.21551	0.21551	0.21551	0.19321	0.00581	32	
Cu	0.37142	0.37142	0.37142	0.03179	0.07278	32	
	$Cu_{1.83}Se$ (a = 5.76(9) Å) Cubic system, *Fm*3*m*						
Se	0	0	0	1	0.025	4	5.73
Cu	0.22404	0.22404	0.224045	0.20145	0.01408	32	
Cu	0.37346	0.37346	0.37346	0.0273	0.0612	32	

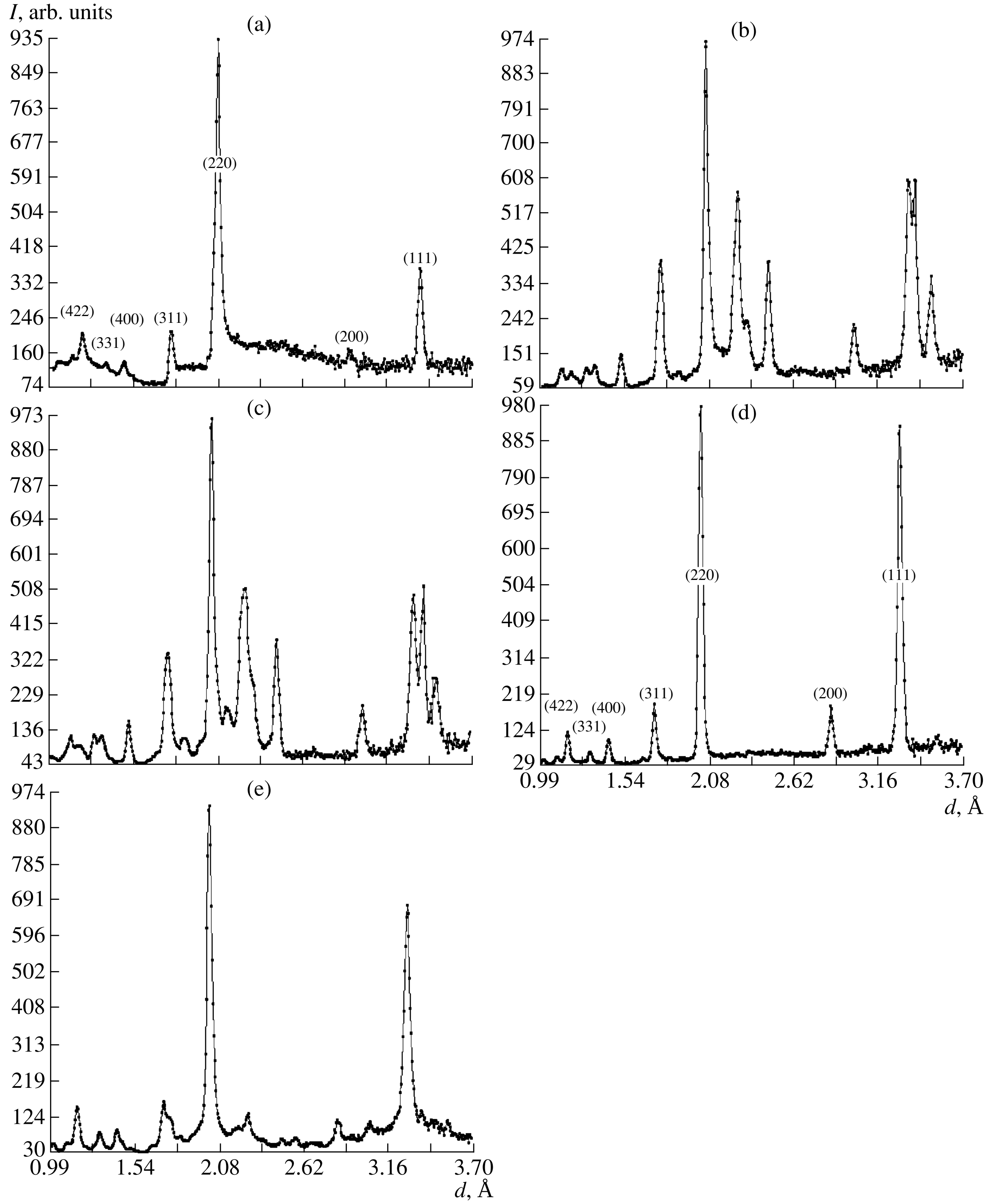

Fig. 3. Splitting of the (111) and (220) peaks for Cu_2Se at (a) 443, (b) 300, and (c) 10 K and for $Cu_{1.75}Se$ at (d) 300 and (e) 10 K.

sponding to composition $Cu_{1.83}Se$) and the low-temperature α phase.

The boundary of existence for the cubic phase at room temperature was determined from the dependence of the lattice constant *a* on the chemical composition of the samples (Fig. 1). It is seen from Fig. 1 that this boundary corresponds to the composition $x = 1.83$, which is consistent with the phase diagram of the Cu_{2-x}–Se system reported in [9].

The lattice constants obtained also agree with the data in [10], where the lattice constant of a $Cu_{1.81}Se$ single crystal was determined as $a = 5.76(3)$ Å.

The refinement of the cubic structures of the $Cu_{1.75}Se$, $Cu_{1.78}Se$, and $Cu_{1.83}Se$ polycrystalline samples was performed by full-profile analysis using the GSAS program package [11]. Figure 2 shows the observed and calculated X-ray diffraction patterns together with the difference curve for the composition $Cu_{1.78}Se$. The results of calculations for the $Cu_{1.75}Se$, $Cu_{1.78}Se$, and $Cu_{1.83}Se$ samples are presented in the table, from which it is clear that lattice cations are not redistributed over the lattice positions with a change in the chemical composition. The cations in $Cu_{1.75}Se$, $Cu_{1.78}Se$, and $Cu_{1.83}Se$ are shifted from the tetrahedral positions toward selenium anions, with some cations being located in octahedral pores with the coordinates x ranging within 0.370–0.410.

The data on the structure of the low-temperature phase are rather contradictory. Therefore, we also studied the structure of $Cu_{1.75}Se$ and $Cu_{1.98}Se$ samples by X-ray diffraction at 300 K and by elastic neutron scattering in the temperature range 10–300 K. The latter measurements were performed on a DN-2 neutron diffractometer.

Indexing the diffraction patterns of the non-superionic low-temperature phase $Cu_{1.98}Se$ at room temperature showed best results for the triclinic system with the following unit-cell parameters: $a = 7.10(1)$ Å, $b = 12.34(6)$ Å, $c = 7.13(2)$ Å, $\alpha = 90.26°$, $\beta = 107.94°$, and $\gamma = 89.56°$. According to data in [3] drawn from an analysis of several publications, the non-superionic low-temperature phase ($0 \le x \le 0.04$) at room temperature can be indexed as monoclinic. Comparing the interplanar distances in [3] with our data shows that our diffraction patterns had a higher resolution.

The analysis of the X-ray and neutron diffraction data shows that the transition from the superionic to the low-temperature non-superionic state is accompanied by the distortion of the selenium sublattice and ordering of the copper ions. The lattice distortion of the cubic structure is seen from splitting of the lines on the diffraction patterns of the $Cu_{1.75}Se$ and $Cu_{1.98}Se$ low-temperature phases (Fig. 3). Comparison of the X-ray and neutron diffraction patterns of $Cu_{1.75}Se$ and $Cu_{1.98}Se$ samples and, in particular, of the (111) and (220) lines, leads to the conclusion that, with the approach to stoichiometry, the transition to the non-superionic α phase is accompanied by line splitting, and the closer the composition to stoichiometric, the more pronounced the line splitting.

CONCLUSION

At room temperature, the $Cu_{1.75}Se$ and $Cu_{1.78}Se$ samples are cubic with the lattice constants $a = 5.74(7)$ and 5.75(5) Å, respectively, whereas the $Cu_{1.86}Se$, $Cu_{1.91}Se$, and $Cu_{1.95}Se$ samples are mixtures of the cubic β phase (corresponding to the composition $Cu_{1.83}Se$ with lattice constant $a = 5.76(9)$ Å) and the α phase. In the $Cu_{1.75}Se$, $Cu_{1.78}Se$, and $Cu_{1.83}Se$ samples, cations are not redistributed over lattice positions with a change of composition. Copper ions in these samples are shifted from the tetrahedral positions toward selenium anions, with some of them being located in the octahedral pores with the x coordinate ranging within 0.370–0.410.

The analysis of the X-ray and neutron diffraction data obtained shows that the phase transition from the superionic to the low-temperature non-superionic state is accompanied by the distortion of the fcc lattice and ordering of copper ions.

ACKNOWLEDGMENTS

This study was supported by the Russian Foundation for Basic Research, project no. 01-02-96017, and by the Ministry of Industry, Science, and Technologies of the Russian Federation (grant for the support of unique facilities of Russia).

REFERENCES

1. *Physics of Superionic Conductors*, Ed. by M. B. Salamon (Zinatne, Riga, 1982).
2. P. Ralfs, Z. Phys. Chem. (Leipzig) **31** (1), 157 (1936).
3. Z. Vucic, V. Horvatic, O. Milat, and Z. Ogorelec, Phys. Rev. B **24**, 5398 (1981).
4. A. L. N. Stevels and F. Jellinek, Recl. Trav. Chim. Pays-Bas. **90**, 273 (1971).
5. R. M. Murray and R. D. Heyding, Can. J. Chem. **53**, 878 (1975).
6. J. B. Boyce, T. M. Hayes, and J. C. Mikkelsen, Solid State Ionics **5**, 497 (1981).
7. M. Olveria, R. K. McMullan, and B. J. Wuensch, Solid State Ionics **28–30**, 1332 (1988).
8. T. Sakuma and K. Shibata, J. Phys. Soc. Jpn. **58**, 3061 (1989).
9. V. V. Gorbachev, *Semiconductor Compounds* (Metallurgiya, Moscow, 1980), p. 8.
10. T. Ohtani, Y. Okada, Y. Yokota, *et al.*, J. Alloys Compd. **279**, 136 (1998).
11. A. C. Larson and R. B. von Dreele, GSAS, LANSCE, MS-H805 Los Alamos National Laboratory, NM 87545.

Translated by K. Kugel

Crystallography Reports, Vol. 48, No. 3, 2003, pp. 374–376. Translated from Kristallografiya, Vol. 48, No. 3, 2003, pp. 418–420.
Original Russian Text Copyright © 2003 by Glazkov, Savenko, Somenkov, Sheptyakov, Shilshtein.

DIFFRACTION AND SCATTERING OF IONIZING RADIATIONS

High-Pressure Neutron Diffraction Study of the $Nd_{1.85}Ce_{0.15}CuO_4$ Structure

V. P. Glazkov*, B. N. Savenko, V. A. Somenkov*, D. V. Sheptyakov**, and S. Sh. Shilshtein*****

** Russian Research Centre Kurchatov Institute, pl. Kurchatova 1, Moscow, 123182 Russia*
e-mail: glazkov@isssph.kiae.ru
*** Joint Institute for Nuclear Research, p/ya 79, Dubna, Moscow oblast, 123182 Russia*
**** Weizmann Institute of Science, Rehovot, 76100 Israel*

Received November 6, 2001; in final form, June 20, 2002

Abstract—The changes in the positional parameter of neodymium in $Nd_{1.85}Ce_{0.15}CuO_4$ under high pressures differ from those observed in Nd_2CuO_4; in fact, practically no changes in the positional parameter in the doped oxide are observed. The different behavior of the positional parameter in these materials is explained by the compensation of the interlayer charge transfer by the interlayer repulsion occurring during doping or under the action of high pressures. *© 2003 MAIK “Nauka/Interperiodica”.*

Structural studies of hole oxide-based superconductors and related systems (mercury, yttrium–barium, etc.) under high pressures showed the existence of a weak link—the interlayer (or interatomic) distances are more sensitive to the changes in the unit-cell volume than any other distances in the lattice and the unit cell as a whole [1–4]. Although these changes are rather small, they are of a regular nature and are analogous to the changes observed in doping with ions of different valence or with oxygen. Therefore, these changes may be considered as related to the changes in the electron subsystem, i.e., the changes occurring with the transfer of the charge to the copper–oxygen planes or with variation in the ion valence in the “reservoir of ions of variable valence” [5–7]. In this respect, electron-type oxide superconductors have been studied in less detail. When doping Nd_2CuO_4 with cerium, one also observes, along with the change in the cation charges, regular changes in the interlayer spacings [8]. Analogous changes were also revealed in pure (undoped) Nd_2CuO_4 under high pressures [9, 10]. The aim of our study was to establish the structural changes occurring during compression of doped $Nd_{1.85}Ce_{0.15}CuO_4$ crystals, i.e., to establish whether the changes in the positional parameter provided by the variations in the composition and unit-cell volume are summed up or not.

Polycrystal line $Nd_{1.85}Ce_{0.15}CuO_4$ samples were obtained by grinding the crystals grown by the method of spontaneous crystallization from melt in an excess of CuO in air [11–14]. The structure was studied by the time-of-flight technique on a DN-12 diffractometer [15] on an IBR-2 reactor (JINR, Dubna). Quasi-hydrostatic pressures up to ~6 GPa were created in a cell using sapphire anvils [16], with the sample volume being ~2.5 mm^3. In this case, we used combined gaskets: the inner ring was prepared from the alloy vanadium–niobium (the zero matrix) and the outer ring was prepared from softer nickel. The pressure was determined from the shift of the ruby fluorescence line with an accuracy of about 0.1 GPa. The structure parameters were determined by the Rietveld method using the isotropic thermal parameters for all the atoms and the MRIA program complex [17]. The experimental and calculated intensities are shown in Figs. 1a and 1b. The profile R factors were determined as R_w 4.9 and 5.7 and R_e ~ 5.1 and 5.1% under normal pressure and a pressure of 5.8 GPa, respectively.

Under the action of high pressures, the diffraction peaks on the neutron diffraction patterns were displaced from their initial positions (Fig. 1). The values of these displacements provided the determination of the periods of the tetragonal $Nd_{1.85}Ce_{0.15}CuO_4$ lattice as functions of pressure (Fig. 2a). As in pure neodymium cuprate [8, 9], the compressibility along the c axis was about 1.5 times higher than the compressibility along the a axis, which resulted in a noticeable change in the axial c/a ratio with pressure (Fig. 2b). The change in the unit-cell volume under pressures of up to ~5 GPa was about 3%, which agreed quite well with the X-ray and neutron diffraction data for Nd_2CuO_4 [8, 9]. Thus, the volume compressibilities of the pure and doped oxides are rather close.

The intensity ratios of the diffraction peaks of $Nd_{1.85}Ce_{0.15}CuO_4$ can vary depending on the value of the positional parameter of the Nd(Ce) ions, because all the other ions in this lattice occupy special positions. The z_{Nd} value determines the interlayer distances. The value z ~ 0.15 corresponds to the displacement of the neodymium layer from its position in the middle

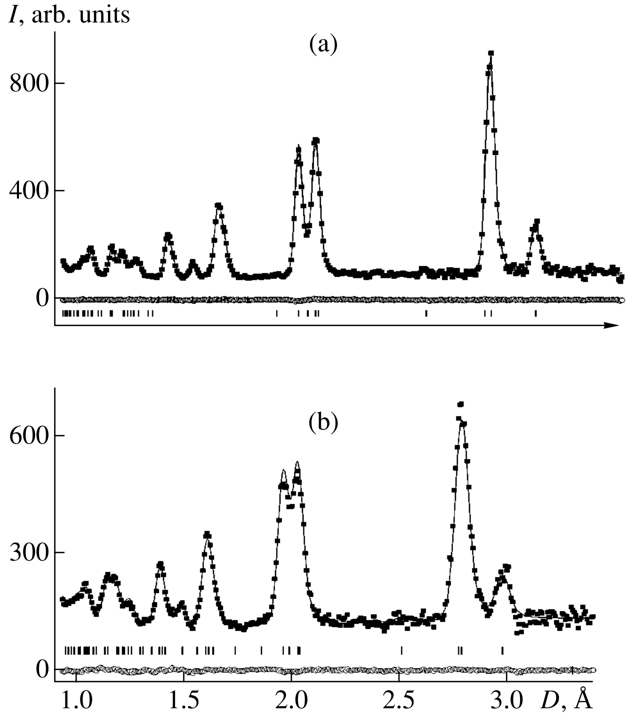

Fig. 1. Neutron diffraction patterns of $Nd_{1.85}Ce_{0.15}CuO_4$ under normal conditions (a), under a pressure of (b) 5.8 GPa.

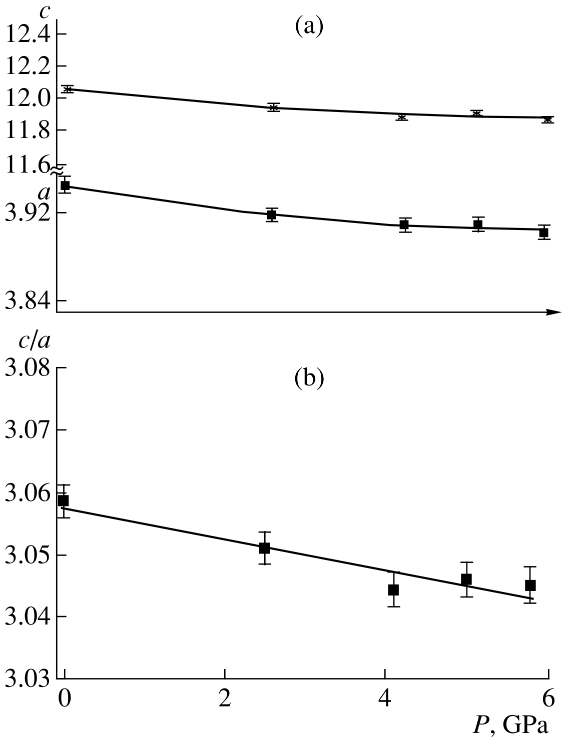

Fig. 2. Pressure-induced variation of (a) the lattice parameters and (b) the axial ratio c/a in $Nd_{1.85}Ce_{0.15}CuO_4$.

between the neighboring O_2 and CuO_2 layers ($z = 0.125$). The value of this parameter calculated from the experimental intensities varies only slightly and remains almost unchanged in the whole pressure range studied (Fig. 3). Unlike this, the z_{Nd} parameter of the undoped oxide decreased in the pressure range $P < 5$ GPa (Fig. 3) in a way similar to its decrease during doping to the composition $Nd_{1.85}Ce_{0.15}CuO_4$.

According to the known data reviewed in [8], the introduction of cerium into neodymium cuprate results in a decrease in the positional parameter. On the other hand, the excessive positive charge of Ce^{+4} ions is compensated by the interlayer charge transfer, i.e., the appearance of an additional negative charge (conduction electrons) with respect to Nd_2CuO_4. Structural changes similar to those caused by the introduction of cerium also take place in Nd_2CuO_4 under high pressures. In [8], this fact was interpreted under the assumption that baric interlayer charge transfer occurs. The results obtained in the present study indicate that the effect of high pressure on $Nd_{1.85}Ce_{0.15}CuO_4$ does not give rise to further changes in the positional parameter.

The different behavior of $Nd_{1.85}Ce_{0.15}CuO_4$ and Nd_2CuO_4 under a pressure of 5–6 GPa is consistent with the structural changes in Nd_2CuO_4 observed over a wider pressure range in the experiments using synchrotron radiation [9, 10]. According to the latter studies, the value of the parameter z_{Nd} decreases at pressures $P < 8$ GPa and then becomes constant. If one takes into account that the only difference in the $Nd_{1.85}Ce_{0.15}CuO_4$ and Nd_2CuO_4 lattices reduces to the value of the period c, one can draw the conclusion that the change from the varying to the constant z_{Nd} parameter is associated with the attainment of a certain value of the axial ratio c/a. Indeed, in pure Nd_2CuO_4, the positional parameter stops changing at c/a = 3.057–3.060 (7–8 GPa). This c/a value (3.058) in doped $Nd_{1.85}Ce_{0.15}CuO_4$ is attained even in the initial state

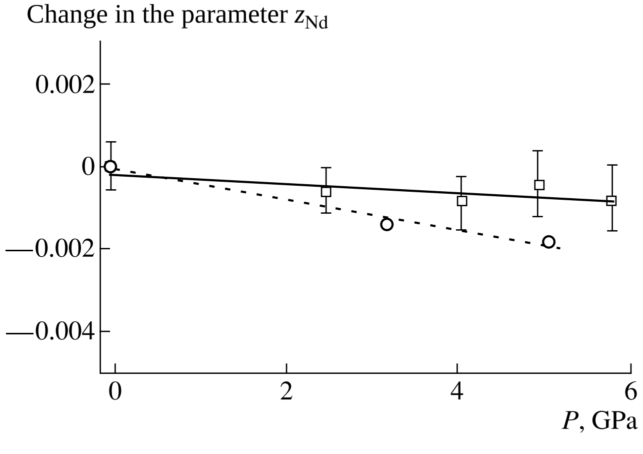

Fig. 3. Change in the positional parameter z_{Nd} as a function of pressure in $Nd_{1.85}Ce_{0.15}CuO_4$ (squares) and Nd_2CuO_4 (circles) [8].

(without high pressures). Therefore, it is not surprising that the z parameter remains unchanged with an increase in the pressure. One can expect the influence of high pressures at lower dopant concentrations (at high c/a values).

The positively charged neodymium layer in the neodymium cuprate lattice has a nonsymmetrical environment: $z = 1/2 - \mathrm{CuO}_2^{-2}$, $z \sim 0.35 - \mathrm{Nd}^{+3}$, $z = 1/4 - \mathrm{O}_2^{-4}$, $z \sim 0.15 - \mathrm{Nd}^{+3}$, $z = 0 - \mathrm{CuO}_2^{-2}$; Cu – 0; 0; 0, O(1) – 0; 1/2; 0, O(2) – 0; 1/2; 1/4, Nd – 0; 0; z. The neighboring O_2 and CuO_2 layers consist of similarly arranged oxygen ions, but, in addition, the copper–oxygen layer also has positive copper ions. Therefore, the oxygen layer has a higher negative charge and, therefore, can readily be polarized. Therefore, the environment asymmetry provides an increase in z_{Nd}, i.e., the displacement of the neodymium layer from the middle position. A decrease in the parameter with the introduction of cerium is explained by a decrease in the difference between the charges of the oxygen and copper–oxygen layers (because the latter layer has additional negative charges that are absent in pure cuprate). The constancy of z_{Nd} in $Nd_{1.85}Ce_{0.15}CuO_4$ under high pressures may signify that the influence of the charge transfer (because of a decrease in the unit-cell volume or doping) is compensated by a more pronounced repulsion between the neodymium and neighboring layers. The results obtained show that both pressure and doping influence the behavior of the positional parameter z_{Nd} in the same way and, therefore, it is expedient to verify whether this analogy is also valid for the electric characteristics of Nd_2CuO_4. In other words, it is expedient to check whether high pressures promote the same metallization of Nd_2CuO_4 as its doping with cerium.

Thus, contrary to the situation with the positional parameter, changes in the unit-cell volume and the lattice parameters in $Nd_{1.85}Ce_{0.15}CuO_4$ at high pressures proceeds in the same way as in Nd_2CuO_4. Unlike the situation in pure oxide, in the doped oxide, the positional parameter z_{Nd} remains constant as in the pure oxide at pressures exceeding 8 GPa. This seems to be explained by the similar influence of high pressure and doping on the structural characteristics of Nd_2CuO_4 and the absence of such influence upon the attainment of a certain pressure or dopant concentration.

ACKNOWLEDGMENTS

The authors are grateful to N.N. Parshin for his help in the experiment. The study was supported by the program "Actual Problems of Condensed Media: Superconductivity," project no. 96038, the program "Neutron Studies of Condensed Media," and the federal program for the Support of Prominent Scientists and Leading Scientific Schools, project no. 00-15-96712. One of us (S. Sh. Sh.) is grateful for the support received from the Ministry of Emigrant Absorption of the State of Israel.

REFERENCES

1. A. K. Tkalich, V. P. Glazkov, V. A. Somenkov, *et al.*, Sverkhprovodimost: Fiz., Khim., Tekh. **4**, 903 (1991).
2. J. D. Jorgensen, B. W. Veal, A. P. Paulikas, *et al.*, Phys. Rev. B **41**, 1863 (1990).
3. R. J. Cava, A. W. Hewat, B. Battlog, *et al.*, Physica C (Amsterdam) **165**, 419 (1990).
4. V. L. Aksenov, A. M. Balagurov, B. N. Savenko, *et al.*, Physica C (Amsterdam) **275**, 87 (1997).
5. S. Sh. Shilstein, A. S. Ivanov, and V. A. Somenkov, Physica C (Amsterdam) **245**, 181 (1995).
6. S. Sh. Shil'shteĭn and A. S. Ivanov, Fiz. Tverd. Tela (St. Petersburg) **37**, 3268 (1995) [Phys. Solid State **37**, 1796 (1995)].
7. S. Sh. Shil'shteĭn, in *Proceedings of 23rd Winter School of the Institute of Nuclear Physics, Russian Academy of Sciences* (S.-Peterb. Inst. Yad. Fiz., St. Petersburg, 1999).
8. V. P. Glazkov, B. N. Savenko, V. A. Somenkov, *et al.*, High Press. Res. **17**, 201 (2000).
9. H. Wilhelm, C. Cros, F. Arrouy, and G. Demanzeau, J. Solid State Chem. **126**, 88 (1996).
10. H. Wilhelm, C. Cros, E. Reny, *et al.*, J. Mater. Chem., No. 8, 2729 (1998).
11. V. V. Kvardakov, V. A. Somenkov, S. N. Barilo, and D. I. Zhigunov, Sverkhprovodimost: Fiz., Khim., Tekh., No. 1, 1263 (1991).
12. V. V. Kvardakov and V. A. Somenkov, Sverkhprovodimost: Fiz., Khim., Tekh., No. 5, 448 (1992).
13. V. V. Kvardakov, V. A. Somenkov, V. Paulus, *et al.*, Pis'ma Zh. Éksp. Teor. Fiz. **60**, 711 (1994) [JETP Lett. **60**, 731 (1994)].
14. S. Pinol, J. Fontcuberta, C. Miravitlles, and D. McK. Paul, Physica C (Amsterdam) **165**, 265 (1990).
15. V. L. Aksenov, A. M. Balagurov, V. P. Glazkov, *et al.*, Physica B (Amsterdam) **265**, 258 (1999).
16. V. P. Glazkov and I. N. Goncharenko, Fiz. Tekh. Vys. Davleniĭ, No. 1, 56 (1991).
17. V. B. Zlokazov and V. V. Chernyshev, J. Appl. Crystallogr. **25**, 447 (1990).

Translated by L. Man

Crystallography Reports, Vol. 48, No. 3, 2003, pp. 377–383. Translated from Kristallografiya, Vol. 48, No. 3, 2003, pp. 421–427.
Original Russian Text Copyright © 2003 by Reznichenko, Shilkina, Titov, Razumovskaya.

DIFFRACTION AND SCATTERING OF IONIZING RADIATIONS

Magnéli Phases in Ti-containing Oxides and Their Solid Solutions

L. A. Reznichenko, L. A. Shilkina, S. V. Titov, and O. N. Razumovskaya

Institute of Physics, Rostov State University, pr. Stachki 194, Rostov-on-Don, 344090 Russia
e-mail: sadkov@ip.rsu.ru

Received December 20, 2000

Abstract—The ordered planes of crystallographic shear inherited from titanium dioxide TiO_2 were revealed in complex Ti-containing oxides (Magnéli phases) by powder X-ray diffraction. It is assumed that periodic shear in the structure results in the modulation of titanium and oxygen displacements along the direction normal to the shear planes. A method of calculating the amplitude of the displacements of titanium atoms from the centers of oxygen octahedra is suggested. The method provides good agreement of the calculated and experimental data for single crystals. The degree of *A*-nonstoichiometry in alkaline earth, cadmium, and lead titanates is evaluated as 2–3%. *© 2003 MAIK “Nauka/Interperiodica”.*

INTRODUCTION

Earlier [1–3], we obtained direct experimental confirmation (X-ray powder diffraction) of the existence of modulated (long-period) structures in Ti- and Nb-containing oxides (including complex oxides). It was assumed that the structures described are formed as a result of superlattice ordering of the vacant positions associated with the propensity of Ti and Nb to easily change their degrees of oxidation and, as a result, form phases of variable composition. In this case, the point defects (anion vacancies) disappear because of the shear of one part of the structure with respect to the other part along a certain crystallographic direction with the simultaneous formation of planar defects, planes of crystallographic shear [4–6], which can be considered as translational modulations of the initial structure [7]. The boundaries of the translations (blocks of the undistorted structure) are planes of crystallographic shear whose formation is provided by a regrouping of the bonds between the coordination polyhedra [7–9] such that the oxygen octahedra share not vertices but edges. This is also accompanied by an increase in the cation/anion ratio without a change in the coordination number of cations nor the appearance of oxygen vacancies in monoxides [5–9], and considerable macroscopic compression of the material as a whole occurs. Metal atoms are displaced by half of the octahedron diagonal but preserve their octahedral coordination and are located at two levels, $z = 0$ and $1/2$. Thus, the ReO_3 structure built by sharing-vertex ReO_6 octahedra is characterized by shear along the $(\bar{1}20)$, $(\bar{1}30)$, (001), etc., planes. In the rutile structure of titanium dioxide, TiO_2, the shear plane coincides with $(\bar{1}21)$ [10]. These structural order–disorder transformations in the above crystals may be accompanied by the transition from the nonpolar to the polar (quasi-ferroelectric) state [11].

The rigorously periodic ordered spatial distribution of shear planes over the crystal results in the formation of Magnéli phases possessing constant, although sometimes unusual, compositions. The nonstoichiometry (variable composition) can be associated with randomly located or irregularly shaped shear planes (Wadsley defects) or with the intergrowth of locally ordered domains of the type of Magnéli phases [12–16]. Although the compositions of the latter phases differ from the composition of the matrix crystal and are usually characterized by rather complicated subscripts in the chemical formula, these phases are, in fact, compounds of a certain constant composition. The real unit-cell of these phases is rather large and includes the fragments of shear planes and, thus, reflects the periodicity of their distribution in a crystal. There exist homologous series of closely related discrete compounds that have similar structures and are described by the formulas Ti_nO_{2n-1}, V_nO_{2n-1}, and Mo_nO_{3n-1}, which allow the reorientation of octahedra either by shear or by rotation [9, 14, 17]. The spacings between the ordered shear planes in various members of these homologous series are different. Table 1 lists the typical homologous series of oxides with Magnéli phases.

As was indicated elsewhere [16], shear planes in a perovskite-type lattice are essentially different from shear planes in the classical shear structures: irrespective of the shear-plane orientation, the shear is equivalent to the removal of exactly the same numbers of *A* and O ions from the perovskite lattice with the preservation of the electroneutrality of a forming extended defect, whereas crystallographic shear in dioxides changes the charge state of the structural elements of the crystal.

1063-7745/03/4803-0377$24.00 © 2003 MAIK “Nauka/Interperiodica”

Table 1. Typical homologous series of oxides with crystallographic shear [7]

Initial structure	Shear planes	Formula	Approximate composition range
WO_3	$\{\bar{1}20\}ReO_3$	W_nO_{3n-1}	WO_3–$WO_{2.93}$
	$\{\bar{1}30\}ReO_3$	W_nO_{3n-2} (n = 20, 24, 25, 40)	$WO_{2.93}$–$WO_{2.87}$
MoO_3	$\{\bar{1}20\}ReO_3$	Mo_nO_{3n-1} (n = 8, 9)	
	$\{311\}MoO_3$	Mo_nO_{3n-2} (n = 18)	
TiO_2	$\{\bar{1}21\}$ rutile	Ti_nO_{2n-1} ($4 < n < 10$)	$TiO_{1.75}$–$TiO_{1.90}$
	$\{\bar{1}32\}$ rutile	Ti_nO_{2n-1} ($16 < n < 37$)	$TiO_{1.90}$–$TiO_{1.9375}$

High-resolution transmission electron microscopy revealed shear planes in the following crystals of the perovskite family $PbTiO_3$, $PbZrO_3$, Pb(Ti, Zr)O_3, and La($BaTiO_3$) [12, 16, 18]. In the former three oxides, the appearance of shear planes is explained in [16] by an elevated volatility of lead oxide at $t > 700°C$ [19].

Below, we show that the ordered shear planes in complex Ti-containing oxides are inherited from titanium dioxide TiO_2.

EXPERIMENTAL

We studied powders of binary oxides with a perovskite structure obtained by grinding $CaTiO_3$, $CdTiO_3$, $BaTiO_3$, $PbTiO_3$, and $SrTiO_3$ single crystals and ceramics. Single crystals were grown from flux; ceramics were obtained using the conventional ceramic technology.

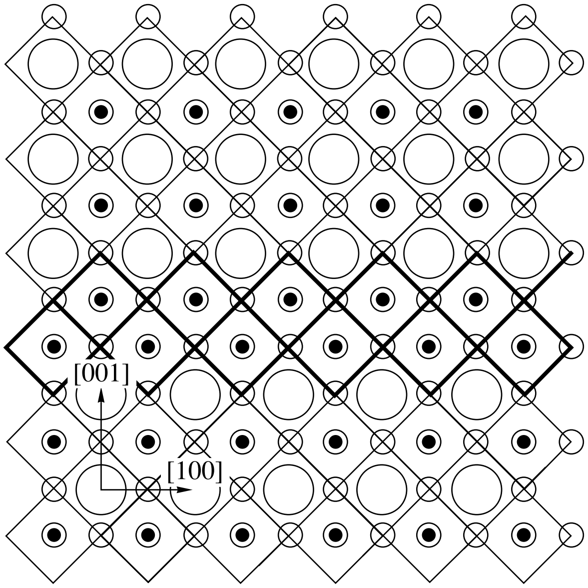

Fig. 1. Shear (001) plane in the perovskite ABO_3 structure projected along the [010] direction. ● denote *B* cations in oxygen octahedra, ◯ denote *A* cations in cuboctahedra displaced from the drawing plane by *b*/2, and ○ denote oxygen ions.

X-ray diffraction studies were performed on DRON-2 and DRON-3 diffractometers (Bragg–Brentano focusing, two systems of slits, FeK_α and CoK_α radiations with the use of Mn- and Fe-filters, respectively, and FeK_β radiation). Powders were pressed and placed into quartz vessels without the use of a plastifier in order to exclude additional diffuse scattering. The profiles of X-ray diffraction lines were obtained with a 2θ scan at a step of 0.01° with the time of pulse recording at each point being 10 s and by recording the profiles onto the diagram tape with a θ-2θ scan at rates of counter motion of 1/2 and 1/4 deg/min. The integrated intensities of reflections were calculated as an area under the intensity-distribution curve by the Simpson method. The displacements of Ti atoms (Δz) were averaged over 5–10 measurements, the deviation of an individual measurement from the average value did not exceed ±10%.

DISCUSSION

The structural changes considered above manifest themselves on X-ray powder diffraction patterns as changes in the diffuse scattering. Figure 1 shows the (001) shear plane in the perovskite structure described by the general formula ABO_3. It is seen that the row of *A* cations intersecting the (001) shear plane along the [001] direction is continued by the row of oxygen ions and, vice versa, a row of oxygen ions is continued by a row of *A* cations. In other words, on the one hand, the geometric order of arrangement of the ions in the (100) and (010) planes is violated, with the degree of disorder being described as $\delta = \frac{r_A - r_O}{r_A + r_O}$ (r_A and r_O are the ionic radii). On the other hand, there is also a substitutional disorder determined by the difference of the atomic scattering factors f_A and f_O. The periodic arrangement of shear planes and the correlation between these two types of disorder result in the formation of a diffuse maximum in the vicinity of the $h00$ reflections. The position of this maximum with respect to the regular reflection is determined by the sign of the product $\delta(f_A - f_O)$. If this product is positive, the additional maximum should be located on the side of smaller θ angles [20].

This effect is clearly seen on the X-ray diffraction pattern of $PbTiO_3$ with a high value of the *c*/*a* ratio (~1.065) and, therefore, a large spacing between the 100 and 001 lines (Fig. 2, 100 and 200 lines). Along other directions, a row of *A* cations is substituted by a row of Ti–O with an average ionic radius of 1.0 Å and an average scattering factor $f_{(\text{Ti–O})} = 15.0$. Therefore the diffuse maximum on the diffraction patterns of Cd, Sr, and Ca titanates studied in this paper can appear both in front of and behind the main reflections (Table 2).

In the planes parallel to the shear plane, the periodicity of atomic arrangement is not broken, but the shear of the planes parallel to one another (pure displacive disorder) results in symmetric broadening of the 00*l* lines (Fig. 2, 001 line). In the general case of the crystallographic shear along an arbitrary plane, the reflections from all the planes not parallel to the shear plane would have asymmetric shapes, whereas the reflections from the planes parallel to the shear plane would be symmetrically broadened ($CaTiO_3$, $CdTiO_3$, $BaTiO_3$, and $SrTiO_3$, Fig. 3). It should be indicated that the 100 and 110 lines of cubic $SrTiO_3$ are obviously asymmetric, whereas the 111 line is symmetric. This leads to the assumption that cubic $SrTiO_3$ has a shear plane coinciding with the (111) plane.

The X-ray profiles in Fig. 3 show that the structures of all the titanates have shear planes. Moreover, these shear planes are also inherited by the Ti-containing solid solutions. Figures 4a–4c show the fragments of X-ray diffraction patterns of the $Pb[Ti_{0.6}Zr_{0.3}(W, Nb, Mn)_{0.1}O_3$, $(Pb, Ca)[Ti_{1-x}(W, Co, Mg)_x]O_3$, and $Pb[Ti_{0.3}Zr_{0.6}(W, Nb, Mn)_{0.1}]O_3$ solid solutions used as the basis of piezoelectric materials designed at the Institute of Physics of Rostov State University. The first two oxides have tetragonal structures; the patterns of diffuse scattering from these materials are similar to the pattern of $PbTiO_3$. The latter solid solution has a rhombohedral structure; we failed to reveal the symmetric profile of the corresponding X-ray diffraction line because of the superposition of the multiplet components. Nevertheless, the symmetric profile of the single 100 peak with nonmonotonically varying intensity indicates the presence of a shear plane in the structure. The position of the satellite maximum in the vicinity of the 100 reflection allowed us to calculate the modulated wavelength λ along the [100] direction for all the titanates under study using the formula $\lambda = \frac{1}{|k|}$, where *k* is the wave vector determined as $|k| = \frac{1}{d_{hkl}} - \frac{1}{d_{c^-}}$ or $|k| = \frac{1}{d_{c^+}} - \frac{1}{d_{hkl}}$ and d_{hkl}, d_{c^-}, and d_{c^+} are the interplanar spacings between the *hkl* line and the satellites that appear in front of or behind the line, respectively [20]. The results are listed in Table 3.

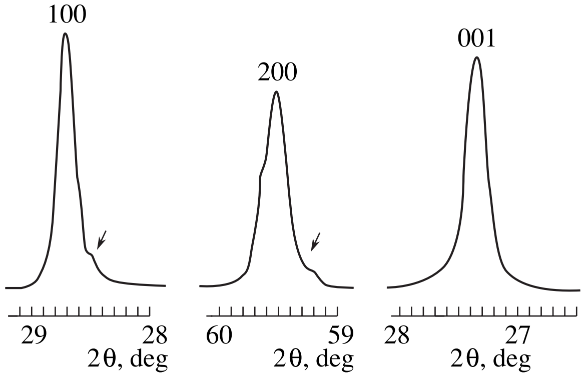

Fig. 2. 100, 200, 001 X-ray diffraction lines of $PbTiO_3$ (ground single crystals). Arrows indicate diffuse maxima. FeK_α radiation.

Table 3 also indicates the pressures (*P*) of saturated vapors of AO oxides at the temperatures of titanate synthesis (T_{syn}). It is seen that, irrespective of the volatility of the initial oxides, λ ranges within 400–500 Å for all the oxides except for $SrTiO_3$; in other words, the number of shear planes are approximately the same in all the titanates and seem to be determined by the specific features of TiO_2 structures rather than the volatility of *A*O oxides.

The formation of shear planes in TiO_2 is also favored by mechanically activated defects [21–23] in the synthesis of various ceramics. Figure 5 shows X-ray

Table 2. Characteristics determining asymmetry of X-ray diffraction lines for alkaline metal, cadmium, and lead titanates

A cations	r_A [12]	For *A*–O row			For *A*–(Ti–O) row		
		δ	$f_A - f_O$ (at θ = 0)	$\delta x(f_A - f_O)$	δ	$f_A - f_{\text{Ti–O}}$ (at θ = 0)	$\delta x(f_A - f_{\text{Ti–O}})$
Ca	1.16	–0.08	+12	–0.9	+0.07	+5	+0.4
Sr	1.34	–0.007	+30	–0.2	+0.14	+23	+3.2
Ba	1.54	+0.06	+48	+3.1	+0.2	+41	+8.7
Cd	1.11	–0.10	+40	–4.0	+0.05	+33	+1.7
Pb	1.41	+0.02	+74	+1.4	+0.17	+67	+11.4

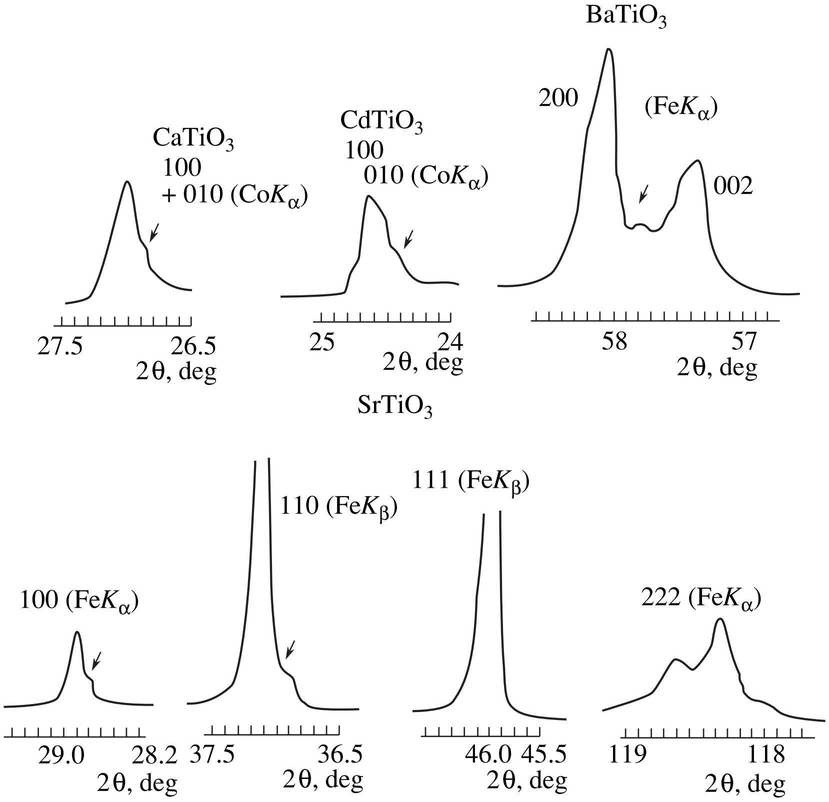

Fig. 3. Fragments of X-ray diffraction patterns from $CaTiO_3$, $CdTiO_3$, and $BaTiO_3$ (ground ceramics) and $SrTiO_3$ (ground single crystals).

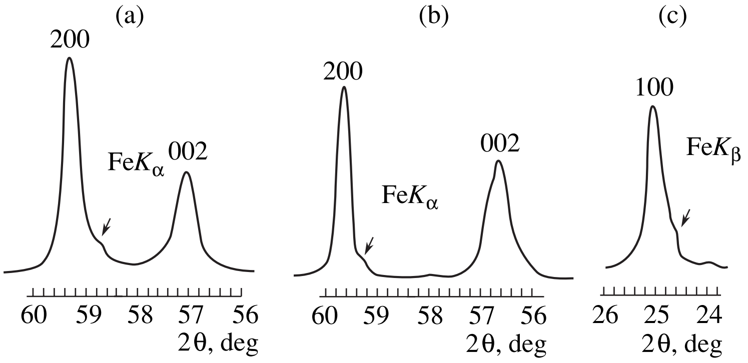

Fig. 4. Fragments of X-ray diffraction patterns from (a) $Pb[Ti_{0.6}Zr_{0.3}(W, Nb, Mn)_{0.1}]O_3$, (b) $(Pb, Ca)[Ti_{1-x}(W, Co, Mg)_x]O_3$, and (c) $Pb[Ti_{0.3}Zr_{0.6}(W, Nb, Mn)_{0.1}]O_3$ solid solutions (ground ceramics).

diffraction lines of TiO_2 corresponding to the symmetrically broadened reflections from the shear $(\bar{1}21)$ plane and from the (101) plane not parallel to the shear plane (clearly seen diffuse maximum on the side of smaller θ angles) obtained before (Fig. 5a) and after (Fig. 5b) 4-h-grinding in the vibration mill. The half-width of the $\bar{1}21$ diffraction line in the first case equals 0.15°, and the modulated wavelength along the [101] direction equals $\lambda \sim 550$ Å; in the second case, the half-width of the line equals 0.17° and $\lambda \sim 450$ Å. Thus, grinding results in a decrease in λ, which indicates an increase in the number of shear planes. In turn, this facilitates an easy and reversible change of the type of connection of coordination polyhedra, which is characteristic of transition metal (from groups V–VII of the Periodic System) oxides [24].

Elastic stresses in the lattice caused by the regrouping of TiO_6 octahedra decrease with the displacements of Ti^{4+} and O^{2-} ions from their ideal positions along the opposite directions normal to the shear plane [8, 9]. It is natural to assume that the periodic shear planes give rise to modulation of these displacements along the displacement direction. Then, analyzing the X-ray diffraction profiles corresponding to the reflection from the planes parallel to the shear plane and using the formula for purely displacive disorder from [20], one can calculate the amplitude Δz of the titanium displacement associated with the higher value of the atomic scattering factor of titanium in comparison with the atomic scattering factor of oxygen:

$$\Delta z = \frac{d_{hkl}\sqrt{I_s/I_{hkl}}}{\pi l}, \qquad (1)$$

where d_{hkl} is the interplanar spacing; I_s and I_{hkl} are the intensities of the satellite and main reflections, respectively; I_s is determined as a half of the difference $I_{int} - I_{hw}$, where I_{int} is the integrated intensity of the X-ray diffraction line; $I_{hw} = Bh$; B is a half-width, and h is the peak height. The calculation was performed using first-order reflections and therefore $l = 1$. In the derivation of this formula, we used the following expressions:

$$\Delta z = \frac{\lambda\varepsilon}{2\pi}\cos\frac{2\pi na}{\lambda}, \qquad (2)$$

where ε is the amplitude of scatter in interplanar spacings and a is the interplanar spacing

$$I_s/I_{hkl} = \frac{\lambda^2\varepsilon^2 l^2}{4a^2}, \qquad (3)$$

where I_s and I_{hkl} are the intensities of the satellite and main reflections, respectively, and l/a is the projection of the reciprocal-space vector onto the normal to the hkl plane. Determining ε from Eq. (3) and substituting it into Eq. (2), we have

$$\Delta z = \frac{a\sqrt{I_s/I_{hkl}}}{\pi l}\cos\frac{2\pi na}{\lambda}. \qquad (4)$$

The amplitude Δz is obtained at $\cos\frac{2\pi na}{\lambda} = 1$.

Table 4 lists the displacements of a titanium atom calculated by Eq. (1) and determined for single crystals in [25] and also indicates the displacement direction. Except for $PbTiO_3$, all the displacements of Ti^{4+} determined are consistent with the Δz values for single crystals. As was shown in [26], some Pb^{4+} and Pb^{2+} ions are located in octahedral positions along the shear plane in the $PbTiO_3$ structure. This explains the fact that the Δz value determined in the present study for $PbTiO_3$ coincides with the displacement of the lead atom from its ideal position known for single crystals. The displacement of the Ti atom in single crystals of cubic $SrTiO_3$ is unknown.

Table 3. Characteristics of *A*O oxides

Oxide formula	Temperature of solid-phase synthesis of titanate, t_{syn}, °C	P, mm Hg at t_{syn}, °C	Modulated wavelength λ along the [100] direction
CaO	1100–1150	5.9×10^{-11}	520
SrO	1100–1150	2.2×10^{-8}	1000
BaO	1100–1150	3.4×10^{-6}	470
CdO	800–850	1.2×10^{-2}	400
PbO	850–900	1.6×10^{-1}	480

As has already been indicated, in perovskites not only oxygen but also *A* positions disappear. If a structure has a shear plane, it manifests itself as a Wadsley defect; then, the deficit in *A* cations is insignificant. However, if there are several shear planes, the deficit of cations in the *A* positions can be quite pronounced. As a result, when performing solid-phase synthesis, one uses the charge with excessive *A* cations, which results

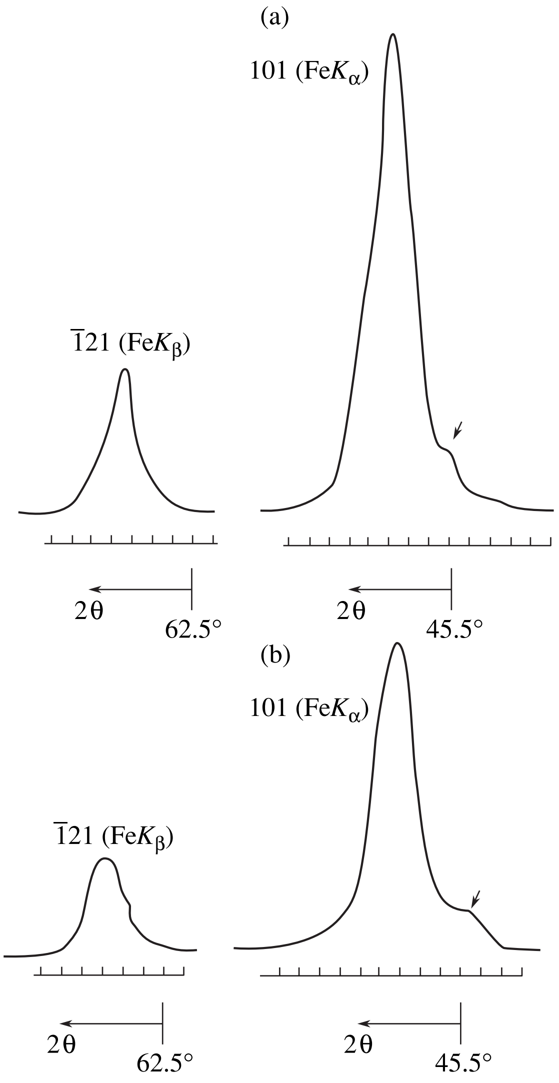

Fig. 5. $\bar{1}21$ and 101 X-ray diffraction lines from TiO_2 (a) before and (b) after grinding.

Table 4. Atomic displacements and their directions determined by X-ray powder and single-crystal diffraction

	Δz, Å		Direction of displacement	Displaced atom
	single crystal [26]	polycrystal		
$CaTiO_3$	0.22	0.24	$[20\bar{1}]$	Ti
$SrTiO_3$		0.22	[111]	Ti
$BaTiO_3$	0.15	0.14	[001]	Ti
$CdTiO_3$	0.35	0.37	$[10\bar{1}]$	Ti
$PbTiO_3$	0.465	0.47	[001]	Pb

Table 5. Characteristics of ATiO$_3$ oxides

Oxide formula	$\tilde{a}_{\mathrm{calcd}}$	$\tilde{a}_{\mathrm{obs}}$ [25]	x
$CaTiO_3$	3.857	3.825	0.027
$SrTiO_3$	3.941	3.907	0.027
$BaTiO_3$	4.036	4.007	0.022
$CdTiO_3$	3.830	3.806	0.021
$PbTiO_3$	3.973	3.985	0.025

in the formation of impurity phases during synthesis and, sometimes, prevents synthesis of the pure phase of composition $A_{1-x}\mathrm{TiO}_{3-x}$. The lattice parameters of single crystals of oxides considerably differ from the lattice parameters of oxides obtained by solid-phase synthesis. The lattice parameters are strongly dependent on the synthesis and sintering modes, which explains the considerable discrepancy in the lattice parameters reported by various researchers. This fact is associated with the pronounced dependence of x on the synthesis temperature. Comparing the average parameter $\tilde{a} = \sqrt[3]{V}$ calculated by the formula

$$\tilde{a}_{\mathrm{calcd}} = \frac{n_A a_A + n_B a_B}{n_A + n_B}, \qquad (5)$$

where $a_A = \sqrt{2}\,L_{AO}$, $a_B = 2L_{BO}$, n_A and n_B are the valences of A and B cations, and L_{AO} and L_{BO} are the "unstressed" A–O and B–O distances [27], with the experimentally observed parameter $\tilde{a}_{\mathrm{obs}}$, we see that the $\tilde{a}_{\mathrm{obs}}$ has a considerably lower value for all the oxides except for $PbTiO_3$ (Table 5). Taking into account that Ba^{2+} ions can only occupy cuboctahedral positions, one can evaluate the deficit in A positions in $BaTiO_3$ by equating the right-hand side of Eq. (5) to $\tilde{a}_{\mathrm{obs}}$. We used the sums of ionic radii from [28] as unstressed bond lengths:

$$\frac{(1-x)\cdot 2\sqrt{2}L_{\mathrm{BaO}} + 2\cdot 4L_{\mathrm{TiO}}}{6} = 4.0066$$
$$\longrightarrow x = 0.0217.$$

Table 5 lists the x values for other titanates calculated in the same way. For $PbTiO_3$ with $\tilde{a}_{\mathrm{obs}} > \tilde{a}_{\mathrm{calcd}}$, the value of x is determined in a more complicated way with allowance for the specific characteristics of this oxide (the presence in the structure of Pb^{4+} and Pb^{2+} ions in octahedral positions along the shear plane). The calculation with due regard for these factors yielded $x \simeq 0.025$.

CONCLUSIONS

The analysis of the character of distortion of X-ray profiles on diffraction patterns of Ti-containing binary oxides with a perovskite structure and the comparison of the average lattice parameter observed experimentally and calculated for the perovskite unit cell lead to the conclusion that the distortions of the crystal lattice by shear planes are periodic and, as a result, the structure is modulated.

The absence of a correlation between the pressure of the saturated vapors of AO oxide at the temperature of its synthesis and the modulated wavelength indicates that the development of shear structures is not associated with the volatility of the AO component but is an effect inherent in the objects studied and, most probably, inherited from titanium dioxide TiO_2.

The equal displacements of titanium atoms (B cations) in binary oxides calculated by the method suggested in the present study and the displacements observed in the corresponding single crystals allow us to draw the conclusion that, first, titanium atoms are displaced along the direction normal to the shear plane and, second, the periodic arrangement of shear planes results in modulation of these displacements.

ACKNOWLEDGMENTS

This study was supported by the Russian Foundation for Basic Research, project no. 99-02-17575.

REFERENCES

1. L. A. Reznichenko, O. N. Razumovskaya, and L. A. Shilkina, in *Proceedings of International Scientific and Practical Conference on Piezoelectric Materials, Piezotekhnika-97* (Obninsk, 1997), p. 191.
2. L. A. Shilkina, L. A. Reznichenko, and O. N. Razumovskaya, in *Abstracts of 8th International Symposium on Physics of Ferroelectrics-Semiconductors* (Rostov-on-Don, 1998), No. 7, p. 192.
3. L. A. Reznichenko, L. A. Shilkina, and O. N. Razumovskaya, in *Abstracts of XV All-Russian Conference on Physics of Ferroelectrics* (Rostov-on-Don, 1999), p. 294.
4. A. D. Wadsley, Rev. Pure Appl. Chem. **5** (1), 165 (1955).
5. A. D. Wadsley, *Non-Stoichiometric Compounds* (Academic, London, 1964).
6. J. S. Anderson, Chem. Soc. Rev. **1**, 5 (1972).

7. C. N. R. Rao and J. Gopalakrishnan, *New Directions in Solid State Chemistry* (Cambridge Univ. Press, Cambridge, 1986; Nauka, Novosibirsk, 1990).
8. Yu. D. Tret'yakov, *Chemistry of Nonstoichiometric Oxides* (Mosk. Gos. Univ., Moscow, 1974).
9. Yu. D. Tret'yakov, *Solid-Phase Reactions* (Khimiya, Moscow, 1978).
10. L. A. Bursill and B. G. Hyde, *The Progress in Solid State Chemistry* (Pergamon Press, Oxford, 1972), Vol. 7.
11. A. H. Meitzler, Ferroelectrics **11**, 503 (1975).
12. V. V. Prisedskiĭ, V. P. Komarov, G. F. Pan'ko, *et al.*, Dokl. Akad. Nauk SSSR **247** (3), 620 (1979).
13. J. S. Anderson, Acta Chem. Scand. **8** (8), 1599 (1954).
14. J. S. Anderson, B. Collen, U. Knylenstiren, and A. Magneli, Acta Chem. Scand. **11**, 1641 (1957).
15. M. G. Blanchin, L. A. Bursil, and D. Smith, Proc. R. Soc. London, Ser. A **391**, 35 (1984).
16. A. G. Petrenko and V. V. Prisedskiĭ, *Structural Defects in Ferroelectics* (Uchebno-Metod. Kab. Vyssh. Obraz., Kiev, 1989).
17. Y. Le Page and P. J. Stroubel, Solid State Chem. **43**, 314 (1982).
18. A. A. Dobrikov and O. V. Presnyakova, Neorg. Mater. **17** (12), 2239 (1981).
19. R. L. Hollman and R. M. Fulrath, J. Appl. Phys. **44** (12), 5227 (1973).
20. A. Guinier, *Théorie et Technique de la Radiocristallographie* (Dunod, Paris, 1956; Fizmatgiz, Moscow, 1961).
21. E. G. Avvakumov, N. V. Kosova, and V. V. Aleksandrov, Izv. Akad. Nauk SSSR, Neorg. Mater. **17** (7), 1118 (1983).
22. E. G. Avvakumov, V. F. Anufrienko, S. V. Vosel', *et al.*, Izv. Sib. Otd. Akad. Nauk SSSR, Ser. Khim. Nauk, No. 2 (431), 41 (1987).
23. E. G. Avvakumov, V. V. Molchanov, R. A. Buyanov, and V. V. Boldyrev, Dokl. Akad. Nauk SSSR **306** (2), 367 (1989).
24. E. Haber, Kinet. Katal. **21** (1), 123 (1980).
25. H. Landolt and L. Börnstein, *Ferroelektrika und Verwandte Substanzen* (Springer, Berlin, 1981), T.B.16-(2).
26. S. V. Titov, L. A. Shilkina, O. N. Razumovskaya, *et al.*, Neorg. Mater. **37** (7), 849 (2001).
27. V. P. Sakhnenko, E. G. Fesenko, and A. T. Shuvaev, Kristallografiya **17** (2), 316 (1972) [Sov. Phys. Crystallogr. **17**, 268 (1972)].
28. G. B. Bokiĭ, *Crystal Chemistry* (Nauka, Moscow, 1971).

Translated by L. Man

Crystallography Reports, Vol. 48, No. 3, 2003, pp. 384–389. Translated from Kristallografiya, Vol. 48, No. 3, 2003, pp. 428–433.
Original Russian Text Copyright © 2003 by Rozenberg, Rastsvetaeva, Verin.

STRUCTURE OF INORGANIC COMPOUNDS

Crystal Structure of Surkhobite: New Mineral from the Family of Titanosilicate Micas[1]

K. A. Rozenberg*, R. K. Rastsvetaeva, and I. A. Verin****
** Moscow State University, Vorob'evy gory, Moscow, 119992 Russia*
*** Shubnikov Institute of Crystallography, Russian Academy of Sciences, Leninskiĭ pr. 59, Moscow, 119333 Russia*
e-mail: rast@ns.crys.ras.ru

Received October 22, 2002

Abstract—The crystal structure of surkhobite, a new mineral from Tajikistan, was determined by methods of X-ray diffraction analysis ($a = 10.723$ Å, $b = 13.826$ Å, $c = 20.791$ Å, $\beta = 95°$, sp. gr. $C2$, $R = 0.047$). The structure is a derivative of the bafertisite structure but differs from it and other representatives of the titanosilicate micas: three-layered slabs are connected to form isolated channels orderly filled with Ca, Na, Ba, and K atoms. *© 2003 MAIK "Nauka/Interperiodica".*

Minerals of the family of titanosilicate micas are rather rare. They are formed in alkali rocks of various types and characterized by both chemical and structural diversity. The family contains thirty minerals. Titanosilicate micas have a heterolayer structure, which, unlike micas with *T*–*O*–*T*-layers, consists of *H*–*O*–*H*-layers [1] (*T* is a layer of tetrahedra, *O* is a layer of octahedra, *H* denotes a mixed tetrahedral–octahedral layer). The majority of the minerals of this family contains barium, of which lamprophyllite and bafertisite are the most widespread minerals. Less widespread barium-containing minerals are nabalamprophyllite, jinshajiangite, perraultite, Ba-lamprophyllite, K-baritolamprophyllite, and delindeite.

We studied the crystal structure of a newly discovered Ca–F-analogue of perraultite from pegmatites of the Darai-Piez alkali massif (central Tajikistan). The mineral surkhobite was found in a peripheral zone of syenite–pegmatite in association with aegirine, microcline, albite, quartz, bafertisite, astrophyllite, and polylithionite. Surkhobite, together with astrophyllite, replaces bafertisite and occurs as flattened brownish red crystals up to 1 mm in length. The chemical composition of surkhobite was studied by the methods of analytical chemistry. The simplified empirical formula calculated for 12 cations looks like: $(Ca_{0.76}Na_{0.46})(Ba_{0.85}K_{0.25}Sr_{0.01})(Fe^{2+}_{1.63}Mn_{1.62}Fe^{3+}_{0.39}Al_{0.19}) \cdot (Ti_{1.58}Zr_{0.18}Nb_{0.07})(Si_{4.01}O_{14})O_{2.26}F_{1.93}(OH)_{1.17}$.

The basic characteristics of the crystal and the diffraction experiment are indicated in Table 1. The set of atomic coordinates of perraultite from Priazovye territory [2] was used as the initial set in the structure refinement. At the final stage, the absorption correction was introduced, the mixed atomic-scattering curves were used, and the model was refined in the anisotropic approximation of atomic displacements. The separation of the F, OH, and O anions was made on the basis of the calculated local balance of valence at anions. The final atomic coordinates are given in Table 2; the site composition and the characteristic of the coordination polyhedra, in Table 3. The crystallochemical formula of the

Table 1. Main characteristics of the crystal and experiment

Characteristic	Value
Unit-cell parameters, Å, deg	$a = 10.723(1)$
	$b = 13.826(2)$
	$c = 20.791(4)$
	$\beta = 95.00(1)$
Unit-cell volume, Å^3	$V = 3070.7$
Sp. gr.	$C121$
Radiation; λ, Å	MoK_α; 0.71073
Density ρ_{calcd}, g/cm^3	3.87
Crystal dimensions, mm	0.2 × 0.2 × 0.4
Diffractometer	ENRAF-NONIUS
Ranges of measurements	$-17 < h < 17$
	$-22 < k < 22$
	$0 < l < 33$
$\sin\theta/\lambda$	< 0.81
Total number of reflections	5292 $F > 3\sigma(F)$
Number of crystallographically independent reflections	3618 $F > 3\sigma(F)$
R-factor	0.047
Program used for refinement	AREN [3]
Program for allowance for absorption	DIFABS [4]

---

[1] This work was presented at the symposium "Order, Disorder and Properties of Oxides" (ODPO), Sochi, 2002.

1063-7745/03/4803-0384$24.00 © 2003 MAIK "Nauka/Interperiodica"

Table 2. Atomic coordinates and equivalent parameters of atomic displacements

Atom	*x*/*a*	*y*/*b*	*z*/*c*	$U_{eq} \times 100$, Å^2	Atom	*x*/*a*	*y*/*b*	*z*/*c*	$U_{eq} \times 100$, Å^2
Ba(1)	0	0.0265(0)	0	1.46(1)	O(8)	0.9638(6)	0.6565(4)	0.3025(3)	1.3(3)
Ba(2)	0.7501(1)	0.7725(1)	0.5005(1)	3.60(3)	O(9)	0.2887(7)	0.9044(5)	0.1979(3)	1.3(3)
K*	0	0.5658(2)	0	3.84(5)	O(10)	0.9622(7)	0.8972(6)	0.3035(3)	1.7(3)
Na(1)*	0	0.523(1)	0.5	3.4(1)	O(11)	0.3786(5)	0.2045(3)	0.0842(2)	0.8(1)
Na(2)*	0	0.023(1)	0.5	3.1(1)	O(12)	0.7193(6)	0.026(1)	0.3143(3)	3.0(3)
Ca	0.2503(6)	0.776(4)	–0.0006(2)	2.54(6)	O(13)	0.0290(7)	0.7885(6)	0.1870(2)	1.4(1)
Mn(1)	0.8742(1)	0.0244(2)	0.2544(1)	1.33(3)	O(14)	0.1492(6)	0.7043(3)	0.0867(2)	0.9(3)
Mn(2)	0.8769(1)	0.5248(2)	0.2559(1)	1.32(3)	O(15)	0.0271(8)	0.2629(5)	0.1892(3)	1.5(3)
Mn(3)*	0.1225(1)	0.4000(1)	0.2503(1)	1.48(4)	O(16)	0.7204(5)	0.522(1)	0.3127(3)	3.0(3)
Mn(4)	0.1229(1)	0.6512(1)	0.2497(1)	1.48(4)	O(17)	0.3248(4)	0.0214(6)	0.1016(2)	0.5(1)
Fe(1)	0.8751(1)	0.2737(1)	0.2442(1)	1.19(4)	O(18)	0.862(1)	0.643(1)	0.4122(5)	4.8(3)
Fe(2)	0.8745(1)	0.7771(1)	0.2444(1)	1.20(4)	O(19)	0.6036(9)	0.946(1)	0.4124(4)	5.4(3)
Fe(3)	0.1249(1)	0.9043(1)	0.2471(1)	1.62(4)	O(20)	0.1068(7)	0.646(1)	0.4156(5)	5.7(4)
Fe(4)	0.1238(1)	0.1512(1)	0.2478(1)	1.16(4)	O(21)	0.8639(9)	0.913(1)	0.4142(4)	6.5(3)
Ti(1)	0.7333(1)	0.0427(2)	0.3997(1)	2.84(5)	O(22)	0.3776(6)	0.8466(4)	0.0878(2)	1.1(3)
Ti(2)	0.7330(1)	0.5446(1)	0.3981(1)	2.16(5)	O(23)	0.870(1)	0.112(2)	0.4163(5)	8.7(3)
Ti(3)*	0.0167(1)	0.2570(1)	0.1009(1)	1.62(4)	O(24)	0.1081(7)	0.146(1)	0.4137(5)	4.8(4)
Ti(4)*	0.0160(1)	0.7960(1)	0.1005(1)	1.75(3)	O(25)	0.6027(9)	0.447(1)	0.4116(4)	4.8(4)
Si(1)	0.9793(2)	0.1647(2)	0.3806(1)	1.18(8)	O(26)	0.1507(6)	0.3449(4)	0.0860(3)	1.3(3)
Si(2)	0.9810(2)	0.6660(2)	0.3802(1)	1.34(7)	O(27)	0.1390(6)	0.1482(4)	0.2442(3)	1.3(1)
Si(3)	0.2574(2)	0.4187(1)	0.1195(1)	1.15(6)	O(28)	0.8715(8)	0.441(1)	0.4121(5)	6.2(3)
Si(4)	0.2852(2)	0.9181(1)	0.1195(1)	0.97(6)	O(29)	0.2092(4)	0.5253(8)	0.0995(2)	1.1(3)
Si(5)	0.2819(2)	0.1350(2)	0.1199(1)	1.28(8)	O(30)	0.0408(6)	0.275(1)	0.3971(8)	6.1(4)
Si(6)	0.2553(2)	0.6349(2)	0.1188(1)	1.20(6)	O(31)	0.0416(6)	0.774(1)	0.4032(7)	6.0(4)
Si(7)	0.9796(2)	0.3838(1)	0.3810(1)	1.44(8)	O(32)	0.3867(6)	0.6480(4)	0.0894(3)	1.3(1)
Si(8)	0.9793(3)	0.8849(1)	0.3797(1)	1.60(8)	OH(1)	0.0381(5)	0.524(1)	0.2076(3)	2.3(3)
O(1)	0.9693(9)	0.3924(7)	0.3062(4)	2.4(1)	OH(2)	0	0.2462(6)	0	1.4(4)
O(2)	0.2789(6)	0.4054(5)	0.1981(3)	1.3(1)	OH(3)	0	0.8019(4)	0	0.76(3)
O(3)	0.9631(7)	0.1543(4)	0.3042(4)	1.65(3)	F(1)	0.0349(6)	0.023(1)	0.2052(3)	3.6(1)
O(4)	0.2780(5)	0.6487(6)	0.1977(3)	1.3(3)	F(2)	0.213(1)	0.7778(5)	0.2947(5)	3.2(1)
O(5)	0.2888(6)	0.1495(5)	0.1988(2)	1.3(1)	F(3)	0.7499(5)	0.0086(9)	0.5008(2)	2.5(1)
O(6)	0.1404(7)	0.9009(5)	0.0868(3)	0.5(1)	F(4)	0.7102(8)	0.7751(4)	0.2921(4)	1.9(1)
O(7)	0.3887(5)	0.4006(3)	0.0843(3)	0.6(1)					

Note: OH(2) and OH(3) = (OH, O).
* Site with mixed composition.

sample studied ($Z = 4$) can be written as $\{[Ba_{1.65}K_{0.35}][Ca_{1.2}Na_{0.8}]\}\{[Fe_4][Mn_{3.7}Na_{0.3}]\}\{[Ti_{3.2} \cdot (Zr, Nb)_{0.8}O_4F(OH, O)][Si_2O_7]_4\}\{[F_3OH]\}$, where the compositions corresponding to the interlayer cations, plane *O*-layer, *H*-layers, and additional anions are given in braces.

Like perraultite, the structure of surkhobite (Fig. 1) is a derivative of bafertisite [5] (Fig. 2), but it differs from it and other representatives of titanosilicate micas in that the three-layer slabs in the structure are not isolated; they are shifted from each other by 0.25 along the *x* and *y* axes. As a result, the vertices of Ti-octahedra protruding from the *H*-layer close up through the shared OH, O, or F vertices. Because of this, the common interslab space is divided into isolated channels—broad channels with an octagonal cross-section along the *x* axis (Fig. 1a) and narrow channels with a hexagonal cross-section along the *y* axis (Fig. 1b)—which makes them somewhat similar to zeolite-like minerals,

Table 3. Characteristics of coordination polyhedra

Position	Composition	C.N.	Cation–anion distances, Å		
			minimum	maximum	average
Ba(1)	2Ba	10	2.81(1)	3.11(1)	2.88
K	1.4K + 0.6Ba	9	2.97(1)	3.26(1)	3.02
Ba(2)	4Ba	12	2.82(1)	3.64(1)	3.11
Na(1)	1.6Na + 0.4Ca	10	2.45(1)	2.79(1)	2.63
Na(2)	1.6Na + 0.4Ca	10	2.45(1)	2.79(1)	2.61
Ca	4Ca	10	2.34(1)	2.88(1)	2.63
Mn(1)	4Mn	6	2.08(1)	2.28(1)	2.20
Mn(2)	4Mn	6	2.07(3)	2.29(1)	2.20
Mn(3)	2.8Mn + 1.2Na	6	2.08(1)	2.46(1)	2.20
Mn(4)	4Mn	6	2.06(1)	2.47(1)	2.22
Fe(1)	4Fe	6	2.08(1)	2.27(1)	2.18
Fe(2)	4Fe	6	2.10(1)	2.23(1)	2.18
Fe(3)	4Fe	6	2.05(1)	2.30(1)	2.18
Fe(4)	4Fe	6	2.12(1)	2..41(1)	2.19
Ti(1)	4Ti	6	1.76(1)	2.28(1)	2.00
Ti(2)	4Ti	6	1.79(1)	2.15(1)	1.99
Ti(3)	2.4Ti + 1.6(Zr, Nb)	6	1.83(1)	2.10(1)	1.98
Ti(4)	2.4Ti + 1.6(Zr, Nb)	6	1.80(1)	2.08(1)	1.96

Table 4. Comparative characteristics of bafertisite-like minerals

Mineral	Interlayer cations	Octahedra of *O*-layer	Octahedra of *H*-layer	Additional anions
Surkhobite (Tajikistan)	$Ba_{1.65}Ca_{1.2}Na_{0.8}K_{0.35}$	$Fe_4Mn_{3.7}Na_{0.3}$	$Ti_{3.2}(Zr, Nb)_{0.8}$	$F_4OH(OH, O)$
Perraultite (Canada) [11]	$Na_{2.02}Ba_{1.02}K_1$	$Mn_{7.73}Fe_{0.27}Mg_{0.03}$	$Ti_{2.08}Nb_{1.77}Zr_{0.02}\square_{0.13}$	$(OH)_{5.62}F_{0.78}H_2O_{0.6}$
Perraultite (Priazovye territory) [2]	$Na_{1.5}Ba_{1.25}K_{0.6}Ca_{0.5}\square_{0.15}$	$Mn_{4.7}Fe_{3.05}Zr_{0.15}\square_{0.1}$	$Ti_{3.84}Nb_{0.16}$	$(OH, F)_4(OH)_2$
Jinshajiangite (China) [12]	$(Na, Ca)_2(Ba, K)_2$	$(Fe, Mn)_8$	Ti_4	$(O, F, H_2O, OH)_6$
Bafertisite (China) [5]	Ba_4	Fe_8	Ti_4	$(OH)_8$
Hejtmanite (Kirgizia) [10]	Ba_4	Mn_8	Ti_4	$(OH)_8$

e.g., labuntsovites. The contacting vertices of Ti-octahedra are also observed in some other titanosilicate micas, Na- and K-containing astrophyllite and nafertisite [1]. In bussenite [6], nabalamprophyllite [7], K-baritolamprophyllite [8], and Ba-lamprophyllite [9], three-layer *H*–*O*–*H* slabs are isolated, and Ba, K, Sr, and Na cations are located in the common interslab space. In nabalamprophyllite (Fig. 3), Ba-lamprophyllite, and K-baritolamprophyllite, the heterolayers have no bulges, because the Ti atom is displaced from the octahedron center to the *O*-layer and no longer has any contact with the sixth vertex, whereas Ti-octahedra are reduced to five-vertex polyhedra.

Earlier, we established the existence of two Mn-bafertisite modifications [10], one of which (hejtmanite) is isostructural to bafertisite, and the other has a "protostructure" with $a/2 = 5.361$ Å and $b/2 = 6.906$ Å characteristic of the majority of minerals of the family of titanosilicate micas. The doubling of these parameters in bafertisite and hejtmanite is associated with the displacement of Ba atoms from their sites related by a pseudotranslation and a change in their coordination polyhedron. As in perraultite from Priazovye territory, the doubling of the *a* and *b* parameters in the surkhobite structure is explained by shifts of the interlayer cations and their positional ordering, including the redistribution of Fe, Mn, and Na cations in the *O*-layer. The distribution of large F and OH anions confirms the pseudoperiodicity of the framework: of the four F atoms, one is located at the vertex shared by two Ti-octahedra, while the shared vertices of (Ti, Zr, Nb)-octahedra are filled with OH-groups. The remaining F atoms are located at shared vertices of three (Fe, Mn)-octahedra of the *O*-layer. The doubling of the *c* parameter is pro-

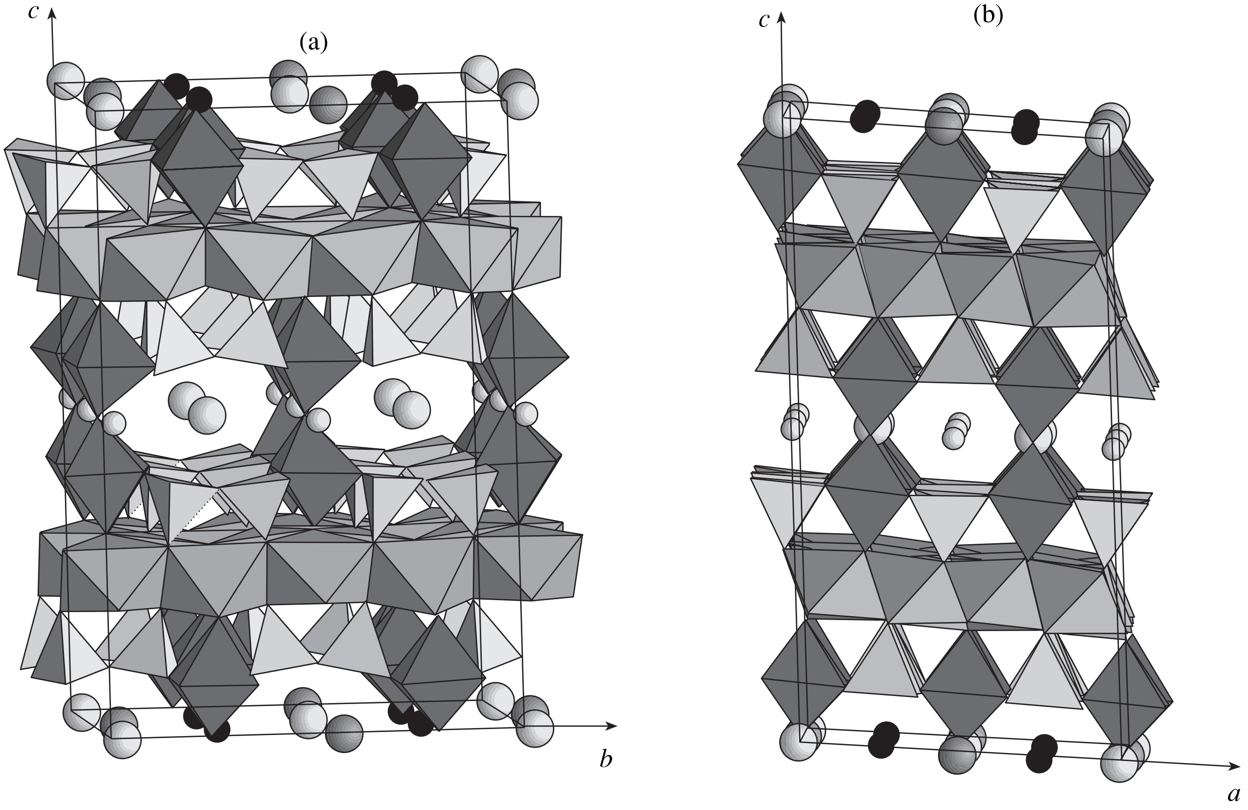

Fig. 1. Surkhobite structure; one can see channels along the (a) [100] and (b) [010] directions. Interlayer cations are shown by different circles: Ba, large white circles; K, large gray circles; (Na, Ca), small white circles; and Ca, small black circles.

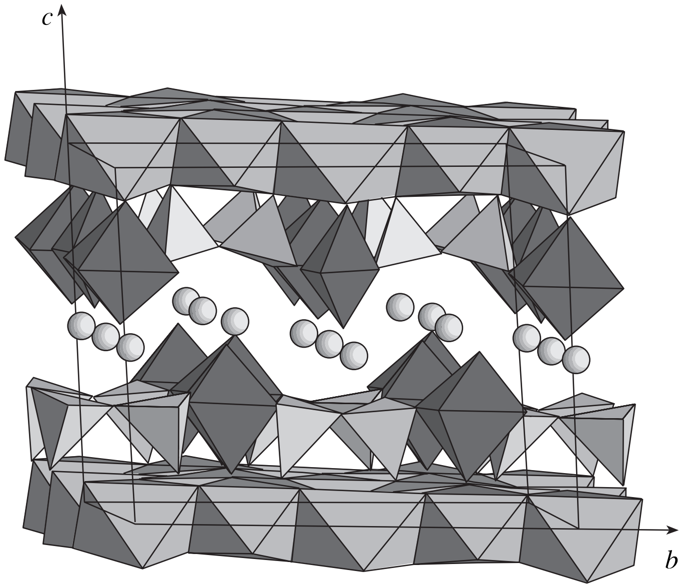

Fig. 2. Bafertisite structure; Ba atoms are shown by circles.

vided mainly by the mutual shift of the *H*–*O*–*H*-slabs; therefore two three-layer slabs become independent in the structure type of perraultite in comparison with only one in the bafertisite structure.

The distributions of intraframework cations over the sites in the structures of surkhobite and perraultite from Priazovye territory are somewhat similar (cations are ordered over different positions in the channels) but are

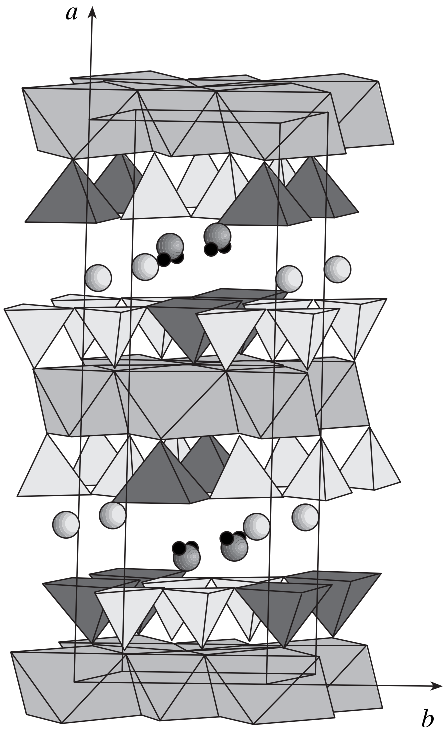

Fig. 3. Nabalamprophyllite structure. Ti-pentagons are shown in dark gray; Na atoms are shown by black circles, Ba atoms are shown by white circles, and (Ba + K) atoms are shown by gray circles.

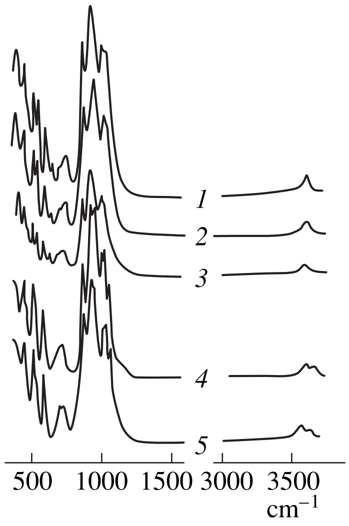

Fig. 4. IR spectra of (*1*) surkhobite, (*2*) jinshajiangite, (*3*) perraultite, (*4*) bafertisite, and (*5*) hejtmanite.

not identical. In surkhobite, Ca atoms fully occupy the sites in one small channel, whereas in another channel, the sites are occupied by both Ca and Na (the latter atoms prevail), and large Ba atoms fill one broad channel completely and another only partly with prevailing K atoms. In perraultite from Priazovye territory, Na atoms fully occupy the site in one narrow channel, whereas in another channel Na and Ca atoms are located; in surkhobite, Ba and K atoms are distributed in a similar way but with a change in the positions in the broad channels. Thus, the main structural feature of the new mineral is the ordering of Ca and Na resulting in the alternation of Ca- and Na-containing narrow channels. Unlike perraultite from Priazovye territory, sodium atoms in surkhobite are located not only in the channels but, together with Fe and Mn, in octahedra of the *O*-layer.

Thus, the family of Ba-containing titanosilicate micas (Table 4) includes minerals with various distributions of Ba, Na, Sr, Ca, and K atoms located either in the interslab space or in channels. Sodium atoms together with Fe, Mn, and Ti (delindeite [13]) are often incorporated into the octahedral layer. The octahedral layers in the groups of bafertisite and perraultite show continuous isomorphism between Mn and Fe^{2+}. In minerals with isolated slabs, i.e., in bafertisite, Ba-lamprophyllite, and K-baritolamprophyllite, Ba, Sr, and K atoms are disorderly distributed over the common interslab space. In bussenite and nabalamprophyllite, Ba, Na, K, and Sr cations are ordered over several positions, which results in lowering the symmetry in nabalamprophyllite from $C2/m$ to $P2/m$. The most complex ordering is observed in titanosilicate micas with combined *H*–*O*–*H*-slabs, i.e., in perraultite and its Ca–F-analogue, where Ba, K, Na, and Ca atoms occupy the sites in the channels. As a result, all three unit-cell parameters are doubled. Comparing surkhobite with perraultite and its analogues shows that the specimen studied differs from known perraultites and is characterized by high Ca, Ba, Fe, and F contents. Different structural and chemical characteristics of minerals of this family also manifest themselves in their IR spectra (Fig. 4). The IR spectra of surkhobite and perraultite and jinshajiangite are almost identical but differ from the spectra of bafertisite and its Mn-dominant analogue hejtmanite. Specifically, the IR spectra of bafertisite and perraultite have no band at 1056 cm^{-1} characteristic of the spectra of surkhobite and its analogues. Instead, there are additional bands at 633 and 532 cm^{-1}, which are most likely explained by valence vibrations of the Ti–(OH)–Ti and Ti–F–Ti bridges. Moreover, the band of O–H-valence vibrations in the spectra of surkhobite, perraultite, and jinshajiangite is not split, which can be explained by the high content of fluorine in the samples of these minerals.

ACKNOWLEDGMENTS

This study was supported by the Russian Foundation for Basic Research, project nos. 02-05-64080 and 02-05-06377, and by the federal program on Support of Prominent Scientists and Leading Scientific Schools, project no. 00-15-96633.

REFERENCES

1. G. Ferraris, G. Ivaldi, P. Khomyakov, *et al.*, Eur. J. Mineral. **8**, 241 (1996).
2. N. A. Yamnova, Yu. K. Egorov-Tismenko, and I. V. Pekov, Kristallografiya **43** (3), 439 (1998) [Crystallogr. Rep. **43**, 401 (1998)].
3. V. I. Andrianov, Kristallografiya **32** (1), 228 (1987) [Sov. Phys. Crystallogr. **32**, 130 (1987)].
4. N. Walker and D. Stuart, Acta Crystallogr. Sect. A: Found. Crystallogr. **39** (2), 158 (1983).
5. Guan Ya-Syan, V. I. Simonov, and N. V. Belov, Dokl. Akad. Nauk SSSR **190** (4), 831 (1970).
6. H. Zhou, R. K. Rastsvetaeva, A. P. Khomyakov, *et al.*, Kristallografiya **47** (1), 50 (2002) [Crystallogr. Rep. **47**, 43 (2002)].
7. R. K. Rastsvetaeva and N. V. Chukanov, Dokl. Akad. Nauk **368** (4), 492 (1999).
8. R. K. Rastsvetaeva, V. G. Evsyunin, and A. A. Konev, Kristallografiya **40** (3), 517 (1995) [Crystallogr. Rep. **40**, 472 (1995)].
9. R. K. Rastsvetaeva and M. D. Dorfman, Kristallografiya **40** (6), 1026 (1995) [Crystallogr. Rep. **40**, 951 (1995)].
10. R. K. Rastsvetaeva, R. A. Tamazyan, E. V. Sokolova, and D. I. Belakovskiĭ, Kristallografiya **36** (2), 354 (1991) [Sov. Phys. Crystallogr. **36**, 186 (1991)].
11. G. Y. Chao, Can. Mineral. **29**, 235 (1991).
12. H. Wenxing and F. Pinqiu, Geochemistry (China), No. 1, 458 (1982).
13. G. Ferraris, G. Ivaldi, D. U. Pushcharovsky, *et al.*, Can. Mineral. **39**, 1307 (2001).

Translated by E. Shtykova

Crystallography Reports, Vol. 48, No. 3, 2003, pp. 390–395. Translated from Kristallografiya, Vol. 48, No. 3, 2003, pp. 434–439.
Original Russian Text Copyright © 2003 by Khomchenko, Troyanchuk, Chobot, Szymczak.

STRUCTURE OF INORGANIC COMPOUNDS

Structural and Magnetic Phase Transformations in $La_{0.88}MnO_{3-x}$ Crystals

V. A. Khomchenko*, I. O. Troyanchuk*, A. N. Chobot*, and H. Szymczak**

** Institute of Solid State and Semiconductor Physics, National Academy of Sciences of Belarus, Minsk, 220072 Belarus*

e-mail: troyan@itttp.bas-net.by

*** Institute of Physics, Polish Academy of Sciences, Warsaw, 02-668 Poland*

Received May 29, 2002

Abstract—The crystal structure and elastic, magnetic, and transport properties of the $La_{0.88}MnO_{3-x}$ system are studied. It is established that, depending on the oxygen content at $x > 0.13$, the system is orbitally ordered by the $LaMnO_3$ type and consists of a mixture of orbitally ordered and disordered orthorhombic phases ($0.11 \le x \le 0.13$); at $x < 0.11$, the system is monoclinically distorted. The orbitally ordered samples show properties inherent in both antiferro- and ferromagnetics, whereas the orbitally disordered samples are ferromagnetics and possess extremely high magnetic resistance. Analysis of the structure and properties of the samples showed that no oxygen vacancies are formed in the $La_{0.88}MnO_{3-x}$ system. It is assumed that the excessive Mn^{3+} is incorporated into interstitials in the vicinity of lanthanum vacancies. *© 2003 MAIK "Nauka/Interperiodica".*

INTRODUCTION

The establishment of extremely high magnetic resistance (up to 10^5% at $T \sim 100$ K) [1, 2] in substituted lanthanum manganites with a perovskite structure gave rise to considerable interest in this class of compounds. Despite the long history of studies of lanthanum manganites, the question of the nature of the relation between their magnetic and electric properties is still open. Several models of exchange interactions were suggested to interpret the evolution of the magnetic state observed during doping and the metal–dielectric transition at the Curie point. The most widespread theory is that of double exchange, within which it is assumed that the antiferromagnetic–ferromagnetic transition proceeds via the formation of a noncollinear magnetic structure [3]. However, some facts indicate that a mixed magnetic state is formed in lanthanum manganites [4, 5]. This state is often interpreted in terms of electron and impurity phase separation [6, 7]. Goodenough [8, 9] took into account the effect of orbital ordering and assumed that the ferromagnetic properties of manganites are provided not only by double exchange but also by the specific character of superexchange interactions in the Mn^{3+}–O–Mn^{3+} and Mn^{3+}–O–Mn^{4+} systems containing Jan–Teller ions.

The initial compound of composition $LaMnO_3$ is an *A*-type antiferromagnetic [10] with $T_N = 140$ K and a Dzyaloshinskii-exchange-induced weak ferromagnetic moment [11]. The transition to the ferromagnetic state in this compound proceeds either via the replacement of lanthanum ions by divalent alkali earth ions or via oxidation of stoichiometric samples (to which most publications on this subject are dedicated).

Comparatively recently, it was shown that ferromagnetic ordering in lanthanum manganites can also proceed in another way associated with the deficit of La^{3+} cations [12]. Lanthanum manganites of different compositions but with the same deficit of lanthanum ions show different properties [13–15]. In this connection, it seems to be expedient to study the properties of La-deficient samples depending on their oxygen content using the analogy with the $LaMnO_{3+\delta}$ system.

In the present study, we established that, depending on the oxygen content, the $La_{0.88}MnO_{3-x}$ system can be in different orbital and magnetic states, with orbital order–orbital disorder and antiferromagnetic–ferromagnetic transitions taking place simultaneously via the formation of two-phase states.

EXPERIMENTAL

A polycrystalline $La_{0.88}MnO_{2.87}$ sample was synthesized by the conventional ceramic technology. After a preliminary 1-h annealing of a mixture of La_2O_3 and Mn_2O_3 oxides at 1000°C, the product thus obtained was ground, pressed into tablets, annealed for five hours in air at $T = 1550$°C, and, finally, cooled at a rate of 100 °C/h. The oxygen content in this compound was determined by gravimetric analysis by decomposing the compound into simple La_2O_3 and MnO oxides. In order to avoid possible chemical inhomogeneity, the oxidation and reduction of the samples were performed in evacuated sealed quartz ampules at T = 900°C for rather long time. The reductant was a metallic tantalum, and the oxidant was MnO_2.

The X-ray diffraction analysis was performed on a DRON-3 diffractometer (CrK_α radiation). Specific magnetization was measured on a commercial OI-3001 vibrating-coil magnetometer. The electrical conductivity of the sample was measured by the four-contact method. The elastic properties were studied by the resonance method on rodlike samples 60 mm in length and 6 mm in diameter in the acoustic frequency range.

RESULTS

According to the X-ray diffraction data obtained, the unit cell ($c/\sqrt{2} < a < b$, sp. gr. *Pbnm*.) of the $La_{0.88}MnO_{3-x}$ samples (x = 0.18, 0.16, and 0.14) is characterized by O'-type (orthorhombic) distortion. With an increase in the oxygen content, the unit-cell volume decreases, which is explained by the transition of manganese ions from the trivalent into the tetravalent state. The X-ray diffraction patterns of the $La_{0.88}MnO_{2.87}$ and $La_{0.88}MnO_{2.89}$ samples showed not only the reflections of the orthorhombic O' lattice but also some additional lines. The calculation of the respective diffraction patterns leads to the assumption that the $La_{0.88}MnO_{3-x}$ samples (x = 0.13 and 0.11) are characterized by the coexistence of the O-($c/\sqrt{2} \approx a < b$) and O'-orthorhombic phases (Fig. 1). It should be indicated that, according to Goodenough [8], O'-type orthorhombic distortions in manganites are provided by orbital ordering, whereas the orthorhombic O structure corresponds to the orbitally disordered state. The $La_{0.88}MnO_{3-x}$ samples with x = 0.09 and 0.07 can also be considered in the monoclinic system, sp. gr. $I2/a$.

Figure 2 shows the temperature dependence of the Young's modulus for the samples with different oxygen content (the squared resonance frequency is directly proportional to the Young's modulus). The most reduced $La_{0.88}MnO_{2.82}$ sample shows a well-pronounced orbital order–orbital disorder transition in the vicinity of 660 K. In this region, there is also a temperature hysteresis in the vicinity of 12 K. With an increase in the oxygen content within the concentration limits of the orthorhombic phase, the temperature of the phase transition associated with the violation of the orbital order gradually decreases and the transition is spread over the temperature. The monoclinic samples with x = 0.09 and 0.07 show a pronounced minimum of the Young's modulus at 656 K. Like the sample with x = 0.18, pronounced attenuation was observed in the vicinity of this minimum.

Study of the magnetic properties revealed a correlation between the type of magnetic state and the crystal structure. The field dependences of magnetization measured in the $La_{0.88}MnO_{3-x}$ system at a temperature of 5 K are shown in Fig. 3. The $La_{0.88}MnO_{2.82}$ sample with the minimum oxygen content has a rather low spontaneous magnetic moment (about 0.09 μ_B per manganese ion) and a very high coercive force value (15 kOe). The temperature dependence of magnetization for this sample is shown in Fig. 4a. A sharp transition to the paramagnetic state is observed at 140 K. The application of the external magnetic field practically does not change the phase-transformation temperature. An increase in the oxygen content within the concentration range of the orthorhombically distorted O' samples decreases the Néel point, increases the spontaneous magnetization, and reduces the magnetic anisotropy. Thus, the spontaneous magnetization for the samples with x = 0.14 equals 0.6 μ_B/Mn, the coercive force equals 3 kOe, and the temperature of magnetic ordering equals 123 K (Figs. 4b, 4c). In this case, the transition to the paramagnetic state is still well pronounced. As in the case of the sample with x = 0.18, the application of an external magnetic field only slightly affects the temperature of the transition to the paramagnetic state.

The magnetic state of the samples with coexisting O and O' phases dramatically changes. In the sample with x = 0.13, two magnetic phase transitions take place at the temperature T_N = 120 K and below the temperature T_C = 250 K (Figs. 4b, 4c). The magnetic phase transition that begins below 250 K is considerably spread over the temperature, whereas the transition at T_N = 120 K is more clearly pronounced. The slight difference between ZFC and FC magnetization in the high-temperature magnetic phase is characteristic of weakly anisotropic magnetics. The magnetic anisotropy considerably increases below T_N = 120 K. Within the concentration range of the coexistence of the O and O' phases, spontaneous magnetization dramatically increases (2.9 μ_B/Mn for $La_{0.88}MnO_{2.89}$), whereas the coercive force decreases (Fig. 3).

The maximum spontaneous magnetization (3.3 μ_B) close to its theoretical value expected for a collinear ferromagnetic is observed for the monoclinically distorted compound $La_{0.88}MnO_{2.91}$ (Fig. 3). The run of the FC and ZFC curves indicates that the monoclinic samples with x = 0.09 and 0.07 undergo the paramagnetic–ferromagnetic transition at 233 K (Figs. 4b, 4c). Unlike the situation in the orthorhombic O' samples, the application of the external fields in this case noticeably shifts the transition to the high-temperature range.

Study of electric and transport properties shows that in the $La_{0.88}MnO_{3-x}$ compounds ($0.11 \le x \le 0.18$), the electric conductivity ρ depends on temperature, which is characteristic of semiconductors. Figure 5 shows the temperature dependence of $\rho(T)$ and magnetoresistance $MR(T)$ in the $La_{0.88}MnO_{2.89}$ sample with two coexisting orthorhombic phases. At the temperatures corresponding to the magnetic phase transformations, the $MR(T)$ curve (where $MR = \{[\rho(H = 9\text{ kOe})\text{-}\rho(H = 0)]/\rho(H = 0)\}100\%$) shows some magnetoresistance maxima.

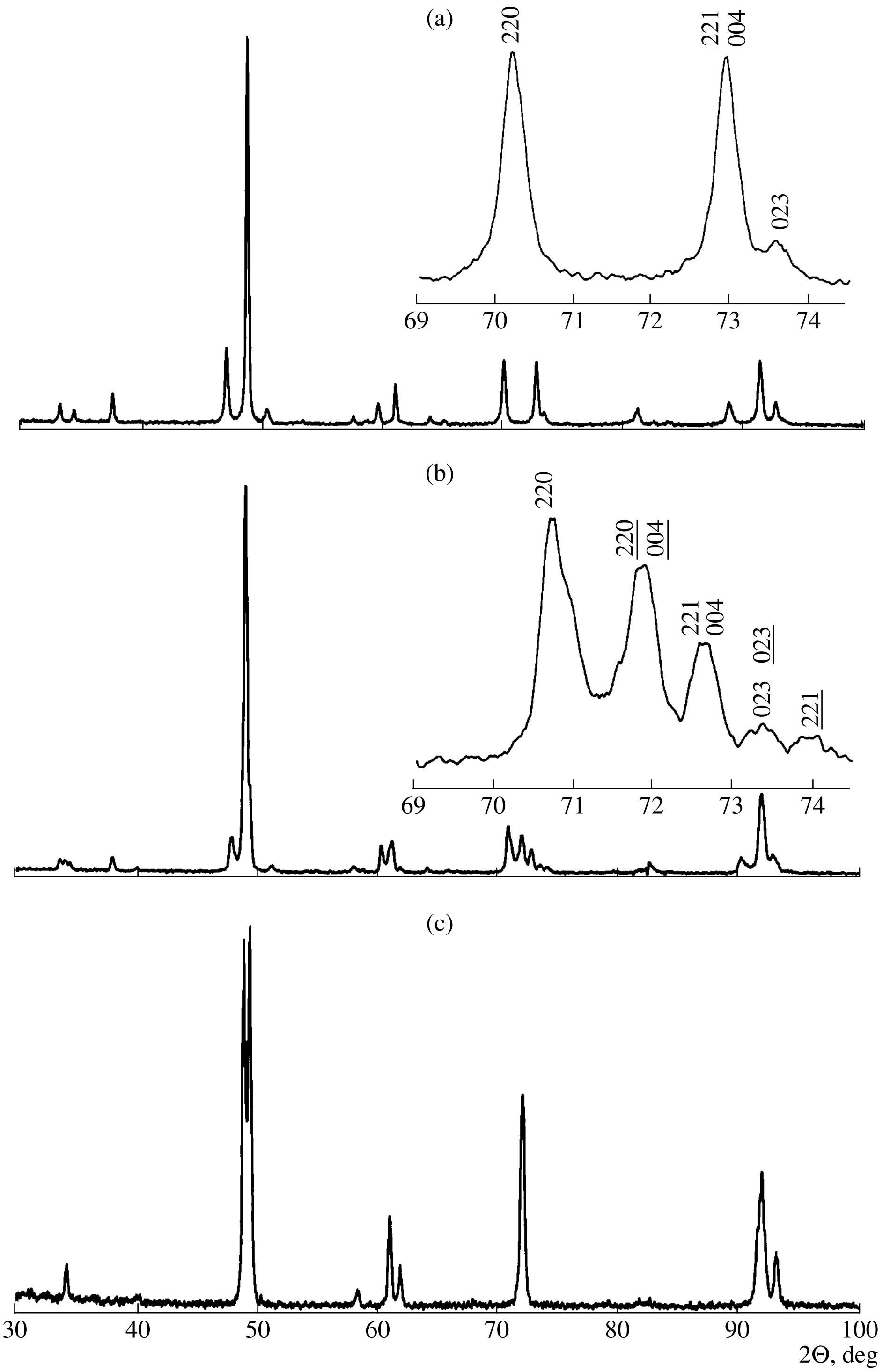

Fig. 1. X-ray diffraction patterns of the (a) $La_{0.88}MnO_{2.82}$, (b) $La_{0.88}MnO_{2.89}$, and (c) $La_{0.88}MnO_{2.93}$ samples. In the insets: some parts of the X-ray diffraction patterns on a larger scale. The Miller indices of the reflections of the orthorhombic *O* phase are underlined.

With an increase in the oxygen content, the magnetoresistance maximum in the low-temperature range decreases, whereas the high-temperature magnetoresistance maximum dramatically increases. The monoclinically distorted samples undergo the transition to the metal state in the vicinity of T_C.

DISCUSSION

First, consider the properties of the strongly reduced samples. It is well known that the stoichiometric lanthanum manganite $LaMnO_3$ is a weak ferromagnetic with a Néel temperature of ~140 K [16]. This sample shows antiferromagnetic distortional cooperative ordering of the d_{z^2} orbitals, which looks like a first-order phase transition at a temperature of about 700 K. The properties of the strongly reduced $La_{0.88}MnO_{2.82}$ sample, which contains no tetravalent manganese ions, are similar to the properties of the stoichiometric $LaMnO_3$. The unit-cell parameters of both compounds are rather close, and they also have close values of spontaneous magnetization and temperature of magnetic (Fig. 3a) and orbital (Fig. 2) ordering. On the other hand, the reduced $La_{0.7}Ca_{0.3}MnO_{2.85}$ sample, which does not contain Mn^{4+} ions, is a spin glass with a temperature of magnetic-moment freezing of about 40 K, which shows no signs of cooperative orbital ordering [17]. This is explained by the fact that the formation of oxygen vacancies changes the nature of the exchange interactions between manganese ions and removes orbital ordering [17]. Indeed, the d_{z^2} orbitals of Mn^{3+} ions in the pentahedral coordination are usually directed toward oxygen vacancies, which is inconsistent with the type of orbital ordering in $LaMnO_3$. Therefore, we assumed that no oxygen vacancies could be formed in $La_{0.88}MnO_{2.82}$. Then the question arises as to how the charge in $La_{0.88}MnO_{2.82}$ is compensated. In principle, manganese can be in a divalent state. A Mn^{2+} ion has a much larger radius that a Mn^{3+} ion, and, therefore, it is possible to assume that it can substitute La^{3+} ions. In this case, the electroneutrality demands the existence of the equivalent number of Mn^{4+} ions, which is inconsistent with the crystal structure and the magnetic and elastic properties of the compound. Therefore, we assumed that all the manganese ions in $La_{0.88}MnO_{2.82}$ are in the trivalent state. The charge compensation most probably occurs due to the incorporation of excessive manganese into interstitials in the vicinity of lanthanum vacancies and the formation of linear chains of lanthanum vacancies alternating with the interstitial Mn^{3+} ions.

With an increase in the oxygen content up to $x = 0.14$, the temperatures of magnetic and orbital ordering decrease, whereas the spontaneous magnetization increases (Figs. 2–4). Such a behavior, characteristic of $La_{1-x}A_xMnO_3$ manganites (A = Ca, Sr, and Ba, $x \leq 0.05$), is explained by the formation of either a noncollinear magnetic structure [3] or a ferromagnetic phase in which the charge-carrier concentration is higher than the charge-carrier concentration averaged over the sample [6]. Our measurements do not allow us to distinguish between these two possibilities; however, it should be noted that the critical temperatures characteristic of the ferromagnetic and antiferromagnetic components are practically the same.

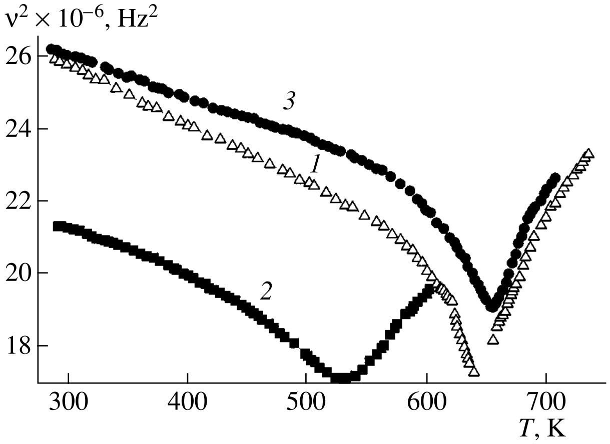

Fig. 2. Temperature dependence of the squared resonance frequency (proportional to the Young's modulus) of the (*1*) $La_{0.88}MnO_{2.82}$, (*2*) $La_{0.88}MnO_{2.87}$, and (*3*) $La_{0.88}MnO_{2.93}$ samples.

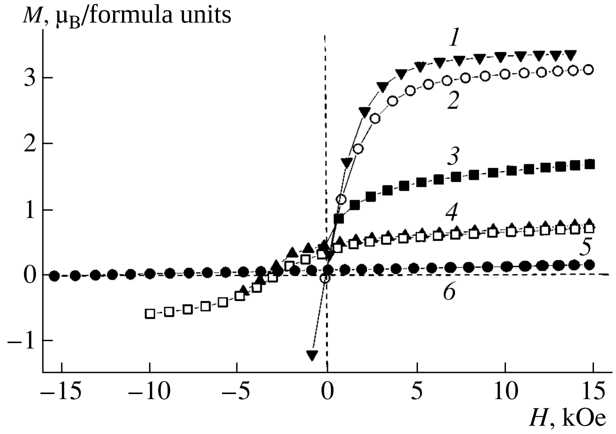

Fig. 3. Magnetization of the $La_{0.88}MnO_{3-x}$ samples as a function of the applied magnetic field at a temperature of 5 K. The compositions x are: (*1*) 0.09, (*2*) 0.11, (*3*) 0.13, (*4*) 0.14, (*5*) 0.16, and (*6*) 0.18.

The samples in the concentration range $0.11 \leq x \leq 0.13$ undergo two well-pronounced magnetic transitions (Figs. 4a–4c). Taking into account the two-phase nature of the samples, the low-temperature magnetic transition should be attributed to the ordered antiferromagnetic phase, whereas the weakly anisotropic high-temperature phase should be considered an orbitally disordered ferromagnetic phase, because it is well known [5, 8] that orbital disordering leads to sign reversal in exchange interactions. It should also be noted that the two-phase nature of the samples in the concentration range, where the orbital or charge-ordered states transit to the disordered states, is the consequence of the martensite character of these phase transitions [18, 19]. It seems that the transient state of Jan–Teller

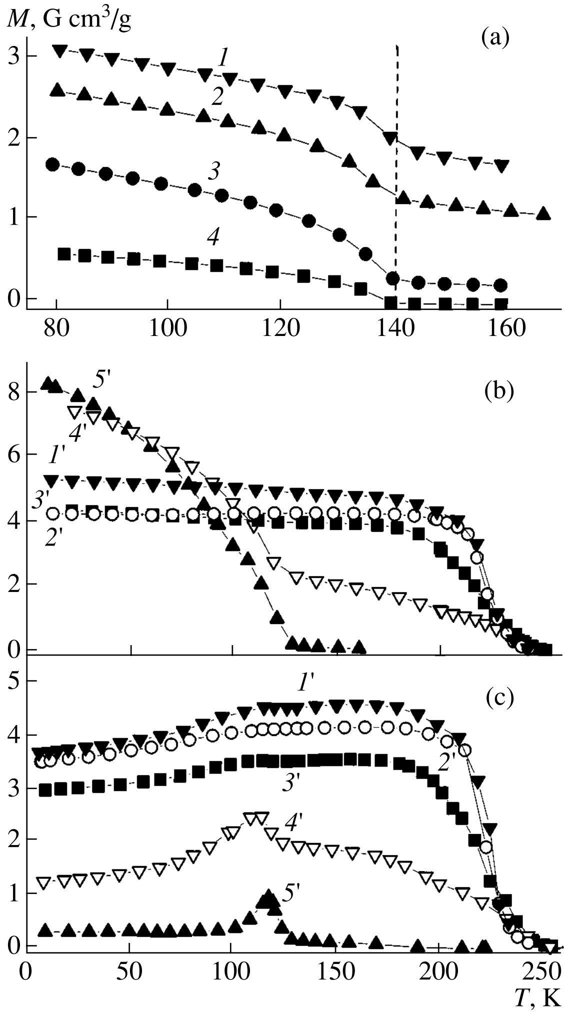

Fig. 4. Temperature dependence of magnetization of $La_{0.88}MnO_{2.82}$ samples in various magnetic fields H for the $La_{0.88}MnO_{3-x}$ samples ($0.07 \le x \le 0.14$) in the (a) heating mode upon cooling in a 100-Oe field (FC) and (c) heating upon cooling in the absence of the field (ZFC). The field H, kOe: (*1*) 14.8, (*2*) 10.0, (*3*) 2.0, (*4*) 0.02; the compositions x: (*1*') 0.07, (*2*') 0.09, (*3*') 0.11, (*4*') 0.13, (*5*') 0.14.

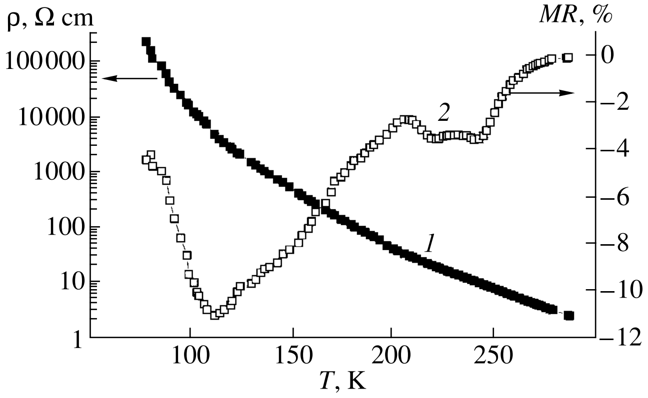

Fig. 5. (*1*) Resistivity ρ and (*2*) magnetic resistivity *MR* of $La_{0.88}MnO_{2.89}$ as functions of temperature.

glass type in lanthanum manganites is rather unstable, and the system shows a tendency to transit to the two-phase state, which is stabilized by the fields of elastic stresses and defects. In two-phase samples, these phases have different orbital or charge ordering and slightly different charge-carrier concentrations and chemical compositions. The charge carriers in the disordered phase become rather mobile because of the removal of the Jan–Teller distortions.

The monoclinic samples consist of only one phase and are characterized by a well-pronounced transition to the paramagnetic state (Figs. 4b, 4c). The established relation between the magnetic state and conductivity and the strong dependence of the ferromagnetic order on the applied magnetic field result in extremely high magnetoresistance at temperatures slightly lower than room temperature.

It is generally accepted [12] that the nonstoichiometry with respect to oxygen in $LaMnO_{3+\delta}$ is associated with the formation of an equivalent number of lanthanum and manganese vacancies. In $La_{0.88}MnO_{3-x}$, one observes nonstoichiometry with respect to both cations and anions. However, comparing the properties of $LaMnO_3$ and $La_{0.88}MnO_{2.82}$, it is possible to assume that the compounds that are nonstoichiometric with respect to cations also have an oxygen framework and the manganese ions do not transit to the divalent state. The most probable mechanism of nonstoichiometry is the formation of extended defects. To refine this mechanism, one has study the problem in more detail using high-resolution electron microscopy. Both $LaMnO_{3+\delta}$ and $La_{0.88}MnO_{3-x}$ have three intervals of oxygen concentration and different types of crystal structure. However, the temperature of ferromagnetic ordering in the cation-nonstoichiometric system is much higher, and, unlike $LaMnO_{3+\delta}$, the transition to the metal state occurs in the vicinity of T_C. This difference follows from the fact that in the cation-nonstoichiometric system, no manganese vacancies are formed in the *B* sublattice of the perovskite structure ABO_3. Another difference consists in the fact that the strongly oxidized samples of the cation-deficient lanthanum manganite are monoclinic, whereas the strongly oxidized samples of $LaMnO_{3+\delta}$ are rhombohedral. We believe that the high-temperature phase transition results in a change of the monoclinic symmetry to rhombohedral (Fig. 2).

CONCLUSION

The results obtained lead to the conclusion that the magnetic state of the samples studied correlates with the type of their crystal structure. Thus, the orbitally ordered samples manifest properties characteristic of antiferromagnetics, whereas the loss of orbital ordering results in antiferromagnetism. The antiferromagnetic–ferromagnetic and orbital order–orbital disorder transitions take place simultaneously via the formation of two-phase states. Both phases are determined by the type of the orbital order, whereas their charge-carrier concentrations are slightly different. The charge carriers become mobile after the removal of the cooperative static Jan–Teller effect.

The obvious minimum value of the Young's modulus in the monoclinic samples indicates that, at the temperature of about 650 K, this type of unit-cell distortion does not exist any more and the sample acquires rhombohedral symmetry.

Moreover, analysis of the crystal structure and the magnetic and elastic properties of the samples allow us to state that no oxygen vacancies are formed in the $La_{0.88}MnO_{3-x}$ system.

ACKNOWLEDGMENTS

This study was supported by the Foundation for Basic Research of the Republic of Belarus, project no. F00-223, and the Polish Committee on Science, project no. 5 P03B 01620.

REFERENCES

1. M. McCormack, S. Jin, T. H. Tiefel, *et al.*, Appl. Phys. Lett. **64**, 3045 (1994).
2. S. Jin, T. H. Tiefel, M. McCormack, *et al.*, Science **264**, 413 (1994).
3. P. G. De Gennes, Phys. Rev. **118**, 141 (1960).
4. G. Allodi, R. De Renzi, G. Guidi, *et al.*, Phys. Rev. B **56**, 6036 (1997).
5. I. O. Troyanchuk, Zh. Éksp. Teor. Fiz. **102**, 251 (1992) [Sov. Phys. JETP **75**, 132 (1992)].
6. E. L. Nagaev, Phys. Rep. **346**, 387 (2001).
7. E. Dogatto, T. Hotta, and A. Moreo, Phys. Rep. **344**, 1 (2001).
8. J. B. Goodenough, A. Wold, R. J. Arnott, and N. Menyuk, Phys. Rev. **124**, 373 (1961).
9. J.-S. Zhou, H. Q. Yin, and J. B. Goodenough, Phys. Rev. B **63**, 184423 (2001).
10. E. O. Wollan and W. C. Koehler, Phys. Rev. **100**, 545 (1955).
11. I. E. Dzyaloshihskii, J. Solid State Chem. **4**, 241 (1958).
12. J. A. M. van Roosmalen, E. H. P. Cordfunke, R. B. Helmholdt, and H. W. Zandbergen, J. Solid State Chem. **110**, 100 (1994).
13. B. C. Hauback, H. Fjellag, and N. Sakai, J. Solid State Chem. **124**, 43 (1996).
14. J. Topfer and J. B. Goodenough, Chem. Mater. **9**, 1467 (1997).
15. A. Maignan, C. Michel, M. Hervieu, and B. Raveau, Solid State Commun. **101**, 277 (1997).
16. G. Matsumoto, J. Phys. Soc. Jpn. **29**, 606 (1970).
17. I. O. Troyanchuk, S. V. Trukhanov, H. Szymczak, *et al.*, Zh. Éksp. Teor. Fiz. **120**, 183 (2001) [JETP **93**, 161 (2001)].
18. N. V. Kasper and I. O. Troyanchuk, J. Phys. Chem. Solids **57**, 1601 (1996).
19. V. Podzorov, B. G. Kim, V. Kiryukhin, *et al.*, Phys. Rev. B **64**, 140406 (2001).

Translated by L. Man

Crystallography Reports, Vol. 48, No. 3, 2003, pp. 396–400. Translated from Kristallografiya, Vol. 48, No. 3, 2003, pp. 440–444.
Original Russian Text Copyright © 2003 by Beskrovnyĭ, Vasilovskiĭ, Belushkin, Smirnov, Balagurov, Martinez Sarrion, Mestres, Herriaz.

STRUCTURE
OF INORGANIC COMPOUNDS

Structural Study of New Compound $Bi_{2.53}Li_{0.29}Nb_2O_9$ by the Powder Neutron Diffraction Method

A. I. Beskrovnyĭ*, S. G. Vasilovskiĭ*, A. V. Belushkin*, L. S. Smirnov*, A. M. Balagurov*, M. L. Martinez Sarrion, L. Mestres**, and M. Herriaz****

** Joint Institute of Nuclear Research, p/ya 79, Dubna, Moscow oblast, 141980 Russia*
e-mail: vassg@nf.jinr.ru
*** Laboratory of Inorganic Chemistry, Barcelona University, Barcelona, 08028 Spain*

Received November 19, 2001; in final form, July 1, 2002

Abstract—A new compound of composition $Bi_{2.53}Li_{0.29}Nb_2O_9$ was synthesized in the course of the search for new materials with high ionic conductivity. Its crystal structure was determined from the neutron diffraction data. The new compound $Bi_{2.53}Li_{0.29}Nb_2O_9$ is crystallized in the orthorhombic system, sp. gr. $Cmc2_1$, and unit-cell parameters a = 24.849(1) Å, b = 5.4536(3) Å, and c = 5.4619(2) Å at T = 290 K (a = 24.843(2) Å, b = 5.4456(5) Å, and c = 5.4546(5) Å at T = 10 K). Within the temperature range 10–870 K, no structural phase transitions were revealed. The atomic coordinates and the thermal factors in the isotropic approximation were refined by the Rietveld method at 290 and 10 K. The data obtained were analyzed based on the calculated local balance of bond strengths. © *2003 MAIK "Nauka/Interperiodica".*

INTRODUCTION

The Aurivillius phases form the group of Bi-based layer compounds whose general formula can be represented as $(Bi_2O_2)^{2+}(A_{m-1}B_mO_{3m+1})^{2-}$, where A are cations with large radii (Bi^{3+}, Pb^{2+}, Ba^{2+}, Ca^{2+}, Sr^{2+}, Na^+, K^+), B are cations with small radii (Mo^{6+}, Nb^{5+}, Ta^{5+}, Ti^{4+}, Fe^{3+}), and m = 1, 2, 3, 4, 5, 8 [1, p. 105]. For example, the Bi_2MoO_6 compound corresponds to m = 1; the $BaBi_2Nb_2O_9$, $Bi_4Ti_3O_{12}$, and $SrBi_4Ti_4O_{15}$ compounds correspond to m = 2, 3, and 4. The $(A_{m-1}B_mO_{3m+1})^{2-}$ fragment located between the $(Bi_2O_2)^{2+}$ layers normal to the a axis of the unit cell has a perovskite-like structure (hereafter it is referred to as a perovskite-like layer). The $(Bi_2O_2)^{2+}$ layer consists of planes of Bi and O atoms forming BiO_4 pyramids (fluorite-type structure).

Denoting the perovskite-like layer of the minimum thickness (m = 1) by P and the (Bi_2O_2)-layer by B, we can describe the above compounds as $\ldots BP_mBP_m\ldots$. The neighboring layers are displaced with respect to one another along the [011] direction by a half-diagonal of the unit-cell base, which results in a doubling of the a period (Fig. 1) [1, p. 104].

Beginning with the first study performed by Smolenskiĭ *et al.* [2], the Aurivillius phases were synthesized and studied as possible ferroelectrics with high Curie temperatures, which, in particular, strongly depend on the radius of the cations located in the A and B positions [3]. The interest in the ferroelectrics of this family in recent years is explained by their possible participation in the synthesis of composite film systems. Thus, of great interest is the possible use of thin $SrBi_2Nb_2O_9$ films in energy-independent memory cells [4] and the design of devices for the processing and storage of information that would make provision for rewriting and permanent storage.

The Aurivillius phases are also studied as potential ionic conductors that can be used, e.g., in the manufacture of lithium accumulators. A number of $Li_{0.5-3x}B_{0.5+x}TiO_3$ compounds (B = La, Pr, Nd) with a perovskite structure and high ionic conductivity were recently synthesized in [5]. In these compounds, one position is occupied by $(0.5 - 3x)$ Li cations and $(0.5 + x)$ B cations, which results in the formation of $(2x)$ vacancies.

We synthesized a new Aurivillius phase of composition $Bi_{2.53}Li_{0.29}Nb_2O_9$ with m = 2 (BLNO) in which a perovskite-like $(Bi_{0.53}Li_{0.29}Nb_2O_7)^{2-}$-layer structurally similar to a $Li_{0.5-3x}B_{0.5+x}TiO_3$ layer is located between the $(Bi_2O_2)^{2+}$ layers.

The present study was undertaken with the aim of determining the crystal structure of BLNO by the neutron powder diffraction method.

EXPERIMENTAL

Synthesis. The compound $Bi_{2.5+x}Li_{0.5-3x}Nb_2O_9$ was synthesized by the method of solid-phase reaction (traditionally used for synthesis of the Aurivillius phases) at the Laboratory of Inorganic Chemistry of the University of Barcelona, Spain. The starting materials were Bi_2O_3, Li_2CO_3, and Nb_2O_5 (6.8555, 3.0795, and 0.1625 g, respectively). The starting materials were mixed in acetone; the mixture was dried and heated for

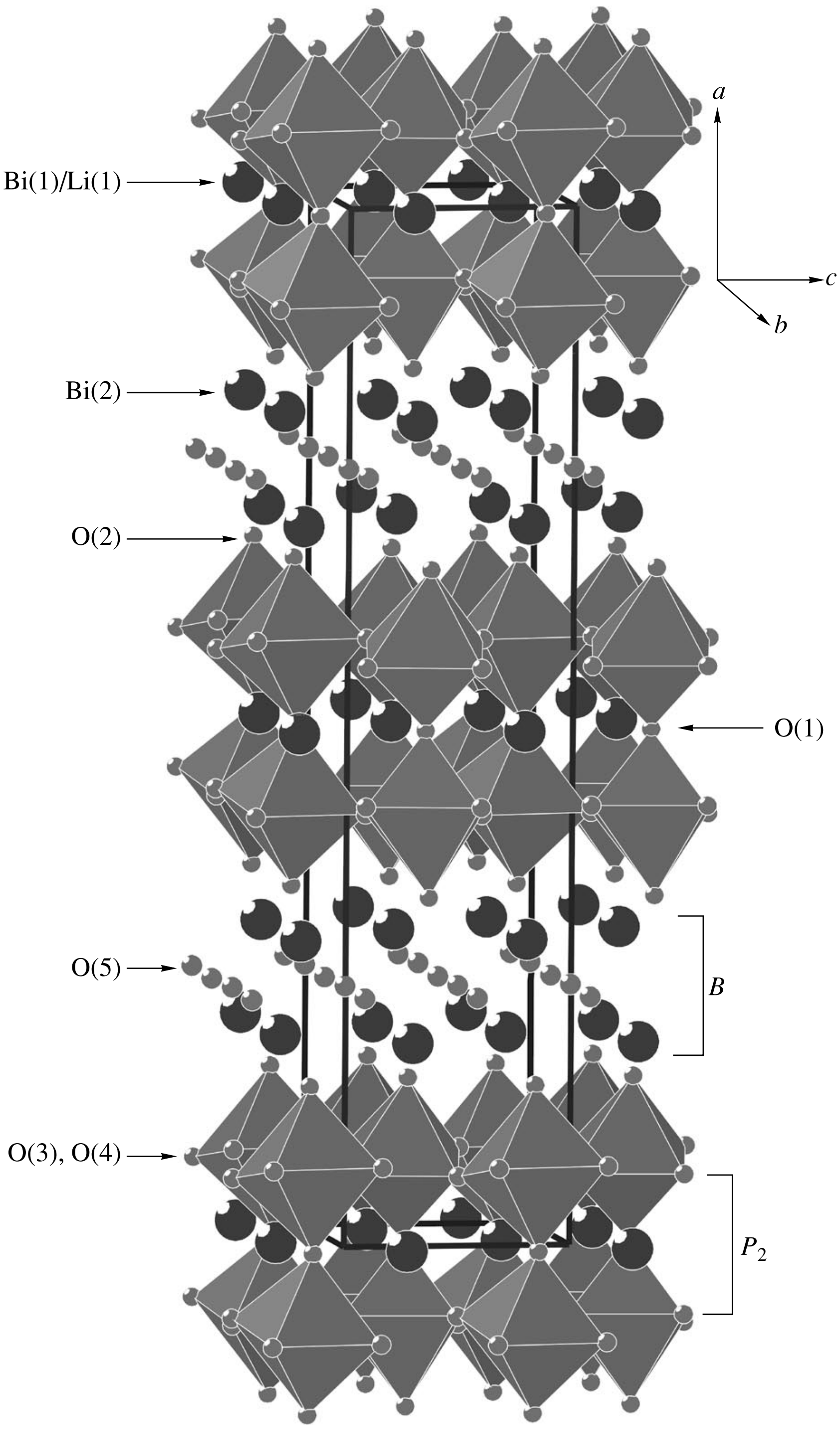

Fig. 1. Crystal structure of $Bi_2(Bi_{0.53}Li_{0.29})Nb_2O_9$; B is the Bi_2O_2 layer, and P_2 is the perovskite-like $Bi_{0.53}Li_{0.29}Nb_2O_7$ layer. Nb atoms are located inside the octahedra.

three hours at 920 K. Upon grinding the mixture in an agate mortar, the powder thus obtained was pressed into a tablet, which was annealed for 4 h at 1225 K. Upon the second cycle of grinding and pressing, the new tablet was annealed for 12 h at 1300 K and then for 10 h at 1370 K.

The content of the constituent elements was determined by inductively coupled plasma mass spectrometry as Bi 2.53(4), Li 0.29(2), Nb 2.0, and O 9.0 atoms per formula unit. The calculated Li content at a Bi concentration of 2.53 (x = 0.03) equals 0.41; in other words, the structure is deficient in Li cations.

Table 1. Atomic coordinates and thermal parameters refined by the Rietveld method at 290 K (upper lines) and 10 K (lower lines) and the occupancy *g* of the crystallographic positions

Atom	ι	*y*	*z*	*g*	U_{iso}, Å^2
Bi(1)	0	0.239(2)	0.225(2)	0.215	0.0562(3)
	0	0.228(3)	0.274(3)		0.0286(3)
Li(1)	0	0.241(8)	0.224(7)	0.145	0.0562(3)
	0	0.236(5)	0.285(6)		0.0286(3)
Bi(2)	0.2998(1)	0.7389(4)	0.2513(7)	1.0	0.0671(3)
	0.2991(7)	0.7484(7)	0.258(1)		0.0241(1)
Nb	0.415(1)	0.2552(7)	0.272(1)	1.0	0.0494(1)
	0.4159(1)	0.254(1)	0.281(1)		0.0078(1)
O(1)	0	0.702(1)	0.329(1)	0.5	0.0601(2)
	0	0.709(1)	0.345(1)		0.0185(1)
O(2)	0.341(1)	0.310(1)	0.303(1)	1.0	0.0517(1)
	0.342(1)	0.306(1)	0.306(1)		0.0149(2)
O(3)	0.415(1)	0.051(1)	0.592(1)	1.0	0.0595(2)
	0.413(1)	0.054(1)	0.601(1)		0.0175(2)
O(4)	0.432(1)	0.531(1)	0.506(1)	1.0	0.0732(1)
	0.435(2)	0.531(1)	0.511(1)		0.0162(2)
O(5)	0.750(1)	0.506(1)	0.516(1)	1.0	0.0408(1)
	0.751(2)	0.505(1)	0.513(1)		0.0155(2)
R_{exp}(%)			8.3 7.7		
R_{wp}(%)			7.3 6.1		
χ^2			6.6 3.2		

X-ray diffraction study. The phase analysis of the samples was made on a Siemens D-500 diffractometer (CuK_α radiation). No additional phases or traces of the initial components was revealed. The diffractometer was calibrated using the Si standard.

Neutron diffraction study. The neutron diffraction experiment was performed on a pulsed IBR-2 reactor using two diffractometers: DN-2 (time-of-flight neutron diffractometer) and FDVR (high-resolution Fourier diffractometer), which was dictated by a large unit-cell volume of BLNO. The neutron diffraction patterns were measured on a DN-2 diffractometer (which is a conventional time-of-flight diffractometer with the resolution determined by the width of the pulse from a neutron source, $\Delta d/d = 0.01$) in the range of the interplanar spacings d_{hkl} from 1 to 12 Å. To improve the resolution of the FDVR diffractometer, we used a fast Fourier chopper and the correlation method for recording diffraction spectra [6]. The spectra recorded on the FDVR diffractometer covered a relatively narrow range of d_{hkl} values: from 1 to 3.2 Å; however, the instrumental resolution was rather high $\Delta d/d = 0.001$.

EXPERIMENTAL DATA PROCESSING

As was shown in [7, 8], the crystal structures of the Aurivillius phases $Bi_2AB_2O_9$ (*A* = Sr and Ca; *B* = Nb and Ta) determined by the X-ray and neutron powder diffraction methods are described by the orthorhombic sp. gr. $Cmc2_1$, whereas the structure of the $Bi_2BaNb_2O_9$ phase is described by the tetragonal sp. gr. *I*4/*mmm*. The diffraction peaks on the neutron diffraction pattern from BLNO were indexed using the AUTOX program [9]. The positions of all the diffraction peaks were described within the orthorhombic sp. gr. $Cmc2_1$ (lattice parameters $a = 24.849(1)$ Å, $b = 5.4536(3)$ Å, and $c = 5.4619(2)$ Å, $V = 740.177(2)$ Å^3). The calculated density of BLNO is $\rho_{calcd} = 6.772$ g/cm^3.

The BLNO crystal structure was refined by the Rietveld method using the MRIA program [10]. The starting coordinates of the refinement were the atomic coordinates determined for the $Bi_2(Sr, Ca)Nb_2O_9$ structures [7].

Earlier studies of the Aurivillius phases show that the valence of bismuth in (Bi_2O_2)- and perovskite-like layers is 3+ [7]. In this case, lithium atoms in the BLNO structure can be located in both perovskite-like and (Bi_2O_2)-layers. A possible variant of the replacement of bismuth by lithium in these layers was checked in the course of the structure refinement. The lithium occupancy in a (Bi_2O_2) layer was calculated to be zero.

Thus, the data obtained show that the replacement of a divalent *A* ion by a trivalent bismuth and monovalent lithium in the $Bi_2ANb_2O_9$ structure results in the formation of structural vacancies in the perovskite-like layer.

The positional parameters of atoms in the structure and the thermal factors in the isotropic approximation were determined at two temperatures (290 and 10 K). The results of the structure refinement are listed in Table 1 and shown in Fig. 2. The unit-cell parameters are: $a = 24.849(1)$ Å, $b = 5.4536(3)$ Å, and $c = 5.4619(2)$ Å at $T = 290$ and $a = 24.843(2)$ Å, $b = 5.4456(5)$ Å, and $c = 5.4546(5)$ Å at 10 K.

The coordinates obtained were used to calculate the rotation angles of oxygen octahedra (NbO_6) at 290 K. The rotation angle in the *bc* plane equals 7.86°, whereas its deviation from the *a* axis equals 4.48°.

The diffraction spectra measured on a DN-2 diffractometer in the temperature range from 10 to 870 K showed no phase transitions. The temperature dependences of the unit-cell parameters are shown in Fig. 3. Some experimental points were interpolated.

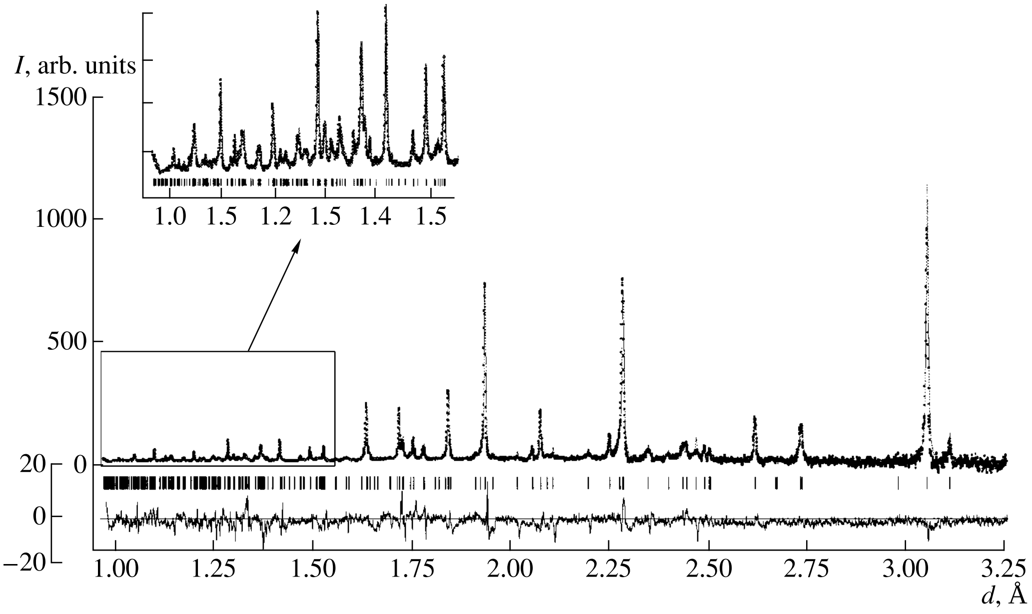

Fig. 2. Neutron diffraction spectrum of BLNO measured on a high-resolution Fourier diffractometer (dots) at $T = 290$ K. The solid line shows the same spectrum processed by the Rietveld method. Vertical lines indicate the calculated positions of the diffraction spectra. Below, the difference (experiment minus calculation) curve normalized to the mean square deviation at the point is shown.

DISCUSSION

The stability of the perovskite-type ABO_3 structures can be considered in terms of the tolerance factor t. For the ion model, this geometrical factor is defined as

$$t = \frac{r_A + r_O}{\sqrt{2}(r_B + r_O)}, \tag{1}$$

where r_A, r_B, and r_O are the ionic radii of the cations and the anions in the positions A, B, and O, respectively. The tolerance factor for the ideal perovskite structure is unity. If $t < 1$, then the BO_2 plane of the structure is under compressive stress, whereas the AO plane is under tensile stress [8]. In perovskite structures, this usually results in mutual rotations of BO_6 octahedra [1, p. 12]. The calculated tolerance factor for BLNO is $t = 0.94$. The existence of tensile and compressive stresses in the perovskite structures in the presence of (Bi_2O_2) layers usually gives rise not only to mutual rotations of BO_6 octahedra but also to the distortion of the bonds. Table 2 lists the bond lengths for atoms in the octahedra and Bi_2O_2 layer. It is seen that the bonds in the octahedra are really considerably distorted, but their lengths are close to the bond lengths in the octahedra of the $Bi_2ANb_2O_9$ structures with A = Ca and Sr [7].

Using the coordinates obtained and the summation rule for bond valences [11], we calculated the valences V_{ij} of the cations in the structure

$$V_{ij} = \sum_{i}^{\nu} s_{ij}(d_{ij}), \tag{2}$$

where ν is the coordination number and $s_{ij}(d_{ij})$ is the valence strength. The dependence of the valence strength s_{ij} on the bond length d is determined as

$$s_{ij}(d_{ij}) = \exp[(d_{1j} - d_{ij})/b], \tag{3}$$

where d_1 has the meaning of the length of the bond of unit strength, whereas the empirical parameter b equals 0.37 Å. The results of the calculations are listed in Table 3 and, as is seen, are consistent with the model assumptions.

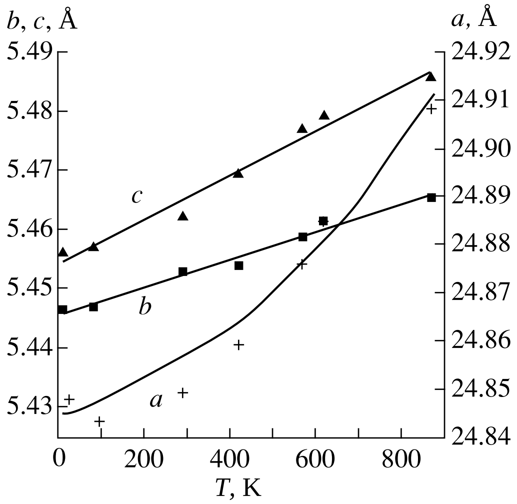

Fig. 3. Temperature dependence of the unit-cell parameters of BLNO.

Table 2. Bond lengths *d* (Å) in NbO_6 octahedra and Bi_2O_2-layers

Bond	*d*	
	T = 10 K	*T* = 290 K
NbO_6-octahedron		
Nb–O(1)[1]	2.133(4)	2.155(4)
Nb–O(2)	1.863(3)	1.871(5)
Nb–O(3)	2.061(3)	2.072(6)
Nb–O(3)[2]	1.948(3)	1.938(6)
Nb–O(4)	1.988(4)	2.018(5)
Nb–O(4)[3]	1.947(4)	1.910(5)
Bi_2O_2-layer		
Bi(2)–O(5)[4]	2.242(4)	2.230(6)
Bi(2)–O(5)[5]	2.291(4)	2.264(6)
Bi(2)–O(5)[6]	2.292(4)	2.289(6)
Bi(2)–O(5)[7]	2.308(4)	2.398(6)

Note: Symmetric transformations of the coordinates of oxygen atoms [1] $x + 1/2, y - 1/2, z$; [2] $x, -y, z - 1/2$; [3] $x, -1 - y, z - 1/2$; [4] $1 - x, 1 - y, z - 1/2$; [5] $x - 1/2, 3/2 - y, z - 1/2$; [6] $1 - x, y, z$; [7] $x - 1/2, y + 1/2, z$.

Table 3. Calculated bond valences of the cations in the structure

Atom	Bond valence		
	T = 10 K	*T* = 290 K	model
Bi	3.03	2.89	3
(Bi/Li)	1.89	1.81	1.88
Nb	4.94	5.14	5

CONCLUSIONS

The neutron powder diffraction data show that no structural phase transitions take place in the newly synthesized Bi-based compound $Bi_{2.53}Li_{0.29}Nb_2O_9$ over the wide temperature range from 10 to 870 K. In this temperature range, the orthorhombic phase described by the sp. gr. $Cmc2_1$ is isostructural to the $Bi_2AB_2O_9$ Aurivillius phases (where A = Sr and Ca and B = Nb and Ta). The structure is refined by the Rietveld method at two temperatures—10 and 290 K. The data processing shows that the monovalent lithium substituting the bismuth atoms in the $Bi_{2.53}Li_{0.29}Nb_2O_9$ structure occupies the 4*a* positions in the perovskite-like layer. The analysis of the data obtained and the calculation of the local balance of the valence strengths agrees with this result. Thus, the existence of a large number of vacancies (0.18 per formula unit) creates in the structure the conditions necessary for high ionic conductivity with respect to lithium.

ACKNOWLEDGMENTS

This study was supported by the International Foundation for Support of the Scientists in the Commonwealth of Independent States, project no. 97-10177, the Russian Foundation for Basic Research, project no. 00-15-96797, and the Ministry of Industry, Science, and Technologies of the Russian Federation (grant for the support of unique setups in Russia). The authors are also grateful to V.G. Simkin for his help with the measurements.

REFERENCES

1. K. S. Aleksandrov and V. B. Beznosikov, *Perovskite-like Crystals* (Nauka, Novosibirsk, 1999).
2. G. A. Smolenskiĭ, Fiz. Tverd. Tela (Leningrad) **3** (2), 651 (1959) [Sov. Phys. Solid State **3**, 477 (1961)].
3. V. A. Isupov, Zh. Neorg. Khim. **39** (5), 731 (1994).
4. Yu. A. Boĭkov, Z. G. Ivanov, D. Érts, *et al.*, Fiz. Tverd. Tela (St. Petersburg) **39** (4), 683 (1997) [Phys. Solid State **39**, 598 (1997)].
5. K. Inaguma, Solid State Commun. **86**, 689 (1993).
6. V. L. Aksenov, A. M. Balagurov, V. G. Simkin, *et al.*, J. Neutron Res. **5**, 181 (1997).
7. S. M. Blake, M. J. Falconer, and M. McCredy, J. Mater. Chem. **7**, 1609 (1997).
8. Y. Shimacawa and Y. Cubo, Phys. Rev. B **61** (10), 6559 (2000).
9. V. B. Zlokazov, J. Appl. Crystallogr. **30**, 996 (1997).
10. V. B. Zlokazov and V. V. Chernyshev, J. Appl. Crystallogr. **25**, 447 (1992).
11. V. S. Urusov and I. P. Orlov, Kristallografiya **44** (4), 736 (1999) [Crystallogr. Rep. **44**, 686 (1999)].

Translated by L. Man

Crystallography Reports, Vol. 48, No. 3, 2003, pp. 401–405. Translated from Kristallografiya, Vol. 48, No. 3, 2003, pp. 445–449.
Original Russian Text Copyright © 2003 by Zubkova, Kabalov, Orlova, Kitaev, Kurazhkovskaya.

The Synthesis and Structure of Alkaline Earth and Cerium (IV) Phosphates (Ce, B, □)[PO_4] (B = Mg, Ca)

N. V. Zubkova*, Yu. K. Kabalov*, A. I. Orlova, D. B. Kitaev**, and V. S. Kurazhkovskaya***

** Moscow State University, Vorob’evy gory, Moscow, 119899 Russia*
e-mail: nata_zubkova@rambler.ru
*** Nizhni Novgorod State University, pr. Gagarina 23, Nizhni Novgorod, 603600 Russia*

Received February 21, 2002

Abstract—Double orthophosphates (Ce(IV), B, □)[PO_4] (B = Mg, Ca) were obtained after thermal treatment of gels with stoichiometric contents of components. The compounds obtained were characterized by X-ray diffraction analysis, infrared spectroscopy, and the electron spin resonance technique. The crystal structures were refined by the Rietveld method within the sp. gr. $P2_1/n$. The refinement was performed in the anisotropic approximation of atomic displacements for cations and isotropic approximation for oxygen. © *2003 MAIK “Nauka/Interperiodica”.*

INTRODUCTION

There are only a few papers on the crystal chemistry of compounds of *f*-elements with tetrahedrally coordinated anions (such as phosphates, arsenates, silicates, etc.). At the same, one can see growing interest in such studies. It is explained by the search for synthetic analogs of natural compounds that can play the role of sorbents of lanthanides and actinides present in nuclear wastes and isolate them from the biosphere. Phosphate compounds attract widespread attention because of the geological stability of phosphate-based minerals containing cerium and other lanthanides, thorium, and uranium.

The phosphate of Ce(III), $CePO_4$, and phosphates of other lanthanides (La–Tb) and actinides (Pu, Am, Cm) with a similar chemical composition have the structure of natural mineral monazite (Ce, La, Y, Ca, Th)PO_4 and its variety cheralite (Ce, La, Y, Th, Ca, Pb, U)(P, Si)O_4 (monoclinic unit cell, sp. gr. $P2_1/n$) [1–6]. The same structures are also characteristic of the known phosphates of *f*-elements of more complicated composition, such as $A_3R_2(PO_4)_3$, A = Na, K, R = Ce–Gd, Pu(III), Am, Cm [7]; $NaNp_2(PO_4)_3$ [8]; $BM(PO_4)_2$, B = Mg, Ca, Sr, Cd, Pb, M = Th and B = Ca, Sr, Ba, M = U [9]; $B_{0.5}Np_2(PO_4)_3$, B = Mg, Ca, Sr [8]; and $NaCaNd(PO_4)_3$ and $CaNdM(PO_4)_3$, M = Th, U [9], and also of solid solutions of various compositions.

Analysis of the available literature on the phosphates of *f*-elements clearly shows the absence of any data on phosphates of Ce(IV) and other lanthanides in the 4^+ oxidation state. Studies of such compounds would provide an additional insight into the crystal chemistry of lanthanide phosphates, the characteristics of their structure, and manifestations of isomorphism. The systems containing cerium and other lanthanides are model systems for studying chemistry and crystal chemistry of highly active actinide compounds.

Below, we present the results of synthesis and structural studies of new double phosphates of Ce(IV) (such as $B_{0.5}Ce_2(PO_4)_3$, B = Mg, Ca) and compare with the known data on the phosphates of *f*-elements.

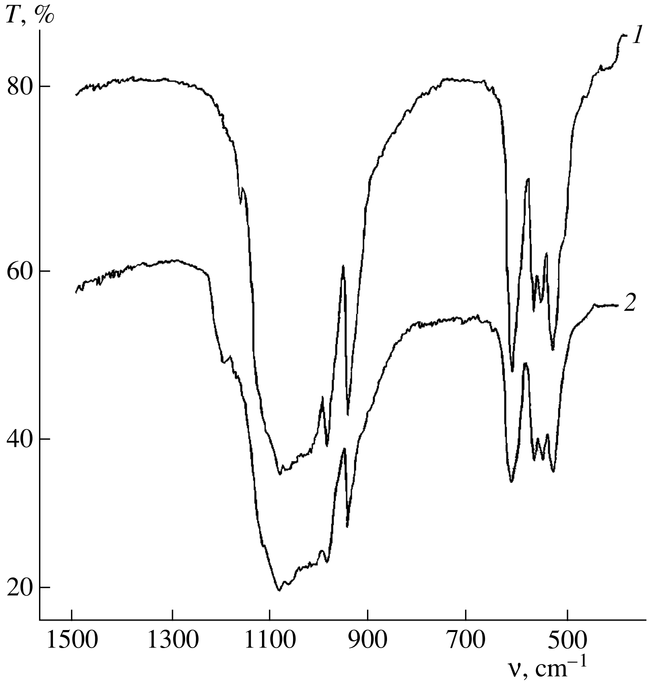

Fig. 1. IR spectra of (Ce, Mg, □)[PO_4] (*1*) and (Ce, Ca, □)[PO_4] (*2*) phosphates.

Table 1. Main characteristics and the results of the Rietveld refinement of the (Ce, Mg, □)[PO_4] (1) and (Ce, Ca, □)[PO_4] (2) crystal structures

Characteristic	Compound	
	1	2
a, Å	6.794(1)	6.786(1)
b, Å	7.020(1)	7.010(1)
c, Å	6.468(1)	6.462(1)
β, deg	103.46(1)	103.50(1)
V, Å^3	300.03	298.92
Sp. gr.	$P2_1/n$	$P2_1/n$
2θ range, deg	15.00–108.00	15.00–110.00
Number of reflections	791	816
Number of parameters to be refined	53	53
R_{wp}	2.74	2.77
R_B	3.23	2.49
R_F	2.62	2.70
DWD	1.30	1.35

Note: $R_{wp} = [\Sigma w|I_{obs} - I_{calcd}|^2/\Sigma w I^2_{obs}]^{1/2}$, $R_B = \Sigma I'_{obs} - I'_{calcd}/\Sigma I'_{obs}$, where I'_{obs} and I'_{calcd} are the observed and calculated values of integrated intensities for Bragg reflections, $R_F = \Sigma|F_{obs} - F_{calcd}/\Sigma F_{obs}$, and *DWD* is the Durbin–Watson statistics [3].

EXPERIMENTAL

The double phosphates of Ce(IV), such as $B_{0.5}Ce_2(PO_4)_3$, where B = Mg or Ca, were synthesized by sol–gel technology, often used for obtaining phosphates [10]. The initial components were $(NH_4)_2Ce(NO_3)_6$ (pure grade), $Mg(NO_3)_2 \cdot 6H_2O$ (pure grade), $Ca(NO_3)_2 \cdot 4H_2O$ (pure grade), and H_3PO_4 (pure grade). The stoichiometric amounts of aqueous solutions of cerium and magnesium salts were poured together with simultaneous stirring. Then a 1-M solution of phosphoric acid was added to solution under constant stirring. The gel thus formed was dried for 24 h at 80°C, then heated, and kept for 24 h at 600, 800, and 1000°C. The thermal treatment was alternated with dispersion. In some experiments, heating to 800°C was performed in an oxygen atmosphere (flow rate of about 0.4 l/h).

Identification of the phases and their further study were performed with the use of various physical and chemical techniques such as infrared (IR) absorption spectroscopy, electron spin resonance (ESR), and X-ray diffraction analysis. The IR absorption spectra of the samples prepared by the fine-dispersion film technique on a KBr substrate were obtained on a Specord-75 IR spectrophotometer within the 1800–400 cm^{-1} frequency range. The ESR spectra of the synthesized materials were obtained on a Bruker ESP-300 radiospectrometer. A 50-mg-phosphate sample was placed into a glass capillary. The experiments were performed at room temperature and at 140 K. The preliminary X-ray diffraction data were obtained on a DRON-3.0 diffractometer (CuK_α radiation) and were then refined on a ADP-2 diffractometer (CuK_α radiation, λ = 1.54078 Å, Ni filter, 2θ scan, scan step 0.02°, and exposure 10 s).

The samples synthesized were polycrystalline white Mg–Ce and gray-greenish Ca–Ce phosphate powders.

Table 2. Atomic positions and parameters of atomic thermal vibrations in the (Ce, Mg, □)[PO_4] (1) and (Ce, Ca, □)[PO_4] (2) structures

Atom	*x*	*y*	*z*	B_{eq}
1				
0.683(4)Ce + 0.167(7)Mg	0.2190(3)	0.1594(4)	0.4004(4)	0.44(3)
0.987(7)P	0.199(1)	0.159(1)	0.887(2)	2.4(2)
O(1)	0.236(3)	0.499(2)	0.436(3)	1.7(4)
O(2)	0.018(2)	0.112(3)	0.686(2)	1.5(4)
O(3)	0.377(2)	0.213(3)	0.787(6)	1.8(4)
O(4)	0.112(2)	0.337(3)	–0.009(3)	1.6(3)
2				
0.700(4)Ce + 0.167(4)Ca	0.2190(4)	0.1597(4)	0.4003(4)	0.60(2)
0.973(7)P	0.200(1)	0.161(1)	0.887(1)	1.9(1)
O(1)	0.242(3)	0.507(2)	0.436(3)	2.0(5)
O(2)	0.017(2)	0.112(2)	0.698(2)	2.6(5)
O(3)	0.376(2)	0.213(2)	0.786(2)	2.0(4)
O(4)	0.120(2)	0.343(3)	–0.008(2)	1.6(4)

Note: The occupancies of oxygen positions were taken to be unity and were not refined.

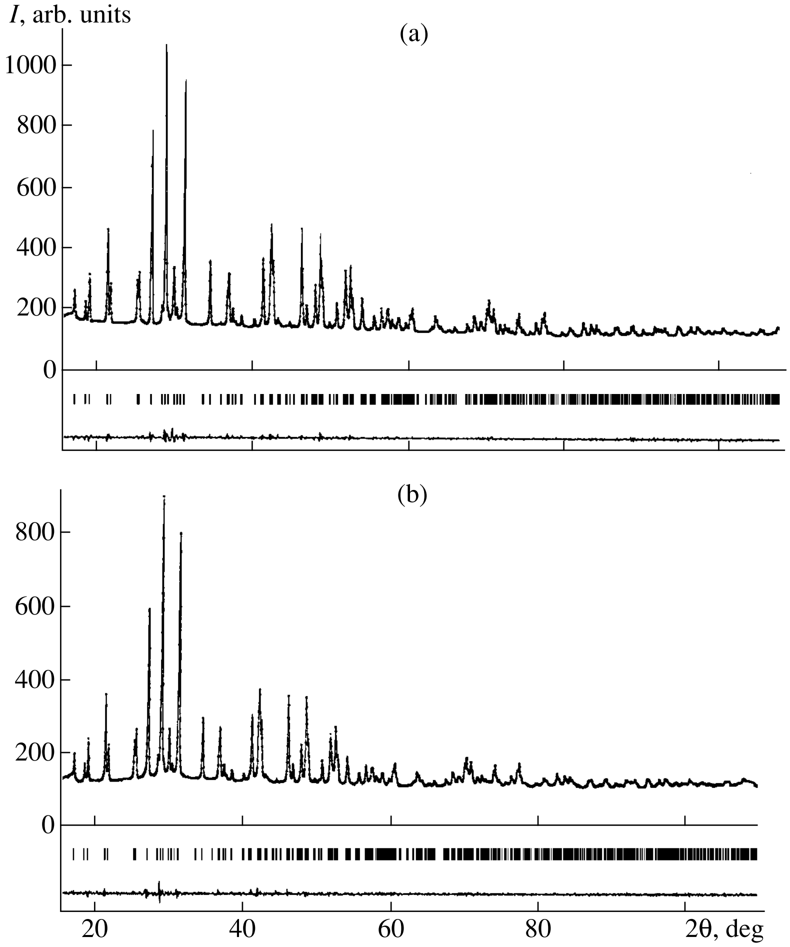

Fig. 2. Observed (a) and calculated (b) X-ray diffraction patterns of (a) (Ce, Mg, □)[PO$_4$] and (b) (CeCa□)[PO$_4$] compounds.

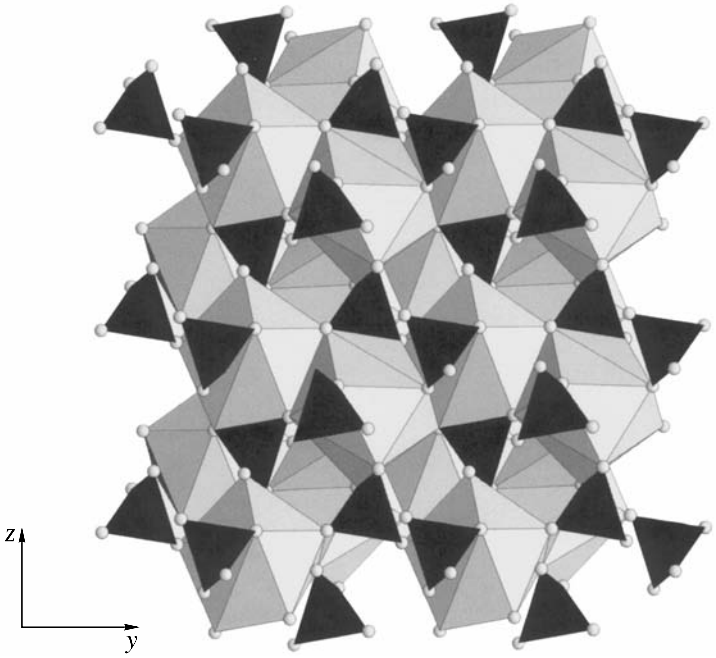

Fig. 3. Projection of the (Ce, Ca, □)[PO$_4$] crystal structure onto the *bc* plane.

Table 3. Interatomic distances (Å) for (Ce, Mg, □)[PO_4] (1) and (Ce, Ca, □)[PO_4] (2) structures

Interatomic distances in polyhedra	Compounds	
	1	2
[Ce, Mg/Ca]–O(1)	2.39(1)	2.44(1)
O(1)	2.53(2)	2.49(1)
O(2)	2.56(1)	2.63(1)
O(2)	2.47(1)	2.47(1)
O(3)	2.51(1)	2.50(1)
O(3)	2.44(1)	2.44(1)
O(4)	2.86(1)	2.87(1)
O(4)	2.56(1)	2.50(1)
O(4)	2.60(1)	2.65(1)
Average value	〈2.55〉	〈2.55〉
P–O(1)	1.59(1)	1.56(1)
O(2)	1.61(1)	1.57(1)
O(3)	1.55(1)	1.53(1)
O(4)	1.59(2)	1.60(1)
Average value	〈1.59〉	〈1.57〉

The IR spectra (Fig. 1) indicate that the compounds belong to the class of orthophosphates. The bands in the 1100–950 cm^{-1} range can be attributed to the stretching (valence) vibrations of a PO_4 ion; those in the 620–530 cm^{-1} range, to its distortional vibrations. In the structure under study, PO_4 tetrahedra are distorted, and their symmetry is lowered to C_1 (phosphorous atoms are located in the general position). As a result, the degeneracy of vibrations is completely removed. The IR spectra of both phosphates are similar and are very close to the spectrum of monazite [11]. However, the bands corresponding to valence vibrations are shifted by about 40 cm^{-1} toward higher frequencies, which is explained by the smaller size of the cations filling the nine-vertex polyhedra of the structure in comparison with the size of the Ce^{3+} cations in monazite (cheralite) [3].

The ESR technique was used for studying phosphates to reveal the possible presence of Ce(III) ions (in some papers, the possible formation of these ions in cerium phosphates at high temperature was mentioned [12–14]). The ESR spectra virtually coincided with the background spectra. Therefore, we did not manage to reveal Ce(III) ions in the compounds under study.

The X-ray diffraction patterns were characterized by the close values of reflection angles. The general arrangement of the characteristic groups of reflections remained the same, which indicated the crystallographic similarity of Mg–Ce and Ca–Ce phosphates. The X-ray diffraction patterns of the samples obtained in an oxygen atmosphere and in air (800°C, 24 h) were identical.

The X-ray diffraction spectra of Mg–Ce and Ca–Ce phosphates obtained on an ADP-2 diffractometer were processed using the WYRIET program, version 3.3 [15]. We used as the initial model the structure of cheralite (sp. gr. $P2_1/n$) [16]. The peak shapes were described using the Pearson VII function. The peak asymmetry was refined at $2\theta < 60°$. For all the chemical elements, the ionic scattering curves were used. The structures were refined by consecutive addition of the refined parameters with a constant graphical modeling of the background up to the stabilization of *R*-factor values. For each structure, the structural parameters of six independent positions were refined: [Ca(Mg), Ce], P, and four oxygen positions. According to the results obtained, the chemical formulas of the compounds studied can be written as follows: $Mg_{0.50}(2)Ce_{2.05}(3)P_{2.96}(2)O_{12}$ (1) and $Ca_{0.50}(1)Ce_{2.10}(1)P_{2.92}(2)O_{12}$ (2). The general crystal-chemistry formula of these compounds is $(Ce_{1-x-y}B_x\square_y)[PO_4]$, where B = Ca or Mg, $x \approx 1/6$, and $y \approx 0.14$.

Some parameters of the data acquisition and the results of structure refinement of compounds 1 and 2 are presented in Table 1. The observed and calculated X-ray diffraction spectra of the compounds are shown in Fig. 2. The atomic positions, isotropic and anisotropic thermal parameters, and occupancies of the cationic positions are listed in Table 2. The interatomic distances are given in Table 3.

DESCRIPTION OF THE STRUCTURE AND DISCUSSION

The data obtained show that, like mineral cheralite [17], the compounds under study have a monazite-type structure.

According to the refined data in [4, 5, 9], this structure is characterized by a three-dimensional framework formed by connected PO_4 tetrahedra and MO_9 polyhedra, forming distorted single-cap square antiprisms. Each oxygen atom forms bridge bonds with two metal atoms, whereas one of the four oxygen atoms of a tetrahedron is bonded to three atoms. Thus, MO_9 polyhedra with a cation composition corresponding to the chemical formula $(Ce_{1-x-y}B_x\square_y)^{3+}$ (where B = Mg or Ca) share vertices and edges and form the framework structure. The vacancies in the M positions of this structure (Table 2) provide a wide spectrum of isomorphous substitutions of Ce(IV) by cations that have lower valences, including lanthanides and actinides. Such substitutions result in the filling of vacancies or in partial transition of Ce(IV) to Ce(III) accompanied by incorporation of another cation with a valence not higher than 3^+. In turn, this can favor the formation of compounds that are more energetically favorable. This seems to explain the existence and geological stability of the minerals monazite and cheralite, which always contain not only cerium but also a varying number of doubly, triply, or quadruply charged cations [5].

Phosphorus atoms in the compounds occupy isolated tetrahedra. The [Ce, Mg(Ca)] cations are located in nine-vertex polyhedra formed by three monodentant and three bidentant PO_4 groups (Fig. 3). In contrast to monazite, in the structures of cheralite and the compounds studied, phosphorus tetrahedra are rotated with respect to each other [18]. In cheralite, this rotation is caused by the isomorphous substitution of cerium atoms by thorium and calcium cations. Structures 1 and 2 are rather close to the structure of cheralite; therefore, the rotation of phosphorus tetrahedra in the compounds studied is also associated with the fact that magnesium and calcium enter into the cerium positions.

The interatomic distances and valence angles in phosphate tetrahedra in compounds 1, 2, and in $CePO_4$ [3] are rather close: $\langle 1.59 \rangle$ Å, $\langle 1.57 \rangle$ Å, and $\langle 1.527 \rangle$ Å and $\langle 109.4° \rangle$, $\langle 109.4° \rangle$, and $\langle 109.5° \rangle$ in compounds 1, 2, and $CePO_4$, respectively. The maximum discrepancy in the interatomic P–O distances and O–P–O angles within the same tetrahedron in these compounds are 0.06, 0.07, and 0.016 Å and 14.4°, 12.7°, and 9.3°, respectively, which indicates the more pronounced distortion of the phosphate tetrahedron in the compounds synthesized than in the phosphate $CePO_4$.

The M–O distances in MO_9 polyhedra are close in all three compounds: $\langle 2.55 \rangle$, $\langle 2.55 \rangle$, and $\langle 2.62 \rangle$ Å, respectively; one of the M–O bonds is longer than the others: 2.86, 2.87, and 2.779 Å, respectively. The differences in lengths of the longest and the shortest bonds are equal to 0.47 and 0.43 Å for the new compounds and 0.33 Å for the phosphate $CePO_4$. Thus, like PO_4, the least distorted MO_9 polyhedron also exists in the $CePO_4$ compound.

Thus, the distortions of a monazite-type structure become more pronounced for compounds with more complex chemical composition.

ACKNOWLEDGMENTS

This study was supported by the Russian Foundation for Basic Research, project no. 01-03-33013.

REFERENCES

1. *X-ray Date File ASTM* (Philadelphia, 1966), Cards Nos. 18-506, 18-523.
2. Y.-X. Ni, J. Haghes, and A. Mariano, Am. Mineral. **80**, 21 (1995).
3. G. W. Beall, L. A. Boatner, D. F. Millica, and W. O. Milligan, J. Inorg. Nucl. Chem. **43** (1), 101 (1981).
4. D. F. Millica, C. K. Loc, and D. A. Crossie, J. Solid State Chem. **63** (3), 452 (1986).
5. C. Keller and K. H. Walter, J. Inorg. Nucl. Chem. **27**, 1253 (1965).
6. F. Weiger, R. Maraquart, and R. Kohl, Inorg. Chim. Acta **94** (1), 31 (1983).
7. A. A. Burnaeva, Yu. F. Volkov, and A. I. Kryukova, Radiokhimiya **36** (4), 289 (1994).
8. Yu. F. Volkov and A. I. Orlova, Tr. Gos. Nauchn. Tsentra Ross. Feder. Nauchno-Issled. Inst. At. Reak., No. 2, 25 (1996).
9. Yu. F. Volkov, Radiokhimiya **42** (2), 161 (1999).
10. A. I. Orlova, V. I. Pet’kov, and O. V. Egor’kova, Radiokhimiya **38** (1), 15 (1996).
11. V. V. Pechkovskiĭ, R. Ya. Mel’nikova, E. D. Dzyuba, *et al.*, *Atlas of Infrared Spectra of Phosphates. Orthophosphates* (Nauka, Moscow, 1981).
12. C. E. Bamberger, R. G. Haire, G. M. Begun, and L. C. Elingboe, Inorg. Chim. Acta **95**, 49 (1984).
13. C. W. Bjorklund, J. Am. Chem. Soc. **79**, 6347 (1958).
14. I. L. Botto and E. J. Baran, Z. Anorg. Allg. Chem. **430**, 283 (1977).
15. J. Schneider, in *Proceedings of International Workshop on the Rietveld Method* (Petten, 1989).
16. J. J. Finney and N. N. Rao, Am. Mineral. **52**, 13 (1967).
17. T. Ueda, J. Jpn. Assoc. Mineral. Petrol. Econ. Geol. **58**, 170 (1967).
18. R. Miyawaki and I. Nakai, Cryst. Struct. Rare-Earth Miner. Rare Earths, No. 11, 134 (1987).

Translated by K. Kugel

Crystallography Reports, Vol. 48, No. 3, 2003, pp. 406–412. Translated from Kristallografiya, Vol. 48, No. 3, 2003, pp. 450–457.
Original Russian Text Copyright © 2003 by Geguzina, Shuvayev, Vlasenko, Shuvayeva, Shilkina.

STRUCTURE OF INORGANIC COMPOUNDS

Synthesis and Structure of New $A_{m-1}Bi_2B_mO_{3m+3}$ (m = 3) Phases[1]

G. A. Geguzina, A. T. Shuvayev, V. G. Vlasenko, E. T. Shuvayeva, and L. A. Shilkina
Institute of Physics, Rostov State University, pr. Stachki 194, Rostov-on-Don, 344090 Russia
e-mail: denis@ip.rsu.ru

Received November 18, 2002

Abstract—Six new polycrystalline bismuth-containing layered perovskite-like oxides described by the general formula $A_{m-1}Bi_2B_mO_{3m+3}$ (m = 3) were synthesized by high-temperature solid-state reactions. The unit-cell parameters of these compounds were determined as a = 5.438(9) Å, b = 5.462(7) Å, and c = 33.08(6) Å for $Bi_4Ti_2Nb_{0.5}Fe_{0.5}O_{12}$; a = 5.408(6) Å, b = 5.425(9) Å, and c = 32.85(6) Å for $Ca_{0.5}Bi_{3.5}Ti_{2.75}W_{0.25}O_{12}$; a = 5.457(0) Å, b = 5.482(2) Å, and c = 32.75(2) Å for $NaCaBi_2Nb_3O_{12}$; $a = b$ = 3.826(2) Å and c = 32.82(6) Å for $Ca_{0.25}Th_{0.25}Bi_{3.5}Ti_3O_{12}$; $a = b$ = 3.816(2) Å and c = 32.81(5) Å for $Nd_{0.5}Gd_{0.5}Bi_3Ti_3O_{12}$; and $a = b$ = 3.826(4) Å and c = 32.95(8) Å for $Th_{0.5}Bi_{3.5}Ti_{2.5}Ga_{0.5}O_{12}$. The compositions of these compounds are based on the composition of the basic Bi-containing layered perovskite-like $Bi_4Ti_3O_{12}$ oxide in which Bi^{III} and Ti^{IV} atoms are partially or completely replaced with other atoms. The experimental and calculated interplanar spacings determined from X-ray diffraction patterns and the reliability factors of their indexing are reported. *© 2003 MAIK “Nauka/Interperiodica”.*

INTRODUCTION

Bismuth-containing layered perovskite-like oxides described by the general formula

$$A_{m-1}Bi_2B_mO_{3m+3} \quad (1)$$

were studied. The known compounds described by formula (1), where m = 1, 1.5, 2, 2.5, 3, 3.5, 4, 5, 6, 7, 8, and 10 [1–14] are the members of a rather small structural family. In these compounds, only a few different types of atoms can occupy the A and B positions [15]. The regions of existence of these compounds are rather narrow [11] compared to the regions of existence, e.g., of complex perovskite-like oxides [16].

The limitations imposed on the chemical diversity of Bi-containing layered perovskite-like oxides are explained, primarily, by the characteristic features of layered perovskite-like structures, on the one hand, and by the technological difficulties of their preparation, on the other [17]. The unit cells of these compounds [6, 10] are built by alternating stacks of perovskite-like layers of composition $[A_{m-1}B_mO_{3m+1}]^{2-}$ and bismuth–oxygen layers $[Bi_2O_2]^{2+}$ located between these stacks. All the layers are parallel and perpendicular to the c axis. The number of perovskite-like layers in each stab is equal to m. The existence of these layers and “binding” bismuth–oxygen layers imposes additional limitations on the formation of such structures [10].

Nevertheless, almost all the representatives of this family have ferroelectric properties and rather high Curie temperatures [10–14]. These facts stimulated the search for new representatives of this family and gave impetus to their preparation [17–22]. The present study was undertaken to solve these problems. The classification of Bi-containing layered perovskite-like oxides [15] and the conditions of their existence [11, 16] give grounds to believe that new compounds of this family may be synthesized. The preparation and study of the structures of new Bi-containing layered perovskite-like oxides would allow one not only to extend this family but also to follow the influence of various atoms in the A and B positions on the formation of layered structures and their unit-cell parameters.

The known compounds of this family with m = 3 are much smaller in number compared to compounds with other m. In most of the above-mentioned reviews [1–14], only one such compound with the simple composition $Bi_4Ti_3O_{12}$ was described. This best studied compound is characterized by a rather high Curie temperature (T_C = 948 K) and very interesting electrophysical properties [10]. $Bi_4Ti_3O_{12}$ was used as the basic compound for synthesis of more complex hypothetical compounds of this family with m = 3. In this study, we prepared and characterized six new polycrystalline oxides with m = 3 and determined their symmetry, space groups, and unit-cell parameters.

CHEMICAL COMPOSITIONS OF BISMUTH-CONTAINING LAYERED PEROVSKITE-LIKE OXIDES AND THEIR SYMMETRY

The chemical compositions were formed starting from the basic composition $Bi_4Ti_3O_{12}$ by partial or complete replacement of the Bi^{III} atoms in the A posi-

---

[1] This study was presented at the symposium “Order, Disorder, and Properties of Oxides” (ODPO), Sochi, Russia, 2002.

tions and Ti^{IV} atoms in the B positions by other elements in the appropriate valence states so as not to the valence balance in their chemical formulas.

We made attempts to synthesize 30 new compounds with $m = 3$ by performing different replacements in the basic composition. As a result, we obtained nine new single-phase Bi-containing layered perovskite-like oxides. The experimental data on three of these oxides were published earlier [21, 22]. Here, we describe six new compounds. For comparison, we also synthesized $Bi_4Ti_3O_{12}$, whose crystal lattice is the prototype of the lattices of these new compounds.

To demonstrate the positions of all the atoms in the A^i and B^j sites of the crystal lattice, we write here the chemical formula of Bi-containing layered perovskite-like oxides of a complex composition in the most general form:

$$(A^1_{\alpha_1}\ldots A^i_{\alpha_i}\ldots A^p_{\alpha_p})Bi_2(B^1_{\beta_1}\ldots B^j_{\beta_j}\ldots B^q_{\beta_q})O_{3m+3}, \qquad (2)$$

where $\sum_{i=1}^{p}\alpha_i = m - 1$ and $\sum_{j=1}^{q}\beta_j = m$.

Taking into account formulas (1) and (2), the compositions of the new oxides can be represented in two forms:

1. $Bi_4Ti_2Nb_{0.5}Fe_{0.5}O_{12} = (\underline{Bi_2})Bi_2(Ti_2\mathbf{Nb_{0.5}Fe_{0.5}})O_{12}$;
2. $Ca_{0.5}Bi_{3.5}Ti_{2.75}W_{0.25}O_{12} = (\mathbf{Ca_{0.5}}Bi_{1.5})Bi_2(Ti_{2.75}\mathbf{W_{0.25}})O_{12}$;
3. $CaNaBi_2Nb_3O_{12} = (\mathbf{CaNa})Bi_2(\mathbf{Nb_3})O_{12}$;
4. $Ca_{0.25}Th_{0.25}Bi_{3.5}Ti_3O_{12} = (\mathbf{Ca_{0.25}Th_{0.25}}Bi_{1.5})Bi_2(\underline{Ti_3})O_{12}$;
5. $Nd_{0.5}Gd_{0.5}Bi_3Ti_3O_{12} = (\mathbf{Nd_{0.5}Gd_{0.5}}Bi)Bi_2(\underline{Ti_3})O_{12}$;
6. $Th_{0.5}Bi_{3.5}Ti_{2.5}Ga_{0.5}O_{12} = (\mathbf{Th_{0.5}}Bi_{1.5})Bi_2(Ti_{2.5}\mathbf{Ga_{0.5}})O_{12}$.

In the second form of the formulas, two Bi atoms are located in the $(Bi_2O_2)^{2-}$ layers (they are outside the parentheses); inside the parentheses, there are atoms in the A^i and B^j positions located in the perovskite-like layers. The atoms indicated by bold letters replace (partially or completely) in the $Bi_4Ti_3O_{12}$ lattice the Bi atoms in the A positions, or the Ti atoms in the B positions, or both simultaneously. The atoms of the basic composition, which are not replaced at all, are underlined.

In composition 1, the Ti^{IV} atom is replaced by 0.5 Nb^{V} and 0.5 Fe^{III}, whereas the Bi atoms remain unchanged. In composition 2, 0.5 Bi and 0.25 Ti are replaced with 0.5 Ca^{II} and 0.25 W^{VI}, respectively. In composition 3, two Bi atoms in the A positions and three Ti atoms in the B positions are simultaneously and completely replaced by the Na^{I}, Ca^{II}, and three Nb^{V} atoms, respectively. In the perovskite-like layers of the compound of composition 3, there are no Bi^{III} and Ti^{IV} atoms at all. The percentage of Ca^{II} atoms increases from composition 2 to composition 3. According to X-ray diffraction analysis, Bi-containing layered perovskite-like oxides with compositions 1–3 are crystallized in the orthorhombic system (sp. gr. $Fmmm = D^{23}_{2h}$) (Table 1).

In composition 4, 0.25 Bi^{III} are replaced by Ca^{II} atoms and 0.25 Bi^{III} by Th^{IV} atoms. By contrast, the Bi atoms in the compound with composition 6 are replaced only by Th^{IV} atoms. This structure contains twice as many Th atoms as composition 4. To preserve the stoichiometry of composition 6, 0.5 Th^{IV} atoms are simultaneously replaced by Ga^{III}. Synthesis of two new Bi-containing layered perovskite-like oxides containing tetravalent Th in the A positions is quite unique. The valence of atoms replacing Bi in the perovskite-like layers of the known Bi-containing oxides studied earlier does not exceed three, as in the new compound with composition 5, where one Bi^{III} atom is replaced by two trivalent ones. According to X-ray diffraction analysis, the compounds with compositions 4–6 are crystallized in the tetragonal system (sp. gr. $I4/mmm = D^{12}_{4h}$) (see Table 1).

PREPARATION OF SAMPLES AND STUDY OF THEIR STRUCTURES

Polycrystalline (ceramic) samples of new Bi-containing layered perovskite-like oxides and $Bi_4Ti_3O_{12}$ were prepared by solid-phase reactions in two or three stages with a thorough mixing of the stoichiometric mixture of the starting components and then of the intermediate products of the reaction. The synthesis of such compounds, all the more so of compounds with more complex compositions, encounters certain difficulties. Here, it is very important to choose both the appropriate initial reagents and the optimum combination of the temperature and duration of the intermediate and final sintering to ensure complete occurrence of the reaction.

The synthesis was performed with the use of the starting components Bi_2O_3, $CaCO_3$, $NaHCO_3$, Nb_2O_5, TiO_2, WO_3, Nd_2O_3, Gd_2O_3, and $Th(OH)_4$ (primarily, of special-purity, analytical, or reagent grade). The samples for sintering were formed from powdered mixtures of the starting components as 3 to 4-mm-thick discs 10 mm in diameter. The synthesis was performed in a laboratory muffle furnace in air. The synthesis temperatures and duration of successive sintering are given in Table 1.

Initially, sintering was made at comparatively low temperatures (from 1013 to 1123 K). The temperatures of the subsequent cycles of sintering were 100–200 K higher. The duration of each cycle of sintering was rather short (no more than 4 h), although the sintering duration reported in most studies, particularly in foreign publications, was an order of magnitude longer. Nevertheless, it has been mentioned that samples with the above compositions obtained at the first stage of synthesis consisted predominantly of a layered phase with the necessary composition and an orthorhombic or

Table 1. Chemical compositions, X-ray densities, modes of preparation, parameters of the orthorhombic unit cells (a_{orth}, b_{orth}, c), average experimentally observed ($\bar{a}_{\text{pt}}^{\text{obs}}$) and calculated ($\bar{a}_{\text{pt}}^{\text{calcd}}$) parameters of the pseudotetragonal and tetragonal unit cells ($a_{\text{tetr}} = b_{\text{tetr}}$ and c) of bismuth-containing layered perovskite-like oxides and their experimental volumes ($V_{\text{un. cell}}$ and $V_{\text{pt. cell}}$)

Sample	Chemical composition, ($V_{\text{un. cell}}$, Å^3, and ρ_{exp}, g/cm^3)	Sintering modes:	Unit-cell parameters, Å, and volume, Å^3		
		temperature (°C)–time (h);	$a_{\text{orth(tetr)}}$ ($\bar{a}_{\text{pt}}^{\text{exp}}$)	$b_{\text{orth(tetr)}}$ ($\bar{a}_{\text{pt}}^{\text{calcd}}$)	c ($V_{\text{pt. cell}}$)
Orthorhombic unit cells, sp. gr. *Fmmm* = D_{2h}^{23}					
1	$Bi_4Ti_2Nb_{0.5}Fe_{0.5}O_{12}$ (983.0 and 8.15)	t_1 = 800–2; t_2 = 950–1.5	5.438(9) (3.854)	5.462(7) (3.856)	33.08(6) (491.4)
2	$Ca_{0.5}Bi_{3.5}Ti_{2.75}W_{0.25}O_{12}$ (964.2 and 7.77)	t_1 = 740–3; t_2 = 850–4	5.408(6) (3.831)	5.425(9) (3.832)	32.85(6) (481.9)
3	$NaCaBi_2Nb_3O_{12}$ (979.8 and 6.49)	t_1 = 800–1.5; t_2 = 1000–1	5.457(0) (3.868)	5.482(2) (3.892)	32.75(2) (490.1)
Basic	$Bi_4Ti_3O_{12}$ (967.7 and 8.04)	t_1 = 800–2.5; t_2 = 1000–1	5.410(2) (3.839)	5.449(2) (3.844)	32.82(5) (483.7)
Tetragonal unit cells, sp. gr. *I*4/*mmm* = D_{4h}^{17}					
4	$Ca_{0.25}Th_{0.25}Bi_{3.5}Ti_3O_{12}$ (484.3 and 7.89)	t_1 = 800–4; t_2 = 900–2; t_3 = 950–2	3.826(4)	3.826(2) (3.829)	32.82(6)
5	$Nd_{0.5}Gd_{0.5}Bi_3Ti_3O_{12}$ (477.9 and 7.78)	t_1 = 800–3; t_2 = 900–2; t_3 = 1000–1	3.816(2)	3.816(2) (3.836)	32.81(5)
6	$Th_{0.5}Bi_{3.5}Ti_{2.5}Ga_{0.5}O_{12}$ (482.5 and 8.26)	t_1 = 850–2; t_2 = 950–2	3.826(4)	3.826(4) (3.822)	32.95(8)

tetragonal structure, and all the subsequent cycles of sintering were made with the sole aim of bringing the reactions to a higher degree of completion.

The optimum synthesis modes were chosen based on the results of powder X-ray diffraction, and the unit-cell parameters of Bi-containing layered perovskite-like oxides were determined with a relative error not exceeding ±0.05%. All the samples were studied at room temperature.

The X-ray diffraction patterns of compounds 4 and 5 and the parent compound $Bi_4Ti_3O_{12}$ were measured on a modified DRON-3M automated diffractometer equipped with a GP-13 attachment. A 1.5BSV29-Cu X-ray tube operated at a voltage of 40 kV and current of 20 mA was used as a source of X-ray radiation. The $\text{Cu}K_{\alpha_{1,2}}$ radiation was isolated from the spectrum with the aid of an Ni filter. The X-ray data were collected in the angle-scan range of 4° to 90°, the scan step was 0.02°, and the intensity was recorded at each point for 4 s.

The spectrum profiles were analyzed with the use of the PCW-2.3 software [23] providing an automatic search for positions of the lines and their indexing within the chosen model unit cell. For compounds 4 and 5, profile analysis and indexing were made within sp. gr. *I*4*mmm* (139). For $Bi_4Ti_3O_{12}$, sp. gr. *Fmmm* (69) was chosen. The background subtracted from the spectrum was represented as a polynomial of the seventh degree. The X-ray line profiles were described by the pseudo-Voigt function, which was a linear combination of the Gaussian and Lorentz functions. The model spectrum was fitted to the experimental data by varying 16 parameters, including eight background parameters, three parameters of the line shape, the shift of the goniometer zero, the scale factor, and three unit-cell parameters. It was assumed that the atoms that substitute bismuth in the 8*i* position are statistically distributed over the crystal lattice. The unit-cell parameters were refined using the unit-cell parameters of $Bi_4Ti_3O_{12}$ [2] as the starting values.

The *R* factors used as the numerical reliability criteria of the evaluation of the line intensities, line indexing, and determination of the unit-cell parameters within the chosen space groups were calculated according to the following formulas:

$$R_p = \frac{\sum_{i=1}^{N} \left|I_i^{\text{obs}} - I_i^{\text{calcd}}\right|}{\sum_{i=1}^{N} \left|I_i^{\text{obs}}\right|},$$

$$R_{wp} = \left[\frac{\sum_{i=1}^{N} w_i\left(\left|I_i^{\text{obs}} - I_i^{\text{calcd}}\right|^2\right)}{\sum_{i=1}^{N} \left|I_i^{\text{obs}}\right|^2}\right]^{1/2}, \qquad (3)$$

where I_i^{obs} and I_i^{calcd} are the observed and calculated intensities at the *i*th scan step, respectively; N is the total number of the points in the spectrum; and $w_i = 1/I_i^{\mathrm{obs}}$ is the weighting coefficient for each point.

In addition, the F_{30} factors were calculated for all the compounds studied in order to demonstrate the quality of the determination of unit-cell parameters according to Smith and Snyder [24]. This factor characterizes the absolute value of the average deviation of the 2θ angles of the first 30 lines of the experimental spectrum from the corresponding 2θ angles calculated based on the assumed model of the lines that could be present in the angular range, where the first 30 lines were observed. This factor depends on both the number of these possible (calculated) lines (N_{poss}) and the absolute value of the average deviation $|\overline{\Delta 2\theta}|$ and is calculated according to the following formula (see Tables 2 and 3):

$$F_{30} = \frac{1}{|\overline{\Delta 2\theta}|}\frac{30}{N_{\mathrm{poss}}}(|\overline{\Delta 2\theta}|, N_{\mathrm{poss}}). \tag{4}$$

The structures of compounds 1–3 and 6 were studied on a DRON-2 diffractometer using $\mathrm{Fe}K_{\alpha_{1,2}}$ radiation, which was isolated from the total spectrum using a Mn filter. The X-ray line spectra were recorded in the range of 2θ angles from 4° to 110° by a plotter, the scan rate was 1 or 0.5 deg/min, and the chart-paper speed was 600 mm/h.

The intensities of all the diffraction lines were determined from the heights of the maxima above the background. The X-ray patterns of compounds 1–3 were indexed using the X-ray diffraction pattern of $\mathrm{Bi_4Ti_3O_{12}}$ as a model pattern, because the line arrangement on the X-ray diffraction patterns of new orthorhombic Bi-containing layered perovskite-like oxides was identical to the X-ray pattern of the basic compound. The X-ray patterns of compounds 4 and 5 were also indexed according to the same automated procedure and then were used as model patterns for compound 6. X-ray diffraction patterns of compounds 1–3 were indexed by the analytical method, which showed that these compounds, like the basic compound, are described by sp. gr. *Fmmm*. The space group *I*4/*mmm* was also chosen for compound 6. The unit-cell parameters were refined by the least-squares method with the use of all the observed intensities.

We managed to index all the lines on the X-ray diffraction patterns of all the compounds synthesized in this study, which indicated that the samples contained no components of the starting charge or other phases that could have been formed in the course of sintering; in other words, this confirmed that we had synthesized single-phase compounds.

STRUCTURES OF NEW BISMUTH-CONTAINING LAYERED PEROVSKITE-LIKE OXIDES

The sets of experimental interplanar spacings and the corresponding spacings calculated based on the chosen structure model, *hkl* indices, and the relative intensities of reflections are given in Table 2 for orthorhombic structures and $\mathrm{Bi_4Ti_3O_{12}}$ and in Table 3 for tetragonal structures. In the crystal structures of new compounds, the A^i and B^j positions are filled with atoms, with the scattering power differing from the scattering power of $\mathrm{Bi^{III}}$ and $\mathrm{Ti^{IV}}$ atoms. This fact is responsible for the redistribution of the intensities of reflections on the X-ray diffraction patterns of new compounds compared to the distribution on the X-ray pattern of $\mathrm{Bi_4Ti_3O_{12}}$. The calculated reliability factors F_{30} for all the compounds and, particularly, the small average deviations of the calculated 2θ angles from the observed values (Tables 2, 3) indicate that the X-ray patterns are reliably indexed within the chosen space groups.

The unit-cell parameters of new orthorhombic Bi-containing layered perovskite-like oxides and the basic $\mathrm{Bi_4Ti_3O_{12}}$ compound are listed in Table 1. This table also lists the average parameters of the pseudotetragonal unit cells $\bar{a}_{pt}$ (both those observed ($\bar{a}_{pt}^{\mathrm{exp}}$) and those calculated according to the procedure suggested in [11] directly from the compound compositions ($\bar{a}_{pt}^{\mathrm{calcd}}$)) and the corresponding unit-cell volumes determined experimentally ($V_{\mathrm{un.\,cell}}$ and $V_{\mathrm{pt.\,cell}}$). The $\bar{a}_{pt}^{\mathrm{exp}}$ parameters were determined from the experimentally observed parameters of the orthorhombic unit cells a_{orth} and b_{orth} according to the following formula [9]:

$$\bar{a}_{pt}^{\mathrm{exp}} = (a_{\mathrm{orth}} + b_{\mathrm{orth}})/2\sqrt{2}. \tag{5}$$

The unit-cell parameters of the tetragonal compounds ($a_{\mathrm{tetr}} = b_{\mathrm{tetr}}$ and c) and their volumes $V_{\mathrm{un.\,cell}}$ are also given in Table 1 along with the $\bar{a}_{\mathrm{tetr}}^{\mathrm{calcd}}$ parameters calculated by the same method [11]. The $\bar{a}_{pt}$ parameters enable one to compare the dimensions (both experimentally observed and calculated) of the unit cells of orthorhombic and tetragonal Bi-containing layered perovskite-like oxides and also their volumes.

The reliability of the determination of the unit-cell parameters and volumes and the consistency of the assumed and obtained compositions (i.e., the existence of one phase) were indirectly confirmed by two more facts. First, the $\bar{a}_{pt}^{\mathrm{calcd}}$ parameters calculated using unstrained A^i–O and B^j–O interatomic bonds within the given chemical composition differ from the experimental $\bar{a}_{pt}^{\mathrm{exp}}$ values by less than 1% (the computational accuracy established in [11]), which indicates that the compositions of the compounds synthesized fully correspond to the set compositions. Second, the volumes of

Table 2. Experimentally observed (d_{obs}) and calculated (d_{calcd}) interplanar spacings (Å), relative intensities (I/I_0), $h\ k\ l$ indices, and reliability factors of line indexing on the X-ray diffraction patterns of orthorhombic bismuth-containing layered perovskite-like oxides

Phase	$Bi_4Ti_3O_{12}$			$Bi_4Ti_2Nb_{0.5}Fe_{0.5}O_{12}$			$Ca_{0.5}Bi_{3.5}Ti_{2.75}W_{0.25}O_{12}$		
$h\ k\ l$ and factors	I/I_0	d_{obs}	d_{calcd}	I/I_0	d_{obs}	d_{calcd}	I/I_0	d_{obs}	d_{calcd}
0 0 4	10	8.204	8.210	9	8.28	8.27	14	8.24	8.2
0 0 6	41	5.470	5.473	21	5.520	5.514	23	5.483	5.4
0 0 8	27	4.101	4.105	13	4.135	4.136	10	4.109	4.1
1 1 1	16	3.814	3.813	17	3.828	3.828	18	3.810	3.8
1 1 3	2	3.623	3.622	3	3.638	3.638	4	3.618	3.6
1 1 5	4	3.315	3.314	5	3.331	3.330	7	3.310	3.3
0 0 10	4	3.281	3.282	3	3.309	3.309	3	3.286	3.2
1 1 7	100	2.970	2.971	100	2.988	2.987	100	2.969	2.9
0 0 12	5	2.735	2.737	7	2.757	2.757	5	2.739	2.7
0 2 0	10	2.725	2.724	21	2.731	2.731	22	2.713	2.7
2 0 0	8	2.705	2.705	21	2.720	2.720	27	2.704	2.7
0 2 4	1	2.570	2.585	2	2.594	2.594	5	2.578	2.5
0 2 6	2	2.439	2.439				3	2.433	2.4
2 0 6	2	2.423	2.425	4	2.448	2.448	3	2.424	2.4
1 1 11			2.356						
0 0 14	33	2.344	2.345	21	2.363	2.363	11	2.347	2.3
0 2 8	6	2.270	2.270	13	2.278	2.278			
2 0 8	6	2.258	2.258	13	2.272	2.272	14	2.260	2.2
1 1 13	4	2.109	2.110	4	2.123	2.124	4	2.109	2.1
0 2 10									
2 0 10							2	2.088	2
0 0 16	5	2.051	2.052	4	2.0684	2.0679			
2 0 12	9	1.9198	1.923				6	1.925	1.92
2 2 0	9	1.9198	1.9196	16	1.9259	1.9266	18	1.9151	1.9
1 1 15	1	1.9007	1.9012	9	1.9142	1.9144	6	1.9016	1.90
0 0 18	2	1.8231	1.8236	3	1.8374	1.8381			
2 2 6	1	1.8113	1.8113	4	1.8193	1.8192	4	1.8084	1.80
0 2 14				4	1.7878	1.7872			
2 0 14	14	1.7722	1.7722	14	1.7842	1.7838	15	1.7725	1.75
2 2 8	2	1.7383	1.7383	4	1.7459	1.7468	3	1.7348	1.75
1 1 17	2	1.7249	1.7250				3	1.7243	1.75
1 3 1	1	1.7199	1.7197			1.7244	3	1.7132	1.7
3 1 1	1	1.7105	1.7192	4	1.7199	1.7184	3	1.7085	1.70
1 3 5	<1	1.6654	1.6656						
2 2 10			1.6571						
1 3 7	5	1.6163	1.6162				11	1.6121	1.6
3 1 7	4	1.6080	1.6082	15	1.6168	1.6169	17	1.6074	1.60
1 1 19	2	1.5753	1.5755	5	1.5871	1.5869	3	1.5764	1.55
2 2 12	2	1.5712	1.5714	3	1.5790	1.5796	3	1.5706	1.50
1 3 9			1.5570				3	1.5527	1.555
2 0 18			1.5121						
0 0 22	3	1.4918	1.4920				3	1.4936	1.49
2 2 14	3	1.4853	1.4855	12	1.4932	1.4936	6	1.4839	1.48
1 1 21	6	1.4475	1.4477	9	1.4582	1.4584	5	1.4483	1.44
0 0 24	3	1.3673	1.3677						
0 4 0	<1	1.3626	1.3622	5	1.3657	1.3658	4	1.3565	1.35
1 3 15	2	1.3529	1.3532				5	1.3504	1.35
4 0 0	3	1.3529	1.3525	5	1.3602	1.3598			
4 0 4			1.3345						
4 0 6	<1	1.3129	1.3130						
3 1 17	<1	1.2807	1.2808						
0 0 26	<1	1.2621	1.2621						
3 3 7	1	1.2346	1.2345	9	1.2396	1.2398	5	1.2317	1.2
1 1 25	<1	1.2424	1.2423						
2 0 24				5	1.2299	1.2296	5	1.2212	1.22
R_p	3.53								
R_{wp}	4.93								
F_{30}	114.9 (0.0063, 39)			33.1 (0.015, 61)			29.3 (0.020, 51)		

Table 3. Experimentally observed (d_{obs}) and calculated (d_{calcd}) interplanar spacings (Å), observed relative intensities of reflections (I/I_0), *h k l* indices, and reliability factors of line indexing on the X-ray diffraction patterns of tetragonal bismuth-containing layered perovskite-like oxides

Phase	$Nd_{0.5}Gd_{0.5}Bi_3Ti_3O_{12}$			$Ca_{0.25}Th_{0.25}Bi_{3.5}Ti_3O_{12}$			$Th_{0.5}Bi_{3.5}Ti_{2.5}Ga_{0.5}O_{12}$		
h k l and factors	I/I_0	d_{obs}	d_{calcd}	I/I_0	d_{obs}	d_{calcd}	I/I_0	d_{obs}	d_{calcd}
0 0 4	5	8.202	8.203	4	8.201	8.205	8	8.231	8.240
0 0 6	17	5.469	5.468	12	5.475	5.470	17	5.491	5.493
0 0 8	12	4.101	4.101	10	4.103	4.102	9	4.115	4.120
1 0 1	12	3.792	3.791	19	3.802	3.800	2	3.801	3.800
1 0 3	2	3.603	3.603	2	3.623	3.612			
1 0 5	6	3.299	3.299	4	3.300	3.305	6	3.311	3.309
1 0 7	100	2.959	2.959	100	2.964	2.964	100	2.970	2.969
0 0 12	6	2.734	2.734						
1 1 0	24	2.698	2.698	33	2.705	2.705	33	2.706	2.706
1 1 4				2	2.575	2.569	2	2.561	2.570
1 1 6	2	2.418	2.418	3	2.423	2.425	8	2.428	2.427
0 0 14	22	2.343	2.344	11	2.345	2.344	8	2.354	2.352
1 1 8	12	2.253	2.254	20	2.257	2.259	16	2.260	2.262
1 0 13	4	2.105	2.105	3	2.107	2.107	2	2.110	2.113
0 0 16	2	2.0511	2.0506	2	2.0510	2.0512	2	2.060	2.060
2 0 0	15	1.9081	1.9081	13	1.9130	1.9125	17	1.9135	1.9132
1 0 15	6	1.8983	1.8979	5	1.8981	1.8993	6	1.9059	1.9054
0 0 18	2	1.8250	1.8228	3	1.8246	1.8235			
2 0 6				2	1.8040	1.8058			
1 1 14	15	1.7687	1.7694	14	1.7712	1.7717	16	1.7759	1.7760
1 0 17	2	1.7231	1.7222						
2 0 8				3	1.7334	1.7338	4	1.7353	1.7352
2 1 1	2	1.7047	1.7044	3	1.7087	1.7087	2	1.7089	1.7089
2 1 7	12	1.6030	1.6037	17	1.6069	1.6074	12	1.6085	1.6083
1 0 19	2	1.5731	1.5733	3	1.5747	1.5744	2	1.5794	1.5798
0 0 22	2	1.4922	1.4914				2	1.4983	1.4981
2 0 14	3	1.4806	1.4797	6	1.4821	1.4821	5	1.4845	1.4846
1 0 21	7	1.4465	1.4459	6	1.4469	1.4468	9	1.4520	1.4520
2 0 16							2	1.4020	1.4018
2 2 0	3	1.3496	1.3492	2	1.3531	1.3527	4	1.3529	1.3527
2 1 15	4	1.3454	1.3455	3	1.3480	1.3478	3	1.3503	1.3501
1 1 22	4	1.3052	1.3053	1	1.3072	1.3064	3	1.3103	1.3106
3 0 7	4	1.2277	1.2277	4	1.2306	1.2306	9	1.2310	1.2310
3 1 0	5	1.2069	1.2068	4	1.2099	1.2099	4	1.2098	1.2099
2 0 22	3	1.1751	1.1750	2	1.1761	1.1764	3	1.1798	1.1795
2 2 14	3	1.1691	1.1693	3	1.1718	1.1716	4	1.1728	1.1729
3 1 8	4	1.1575	1.1577	3	1.1605	1.1605	3	1.1607	1.1609
2 1 21	6	1.1524	1.1524				6	1.1566	1.1566
R_p	7.05			6.83					
R_{wp}	9.40			8.91					
F_{30}	45.6 (0.0124, 53)			35.9(0.0144, 58)			27.2 (0.0150, 71)		

the pseudotetragonal (for the orthorhombic compounds) and tetragonal unit cells of all the newly synthesized compounds are determined as was expected, primarily by the dimensions of the oxygen–octahedral framework of the structure formed by the B^j atoms. Therefore, the unit-cell volume either increases or decreases (compared to the unit-cell volume of the basic compound) depending on the valence state of the B^j atoms that replace Ti^{IV} in the structure of the basic compound and on the lengths of the unstrained B^j–O interatomic bonds [11].

The unit-cell volumes decrease with an increase in the valence of the B^j atoms that replace Ti atoms in the perovskite-like layers of the basic lattice and with a decrease in the lengths of unstrained B^j–O interatomic bonds. And vice versa, the unit-cell volume increases with an increase in the lengths of unstrained B^j–O bonds and a simultaneous increase in the valence of B^j atoms. The A^i atoms that replace Bi^{III} atoms produce only a slight effect on the change of volumes.

The replacement of only Bi atoms in the A^i positions by the atoms forming shorter unstrained A^i–O bonds (compared to those formed by Bi) but having the same valence state (e.g., in $Nd^{III}_{0.5}Gd^{III}_{0.5}Bi_3\underline{Ti}_3O_{12}$) leads to a regular more pronounced decrease in the unit-cell volume and, sometimes, to a rearrangement of the orthorhombic structure into tetragonal form. Upon the replacement of Bi^{III} atoms by a rather small number of atoms with a lower and higher valency (Ca^{II} and Th^{IV}, respectively; 25% of each atom) and, all the more so, in the case of a simultaneous decrease in the unstrained A^i–O bond length (e.g., in $Ca_{0.25}Th_{0.25}Bi_{3.5}Ti_3O_{12}$), the unit-cell volumes remain virtually unchanged, but the A^i–O interatomic bonds become more strained.

Thus, we managed to synthesize six new bismuth-containing complex oxides with $m = 3$, whose existence is confirmed by X-ray diffraction study and the fact that the experimental characteristics of their structures are close to the corresponding calculated values. The unit-cell parameters and volumes of these compounds are determined. It is demonstrated that the change in the unit-cells dimensions correlates with the change in the chemical compositions.

ACKNOWLEDGMENTS

This study was supported by the Ministry of Education of the Russian Federation, grant no. E00-3.4-560.

REFERENCES

1. B. Aurivillius, Ark. Kemi **1**, 463 (1949).
2. B. Aurivillius, Ark. Kemi **1**, 499 (1949).
3. B. Aurivillius, Ark. Kemi **2**, 512 (1950).
4. B. Aurivillius and P. H. Fang, Phys. Rev. **126**, 893 (1962).
5. E. C. Subbarao, J. Phys. Chem. Solids **23**, 665 (1962).
6. G. I. Ismailzade, V. I. Nesterenko, F. A. Mirishli, and P. G. Rustamov, Kristallografiya **12** (3), 468 (1967) [Sov. Phys. Crystallogr. **12**, 400 (1967)].
7. G. A. Smolenskiĭ, V. A. Isupov, and A. I. Agranovskaya, Fiz. Tverd. Tela (Leningrad) **3**, 895 (1971) [Sov. Phys. Solid State **3**, 651 (1971)].
8. T. Kikuchi, A. Watanabe, and K. Uchida, Mater. Res. Bull. **12**, 299 (1977).
9. T. Kikuchi, Mater. Res. Bull. **14**, 1561 (1979).
10. *Physics of Ferroelectric Phenomena*, Ed. by G. A. Smolenskiĭ (Nauka, Leningrad, 1985).
11. G. A. Geguzina, E. G. Fesenko, and E. T. Shuvayeva, Ferroelectrics **167**, 311 (1995).
12. V. A. Isupov, Ferroelectrics **189**, 211 (1996).
13. L. A. Reznichenko, O. N. Razumovskaya, L. A. Shilkina, and N. V. Dergunova, Neorg. Mater. **32**, 474 (1996).
14. V. A. Isupov, Izv. Akad. Nauk SSSR, Neorg. Mater. **33**, 1106 (1997).
15. G. A. Geguzina, Kristallografiya **47** (6), 983 (2002) [Crystallogr. Rep. **47**, 913 (2002)].
16. G. A. Geguzina, in *Advances in Structure Analysis* (Chech and Slovak Crystallographic Association, Prague, 2000), p. 223.
17. G. A. Geguzina, A. T. Shuvaev, S. G. Gakh, and E. T. Shuvaeva, in *Proceedings of International Symposium on Phase Transitions in Solid Solutions and Alloys, Sochi* (2002), p. 52.
18. G. A. Geguzina, A. T. Shuvaev, E. T. Shuvaeva, *et al.*, in *Proceedings of International Symposium on Phase Transitions in Solid Solutions and Alloys*, *Sochi* (2002), p. 56.
19. E. G. Fesenko, V. G. Smotrakov, G. A. Geguzina, *et al.*, Neorg. Mater. **30**, 1446 (1994).
20. E. G. Fesenko, A. T. Shuvaev, V. G. Smotrakov, *et al.*, Neorg. Mater. **30**, 1057 (1994).
21. I. A. Trifonov, G. A. Geguzina, E. S. Gagarina, *et al.*, Neorg. Mater. **36**, 237 (2000).
22. I. A. Trifonov, G. A. Geguzina, A. T. Shuvaev, *et al.*, Neorg. Mater. **36**, 1358 (2000).
23. W. Kraus and G. Nolze, *PowderCell for Windows. Version 2.3* (Federal Inst. for Materials Research and Testing, Berlin, 1999).
24. G. S. Smith and R. L. Snyder, J. Appl. Crystallogr. **12**, 60 (1979).

Translated by T. Safonova

Crystallography Reports, Vol. 48, No. 3, 2003, pp. 413–415. Translated from Kristallografiya, Vol. 48, No. 3, 2003, pp. 458–460.
Original Russian Text Copyright © 2003 by Zyuzin, Moroz, Ivanova, Shmakov.

STRUCTURE OF INORGANIC COMPOUNDS

Structure Characteristics of Disordered Zirconium Hydroxoxides[1]

D. A. Zyuzin, E. M. Moroz, A. S. Ivanova, and A. N. Shmakov
Boreskov Institute of Catalysis, Siberian Division, Russian Academy of Sciences,
pr. Akademika Lavrent'eva 5, Novosibirsk, 630090 Russia
e-mail: zyuzin@catalysis.nsk.ru

Received December 3, 2002

Abstract—The structural characteristics of low-temperature zirconium hydroxoxide and zirconium dioxide obtained from zirconyl nitrate and treated at 383 and 653 K have been studied by the X-ray method of distribution of radial electron density. It is shown that the low-temperature hydroxide contains a ~10 to 15-Å nucleus of the crystalline phase with a structure of short-range order similar to the short-range order in ZrO_2. An increase in treatment temperature of zirconium hydroxide results in the formation of a mixture of cubic and monoclinic zirconium dioxide with a particle size of ~60 Å. *© 2003 MAIK "Nauka/Interperiodica".*

INTRODUCTION

At the present time, great interest is being shown in zirconium dioxides because of their widespead use in the manufacturing of ceramics, solid electrolytes, and catalysts. The structure and properties of zirconium dioxide depend on the method of their preparation and thermal treatment. It is well known that the cubic phase of zirconium dioxide belongs to the fluorite structure type and that the tetragonal and monoclinic phases are derived from this structure type.

The process of formation of zirconium hydroxide and dioxide from zirconyl chlorides is described in detail. It is shown [1] that zirconyl chloride hydrate, both in the solid state and in aqueous solution, contains a structural fragment, zirconium tetramer, which forms no direct bonds with chlorine ions. The tetramer is a square whose vertices are occupied by four zirconium atoms bound with four pairs of bridge hydroxyl groups. The interatomic distances in the tetramer are close to the corresponding distances in the first coordination spheres in the cubic, tetragonal, and monoclinic phases.

In solution, these tetramers are polymerized and form zirconium hydroxide $Zr(OH)_4 \cdot xH_2O$. At further annealing or aging, a dehydration of hydroxide takes place according to the scheme $Zr(OH)_4 \cdot xH_2O \longrightarrow ZrO(OH)_2 \cdot xH_2O \longrightarrow$ amorphous $ZrO_2 \cdot xH_2O \longrightarrow$ amorphous ZrO_2, which can slightly change depending on the conditions of the treatment [2].

The published data on further transformations of amorphous zirconium dioxide with an increase in the treatment temperature up to 400°C are inconsistent. There are data on the crystallization of the cubic, tetragonal, and monoclinic phases. However, an increase in the treatment temperature up to ~600°C results in the transformation of ZrO_2 into the monoclinic phase, which is stable up to ~1100°C [2].

The data concerning the preparation of ZrO_2 from zirconium nitrates are very scant. It is reported in [3] that, according to known data on chemical balance, as in zirconyl chloride, all the zirconium in the $Zr(NO_3)_4$ aqueous solution should exist in the form of tetramers. It was shown by small-angle X-ray scattering [4] that such solutions contain ~5-Å particles; however, their exact geometry has not been established. We found no data on the mechanism of the formation of zirconium dioxide from zirconyl nitrate.

Below, we descibe a study of structural characteristics of the compounds formed from aqueous solutions of zirconyl nitrate during the preparation of zirconium dioxide.

EXPERIMENTAL

The samples were prepared by the deposition of zirconyl nitrate solution by an aqueous solution of ammonia (1 : 1, pH 9) at a temperature of 343 ± 2 K with the subsequent filtration and washing of precipitates with distilled water until the disappearance of nitrates in the filter. The thermal treatment was performed for 4 h in a flow of dried air at 653 K (sample 2).

X-ray diffraction patterns were obtained on a high-resolution diffractometer on a synchrotron-radiation station in the Siberian Center of the Institute of Nuclear Physics of the Siberian Division of the Russian Academy of Sciences. An Si (111) crystal-monochromator provided the wavelength $\lambda = 0.695$ Å and the radiation monochromatization $\Delta\lambda/\lambda \sim 10^{-4}$. Scanning was performed in the angular range from 5° to 135° (by 2θ). The radial distribution functions (RDF) of electron-

---

[1] This study was submitted to the Symposium "Order, Disorder, and Properties of Oxides" (ODPO), Sochi, 2002.

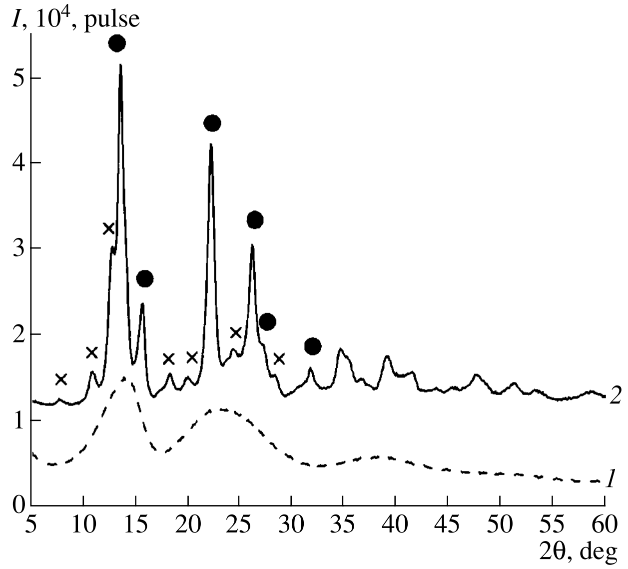

Fig. 1. X-ray diffraction patterns of samples (*1*) 1 and (*2*) 2. ● Cubic phase, × monoclinic phase.

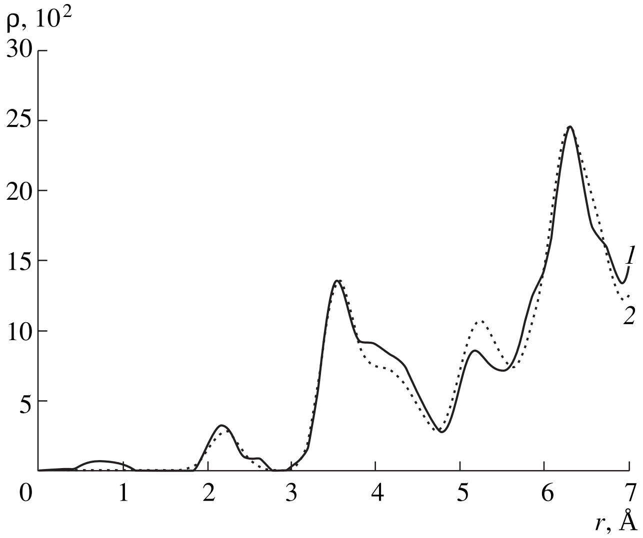

Fig. 2. (*1*) Experimental RDF of electron density of sample 2 and (*2*) the model RDF of electron density of the mixture of the monoclinic and cubic ZrO_2 phases in a 1 : 1 ratio. ρ is electron density, el^2/Å.

density were calculated using the technique suggested in [5].

RESULTS AND DISCUSSION

X-ray diffraction patterns from samples 1 and 2 are shown in Fig. 1. The maxima on the diffraction pattern from sample 1 are located in the ranges of diffraction peaks of the low-temperature cubic phase of zirconium dioxide. The crystallite size evaluated from the half-width of the diffraction peaks does not exceed 10–15 Å. On the diffraction pattern of sample 2, the diffraction peaks of the cubic and monoclinic phases are observed. Quantitative analysis with the use of an external standard showed that the content of the monoclinic phase in the sample is ~50%. The size of the crystallites of both phases is ~60 Å.

To interpret the curves of the radial electron density distribution of sample 1, we calculated the model RDF of electron-density for cubic zirconium dioxide using data in [6]. A comparison of these curves shows that the short-range order in sample 1 (up to distances of ~4 Å) is similar to the short-range order of the cubic phase. However, the interatomic distances in sample 1 are shorter, the coordination numbers (CN) of oxygen with respect to zirconium are higher (r = 2.15 Å, CN = 9.7, r = 3.99 Å, and CN = 35 instead of r = 2.2 Å, CN = 8, r = 4.22 Å, and CN = 24), and the coordination numbers of zirconium with respect to zirconium are lower (r = 3.4 Å and CN = 5.9 instead of r = 3.6 Å and CN = 12) than for the cubic phase. Earlier, we reported the formation of similar distorted structures in [7]. Moreover, the radial electron-density distribution in sample 1 has a peak at r = 2.58 Å, which we also identified with the Zr–O distances with CN = 3.9. Beginning from a distance of ~5 Å, the shape of the RDF of electron density of sample 1 does not differ from the curve of average electron density, which is explained by the small size of crystallites (~10 Å); this is also confirmed by the X-ray diffraction data. The high coordination numbers of oxygen with respect to zirconium are explained by the presence of OH-groups and coordination water in the sample. This is confirmed by the data on water losses during calcination—hydroxide loses 0.85 mol of H_2O per 1 mol of ZrO_2. The reduced coordination numbers of zirconium are explained by the small size of crystallites and distortion of the short-range order.

With an increase in temperature up to 653 K, the OH-groups are removed. The RDF of electron density of sample 2 and the model RDF of electron density for a mixture of the monoclinic and cubic zirconium dioxide phases in a 1 : 1 ratio are shown in Fig. 2 (curves *1* and *2*, respectively). The comparison of RDFs indicates that the Zr–Zr distances and the corresponding coordination members on the experimental curve correspond to the above composition. Almost all the Zr–O distances are characterized by high coordination numbers of oxygen with respect to zirconium in both monoclinic and cubic phases. This means that, during calcination, the monoclinic and cubic zirconium dioxide phases are formed based on the already formed cation sublattice and the anion sublattice still containing OH-groups.

CONCLUSIONS

The results obtained allow us to draw the following conclusions:

—Zirconium hydroxide prepared from zirconyl hydrate at 383 K is a highly dispersive system containing the nuclei of the crystalline phase with sizes not exceeding 15 Å; the short-range order of this hydroxide is similar to the short-range order in cubic ZrO_2.

—An increase in the treatment temperature up to 653 K results in the removal of OH-groups and a simultaneous increase in the particle size up to ~60 Å with the formation of the monoclinic and cubic zirconium dioxide phases. The structure of the latter phases differs from the structures of the known compounds in that it has high coordination numbers of oxygen with respect to zirconium.

REFERENCES

1. T. C. W. Mak, Can. J. Chem. **46**, 3491 (1968).
2. *Physical and Chemical Aspects of Adsorbents and Catalysts*, Ed. by B. G. Linsen (Academic, London, 1970; Mir, Moscow, 1973).
3. C. F. Baes, Jr. and R. E. Mesmer, *The Hydrolysis of Cations* (Wiley, New York, 1976).
4. L. M. Toth, J. S. Lin, and L. K. Felker, J. Phys. Chem. **95**, 3106 (1991).
5. E. M. Moroz, Russ. Chem. Rev. **61**, 188 (1992).
6. L. Katz, J. Am. Ceram. Soc. **54**, 531 (1971).
7. E. M. Moroz, A. S. Ivanova, and D. A. Zyuzin, J. Mol. Catal. A: Chem. **158**, 313 (2000).

Translated by T. Dmitrieva

Crystallography Reports, Vol. 48, No. 3, 2003, pp. 416–421. Translated from Kristallografiya, Vol. 48, No. 3, 2003, pp. 461–466.
Original Russian Text Copyright © 2003 by Gurskaya, Zavodnik, Shutalev.

STRUCTURE OF ORGANIC COMPOUNDS

X-ray Diffraction Studies of 5-Functionalized 1,2,3,4-Tetrahydropyrimidin-2-ones(thiones): II. Molecular and Crystal Structures of 5-Benzoyl-4,6-Dimethyl-1,2,3,4-Tetrahydropyrimidine-2-Thione and Ethyl 6-Phenyl-2-Thioxo-1,2,3,4-Tetrahydropyrimidine-5-Carboxylate

G. V. Gurskaya*, V. E. Zavodnik, and A. D. Shutalev*****
** Engelhardt Institute of Molecular Biology, Russian Academy of Sciences,*
ul. Vavilova 32, Moscow, 119991 Russia
e-mail: gurskaya@genome.eimb.relarn.ru
*** Karpov Research Institute of Physical Chemistry, State Scientific Center,*
ul. Vorontsovo pole 10, Moscow, 103064 Russia
**** Lomonosov State Academy of Fine Chemical Technology,*
pr. Vernadskogo 86, Moscow, 117571 Russia

Received July 19, 2002

Abstract—The structures of two new tetrahydropyrimidine-2-thiones, namely, 5-benzoyl-4,6-dimethyl-1,2,3,4-tetrahydropyrimidine-2-thione and ethyl 6-phenyl-2-thioxo-1,2,3,4-tetrahydropyrimidine-5-carboxylate, which are potential medicinals, are investigated using X-ray diffraction analysis. The conformational features of the molecules studied are analyzed. © *2003 MAIK "Nauka/Interperiodica".*

INTRODUCTION

In recent years, a large number of works have been concerned with the synthesis and structural investigation of 5-functionalized 1,2,3,4-tetrahydropyrimidin-2-ones and their 2-thioxo analogues (**I**) [1–6].

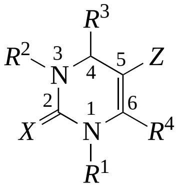

I

X = O, S
Z = COOR, COOH, C(O)NR_2, CN, NO$_2$, C(O)R

Scheme I

The considerable interest expressed by researchers in these compounds is associated primarily with the wide spectrum of their biological activities. In particular, it has been found that a number of tetrahydropyrimidine compounds exhibit antiviral, antibacterial, antihypertensive, and other activities [1–5].

It should be noted that, for the most part, these studies have dealt with compounds containing aryl groups at the C(4) atom. At the same time, compounds **I** that either contain no substituents at the C(4) atom or contain alkyl groups have been studied to a considerably smaller degree because of the lack of a unified convenient approach to their chemical synthesis.

In our earlier works [7, 8], we developed a new general method for preparing different 5-functionalized 1,2,3,4-tetrahydropyrimidin-2-ones(thiones). This method is based on the reaction of α-tosyl-substituted ureas or thioureas with enolates of α-substituted carbonyl compounds, followed by dehydration of the reaction products, namely, 4-hydroxyhexahydropyrimidin-2-ones(thiones). The method proposed makes it possible to synthesize not only 4-aryl-substituted pyrimidines **I** but also 4-unsubstituted or 4-alkyl-substituted pyrimidines. This study is a continuation of our X-ray structure investigations of 5-functionalized 1,2,3,4-tetrahydropyrimidin-2-ones(thiones) (**II**–**IV**) [9]. In the present work, we carried out X-ray diffraction analysis of two new compounds, namely, 5-benzoyl-4,6-dimethyl-1,2,3,4-tetrahydropyrimidine-2-thione (**V**) and ethyl 6-phenyl-2-thioxo-1,2,3,4-tetrahydropyrimidine-5-carboxylate (**VI**).

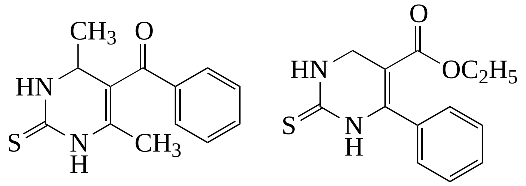

V **VI**

Scheme II

1063-7745/03/4803-0416$24.00 © 2003 MAIK "Nauka/Interperiodica"

Table 1. Atomic coordinates ($\times 10^4$ for C, N, O, and S; $\times 10^3$ for H) and thermal parameters (Å$^2 \times 10^3$ for C, N, O, and S; Å$^2 \times 10^2$ for H) for structure **V**

Atom	x/a	y/b	z/c	U_{iso}	Atom	x/a	y/b	z/c	U_{iso}
S	9372(1)	7435(1)	5538(1)	56(1)	H(1)	859(3)	704(5)	691(2)	4(1)
O(51)	8502(3)	–307(3)	7356(2)	53(1)	H(3)	922(4)	370(6)	537(2)	8(1)
N(1)	8498(3)	5953(4)	6719(2)	38(1)	H(4)	904(3)	129(5)	621(2)	3(1)
N(3)	8925(3)	3894(4)	5816(2)	48(1)	H(411)	641(4)	256(6)	561(2)	7(1)
C(2)	8911(4)	5638(5)	6039(2)	40(1)	H(412)	726(4)	127(6)	512(2)	8(1)
C(4)	8368(4)	2293(5)	6156(2)	41(1)	H(413)	671(4)	48(6)	583(2)	8(1)
C(5)	8160(3)	2774(4)	6964(2)	35(1)	H(53)	794(3)	–56(4)	873(2)	3(1)
C(6)	8230(3)	4546(5)	7210(2)	35(1)	H(54)	637(3)	–69(5)	950(2)	4(1)
C(41)	7089(5)	1652(7)	5643(3)	56(1)	H(55)	440(4)	103(5)	924(2)	6(1)
C(51)	7948(3)	1171(4)	7437(2)	37(1)	H(56)	401(4)	302(5)	811(2)	7(1)
C(52)	6964(4)	1230(4)	7963(2)	38(1)	H(57)	564(3)	308(4)	736(2)	3(1)
C(53)	7160(5)	81(5)	8603(2)	46(1)	H(611)	727(5)	582(6)	796(2)	8(2)
C(54)	6212(5)	6(6)	9071(3)	57(1)	H(612)	875(4)	633(6)	813(2)	8(1)
C(55)	5078(5)	1073(6)	8900(3)	59(1)	H(613)	828(4)	430(5)	842(2)	6(1)
C(56)	4867(4)	2204(6)	8263(2)	50(1)					
C(57)	5801(4)	2273(5)	7787(2)	44(1)					
C(61)	8125(5)	5265(6)	7995(2)	42(1)					

EXPERIMENTAL

The tetrahydropyrimidines studied in the present work were synthesized according to the procedure proposed in [7, 8]. Crystals suitable for X-ray diffraction analysis were prepared by slow evaporation of a solvent at room temperature from saturated solutions of compounds **V** and **VI** in methanol and acetonitrile, respectively.

The X-ray diffraction data and three-dimensional sets of intensities of reflections with $I > 2\sigma(I)$ for the crystals were collected on a CAD4 four-circle automated diffractometer (MoK_α radiation, β filter, θ/2θ scan mode).

The main crystallographic parameters are as follows:

Crystals **V** are monoclinic, a = 10.202(2) Å, b = 7.202(1) Å, c = 17.618(4) Å, β = 101.09(3)°, V = 1270.3(4) Å^3, Z = 4, d_{calcd} = 1.288 g/cm^3, and space group $P2_1/c$.

Crystals **VI** are triclinic, a = 8.630(1) Å, b = 9.556(1) Å, c = 16.597(1) Å, α = 80.89(1)°, β = 83.13(1)°, γ = 86.30(1)°, V = 1340.3(2) Å^3, Z = 4, d_{calcd} = 1.300 g/cm^3, and space group $P\bar{1}$.

The structures were solved by direct methods and refined using the full-matrix least-squares procedure in the anisotropic approximation for the non-hydrogen atoms. The hydrogen atoms were located from difference Fourier syntheses and refined by the least-squares method in the isotropic approximation. The discrepancy factors R are equal to 0.025 for 796 reflections with $I > 2\sigma(I)$ in structure **V** and 0.030 for 2895 reflections in structure **VI**. All the calculations were performed using the SHELX97 program package [10]. The atomic coordinates and thermal parameters for the studied structures are listed in Tables 1 and 2.

RESULTS AND DISCUSSION

The molecular structures of compound **V** and two crystallographically independent molecules of compound **VI** with the atomic numbering used in this work are shown in Figs. 1 and 2, respectively. The graphical calculations were performed with the SHELXTL81 program package [11]. The C, N, O, and S atoms are drawn in the form of thermal ellipsoids at the 50% probability level, and the H atoms are depicted as spheres of arbitrary radius.

By analogy with our previous work [9], the conformation (puckering) of the pyrimidine rings is described in two ways: (i) as is customary when analyzing the tetrahydropyrimidine structures [6], the conformation is treated in terms of a distorted boat: the boat bottom is represented by the plane passing through the C(2), N(3), C(5), and C(6) atoms (hereafter, this plane will be referred to as the plane of the pyrimidine ring) and the N(1) and C(4) atoms deviate from the bottom plane toward the same direction; and (ii) the conformation is examined on the basis of the dihedral angles ϕ between the least-squares planes that pass through the two planar groupings composed of the N(1), C(2), N(3), and S atoms (the thiourea fragment) and the N(1), C(4), C(5), and C(6) atoms [the fragment containing the C(5)=C(6)

Table 2. Atomic coordinates ($\times 10^4$ for C, N, O, and S; $\times 10^3$ for H) and thermal parameters ($Å^2 \times 10^3$ for C, N, O, and S; $Å^2 \times 10^2$ for H) for structure **VI**

Molecule 1					Molecule 2				
Atom	x/a	y/b	z/c	U_{eq}/U_{iso}	Atom	x/a	y/b	z/c	U_{eq}/U_{iso}
S	5270(1)	3379(1)	6630(1)	60(2)	Sa	502(1)	3364(1)	5947(1)	63(1)
O(51)	7641(2)	2657(2)	2747(1)	75(1)	O(51a)	−1664(2)	1252(3)	9908(1)	103(1)
O(52)	5619(2)	1312(3)	3018(1)	110(1)	O(52a)	156(2)	2795(2)	9940(1)	78(1)
N(1)	4431(2)	2945(2)	5206(1)	53(1)	N(1a)	1431(2)	2664(2)	7430(1)	57(1)
N(3)	6990(2)	3394(2)	5193(1)	52(1)	N(3a)	−1147(2)	2433(2)	7364(1)	66(1)
C(2)	5604(2)	3238(2)	5626(1)	47(1)	C(2a)	228(2)	2789(2)	6955(2)	54(1)
C(4)	7309(3)	3411(3)	4316(2)	58(1)	C(4a)	−1297(3)	1619(4)	8184(2)	76(1)
C(5)	6087(2)	2668(2)	4001(1)	47(1)	C(5a)	−144(3)	2088(3)	8681(2)	60(1)
C(6)	4673(2)	2529(2)	4436(1)	45(1)	C(6a)	1229(2)	2532(2)	8284(1)	52(1)
C(51)	6528(2)	2236(3)	3199(1)	53(1)	C(51a)	−619(3)	1983(3)	9567(2)	69(1)
C(52)	5882(5)	877(9)	2205(4)	129(2)	C(52a)	−185(6)	2743(6)	10 823(2)	106(1)
C(53)	4447(6)	642(7)	1946(3)	126(2)	C(53a)	872(8)	3708(7)	11 073(3)	130(2)
C(61)	3268(2)	1989(2)	4174(1)	45(1)	C(61a)	2610(2)	2903(2)	8647(1)	50(1)
C(62)	2810(3)	636(3)	4469(2)	68(1)	C(62a)	3250(3)	4202(3)	8394(2)	62(1)
C(63)	1533(3)	133(3)	4195(2)	79(1)	C(63a)	4549(4)	4538(4)	8726(2)	81(1)
C(64)	705(3)	983(3)	3648(2)	73(1)	C(64a)	5217(4)	3576(4)	9295(2)	84(1)
C(65)	1119(3)	2347(4)	3374(2)	72(1)	C(65a)	4611(3)	2276(4)	9539(2)	76(1)
C(66)	2412(3)	2855(3)	3632(2)	59(1)	C(66a)	3301(3)	1931(3)	9224(2)	63(1)
H(1)	356(3)	295(2)	545(1)	5(1)	H(1a)	230(3)	288(3)	718(2)	6(1)
H(3)	772 (3)	349(3)	549(1)	6(1)	H(3a)	−193(4)	260(3)	708(2)	9(1)
H(41)	829(3)	299(3)	419(2)	8(1)	H(41a)	−224(4)	171(3)	841(2)	8(1)
H(42)	729(3)	442(3)	405(2)	8(1)	H(42a)	−112(3)	54(4)	811(2)	10(1)
H(521)	613(8)	158(6)	179(4)	20(3)	H(521a)	−128(5)	299 (4)	1087(2)	13(1)
H(522)	677(5)	40(4)	218(2)	10(1)	H(522a)	11(6)	179(5)	1106(3)	17(2)
H(531)	503(10)	−47(9)	253(5)	29(3)	H(531a)	63(6)	367(6)	1166(4)	20(2)
H(532)	360(7)	126(6)	206(3)	18(2)	H(532a)	204(8)	342(6)	1086(4)	21(3)
H(533)	458(4)	28(4)	141(2)	13(1)	H(533a)	54(8)	485(8)	1072(4)	27(3)
H(62)	336(3)	7(3)	487(2)	8(1)	H(62a)	279(3)	486(3)	801(2)	8(1)
H(63)	119(4)	−76(4)	442(2)	10(1)	H(63a)	493(4)	539(4)	856(2)	9(1)
H(64)	−18(3)	64(3)	344(2)	9(1)	H(64a)	611(4)	380(3)	951(2)	9(1)
H(65)	46(3)	293(3)	302(2)	9(1)	H(65a)	508(4)	163(3)	991(2)	10(1)
H(66)	275(3)	376(3)	341(2)	7(1)	H(66a)	278(3)	104(3)	939(2)	7(1)

double bond] in the pyrimidine rings. The ϕ angles clearly demonstrate the degree of puckering of the pyrimidine rings.

The conformations of the side radicals (substituents) are also analyzed using two parameters, namely, the angles between the least-squares planes of the flattened molecular fragments and the torsion angles.

Compounds **V** and **VI** differ from each other in the substituent at the C(4), C(5), and C(6) atoms of the pyrimidine rings.

The calculated bond lengths and angles in the structures studied are in agreement within the accuracy of their determination and are close to those available in the literature. Therefore, below we dwell only on the analysis of the conformational features of the molecules.

The presence of identical radicals (methyl groups) at the C(4) and C(6) atoms in molecule **V** leads to a certain flattening of its pyrimidine ring as compared to that in molecules **VI**. The latter molecules involve the phenyl substituent at the C(6) atom and no substituent at

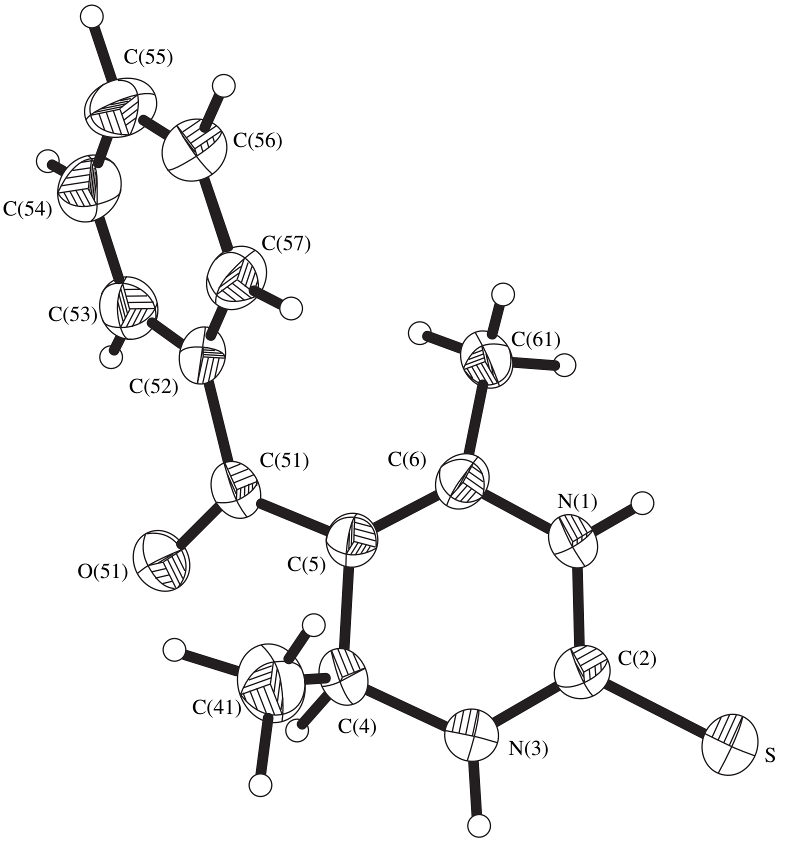

Fig. 1. Molecular structure of compound **V**.

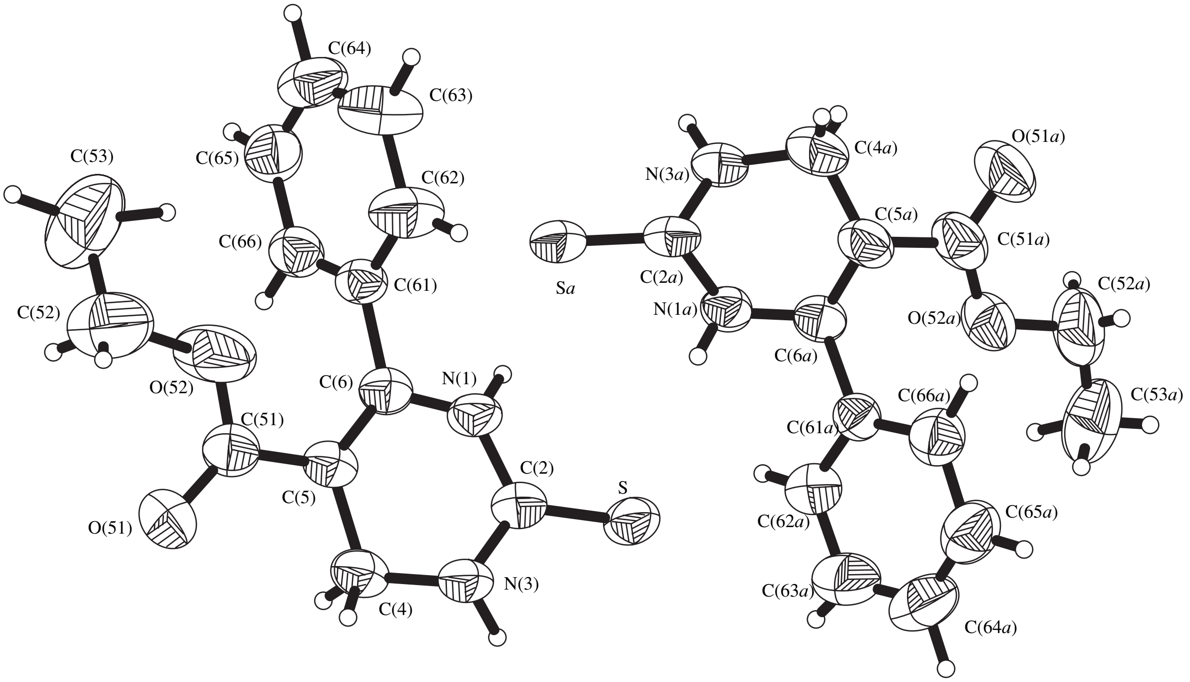

Fig. 2. Structures of crystallographically independent molecules 1 and 2 in compound **VI**.

Table 3. Selected torsion angles (deg) characterizing the conformation of the pyrimidine rings and relative orientations of the substituents at the C(4), C(5), and C(6) atoms in molecules of compounds **V** and **VI**

Torsion angle	**V**	**VI**		Torsion angle	**V**	**VI**	
		Molecule				Molecule	
		1	2			1	2
C(4)–N(3)–C(2)–S	–170.6(3)	–174.1(2)	164.4(2)	C(6)–C(5)–C(51)–C(52)	41.6(6)		
C(6)–N(1)–C(2)–S	–173.2(3)	–166.2(2)	163.7(2)	C(6)–C(5)–C(51)–O(52)		–19.6(3)	22.0(4)
N(1)–C(6)–C(5)–C(4)	–0.2(5)	–6.7(3)	6.4(4)	C(5)–C(51)–C(52)–C(57)	32.2(5)		
C(6)–C(5)–C(4)–N(3)	12.9(5)	22.3(3)	–32.5(4)	C(51)–O(52)–C(52)–C(53)		–144.9(5)	178.2(4)
C(5)–C(4)–N(3)–C(2)	–18.5(6)	–23.0(3)	39.1(4)	C(51)–C(5)–C(6)–C(61)	0.6(6)	–3.5(4)	5.3(4)
C(4)–N(3)–C(2)–N(1)	9.6(6)	6.2(3)	–16.3(4)	C(51)–C(5)–C(4)–C(41)	72.1(4)		
N(3)–C(2)–N(1)–C(6)	6.6(5)	13.5(3)	–15.6(3)	C(53)–C(52)–C(51)–O(51)	32.3(5)		
C(2)–N(1)–C(6)–C(5)	–11.0(5)	–13.0(3)	20.3(4)	C(52)–O(52)–C(51)–O(51)		–5.9(6)	4.3(5)
C(2)–N(3)–C(4)–C(41)	105.4(4)			O(51)–C(51)–C(52)–C(57)	–141.6(4)		
C(6)–C(5)–C(4)–C(41)	–110.5(4)			C(2)–N(1)–C(6)–C(61)	165.9(4)	168.2(2)	–160.1(2)
N(3)–C(4)–C(5)–C(51)	–164.6(3)	–161.7(2)	149.0(2)	C(4)–C(5)–C(6)–C(61)	–176.5(4)	172.0(2)	–173.1(3)
N(1)–C(6)–C(5)–C(51)	177.0(3)	177.8(2)	–175.2(2)	N(1)–C(6)–C(61)–C(62)		–78.5(3)	54.7(3)
C(4)–C(5)–C(51)–O(51)	32.7(5)	–13.7(3)	18.0(4)	C(5)–C(6)–C(61)–C(62)		102.8(3)	–125.7(3)
C(6)–C(5)–C(51)–O(51)	–144.6(4)	162.0(2)	–160.5(3)	N(1)–C(6)–C(61)–C(66)		101.3(2)	–123.1(2)
C(4)–C(5)–C(51)–C(52)	–141.0(4)			C(5)–C(6)–C(61)–C(66)		–77.4(3)	56.4(3)
C(4)–C(5)–C(51)–O(52)		164.7(2)	–159.6(3)	C(5)–C(51)–O(52)–C(52)		175.7(4)	–178.1(3)
C(5)–C(51)–C(52)–C(53)	–153.9(4)						

Table 4. Geometric parameters of the intermolecular hydrogen bonds in structures **V** and **VI**

D–H···*A* hydrogen bond*	*D*···*A* distance, Å	H···*A* distance, Å	*D*–H···*A* angle, deg	Symmetry operation for *A*
V				
N(3)–H···S	3.350(3)	2.48(4)	160(4)	(2 –*x*, 1 – *y*, 1 – *z*)
N(1)–H···O(51)	2.917(4)	2.08(3)	171(3)	(*x*, *y* + 1, *z*)
VI				
N(1)–H···S*a*	3.486(2)	2.69(3)	167(2)	(*x*, *y*, *z*)
N(1*a*)–H···S	3.487(2)	2.66(3)	170(2)	(*x*, *y*, *z*)
N(3)–H···S*a*	3.411(2)	2.59(3)	159(2)	(*x* + 1, *y*, *z*)
N(3*a*)–H···S	3.472(2)	2.64(3)	162(3)	(*x* – 1, *y*, *z*)
C(65)–H···O(51)	3.273(3)	2.56(3)	131(2)	(*x* – 1, *y*, *z*)
C(62*a*)–H···O(51)	3.382(4)	2.52(3)	152(2)	(1–*x*, 1 – *y*, 1 – *z*)
C(66*a*)–H···O(51*a*)	3.465(4)	2.50(3)	168(2)	(–*x*, –*y*, 2 – *z*)
C(53*a*)–H···O(52*a*)	3.603(6)	2.42(8)	178(5)	(–*x*, 1 – *y*, 2 – *z*)

* *D* is a donor atom, H is a hydrogen atom, and *A* is an acceptor atom.

the C(4) atom. The deviations of the N(1) and C(4) atoms from the least-squares plane of the C(2), N(3), C(5), and C(6) atoms in compound **V** are equal to 0.088(5) and 0.189(6) Å, respectively. The corresponding deviations in compound **VI** are 0.132(3) and 0.271(4) Å in molecule 1 and 0.179(3) and 0.426(5) Å in molecule 2, respectively. The ϕ angles are proportional to the above deviations. The ϕ angle in the molecule of compound **V** is equal to 9.3(3)°. In compound **VI**, these angles are as follows: ϕ = 16.0(2)° in molecule 1 and ϕ = 21.3(1)° in molecule 2. As can be seen, the ϕ angles clearly reflect a higher degree of puckering of the pyrimidine ring in the molecules of compound **VI**, especially, in molecule 2.

In molecules of compound **V**, the bulky benzoyl radical at the C(5) atom has a nonplanar structure. In this radical, the plane of the benzene ring is rotated by an angle of 33.4(4)° with respect to the plane of the C(5)C(51)O(51) carbonyl fragment. The planes of the phenyl group and the carbonyl fragment make angles of 60.5(2)° and 29.3(5)° with the plane of the pyrimidine ring.

The crystallographically independent molecules of compound **VI** differ not only in the degree of puckering of the pyrimidine ring but also in the orientation of the phenyl rings with respect to the pyrimidine rings and in the structure and orientation of the ethoxycarbonyl fragments.

In compound **VI**, the plane of the benzene ring in molecule 1 forms an angle of 74.7(1)° with the plane of the pyrimidine ring. The ethoxycarbonyl fragment adopts a nonplanar conformation. The angle between the planes that pass through the O(52), C(52), and C(53) atoms of the ethoxy group and the C(5), C(51), and O(51) atoms of the carbonyl fragment is equal to 31.5(6)°. The plane of the ethoxy group makes an angle of 11.1(4)° with the plane of the pyrimidine ring and an angle of 83.8(4)° with the plane of the benzene ring. The angles formed by the plane of the carbonyl fragment with the planes of the pyrimidine and phenyl rings are equal to 23.2(3)° and 74.4(2)°, respectively.

At the same time, in molecule 2 of compound **VI**, the angle between the benzene and pyrimidine rings is equal to 51.3(1)°. The non-hydrogen atoms of the ethoxycarbonyl group are arranged in the same plane, to within the mean deviation of 0.011 Å. The least-squares plane of the ethoxycarbonyl group forms an angle of 32.6(2)° with the plane of the pyrimidine ring and an angle of 57.0(1)° with the plane of the benzene ring.

All the aforementioned conformational features of the molecules clearly manifest themselves in the torsion angles (Table 3).

In molecules of the tetrahydropyrimidines studied by X-ray diffraction in [9] and the present work, the phenyl fragments of the side radicals exhibit a tendency to lie almost perpendicularly with respect to the pyrimidine rings.

As in nucleosides and nucleotides, the molecular packing in the crystal structure of tetrahydropyrimidines is characterized by a tendency to dimerization due to the formation of intermolecular hydrogen bonds between the pyrimidine rings. In crystals of compound **V** with one molecule in the asymmetric part of the unit cell, the molecules related by the symmetry center form dimers through two N(3)–H···S symmetric intermolecular hydrogen bonds (see Table 4). The dimers are linked together into a three-dimensional crystal structure through the N(1)–H···O(51) intermolecular hydrogen bonds and van der Waals forces.

In crystals of compound **VI** with two molecules in the asymmetric part of the unit cell, the crystallographically independent molecules form dimers through the N(1)(x, y, z)–H··Sa(x, y, z) and N(1a)(x, y, z)–H··S(x, y, z) hydrogen bonds. These dimers are joined together to form a three-dimensional crystal via the N(3)(N(3a))–H··Sa(S) intermolecular hydrogen bonds and van der Waals forces. By analogy with structure **IV** studied in [9], intermolecular hydrogen bonds of the C–H··O type can contribute to the stabilization of the crystal structure. These hydrogen bonds can involve the O(51), O(52), O(51a), and O(52a) atoms (in the ethoxycarbonyl fragments) that do not participate in other hydrogen bonds. The geometric parameters of the selected hydrogen bonds are presented in Table 4.

CONCLUSIONS

Thus, we performed X-ray structure investigations of two new tetrahydropyrimidine-2-thiones, namely, 5-benzoyl-4,6-dimethyl-1,2,3,4-tetrahydropyrimidine-2-thione **V** and ethyl 6-phenyl-2-thioxo-1,2,3,4-tetrahydropyrimidine-5-carboxylate **VI**. The conformational features of the molecules in the compounds studied were analyzed. In the future, they can be used to reveal a correlation between the three-dimensional structure and biological activity in the series of pyrimidine derivatives.

ACKNOWLEDGMENTS

This work was supported by the Russian Foundation for Basic Research, project no. 00-15-74835.

REFERENCES

1. C. O. Kappe, Tetrahedron **49**, 6937 (1993).
2. C. O. Kappe, Acc. Chem. Res. **33**, 879 (2000).
3. K. S. Atwal, B. N. Swanson, S. E. Unger, *et al.*, J. Med. Chem. **34**, 806 (1991).
4. G. J. Grover, S. Dzwonczyk, D. M. McMullen, *et al.*, J. Cardiovasc. Pharmacol. **26**, 289 (1995).
5. G. C. Rovnyak, S. D. Kimball, B. Beyer, *et al.*, J. Med. Chem. **38**, 119 (1995).
6. C. O. Kappe, W. M. F. Fabian, and M. A. Semones, Tetrahedron **53**, 2803 (1997).
7. A. D. Shutalev and V. A. Kuksa, Khim. Geterotsikl. Soedin., No. 1, 97 (1995).
8. A. D. Shutalev, E. A. Kishko, N. V. Sivova, and A. Yu. Kuznetsov, Molecules **3**, 100 (1998).
9. G. V. Gurskaya, V. E. Zavodnik, and A. D. Shutalev, Kristallografiya **48** (1), 97 (2003) [Crystallogr. Rep. **48**, 92 (2003)].
10. G. M. Sheldrick, *SHELX97: System of Computer Programs for the Solution and Refinement of Crystal Structures* (Univ. of Göttingen, Göttingen, 1997).
11. G. M. Sheldrick, *SHELXTL81: User Manual, Revision 3* (1981).

Translated by O. Borovik-Romanova

Crystallography Reports, Vol. 48, No. 3, 2003, pp. 422–425. Translated from Kristallografiya, Vol. 48, No. 3, 2003, pp. 467–470.
Original Russian Text Copyright © 2003 by Antsyshkina, Sadikov, Sergienko, Garnovskiĭ.

STRUCTURE OF ORGANIC COMPOUNDS

Specific Stereochemical Features of Metallochelate Complexes with Tridentate *N*,*N*,*N*(*N*,*N*,O)-Donating Ligands

A. S. Antsyshkina*, G. G. Sadikov*, V. S. Sergienko*, and D. A. Garnovskiĭ**

** Kurnakov Institute of General and Inorganic Chemistry, Russian Academy of Sciences,*
Leninskiĭ pr. 31, Moscow, 119991 Russia
e-mail: antas@igic.ras.ru
*** Research Institute of Physical and Organic Chemistry, Rostov State University,*
pr. Stachki 194, Rostov-on-Don, 344104 Russia

Received May 6, 2002

Abstract—Earlier X-ray diffraction studies of a series of 12 adducts (**I**–**XII**) between metallochelate complexes [M = Co(II), Ni(II), and Cu(II)] with tridentate *N*,*N*,*N*(*N*,*N*,O)-donating Schiff bases (L) and monodentate or bidentate ligands (L') revealed a similarity in the stereochemistry of these compounds. The coordination polyhedron of metal atoms in compounds **I**–**XII** is a tetragonal pyramid (bipyramid) with two vertices occupied competitively. The L ligand occupies three coordination sites in the base of the pyramid. The L' ligand approaches the metal atom, as a rule, in a direction perpendicular to the basal plane. The fourth site in the base of the pyramid and the apical vertex are occupied competitively. Different patterns of occupation of these positions are observed: they include the donor atoms of both the L and L' ligands. *© 2003 MAIK "Nauka/Interperiodica".*

By now, a series of metal [Co(II), Ni(II), and Cu(II)] complexes (**I**–**XII**) with tridentate chelate *N*,*N*,*N*(*N*,*N*,O)-donating Schiff bases as ligands has been studied by X-ray diffraction.

X-ray diffraction studies revealed that the structures of these compounds are similar in many respects.

Some stereochemical characteristics of compounds **I**–**XII** are summarized in the table.

Structural characteristics of compounds **I**–**XII**

Structure no.	Compound MLL'	Accompanying equatorial ligand	Apical ligand	Δ, Å	Δ', Å	d, Å			Reference
						mean M–L_{eq}		M–L_{ap}	
						M–N	M–O		
I	NiL^1(AP)	O(L)	N(AP)	±0.06	0.40	1.96	2.41	2.01	[1]
II	CuL^1(*Me*OH)	O(*Me*OH)	O(L)	±0.44	0.22	1.91	2.06	2.64	[1]
III	CuL^2(MABI)	N(MABI)	O(L)	±0.38	0.06	1.97	1.89	3.13	[2]
IV	CoL^2(H_2O)(MABI)	O(H_2O)	N(MABI)	±0.04	0.49	2.06	2.03	2.04	[3]
V	CoL^3(MABI)$_2$	N(MABI)$_1$	N(MABI)$_2$	±0.27	0.35	2.11	2.00	2.11	[4]
VI	CuL^4(*Phen*)	N(*Phen*)	N(*Phen*)	±0.18	0.12	1.99	1.94	2.32	[5]
VII	CuL^3(*Bipy*)	N(*Bipy*)	N(*Bipy*)	±0.23	0.16	1.99	1.94	2.35	[6]
VIII	CuL^5(O*Ac*)	O(*Ac*)	O(O*Ac*)	±0.26	0.55	1.98	1.97	2.65	[7]
IX	[CoL^3(*Me*OH)]$_2$	O'(L)	[O(*Me*OH)	±0.26	0.33	2.06	2.02	2.04	[8]
X	[NiL^3(*Me*OH)$_2$]$_2$	O'(L)	2[O(*Me*OH)	0.0	0.0	2.05	2.05	2.11	[6]
XI	[NiL^4(*Phen*)]$_2$	N(*Phen*)	N(*Phen*); O'(L)	±0.09	0.0	2.09	2.11	2.13	[5]
XII	[CuL^6(O*Ac*)]$_2$	O(O*Ac*)	O'(O*Ac*)	±0.08	0.27	1.98	1.96	2.53	[7]

Note: AP is aminopyridine, MABI is 1-methyl-2-aminobenzimidazole, H_2L^1 is 2-N-tosylamino(2'-tosylaminobenzal)aniline, H_2L^2 is 2-N-tosylamino(N'-benzylideneaniline), H_2L^3 is 2-N-tosylaminophenyl(iminomethyl)phenol, H_2L^4 is [N-(2-oxophenyl)methylidene]-N'-tosylbenzene-1,2-diamine, H_2L^5 is (2-N-tosylaminobenzylideneimino)quinoline, H_2L^6 is (5-chlorosalicilideneimino)quinoline, Δ is the largest deviation of the equatorial atoms from the rms plane, and Δ' is the deviation of the metal atom from the equatorial plane toward the apical vertex.

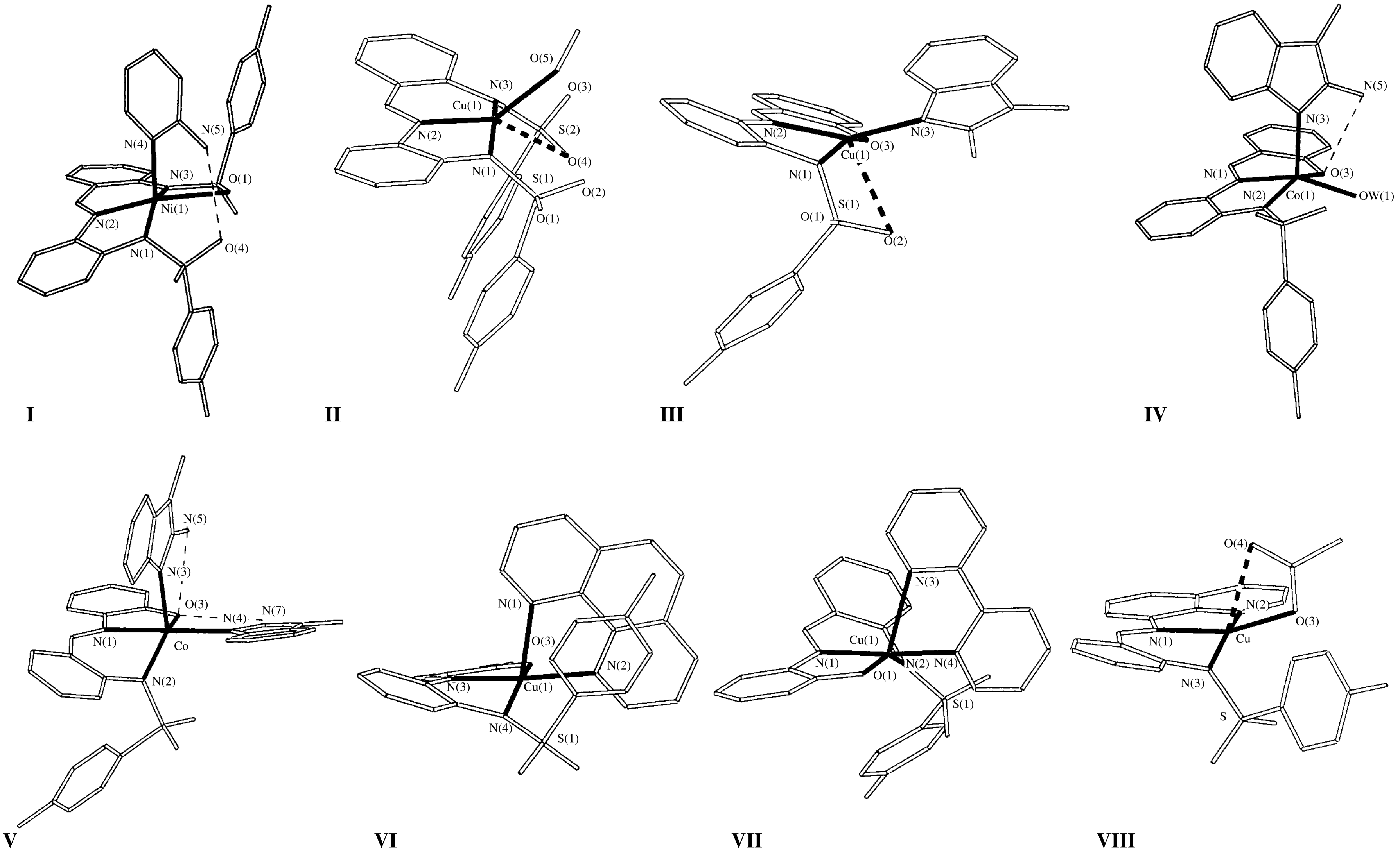

Structures of complexes **I**–**XII**.

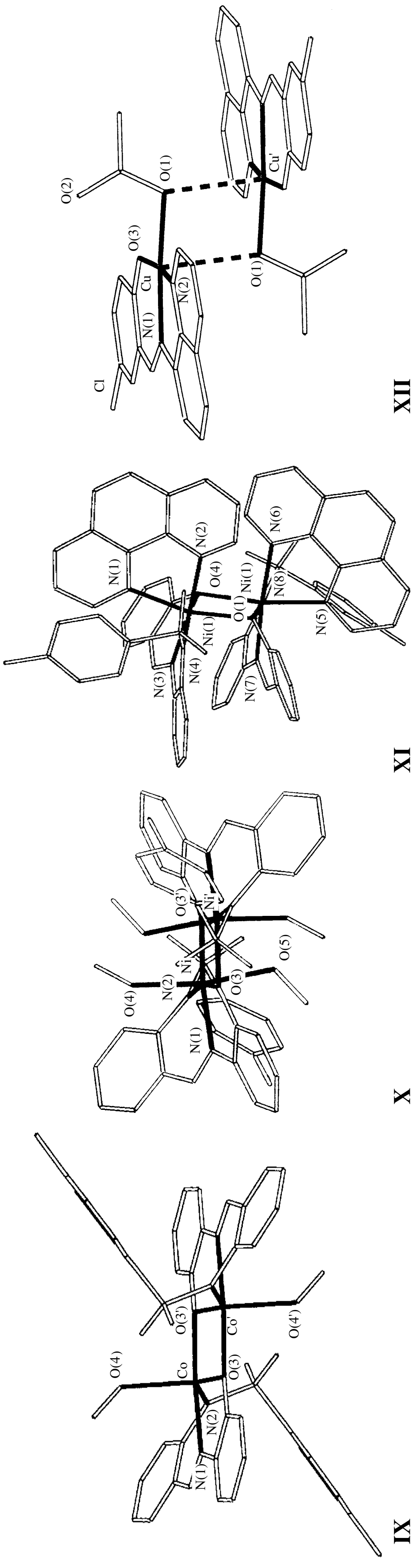

Figure. (Contd.)

In compounds **I**–**XII**, the planar tridentate bischelate ligand *L* forms the basal plane of the coordination polyhedron. As a rule, the base of the polyhedron is a tetrahedrally distorted square whose fourth vertex is competitively occupied, so various patterns of its occupation are observed. The degree of distortion of the square base Δ (the largest deviation of the four donor atoms from the rms plane) varies from zero (compound **X**) to significant values (complexes **II** and **III**). If the accompanying ligand *L*' (or a fragment of ligand *L*) approaches the metal atom as viewed from the direction perpendicular to the equatorial plane, the coordination of the central atom is added to the tetragonal pyramid, or in some cases, the tetragonal bipyramid. The apical vertex in the tetragonal pyramid, like the fourth site in its base, is occupied competitively.

The metal atom usually deviates from the base of the pyramid toward the apical vertex. This deviation (Δ') varies from zero (compound **XI**) to a value larger than 0.5 Å (complex **VIII**).

The variants of competitive occupation of the positions in the tetragonal pyramids (bipyramid) of compounds **I**–**XII** are shown in the figure.

In structure **I** [1], the fourth site in the base of the pyramid is occupied by the peripheral (not involved in the planar fragment) oxygen atom of the *L* ligand. This variant has never been observed before. The fourth site can be occupied by an accompanying ligand, for example, a methanol molecule in structure **II** [1] or a 1-methyl-2-aminobenzimidazole (MABI) molecule in **III** [2].

Molecules of additional ligands (identical or different) most commonly occupy both vacant vertices of the tetragonal pyramid. In the structure of Co*LL*' (H_2O) (**IV**) [3], the vertex in the base of the tetragonal pyramid is occupied, apart from the tridentate ligand *L*, by a water molecule, whereas the apical position is occupied by the accompanying ligand *L*' (MABI). In the $\mathrm{Co}LL_2'$ complex (**V**) [4], both the sites occupied competitively include identical MABI ligands.

In Cu*LL*' complexes, both the sites occupied competitively can include a bidentate ligand of the *Phen* (**VI**) [5] or *Bipy* (**VII**) [6] type or simply the bidentate acetate group (**VIII**) [7]. In the latter compound, the tetragonal-pyramidal metal coordination is severely distorted.

One of the atoms of the *L* ligand that coordinate the metal atom can additionally form a bond with the metal atom of the neighboring complex and occupy the vacant site in the base of the tetragonal pyramid. This results in the formation of a dimer structure similar to that observed in $(\mathrm{Co}LL_2')_2$ (**IX**) [8], in which two *L* ligands of the dimer fulfill the tetradentate bischelate bridging function.

In the $(\mathrm{Ni}LL_2')_2$ dimer compound (**X**) [6], the Ni polyhedron is added to the pseudooctahedron by including the second methanol molecule in the second apical vertex.

A distinctly different pattern of dimer formation is observed in the $(\mathrm{Ni}LL')_2$ complex (**XI**) [5], where *L*' is the accompanying bidentate ligand *Phen*. In this complex, the fourth site in the base of the pyramid is occupied by one of the atoms of the chelate *L*' ligand and the oxygen atom of the *L* ligand serves as a bridge: it is located at the equatorial site of one half of the dimer and at the apical site of the other half. The asymmetric parts of the dimer in this complex are related by the C_2 pseudoaxis, not the center of symmetry as in **IX** or **X**, and the dimer as a whole is essentially polar.

The *L*' ligand can also play a bridging role to form a pseudodimer, for example, in the structure of $(\mathrm{Cu}LL')_2$ (**XII**) [7], where $L' = CH_3C(O)O^-$.

Some of the complexes considered, for example, Ni*LPy*, where H_2L = [2-(2'-tosylaminophenyl)iminomethyl]mercaptophenol [9], have planar structures (with a vacant apical position).

Intramolecular and intermolecular hydrogen bonds (some of them are shown in the figure) additionally stabilize the structures of the compounds described above. The components of these bonds are usually fragments of the *L*' ligand (donors) and atoms (usually, O) of the *L* ligand (acceptors). In some structures, uncoordinated solvent molecules are also involved in hydrogen bonding.

REFERENCES

1. D. A. Garnovskiĭ, A. S. Antsyshkina, G. G. Sadikov, *et al.*, Kristallografiya **48** (2), 259 (2003) [Crystallogr. Rep. **48**, 322 (2003)].
2. D. A. Garnovskiĭ, A. Sousa, A. S. Antsyshkina, *et al.*, Izv. Akad. Nauk, Ser. Khim., No. 8, 2093 (1996).
3. D. A. Garnovskiĭ, A. S. Antsyshkina, G. G. Sadikov, *et al.*, Zh. Neorg. Khim. **43** (11), 1852 (1998).
4. A. S. Antsyshkina, G. G. Sadikov, A. S. Burlov, *et al.*, Koord. Khim. **26** (10), 779 (2000).
5. M. Bernal, J. A. García-Vázquer, J. Romero, *et al.*, Inorg. Chim. Acta **295** (1), 39 (1999).
6. A. D. Garnovskii, A. S. Burlov, and D. A. Garnovskii, Polyhedron **18**, 863 (1999).
7. I. S. Vasil’chenko, A. S. Antsyshkina, A. S. Burlov, *et al.*, Zh. Neorg. Khim. **44** (8), 1278 (1999).
8. A. S. Antsyshkina, G. G. Sadikov, A. S. Burlov, *et al.*, Zh. Neorg. Khim. **45** (11), 1811 (2000).
9. A. S. Burlov, A. S. Antsyshkina, H. Romero, *et al.*, Zh. Neorg. Khim. **40** (9), 1480 (1995).

Translated by I. Polyakova

Crystallography Reports, Vol. 48, No. 3, 2003, pp. 426–434. Translated from Kristallografiya, Vol. 48, No. 3, 2003, pp. 471–479.
Original Russian Text Copyright © 2003 by D. Garnovskiĭ, Sadikov, Antsyshkina, Burlov, Vasil'chenko, Garnovskaya, Sergienko, A. Garnovskiĭ.

STRUCTURE OF ORGANIC COMPOUNDS

Adducts of Metallochelate Complexes of Tridentate *N,N,N*-Donating Azomethine Ligands: Crystal Structures of (2-Aminopyridine)[2-*N*-Tosylamino(2'-Tosylaminobenzal)anilinato]nickel(II) and (Methanol)[2-*N*-Tosylamino(2'-Tosylaminobenzal)anilinato]copper(II)

D. A. Garnovskiĭ*, G. G. Sadikov, A. S. Antsyshkina**, A. S. Burlov*,**
I. S. Vasil'chenko*, E. D. Garnovskaya*, V. S. Sergienko, and A. D. Garnovskiĭ***

** Research Institute of Physical and Organic Chemistry, Rostov State University,*
pr. Stachki 194, Rostov-on-Don, 334104 Russia

*** Kurnakov Institute of General and Inorganic Chemistry, Russian Academy of Sciences,*
Leninskiĭ pr. 31, Moscow, 119991 Russia

e-mail: sadgg@igic.ras.ru

Received May 6, 2002

Abstract—The reaction between 2-*N*-tosylamino-(2'-tosylaminobenzal)aniline (H_2L), 2-aminopyridine (L'), and a zero-valent metal (M) in methanol results in the electrochemical synthesis of the $ML \cdot L'$ adducts [M = Ni (**I**) or Co]. The copper complex obtained under the same conditions has the composition $CuL \cdot CH_3OH$ (**II**). The structures of the compounds obtained are investigated using IR spectroscopy, FAB^+ mass spectrometry, and magnetochemistry. The crystal structures of compounds **I** and **II** are determined by X-ray diffraction. In molecules **I** and **II**, the metal atoms are coordinated by three N atoms of the L ligand. The mean M–N distances are 1.97 in **I** and 1.89 Å in **II**. The fourth site in the coordination sphere of the central atom in **I** and **II** is occupied by the endocyclic N atom of the L' ligand (Ni–N, 2.01 Å) and the O atom of the methanol molecule (Cu–O, 2.06 Å), respectively. The coordination polyhedra of the metal atoms in **I** and **II** are complemented by the O atom of the tosyl fragment of the L ligand (Ni–O, 2.41 Å in **I**; Cu–O, 2.64 Å in **II**). *© 2003 MAIK "Nauka/Interperiodica".*

INTRODUCTION

Molecules of tridentate azomethine compounds (H_2L, Scheme 1a) that contain protonated donor groups (XH and YH) in the *o*-positions of the phenyl rings are able to form complexes of variable composition and structure (Schemes 1b, 1c) [1–5].

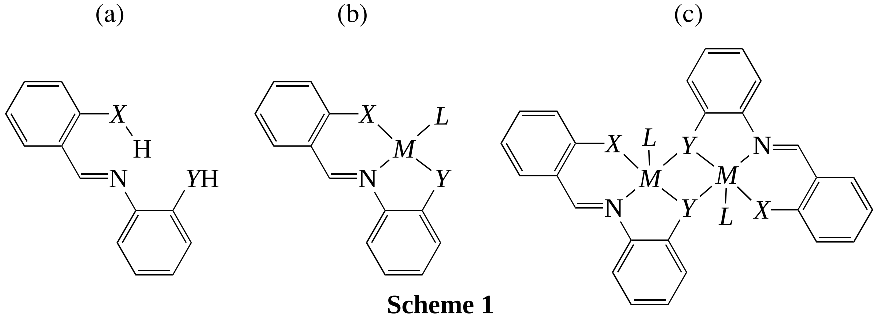

Scheme 1

Adducts with 2-aminoheterocycles [6–8], which simulate fragments of some biologically important objects (purine bases) responsible for binding metals in nature [9, 10], are of the greatest interest among the compounds of type (b). Aminoazole and aminoazine systems, whose molecules contain two or several potential donor centers, play an important role in the solution of the problem of competitive coordination of ambidentate ligands [11–23]. In this connection, we continued our earlier studies and conducted the electrochemical synthesis of adducts of the chelate complexes $NiL \cdot L'$ (**I**) and $Co\,L \cdot L'$ (**III**) [(for L, see Scheme 1a); $X = Y = p$-N-Ph-CH_3 (*NTS*); L' = 2-aminopyridine], obtained the adduct $CuL \cdot CH_3OH$ (**II**), and studied the physicochemical properties of **I**–**III** (IR and ^1H NMR

1063-7745/03/4803-0426$24.00 © 2003 MAIK "Nauka/Interperiodica"

spectra, *FAB*$^+$ mass spectra, and magnetochemical measurements). The crystal structures of complexes **I** and **II** were determined by the X-ray diffraction technique.

EXPERIMENTAL

Synthesis and Physicochemical Properties

The elemental analysis for C, H, N, and S was performed on a Carlo Erba 1108 microanalyzer. The melting points were determined on a Kofler stage. The *FAB*$^+$ mass spectra were measured on a Trio-2000 instrument. The IR spectra (4000–400 cm^{-1}) were recorded on a Bio-RAD FTS 3000 MX spectrophotometer (KBr pellets). The ^{1}H NMR spectra were taken on a Varian UNITY 300 spectrometer at room temperature. The magnetochemical measurements were performed by the Faraday method using a setup designed at Rostov University [24].

The initial compound, 2-*N*-tosylamino(2'-tosylaminobenzal)aniline (H_2L), was synthesized according to the procedure reported in [2]. The electrochemical synthesis of complexes **I**–**III** was performed according to the standard procedure [25–30] using the reaction of H_2L and L' with the corresponding metal ions obtained in the course of electrolysis of the anode. The electrochemical cell can be represented as follows: Pt(–)/CH_3OH, H_2L, L'/M(+). The stock solution of methanol (25 ml) contained H_2L (0.262 g, 1 mmol), L' (0.095 g, 1 mmol), and $[Et_4N]ClO_4$ (0.01 g) as a conductive additive. The electrolysis was conducted at a constant current of 10 mA and a voltage of 15 V for 2 h. The residues of complexes **I**–**III** were filtered off, washed three times with 10 ml of hot methanol, and dried under vacuum.

Complex I

For $C_{32}H_{29}N_5O_4S_2Ni$ anal. calcd. (%): C, 57.32; H, 4.36; N, 10.45; S, 9.57.

Found (%): C, 57.14; H, 4.35; N, 10.45; S, 9.60.

FAB$^+$ mass spectrum (*m*/*z*): 670, $[M]^+$; 598, $[M–L + Na–H]^+$; 421, $[M–L–SO_2C_6H_4\text{-}4\text{-}CH_3]^+$. t_{decomp} = 172°C. IR spectrum (KBr; cm^{-1}): 3419, $\nu_{as}(NH_2)$; 3344, $\nu_s(NH_2)$; 3242, $\nu_s(NH_2)$; 1649, $\delta(NH_2)$; 1608, ν(C=N).

Complex II

For $C_{28}H_{27}N_3O_5S_2Cu$ anal. calcd. (%): C, 54.90; H, 4.40; N, 6.85; S, 10.44.

Found (%): C, 55.01; H, 4.27; N, 7.09; S, 10.46.

FAB$^+$ mass spectrum (*m*/*z*): 582, $[M–CH_3OH]$; 581, $[M–CH_3OH–H]$; 426, $[M–CH_3OH–H–SO_2C_6H_4\text{-}4\text{-}CH_3]^+$; 271, $[M–CH_3OH–H–2SO_2C_6H_4\text{-}4\text{-}CH_3]^+$. t_{decomp} = 174°C. IR spectrum (KBr; cm^{-1}): 1602, ν(C=N). $\mu_{eff} = 1.92\ \mu_B$.

Complex III

For $C_{32}H_{29}N_5O_4S_2Co$ anal. calcd. (%): C, 57.30; H, 4.36; N, 10.44; S, 9.56.

Found (%): C, 57.16; H, 4.30; N, 10.44; S, 10.00.

FAB$^+$ mass spectrum (*m*/*z*): 599, $[M–L + Na–H]^+$; 422, $[M–L–SO_2C_6H_4\text{-}4\text{-}CH_3]^+$. t_{decomp} = 179–180°C. IR spectrum (KBr; cm^{-1}): 3416, $\nu_{as}(NH_2)$; 3343, $\nu_s(NH_2)$; 3238, $\nu_s(NH_2)$; 1651, $\delta(NH_2)$; 1610, ν(C=N). $\mu_{eff} = 4.08\ \mu_B$.

X-ray Diffraction Studies

Crystals **I** are monoclinic, $a = 9.161(3)$ Å, $b = 13.091(3)$ Å, $c = 25.408(8)$ Å, $\beta = 98.86(3)°$, $V = 3010(1)$ Å^3, $M = 670.4$, $\rho_{calcd} = 1.479$ g/cm^3, $\mu_{Mo} = 0.83$ mm^{-1}, $Z = 4$, and space group $P2_1/c$.

Crystals **II** are triclinic, $a = 8.824(3)$ Å, $b = 10.740(5)$ Å, $c = 14.478(9)$ Å, $\alpha = 98.06(5)°$, $\beta = 92.21(5)°$, $\gamma = 98.72(4)°$, $V = 1340(1)$ Å^3, $M = 612.2$, $\rho_{calcd} = 1.517$ g/cm^3, $\mu_{Mo} = 1.02$ mm^{-1}, $Z = 2$, and space group $P\bar{1}$.

The experimental data (5179 and 6500 reflections for **I** and **II**, respectively) were obtained on an Enraf–Nonius CAD4 diffractometer (λMoK_α, graphite monochromator, $\theta/2\theta$ scan mode, $2\theta_{max} = 52°$ for **I** and 56° for **II**). Structures **I** and **II** were solved by the heavy-atom method. The non-hydrogen atoms were located from a series of successive difference Fourier syntheses. The X-ray diffraction analysis of structure **I** revealed that many structural fragments are statistically disordered. The positions of the hydrogen atoms were introduced based on the geometrical model of the structure. The Ni, S, N, and O atoms in **I** and all the non-hydrogen atoms in **II** were refined by the least-squares full-matrix procedure in the anisotropic approximation. The C atoms in **I** were refined in the isotropic approximation. The H atoms in **I** and **II** were refined within a riding model (C–H, 0.96 Å). In **I**, the thermal parameters U_j of the H atoms were larger than the U_j values of the corresponding carbon atoms by a factor of 1.5 (for CH_3 groups) or 1.2 (for all the other H atoms). In **II**, the individual isotropic thermal parameters of the H atoms were refined objectively.

The final discrepancy factors are as follows: $R_1 = 0.0619$, $wR_2 = 0.1440$, and *GOOF* = 1.093 for **I**; and $R_1 = 0.0576$, $wR_2 = 0.1474$, and *GOOF* = 1.042 for **II**. The number of reflections with $F_0 \geq 4\sigma(F_0)$ was 1099 in **I** and 1161 in **II**. The residual electron density varied from $\Delta\rho_{max} = 0.453$ e Å^{-3} to $\Delta\rho_{min} = -0.770$ e Å^{-3} in **I** and from $\Delta\rho_{max} = 0.523$ e Å^{-3} to $\Delta\rho_{min} = -0.332$ e Å^{-3} in **II**. All the calculations were performed with the SHELX86 [31] and SHELXL93 [32] program packages. The structural data for the complexes studied were deposited as CIF files in the Cambridge Structural Database (CCDC nos. 196745 and 196746). The geo-

Table 1. Bond lengths *d* (Å) in compounds **I** and **II**

Bond	*d*	Bond	*d*	Bond	*d*	Bond	*d*
I				**II**			
Ni(1)···O(1)	2.408(9)	Ni(1)–N(1)	1.95(1)	Cu(1)–N(1)	1.93(3)	Cu(1)–N(2)	1.91(3)
Ni(1)–N(2)	1.99(1)	Ni(1)–N(3)	1.95(1)	Cu(1)–N(3)	1.89(3)	Cu(1)–O(4)	2.64(2)
Ni(1)–N(4)	2.01(1)	S(1)–O(1)	1.47(1)	Cu(1)–O(5)	2.06(2)	S(1)–N(1)	1.64(3)
S(1)–O(2)	1.43(1)	S(1)–N(3)	1.61(1)	S(1)–O(1)	1.39(3)	S(1)–O(2)	1.40(2)
S(1)–C(14)	1.71(5)	S(1)–C(14′)	1.81(5)	S(1)–C(14)	1.78(4)	S(2)–N(3)	1.58(3)
S(2)–O(3)	1.43(1)	S(2)–O(4)	1.45(1)	S(2)–O(3)	1.37(2)	S(2)–O(4)	1.41(2)
S(2)–N(1)	1.64(1)	S(2)–C(26)	1.67(3)	S(2)–C(21)	1.74(4)	N(1)–C(1)	1.32(4)
S(2)–C(26′)	1.93(4)	N(1)–C(1)	1.42(2)	N(2)–C(2)	1.49(4)	N(2)–C(7)	1.30(4)
N(2)–C(6)	1.40(2)	N(2)–C(7)	1.29(2)	N(3)–C(9)	1.54(4)	O(5)–C(28)	1.39(4)
N(3)–C(13)	1.43(2)	N(4)–C(21)	1.34(2)	C(1)–C(2)	1.42(5)	C(1)–C(6)	1.41(5)
N(4)–C(25)	1.35(2)	N(5)–C(25)	1.35(2)	C(2)–C(3)	1.35(4)	C(3)–C(4)	1.36(4)
C(1)–C(2)	1.53(4)	C(1)–C(2′)	1.32(4)	C(4)–C(5)	1.37(5)	C(5)–C(6)	1.36(5)
C(1)–C(6)	1.40(3)	C(2)–C(3)	1.36(5)	C(7)–C(8)	1.38(4)	C(8)–C(9)	1.37(4)
C(3)–C(4)	1.41(5)	C(4)–C(5)	1.46(5)	C(8)–C(13)	1.42(4)	C(9)–C(10)	1.39(5)
C(5)–C(6)	1.37(4)	C(2′)–C(3′)	1.45(5)	C(10)–C(11)	1.40(5)	C(11)–C(12)	1.32(5)
C(3′)–C(4′)	1.37(5)	C(4′)–C(5′)	1.38(6)	C(12)–C(13)	1.31(5)	C(14)–C(15)	1.32(5)
C(5′)–C(6)	1.44(4)	C(7)–C(8)	1.39(2)	C(14)–C(19)	1.35(5)	C(15)–C(16)	1.42(5)
C(8)–C(9)	1.42(2)	C(8)–C(13)	1.45(2)	C(17)–C(18)	1.37(6)	C(17)–C(16)	1.35(5)
C(9)–C(10)	1.35(3)	C(10)–C(11)	1.35(3)	C(17)–C(20)	1.46(6)	C(18)–C(19)	1.33(6)
C(11)–C(12)	1.37(2)	C(12)–C(13)	1.37(3)	C(21)–C(22)	1.38(6)	C(21)–C(26)	1.33(6)
C(14)–C(15)	1.48(6)	C(14)–C(19)	1.40(6)	C(22)–C(23)	1.44(7)	C(23)–C(24)	1.30(7)
C(15)–C(16)	1.35(5)	C(16)–C(17)	1.35(5)	C(24)–C(25)	1.35(7)	C(24)–C(27)	1.51(7)
C(17)–C(18)	1.37(6)	C(17)–C(20)	1.52(4)	C(25)–C(26)	1.35(7)		
C(18)–C(19)	1.47(6)	C(21)–C(22)	1.40(2)				
C(22)–C(23)	1.42(2)	C(23)–C(24)	1.32(2)				
C(24)–C(25)	1.38(2)	C(26)–C(27)	1.39(5)				
C(26)–C(31)	1.42(4)	C(27)–C(28)	1.39(5)				
C(28)–C(29)	1.37(5)	C(29)–C(30)	1.43(5)				
C(29)–C(32)	1.49(5)	C(30)–C(31)	1.34(4)				
C(15')–C(16')	1.40(5)	C(16')–C(17')	1.42(5)				
C(17')–C(18')	1.37(5)	C(17')–C(20')	1.51(4)				
C(18')–C(19')	1.25(6)	C(26')–C(27')	1.41(6)				
C(26')–C(31')	1.34(5)	C(27')–C(28')	1.38(7)				
C(28')–C(29')	1.31(6)	C(29')–C(30')	1.32(5)				
C(29')–C(32')	1.52(6)	C(30')–C(31')	1.44(5)				

metric parameters of complexes **I** and **II** are listed in Tables 1 and 2.

RESULTS AND DISCUSSION

The electrochemical oxidation of the Co and Ni atoms in the presence of 2-*N*-tosylamino(2'-tosylaminobenzal)aniline (H_2L) and 2-aminopyridine (*L*') leads to the formation of the $ML \cdot L'$ complexes (*L* is the double-deprotonated form of the ligand). For the copper anode, the $CuL \cdot CH_3OH$ (**II**) product is isolated under the same conditions. The overall electrochemical process proceeding in the cell can be represented by the following scheme:

At the cathode: $H_2L + 2\bar{e} \longrightarrow L^{2-} + H_2$.

At the anode: $M^0 + L' + L^{2-} \longrightarrow ML \cdot L' + 2\bar{e}$

for $M = $ Co, Ni, and Zn or $[ML \cdot CH_3OH] + 2\bar{e}$ for $M = $ Cu.

Table 2. Bond angles ω (deg) in compounds **I** and **II**

Angle	ω	Angle	ω	Angle	ω	Angle	ω
I				**II**			
O(1)Ni(1)N(1)	113.3(5)	O(1)Ni(1)N(2)	151.9(4)	N(1)Cu(1)N(2)	83(1)	N(1)Cu(1)N(3)	164(1)
O(1)Ni(1)N(3)	64.6(4)	O(1)Ni(1)N(4)	92.7(4)	N(1)Cu(1)O(4)	113.5(9)	N(1)Cu(1)O(5)	97(1)
N(1)Ni(1)N(2)	82.2(5)	N(1)Ni(1)N(3)	151.9(5)	N(2)Cu(1)N(3)	94(1)	N(2)Cu(1)O(4)	135.2(9)
N(1)Ni(1)N(4)	106.0(5)	N(2)Ni(1)N(3)	90.6(5)	N(2)Cu(1)O(5)	141(1)	N(3)Cu(1)O(4)	58.6(9)
N(2)Ni(1)N(4)	105.7(5)	N(3)Ni(1)N(4)	102.0(5)	N(3)Cu(1)O(5)	95(1)	O(4)Cu(1)O(5)	80.5(8)
O(1)S(1)O(2)	117.1(6)	O(1)S(1)N(3)	99.7(6)	N(1)S(1)O(1)	115(1)	N(1)S(1)O(2)	108(1)
O(1)S(1)C(14)	107(2)	O(1)S(1)C(14′)	108(2)	N(1)S(1)C(14)	103(1)	O(1)S(1)O(2)	117(1)
O(2)S(1)N(3)	114.4(6)	O(2)S(1)C(14)	103(2)	O(1)S(1)C(14)	105(2)	O(2)S(1)C(14)	108(2)
O(2)S(1)C(14′)	112(2)	N(3)S(1)C(14)	116(2)	N(3)S(2)O(3)	113(1)	N(3)S(2)O(4)	101(1)
N(3)S(1)C(14′)	105(2)	O(3)S(2)N(1)	114.1(7)	N(3)S(2)C(21)	108(2)	O(3)S(2)O(4)	118(1)
O(3)S(2)O(4)	117.2(7)	O(3)S(2)C(26′)	97(1)	O(3)S(2)C(21)	108(2)	O(4)S(2)C(21)	108(1)
O(3)S(2)C(26)	117(1)	O(4)S(2)C(26)	106(1)	Cu(1)N(1)S(1)	119(1)	Cu(1)N(1)C(1)	115(2)
O(4)S(2)N(1)	104.5(7)	N(1)S(2)N(26)	95(1)	S(1)N(1)C(1)	122(2)	Cu(1)N(2)C(2)	113(2)
O(4)S(2)N(26′)	106(1)	N(1)S(2)S(26′)	119(1)	Cu(1)N(2)C(7)	127(2)	C(2)N(2)C(7)	120(3)
Ni(1)O(1)S(1)	90.6(5)	Ni(1)N(1)S(2)	121.2(8)	Cu(1)N(3)S(2)	114(2)	Cu(1)N(3)C(9)	125(2)
Ni(1)N(1)C(1)	114(1)	S(2)N(1)C(1)	119(1)	S(2)N(3)C(9)	118(2)	Cu(1)O(4)S(2)	86(1)
Ni(1)N(2)C(6)	113(2)	Ni(1)N(2)C(7)	122(1)	Cu(1)O(5)C(28)	128(2)	N(1)C(1)C(2)	118(3)
C(6)N(2)C(7)	124(1)	Ni(1)N(3)S(1)	105.1(6)	N(1)C(1)C(6)	129(3)	C(2)C(1)C(6)	113(3)
Ni(1)N(3)C(13)	132(1)	S(1)N(3)C(13)	123(1)	N(2)C(2)C(1)	109(3)	N(2)C(2)C(3)	128(3)
Ni(1)N(4)C(21)	116(1)	Ni(1)N(4)C(25)	128(1)	C(1)C(2)C(3)	123(3)	C(2)C(3)C(4)	121(3)
C(21)N(4)C(25)	115(1)	N(1)C(1)C(2)	121(2)	C(3)C(4)C(5)	119(3)	C(4)C(5)C(6)	119(3)
N(1)C(1)C(2′)	129(2)	N(1)C(1)C(6)	115(2)	C(1)C(6)C(5)	124(3)	N(2)C(7)C(8)	127(3)
C(2)C(1)C(6)	123(2)	C(1)C(2)C(3)	118(3)	C(7)C(8)C(9)	128(3)	C(7)C(8)C(13)	118(3)
C(2′)C(1)C(6)	113(2)	C(2)C(3)C(4)	120(3)	C(9)C(8)C(13)	115(3)	N(3)C(9)C(8)	118(3)
C(3)C(4)C(5)	115(3)	C(4)C(5)C(6)	131(3)	N(3)C(9)C(10)	119(3)	C(8)C(9)C(10)	123(3)
C(1)C(2′)C(3′)	120(3)	C(2′)C(3′)C(4′)	118(3)	C(9)C(10)C(11)	118(3)	C(10)C(11)C(12)	117(3)
C(3′)C(4′)C(5′)	127(4)	C(4′)C(5′)C(6′)	106(3)	C(11)C(12)C(13)	126(3)	C(8)C(13)C(12)	120(3)
N(2)C(6)C(1)	115(1)	N(2)C(6)C(5)	134(2)	S(1)C(14)C(15)	121(3)	S(1)C(14)C(19)	120(3)
N(2)C(6)C(5')	113(2)	C(1)C(6)C(5)	110(2)	C(15)C(14)C(19)	119(3)	C(14)C(15)C(16)	121(3)
C(1)C(6)C(5')	132(2)	C(7)C(8)C(9)	119(1)	C(18)C(17)C(16)	119(4)	C(18)C(17)C(20)	124(4)
N(2)C(7)C(8)	131(1)	C(9)C(8)C(13)	114(1)	C(16)C(17)C(20)	118(3)	C(17)C(18)C(19)	122(4)
C(7)C(8)C(13)	126(1)	C(9)C(10)C(11)	119(2)	C(15)C(16)C(17)	118(3)	C(14)C(19)C(18)	120(4)
C(8)C(9)C(10)	124(2)	C(11)C(12)C(13)	121(2)	S(2)C(21)C(22)	121(3)	S(2)C(21)C(26)	123(3)
C(10)C(11)C(12)	121(2)	N(3)C(13)C(12)	126(1)	C(22)C(21)C(26)	115(4)	C(21)C(22)C(23)	120(4)
N(3)C(13)C(8)	114(1)	S(1)C(14)C(15)	125(3)	C(22)C(23)C(24)	119(4)	C(23)C(24)C(25)	121(4)
C(8)C(13)C(12)	120(1)	S(1)C(14)C(19)	113(3)	C(23)C(24)C(27)	117(4)	C(25)C(24)C(27)	121(4)
C(15)C(14)C(19)	122(4)	C(14)C(15)C(16)	117(3)	C(24)C(25)C(26)	118(4)	C(21)C(26)C(25)	126(5)
C(15)C(16)C(17)	127(3)	C(16)C(17)C(18)	113(3)				
C(16)C(17)C(20)	122(3)	C(18)C(17)C(20)	125(3)				
C(17)C(18)C(19)	130(4)	C(14)C(19)C(18)	111(3)				
N(4)C(21)C(22)	126(2)	C(21)C(22)C(23)	115(2)				
C(22)C(23)C(24)	119(2)	C(23)C(24)C(25)	121(2)				
N(4)C(25)N(5)	117(1)	N(4)C(25)C(24)	123(1)				
N(5)C(25)C(24)	120(1)	S(2)C(26)C(27)	125(3)				
S(2)C(26)C(31)	121(2)	C(31)C(26)C(27′)	98(3)				
C(26)C(27)C(28)	123(4)	C(26)C(27)C(28′)	103(3)				
C(28)C(27)C(26′)	112(3)	C(27)C(28)C(29)	121(3)				
C(28)C(29)C(30)	116(3)	C(28)C(29)C(32)	122(3)				
C(30)C(29)C(32)	123(3)	C(29)C(30)C(31)	123(3)				
C(26)C(31)C(30)	122(3)	S(1)C(14')C(15')	113(4)				
S(1)C(14')C(19')	129(4)	C(15')C(14')C(19')	118(4)				
C(14')C(15')C(16')	116(4)	C(15')C(16')C(17')	120(3)				
C(16')C(17')C(18')	120(3)	C(16')C(17')C(20')	118(3)				
C(18')C(17')C(20')	122(3)	C(14')C(19')C(18')	132(4)				
S(2)C(26')C(27')	111(3)	S(2)C(26')C(31')	123(3)				
C(27')C(26')C(31')	125(4)	C(26')C(27')C(28')	113(4)				
C(27')C(28')C(29')	124(4)	C(28')C(29')C(30')	121(4)				
C(28')C(29')C(32')	123(3)	C(30')C(29')C(32')	115(3)				
C(29')C(30')C(31')	120(3)	C(26')C(31')C(30')	115(3)				

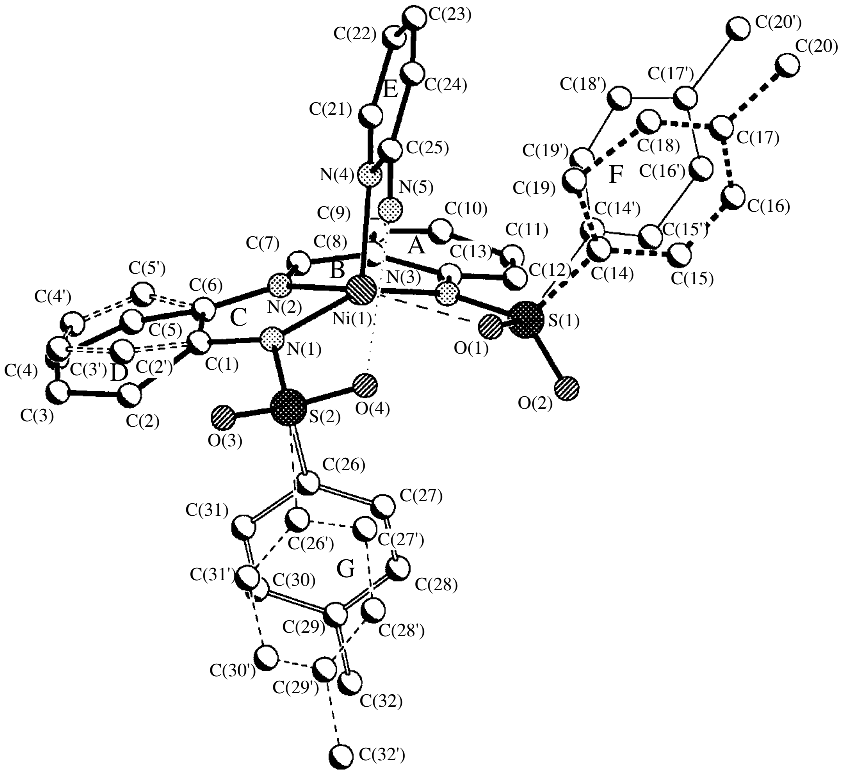

Fig. 1. Structure of molecular complex **I**. The second orientation of the statistically disordered fragments D, F, and G is shown by dashed lines.

In the IR spectra of compounds **I**–**III** (as compared to the spectrum of a free H_2L molecule), the ν(NH) band of stretching vibrations of the tosylated amino group at 3297 cm^{-1} disappears and the band of stretching vibrations of the azomethine bond shifts by ~10 cm^{-1} toward the low-frequency range (1630–1600 cm^{-1}). These data count in favor of the formation of complex compounds containing the MN_4 metallochelate group with two deprotonated nitrogen atoms of the aminotosyl fragments and the nitrogen atoms of the imino group and the pyridine ring. In the high-frequency range (3500–3200 cm^{-1}), the spectra of complexes **I** and **III** additionally contain the stretching vibration bands of the amino group of coordinated 2-aminopyridine. In the spectra of these complexes, the $\nu_{as}(NH_2)$ band of asymmetric stretching vibrations of the amino group is shifted by ~30 cm^{-1} toward the low-frequency range. According to [6, 7], this shift is most likely caused by the formation of the N–H…O intramolecular hydrogen bond between the amino group and the tosyl fragment.

The ^{1}H NMR spectrum of the H_2L molecule, which was recorded in the DMSO-d^6 solution, exhibits two singlet signals at 9.6 and 11.4 ppm due to protons of the tosylated amino groups, an aromatic multiplet at 6.9–7.8 ppm, and a signal of the azomethine proton at 8.2 ppm.

The FAB^+ mass spectra of complexes **I** and **III** contain peaks corresponding to the $[M–L + Na–H]^+$ fragment. In the mass spectrum of copper complex **II**, the peak with m/z = 582 corresponds to the $[MO(H)CH_3]^+$ fragment.

The magnetic moments (μ_{eff}) of compounds **II** and **III** at room temperature (4.08 and 1.92 μ_B, respectively) indicate that the complexes have mononuclear structures.

According to the X-ray diffraction data, crystal **I** consists of Ni$L \cdot L'$ molecular complexes (Fig. 1). The Ni atom is coordinated by three N atoms of the L ligand, which is planar within ±0.4 Å. One more site in the coordination sphere of the Ni atom in **I** is occupied by the N atom of the aminopyridine L' ligand. The coordination polyhedron of the Ni atom is a severely distorted tetrahedron (the NNiN angles vary between 82.2° and 151.9°). The oxygen atom of one of the tosyl groups of the L ligand complements the coordination environment of the metal by the weak Ni–O(1) interaction. With due regard for this additional contact, the coordination polyhedron of the Ni atom can be described as a tetragonal pyramid with the N(1), N(2), N(3) (mean Ni–N, 1.97 Å), and O(1) [Ni–O(1), 2.41 Å] atoms in the base and the N(4) atom [Ni–N(4), 2.01 Å] at the apical vertex. The basal plane of the pyramid is slightly distorted (±0.06 Å), and the Ni atom deviates

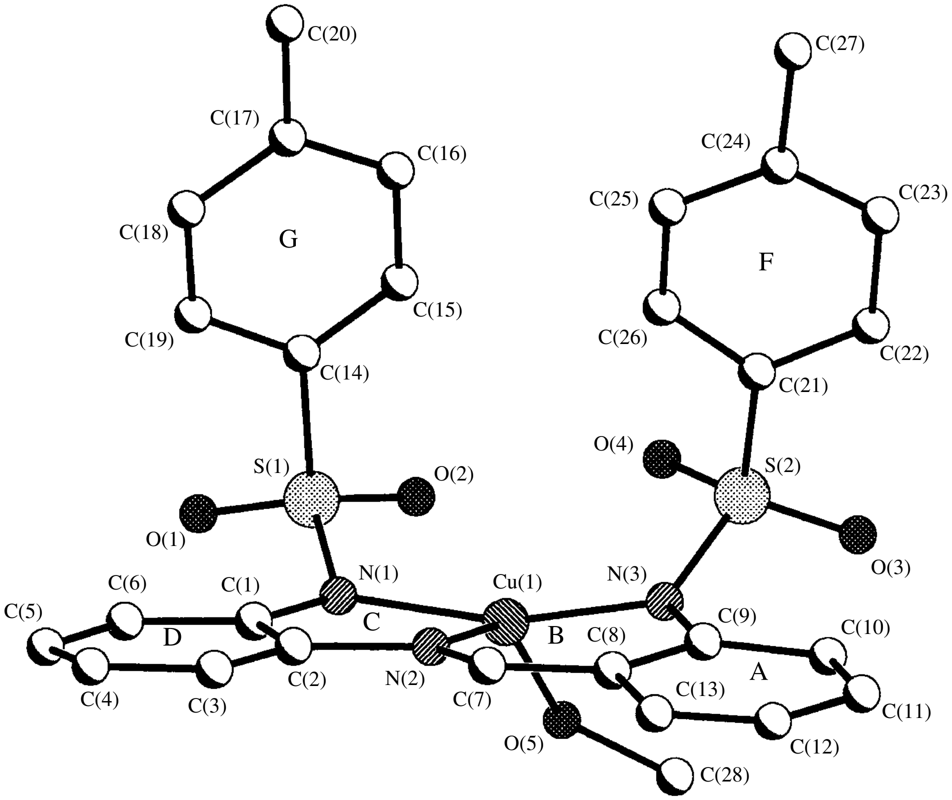

Fig. 2. Structure of molecular complex **II**.

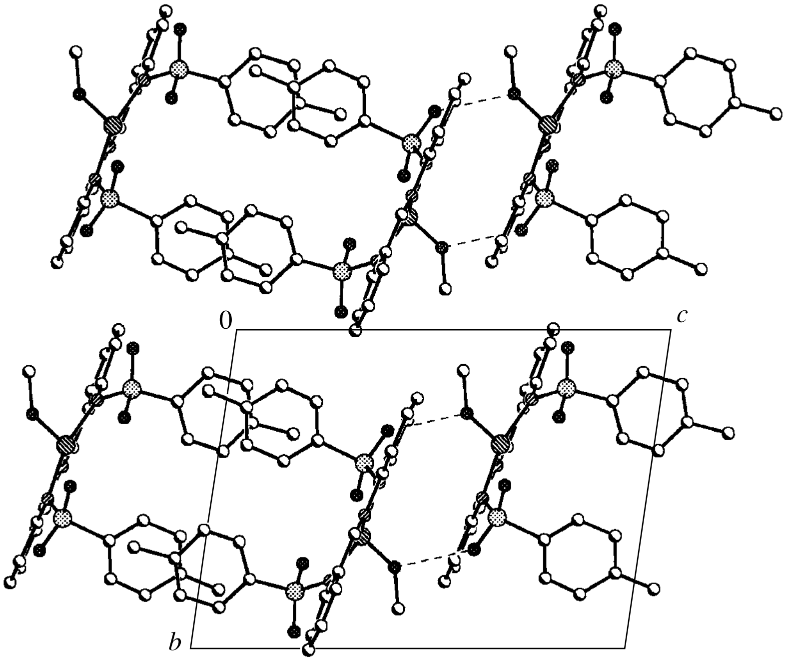

Fig. 3. Crystal packing of complexes **II**. The hydrogen bonds in the dimers are indicated by dashed lines. The chains formed of dimers are perpendicular to the plane of the figure, i.e., the (100) plane, and the layers are parallel to the (001) plane.

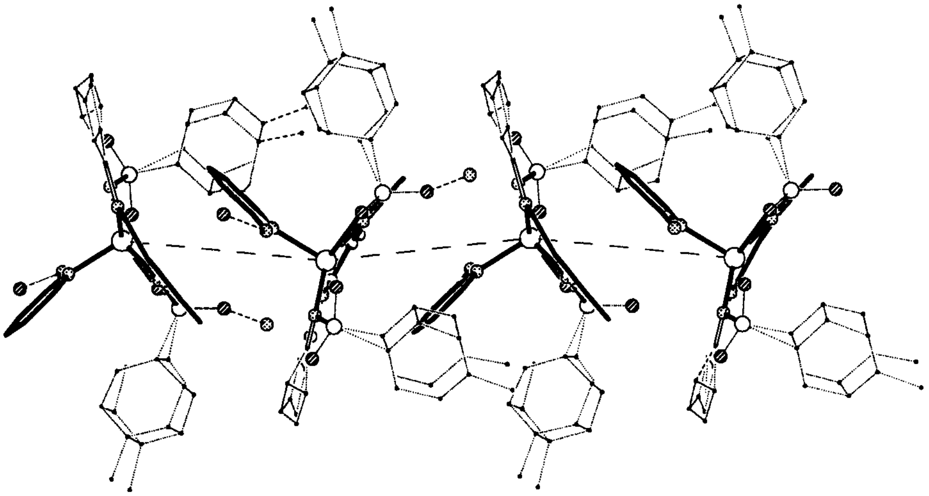

Fig. 4. Projection of the supramolecular chain ensemble of structure **I** showing the mutual orientation of the contacts between the complexes in the chain. The twofold screw axis relating the complexes lies in the plane of the figure. The rigid fragments of the complexes *A*, *B*, and *E* are shown by solid lines; the *B* ring is shown by thin lines; and the disordered fragments are shown by dotted lines.

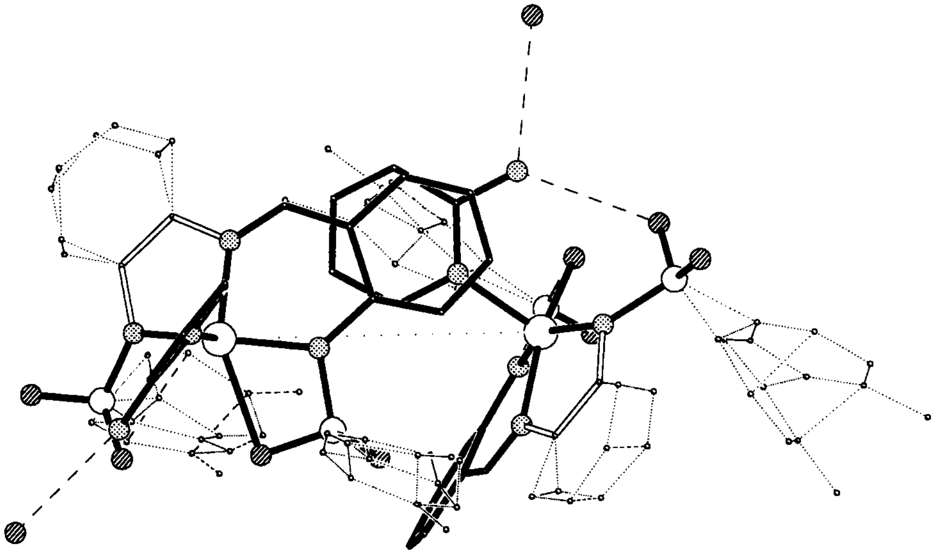

Fig. 5. Contact between the neighboring complexes in the chain of the supramolecular ensemble. The Ni···Ni vector (dotted line) lies in the plane of the figure. The plane-parallel fragments *A* and *E* of the neighboring complexes overlap almost completely. The disordered fragments are shown by dotted lines.

from it by 0.40 Å toward the N(4) atom. The N(4)NiN(1–3) angles lie in the range 102.0°–106.0°, and the N(4)NiO(1) angle is 92.7°.

In structure **II** (Fig. 2), the *L* ligand is planar within 0.1 Å and coordinates the metal atom in the same manner as in **I**, that is, by three nitrogen atoms (mean Cu–N, 1.89 Å). The fourth vertex in the copper polyhedron is occupied by the oxygen atom of the methanol molecule [Cu–O(5), 2.06 Å]. We can assume that the tetrahedrally distorted (within 0.44 Å) square of CuN_3O forms the base of the tetragonal pyramid with the tosyl O(4) atom of the *L* ligand at the apical vertex, which is removed from the copper atom by 2.64 Å. As in **I**, the central copper atom in **II** deviates from the rms plane of the base by 0.22 Å toward the apical vertex. In distinction to **I**, in which the tosyl groups lie on both sides of the plane of the *L* ligand, the tosyl fragments in **II** lie on one side of this plane and are nearly parallel to one another (the dihedral angle between their planes is 13°).

The structural features of complexes **I** and **II** are typical of adducts of the tridentate Schiff bases obtained by the electrochemical procedure [33].

Although there are few hydrogen bonds in structures **I** and **II**, they play an important role in crystal formation. In **II**, only one intermolecular hydrogen bond is formed, namely, O(5)–H(5*D*)···O(1) (2 – *x*, 1 – *y*, 1 – *z*)

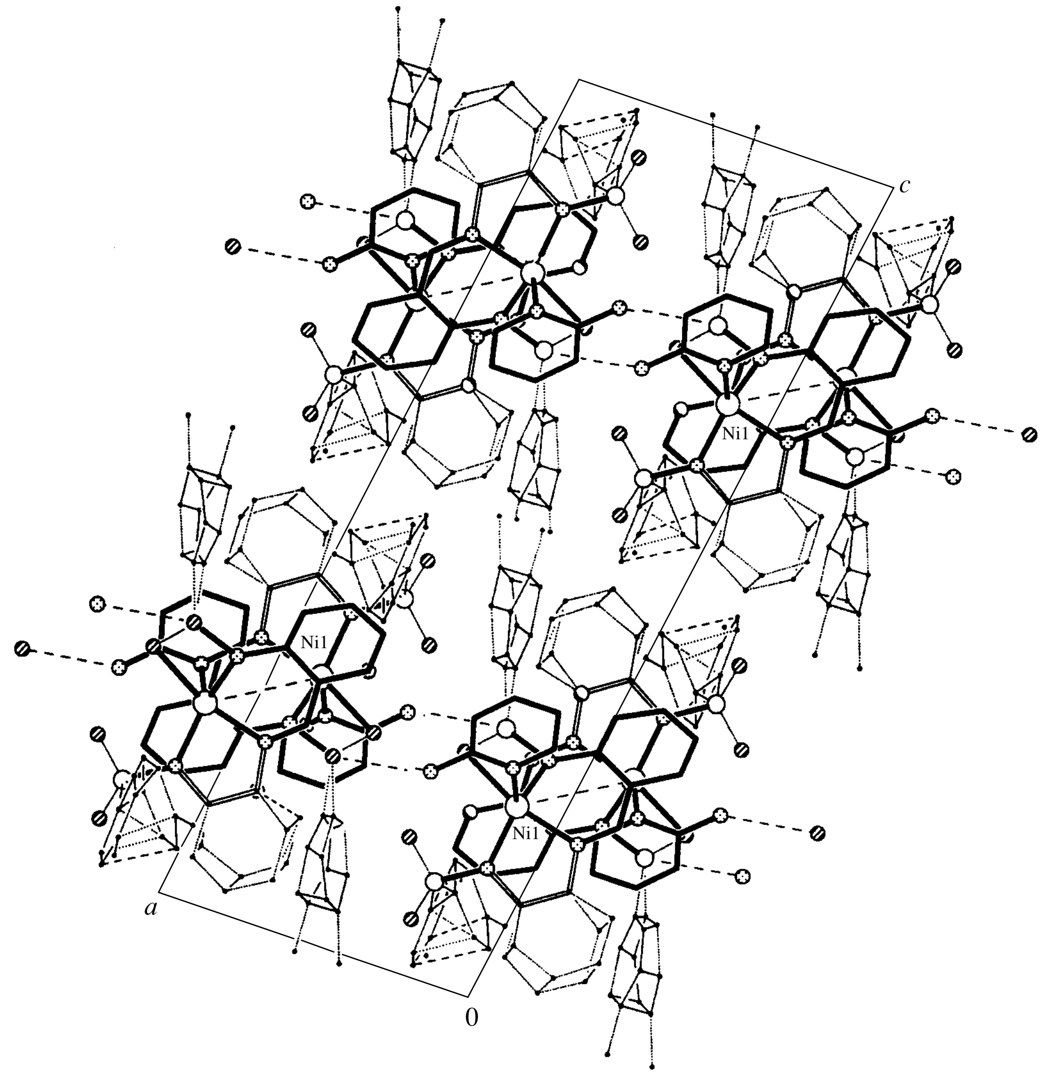

Fig. 6. Packing of the chains in crystal **I**. Weak hydrogen bonds form layers parallel to the (100) plane. The projection is orthogonal to that shown in Fig. 4. All the disordered fragments of complexes lie in the region of the interlayer contacts.

[O(5)–H(5*D*), 0.85 Å; H(5*D*)··O(1), 2.21 Å; O(5)··O(1), 2.79(2) Å; the O(5)H(5*D*)O(1) angle, 130°]. This bond links complexes into step-shaped centrosymmetric supramolecular dimers [34]. The protruding plane-parallel fragments of the dimers on their sides opposite to the tosylamine (*NTS*) groups overlap to form chains along the *a* axis (Fig. 3). The distance between the Cu atoms is 7.055 Å in the dimers and 7.092 Å between the dimers. This is an indirect indication of the comparable strength of the van der Waals contacts and hydrogen bonds. The chains are packed into layers parallel to the (001) coordinate plane. The distance between the Cu atoms of the neighboring chains is 8.15 Å. The planar fragments of the complexes (*L* ligands) are almost parallel to the layers, and the phenyl rings of the *NTS* groups are perpendicular to the layer and protrude evenly on either side of the layer. These groups are directed to the interlayer space and form contacts between the layers. Thus, the intermolecular hydrogen bond is responsible for the shape of the supramolecular dimer, which serves as a starting building unit, and, therefore, determines the crystal structure as a whole.

In **I**, two different hydrogen bonds are formed, namely, the intramolecular bond N(5)–H(5*A*)···O(4) [N(5)–H(5*A*), 0.86 Å; H(5*A*)···O(4), 2.10 Å; N(5)···O(4), 2.95(1) Å; the N(5)H(5*A*)O(4) angle, 164°] and the weak intermolecular bond N(5)–H(5*B*)···O(2) (–1 –*x*, –0.5 + *y*, –0.5 + *z*) [N(5)–H(5*B*), 0.87 Å; H(5*B*)···O(2), 2.23 Å; N(5)···O(2), 3.08(2) Å; the N(5)H(5*B*)O(2) angle, 170°].

These hydrogen bonds account for the main feature of structure **I**: although it is formally not the OD structure, it contains a large number of statistically disordered fragments in the molecular complex. The phenyl rings of both *NTS* groups are disordered. In the main tridentate ligand, which contains (with consideration for the Ni atom) four almost planar adjacent rings, one of the outer rings (*A*) is rigid and the other (*D*) is disordered (Fig. 1).

The role of the intramolecular hydrogen bond consists in fixing the additional ligand *L*' (ring *E*) with respect to the complex, so that the plane of its phenyl ring is perpendicular to the main plane of ligand *L* (the angle is 98°). Rigid rings *A* and *E* are mutually perpendicular and form angles of ~45° with the *b* axis. These rings serve as basic elements in the packing of complexes. The complexes are arranged in chains along the twofold screw axis. The shortest distances between the centers of complexes are 7.33 Å in the chains (Fig. 4) and 9.5 Å between the chains. The contacts between the adjacent complexes in the chain are due to the parallel arrangement of the rigid six-membered rings *A* and *E*, which are eclipsed relative to each other (Figs. 4, 5). These contacts are formed on different sides of the twofold screw axis and stabilize the supramolecular chain ensemble.

The weak intermolecular hydrogen bond, which is located in the plane of the rigid ring *E* close to the plane of the strong intramolecular hydrogen bond, links the supramolecular chain ensembles into layers parallel to the (001) plane.

The packing of the chains in the crystal lattice (Fig. 6) shows that all the disordered fragments lie in the region of the interlayer contacts. This, in turn, indicates that the contacts in the chains mentioned above are strong.

Thus, the plane-parallel contacts in structure **I**, which are shown in Fig. 5, are able to form the base for the construction of a single crystal.

REFERENCES

1. A. S. Burlov, A. S. Antsyshkina, H. Romero, *et al.*, Zh. Neorg. Khim. **40** (9), 1480 (1995).
2. A. S. Burlov, D. A. Garnovskiĭ, L. I. Kuznetsova, *et al.*, Koord. Khim. **24** (12), 915 (1998).
3. B. I. Kharisov, D. A. Garnovskii, L. M. Blanco, *et al.*, Polyhedron **18** (7), 985 (1999).
4. M. Bernal, J. A. Garcia-Väzquez, J. Romero, *et al.*, Inorg. Chim. Acta **295** (1), 39 (1999).
5. A. S. Antsyshkina, G. G. Sadikov, A. S. Burlov, *et al.*, Zh. Neorg. Khim. **45** (11), 1811 (2000).
6. D. A. Garnovskiĭ, A. Sousa, A. S. Antsyshkina, *et al.*, Izv. Ross. Akad. Nauk, Ser. Khim., No. 8, 2093 (1996).
7. D. A. Garnovskiĭ, A. S. Antsyshkina, G. G. Sadikov, *et al.*, Zh. Neorg. Khim. **43** (11), 1852 (1998).
8. A. S. Antsyshkina, G. G. Sadikov, A. S. Burlov, *et al.*, Koord. Khim. **26** (10), 779 (2000).
9. *Inorganic Biochemistry*, Ed. by G. Eichhorn (Elsevier, Amsterdam, 1975; Mir, Moscow, 1978), Vols. 1 and 2.
10. *Metal Ions in Biological Systems*, Ed. by H. Sigel (Marcel Dekker, New York, 1979; Mir, Moscow, 1982).
11. D. A. Garnovskiĭ, A. P. Sadimenko, O. A. Osipov, *et al.*, Inorg. Chim. Acta **160** (2), 177 (1989).
12. D. A. Garnovskiĭ, A. D. Garnovskiĭ, A. P. Sadimenko, and S. G. Sigeĭkin, Koord. Khim. **20** (2), 83 (1994).
13. F. A. Cotton and A. Yokoshi, Inorg. Chem. **37** (11), 2723 (1998).
14. M. A. Garralda, R. Hernández, E. Pinilla, and M. R. Torres, J. Organomet. Chem. **586** (2), 150 (1999).
15. A. Garcia-Raso, J. J. Fiol, A. López-Zafra, *et al.*, Polyhedron **18** (6), 871 (1999).
16. S. A. Komaei, G. A. van Albada, I. Mutikainen, *et al.*, Polyhedron **18** (14), 1991 (1999).
17. D. A. Garnovskiĭ, A. S. Antsyshkina, G. G. Sadikov, *et al.*, Zh. Strukt. Khim. **41** (3), 572 (2000).
18. H. Kitamura, T. Ozawa, K. Jitsukawa, *et al.*, Inorg. Chem. **39** (15), 3294 (2000).
19. J. L. Manson, J. A. Schlueter, U. Geiser, *et al.*, Polyhedron **20** (11–14), 1423 (2001).
20. O. Castillo, A. Luque, M. Julve, *et al.*, Inorg. Chim. Acta **315** (1), 9 (2001).
21. K. J. La Chance-Galang, I. Maldonaldo, M. L. Gallagher, *et al.*, Inorg. Chem. **40** (3), 485 (2001).
22. L. E. Kapinos, A. Holy, J. Gunter, and H. Sigel, Inorg. Chem. **40** (11), 2500 (2001).
23. O. Castillo, A. Luque, P. Román, *et al.*, Inorg. Chem. **40** (11), 5526 (2001).
24. V. P. Kurbatov, A. V. Khokhlov, A. D. Garnovskiĭ, *et al.*, Koord. Khim. **5** (3), 351 (1979).
25. D. G. Tuck, Pure Appl. Chem. **51** (11), 2005 (1979).
26. D. G. Tuck, in *Molecular Electrochemistry of Inorganic, Bioinorganic, and Organometallic Compounds*, Ed. by A. J. L. Pombeiro and J. A. McCleverty (Kluwer, Dordrecht, 1993), pp. 15–31.
27. M. C. Chakravorti and G. V. B. Subrahmanyam, Coord. Chem. Rev. **135/136** (1), 65 (1994).
28. *Direct Synthesis of Coordination Compounds*, Ed. by V. V. Skopenko (Venturi, Kiev, 1997).
29. *Direct Synthesis of Coordination and Organometallic Compounds*, Ed. by A. D. Garnovskii and B. I. Kharisov (Elsevier, Amsterdam, 1999).
30. A. D. Garnovskiĭ, I. S. Vasil'chenko, and D. A. Garnovskiĭ, *Modern Aspects of Metallocomplex Synthesis: Basic Ligands and Methods* (Lab. Perspekt. Obraz., Rostov-on-Don, 2000).
31. G. M. Sheldrick, Acta Crystallogr., Sect. A: Found. Crystallogr. **46**, 467 (1990).
32. G. M. Sheldrick, *SHELXL93: Program for the Refinement of Crystal Structures* (Univ. of Göttingen, Germany, 1993).
33. A. S. Antsyshkina, G. G. Sadikov, V. S. Sergienko, and D. A. Garnovskiĭ, Zh. Neorg. Khim. **48** (2003) (in press).
34. J.-M. Lehn, *Supramolecular Chemistry: Concepts and Perspectives* (VCH, Weinheim, 1995; Nauka, Novosibirsk, 1998).

Translated by I. Polyakova

Crystallography Reports, Vol. 48, No. 3, 2003, pp. 435–442. Translated from Kristallografiya, Vol. 48, No. 3, 2003, pp. 480–487.
Original Russian Text Copyright © 2003 by Smirnov, Kazimirov.

LATTICE DYNAMICS AND PHASE TRANSITIONS

Theoretical Study of Structural Phase Transition in a $RbMnCl_3$ Crystal by the Kim–Gordon Method

M. B. Smirnov* and V. Yu. Kazimirov**
** St. Petersburg State University, Universitetskaya nab. 7/9, St. Petersburg, 199164 Russia*
*** Joint Institute for Nuclear Research, Dubna, Moscow oblast, 141980 Russia*

Received November 21, 2002

Abstract—Symmetry analysis of the low-temperature phase of $RbMnCl_3$ crystals with the monoclinic axis perpendicular to the sixfold axis of the high-temperature phase showed that its space group is either C_{2h}^3 or C_{2h}^6. The distribution of normal vibrations over the irreducible representations of the high-temperature phase is refined, and the symmetry relationships for normal vibrations of all possible low-temperature phases are tabulated. The model of the potential function of the crystal is obtained by the nonempirical Kim–Gordon method. This model allows one to establish the existence of the saddle point of the potential surface and several harmonically unstable modes corresponding to correlated rotations of rigid $MnCl_6$ and Mn_2Cl_9 polyhedra. The absolute energy minimum is determined by deforming the lattice along the eigenvector of the E_{1g} mode within the sp. gr. C_{2h}^6. *© 2003 MAIK “Nauka/Interperiodica”.*

INTRODUCTION

Perovskite-like crystals described by the general formula $A^{I}B^{II}Hal_3$ attract the attention of researchers because of their numerous phase transitions and, as a result, diverse magnetic and crystal structures. The relatively simple structure and mainly ionic interactions of the atoms facilitate the use of the direct computational methods of the theory of lattice dynamics. Often, it is the lattice instability with respect to some phonon modes that can give rise to phase transitions.

The structural phase transition in $RbMnCl_3$ crystals was first observed in [1]. In the course of a complex experimental investigation, it was established that the high-temperature phase of these crystals is described by the hexagonal sp. gr. *P*63/*mmc* [2]. The study of their twin structure, temperature dependences of birefringence, rigidity (theory of elasticity), and Raman spectra showed that the crystals undergo a displacive-type second-order phase transition at $T \sim 270$ K. The complex twin structure of the crystals did not allow one to definitively determine the space group of the low-temperature phase; however the twinning pattern showed monoclinic distortion of the structure such that the point group of the low-temperature phase was determined as C_{2h}^2 [2]. The presence of a center of inversion indicated that the transition could not be ferroelectric, and the easy untwinning of the crystals under the low mechanical stresses applied proved its ferroelastic nature.

It should be indicated that $RbMnCl_3$ crystals undergo a magnetic phase transition at $T_c \sim 100$ K, which results in antiferromagnetic ordering in the (001) plane and the appearance of a weak magnetic moment along the [001] direction. This additionally complicates the interpretation of the neutron diffraction data obtained for the low-temperature phase ($T < 100$ K) [3, 4]. Hereafter, we ignore this fact and consider the low-temperature phase as the state of $RbMnCl_3$ crystals in the temperature range 100–270 K.

Thus, the experimental studies of the crystal and twin structure, elastic moduli, and Raman spectra of $RbMnCl_3$ crystals allowed Aleksandrov *et al.* [2] to draw the following conclusions:

—The space group of the high-temperature phase is *P*63/*mmc* (D_{6h}^4);

—the phase transition lowers the symmetry to the sp. gr. C_{2h} with the twofold axis being perpendicular to the sixfold axis of the sp. gr. D_{6h};

—the structural phase transition observed in $RbMnCl_3$ is of a ferroelastic nature, with the elastic constant C_{44} tending to zero;

—the behavior of the active mode of the Raman scattering (hereafter referred to as Raman-active mode) from the representation E_{1g} is similar to the behavior of the soft mode.

Proceeding from the above facts and group-theoretical analysis, it was assumed [2] that the symmetry of the low-temperature phase should be *P*21/*mc* (C_{2h}^2). The symmetry analysis performed in the present study gives rise to some doubt about the validity of this statement. Moreover, we also noticed and corrected some errors in the symmetry analysis of the vibrational spec-

Table 1. Atomic positions in the structures of the high- and low-temperature phases of $RbMnCl_3$ crystals

Atom	D_{6h}^4	Z	C_{2h}^3	Z	C_{2h}^6	Z
Rb1	(0, 0, *j*)	2	(0, 0, *j*)	2	(0, 0, *j*)	2
Rb2	(1/3, 2/3, *z*)	4	(0, 1/3, *z*), (1/2, 1/6, *z* – 1/2)	2	(0, 1/3, *z*)	4
Mn1	(0, 0, 0)	2	(0, 0, 0), (0, 0, 1/2)	1	(0, 0, 0)	2
Mn2	(1/3, 2/3, *z*)	4	(0, 1/3, *z*), (1/2, 1/6, *z* + 1/2)	2	(0, 1/3, *z*)	4
Cl1	(*x*, –*x*, *z*)	12	(3/2*x*, *x*/2, *S* + *z*), (3/2*x* – 1/2, *S* – *x*/2, *z*),	4	(–3/2*x*, *x*/2, *S* + *z*), (3/2*x* – 1/2, *S* – *x*/2, *z*),	4
			(0, *x*, *z*), (*S*, *S* – *x*, *S* + *z*)	2	(0, *x*, *z*)	
Cl2	(*x*, –*x*, *j*)	6	(3/2*x* – 1/2, *S* – *x*/2, *j*)	4	(3/2*x* – 1/2, *S* – *x*/2, *j*)	4
			(0, *x*, *j*)	2	(0, *x*, *j*)	2

Table 2. Symmetry relationships for the vibrational modes of the high-temperature phase of $RbMnCl_3$ crystals in the transition to possible low-temperature phases

$D_{6h}^4 \longrightarrow C_{2h}^3$	$D_{6h}^4 \longrightarrow C_{2h}^6$	$D_{6h}^4 \longrightarrow C_{2h}^2$
$25A_g \longleftrightarrow 5A_{1g} + 6B_{1g} + 6E_{1g} + 8E_{2g}$	$20A_g \longleftrightarrow 5A_{1g} + B_{2g} + 6E_{1g} + 8E_{2g}$	$23A_g \longleftrightarrow 5A_{1g} + 2A_{2g} + 16E_{2g}$
$17B_g \longleftrightarrow 2A_{2g} + B_{2g} + 6E_{1g} + 8E_{2g}$	$22B_g \longleftrightarrow A_{2g} + 6B_{1g} + 6E_{1g} + 8E_{2g}$	$19B_g \longleftrightarrow 6B_{1g} + B_{2g} + 12E_{1g}$
$19A_u \longleftrightarrow A_{1u} + 2B_{1u} + 9E_{1u} + 7E_{2u}$	$23A_u \longleftrightarrow A_{1u} + 6B_{2u} + 9E_{1u} + 7E_{2u}$	$22A_u \longleftrightarrow A_{1u} + 7A_{2u} + 14E_{2u}$
$29B_u \longleftrightarrow 7A_{2u} + 6B_{2u} + 9\mathrm{E}_{1u} + 7E_{2u}$	$25B_u \longleftrightarrow 7A_{2u} + B_{1u} + 9\mathrm{E}_{1u} + 7E_{2u}$	$26B_u \longleftrightarrow 2B_{1u} + 6B_{2u} + 18\mathrm{E}_{1u}$

trum of the high-temperature phase [2]. These problems are considered in the first part of the present article.

The absence of reliable experimental data on the structure and IR and Raman spectra of the low-temperature phase hinders analysis of the mechanism of the structural phase transition in $RbMnCl_3$ crystals. In this connection, it is expedient to study the lattice dynamics theoretically and analyze the microscopic nature of the lattice instability with the use of the potential function obtained by direct nonempirical calculation. The following sections of the article are dedicated to a short description of the method and a discussion of the results obtained.

GROUP-THEORETICAL ANALYSIS: VIBRATIONAL SPECTRUM OF THE HIGH-TEMPERATURE PHASE AND POSSIBLE SYMMETRY OF THE LOW-TEMPERATURE PHASE

We proceed from the fact that the structure of the low-temperature $RbMnCl_3$ phase is monoclinic and is described by the point symmetry C_{2h}. The space group D_{6h} has three nonequivalent twofold axes to which there correspond three subgroups C_{2h}. Singling out the operations corresponding to these three subgroups from the operations inherent in the sp. gr. D_{6h}^4, we arrive at three space groups each of which can be considered as a hypothetical group of the low-temperature phase, namely,

—the C_2 axis is aligned along the x axis, $D_{6h}^4 \longrightarrow C_{2h}^3$ ($C2/m11$);

— the C_2 axis is aligned along the y axis: $D_{6h}^4 \longrightarrow C_{2h}^6$ ($C12/c1$);

—the C_2 axis is aligned along the z axis: $D_{6h}^4 \longrightarrow C_{2h}^2$ ($P112/m$).

It should be emphasized that, in the first two cases (the monoclinic axis lies in the *xy* plane), the unit cell becomes base-centered, which corresponds to the transformation of the unit-cell face into a rectangle. The unit-cell dimension along the direction perpendicular to the twofold axis increases by a factor of $\sqrt{3}$. The experimental results obtained in [2] allow one to assume that the monoclinic axis of the low-temperature phase lies in the *xy* plane. Thus, it is possible to reject the sp. gr. C_{2h}^2 with the twofold axis coinciding with the z axis. Table 1 shows the corresponding atomic positions in an $RbMnCl_3$ crystal in the sp. gr. D_{6h}^4 and the subgroups C_{2h}^3 and C_{2h}^6.

Now, proceed to the analysis of the symmetry of the vibrational mode for the low-temperature phase.

According to [5], the structure of the intensity tensor of the Raman spectrum for the sp. gr. D_{6h} (for different representations) looks as follows:

$$\begin{aligned} &A_{1g}\text{: } xx = yy,\ zz; \\ &E_{1g}(1)\text{: } xz; \\ &E_{1g}(2)\text{: } yz; \\ &E_{2g}(1)\text{: } xx = -yy; \\ &E_{2g}(2)\text{: } xy. \end{aligned} \tag{1}$$

Therefore, the modes from the representations A_{1g} and E_{1g} and also from the representation E_{2g} would be Raman-active. Thus, the rejection of the mode E_{2g} from the analysis of the Raman spectra in [2] is unjustified. Also, it should be indicated that the expansion of the central modes of the Brillouin zone in irreducible representations in [2] has an unfortunate misprint. The correct expansion should be written as

$$\Gamma = 5A_{1g} + 2A_{2g} + 6B_{1g} + B_{2g} + 6E_{1g} + 8E_{2g} + A_{1u} + 7A_{2u} + 2B_{1u} + 6B_{2u} + 9E_{1u} + 7E_{2u}.$$

The analysis of the changes in the vibrational spectra in the structural second-order phase transition requires the determination of the relationship between the irreducible representations of the space group and its subgroups. The problem is far from simple; however, it can be solved by comparing the calculated frequencies. The LADY program provides such a comparison because it is based on an algorithm that automatically classifies all the vibrational states of a crystal that has an arbitrary symmetry over the irreducible representations [6]. The relationships thus obtained for the irreducible representations of the sp. gr. D_{6h}^4 and its subgroups with the point symmetry C_{2h} are listed in Table 2.

The transition from D_{6h} to C_{2h} can be induced by the modes from representations E_{1g} and E_{2g}. One of the components of the doubly degenerate E_{1g} or E_{2g} modes should be transformed into the A_g mode of the low-temperature phase. According to Table 2, the phase transition to subgroup C_{2h}^2 can be induced only by the mode from representation E_{2g}, whereas the transitions to subgroups C_{2h}^3 and C_{2h}^6 can be induced by the modes from both representations E_{1g} and E_{2g}.

The measurements made in [2] show that, in the phase transition, the elastic constant C_{44} goes to zero, whereas C_{66} remains almost constant. Obviously, such a behavior of the elastic properties is associated with the structural relaxation, i.e., the interactions of homogeneous deformations with vibrational modes. It is the dramatic decrease in the frequency of one of these modes that gives rise to a ferroelastic phase transition. Proceeding from considerations of symmetry allows one to show that only the Raman-active modes can interact with the homogeneous deformations and that the symmetry of the coefficients of optoacoustic interactions coincides with the symmetry of the intensity tensor of the Raman scattering [7]. It follows from Eq. (1) that the modes from representation E_{1g} interact with elastic deformation U_4, whereas the modes from representation E_{2g} interact with elastic deformation U_6.

Table 3. Parameters of the potential described by Eq. (3a) for the high-temperature phase of $RbMnCl_3$ crystals

Interaction	A (10^{-18} J)	r (E)	C (10^{-18} J Å^6)
Mn^{2+}–Cl^-	445.83	0.3155	4.356
Rb^+–Cl^-	1555.24	0.2897	10.46
Cl^-–Cl^-	637.76	0.3265	46.363

All the above confirms the conclusion drawn in [2] that the phase transition is associated with the softening of mode E_{1g}. However, contrary to [2], we state that the symmetry of the low-temperature phase should be either C_{2h}^3 or C_{2h}^6.

Since there is no relevant reliable experimental data, a justified choice of space group can only be made after

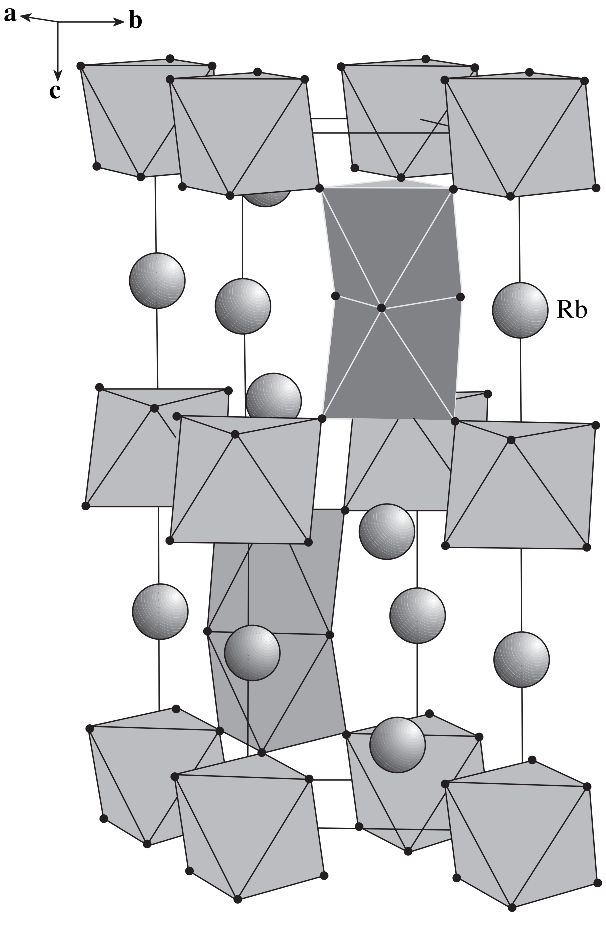

Fig. 1. Structure of the high-temperature phase of $RbMnCl_3$.

Table 4. Experimental and calculated equilibrium structure of the low-temperature phase of $RbMnCl_3$ crystals

Unit-cell parameters (experiment/calculation)			
	a	*b*	*c*
	7.16/7.22	7.16/7.22	17.80/18.03
Atomic positions (experiment/calculation)			
	x/*a*	*y*/*b*	*z*/*c*
Rb1	0/0	0/0	(1/4)/(1/4)
Rb2	(1/3)/(1/3)	(2/3)/(2/3)	0.9165/0.8920
Mn1	0/0	0/0	0/0
Mn2	(1/3)/(1/3)	(2/3)/(2/3)	0.1579/0.1649
Cl1	0.1705/0.1626	0.8295/0.8374	0.0820/0.0877
Cl2	0.4925/0.4770	0.5075/0.5230	(1/4)/(1/4)

Table 5. Frequencies of normal vibrations in the center of the Brillouin zone of the high-temperature phase of $RbMnCl_3$ crystals

Mode	Frequency, cm^{-1}
A_{1g}	40, 161, 254, 339, 368
A_{2g}	63, 71
B_{1g}	26, 62, 99, 174, 296, 356
B_{2g}	53*i*
E_{1g}	51*i*, 44, 120, 157, 171, 301
E_{2g}	39*i*, 39, 55, 80, 143, 216, 242, 306
A_{1u}	20*i*
A_{2u}	35, 56, 146, 202, 271, 352
B_{1u}	44*i*, 74
B_{2u}	53, 112, 221, 276, 339, 391
E_{1u}	40, 56, 64, 119, 171, 242, 244, 330
E_{2u}	7, 42, 82, 135, 166, 215, 328

a quantitative analysis of the situation based on an appropriate microscopic model.

DESCRIPTION OF THE MODEL

The compound $RbMnCl_3$ can be reliably assigned to the class of ionic crystals. For these crystals, quite a good approximation of the potential function is given by the Kim–Gordon method [8], a simplified variant of the method of the local-density functional. Within this approach, an ionic crystal is considered as a number of overlapping spherically symmetric ions, so that the total electron density can be written as a sum of the ionic densities:

$$\rho(\mathbf{R}) = \sum_i \rho_i(\mathbf{R} - \mathbf{r}_i). \tag{2}$$

The summation is performed over all the ions of the crystal, and the electron-density distribution ρ_i is calculated by the Hartree–Fock method for an isolated ion.

The pair interaction potentials of the ions *a* and *b* are calculated within the approximation of the local-density functional as

$$\varphi_{ab}(\mathbf{R}) = E[\rho_a(\mathbf{r}) + \rho_b(\mathbf{r} + \mathbf{R})]. \tag{3}$$

To facilitate the further use of these potentials in studies of crystal structures and crystal dynamics, one has to approximate the numerical dependences obtained using some standard analytical expressions. In our case, it was established that a rather good approximation of the numerical potentials (with an average error of 1–2%) provides the ionic Born–Mayer potential:

$$\varphi_{ab}(R) \approx \frac{Z_a Z_b}{R} + A\exp\left(-\frac{R}{b}\right) - \frac{C}{R^6}. \tag{3a}$$

The complete crystal-lattice potential is written as a sum of all the pair potentials:

$$U(R) = \sum_{a \neq b} \varphi_{ab}(R). \tag{4}$$

The radial electron-density distribution of free Cl^-, Rb^+, and Mn^{2+} ions was calculated by the Hartree–Fock method. For a Mn^{2+} ion, we performed the averaging over all the possible orientations of the 3*d* orbitals. The parameters of the potentials calculated by the Kim–Gordon method and described by Eq. (3a) are listed in Table 3.

RESULTS OF THE CALCULATION

Structure and Vibrational Spectrum of the Low-Temperature Phase

Before proceeding to the consideration of the lattice dynamics of $RbMnCl_3$ crystals, we searched for the local minima of the potential surface. The starting point of our search was the experimentally determined structure of the low-temperature phase. After calculation of the forces at atoms and the homogeneous stresses, we established that these forces do not exceed 0.1 mdyn, whereas the stresses are rather high, U_1 = 2.5 GPa and U_3 = 4.0 GPa. Taking into account that the atomic positions in the crystal structure are determined by seven independent parameters and that the energy gradients calculated using each of these parameters turned out to be close to zero, one can draw the conclusion that the ionic model selected agrees quite well with the observed geometry of the low-temperature phase. The considerable residual stresses, especially along the *z* axis, can be explained by the formation in the structure of a specific fragment—an Mn_2Cl_9 bioctahedron (two sharing-face $MnCl_6$ octahedra) (Fig. 1). This results in the appearance of an unusually short contact *R*(Mn2–Mn2) = 3.27 Å, which provides considerable

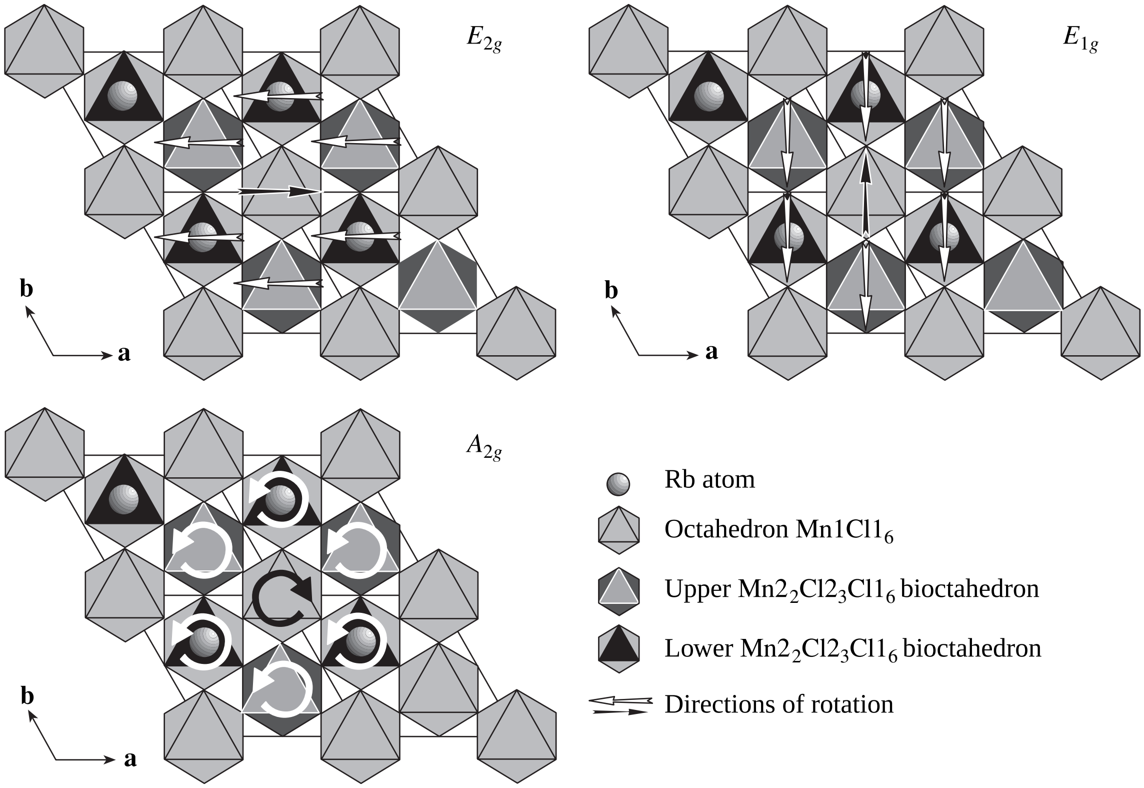

Fig. 2. Harmonically unstable normal vibrations in the high-temperature phase (A_{2g}, E_{1g}, E_{2g}).

uncompensated stresses inside the triangular Mn2–(Cl2)$_3$–Mn2 bipyramid. To take into account this structural fact, we slightly changed the parameters of the potentials; namely, in addition to the above potentials listed in Table 3, we also introduced the van der Waals attraction Mn2–Cl2 with the coefficient C = 30 aJ Å^6 and increased the coefficient A in the exponential repulsion potential Cl2–Cl2 by a factor of 1.5. This correction of the nonempirical potentials resulted in a theoretical structure corresponding to the minimum of the potential energy and close to the experimentally determined structure in both atomic positions and unit-cell parameters (Table 4). After optimizing the structure with the use of the same potential, we calculated the modes and frequencies of the normal vibrations in the center of the Brillouin zone (Table 5).

First of all, it should be indicated that there exist several unstable modes. The fact that some of the modes have imaginary frequencies signifies that the equilibrium geometry of the high-temperature phase determined in our study corresponds not to the minimum of the potential surface but to the saddle point on this surface and that the potential of the deformations corresponding to the eigenvectors of these modes has two wells. This situation is characteristic of most of the high-temperature (usually, highly symmetric) phases of framework crystals whose vibrational modes include almost free rotations of rigid polyhedra with covalent bonds (rigid-unit modes). It is precisely this scenario that we observed in the crystal under study. This is seen from the atomic displacements corresponding to the most unstable modes of the calculated phonon spectra (Fig. 2).

The most unstable mode A_{2g} represents the correlated rotations of Mn1Cl$_6$ octahedra and (Mn2)$_2$Cl$_9$ bio-

Table 6. Frequencies of normal vibrations in the center of the Brillouin zone of an RbMnCl$_3$ crystal stabilized by the introduction of the force constant for Rb–Cl bonds

Mode	Frequency, cm^{-1}
A_{1g}	59, 168, 254, 342, 368
A_{2g}	34, 101
B_{1g}	42, 84, 111, 180, 299, 357
B_{2g}	48
E_{g1}	4, 85, 131, 159, 179, 302
E_{g2}	19, 66, 91, 111, 153, 218, 249, 307
A_{1u}	68
A_{2u}	60, 94, 151, 204, 273, 352
B_{1u}	56, 103
B_{2u}	68, 118, 224, 276, 342, 391
E_{1u}	73, 90, 102, 132, 175, 244, 250, 330
E_{2u}	40, 78, 105, 139, 173, 216, 328

Table 7. Theoretical estimates of elastic constants for an $RbMnCl_3$ crystal (in GPa)

i, *j*	C^{ext}	C
11	79.5	46.2
33	69.7	57.8
44	27.0	–2.0
66	26.5	7.1
12	26.5	32.1
13	27.0	23.7

ctahedra in opposite directions around the z axis, whereas the unstable modes from representations E_{1g} and E_{2g} are the analogous oscillations of the above polyhedra around the y and x axes, respectively. It should be noted that, unlike the unstable mode A_{2g}, the two latter modes are not pure rotations since they also include slight deformations of these polyhedra. The remaining unstable modes (B_{2g}, A_{1u}, and B_{1u}) include, along with rotations, torsional deformations of polyhedra such that the opposite faces of these polyhedra are rotated in opposite directions. Thus, mode B_{2g} corresponds to the rotation of octahedra and torsional distortions of bioctahedra, mode B_{1u} corresponds to the rotation of bioctahedra and torsional distortions of octahedra, and mode A_{1u}, to torsional distortions of both octahedra and bioctahedra.

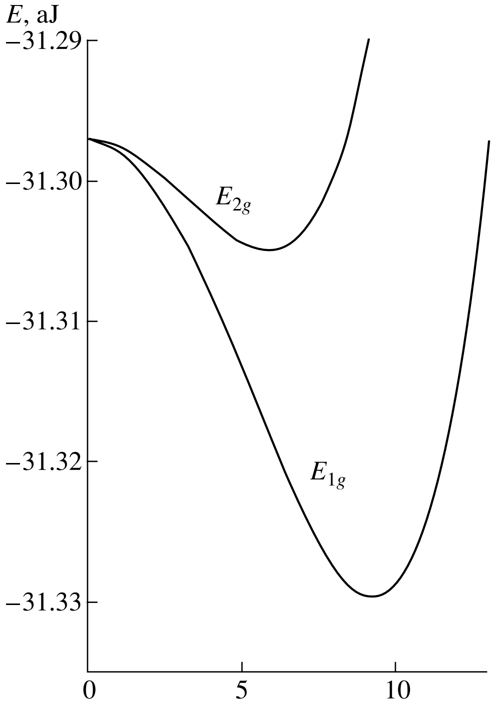

Fig. 3. Potential energy of the unit cell as a function of deformation for unstable E_{1g} and E_{2g} modes in an $RbMnCl_3$ crystal.

The mechanical instability of such deformations can be explained by internal stresses [9], in this case, mainly by Cl–Cl repulsion, which is well reflected in our model. However, one can also assume the existence of some stabilizing factors that are insufficiently reflected by our model. These are, first and foremost, Rb–Cl interactions. Indeed, all the above unstable modes are rigid-unit modes only with respect to the $MnCl_6$ polyhedra, but they inevitably also include the variations in the Rb–Cl bond lengths. Possibly, the nature and energy of these bonds are described insufficiently by our purely ionic model. To verify this assumption, we introduced into our model a small force constant K(Rb–Cl) for Rb–Cl bonds in the first coordination sphere (<3.7 Å). The addition of this interaction stabilized all the unstable modes, with the most potentially unstable mode being the mode from representation E_{1g}. Table 6 lists the vibrational frequencies calculated at K(R–Cl) = 0.056 mdyn/Å.

Using the same potential function, we also calculated elastic constants. In the approximation of long-wave lengths, the expressions for the elastic constants contain the contribution from optoacoustical interactions:

$$C_{\mu\nu} = C^{ext}_{\mu\nu} - \sum_n \frac{1}{\omega_n^2} F_{n\mu} F_{n\nu},$$

where C^{ext} is the contribution of the external homogeneous deformations, ω_n is the frequency of the nth phonon, and $F_{n\mu}$ is the constant of the interaction between the nth mode and μth homogeneous deformation. As was indicated above, the nonzero contribution to this expression comes only from Raman-active modes, with the intensity tensor of the Raman scattering having a nonzero component ($\mu\nu$). We give this expression here to emphasize once again that the softening of the Raman-active mode unavoidably leads to a decrease in the corresponding elastic constant and, thus, can give rise to a ferroelastic phase transition. This does not necessarily require that the frequency of this mode be zero. A decrease in the elastic constant is determined by the constant of the optoacoustical coupling. Table 7 gives the C and C^{ext} values calculated using the same parameters as in the calculation of the frequencies listed in Table 6.

Thus, we see that the elastic constants C_{44} and C_{66} are considerably decreased because of the interaction with modes E_{1g} and E_{2g}, respectively. At the value of the parameter K(Rb–Cl) selected in this study, our model predicts that $\omega(E_{1g}) \sim 4$ cm^{-1} and $C_{44} < 0$. It follows from experimental data [2] that C_{44} goes to zero at $\omega(E_{1g}) \sim 8$ cm^{-1} for the low-temperature phase and $\omega \sim 45$ cm^{-1} for the high-temperature phase. This discrepancy can be explained by anharmonic effects, in particular, dynamic disordering, which is more noticeable in the high-temperature phase. The evaluated diagonal elements of the

Table 8. Structural parameters of the low-temperature phase of an $RbMnCl_3$ crystal (sp. gr. C_{2h}^6) corresponding to the energy minimum

Unit-cell parameters			
	a, Å	b, Å	c, Å
	7.19	12.5054	18.03
	α, deg	β, deg	γ, deg
	90	88	90
Atom	x/a	y/b	z/c
Rb1	0	0.0035	0.25
Rb2	0.0098	0.3376	0.8961
Mn1	0	0	0
Mn2	0.9877	0.3329	0.1635
Cl1	0.6945	0.4061	0.1004
Clb	0.9623	0.1532	0.0943
Clc	0.6977	0.0869	0.5592
Cl2	0.2147	0.2636	0.2403
ClA	0	0.4770	0.25

elastic constants agree quite well with the experimental data $C_{11} = 46$ GPa and $C_{33} = 55$ GPa [2].

Structure of the Low-Temperature Phase

The discrepancies between the results calculated based on the nonempirical model and the experimental data forced us to introduce several empirical corrections into the model. As a result, we arrived at a potential function that allowed us to obtain a structure of the high-temperature phase close to the structure determined experimentally, whereas of all the potentially unstable modes, the most unstable one is the mode from representation E_{1g}. Unavoidably, this would result in the ferroelastic instability $C_{44} \sim 0$. All these results are consistent with the data in [2].

However, there is an unanswered question in [2]: Which subgroup describes the structure of the low-temperature phase? It was indicated above that the appearance of mode E_{1g} in the sp. gr. D_{6h}^4 can result in the transition either to the subgroup C_{2h}^3 or to the subgroup C_{2h}^6. In our model, the geometry of the low-temperature phase corresponds not to the minimum of the potential surface but to the saddle point on it. Each of the unstable modes can be considered as a deformation leading to the point of local energy minima, of which the deepest one is the absolute minimum. It is to this point of the configurational space that the geometry of the low-temperature phase should correspond. Trying to evaluate the relative depth of the local energy minima, we calculated the potential energies as functions of deformation along the normal coordinate, $E(Q)$, for the unstable modes E_{1g} and E_{2g}. These curves show that the minimum for E_{1g} is much deeper than for E_{2g} (Fig. 3), which confirms once again that the role of the soft mode is played here by the mode from representation E_{1g}. Displacing the lattice atoms parallel to the eigenvector of the mode E_{1g} to the minimum point of curve $E(Q)$, we further optimized the structure in both space groups C_{2h}^3 and C_{2h}^6. The energy values thus obtained are –31.3574 and –31.3634 aJ per unit cell. This result can be considered as an indication of the fact that the structure described by the sp. gr. C_{2h}^6 (i.e., with the twofold axis along the y coordinate axis) is energetically more favorable and, therefore, should be regarded as the most probable configuration of the low-temperature phase. Table 8 lists the calculated values of the corresponding structure parameters. These results may be of interest for experimentalists studying this compound.

CONCLUSION

Symmetry analysis of the structure of the low-temperature phase allowed us to draw the conclusion that the symmetry group of the monoclinic phase with the monoclinic axis perpendicular to the sixfold axis of the high-temperature phase is either C_{2h}^3 or C_{2h}^6.

The distribution of normal vibrations over the irreducible representations of the high-temperature phase is refined, and the relationships between normal vibrations for all possible low-temperature phases are tabulated.

The model of the potential function is obtained by the nonempirical Kim–Gordon method and amended by introducing some small empirical corrections. Using this model, we managed to establish that the configuration of the high-temperature phase corresponds to the saddle point on the potential surface and that the vibrational spectrum has several modes that are unstable in the harmonic approximation. The analysis of the corresponding eigenvectors showed that these modes mainly describe the deformations that include the consistent rotations of rigid $MnCl_6$ and Mn_2Cl_9 polyhedra. The absolute minimum of the potential surface (i.e., the geometry of the low-temperature phase) is attained by deformation of the structure (sp. gr. C_{2h}^6) along the eigenvector of the mode from the representation E_{1g}. In fact, this mode describes oscillations of rigid polyhedra around the y axis (in the setting of the high-temperature phase) and interacts with the homogeneous shear deformation xz, which, in the final analysis, determines the ferroelastic nature of the phase transition.

Our calculations show that the height of the energy barrier between the high- and low-temperature phases is 0.0663 aJ per unit cell, which, on the temperature scale, corresponds to 55 K (we used the relationship $\Delta E \approx 3nkT$). Experimentally, the structural phase transition is observed at $T \sim 270$ K. It should be indicated that the height of the energy barrier does not determine the phase-transition temperature and can have both a higher (for order–disorder phase transitions) or a lower (for displacive-type transitions) value [10]. Our estimates allow us to state that the structural phase transition is close to a displacive-type transition characteristic of framework crystals with structural phase transitions induced by rotations of rigid polyhedra.

ACKNOWLEDGMENTS

This study was supported by INTAS, project no. 97-10177, and the Russian Foundation for Basic Research, project no. 00-03-33040. The authors are grateful to I.I. Tupitsyn for the program for quantum-chemical computations by the Hartree–Fock method.

REFERENCES

1. G. G. Vasil'ev, S. V. Mel'nikova, A. V. Malakhovskiĭ, and A. T. Anistratov, Fiz. Tverd. Tela (Leningrad) **19** (12), 3700 (1977) [Sov. Phys. Solid State **19**, 2163 (1977)].
2. K. S. Aleksandrov, A. T. Anistratov, S. V. Mel'nikova, *et al.*, Fiz. Tverd. Tela (Leningrad) **21** (4), 1119 (1979) [Sov. Phys. Solid State **21**, 650 (1979)].
3. M. Melamud, J. Makovsky, N. Shaked, and S. Strikman, Phys. Rev. B **3**, 821 (1971).
4. I. V. Fedoseeva and B. V. Beznosikov, Pis'ma Zh. Éksp. Teor. Fiz. **21**, 108 (1975) [JETP Lett. **21**, 48 (1975)].
5. D. Schonland, *Molecular Symmetry* (Van Nostrand, London, 1965).
6. M. B. Smirnov and V. Yu. Kazimirov, JINR Commun. (Dubna), E14-2001-159 (2001).
7. P. B. Miller and J. D. Axe, Phys. Rev. **163**, 924 (1967).
8. R. G. Gordon and Y. S. Kim, Chem. Phys. **56**, 3122 (1972).
9. A. P. Mirgorodsky, M. B. Smirnov, P. E. Quintard, and T. Merle-Méjean, Phys. Rev. B **52**, 9111 (1995).
10. A. D. Bruce and R. A. Cowley, *Structural Phase Transitions* (Taylor and Francis, London, 1981; Mir, Moscow, 1984).

Translated by L. Man

Crystallography Reports, Vol. 48, No. 3, 2003, pp. 443–447. Translated from Kristallografiya, Vol. 48, No. 3, 2003, pp. 488–492.
Original Russian Text Copyright © 2003 by Sakhnenko, Ter-Oganesyan.

LATTICE DYNAMICS AND PHASE TRANSITIONS

Ferroelectric and Ferroelastic Phase States of Crystals Caused by Atomic Ordering

V. P. Sakhnenko and N. V. Ter-Oganesyan
Institute of Physics, Rostov State University, pr. Stachki 194, Rostov-on-Don, 344090 Russia
e-mail: sakh@ip.rsu.ru

Received December 18, 2002

Abstract—The effect of atomic ordering on displacive-type structural phase transitions is considered for crystals with several atomic sublattices. On the basis of group-theoretical analysis and general crystallographic and thermodynamic principles, it is shown that ordering gives rise to qualitative restructuring of phase diagrams and changes in atomic states up to the formation of new ferroelectric and ferroelastic phases proper. Specific physical properties of crystals provided by atomic ordering are considered in the vicinity of structural transitions within the framework of the phenomenological theory of phase transitions. *© 2003 MAIK “Nauka/Interperiodica”.*

INTRODUCTION

Depending on the thermodynamic history of multiatomic crystals, some atoms, which were equivalent in a disordered crystal, can be distributed over the lattice site with different degree of order. If these crystals undergo structural or magnetic phase transformations, the temperatures of these transitions and the specific features of their physical characteristics in the vicinity of the transition points are dependent on the type and degree of atomic order, which is confirmed by numerous experiments. Among such crystalline compounds there are ordering alloys whose magnetically ordered states are strongly dependent on the degree of atomic order and multiatomic compounds (such as oxides and halides) whose properties are determined, to a large extent, by the degree of cationic order. Numerous intensely studied relaxors also belong to these compounds. We consider here the effect of atomic ordering on structural phase transitions proceeding from the general symmetry and thermodynamic principles.

ATOMIC ORDERING AND SYMMETRY

In many instances, atomic order is formed at temperatures considerably exceeding the temperatures of the structural and magnetic phase transitions observed in these crystals. Therefore, the degree of atomic order described by the order parameter s in such crystals can be considered as a characteristic constant in the whole range of the variation of the thermodynamic parameters of state.

When interpreting various manifestations of atomic ordering, one usually proceeds from the assumption that the order parameter s makes a quantitative contribution to the thermodynamic potential and corresponding thermodynamic functions. Within the framework of the phenomenological theory of phase transitions or some modification of the mean-field approximation, this approach reduces to introducing the dependence on s of the coefficients of the expansion of the thermodynamic potential in degrees of the corresponding order parameter (see, e.g., [1–3]). However, the effect of atomic ordering on phase transitions can be much more pronounced; namely, at $s \neq 0$, some additional contributions to the thermodynamic potential can arise, which are forbidden by the symmetry in the disordered state. If such contributions are small in comparison with the components of the order parameter of a structural or magnetic phase transition, the whole picture of phase transformations is qualitatively changed along with the phase states. These changes can manifest themselves especially clearly in those instances where ordering requires the inclusion into the phase transition of degrees of freedom that are described by tensors, which results in the formation of corresponding macroscopic fields during phase transitions and, as a result, in the divergence of the corresponding susceptibilities.

In the majority of instances, atomic ordering is accompanied by multiplication of the initial unit-cell; in other words, the order parameter s (in general, a multicomponent quantity) is related to the star of the reciprocal-lattice vectors $\mathbf{k} \neq 0$ lying either at the boundary of the Brillouin zone or inside this zone. If a crystal undergoes a structural or magnetic phase transition with the order parameter c relating to the same vector $\mathbf{k}$ as the order parameter s, then, in the general case, the symmetry admits the existence of mixed invariants with the components s_i and c_j and tensor quantities ξ_l. In the simplest case, such an invariant has the form

$$J = \sum_{i,j,l} A_{ijl} s_i c_j \xi_l. \qquad (1)$$

In this case, ξ can possess the symmetry of the vector of electric polarization or magnetization or else that of a tensor of homogeneous deformations. In a disordered crystal, where all $s_i = 0$, there are no interactions between the order parameter c and the tensor ξ described by this invariant. In an ordered crystal ($s \neq 0$), the phase transition induced by the order parameter c acquires the characteristics of a ferroelectric, ferromagnetic, or ferroelastic transition because of the interactions bilinear with respect to c and ξ. In terms of group-theoretical analysis, the condition for the existence of invariants of this type, in general, can be written as

$$\tau_l \in \tau_i \otimes \tau_j, \tag{2}$$

where τ_i is the irreducible representation that describes atomic ordering, τ_j is the irreducible representation according to which the order parameter of a structural or magnetic phase transition is transformed, and τ_l is the irreducible representation that reflects the transformational properties of the components (or their linear combinations) of a certain tensor quantity. Obviously, the presence of τ_l in the direct product of τ_i and τ_j signifies that the symmetry of the initial disordered phase admits the existence of invariants bilinear with respect to the products of (s_i, c_j) and ξ_l, i.e., invariants of form (1).

PHASE TRANSITIONS IN TERNARY OXIDES OF THE PEROVSKITE FAMILY WITH ORDERING CATIONIC SUBLATTICES

Consider examples of ternary oxides with a perovskite-type structure described by the formulas $A'_{1/2}A''_{1/2}BO_3$ and $AB'_{1/2}B''_{1/2}O_3$, which have been repeatedly studied experimentally at different degrees of atomic order (see, e.g., [4]). The experimental data show the considerable effect of the degree of order of A and B atoms on the structural phase transitions in these oxides.

The completely disordered ($s = 0$) oxides of these types are described by the sp. gr. O_h^1 ($Pm3m$). If (1 : 1)-type ordering of the A and B cations proceeds along all the three crystallographic axes, the crystal preserves its cubic symmetry, but the lattice becomes face-centered and the space group changes to O_h^5 ($Fm3m$) with a double volume of the primitive unit-cell. Choosing the origin of the coordinate system at the site A for $A'_{1/2}A''_{1/2}BO_3$ perovskites and at the site B for $AB'_{1/2}B''_{1/2}O_3$ perovskites, we can describe ordering by the one-dimensional irreducible representation $\tau_1(\Gamma_1)$ of the vector $\mathbf{k} = (1/2, 1/2, 1/2)$ of the point R in the Brillouin zone of a primitive cubic lattice (in what follows, we number the irreducible representations τ_i in accordance with [5]). Most of the phase transitions observed in perovskites can be described by three-dimensional irreducible representations of the sp. gr. O_h^1. Consider the structural phase transitions induced by three-dimensional irreducible representations of the vector $\mathbf{k} = (1/2, 1/2, 1/2)$, to which the irreducible representation τ_1 (which describes atomic ordering) belongs. For a given $\mathbf{k}$, the structure of the vibrational representation τ_{vib} is as follows. If the generating symmetry elements of the sp. gr. O_h^1 are related to the point A, then $\tau_{\text{vib}}^{(R)} = \tau_4 + \tau_6 + \tau_7 + \tau_8 + 2\tau_{10}$; if they are related to the point B, then $\tau_{\text{vib}}^{(R)} = \tau_1 + \tau_5 + 2\tau_7 + \tau_9 + \tau_{10}$. In ordering induced by unit-cell doubling, the Brillouin zone of the initial cubic lattice becomes smaller, and the point R lies in the center of a new Brillouin zone of the face-centered cubic lattice described by the sp. gr. O_h^5. Using the table from [5], one can readily establish that, for the irreducible representation of the sp. gr. O_h^1, the following correspondence is valid: $\tau_i(R) \otimes \tau_1(R) = \tau_i(\Gamma)$. This signifies that the phase transition that was described by the irreducible representation $\tau_i(R)$ in the disordered crystal is now described by the irreducible representation $\tau_i(\Gamma)$. Thus, we can obtain correspondence between the phases in the ordered and disordered states of a crystal that are generated by the same order parameter (see table).

Consider the phase transitions described by the irreducible representations $\tau_7(R)$ and $\tau_{10}(R)$. To the symmetry transformation $Pm3m$–$Fm3m$ for τ_7 there corresponds the newly appeared term $sc_1c_2c_3$ in the thermodynamic potential $\Phi(c_i)$. This indicates a violation of the Landau condition for the corresponding order parameter, and, therefore, the structural transition in the ordered crystal ($s \neq 0$) cannot be related to second-order phase transitions. One can readily show that the symmetry admits a mixed invariant $s(c_1U_{xy} + c_2U_{yz} + c_3U_{zx})$, which signifies that, at $s \neq 0$, the proportional components of the tensor of homogeneous deformation U_{jk} should appear. Thus, in the ordered crystal, the structural transition with the order parameter, which is transformed according to the irreducible representation $\tau_7(R)$, becomes a quasi-proper ferroelastic phase transition, which, in the cubic phase, should be accompanied by an anomalous increase in the component s_{44} of the tensor of elastic compliances.

If a phase transition is described by the irreducible representation $\tau_{10}(R)$, the form of the thermodynamic potential $\Phi(c_i)$ remains unchanged. However, now the symmetry admits a mixed invariant $s(c_1P_x + c_2P_y + c_3P_z)$, where P_x, P_y, and P_z are the components of the electric-polarization vector. This results in the appearance of spontaneous polarization in all the dissymmetric phases of the ordered ($s \neq 0$) crystal, which are induced by the irreducible representation $\tau_{10}(R)$.

Now, analyze the crystal structure of the ferroelectric phases thus formed in more detail. Consider, first, Phase states of disordered and ordered $A'_{1/2}A''_{1/2}BO_3$ and $AB'_{1/2}B''_{1/2}O_3$ crystals of the perovskite family induced by three-dimensional irreducible representations of the vector **k** = (1/2, 1/2, 1/2) of the sp. gr. O_h^1

Types of phase states	τ_7		τ_8		τ_9		τ_{10}	
	disordered	ordered	disordered	ordered	disordered	ordered	disordered	ordered
$c\ 0\ 0$	D_{4h}^{17}	D_{2h}^{25}	D_{4h}^{18}	D_{2d}^{11}	D_{4h}^{18}	D_{4h}^{5}	D_{4h}^{17}	C_{4v}^{9}
$c\ c\ c$	D_{3d}^{5}	D_{3d}^{5}	D_{3d}^{6}	D_{3}^{7}	D_{3d}^{6}	C_{3i}^{2}	D_{3d}^{5}	C_{3v}^{5}
$c\ c\ 0$	D_{2d}^{28}	C_{2h}^{3}	D_{2h}^{28}	C_{2v}^{20}	D_{2h}^{28}	C_{2h}^{3}	D_{2h}^{28}	C_{2v}^{20}
$c_1\ c_1\ c_2$	C_{2h}^{3}		C_{2h}^{6}	C_{2}^{3}	C_{2h}^{6}	C_i^1	C_{2h}^{3}	C_s^3
$c_1\ c_2\ 0$	C_{2h}^{3}	C_i^1	C_{2h}^{3}	C_s^3	C_{2h}^{3}		C_{2h}^{3}	C_s^3
$c_1\ c_2\ c_3$	C_i^1		C_i^1	C_i^1	C_i^1		C_i^1	C_i^1

the case of B ordering. In the phase transition associated with the appearance of one of the c_i components of the order parameter $\tau_{10}(R)$, e.g., c_3, the B atoms are displaced from their positions, which leads to the formation of the antiferroelectric state of the crystal (Fig. 1a). As is seen from Fig. 1a, this is accompanied by the loss of the (001) symmetry planes passing through the B sites. If $s \neq 0$, the (001) symmetry planes, where A atoms were located, disappear. As a result, the crystal looses the center of inversion and becomes a ferroelectric with the polar axis z (Fig. 1b). In a similar way, other dissymmetric phases generated by the order parameter $\tau_{10}(R)$ become ferroelectric in a B-ordered crystal.

If the generating elements of the sp. gr. O_h^1 are related to the point A, then $\tau_{10}(R)$ describes the mode formed at the displacements of oxygen atoms. In the phase thus formed, the displacements of oxygen atoms lead to the loss of the planes passing through B cations, whereas the ordering of A cations cause the disappearance of another set of reflection planes. Therefore, in an A-ordered crystal, the corresponding phase also becomes ferroelectric. It is precisely this picture of structure transformations that is reflected by an *scP*-

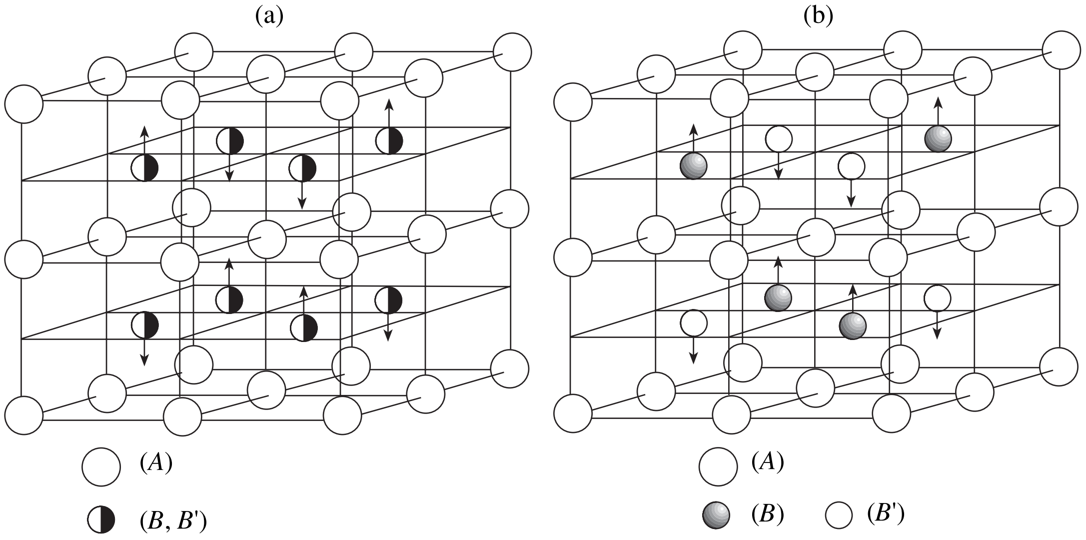

Fig. 1. Structure of the 00*c*-type phase described by the three-component order parameter $\tau_{10}(R)$ for (a) disordered and (b) ordered $AB'_{1/2}B''_{1/2}O_3$ crystals of the perovskite family.

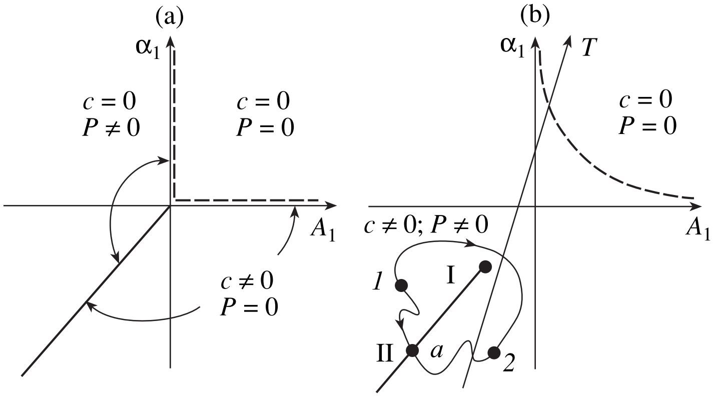

Fig. 2. Phase diagrams of (a) disordered and (b) ordered crystals corresponding to the thermodynamic potential Φ. Dashed lines indicate the lines of second-order phase transitions and solid lines, those of first-order phase transitions.

type invariant in the thermodynamic potential in both cases.

EFFECT OF ORDERING ON PHASE TRANSITIONS WITH COMPETING ORDER PARAMETERS

We believe that the difference in the phase states of ordered and disordered crystals considered above is significant for understanding and theoretically describing diffuse phase transitions. The phase transitions with the characteristic diffuse maximum of the response function corresponding to the order parameter are observed in many complicated compounds, in particular, in magnetic alloys [6, 7] and ferroelectric oxides [4], of which the best studied are ternary oxides with a perovskite structure—$Pb(Sc_{1/2}Nb_{1/2})O_3$, $Pb(Sc_{1/2}Ta_{1/2})O_3$, $(Na_{1/2}Bi_{1/2})TiO_3$, and $Pb(Mg_{1/3}Nb_{2/3})O_3$. It is established that the degree of cationic order produces a considerable effect on their anomalous physical characteristics, which is especially clearly seen during phase transformations.

One of the characteristics of the above lead-containing oxides is the lowering of the lattice symmetry at high temperatures (considerably exceeding the temperature of the diffuse maximum of the dielectric constant) accompanied by the formation, at least locally, of a phase described by the space group $R\bar{3}m\,(D_{3d}^5)$ [8, 9]. In order to describe the behavior of the physical properties of these oxides over a wide temperature range, consider the structural transitions in ordering crystals in the case of two competing order parameters. In our case, these parameters are the three-component order parameter c_i described by the irreducible representation $\tau_{10}(R)$ and the vector order parameter transformed by the irreducible representation $\tau_{10}(\Gamma)$ of the vector $\mathbf{k} = 0$ both in the ordered and disordered phases. The phase D_{3d}^5 is formed if $c_1 = c_2 = c_3 = c \neq 0$, which allows one to use the one-component approximation and to write the model thermodynamic potential in the form

$$\Phi = \frac{1}{2}\alpha_1 c^2 + \frac{1}{4}\alpha_2 c^4 + \frac{1}{2}A_1 P^2 + \frac{1}{4}A_2 P^4 + \frac{1}{2}f c^2 P^2 + kscP - EP.$$

One of the simplest phase diagrams in the (α_1, A_1) plane at $s = 0$ and $E = 0$ corresponding to the above potential is shown in Fig. 2a. This diagram of phase states is valid at $\Delta = \alpha_2 A_2 - f^2 < 0$ and $f > 0$. Ordering ($s \neq 0$) mixes nonferroelectric ($c \neq 0$, $P = 0$) and ferroelectric ($c = 0$, $P \neq 0$) phase states. As a result, a phase of the type $c \neq 0$, $P \neq 0$ is formed in the ordered crystal. The transition of the symmetric phase into this mixed phase proceeds along the line of second-order phase transitions k^2s^2, i.e., $\alpha_1 A_1 = 0$, $\alpha_1 > 0$ (dashed line in Fig. 2b). At the same time, the line of first-order phase transitions between the phases $c \neq 0$, $P = 0$ and $c = 0$, $P \neq 0$ in the vicinity of the point $\alpha_1 = 0$, $A_1 = 0$ in an ordered crystal becomes rather diffuse and begins only at the point with the coordinates $A_1^* = -\frac{2|ks|\alpha_1^{1/4}A_2^{3/4}}{f - (\alpha_2 A_2)^{1/2}}$, $\alpha_1^* = A_1^*\sqrt{\alpha_2/A_2}$. Thus, in an ordered crystal, the transition between states 1 and 2 should proceed either continuously (line I) or via a first-order phase transition (point *a* on line II).

Now consider the phase transformations from the symmetric phase along the line where all the thermodynamic parameters of state, except for temperature, are constant. In the approximation of the phenomenological theory of phase transitions considered here, this is a straight line in the (α_1, A_1) plane (the T axis in Fig. 2b). With a decrease in temperature, i.e., in the thermodynamic path along the direction opposite to the direction indicated by an arrow, a disordered crystal is transformed into a centrosymmetric phase, whereas an ordered crystal shows the transition to the ferroelectric state along the line of second-order phase transitions. With a further decrease in temperature, the thermodynamic path considered above intersects the line of first-order phase transitions to the ferroelectric phase in a disordered crystal. This transition should be accompanied by an increase in the dielectric constant in the vicinity of the phase transition and its jump on the line of the phase transition. As has already been indicated, in an ordered crystal ($s \neq 0$), a region is formed in which no phase transitions take place and which broadens with an increase in s. However, the dielectric constant passes through a broad maximum, which diffuses with an increase in s and, thus, also with an increase in the distance of the critical point from the temperature axis.

Thus, the structural transition in an ordered crystal ($c \neq 0$) is accompanied by the appearance of spontaneous polarization, which can have considerably lower values than polarization observed in intrinsic ferroelectric phase transitions. In this case, the region of a considerable increase in ε, provided by the divergence of permittivity at the transition point, is very narrow because of the low value of the Curie constant. At the same time, with a further decrease in temperature, a broad maximum of permittivity should be formed in the wide range of s values corresponding to the temperature of the ferroelectric transition in a crystal with $s = 0$.

CONCLUSION

The effect of atomic ordering on structural phase transitions can be even more pronounced in the case of spatial inhomogeneity of atomic ordering, which is often the case irrespective of the chemical inhomogeneity of the crystal. The dependence of the phase-transition temperature on the degree of order $s(\mathbf{r})$ results in additional diffusion of the dielectric constant during the formation of a ferroelectric state. However, in many crystals, ordering can be extremely inhomogeneous. Thus, lead-containing perovskites with ordering B cations, in fact, consist of ordered (by the 1 : 1 type) nanometric regions with $s = 1$ distributed over the disordered crystalline matrix with $s = 0$ [10]. In such a crystal, which preserves a continuous oxygen framework, the regions with $s \neq 0$ acquire a dipole moment during the structural phase transition and become the sources of internal electric fields of complex configuration. As a result, a ferroelectric phase transition, which occurs in the whole crystal lattice, proceeds in a crystal containing numerous sources that form an internal electric field. In particular, it was shown above that during the formation of a phase described by the space group D_{3d}^5 recorded at high temperatures, the ordered regions of the crystal have the structure described by the space group C_{3v}. Thus, we believe that it is the ordered regions of the crystal that may be one of the sources of random fields; the existence of these fields should necessarily be assumed in order to interpret specific physical properties.

REFERENCES

1. A. A. Bokov, I. P. Raevskiĭ, and V. G. Smotrakov, Fiz. Tverd. Tela (Leningrad) **25**, 2025 (1983) [Sov. Phys. Solid State **25**, 1168 (1983)].
2. P. Groves, J. Phys. C **19**, 5103 (1986).
3. A. A. Bokov, Ferroelectrics **90**, 155 (1989).
4. Z.-G. Ye, Key Eng. Mater. **155–156**, 81 (1998).
5. O. V. Kovalev, *Representations of the Crystallographic Space Groups: Irreducible Representations, Induced Representations, and Corepresentations* (Nauka, Moscow, 1986; Gordon and Breach, Yverdon, Switzerland, 1993).
6. E. F. Wassermann, *Ferromagnetic Materials* (Elsevier, Amsterdam, 1990), Vol. 6, p. 240.
7. K. P. Belov, *Magnetic Transitions* (Fizmatgiz, Moscow, 1959; Consultants Bureau, New York, 1961).
8. M. Mitsui and E. P. Nakamura, *Ferroelectrics and Related Substances* (Springer, Berlin, 1990), Landolt–Börnstein New Series, Vol. 28.
9. I. W. Chen, J. Phys. Chem. Solids **61**, 197 (2000).
10. A. D. Hilton, D. J. Barber, C. A. Randall, and T. R. Shrout, J. Mater. Sci. **25**, 3461 (1990).

Translated by L. Man

Crystallography Reports, Vol. 48, No. 3, 2003, pp. 448–456. Translated from Kristallografiya, Vol. 48, No. 3, 2003, pp. 493–501.
Original Russian Text Copyright © 2003 by Reznichenko, Shilkina, Gagarina, Raevskiĭ, Dul'kin, Kuznetsova, Akhnazarova.

LATTICE DYNAMICS AND PHASE TRANSITIONS

Structural Instabilities, Incommensurate Modulations and *P* and *Q* Phases in Sodium Niobate in the Temperature Range 300–500 K

L. A. Reznichenko*, L. A. Shilkina*, E. S. Gagarina*, I. P. Raevskiĭ*, E. A. Dul'kin, E. M. Kuznetsova*, and V. V. Akhnazarova***

** Research Institute of Physics, Rostov State University, Rostov-on-Don, 344090 Russia*
e-mail: egag@ip.rsu.ru
*** Advanced School of Applied Science, Hebrew University, Jerusalem, 91904 Israel*

Received November 18, 2002

Abstract—The relation between the phase transition in the vicinity of 420 K discovered earlier and the formation of an incommensurate phase in the temperature range 410–460 K is established based on the X-ray, dielectric, and dilatometric studies of sodium niobate ($NaNbO_3$) single crystals and ceramics. It is also established that this phase is characterized by temperature and temporal instabilities. Anomalies in some physical characteristics in the vicinity of 350 K are revealed. It is also shown that the thermodynamic history of the samples is important for the coexistence of the regions of the ferroelectric *Q* and antiferroelectric *P* phases in $NaNbO_3$. *© 2003 MAIK "Nauka/Interperiodica".*

INTRODUCTION

The studies of the temperature behavior of the dielectric constant ε of sodium niobate $NaNbO_3$ single crystals in [1] showed that, in addition to the seven well-known phases [2] (paraelectric, antiferroelectric, and ferroelectric) and the corresponding six phase transitions, namely, U (paraelectric, O_h^1) $\xleftrightarrow{910\text{ K}}$ $T2$ (paraelectric, D_{4h}^5) $\xleftrightarrow{850\text{ K}}$ $T1$ (paraelectric, D_{2h}^{17}) $\xleftrightarrow{790\text{ K}}$ S (paraelectric, D_{2h}^{13}) $\xleftrightarrow{750\text{ K}}$ R (antiferroelectric, D_{2h}^{13}) $\xleftrightarrow{630\text{ K}}$ P (antiferroelectric, D_{2h}^{11}) $\xleftrightarrow{170\text{ K}}$ N (ferroelectric, C_{3v}^6), the compound undergoes at least one more phase transition in the vicinity of 420 K. The latter transition is accompanied by the formation of a diffuse anomaly in $\varepsilon(T)$. The introduction of lithium or potassium into sodium niobate increases the temperature of this phase transition up to 445–455 K. Insignificant anomalies in the structural and physical parameters in the temperature range from 220 ($N \longrightarrow P$) to 630 K ($P \longleftrightarrow R$) were observed earlier [3–10], but they were not attributed to the existence of structural instabilities in this temperature range. The only exception here is the study of the Raman spectra [11], whose authors came to the conclusion that a phase transition in sodium niobate may exist in the temperature range 420–470 K.

Despite the fact that the anomaly in the behavior of $\varepsilon(T)$ in sodium niobate discovered by us is diffused in comparison with the anomalies corresponding to the well-known phase transitions, the temperature of this phase transition is practically independent of the measuring-field frequency in the range 1–100 kHz and the measuring mode (heating or cooling), whereas the maxima of $\varepsilon(T)$ corresponding to the well-known phase transitions are characterized by a pronounced temperature hysteresis [1, 5–7]. These results allowed us to suggest [1] that the character of the phase transition observed in sodium niobate in the vicinity of 420 K is close to the second-order phase transition, which is confirmed by the studies of these crystals in polarized light. It was established that the propagation of the phase fronts and the change in the extinction character take place only at the temperatures corresponding to the well-known phase transitions.

The studies of the temperature behavior of the structural characteristics of sodium niobate described in our earlier publications [1, 10] showed that the orthorhombic symmetry remains unchanged in the temperature range 300–630 K and that only the slopes of the temperature curves of the lattice parameters of the monoclinically distorted perovskite-type unit cell $a = c > b$, $\alpha = \gamma = 90° < \beta$ are changed in the temperature range 420–470 K.

The polydomain sodium niobate crystals grown from NaF flux [3] had, along with the antiferroelectric *P* phase, the orthorhombic ferroelectric *Q* phase (sp. gr. C_{2v}^2). This phase is usually formed in sodium niobate in an applied electric field, in potassium- or lithium-modified sodium niobate, etc. [12]. The relation between the perovskite-type unit cells of the *P* and *Q* phases and the orthorhombic unit cell is described by the following relationships [12]: $\mathbf{A} = \mathbf{a} - \mathbf{c}$, $\mathbf{B} = 4\mathbf{b}$ (*P* phase) or $\mathbf{B} = 2\mathbf{b}$ (*Q* phase), $\mathbf{C} = \mathbf{a} + \mathbf{c}$, where $\mathbf{A}$, $\mathbf{B}$,

1063-7745/03/4803-0448$24.00 © 2003 MAIK "Nauka/Interperiodica"

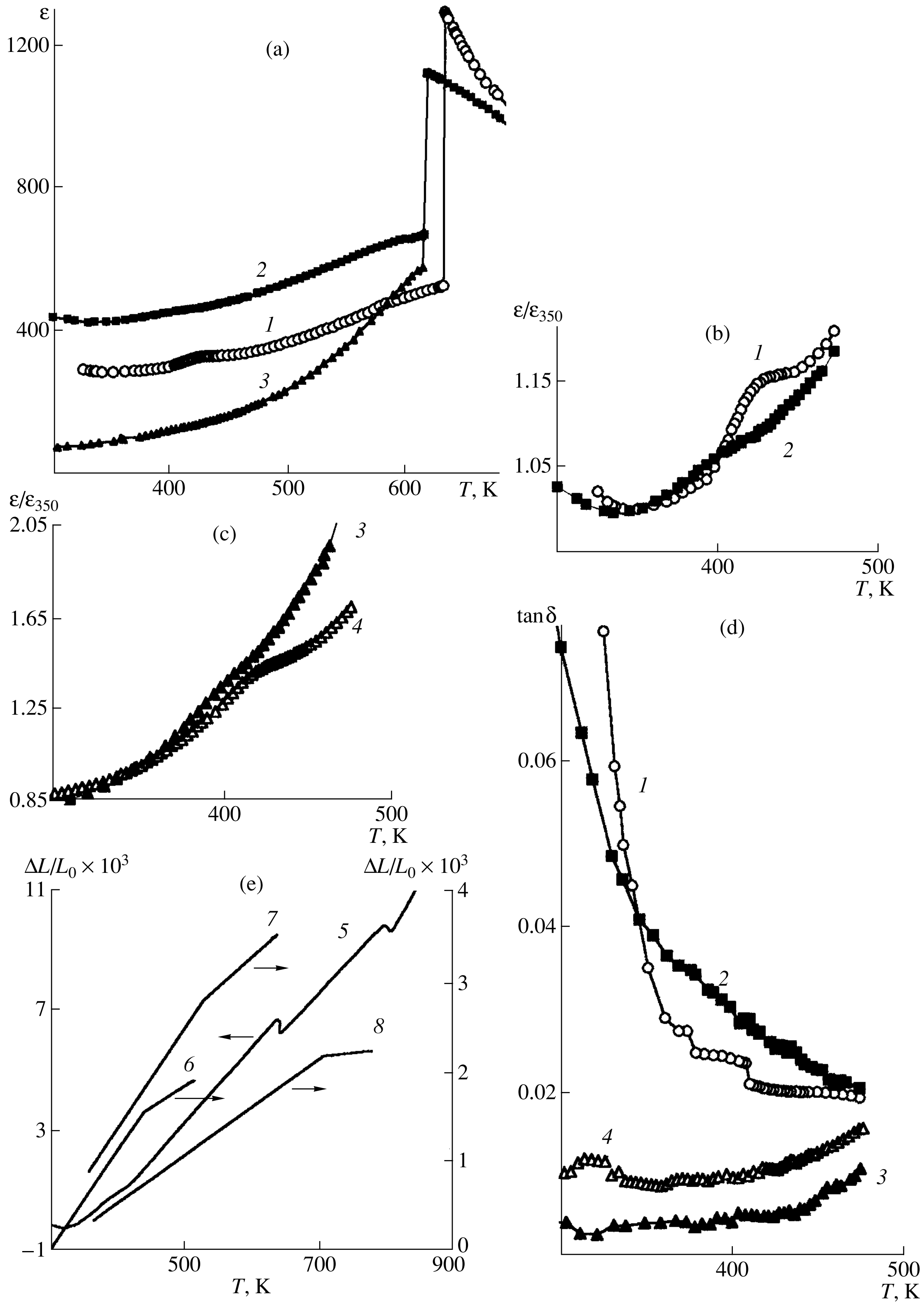

Fig. 1. Temperature curves of (a–c) ε; (d) tan δ of (*1*) *K*1 and (*2*, *3*) *K*2 crystals, and (*4*) $NaNbO_3$ ceramic measured at a frequency of 1 kHz in the heating mode on (*1*, *2*) twinned crystals and (*3*) single-domain crystal; and (e) relative elongation $\Delta L/L_0$ of (*5*) a *K*2 single crystal and (*6*) $NaNbO_3$, (*7*) $Sr_2Nb_2O_7$, and (*8*) $Ca_2Nb_2O_7$ ceramics.

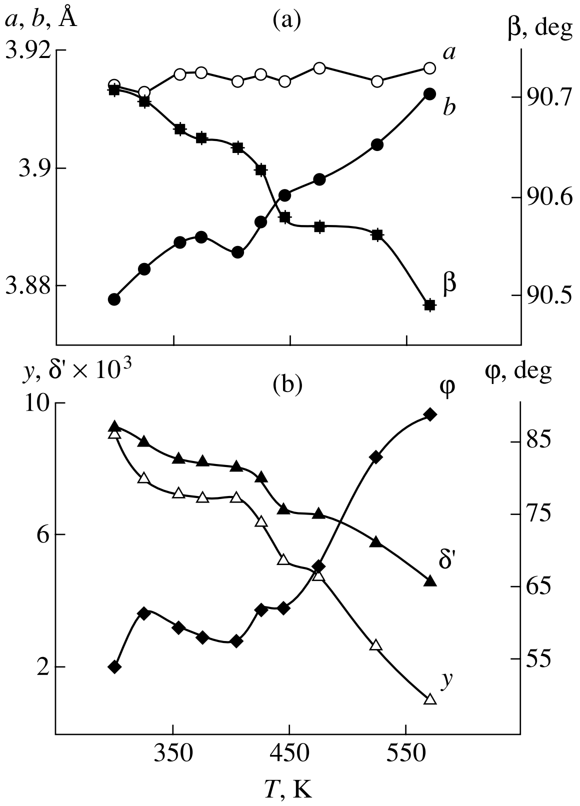

Fig. 2. Temperature curves of (a) the *a*, *b*, and β parameters of the perovskite unit cell and (b) the δ' parameter of uniform deformation, degree of orthorhombicity *y*, and the calculated angle φ of the orientation of 60°-domain boundaries of the (*hhl*) type for *K*1 single crystals ($\Delta a = \Delta b = \pm 0.003$, $\Delta\beta = \pm 0.05°$, $\Delta\delta' = \pm 0.002$, $\Delta y = \pm 0.001$, and $\Delta\varphi = \pm 2°$).

and **C** are the axial vectors of the orthorhombic unit cells. In the temperature range 350–500 K, these crystals also showed the $P \longleftrightarrow Q$ phase transitions characterized by a jumpwise change of the lattice parameters and a more pronounced (50–100 K) temperature hysteresis.

In order to clarify the nature of the phase transition revealed in [1], we undertook detailed X-ray, dielectric, and dilatometric studies of sodium niobate in the temperature range 300–500 K. Taking into account the often encountered inconsistency of the published data on sodium niobate associated with the conditions of sample preparation, we studied single crystals grown from various salt systems and also sodium niobate ceramics.

PREPARATION OF SAMPLES. MEASUREMENT METHODS

Sodium niobate single crystals were grown from flux [13] with the use of the Na_2CO_3–B_2O_3 and Na_2CO_3–NaF–$NaVO_3$ systems as solvents. In the first case, we obtained both platelike colorless transparent crystals with $\{100\}_c$[1] faceting having a thickness of 0.2–0.3 mm and an edge length of up to 2 mm (*K*1 crystals) and gray (because oxygen of deficiency) prismatic crystals with $\{100\}_c$ faceting, a base-edge length of up to 1 mm, and a height of up to 3 mm (*K*1' crystals). In the second case, we obtained yellowish crystals (*K*2) with a faceting analogous to the faceting of *K*1' crystals. Ceramics were prepared by two-stage 4-h solid-phase synthesis at 1070–1120 K and subsequent 2 h-sintering at 1510 K.

The X-ray diffraction studies of both single crystals and ceramics and also the powders obtained by grinding these crystals and ceramics were performed on DRON-3 and ADP diffractometers (Fe_{K_α} radiation, Mn-filter, and Fe_{K_β} radiation). Thermal expansion was studied on prismatic *K*2 crystals along the $[001]_c$ direction and on ceramic samples using a differential dilatometer by methods described elsewhere [14]. The dielectric constant ε was measured at frequencies 1–100 kHz using an alternate-current *P*5083 bridge during heating or cooling at a rate of 2–3 K/min. The Aquadag electrodes were applied to the natural $\{100\}_c$-faces of the crystals. The ceramic samples were metallized by 0.5-h-brazing of a silver-containing paste at 1070 K.

RESULTS AND DISCUSSION

As a rule, all the prepared sodium niobate crystals were obviously twinned. Figure 1a shows the ε(*T*) curves of the twinned *K*1 and *K*2 crystals. Curves *1* and *2* (ε only slightly depends on temperature and increases with a lowering of the temperature below 350 K) are similar to those obtained in [15] for sodium niobate crystals measured along the **b** axis. This is quite understandable since the ε value along the **b** axis is considerably higher than along the perpendicular directions [15], whereas the **b** axes of different twin components are either directed normally to the crystal faces $\{100\}_c$ or form a small angle with these faces because of twinning along the (110) faces. All the sodium niobate samples studied had, in addition to the maximum on ε, weak anomalies in the vicinity of 420 K for *K*1 crystals and ceramics and the same in the vicinity of 400 K for *K*2 crystals. The lower temperatures of the maxima on ε(*T*) for the latter crystals seem to be explained by the incorporation of F^- and V^5 ions into the lattice, which is also consistent with the crystal color. We managed to find among the *K*2 crystals one practically single-domain crystal and measured this crystal normally to its **b** axis. Although the ε values and the run of ε(*T*) of this crystal (Figs. 1a, 1c, curve *3*) differ from those observed for twinned *K*1 and *K*2 crystals (Figs. 1a, 1b), the anomaly in ε(*T*) in the vicinity of 400 K is observed in this case as well. The temperature curves of the tan-

---

[1] The hkl_c indices correspond to pseudocubic perovskite unit cell, *hkl* indices, to monoclinically distorted unit cell.

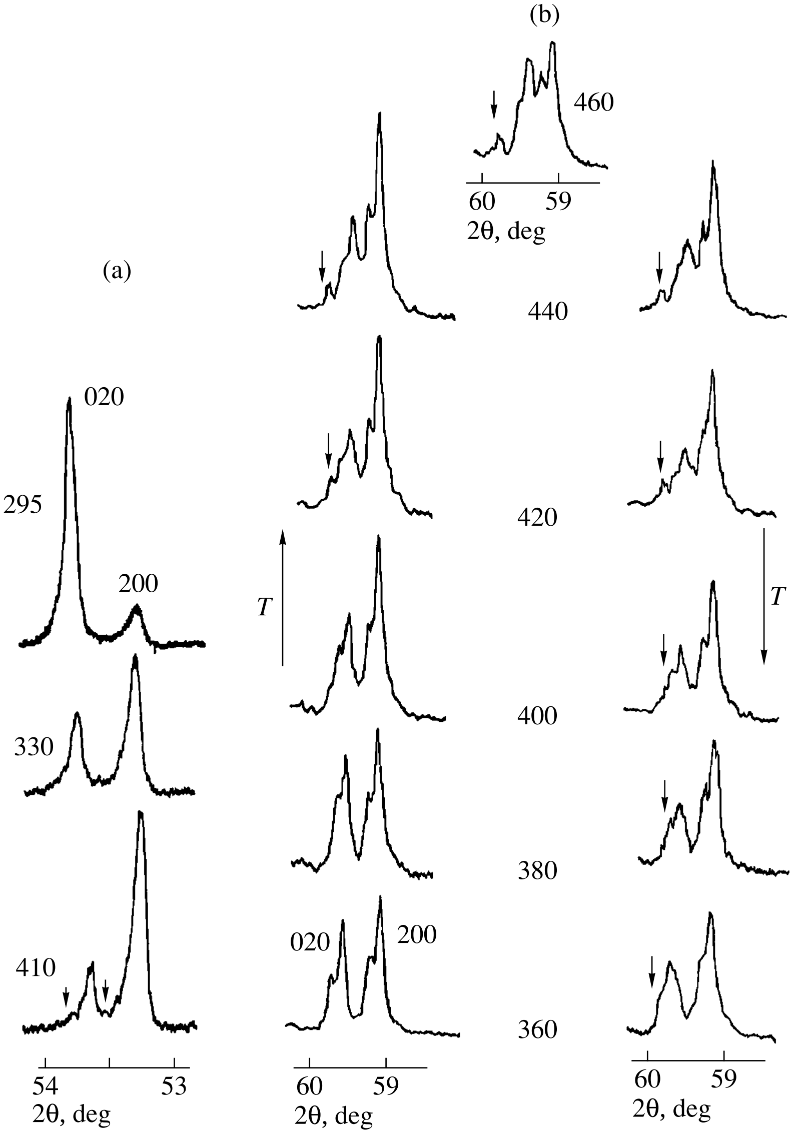

Fig. 3. Evolution of the 020 and 200 reflection profiles with a change in the temperature (K) of (a) *K*2 crystals (FeK_β-radiation, heating mode) and (b) ground *K*1 crystals (FeK_α radiation, heating–cooling mode). Arrows indicate satellite reflections.

gent of the angle of dielectric losses, $\tan\delta$, showed no noticeable anomalies corresponding to the anomaly in $\varepsilon(T)$ in the temperature range 400–420 K for all the crystals studied (Fig. 1d). The temperature dependence of the relative elongation $\Delta L/L_0$ of *K*2 single crystals has, in addition to the anomalies corresponding to the $P \longleftrightarrow R$ and $S \longleftrightarrow T1$ transitions, a kink in the vicinity of 400 K (Fig. 1e). The change in the slope of the $\Delta L/L_0(T)$ curves at 430 K was also observed for ceramic sodium niobate samples (Fig. 1e). The X-ray studies of sodium niobate powders showed no changes in the symmetry in the temperature range from 300 to 630 K. In the temperature range 420–470 K (corresponding to the anomaly in $\varepsilon(T)$), sodium niobate single crystals and ceramics show only feeble jumps on the $b(T)$ and $\beta(T)$ curves (Fig. 2) and related anomalies in the temperature behavior of the uniform deformation parameter $\delta' = a\sqrt{1-\cos\beta}/V^{1/3}$ [16] (where V is the volume of the perovskite unit cell) and the degree of unit-cell orthorhombicity $y = b/(a\sin\beta) - 1$.

Analysis of the X-ray line profiles corresponding to the main 200 and 020 reflections showed the following. With an increase in temperature in the range 410–460 K, satellite reflections appear in the vicinity of the 020 reflection (Fig. 3), which indicates structure modulation along the [010] direction. The maximum intensities of the satellite peaks comprise about 1/5 of the main-reflection intensity. The modulation wavelength continuously varies with the temperature and decreases with an increase in the temperature from 500 Å at 410 K to 350 Å at 460 K and increases with a lowering

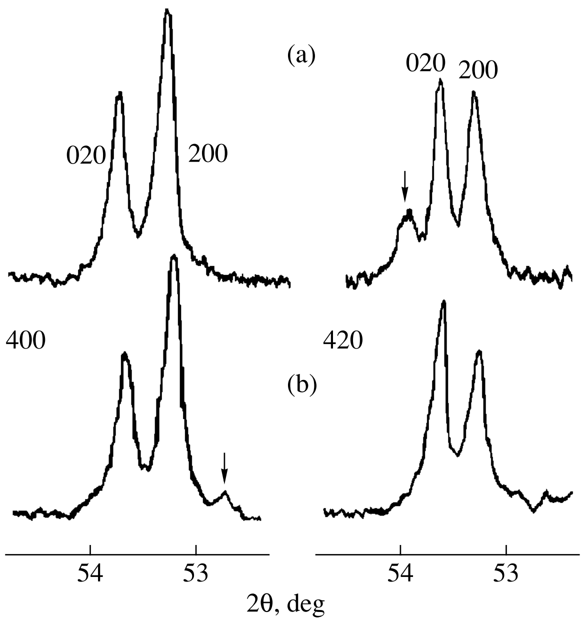

Fig. 4. Profiles of the 020 and 200 diffraction reflections from ground *K*1 crystals (a) after they were kept for 10 min at 400 and 420 K and (b) after they were kept for a further 15 min at these temperatures. Arrows indicate satellite reflections.

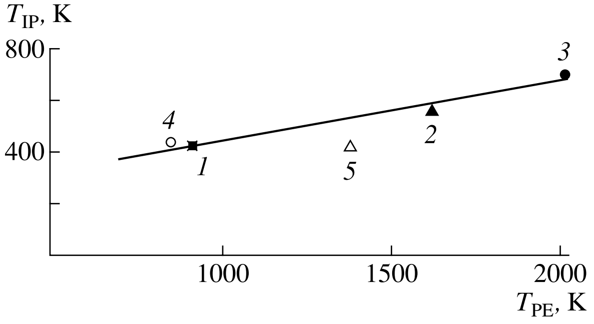

Fig. 5. Correlation between the temperatures of transition to the paraelectric (T_{PE}) and incommensurate phase (T_{IP}) for (*1*) $NaNbO_3$, (*2*) $Sr_2Nb_2O_7$, and (*3*) $Ca_2Nb_2O_7$. For comparison, the empty shapes indicate the temperatures of the anomalies in the electrophysical and structural parameters for (*4*) $AgNbO_3$ and (*5*) $LiNbO_3$ according to [21, 22].

of the temperature, but it has different values at each fixed temperature in the heating and cooling modes (Fig. 3b). This indicates the formation of an incommensurate phase along the [010] direction in the indicated temperature range and the existence of temperature hysteresis of the structural characteristics. Thus, one can state that there exist two phase transitions: commensurate orthorhombic phase $\xrightarrow{410\text{ K}}$ incommensurate phase $\xrightarrow{460\text{ K}}$ commensurate orthorhombic phase. It seems that the diffuse anomaly in ε(*T*) observed at 420 K reflects the occurrence of these two closely located phase transitions. The repeated annealing of the samples resulted in a narrowing of the existence range of the incommensurate phase to ~415–445 K. The character of the appearance and disappearance of the incommensurate phase (gradual diffusion of the 020 line until the formation of a diffuse maximum with an increase in temperature and its gradual transformation into its initial diffused state as the temperature is decreased) indicates that the phase transformations observed are close to second-order phase transitions.

In addition to the observed temperature instability, the incommensurate phase is also characterized by temporal instability—change of the diffraction pattern with time. Figure 4 illustrates the changes in the profiles of the main 020 and 200 reflections at 400 and 420 K as a result of maintaining the samples at these temperatures for 15 min. As is seen from Fig. 4, heating the sample up to 400 K and keeping it at this temperature for 15 min result in the appearance of a satellite (2θ = 52.8°) in the vicinity of the 200 reflection and the diffusion of the profile of the 020 reflection. Further heating up to 420 K is accompanied by the transformation of the diffuse 020 profile into a sharp satellite (2θ = 53.9°), which, after keeping the sample at the given temperature for 15 min, disappears. At 420 K, the satellite in the vicinity of the 200 reflection becomes diffuse.

The existence of intermediate low-temperature incommensurate phases far from the transition to the paraelectric phase was earlier observed in other niobate materials, e.g., in strontium and calcium pyroniobates, $Sr_2Nb_2O_7$ and $Ca_2Nb_2O_7$ [17–20]. Similar to the situation in sodium niobate, in this case, the phase transition from the basic phase into the incommensurate phase is accompanied by the formation of weak anomalies in ε(*T*), i.e., $\Delta L/L_0(T)$ (Fig. 1e). The nature of the incommensurate phase in these compounds has not been understood as yet. Taking into account the close chemical compositions and the related structure types of sodium, strontium, and calcium niobates, one can assume that the formation of the incommensurate phases in these compounds can be caused by similar factors. To some extent, this is confirmed by the almost linear dependence of the temperatures of the transitions to the incommensurate and the paraelectric cubic phases in these three oxides (Fig. 5). It should be emphasized that the temperatures of the anomalies in the lattice parameters and the $\Delta L/L_0$ and ε(*T*) curves of the $LiNbO_3$ [21] and $AgNbO_3$ [22] compounds are also close to this line, which allows us to assume the existence of an incommensurate phase in the vicinity of the above temperatures.

In the course of high-temperature X-ray diffraction studies of sodium niobate samples, we also revealed dramatic changes in the intensities of the main 200 and 020 reflections in the reciprocal-space section θ–2θ. Such a redistribution between the diffraction reflection intensities is caused by the motion of domain walls giving rise to the redistribution of the orientational states. This process depends on the habit of the single crystals

Unit-cell parameters and phase composition of $NaNbO_3$ samples at 300 K

Sample no.	$NaNbO_3$ (sample form)	Phase composition	Phase ratio, P/Q	Parameters of perovskite unit cell
1	Ceramic	P		$a = 3.911$ Å, $b = 3.879$ Å, $\beta = 90.67°$
2	$K1$ single crystal (no. 1)	$P + Q$	≈1 : 2	P phase: $a\sin\beta = 3.915$ Å
				Q phase: $a\sin\beta = 3.922$ Å
3	$K1$ single crystal (no. 2)	$P + Q$	≈2 : 1	P phase: $a\sin\beta = 3.917$ Å
				Q phase: $a\sin\beta = 3.923$ Å
4	Ground $K1$ single crystal	P		P phase: $a = 3.915$ Å, $b = 3.880$ Å, $\beta = 90.72$ Å
				Q phase: $a\sin\beta = 3.919$ Å (appears at $T = 350$ K)
5	$K1'$ single crystal	P		$a\sin\beta = 3.915$ Å, $b = 3.879$ Å
6	Ground $K1'$ crystals	P		$a = 3.914$ Å, $b = 3.878$ Å, $\beta = 90.75°$
7	$K2$ single crystal (no. 1)	P		$a\sin\beta = 3.911$ Å, $b = 3.882$ Å
8	$K2$ single crystal (no. 2)	P		$a\sin\beta = 3.912$ Å, $b = 3.879$ Å

studied: the diffraction pattern obtained from the developed face of the platelike crystals shows an increase in the intensity of the 020 reflections at higher temperatures; for prismatic crystals, the diffraction pattern from the side face of the prism (Fig. 3a) shows an increase in the intensity of the 200 reflection. In other words, the redistribution of reflection intensities proceeds in such a way that the axis **b** of the perovskite cell tries to rotate parallel to the singled-out direction (perpendicular to the developed face of the plate or the long edge of the prism). One of the possible mechanisms of such rearrangement can be the change in the orientations of the 60°-domain boundaries (*hhl*) of the *S*-type observed in sodium niobate with the temperature or stress variations [8, 23]. The orientation of these domain boundaries depends on the unit-cell parameters and can be determined from the coherence condition at the plane boundary of the contacting domains [24]:

$$h/l = (\eta_a^2 - \eta_b^2 + \eta^2)/4\eta\eta_a,$$

where $\eta_a - 1$, $\eta_b - 1$, and η are the elements of the deformation matrix; $\eta_a = a\cos(\mu/2)/a_0$; $\eta_b = b/a_0$; $\eta = a\sin(\mu/2)/a_0$; $\mu = (\beta - 90°)$; $a_0 = V^{1/3}$; and V is the volume of the perovskite unit cell. The calculated temperature curves of the orientation angle $\varphi = \arctan(bl/ah)$ of these boundaries (Fig. 2) show that, in the vicinity of the temperature range 420–450 K, the region of the pronounced changes in φ begins, which is consistent with the optical data [23].

The temperature dependences of ε (Figs. 1, 2) also show anomalies in the vicinity of 350 K. The character of these anomalies is similar to those observed at 420 K, although they are less intense. In the vicinity of this temperature, an additional maximum on the dependence $\tan\delta(T)$ was recorded [9, 25]. The samples that we studied showed no noticeable maxima of $\tan\delta(T)$ in the vicinity of 350 K; however, a dramatic increase in $\tan\delta(T)$ in twinned $K1$ and $K2$ crystals is observed in this temperature range during cooling (Fig. 1d), whereas the curves $\varphi(T)$ (Fig. 2) had a jump. The mechanism of the structural instability of sodium niobate in this temperature range is still unclear.

The manifestation of the above anomalies did not depend on the physicochemical state of the object. These anomalies were well reproducible in the ceramic and in single crystals grown from various salt melts. The thermodynamic history plays the decisive role in the effect of coexistence of the antiferroelectric (P) and ferroelectric (Q) states. The simultaneous presence of these phases in sodium niobate at room temperature was observed experimentally in a number of studies [3, 26].

Thus, among the ten $K2$ crystals studied, none of them showed the presence of the Q phase; with an increase in temperature, this phase did not appear either. In most of the $K1$ crystals, coexistence of the P and Q phases was observed already at room temperature (in the ratios 2 : 1, 1 : 2, etc.) (see table). The content of the P and Q phases was evaluated from the observed splitting of the 200 diffraction reflection associated with a slight difference in the a parameter of the perovskite unit cells corresponding to these phases, $a_Q > a_P$ [3]. We established that the a value of different samples at room temperature ranges within 3.919–3.923 for the Q phase and within 3.911–3.917 Å for the P phase.[2]

In $K1$ crystals that initially have no Q phase (at room temperature), this phase appeared upon crystal heating up to 350–400 K, with its content intensely increasing with the approach to ~420 K. In these cases, the incom-

---

[2] Because of the difference in the a parameter of the P and Q phases (3.916 Å for P and 3.920 Å for Q), the corresponding broadening of the 100 diffraction profile was mistakenly attributed in [27] to the parameters $a \neq c$ of the allegedly existing monoclinic phase and not to the orthorhombic phase in sodium niobate at room temperature.

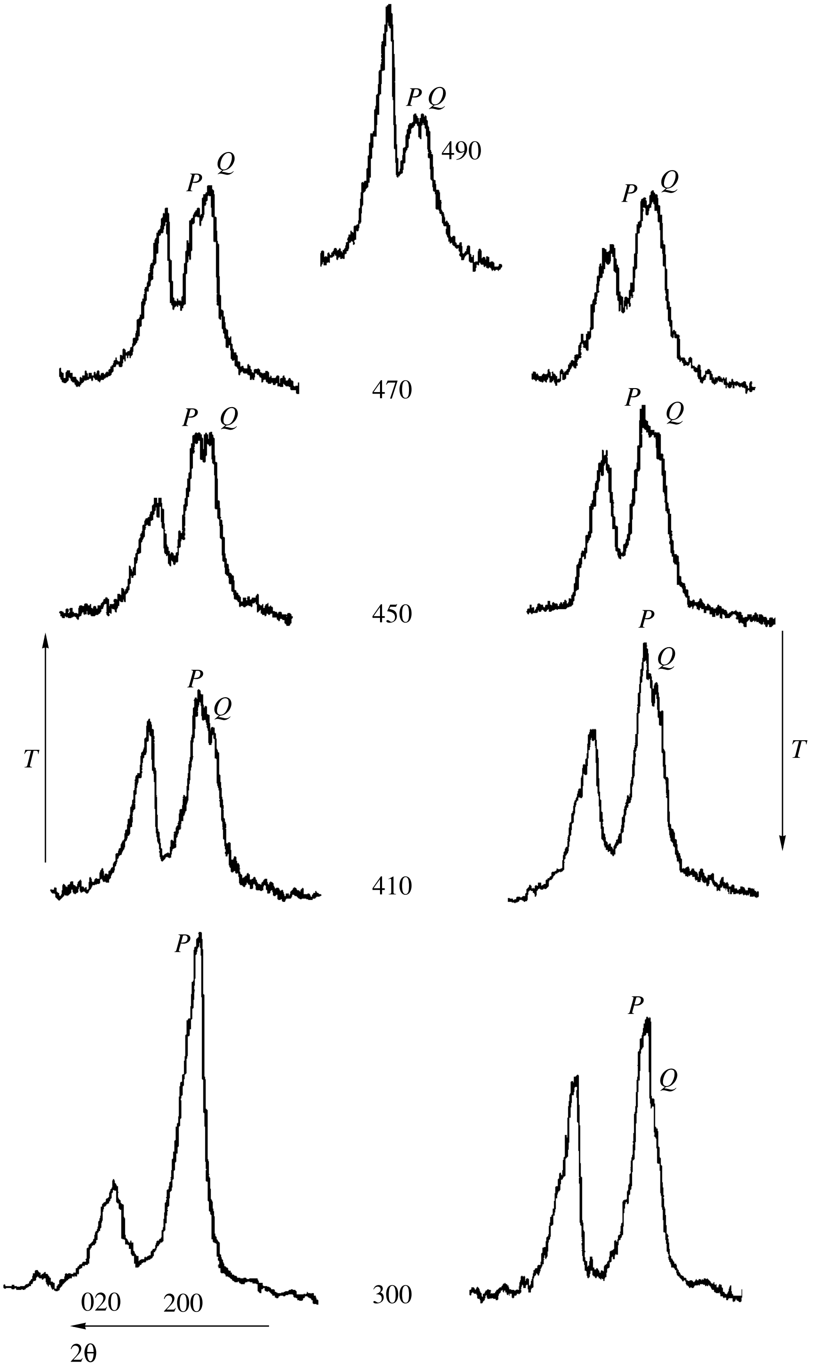

Fig. 6. Changes in the 200 and 020 reflection profiles corresponding to the change in the ratio of the *P* and *Q* phases in a *K*1 single crystal with temperature variation in the heating–cooling mode.

mensurate phase consisted of equal amounts of both phases (as is also the case when heating crystals with initially coexisting *P* and *Q* phases in a 2 : 1 ratio). With further heating, the amount of the *Q* phase decreases and, finally, at *T* ~ 520–570 K, this phase disappears, which is in good accord with data [3]. The more intense formation of the *Q* phase in the vicinity of the range of existence of the incommensurate phase seems to be associated with the high instability of the structure in this range. Cooling of the *K*1 crystals (which contained the *P* phase in the initial state) and their subsequent heating to the temperature at which the amounts of the *P* and newly formed *Q* phases become equal did not return the crystals to the initial *P* state, so they remained heterophase (Fig. 6). Repeated heating of these crystals to 950 K and their subsequent cooling resulted in the

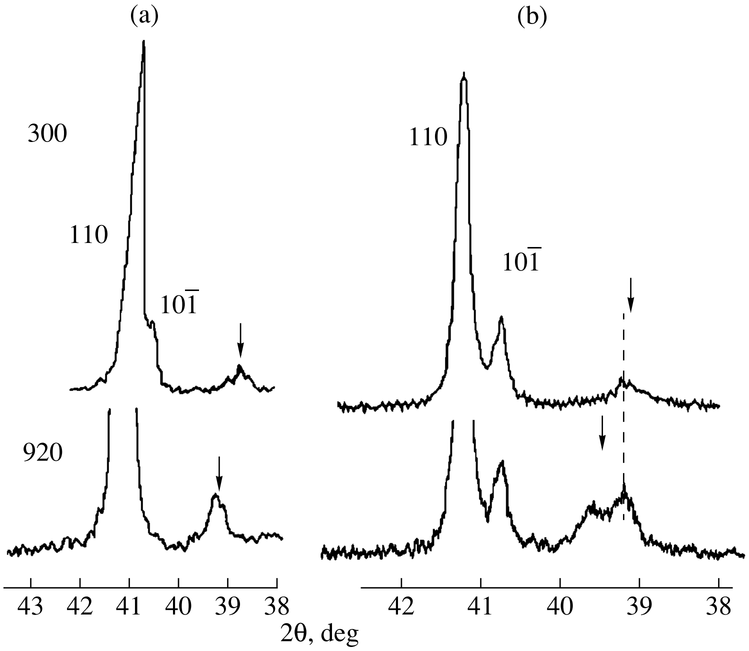

Fig. 7. Fragments of the diffractograms that show the $10\bar{1}$, 110, and satellite reflections (indicated by arrows) at 300 and 920 K from (a) a ceramic and (b) a *K*1' single crystal (no. 5 in table) prior to (above) and after (below) being kept for 10 h at 420 K.

restoration of the single-phase *P* state. Heating of *K*1 crystals with an initial ratio of the *P* and *Q* phases of ~1 : 2 did not lead to a change in this ratio.

Earlier [28], we established that alkali metal niobates, their solid solutions, and ternary niobium oxides have modulated deformed states arising in the same way as in the initial Nb_2O_5 reagent [29] because of the ordering of the shear planes. The appearance of shear planes is associated with the necessity to remove anionic vacancies formed because of the instability of the valence state (4^+, 5^+) Nb. At room temperature, the diffraction pattern of sodium niobate has one or two (in some rare occasions even three) satellite reflections in the form of broad or split maxima located before the $10\bar{1}$ reflection (on the side of smaller θ angles) [28]. The corresponding modulation periods, i.e., the distances between the shear planes along the $[10\bar{1}]$ direction range within ~55–100 Å, which is less by an order of magnitude than in the incommensurate phase described above.

Our studies showed that the satellite peaks do not change their positions with an increase in temperature and are also preserved in the paraelectric cubic phase (Fig. 7a). In this case, the peaks are not split any more and their intensities noticeably increase, which indicates an increase in the degree of order in the arrangement of shear planes. The almost constant modulation period (it is independent of the temperature and observation time) allows one to consider the observed modulated state as a stable state, provided by the stable defect-density wave associated with the periodic distribution of shear planes over the crystal. An incommensurate phase with a varying modulation period along the **b** axis in the vicinity of 420 K can be considered as a metastable state, whose nature is not clear as yet.

It should be noted that satellites along the [010]* direction of the reciprocal lattice were observed in sodium niobate at room temperature [26]. All the attempts to stabilize the incommensurate phase by keeping the crystals at 420 K for 10 h gave no results: the satellite close to the 020 reflection appeared only after the crystal was kept at 420 K for 25 min and then disappeared. At the same time, the X-ray diffraction pattern had one more satellite before the 110_c reflection (Fig. 7b); the intensity of the first reflection considerably increased; i.e., the second wave of defect density was generated. It seems that the long isothermal keeping of the samples at moderate temperatures also provides a more regular arrangement of shear planes and redistribution of point defects which, as a rule, try to arrange along the defect-containing planes and, thus, stabilize the waves of atomic displacements.

CONCLUSION

The anomalies revealed in the temperature curves of ε, thermal expansion, and parameters of the perovskite $NaNbO_3$ unit cell in the vicinity of 420 K are caused by the formation of an incommensurate phase in the temperature range 410–460 K and are characterized by temperature and temporal instability with a modulation period of 350–500 Å along the (010) direction. The above anomalies and the formation of the incommensurate phase are observed in all the sodium niobate single crystals and ceramic samples studied. At the same time, the existence in sodium niobate of ferroelectric regions of the *Q* phase and the total volume of these regions are critically dependent on the thermodynamic history of the samples, so that many samples show no *Q* phase at all. Anomalies in some physical characteristics in the vicinity of 350 K are revealed. The analysis of the diffraction patterns leads to the conclusion that several incommensurate modulations of different character coexist in sodium niobate. The nature of these modulations and the relation between them are not clear as yet.

The pronounced polymorphism, the coexistence of several phases of different nature at the same temperature, in particular, the ferroelectric and antiferroelectric phases, and the high mobility of the domain boundaries indicate the structural instability and extremely high sensitivity of $NaNbO_3$ to various external factors.

ACKNOWLEDGMENTS

This study was supported by the Russian Foundation for Basic Research, project no. 99-02-17575.

REFERENCES

1. I. P. Raevskiĭ, L. A. Reznichenko, V. G. Smotrakov, *et al.*, Pis'ma Zh. Tekh. Fiz. **26** (16), 97 (2000) [Tech. Phys. Lett. **26**, 744 (2000)].
2. H. D. Megaw, Ferroelectrics **7** (1–4), 87 (1974).
3. I. Lefkowitz, K. Lukaszewicz, and H. D. Megaw, Acta Crystallogr. **20**, 670 (1966).
4. N. N. Kraĭnik, Fiz. Tverd. Tela (Leningrad) **2**, 685 (1960) [Sov. Phys. Solid State **2**, 633 (1960)].
5. L. Pardo, P. Duran-Martin, J. P. Mercurio, *et al.*, J. Phys. Chem. Solids **58**, 1335 (1997).
6. K. Konieczny, Mater. Sci. Eng. B **60**, 124 (1999).
7. A. Molak, M. Pawelczyk, and J. Kwapulinski, J. Phys.: Condens. Matter **6**, 6833 (1994).
8. S. Miga, J. Dec, and M. Pawelczyk, J. Phys.: Condens. Matter **8**, 8413 (1996).
9. V. A. Isupov, Izv. Akad. Nauk SSSR, Ser. Fiz. **22** (12), 1504 (1958).
10. L. A. Shilkina, L. A. Reznichenko, M. F. Kupriyanov, and E. G. Fesenko, Zh. Tekh. Fiz. **47** (10), 2173 (1977) [Sov. Phys. Tech. Phys. **22**, 1262 (1977)].
11. X. B. Wang, Z. X. Shen, Z. P. Hu, *et al.*, J. Mol. Struct. **385**, 1 (1996).
12. G. A. Smolenskiĭ, V. A. Bokov, V. A. Isupov, N. N. Kraĭnik, R. E. Pasynkov, A. I. Sokolov, and N. K. Yushin, *Physics of Ferroelectric Phenomena* (Nauka, Leningrad, 1985).
13. V. G. Smotrakov, I. P. Raevskiĭ, M. A. Malitskaya, *et al.*, Neorg. Mater. **16** (5), 1065 (1980).
14. E. A. Dul'kin and I. P. Raevski, Ferroelectrics **239** (1–4), 381 (2000).
15. L. E. Cross and B. J. Nicholson, Philos. Mag. **46**, 453 (1956).
16. E. G. Fesenko, V. S. Filip'ev, and M. F. Kupriyanov, Fiz. Tverd. Tela (Leningrad) **11** (2), 466 (1969) [Sov. Phys. Solid State **11**, 366 (1969)].
17. V. V. Kochetkov, N. A. Zakharov, S. Yu. Stefanovich, and Yu. N. Venevtsev, Kristallografiya **24** (5), 1066 (1979) [Sov. Phys. Crystallogr. **24**, 610 (1979)].
18. K. Ohi, M. Kimura, H. Ishida, and H. Kakinuma, J. Phys. Soc. Jpn. **49** (4), 1387 (1979).
19. N. Yamamoto, Acta Crystallogr., Sect. A: Cryst. Phys., Diffr., Theor. Gen. Crystallogr. **38**, 780 (1982).
20. N. A. Zakharov, V. P. Orlovskiĭ, and V. A. Klyuev, Izv. Ross. Akad. Nauk, Ser. Fiz. **60** (10), 85 (1996).
21. V. A. Chernyshkov, Candidate's Dissertation in Physics and Mathematics (Rostov State Univ., Rostov-on-Don, 1990).
22. A. Kania and J. Kwapulinski, J. Phys.: Condens. Matter **11**, 8933 (1999).
23. O. A. Zhelnova and O. E. Fesenko, Fiz. Tverd. Tela (Leningrad) **27** (1), 8 (1985) [Sov. Phys. Solid State **27**, 4 (1985)].
24. V. Yu. Topolov, L. E. Balyunis, A. V. Turik, and O. E. Fesenko, Kristallografiya **35** (3), 755 (1990) [Sov. Phys. Crystallogr. **35**, 441 (1990)].
25. L. A. Reznichenko, A. V. Turik, E. M. Kuznetsova, and V. P. Sakhnenko, J. Phys.: Condens. Matter **13**, 3875 (2001).
26. J. Chen and D. Feng, Phys. Status Solidi A **109**, 171 (1988).
27. C. N. W. Darlington and K. S. Knight, Physica B (Amsterdam) **266**, 368 (1999).
28. L. A. Reznichenko, L. A. Shilkina, S. V. Titov, *et al.*, in *Proceedings of International Symposium on Odering in Minerals and Alloys, OMA-2000* (Rostov-on-Don, 2000), p. 111.
29. C. N. R. Rao and J. Gopalakrishnan, *New Directions in Solid State Chemistry* (Cambridge Univ. Press, Cambridge, 1986; Nauka, Novosibirsk, 1990).

Translated by L. Man

Crystallography Reports, Vol. 48, No. 3, 2003, pp. 457–460. Translated from Kristallografiya, Vol. 48, No. 3, 2003, pp. 502–505.

Neutron Diffraction Study of Phase Transitions in the Superionic Conductor $Li_{0.25}Cu_{1.75}Se$*

**N. N. Bikkulova[1], S. A. Danilkin[2], A. I. Beskrovnyĭ[3], E. L. Yadrovskiĭ[4], V. A. Semenov[4],
G. N. Asylguzhina[1,5], M. Kh. Balapanov[5], M. B. Sagdatkireeva[5],
and U. Kh. Mukhamed'yanov[5]**

[1] Sterlitamak State Pedagogical Institute, Sterlitamak, pr. Lenina 49, 453103 Bashkortostan, Russia
e-mail: bickulova@mail.rb.ru
[2] Hahn-Meitner-Institut, SF2, Glienicker Str. 100, Berlin, D-14109 Germany
[3] Frank Laboratory of Neutron Physics, Joint Institute for Nuclear Research,
ul. Joliot-Curie, Dubna, Moscow oblast, 141980 Russia
[4] Institute of Physics and Power Engineering, pl. Bondarenko 1, Obninsk, Kaluzhskaya oblast, 249020 Russia
[5] Bashkortostan State University, ul. Frunze 32, Ufa, 450074 Bashkortostan, Russia

Received November 22, 2002

Abstract—Neutron diffraction studies of the superionic conductor $Li_{0.25}Cu_{1.75}Se$ are reported. It is shown that gradual disordering in the cation sublattice with an increase in temperature leads to changes in the symmetry of the crystal lattice at 400 and 500 K. At temperatures close to these values, anomalies in the temperature dependence of both ionic and electron conductivity are observed. *© 2003 MAIK "Nauka/Interperiodica".*

INTRODUCTION

Lithium-substituted copper selenide is a superionic conductor. The substitution of copper by lithium ions results in a lowering of the ionic conductivity, increase in the activation energy, and decrease in the coefficients of chemical diffusion [1]. At present, no structural data on $Li_{0.25}Cu_{1.75}Se$ are available. The aim of this study was to establish the relation between the crystal structure and disorder of the cation sublattice.

EXPERIMENTAL RESULTS AND DISCUSSION

Neutron diffraction studies of the alloy $Li_{0.25}Cu_{1.75}Se$ were performed by the elastic neutron scattering technique on a DN-2 diffractometer within the 300–573 K temperature range at the Joint Institute for Nuclear Research, Dubna, Russia and on a E1 diffractometer at 300 K at the Hahn-Meitner-Institut, Berlin, Germany.

A $Li_{0.25}Cu_{1.75}Se$ sample was prepared by the method of solid-state reaction between lithium and polycrystalline $Cu_{1.75}Se$ in vacuum with its subsequent homogenization for 100 h at 673 K.

Electron conductivity σ was measured by the four-probe method [2]. The experimental error of σ measurements ranged within 6–8%.

The neutron diffraction patterns of materials with the compositions $Cu_{1.75}Se$, $Cu_{1.98}Se$, and $Li_{0.25}Cu_{1.75}Se$ obtained at 300 K on an E1 diffractometer are shown in Fig. 1. The neutron diffraction pattern of $Li_{0.25}Cu_{1.75}Se$ resembles the pattern of α-$Cu_{1.98}Se$, but the reflections are slightly shifted and their intensities differ from the reflection intensities of α-$Cu_{1.98}Se$. For comparison, the same figure also shows the diffraction pattern of fcc β-$Cu_{1.75}Se$ [3]. The neutron diffraction patterns of $Cu_{1.98}Se$ and $Li_{0.25}Cu_{1.75}Se$ are similar to the diffraction pattern corresponding to the cubic phase but with split main Bragg peaks—111 and 220.

Unit cell parameters of the alloy $Li_{0.25}Cu_{1.75}Se$

T, K	a, Å	b, Å	c, Å	α, deg	β, deg	γ, deg	System	R, %
293	7.13(5)	12.35(9)	6.91(0)	90.44	107.68	91.22	Triclinic	1.5
473	7.13(1)	12.28(9)	7.18(4)	90.00	108.34	90.00	Monoclinic	1.8
523	11.37(5)	11.43(9)	11.32(0)	90.00	90.00	90.00	Orthorhombic	1.2
573	11.39(2)	11.47(6)	11.24(6)	90.00	90.00	90.00	Orthorhombic	1.3

---

* This study was presented at the Symposium "Phase Transformations in Solid Solutions" (OMA), Sochi, 2002.

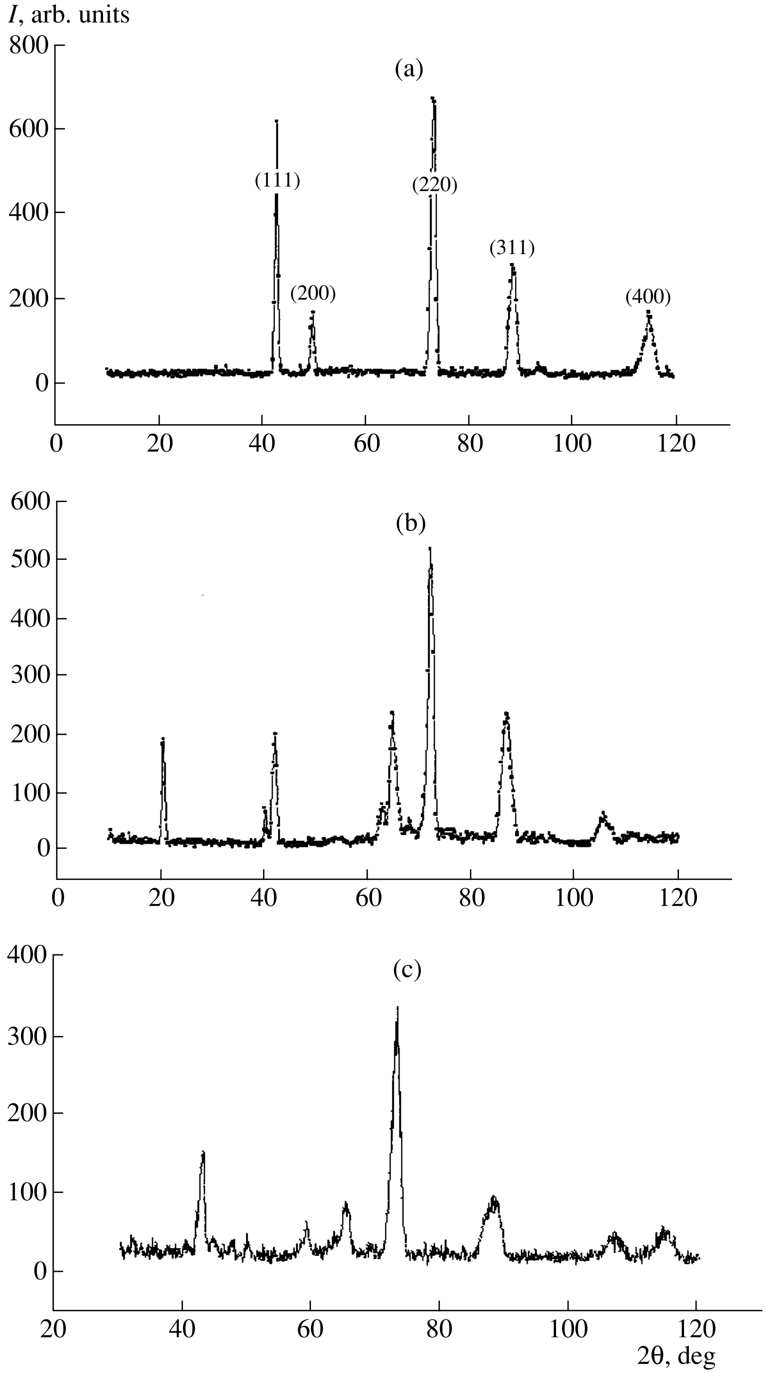

Fig. 1. Neutron diffraction patterns of materials with the compositions (a) $Cu_{1.75}Se$, (b) $Cu_{1.98}Se$, and (c) $Li_{0.25}Cu_{1.75}Se$.

The neutron diffraction patterns of the compound $Li_{0.25}Cu_{1.75}Se$ obtained on a DN-2 diffractometer in the temperature range 300–573 K are shown in Fig. 2. With an increase in the temperature, the neutron diffraction patterns change only slightly. Neutron diffraction patterns obtained on a DN-2 diffractometer were indexed using the INDEX program. It is seen that, like α-$Cu_{1.98}Se$, the α-$Li_{0.25}Cu_{1.75}Se$ phase at 300 K is triclinic. This result follows from the data obtained on different diffractometers (DN-2 and E1) at different times. Despite the low symmetry of the $Li_{0.25}Cu_{1.75}Se$ lattice at 293 K, the compound has a rather high ionic conductivity ($0.020 \pm 0.002\ \Omega^{-1}\ cm^{-1}$), which enables us to consider this phase as a superionic with a mixed type of conductivity (electronic conductivity equals $650\ \Omega^{-1}\ cm^{-1}$). However, the ionic conductivity of this material is by an order of magnitude lower than that in the superionic

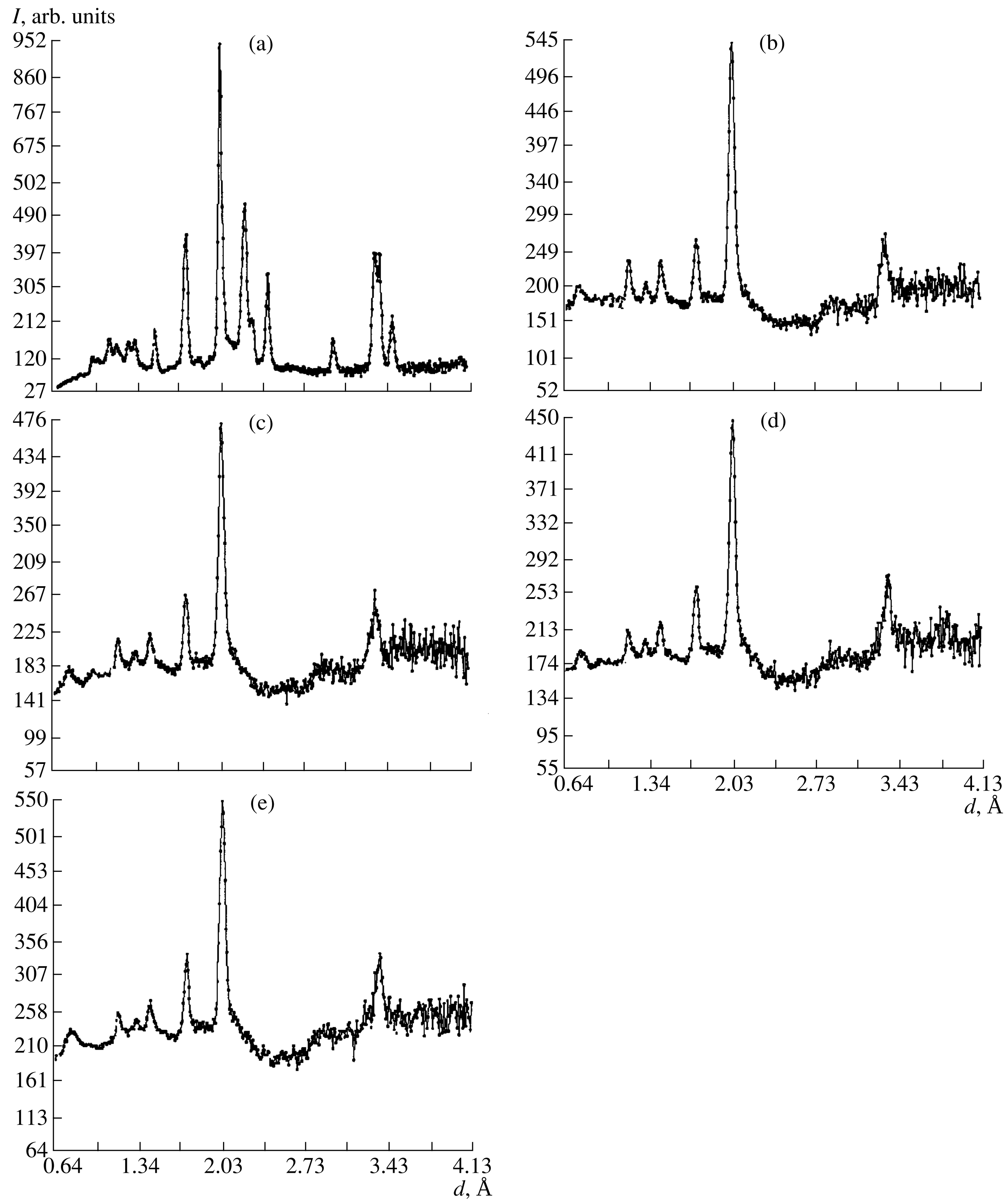

Fig. 2. Neutron diffraction patterns of materials with the compositions (a) Cu_2Se at 300 K and $Li_{0.25}Cu_{1.75}Se$ at (b) 300, (c) 473, (d) 523, and (e) 573 K.

cubic $Cu_{1.75}Se$ phase. The ionic conductivity of $Cu_{1.75}Se$ at the same temperature is $0.45 \pm 0.05\ \Omega^{-1}\ cm^{-1}$.

At 473 K, the $Li_{0.25}Cu_{1.75}Se$ crystal is monoclinic. However, it should be indicated that the lattice parameters at this temperature are slightly different from those at 300 K. The ionic conductivity of this modification is $0.084\ \Omega^{-1}\ cm^{-1}$ at 493 K. At 523 and 573 K, the neutron diffraction pattern of this phase can be indexed in the orthorhombic system (see table). The ionic conductivity of the orthorhombic $Li_{0.25}Cu_{1.75}Se$ phase increases to $0.95\ \Omega^{-1}\ cm^{-1}$ at 623 K.

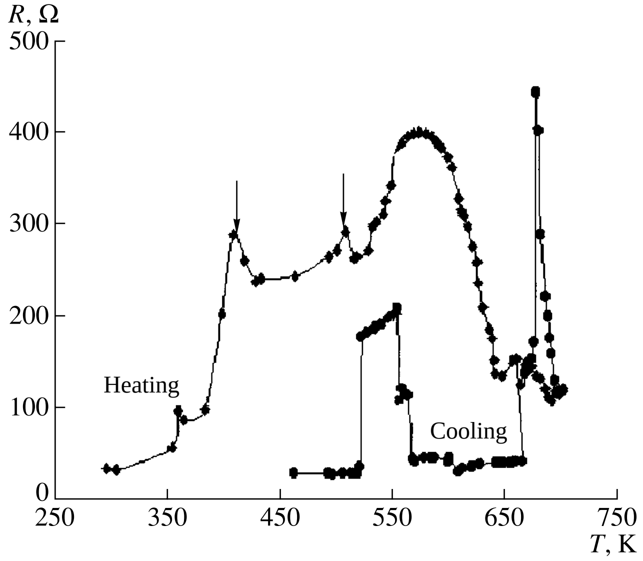

Fig. 3. Temperature dependence of electrical resistivity of an $Li_{0.25}Cu_{1.75}Se$ sample.

With an increase in temperature, gradual disordering in the cation sublattice leads to considerable changes in crystal symmetry—from triclinic to monoclinic and then to orthorhombic—which manifests itself in a change in the electrophysical properties: a gradual increase in the contribution of ionic conductivity to the total conductivity of the material. It is clear from Fig. 3 that the electron conductivity decreases with an increase in temperature.

It should be emphasized that, in contrast to binary copper selenide, no cubic phase was in this case observed in the temperature range studied. It is quite probable that a cubic phase would form at higher temperatures, where some anomalies are observed in the behavior of electrical resistivity in the vicinity of 673 K (see Fig. 3). These anomalies could be explained by the rearrangement of the crystal lattice. In this context, further studies of ionic and electronic characteristics in the vicinity of phase transitions are needed, as well as the refinement of the crystal structures of these phases.

CONCLUSIONS

With an increase in temperature, gradual disordering in the cation sublattice leads to a change in crystal symmetry from triclinic to monoclinic and then to orthorhombic, which is reflected in changes in the electrophysical characteristics—a gradual increase in the ionic contribution to the total conductivity [1]. Structural studies of these phases are now in progress.

ACKNOWLEDGMENTS

This study was supported by the Russian Foundation for Basic Research, project no. 01-02-96017, and the Ministry of Industry, Science, and Technologies of the Russian Federation (grant for the support of unique facilities of Russia).

REFERENCES

1. M. Kh. Balapanov, A. F. Nadejdina, and R. A. Yakshibayev, Ionics **5**, 20 (1999).
2. I. J. Iokota, J. Phys. Soc. Jpn. **16**, 2213 (1961).
3. T. Ohtani, J. Alloys Compd. **279**, 136 (1998).

Translated by K. Kugel

Crystallography Reports, Vol. 48, No. 3, 2003, pp. 461–465. Translated from Kristallografiya, Vol. 48, No. 3, 2003, pp. 506–510.
Original Russian Text Copyright © 2003 by Raevskiĭ, Emel'yanov, Savenko, Zakharchenko, Bunina, Malitskaya, Bogatin, Sakhkar.

Growth and Study of Single Crystals of Solid Solutions of Ferroelectric–Relaxors $(1-x)\mathrm{PbMg_{1/3}Nb_{2/3}O_3}$–$(x)\mathrm{PbSc_{1/2}Nb_{1/2}O_3}$ with Different Degrees of Compositional Order[1]

**I. P. Raevskiĭ, S. M. Emel'yanov, F. I. Savenko, I. N. Zakharchenko, O. A. Bunina,
M. A. Malitskaya, A. S. Bogatin, and E. V. Sakhkar**
Institute of Physics, Rostov State University, pr. Stachki 194, Rostov-on-Don, 344090 Russia
e-mail: rip@ip.rsu.ru

Received November 18, 2002

Abstract—Single crystals of $(1-x)\mathrm{PbMg_{1/3}Nb_{2/3}O_3}$–$(x)\mathrm{PbSc_{1/2}Nb_{1/2}O_3}$ (PMN–PSN) solid solutions are grown from flux. The X-ray diffraction patterns of the crystals with $0.1 \le x \le 0.65$ show superstructural reflections associated with ordering of cations in the *B* sublattice. The changes in the dielectric properties and the degree of phase-transition diffusion with an increase in PSN content qualitatively agree with the model of stoichiometric 1 : 1 random-site ordering of *B* cations in ternary $\mathrm{Pb}(B^{2+}_{1/3}B^{5+}_{2/3})\mathrm{O_3}$ oxides and the monotonic dependence of the temperature of the order–disorder phase transition on *x* in the PMN–PSN system. © *2003 MAIK "Nauka/Interperiodica".*

INTRODUCTION

One of the most important achievements in the physics of ferroelectrics in the last decade is the discovery of the enormous piezoelectric sensitivity of single crystals of solid solutions based on $\mathrm{Pb}B'_nB''_m\mathrm{O_3}$ ferroelectrics–relaxors with a perovskite structure [1, 2].

The much better piezoelectric properties of these crystals in comparison with the properties of ceramics are explained by the fact that in crystals electric fields can be applied along specific crystallographic directions [1, 2]. In this connection, it is timely to improve the methods of growing single crystals of the solid solutions of relaxors and study the dependence of their properties on growth conditions.

In addition to ferroelectric phase transitions, ternary oxides of the perovskite family $\mathrm{Pb}B'_nB''_m\mathrm{O_3}$ also undergo order–disorder phase transitions at high temperatures ($T_t \sim$ 900–1500°C) [3–6]. Above T_t, the *B*' and *B*'' cations are distributed over sites located inside octahedra quite randomly, whereas below this temperature, the ordered state is equilibrium (compositional order). Since a change in the degree *s* of the long-range order proceeds via diffusion, fast cooling of the sample after sintering can "freeze" the high-temperature state. As a result, the properties of compositionally ordered oxides are strongly dependent on the conditions of their synthesis and, first of all, on the ratio of T_t and the temperatures of ceramic sintering or crystal growth.

The influence of compositional ordering on the properties of ternary oxides with a 1 : 1-type perovskite structure are studied in detail for the oxides described by the general formula $\mathrm{Pb}(B^{3+}_{1/2}B^{5+}_{1/2})\mathrm{O_3}$ (B^{3+} = Sc, In, Yb, Lu, Tm, Er; B^{5+} = Nb, Ta) [3–7]. The phase transitions in these oxides are rather sharp at $s \sim 1$ and diffuse at $s \sim 0$. Ternary oxides with a perovskite structure of type 1 : 2 described by the general formula $A^{2+}(B^{2+}_{1/3}B^{5+}_{2/3})\mathrm{O_3}$ (A^{2+} = Pb, Ba, Sr, Ca, B^{2+} = Mg, Zn, and B^{5+} = Nb, Ta), several variants of ordering of *B* cations are observed. An ordering of type 1 : 2 is observed only in lead-free oxides [8–11]. In Pb-containing ternary oxides the so-called stoichiometric 1 : 1 random-site ordering occurs in accordance with the formula $\mathrm{Pb}(B'_{1/2}B''_{1/2})\mathrm{O_3}$, where the *B*'' positions are filled with $\mathrm{Nb^{5+}}$ and the *B*' positions are randomly occupied by the B^{2+} and B^{5+} cations in the ratio 2 : 1. In the classical relaxor $\mathrm{PbMg_{1/3}Nb_{2/3}O_3}$ (PMN), the size of ordered regions does not exceed several nanometers, which is explained by the low value of T_t ($T_t \sim$ 900–950°C) [10, 11]. Ordering at such low temperatures is limited by the low diffusion coefficient of cations. According to [11], the addition of some cations, e.g., $\mathrm{Sc^{3+}}$, increases the temperature T_t in PMN and, thus, considerably facilitates the ordering process. In particular, it was reported that the long thermal treatment of ceramics of $(1-x)\mathrm{PbMg_{1/3}Nb_{2/3}O_3}$–$(x)\mathrm{PbSc_{1/2}Nb_{1/2}O_3}$ solid solu-

---

[1] This work was submitted to the International Meeting "Order, Disorder, and Properties of Oxides," Sochi, Russia, 2002.

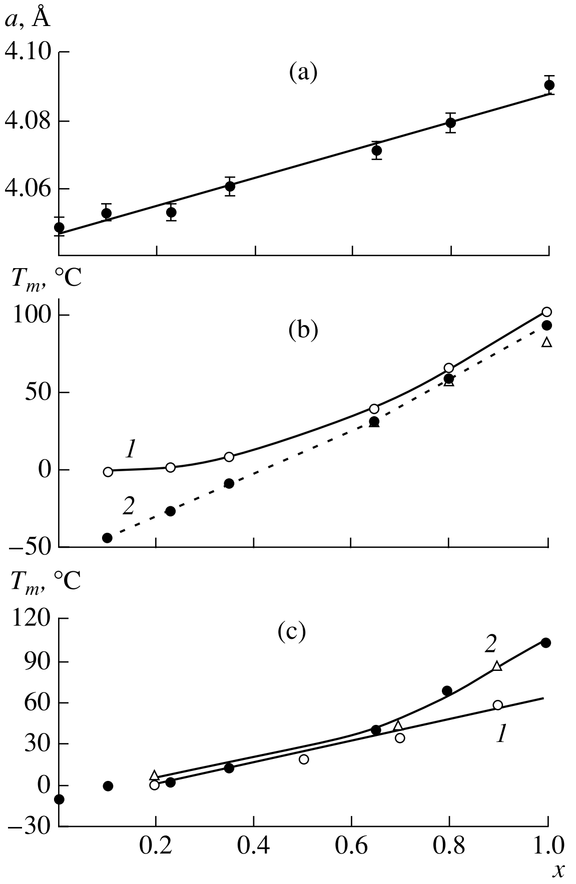

Fig. 1. (a) Lattice parameter *a* of a pseudocubic (1 – *x*)PMN–(*x*)PSN crystal, (b) (*1*) temperature T_m measured at a frequency of 1 kHz (filled circles) and (*2*) the Vogel–Fulcher temperature T_0 (empty circles) for (1 – *x*)PMN–(*x*)PSN crystals (empty circles) as functions of the concentration parameter *x*, and (c) the same curves for (*1*) ordered and (*2*) disordered ceramics determined from data [11].

tions (PMN–PSN) provided the formation of compositionally ordered regions as large as 200 nm [11].

We undertook this study to grow single crystals of PMN–PSN solid solutions, measure their dielectric properties, and verify the validity of the known dependence of *s* on the crystallization conditions established earlier for Pb$B^{3+}_{0.5}B^{5+}_{0.5}$O$_3$-type oxides with a perovskite structure [5, 12].

EXPERIMENTAL

Crystals of continuous series of solid solutions were grown from flux with the use of a lead borate solvent in the temperature range of crystallization 1150–980°C with a cooling rate of the melt of 10 K/h at $T > 1100$°C and 1 K/h in the temperature range 1100–980°C. The yellow transparent crystals grown had an isometric shape faceted by (100) planes of a perovskite basis and an edge length of up to 6 mm. The crystal composition was determined on a Camebax-Micro microanalyzer with an error not exceeding 2%. The standards were PMN and PSN single crystals.

X-ray diffraction studies of powders obtained by grinding the grown crystals were performed on a DRON-3 diffractometer (Co$_{K\alpha}$ radiation).

Dielectric properties were measured on $1 \times 2 \times 4$ mm^3 samples cut out parallel to the natural (100) faces in the frequency range 10^{-2}–10^4 Hz by a method described elsewhere [13]. The aluminum electrodes were deposited onto the samples in vacuum.

EXPERIMENTAL RESULTS

X-ray diffraction analysis of powders obtained by grinding the grown crystals showed a practically linear dependence of the lattice parameter of the pseudocubic perovskite unit cell on *x*, which indicated the formation of a continuous series of solid solutions (Fig. 1a). The powder diffraction patterns from the powders with $0.1 \le x \le 0.65$ showed superstructural lines in the vicinity of the angles $2\theta \approx 22°$ which corresponded to a doubling of the initial perovskite unit cell (Fig. 2). Earlier, it was established in the PMN–PSN ceramic that this superstructural line is associated with the ordering of *B* cations [11]. In all the crystals mentioned above, the dimensions of the ordered regions (determined from broadening the superstructural reflection in comparison with the main line according to the Schemer formula) were approximately the same (~50 nm).

Figure 3a shows the ε(*T*) curves of the (1 – *x*) PMN–(*x*)PSN crystals with different PSN content measured at several frequencies in the range 10^{-2}–10^4 Hz. Although the dimension of the ordered regions was rather large (~50 nm), the dielectric behavior of the crystals with the composition $x < 0.65$ was similar to the behavior of relaxors: the shape of the dependence ε(*T*) and its change with the frequency *f* were analogous to those observed for the classic PMN relaxor. The dependence of the temperature T_m of the dielectric-constant maximum ε is described by the Vogel–Fulcher law (Fig. 3b):

$$f = f_0 \exp[-E_0/k(T_m - T_0)],$$

where f_0 is the frequency of the attempts to overcome the potential barrier E_0, *k* is the Boltzmann constant, T_0 is the Vogel–Fulcher temperature usually interpreted as the temperature of static freezing of electric dipoles or the transition into the dipole-glass state [14]. For PMN–PSN crystals, $f_0 = (0.1–1) \times 10^{11}$ Hz, which is close to the values known for other ferroelectric–relaxors [14]. With an increase in *x*, the T_m values monotonically increase and the difference between T_m (at the frequency 1 kHz) and T_0 decreases (Fig. 1b), whereas the diffusion of the ε(*T*) maximum in the region $x \approx 0.65$ becomes minimal (Fig. 4). At $x > 0.65$, the T_m values of the crystals almost coincide with T_m of the disordered ceramic samples [11] (Fig. 1c).

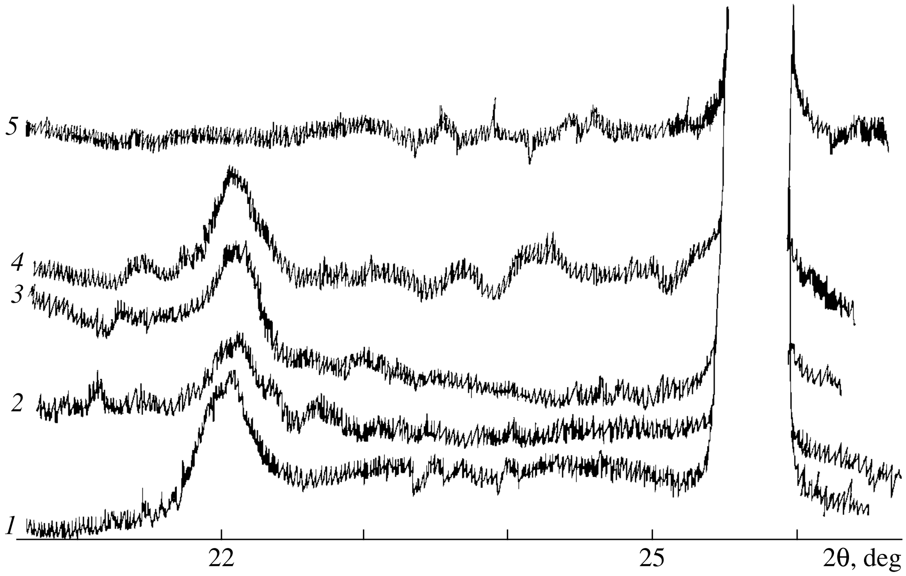

Fig. 2. Fragments of the X-ray diffraction patterns from the powders obtained by grinding (1 – *x*)PMN–(*x*)PSN crystals showing the existence of a superstructure due to ordering; *x*: (*1*) 0.10, (*2*) 0.23, (*3*) 0.35, (*4*) 0.65, (*5*) 0.80.

The ε(T) curves of crystals with $x \geq 0.65$ have a step at a temperature slightly lower than T_m; the step temperature T_s, unlike T_m, is almost independent of *f* (Fig. 3a). For crystals with $0.65 \leq x \leq 0.80$, the T_s temperatures are close to T_0, whereas for PSN crystals, the T_s temperatures are considerably lower than T_0 (Fig. 1b).

DISCUSSION

Earlier, we established that 1 : 1-type perovskite crystals described by the formula Pb$B^{3+}_{0.5}B^{5+}_{0.5}$O$_3$, in particular, PSN crystals, grow in a disordered way (even at temperatures lower than T_t, where the disordered state is nonequilibrium), and only later does the degree of order *s* vary because of diffusion and tends to the value s_e equilibrium at the crystallization temperature [5–7, 12]. Thus, for the given crystal, the *s* value depends on the t/τ ratio, where *t* is the crystallization time and τ is the time necessary for diffusion to attain the equilibrium value s_e at the crystallization temperature T_{cr}. In turn, τ depends on T_{cr}, while s_e depends on the ratio T_{cr}/T_t. According to the experimental data [10, 11], the dependence $T_t(x)$ in the PMN–PSN system is of a parabolic character with the coordinates of the maximum being $x \approx 0.5$ and $T \approx 1370$°C. With due regard for the parabolic shape of the $T_t(x)$ dependence, the results of X-ray diffraction and dielectric measurements of the PMN–PSN crystals qualitatively agree with the above speculation. Thus, the superstructural reflections associated with ordering are not observed in PMN, where T_t is lower than the lower boundary of the crystallization range, but superstructural reflections appear for crystals

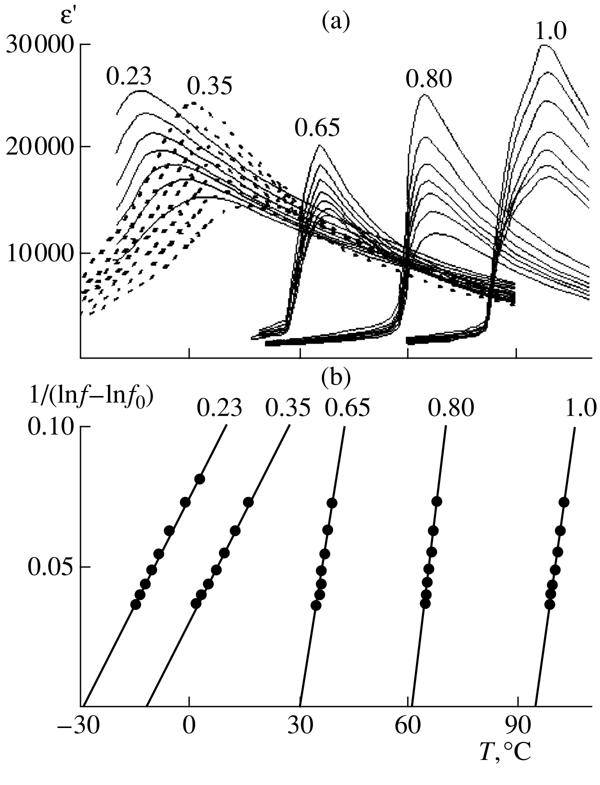

Fig. 3. (a) ε(T) curves measured at the frequencies 10^{-2}, 10^{-1}, 10, 10^2, 10^3, and 10^4 Hz and (b) $(\ln f_0 – \ln f)^{-1}$ measured as functions of T_m for the (1 – *x*)PMN–(*x*)PSN crystals, which confirm the validity of the Vogel–Fulcher law. Figures at the curves indicate *x* values. For each composition, the upper and lower curves correspond to the minimum and maximum frequencies, respectively.

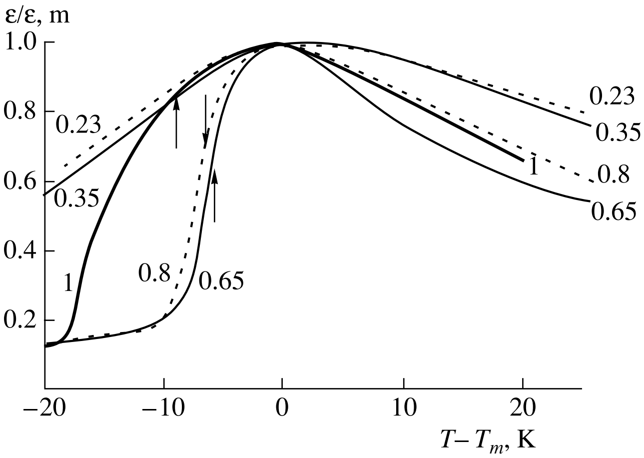

Fig. 4. Dielectric constant measured at a frequency of 1 kHz and normalized to the maximum ε_m as a function of the relative temperature $T - T_m$, where T_m is the temperature of the maximum of the $\varepsilon(T)$ curve for $(1 - x)$PMN–(x)PSN crystals. Figures at the curves indicate x values. Arrows indicate T_0 values for crystals with $x = 0.65$, 0.8, and 1.0.

with $x > 0.1$, where T_t is higher than this boundary. The absence of noticeable superstructural reflections for crystals with the composition $x \geq 0.8$ seems to be explained, on the one hand, by a lower degree of order, and, on the other, by the fact that the intensity of these reflections in PSN is very low even for ordered samples (because of the close scattering factors of Sc^{3+} and Nb^{5+} cations [3]). Another factor affecting s is the ordering rate in the temperature range of crystallization. Earlier, it was established that the ordering rate for crystals of the PSN–$PbSc_{1/2}Ta_{1/2}O_3$ (PST) solid solutions with compositions close to PST is much higher than for the solid solutions with high PSN content [15]. It seems that the analogous dependences would also be characteristic of the $(1 - x)$PMN–(x)PSN system, where crystals with a high PSN content ($x > 0.65$) have high T_m values corresponding to a low degree of order (Fig. 1c).

In crystals with $x = 0.65$ and $x = 0.8$, where the temperature of the step on $\varepsilon(T)$ is close to T_0, this step seems to be associated with the spontaneous phase transition from the relaxor to the normal ferroelectric state. This transition was earlier observed in the PSN ceramic [14] and PSN crystals [16]. At the same time, the step on $\varepsilon(T)$ for PSN crystals, whose temperature T_s is considerably lower than T_0 (Figs. 1b, 4) but is close to T_m of PSN crystals with $s \sim 1$ [3–7], seems to be explained by the presence of macroscopic regions with a high s value in the sample. Indeed, because of the low ordering rate in PSN, one can expect a considerable difference in s values for the internal and external layers of the crystals grown within different periods of time. Such macroscopic inhomogeneities in s and the existence of two temperature anomalies on $\varepsilon(T)$ caused by these inhomogeneities, whose temperatures correspond to the phase transitions in the regions with high and low s values, were observed in our earlier studies of PSN crystals grown in a wide temperature range [12]. This explanation is consistent with the step observed on the $\varepsilon(T)$ dependence of PSN crystals and also with the kink observed below T_m, whose temperature is close to T_0 and which seems to be associated with a spontaneous phase transition from the relaxor to the normal ferroelectric state in the crystal regions with low s values (Fig. 4).

Following [10, 11], we can explain the relaxor behavior of ordered crystals and ceramics in the PMN–PSN system under the assumption that the main part in the frustration of ferroelectric interaction in Pb-containing 1 : 2 perovskites is played not by the dimensions of the compositionally ordered regions (as is the case of PSN and other 1 : 1 perovskites) but by random fields induced by disorder in the B' sublattice containing several types of cations.

CONCLUSION

Thus, for the first time, single crystals of $(1 - x)$ PMN–(x)PSN solid solutions were grown. Taking into account the nonmonotonic dependence of the temperature of the order–disorder phase transition on x in the PMN–PSN system [11], the superstructural reflections on the X-ray diffraction patterns from the crystals with $0.1 < x < 0.65$ (whose formation is associated with ordering of cations in the B sublattice) and the minimum diffusion of the dielectric-constant maximum observed for a crystal with $x \approx 0.65$ allow us to state that the characteristics of the dependence of the degree order x on the crystallization conditions in the PMN–PSN system [11] established earlier for 1 : 1-type oxides with a perovskite structure [12] are also valid for solid solutions of 1 : 2-type ternary oxides with a perovskite structure.

The dielectric behavior of the relaxor type for the crystals with $x < 0.6$ containing rather large ordered regions (~50 nm) qualitatively agree with the model of the stoichiometric random-site 1 : 1 ordering of B cations in ternary $Pb(B^{2+}_{1/3}B^{5+}_{2/3})O_3$ oxides.

ACKNOWLEDGMENTS

This study was supported by the Russian Foundation for Basic Research, project no. 01-03-33119, and the Ministry for Higher Education of the Russian Federation, project no. E00-3.4-287.

REFERENCES

1. S. Park and T. R. Shrout, J. Appl. Phys. **82**, 1804 (1997).
2. H. Fu and R. Cohen, Nature **403**, 281 (2000).
3. C. G. F. Stenger and A. J. Burggraaf, Phys. Status Solidi A **61**, 275 (1980).
4. N. Setter and L. E. Cross, J. Appl. Phys. **51**, 4356 (1980).

5. A. A. Bokov and I. P. Rayevsky, Ferroelectrics **90**, 125 (1989).
6. A. A. Bokov and I. P. Rayevsky, Ferroelectrics **144**, 147 (1993).
7. I. P. Raevski, V. Y. Shonov, M. A. Malitskaya, *et al.*, Ferroelectrics **235**, 205 (1999).
8. Y. Yan, S. J. Pennycook, Z. Xu, and D. Viehland, Appl. Phys. Lett. **72**, 3145 (1998).
9. B. Burton, Phys. Rev. B **59**, 6087 (1999).
10. P. K. Davies and M. A. Akbas, J. Phys. Chem. Solids **61**, 197 (2000).
11. P. K. Davies, L. Farber, M. Valant, and M. A. Akbas, AIP Conf. Proc. **535**, 38 (2000).
12. A. A. Bokov, I. P. Raevskiĭ, V. G. Smotrakov, and S. M. Zaĭtsev, Kristallografiya **32** (6), 1301 (1987) [Sov. Phys. Crystallogr. **32**, 769 (1987)].
13. S. B. Vakhrushev, E. V. Kolla, E. Yu. Koroleva, and R. F. Suramanov, Preprint No. 1505, FTI AN SSSR (Physicotechnical Inst., USSR Academy of Sciences, Leningrad, 1991).
14. F. Chu, I. M. Reaney, and N. Setter, Ferroelectrics **151**, 343 (1994).
15. I. P. Raevski, M. A. Malitskaya, E. S. Gagarina, *et al.*, Ferroelectrics **235**, 221 (1999).
16. I. P. Raevskiĭ, V. V. Eremkin, V. G. Smotrakov, *et al.*, Fiz. Tverd. Tela (St. Petersburg) **42** (1), 154 (2000) [Phys. Solid State **42**, 161 (2000)].

Translated by L. Man

Crystallography Reports, Vol. 48, No. 3, 2003, pp. 466–468. Translated from Kristallografiya, Vol. 48, No. 3, 2003, pp. 511–513.

LATTICE DYNAMICS AND PHASE TRANSITIONS

Characteristic Features of Structure Formation of Nickel Monoaluminide Formed in a Gasless Combustion Wave[1]

A. S. Rogachev*, B. P. Tolochko, N. Z. Lyakhov**, M. P. Sharafutdinov**, N. A. Popkov***, B. Ya. Pirogov**, and E. B. Pis'menskaya***

** Institute of Structural Macrokinetics and Materials Science, Russian Academy of Sciences, Chernogolovka, Moscow oblast, 142432 Russia*

e-mail: rogachev@ism.as.ru

*** Institute of Solid State Chemistry and Mechanical Chemistry, Siberian Division, Russian Academy of Sciences, ul. S. Kutateladze 18, Novosibirsk, 630128 Russia*

**** Institute of Nuclear Physics, Siberian Division, Russian Academy of Sciences, pr. Akademika Lavrent'eva 11, Novosibirsk, 630090 Russia*

Received December 3, 2002

Abstract—The dynamics of structural transformations in the gasless combustion wave is studied. It is shown that crystalline NiAl starts forming behind the wave front at the first milliseconds of the process. The attained time resolution on the order of 5 ms provides an opportunity to extract fundamentally new data on the phase and structural tranformations in the course of a fast high-temperature reaction. *© 2003 MAIK "Nauka/Interperiodica".*

INTRODUCTION

Combustion in a gasless medium is well known as a kind of self-propagating high-temperature synthesis widely used for producing refractory compounds and materials [1]. At the wave front of the gasless combustion, the temperature steeply increases because of the heat release during the chemical reaction. In many instances, this leads to complete or partial melting of the reagents and reaction products. At the same time, the gasification of the main components can be ignored. Thus, all the initial reagents, as well as the intermediate and final products, remain in the condensed (solid or liquid) state, which allows one to perform *in situ* X-ray phase analysis directly in the course of the combustion process and, thus, to study the dynamics of the structural and phase transformations. Intermetallic systems such as Ni–Al are very interesting, although rather complicated, objects for these studies because of the large variety of phases, both ordered and disordered, that can form during synthesis of the final product. Also, nickel aluminides arouse widespread interest owing to their physical, chemical, and mechanical characteristics, ensuring their application as refractory materials, protective coatings, and other products of practical importance.

Nickel monoaluminide is the most refractory phase in the nickel–aluminum system (melting point 1911 K). Therefore, it is natural to expect that this phase would be the first to crystallize from melt in the process of the gasless combustion of the Ni + Al mixture. However, the first experiments involving synchrotron-radiation-based dynamic X-ray analysis of the phase composition directly in the course of combustion revealed a number of structural transformations behind the combustion front [2]. It was assumed that the formation of the final NiAl (*B*2) phase is preceded by the nucleation of two unknown intermediate phases. A similar result but with four intermediate phases was reported in [3], where it was also assumed that some sharp short-lived peaks on the X-ray diffraction pattern could be interpreted as spot reflections formed from individual crystals of the reaction product. The linear detectors used in [2, 3] do not allow one to distinguish between the spot and ring reflections. The existence of intermediate phases was not confirmed in [4, 5], where it was stated that the phase formed behind the combustion front within about a second corresponded to the homogeneity range of NiAl, and its structure corresponded to the structure of the final *B*2 phase but with the interplanar spacings modified because of thermal expansion. In general, it is still unclear whether intermediate phases precede the formation of NiAl and whether there is enough time for the formation of an ordered crystalline phase in the combustion zone.

The aim of the present work was to use the maximum possible spatial and time resolution to follow the formation of the crystal structure inherent in the product of the Ni + Al reaction in the combustion wave.

---

[1] This work was presented at the Symposium "Phase Transitions in Solid Solutions and Alloys" (OMA), Sochi, Russia, 2002.

EXPERIMENTAL TECHNIQUE

To improve the spatial resolution, in spite of the usual geometry of irradiation of the side surface, the synchrotron radiation beam was directed to the end plane of a cylindrical sample. As a result, the region of pattern recording was oriented parallel to the combustion-front plane. For an ideally planar combustion front, the spatial resolution is determined by the penetration depth of the monochromatic synchrotron radiation incident onto the sample. For the system under study, the spatial resolution along the combustion direction was about 50–100 μm. The roughness of the combustion front resulting in nonsimultaneous arrival of different portions of the combustion front to the sample end was estimated using high-speed video recording (500 frames per second). It turned out that this roughness only slightly affects the spatial resolution.

The experiments were made using channel 5a of the VEPP-3 accelerator at the Institute of Nuclear Physics of the Siberian Division of the Russian Academy of Sciences in Novosibirsk. The attainment of a high time resolution was possible because of the use of a specialized source (wiggler) of synchrotron radiation and a focusing X-ray optical system with a high aperture ratio. This allowed us to obtain a photon flux as high as 10^{14} photons per second in the X-ray and gamma-ray ranges. A monochromator pyrolytic graphite ($\Delta\lambda/\lambda$ about 10^{-2}) provided the enhancement of the photon flux by one to two orders of magnitude as compared to conventional monochromators (Si, Ge, $\Delta\lambda/\lambda = 10^{-3}$–$10^{-4}$). The registration of photons was made with the aid of a DED-5 two-coordinate gas-filled detector. Thus, we manage to record the radiation within a considerably larger part of the diffraction cone in comparison with single-coordinate (linear) defectors. This became possible because integration over an arc results in an increase in the aperture for collected quanta. The sample-detector distance was equal to 30 cm. Estimates show that this distance corresponds to the optimum correspondence between the resolution power of the detector and the diffraction-pattern quality at the given degree of monochromatization. In fact, if $\Delta\lambda = \pm 0.01$ Å, the angular error $\Delta\theta$ is $\pm 0.3°$ ($\lambda = 1.54$ Å). At a sample-detector distance equal to 30 cm, this corresponds to a line broadening of about 1.5 mm, that is, the size of one pixel of the detector. The above improvements allowed us to reduce the measurement time for each X-ray diffraction pattern to 5 ms, i.e., to make measurements at a rate of 200 diffraction patterns per second.

RESULTS AND DISCUSSION

The time dependence of the main diffraction peaks obtained by processing two-dimensional diffraction patterns is illustrated in Fig. 1. During the first 20 ms (the front has not yet reached to the sample edge but is rather close to the recording zone), we observe the displacement of the reflections of nickel and aluminum toward lower angles. This indicates that particles of the initial components are rapidly heated. Simultaneously, the intensity of the nickel reflections decreases by 14%, which can be explained by the Debye–Waller effect. It is interesting that the intensity of the aluminum peaks does not decrease despite its lower melting point. During the following 25 ms, the aluminum reflections loose their intensity and, finally, completely vanish. During the same time, the intensity of the nickel reflections decreases by 40%. Instead, the reflections of the reaction product (NiAl) appear and reach up to 50% of their final intensity. The background intensity also dramatically increases, thus indicating the formation of a large amount of melt. It seems that at this stage solid nickel particles are dissolved in aluminum with the simultaneous precipitation of crystalline NiAl grains from the melt. Later on (45–70 ms), the nickel reflections completely disappear as well, whereas the intensity of the nickel monoaluminide reflections continues increasing. The change in the intensity of nickel reflections attains 46% of their initial intensity. The intensity of the diffuse background also continues increasing. It is possible to assume that at this stage the most intense reaction takes place. Because of the thermal inhomogeneity of the medium at the microscopic level, some nickel particles remain solid, while some others melt. Therefore, the mechanism corresponding to the dissolution of solid nickel in the melt is accompanied by the reaction-induced coalescence, i.e., the merging of melted Ni and Al and their simultaneous reaction. At the final stage of the process (70–70 000 ms), an increase in the intensity of reflections of the final product decelerates and eventually stops because the melt as a whole is transformed into the final crystalline product.

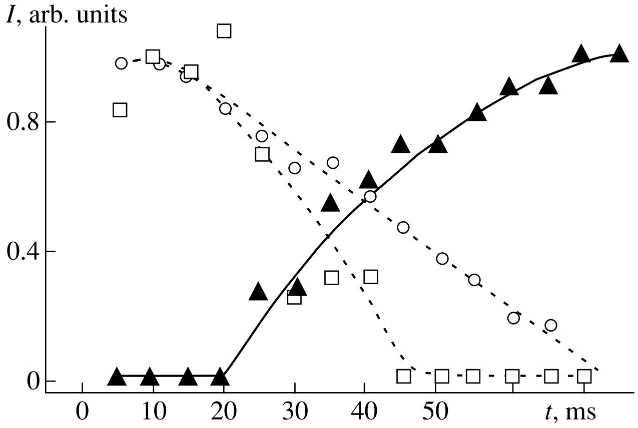

Fig. 1. The time dependence of the phase composition in the gasless combustion wave propagating in the Ni + Al mixture; □, (111) Al; ○, (111) Ni; ▲, (110) NiAl.

Several selected Debye patterns obtained at different stages of the process are shown in Fig. 2. It is seen that the Debye rings of the product consist of individual reflections (spots). In fact, the two-dimensional diffraction pattern of the reaction product is the superposition

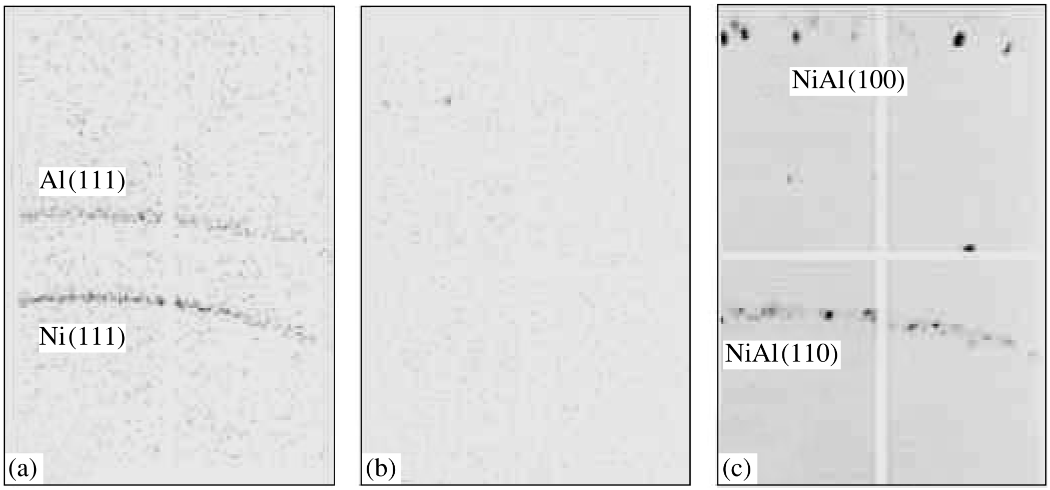

Fig. 2. Selected dynamic X-ray diffraction patterns of the Ni + Al sample: (a) the initial mixture ahead of the combustion front, (b) reaction zone, (c) reaction product.

of a large number of single-crystal patterns of individual crystallites. The number of these crystallites is less than for a typical Debye pattern, but it is still large enough to determine the angles corresponding to the diffraction peaks of the reaction product as a whole (i.e., without the analysis of the Laue diffraction patterns for each individual crystallite) and to calculate the interplanar spacing. The intensities of the spot reflections behind the combustion front gradually increase together with the area of each individual reflection. The data on the change in intensity indicate a rapid increase in the size of crystalline grains (because of crystallization and recrystallization). In addition, small displacements of the individual spot reflections are observed. Apparently, they are caused by the displacements and rotations of individual crystallites in the melt. This supports the assumption made in [3] that the formation and disappearance of sharp short-lived peaks in the X-ray spectra recorded by a linear detector may be associated with intense reflections from individual crystallites.

In our experiments, we managed to detect the (110)NiAl diffraction peak earlier than the (100)NiAl peak, which calls for additional study.

Thus, the results obtained demonstrate that the NiAl phase is formed in the combustion wave within the first milliseconds after the onset of the reaction. The ordering of this phase can proceed behind the combustion wave front. The changes in the X-ray diffraction patterns observed after the passage of the front can be explained by processes of recrystallization, an increase in grain size, and ordering in nickel monoaluminide.

ACKNOWLEDGMENTS

This study was supported by the Russian Foundation for Basic Research, project no. 01-03-33017.

REFERENCES

1. A. G. Merzhanov and I. P. Borovinskaya, Dokl. Akad. Nauk SSSR **204** (2), 366 (1972).
2. V. V. Boldyrev, V. V. Aleksandrov, M. A. Korchagin, *et al.*, Dokl. Akad. Nauk SSSR **259**, 722 (1981).
3. J. Wong, E. M. Larson, and J. B. Holt, Science **249**, 1406 (1990).
4. A. S. Rogachev, I. O. Khomenko, A. Varma, *et al.*, Int. J. Self-Propag. High-Temp. Synth. **3** (3), 239 (1994).
5. A. S. Rogachev, A. Varma, and A. G. Merzhanov, Int. J. Self-Propag. High-Temp. Synth. **2** (1), 25 (1993).

Translated by K. Kugel

Crystallography Reports, Vol. 48, No. 3, 2003, pp. 469–472. Translated from Kristallografiya, Vol. 48, No. 3, 2003, pp. 514–517.
Original Russian Text Copyright © 2003 by Akchurin, Galiulin.

PHYSICAL PROPERTIES OF CRYSTALS

Formation of the Nanocrystalline State by Twinning Crystals[1]

M. Sh. Akchurin and R. V. Galiulin
Shubnikov Institute of Crystallography, Russian Academy of Sciences,
Leninskiĭ pr. 59, Moscow, 119333 Russia
e-mail: galiulin@ns.crys.ras.ru

Received December 3, 2002

Abstract—The formation of the nanocrystalline state under the action of a concentrated load applied to crystals is studied. It is established that the relaxation of the enormous stresses (on the order of the shear modulus) arising under the indenter proceeds through twinning, which results in the fragmentation of the structure into nanoblocks. The properties of the nanocrystalline material thus obtained are explained based on the consideration of grain boundaries as twin boundaries that represent another phase of the material. *© 2003 MAIK “Nauka/Interperiodica”.*

The difference between the properties of nanocrystalline materials and those of the the corresponding single crystals and polycrystals is usually explained by the formation of the specific state of the interfaces, i.e., the high density of defects up to the formation of amorphous layers and agglomerates of vacancies (nanopores) [1–6]. Below, we interpret the unusual properties of nanocrystalline materials (e.g., of such fundamental parameters as the Curie and Debye temperatures, elastic constant, strength, etc.) based on the concept of an ideal crystal. We present the results of our morphological and structural studies of indentations and scratches produced by a diamond indenter on the surfaces of cleavages of natural calcite ($CaCO_3$) single crystals and also review our earlier works on the deformation of single crystals of alkali metal halides and some oxides under the action of concentrated loads. The unusual properties of the nanocrystalline regions are explained based on the representation of grain boundaries as twin boundaries, which in fact consist of another phase of the same material.

EXPERIMENTAL AND DISCUSSION OF RESULTS

We selected $CaCO_3$ single crystals as objects for studying because, being deformed, they show a propensity to twinning [7]. We deformed the $(10\bar{1}1)$ cleavages of $CaCO_3$ crystals by a standard Vickers pyramid under loads ranging within 0.1–10.0 N in air at room temperature. X-ray phase analysis was performed on an AFV-202E powder diffractometer ($\lambda = CuK_\alpha$, Ni-filter). Since the diameter of the X-ray beam was 5 mm, we deformed the sample area with the dimensions 6×6 mm^2. Several hundreds of scratches were made on the cleavage surface of the crystal so close to one another that practically the whole surface was in contact with the indenter. The load applied to the indenter was selected in a way to prevent sample fracture (the absence of scratches was checked in a scanning electron microscope).

Figure 1 shows the X-ray diffraction patterns from the surface of the cleavage and the deformed region. The X-ray diffraction pattern from the cleavage has a strong peak due to scattering from the cleavage plane and a peak formed due to the β component of the radiation. The diffraction pattern from the deformed region (scratch) has a large number of additional reflections, which correspond to the formation of at least one new phase. Table 1 lists the interplanar spacings d and the intensities I of these reflections. Although the peaks marked with asterisks were weak and rather diffuse, they were reliably recorded for all the samples studied and were attributed to a nanophase. The estimate of the grain size D from the half-width of the peaks and the formula $D = K\delta/H$ [8] (H is the microhardness and δ is the specific surface energy) showed that it ranges within 10–20 nm. We could not identify the X-ray diffraction pattern with any of the known $CaCO_3$ modifications [9].

According to [7, 10, 11], the indentation and scratching of the $CaCO_3$ cleavage give rise to deformation proceeding through twinning—one observes mechanical twinning along an obtuse rhombohedron. Twinning of calcite can proceed by three systems: $(\bar{1}012)\,[10\bar{1}1]$, $(1\bar{1}02)\,[\bar{1}101]$, and $(01\bar{1}2)\,[0\bar{1}11]$. Simultaneous twinning by several systems of planes results in the intersection of the twinned interlayers, which can also result in the formation of a new phase. Therefore, it is possible to assume that the additional reflections observed on diffraction patterns correspond

---

[1] This study was presented at the international symposium “Phase Transformations in Solid Solutions and Alloys,” Sochi, Russia, 2002.

1063-7745/03/4803-0469$24.00 © 2003 MAIK “Nauka/Interperiodica”

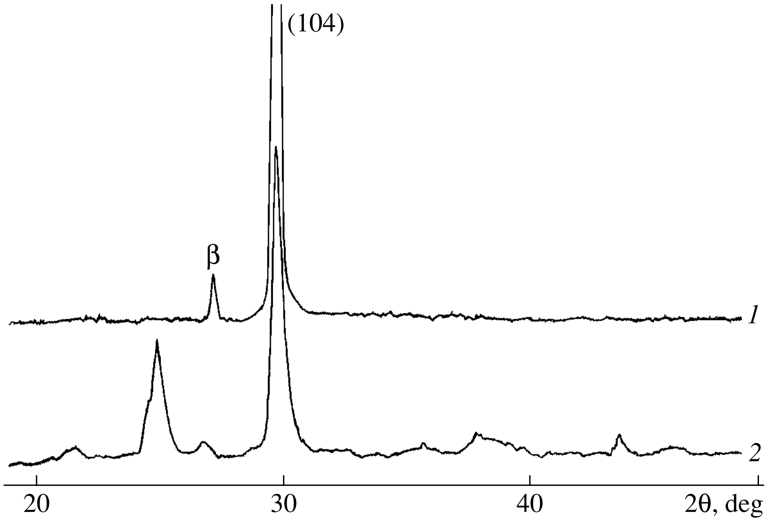

Fig. 1. X-ray diffraction peaks from the cleavage plane of a calcite single crystal (*1*) before and (*2*) after its deformation. CuK_α radiation.

to the location of atoms in a twin boundary of a mechanical twin and at the sites of intersection of twinned interlayers formed by different systems.

Thus, twinning in a $CaCO_3$ crystal under the action of a concentrated load can be considered as fragmentation of the single crystal into nanoblocks whose boundaries are the twin boundaries consisting of a new modification of the material.

Previous studies of the formation of the nanocrystalline state in single crystals of alkali metal halides and some oxides under the action of a concentrated load showed that the relaxation of enormous stresses (on the order of the shear modulus) under the indenter (where the crystal becomes unstable) results in structural rearrangement with the formation of the nanocrystalline state [12]. Directly under the indenter, a nanocrystalline region is formed whose volume depends on the load and corresponds to the volume of a hemisphere with a diameter equal to the diagonal of the indentation or to the scratch width. The properties of these regions differ from the properties of the undeformed matrix—these regions are characterized by an elevated (almost by a factor of 2) hardness and intensity of exciton luminescence. They also have a specific chemical composition. Thus, ionic crystals with nanocrystalline regions show a noticeable deficit in cations, and, the harder the crystal, the more pronounced its nonstoichiometry. Table 2 lists the ratios of the number of cations *K* to the number of anions *A* in the nanocrystalline regions of indentations (the corresponding ratios in undeformed regions (cleavage) are equal to unity). Table 2 also gives microhardness *H* and average dimensions *D* of the grains under the indenter.

The size of the grains formed is characteristic of each crystal and is practically independent of the load applied to the indenter: the harder the material, the smaller the grains; i.e., hardness is determined by the "work of dispersion" [8]. Along with the formation of the nanocrystalline state under stresses exceeding a certain critical value for each crystal, we also observed amorphization of the material directly under the indenter, whereas the nanocrystalline region was located under the amorphous layer [12].

Recently, we obtained atomic force microscopy data which show that, unlike indentations, the grains in this scratch are elongated and form ribbon–columnar structures. Thus, the scratches on MgO crystals form cylindrical structures with a diameter of ~20 nm elongated in the ⟨100⟩ directions (Fig. 2). The formation of the nanocrystalline state during deformation of crystalline

Table 1. Interplanar spacings and intensities of the X-ray diffraction peaks from a new $CaCO_3$ phase

Plane	1	2	3	4	5	6	7	8
d, Å	4.16*	4.01*	3.657	3.601	3.361	3.140	2.786*	2.536*
I, %	5	2	20	35	2	2	2	1

Plane	9	10	11	12	13	14	15	16	17
d, Å	2.400*	2.359*	2.313*	2.295*	2.088*	2.000*	1.796*	1.675*	1.624
I, %	5	4	4	3	3	2	1	2	1

objects by concentrated loads can be considered as the decomposition of the crystals into twinned interlayers in the fields of mechanical stresses.

Two crystalline individuals related by a mirror reflection plane form a twin. It should be noted that twins can be formed, with different probabilities, along any plane that is not a symmetry plane of the initial single crystal. The twin structures formed in the fields of mechanical stresses are more stable, because they are high-pressure phases, e.g., calcite $R\bar{3}c$, aragonite *Pcmn*, diamond *Fd*3*m*, lonsdaleite $P6_3/mmc$, pyrite *Pa*3, and marcasite *Pmnn*.

The results obtained and some other properties of nanocrystalline materials can be explained by representing the grain boundaries as twin boundaries.

The formation of a twinned phase after indentation of $CaCO_3$ crystals allows one to assume that similar twinned phases can also be formed in other crystals. Thus, we observed the formation of a new phase after indentation of fluorite [13] and explained its formation by twinning along the {111} planes.

Now, in the light of this consider indentation of a crystal with a sodium chloride structure [12]. The formation of nanocrystalline regions under the action of a concentrated load applied to the crystals of alkali metal halides can also be explained by mechanical twinning of the crystal under the indenter. It is most probable that, in crystals with an NaCl structure, twinning occurs along an octahedron as follows. In an NaCl structure, anions form cubic close packing, whereas cations occupy all its octahedral voids. During twinning along an octahedron, anions form a hexagonal close packing at the boundary, where the cation octahedra are located above one another, whereas in an ideal NaCl structure they are located above the tetrahedral voids, i.e.; the distances between the cations at the twin boundary are shorter. The approach of the cations can result in a change in stoichiometry—a decrease in the number of cations, which was really observed experimentally (Table 2). In this case, after a decrease in the number of sodium cations in twinned regions, the phase cannot be ideally crystalline; however, the general arrangement of the atoms in it is similar to their arrangement in the cubic crystal. Therefore, this twinned phase can hardly be detected by X-ray diffraction methods in the NaCl structure; moreover, the width of its region can be equal to two or three lattice parameters, i.e., can attain only several percent of the grain size. Microtwinning of crystals under the action of a concentrated load is also confirmed by the unimportant role of dislocation-induced plasticity in stress relaxation under the indenter [8, 14, 15].

Table 2. Stoichiometry, average grain size, and microhardness of the nanocrystalline regions

Crystal	MgO	LiF	NaCl	KCl
$(K/A)_{\text{def}}$	0.91	0.95	0.96	0.98
D, nm	7*	10	12	30
H, GPa	11.00	1.95	0.49	0.23

* Value calculated using the formula from [8].

The results obtained in the experiments on enhancement of exciton luminescence from the nanocrystalline regions in alkali metal halides may also be explained well by considering grain boundaries as twin boundaries. It is commonly accepted that an increase in the intensity of exciton bands characterizes the perfection of the crystal structure. It is well known that, with a decrease in the crystal dimensions, its structure becomes more perfect (e.g., whiskers). It is energetically disadvantageous for defects to be nucleated and exist in small volumes, and, under the action of the image forces, they move to the boundaries, playing the role of sinks of defects. However, if an interface is twinned, one more characteristic should be taken into account. A mirror reflection plane “attracts” the defects of opposite signs from neighboring grains so that they can annihilate at the interface, which makes the structure of individual grains and boundaries in such nanomaterials rather perfect. The boundary plays the part of a symmetry element (in this case, mirror reflection plain), which combines the atoms from neighboring grains, i.e., the grains themselves. In these terms, one can readily explain the high transparency of some nanoceramics and the efficient operation of lasers made on their basis [16]. Thus, twinning seems to be the most natural way of obtaining high-quality nanomaterials.

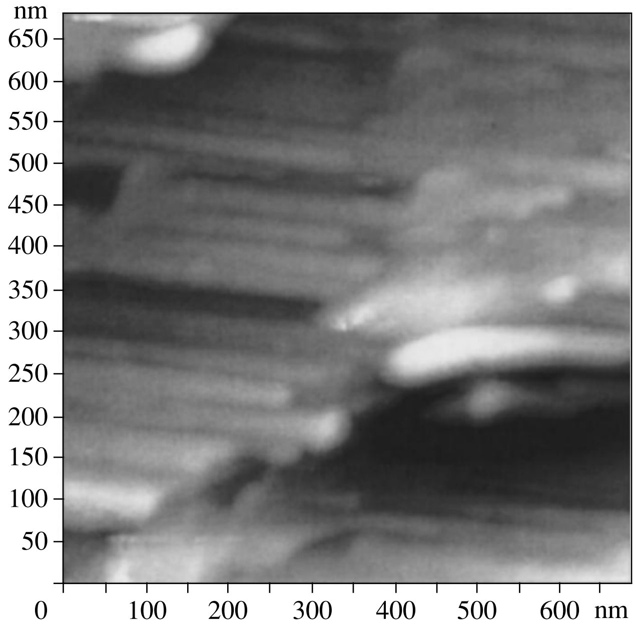

Fig. 2. Two-dimensional image of a scratch on a MgO crystal in an atomic force microscope. $P = 0.1$ N.

The representation of grain boundaries as twin boundaries also allows one to explain the specific mechanical properties of nanomaterials. As was assumed by Rebinder as in 1936 [17] and confirmed by us in [8], the hardness of crystalline materials is determined by the work of dispersion. In other words, the lower the dimensions of the grains formed under the indenter, the higher the microhardness of the material. Therefore, the experimentalists observe an increase in microhardness with a decrease in grain size [5] (the analogue of the Hall–Petch effect). Second, the binding energy of atoms in the vicinity of the twin boundary (high-pressure phase) is higher than in the grain bulk. For example, the Mohs hardness of calcite equals 3, whereas the hardness of aragonite equals 4. Our experiments on the indentation of the boundaries of intergrowths of large blocks in CdS crystals by Si whickers in a scanning electron microscope showed that the microhardness of the regions close to the boundary is about two times higher than in the block center.

A decrease in the grain size such that the interatomic bonds in the grain are oriented mainly toward the opposite twin boundaries and the atomic interactions in the grain center become weaker results in a change of the deformation mechanism, mainly to grain boundary sliding. In this case, the role of grains is played by twinned phases, whereas grain boundary sliding would take place along the weakened sites located approximately in the grain centers. Therefore, a further decrease in the grain size would reduce nanomaterial hardness (the anomaly in the Hall–Petch effect). Thus a decrease in the thickness of twinned interlayers results in a weakening of the bonds inside the grains and, in the limit, in the transition to superfluidity.

Thus, the formation of the nanocrystalline regions under the indenter is associated, first and foremost, with twinning. Mechanical twinning in single crystals results in the fragmentation of the material into nanoblocks whose boundaries are twinning planes—mirror reflection planes. Therefore, the specific physical properties of nanomaterials can be explained by a change in their symmetry and the representation of grains as twinned interlayers.

ACKNOWLEDGMENTS

The authors are grateful to P.P. Fedorov for his help in the X-ray phase analysis of $CaCO_3$ single crystals.

REFERENCES

1. H. Gleiter, Prog. Mater. Sci. **33**, 223 (1989).
2. H. Gleiter, Nanostruct. Mater. **1**, 1 (1992).
3. R. V. Siegel, Annu. Rev. Mater. Sci. **21**, 559 (1991).
4. R. Z. Valiev, A. V. Korznakov, and R. R. Mulyukov, Fiz. Met. Metalloved. **4**, 70 (1992).
5. A. I. Gusev, Usp. Fiz. Nauk **108**, 55 (1998) [Phys. Usp. **45**, 49 (1998)].
6. R. A. Andrievskiĭ and A. M. Gleĭzer, Fiz. Met. Metalloved. **88** (1), 50 (1999); Fiz. Met. Metalloved. **89** (1), 91 (2000).
7. M. V. Klassen-Nekhlyudova, *Mechanical Twinning of Crystals* (Akad. Nauk SSSR, Moscow, 1960; Consultants Bureau, New York, 1964).
8. M. Sh. Akchurin, V. G. Galstyan, and V. R. Regel’, Fiz. Tverd. Tela (St. Petersburg) **37** (3), 845 (1995) [Phys. Solid State **37**, 459 (1995)].
9. E. Yu. Tonkov, *Phase Diagrams of the Compounds and High Pressures* (Nauka, Moscow, 1983).
10. D. B. Gogoberidze, *Mechanical Twinning* (Gos. Nauchn.-Tekh. Izd. Ukr., Kharkov, 1938).
11. A. V. Skropyshev and A. L. Kukuĭ, *Iceland Spar* (Nedra, Leningrad, 1973).
12. M. Sh. Akchurin and V. R. Regel, Chem. Rev. **23**, 59 (1998).
13. M. Sh. Akchurin, V. G. Galstyan, V. R. Regel’, and P. P. Fedorov, in *Abstracts of XIX Russian Conference on Electron Microscopy RKEM-2002* (Chernogolovka, 2002), p. 27.
14. B. Ya. Farber, V. I. Orlov, and A. H. Heuer, Phys. Status Solidi A **166**, 115 (1998).
15. Yu. V. Golovin and A. I. Tyurin, Fiz. Tverd. Tela (St. Petersburg) **42** (10), 1818 (2000) [Phys. Solid State **42**, 1865 (2000)].
16. J. Lu, M. Prabhu, J. Song, *et al.*, Jpn. J. Appl. Phys. **40**, L552 (2001).
17. A. P. Rebinder, Izv. Akad. Nauk SSSR, Ser. Khim. **5**, 639 (1936).

Translated by L. Man

Crystallography Reports, Vol. 48, No. 3, 2003, pp. 473–476. Translated from Kristallografiya, Vol. 48, No. 3, 2003, pp. 518–521.
Original Russian Text Copyright © 2003 by Gan'shina, Granovskiĭ, Vinogradov, Kumaritova, Grenet, Cairo, Revcolevschi, Dhalenne, Berton.

PHYSICAL PROPERTIES OF CRYSTALS

Electronic Structure and Magnetooptical Properties of an $La_{0.7}Ca_{0.25}Ba_{0.05}MnO_3$ Single Crystal[1]

E. A. Gan'shina*, A. B. Granovskiĭ*, A. N. Vinogradov*, R. Yu. Kumaritova*, J.-C. Grenet, R. Cairo**, A. Revcolevschi***, G. Dhalenne***, and J. Berton*****

** Department of Physics, Moscow State University, Vorob'evy gory, Moscow, 119992 Russia*
e-mail: eagan@magn.ru
*** Laboratoire de Termodynamique Experimentale, Université de Nice, BP 71, 06108 Nice Cedex 2, France*
**** Laboratoire de Chimie de Solides, Bat. 414, Université de Paris XI, 91405 Orsay, France*

Received December 3, 2002

Abstract—The spectral and temperature characteristics of the magnetooptical Kerr effect and the optical properties of an $La_{0.7}Ca_{0.25}Ba_{0.05}MnO_3$ single crystal are studied. The data obtained are used to calculate the components of the permittivity tensor, whose behavior is interpreted within the framework of the known models of the electronic structure of manganites. *© 2003 MAIK "Nauka/Interperiodica".*

INTRODUCTION

Despite numerous studies of doped $La_{1-x}(Sr, Ca, Ba)_xMnO_3$-type and La-deficient La_xMnO_3 manganites performed after the discovery of the enormous magnetoresistance in these compounds [1], the problem of a correct description of the electronic energy spectrum in these systems is still unsolved. The nature of low-energy transitions in manganites is also unclear. Various mechanisms are proposed to interpret these transitions. Here, useful information can be obtained with the aid of optical and especially magnetooptical methods, because magnetooptical spectra are extremely sensitive to weak *d*–*d* transitions.

However, the magnetooptical properties of doped manganites were studied in a limited number of works [2–6]. The measurements were performed mainly on polycrystalline ceramic samples and thin films. As far as we know, no low-temperature measurements of magnetooptical effects in doped single crystals of manganites were made in order to obtain the permittivity tensor and determine the anisotropy of magnetooptical effects.

Below, we present the results of the study of spectral and temperature characteristics of magnetooptical properties, measurements of optical properties, and calculation of diagonal and nondiagonal components of the permittivity tensor for an $La_{0.7}Ca_{0.25}Ba_{0.05}MnO_3$ single crystal. The experimental data are discussed in terms of the known models of the electronic structure.

EXPERIMENTAL

Cylindrical $La_{0.7}Ca_{0.25}Ba_{0.05}MnO_3$ samples were grown by the floating zone technique. X-ray diffraction analysis showed that the single crystal had a pseudocubic structure with slight monoclinic deformations; the lattice parameters are $a = 7.783 \pm 0.001$ Å, $b = 7.787 \pm 0.001$ Å, and $c = 7.782 \pm 0.001$ Å; $\beta = 89.838° \pm 0.002°$. The measurements were performed on plates both immediately after mechanical polishing and also after the recovery annealing in air. Magnetooptical properties were studied by the dynamic method in the geometry of the transverse Kerr effect. The relative intensity variation of the reflected *p*-polarized light was measured directly during experiments:

$$\delta = (I(H) - I(0))/I(0),$$

where $I(H)$ and $I(0)$ are the intensities of the reflected light in the presence and absence of a magnetic field, respectively. The applied alternating field attained a value of 3 kOe. Magnetooptical spectra were recorded in the energy range 1.3–3.8 eV. Low-temperature measurements were performed in a flow-type helium cryostat at a continuously varying temperature in the range 20–300 K.

RESULTS AND DISCUSSION

The temperature characteristics of the transverse Kerr effect for two mechanically polished samples cut out from different parts of the single crystal are shown in Figs. 1a and 1b. It is seen that the temperatures of the phase transition to a magnetically ordered state (the temperatures below which the magnetooptical effect is observed) for these two samples are different. The temperature curves of the transverse Kerr effect measured in the heating and cooling modes show a pronounced temperature hysteresis. After a recovery annealing at 900°C and gradual 24-h-cooling, the effect became more pronounced and the hysteresis reduced (Fig. 1c). The magnetooptical spectra of the mechanically pol-

---

[1] This study was presented at the Symposium "Order, Disorder, and Properties of Oxides" (ODPO), Sochi, 2002.

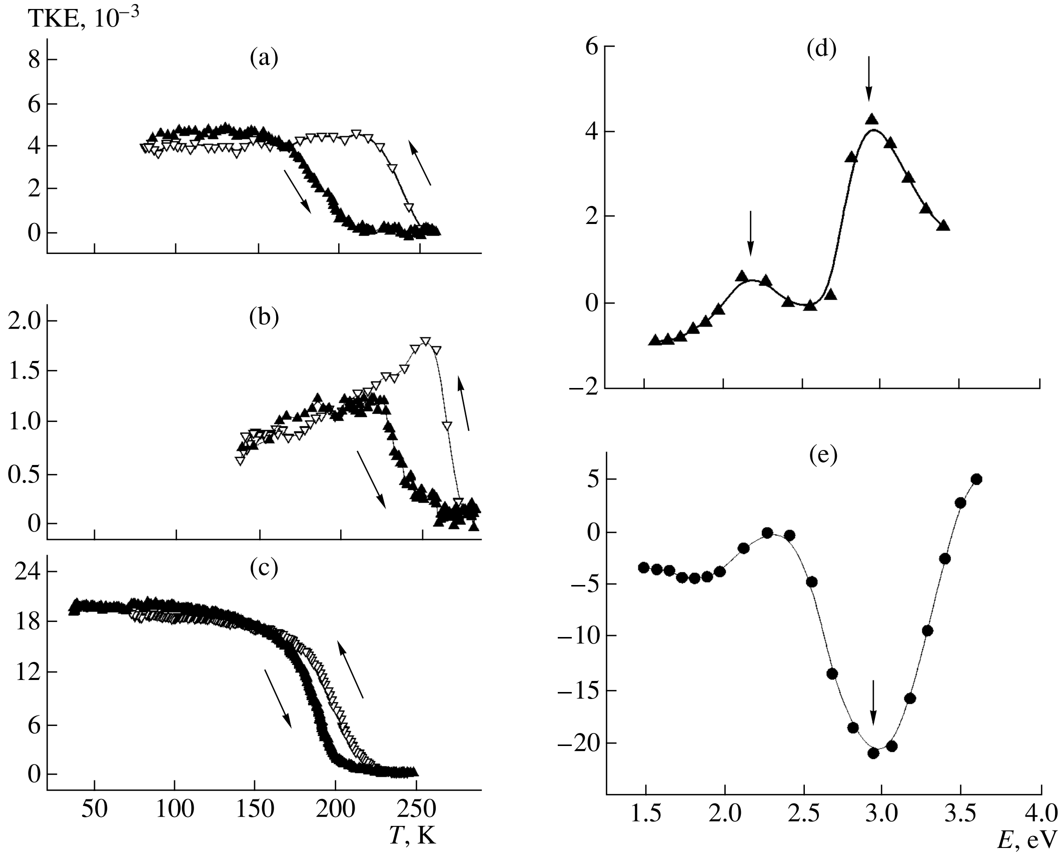

Fig. 1. (a, b, c) Temperature and (d, e) spectral characteristics of the transverse Kerr effect (TKE) for two samples of an $La_{0.7}Ba_{0.05}Ca_{0.25}MnO_3$ single crystal (a, b, d) before and (c, e) after annealing. The directions of the change of temperature are indicated by arrows.

ished samples are shown in Fig. 1d. These spectra significantly differ from the spectra of the $LaMnO_{3+\delta}$ ceramic [3] and $(La_{1-x}Pr_x)_{0.7}(CaSr)_{0.3}MnO_3$ thin films [4–6]. Thus, these spectra of the transverse Kerr effect have two maxima, at 2.1 and 2.9 eV, instead of a high negative peak near 3.0 eV. After annealing, the spectra change (Fig. 1e) and become similar to the spectra obtained earlier for $(La_{1-x}Pr_x)_{0.7}(CaSr)_{0.3}MnO_3$ [4–6]. The spectral characteristics of the transverse Kerr effect in magnetic fields applied along the [100] and [110] directions revealed no anisotropy in their behavior.

To establish the nature of the optical transitions responsible for the behavior of magnetooptical spectra, we calculated the nondiagonal components of the permittivity tensor $\varepsilon_{xy} = -i\varepsilon' = -i(\varepsilon_1' - i\varepsilon_2')$. The spectral characteristics of the nondiagonal components ε_1' and ε_2' of the permittivity tensor were determined from the measurements of the transverse Kerr effect at three different angles of light incidence and from the measurements of the optical constants n and k. It should be noted that the optical constants were determined by direct ellipsometry measurements without recalculating by the Kramers–Kronig method, which allowed us to reveal more clearly the specific features of the optical-conductivity spectra.

The energy curve of the optical conductivity σ (Fig. 2a) had weak singularities in the vicinity of E = 2.1 and 3.1 eV and showed the beginning of strong absorption at $E > 2.3$ eV. The calculated imaginary and real parts of the nondiagonal components of the permittivity tensor are shown in Fig. 2b. The ε_1' and ε_2' curves at energies $E > 2.0$ eV obtained for an $La_{0.7}Ca_{0.25}Ba_{0.05}MnO_3$ single crystal are consistent with the form of the tensor calculated earlier for $LaMnO_{3+\delta}$ [3] and $La_{0.7}Sr_{0.3}MnO_3$ [2]. The ε_1' and ε_2' spectra show a rather pronounced "diamagnetic" transition at E = 3.5 eV and weak singularities at lower energies. The form of magnetooptical spectra of doped manganites does not vary with the substitution of Sr by Ca or of Ba or Ly by Pr. The spectra of manganites with an equal Mn^{3+}/Mn^{4+} ratio, i.e., at equal doping level, are similar. This leads to the conclusion that it is the transitions in the octahedral complexes of manganese ions that possess different valences that are responsible for the behavior of the magnetooptical spectra of these compounds. Therefore, the analysis of the spectra obtained can be based on consideration of the possible transitions in these complexes.

To describe the low-energy transitions, we used a scheme of energy levels obtained as a result of a spin-polarized X_α-DB-calculation of one-electron energy levels for octahedral $(AO_6)^{9-}$ complexes in the $LaAO_3$ structure (A = Mn, Cr) [7]. To analyze the transitions in octahedral $(Mn^{4+}O_6)^{8-}$ complexes, we considered the energy spectrum of a $(Cr^{3+}O_6)^{9-}$ complex, because the Cr^{3+} and Mn^{4+} ions are isoelectronic and, in the first approximation, their spectra should be similar. According to this calculation, a pronounced allowed electric dipole transition with a charge transfer should be observed for octahedral $(Mn^{3+}O_6)^{9-}$ complexes at $E \sim 4.1$ eV, whereas according to our experimental data, this transition occurs at 3.5 eV.

Experimentally this transition was observed only in the systems containing the octahedral $(Mn^{3+}O_6)^{9-}$ complexes [3]. The studies of the magnetooptical properties of pyrochlores $A_2^{3+}Mn_2^{4+}O_7$ containing only magnetoactive Mn^{4+} ions [3] did not reveal this transition, and in the energy range 2.6–3.1 eV, the magnetooptical spectra showed only two maxima, which were attributed to the d–d transitions in Mn^{4+} ions: Mn^{4+}–$^4A_{2g}$–$^4T_{2g}$ and $^4A_{2g}$–$^4T_{1g}$, respectively. According to [8], the transitions with a charge transfer in octahedral $(Mn^{4+}O_6)^{8-}$ complexes may begin at an energy exceeding 3.7 eV. When studying Bi- and Pb-containing manganese perovskites [3], we observed such a transition at $E = 4.3$ eV. The above assumptions about the nature of the transitions in octahedral $(MnO_6)^{8-}$ complexes agree with the data obtained in luminescence studies of compounds containing Mn^{4+} ions [8]. Although the data obtained in magnetooptical experiments are in good agreement with the scheme of one-electron levels for octahedral $(MnO_6)^{9-}$ and $(MnO_6)^{8-}$ complexes, the curves for ε'_1 and ε'_2 in Fig. 2b show that the experimental curves behave in a more complex way than might be obtained for a simple diamagnetic transition (the curves are unusually broad and asymmetric). In the low-energy region, we observed relatively high ε'_2 values. A similar conclusion can also be drawn from the comparison of the experimental and calculated curves for ε'_1 and ε'_2 obtained earlier for $La_{0.7}Sr_{0.3}MnO_3$ [2]. Such a behavior can be explained if one takes into account that the electronic structure in systems similar to doped manganites cannot be adequately described without allowance for multielectronic correlations in the ground and excited states.

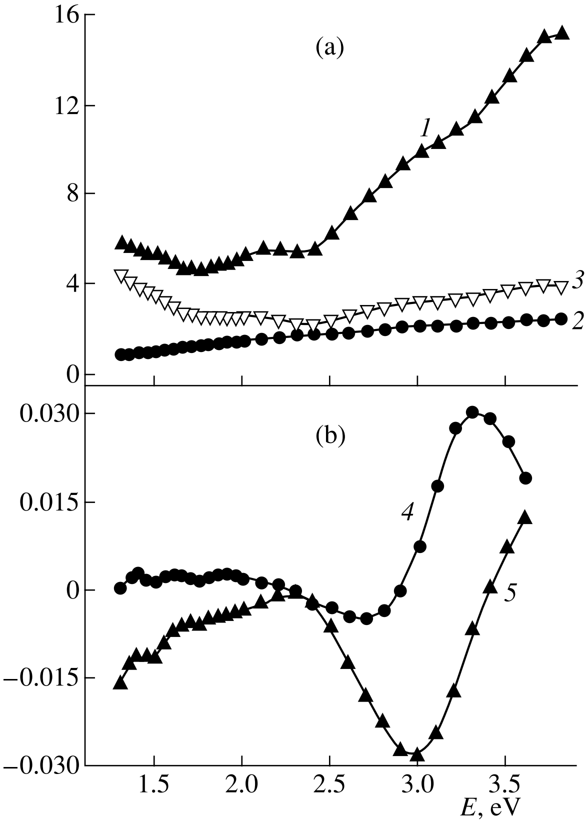

Fig. 2. Spectra of (a) (*1*) optical conductivity σ, the diagonal (*2*) ε_1 and (*3*) ε_2, and (b) the nondiagonal (*4*) ε'_1 and (*5*) ε'_2 components of the permittivity tensor for an $La_{0.65}Ba_{0.05}Ca_{0.3}MnO_3$ single crystal.

Analysis of various transitions accompanied by charge transfer O2p–Mn3d in the $[MnO_6]^{9-}$ octahedra [9] showed that the one-electron transitions from odd oxygen $t_{1u}(\sigma)$, $t_{1u}(\pi)$, and $t_{2u}(\pi)$ orbitals into 3d-cation e_g- or t_{2g}-state accompanied by charge transfer form 60 (!) allowed electric dipole transitions between the corresponding multielectronic configurations over the wide energy spectral range from ~2.5 to ~11 eV. In addition to the allowed transitions accompanied by charge transfer one also has to take into account the set of dipole-forbidden transitions from $a_{1g}(\sigma)$ and $t_{1g}(\pi)$ oxygen states.

Using the above model, we can also describe the behavior of the diagonal and nondiagonal components of permittivity for an $La_{0.7}Ca_{0.25}Ba_{0.05}MnO_3$ single crystal. According to this model, a pronounced magnetooptical activity at energies $E > 1.8$ eV can be induced by two transitions—a weak dipole-allowed $t_{2u}(\pi)$–e_g transition with the maximum at 2.5 eV and a relatively more intense $t_{1u}(\pi)$–e_g transition with the maximum at 3.5 eV. The occurrence of several transitions accompanied by charge transfer explains both the broadening and the asymmetry of the experimental ε'_1 and ε'_2 curves in the vicinity of 3.5 eV.

The theoretical model suggested in [9] was developed for nominally stoichiometric $LaMnO_3$. However, for manganites and many other 3*d*-oxides, oxygen nonstoichiometry with compensation of the charge by holes of an Mn^{4+} or O^{-} type is more typical [10]. The model calculations performed in [10] show that charge transfer with participation of these holes can give a noticeable contribution to the low-frequency optical response near the energy 1.5 eV.

The different behavior of the ε_1' and ε_2' curves for the single crystal studied and for $La_{1-x}Sr_xMnO_3$ and also for an $LaMnO_{3.11}$ single crystal at energies lower than 2 eV can be explained by the different microstructure of the samples and, hence, by the different inhomogeneities of the electronic structure formed in the nonstoichiometric systems doped with nonisovalent dopants. The formation of these inhomogeneities should considerably change the optical and magnetooptical spectra [10, 11].

The different behavior of the magnetooptical properties in the annealed and nonannealed samples also indicates that the structural distortions also change the electronic and magnetic structures of the subsurface layer of mechanically polished samples. As a result, the subsurface layer is characterized by a different value of the Mn^{3+}/Mn^{4+} ratio of magnetoactive ions and the different volume ratio of the ferromagnetic metal phase and dielectric matrix, which, in turn, gives rise to changes in the spectrum.

Thus, we can conclude that it is the transitions in octahedral complexes of manganese ions with different valences and the *d*–*d* transitions in the manganese ions that are responsible for the magnetooptical activity of both doped and oxygen-nonstoichiometric manganites. The high value of the magnetooptical activity and the dispersion dependence of the permittivity tensor are consistent with the predictions (based on the multielectronic band structure) about the transitions accompanied by charge transfer in manganites [9].

REFERENCES

1. E. L. Nagaev, Phys. Rep. **346**, 387 (2001); E. Dagotto, T. Hotta, and A. Moreo, Phys. Rep. **344**, 1 (2001).
2. S. Yamaguchi, Y. Okimoto, K. Ishibashi, and Y. Tokura, Phys. Rev. **58**, 6862 (1998).
3. E. A. Balukina, E. A. Gan'shina, G. S. Krinchik, and A. Yu. Trifonov, J. Magn. Magn. Mater. **117**, 259 (1992).
4. E. A. Gan'shina, O. Yu. Gorbenko, A. R. Kaul, *et al.*, J. Phys.: Condens. Matter **12**, 2857 (2000).
5. E. A. Gan'shina, O. Yu. Gorbenko, A. G. Smechova, *et al.*, in *Proceeding of 8th International Symposium on Non-Linear Electromagnetic Systems, Braunschweig, Germany, 1997* (IOS Press, Amsterdam, 1998), p. 325.
6. E. A. Gan'shina, I. K. Rodin, A. R. Kaul', and O. Yu. Gorbenko, J. Magn. Magn. Mater. **239**, 323 (2002).
7. D. J. Lam, B. W. Veal, and D. E. Ellis, Phys. Rev. B **22**, 5730 (1980).
8. A. G. Paulusz and H. I. Burrus, Chem. Phys. Lett. **17**, 527 (1972).
9. A. S. Moskvin, cond-mat/0111198.
10. N. N. Kovaleva, J. L. Gavartin, A. L. Shluger, *et al.*, cond-mat/0108207.
11. Yu. Sukhorukov, N. N. Loshkareva, E. A. Gan'shina, *et al.*, Zh. Éksp. Teor. Fiz. **123**, 293 (2003).

Translated by T. Dmitrieva

Crystallography Reports, Vol. 48, No. 3, 2003, pp. 477–479. Translated from Kristallografiya, Vol. 48, No. 3, 2003, pp. 522–524.
Original Russian Text Copyright © 2003 by Babaev, Kamilov, Gabibov, Sultanov, Askhabov, Khasbulatov.

PHYSICAL PROPERTIES OF CRYSTALS

Study of Mechanical Amorphization of Mineral Orpiment (As_2S_3) and Arsenic and Germanium Selenide Crystals by Optical Methods[1]

**A. A. Babaev*, I. K. Kamilov*, F. S. Gabibov*, S. B. Sultanov*,
A. M. Askhabov*, and A. M. Khasbulatov****

** Institute of Physics, Dagestan Scientific Center, Russian Academy of Sciences,
ul. M. Yaragskogo 94, Makhachkala, 367003 Russia*

e-mail: kamilov@datacom.ru

*** Dagestan State University, ul. Dzerzhinskogo 12, Makhachkala, 367010 Russia*

Received December 3, 2002

Abstract—Reversible photostructural transformations (darkening and clearing) accompanied by a shift of the edge transmission and a fatigue effect of luminescence have been found in deformed As_2S_3, $GeSe_2$, and As_2Se_3 single crystals and powders at $T = 77$ K. The experimental results are interpreted based on the configurational model of two stable states of molecular groups. © *2003 MAIK "Nauka/Interperiodica".*

Mechanical treatment of solid materials requires allowance for the fact that a pronounced disorder arising in the surface layers "propagates" into the sample depth and can give rise to complete amorphization of the structure [1]. The transition of single crystals of the type of glasslike chalcogenide semiconductors into a disordered state caused by nonthermal treatment is of special interest. The most interesting phenomena characteristic of glasslike chalcogenide semiconductors and not observed in their crystalline analogues are reversible photostructural transformations that modify a complex of properties of glasslike chalcogenide semiconductors.

The present study was aimed at the establishment of the effect of mechanical treatment on structural disordering in As_2S_3, As_2Se_3, and $GeSe_2$ single crystals. For this we studied the photoluminescence properties and optical transmission in initial and deformed single crystals and powders. The photoluminescence (curves *1*, *2*, and *3*) and the luminescence excitation spectra at 77 K of starting (curves *1*', *2*', and *3*') and deformed (curves *1*'', *2*'', and *3*'') As_2Se_3, $GeSe_2$, and As_2S_3 single crystals and powders are shown in Fig. 1a. It is seen from Fig. 1 that the photoluminescence spectra of initial and deformed single crystals and powders are the same, whereas the luminescence excitation spectra are considerably changed. The maxima of the luminescence excitation spectra of starting crystals are equal to the energy of exciton absorption, whereas in the mechanically treated crystals these maxima are shifted to high energies. In this case, the photoluminescence intensity increases, whereas the low energy edge of the lumines-

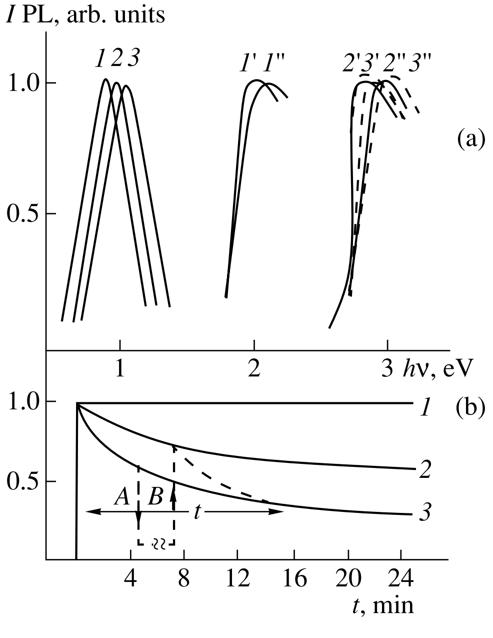

Fig. 1. (a) Photoluminescence (PL) (*1*, *2*, *3*) and photoluminescence-excitation of the initial (*1*', *2*', *3*') and deformed (*1*'', *2*'', *3*'') As_2Se_3, $GeSe_2$, and As_2S_3 single crystals and powders at $T = 77$ K; (b) long-term attenuation of photoluminescence during the process of stationary excitation in (*1*) starting and (*2*) deformed As_2S_3 single crystals and (*3*) in As_2S_3 powder at $T = 77$ K.

---

[1] This study was submitted to the Symposium "Phase Transitions in Solid Solutions and Alloys" (OMA), Sochi, 2002.

1063-7745/03/4803-0477$24.00 © 2003 MAIK "Nauka/Interperiodica"

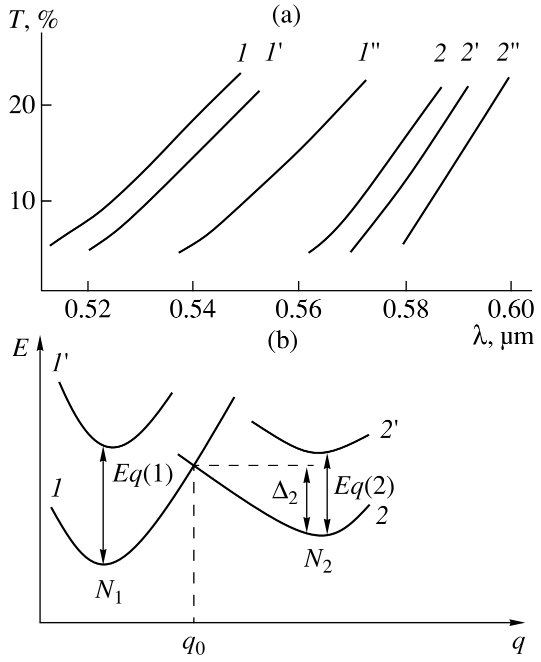

Fig. 2. (a) Edge transmission of the layers of As_2S_3 and $GeSe_2$ powders (*1*, *2*) before irradiation; (*1*'', *2*'') after irradiation; (*1*', *2*') after annealing. (b) The configurational diagram: the electron energy in the (*1*) ground, (*1*') excited, (*2*) metastable ground, and (*2*') metastable excited states.

cence excitation spectra becomes flattened. The Stokes shift and the position of the photoluminescence spectrum and its half-width indicate a strong electron–phonon interaction. The conduction band of the crystals is formed by the antibinding orbitals of covalent bonds, whereas the valent-band bottom is formed by the bonds of lone pairs of chalcogen electrons [2, 3]. It seems that mechanical treatment of crystals gives rise to the formation of defects similar to those in glasslike chalcogenide semiconductors [4]. A chalcogen atom with c.n. = 3, C_3^0 can play the role of a neutral defect with the minimum energy. Two neutral centers are unstable with respect to the $2C_3^0 \longrightarrow C_3^+ + \mathrm{C}1$ reaction. Charged defects in glasslike chalcogenide are diamagnetic, whereas neutral defects (formed as a result of photoexcitation) are paramagnetic [4].

Typical curves characterizing the fatigue of single crystals and powders deformed due to photoluminescence are shown in Fig. 1b using As_2S_3 as an example. The effect of photoluminescence-induced fatigue differs from the effect observed in glasslike chalcogenides. During photoluminescence attenuation, when the stationary excitation is switched off, the intensity drops within a time shorter than 10^{-2} s (*A*), as in glasslike chalcogenides. During subsequent excitation, the signal level *B* exceeds the value recorded at the moment of excitation termination. The photostructural transformations are accompanied by darkening at low temperatures and clearing during annealing and also by a parallel shift of the transmission edge (see Fig. 2a). In As_2S_3 the optical transmission is fully restored at T = 150°C, whereas in a more rigid Ge_2Se_3 structure, it occurs at T = 180°C. The photostimulated change in optical transmission was measured at T = 77 and 300 K. The respective control was made at the wavelength with an initial transmission equal to 20%. Using the model of structural transformations in glasslike chalcogenide semiconductors [5, 6], we proposed a configuration model of two stable structural states of molecular groups for deformed single crystals and powders (these groups are analogues of the unit cell of the starting crystal). These states (ground and metastable states) have different energies (Fig. 2b). The ratio of molecular groups depends on the optical and thermal transitions. Similar to the case of glasslike chalcogenides, the main changes in deformed single crystals and powders take place in the chalcogen sublattice. In the configuration model, the sample transmission is determined by the occupancy of the metastable state β:

$$\beta = N_2/(N_1 + N_2), \tag{1}$$

where N_1 and N_2 are the numbers of molecular groups in the ground and metastable states, respectively. The balance equation for β can be written in the form

$$d\beta/dt = -\left[-\frac{1}{\tau} + Q(\alpha_1 + \alpha_2)\right]\beta + Q\alpha, \tag{2}$$

where Q is the luminous flux, $\alpha(\alpha_2)$ is the absorption cross section for the optical transition from the ground to metastable state (and vice versa), and τ is the lifetime of the system in the metastable state. At

$$Q(t) = \begin{cases} 0, & t = 0 \\ Q_0, & t > 0 \end{cases} \tag{3}$$

the solution of the balance equation yields

$$\beta = (\beta_0 - \beta_\infty)\exp(-\alpha t) + \beta_\infty, \tag{4}$$

$$\beta_\infty = Q_0\alpha_1/\alpha, \tag{5}$$

$$\alpha = Q_0(\alpha_1 + \alpha_2) + 1/t, \tag{6}$$

where β_0 is the initial occupancy at $t = 0$. The quantity α characterizes the dependence of occupancy on the temperature and wavelength of the exciting light. After switching off the light, the occupancy of the metastable state decreases according to the exponential law

$$\beta = \beta_0\exp(-\alpha_T t), \tag{7}$$

where $\alpha_T = \tau^{-1} = \nu\exp(-\Delta_2/kT)$, Δ_2 is the depth of potential well of the metastable state (see Fig. 2b), and ν is the frequency (of the order of the phonon frequency).

To establish the microscopic nature of photostructural transformations in detail, one has to study it by EXAFS and photoelectron spectroscopy.

REFERENCES

1. A. Feltz, *Amorphe und Glasartige Anorganische Festkörper* (Akademie, Berlin, 1983; Mir, Moscow, 1986).
2. M. Lanno and M. Bensonssan, Phys. Rev. B **16** (8), 3546 (1977).
3. E. Tarnov, A. Antonelli, and J. Joaunopoulos, Phys. Rev. B **34** (6), 4059 (1986).
4. N. Mott and E. Davis, *Electronic Processes in Non-Crystalline Materials* (Clarendon Press, Oxford, 1979; Mir, Moscow, 1982).
5. V. L. Averianov, A. V. Kolobov, B. T. Kolomiets, *et al.*, J. Non-Cryst. Solids **45**, 335 (1981).
6. B. T. Kolomiets, A. V. Kolobov, V. M. Lyubin, *et al.*, Rev. Roum. Phys. **45**, 343 (1981).

Translated by T. Dmitrieva

Crystallography Reports, Vol. 48, No. 3, 2003, pp. 480–482. Translated from Kristallografiya, Vol. 48, No. 3, 2003, pp. 525–527.
Original Russian Text Copyright © 2003 by Korshunov.

PHYSICAL PROPERTIES OF CRYSTALS

Distribution of Component Molecules in *p*-Dibromobenzene–*p*-Dichlorobenzene Solid Solutions from Raman Effect Data

M. A. Korshunov
Kirenskiĭ Institute of Physics, Siberian Division, Russian Academy of Sciences,
Akademgorodok, Krasnoyarsk, 660036 Russia
e-mail: mkor@iph.krasn.ru

Received September 25, 2001

Abstract—Distribution of component molecules in the bulk of single crystals of *p*-dibromobenzene–*p*-dichlorobenzene solid solutions grown by the Bridgman method studied by Raman effect. © *2003 MAIK “Nauka/Interperiodica”.*

Mixed organic crystals find ever growing application in molecular electronics [1]. The use of these crystals requires knowledge of the distribution of the component molecules in the bulk of single crystals, because this distribution influences their physical properties. The distribution of the component molecules was studied by X-ray diffraction analysis, nuclear quadrupole resonance, and optical absorption analysis [2–4].

In the present study, we use Raman effect, which allows one to establish the character of the arrangement of impurity molecules among the molecules of the matrix crystal from the spectra of lattice and intramolecular vibrations. In particular, Raman spectra allow one to determine whether the solid solution is substitutional or interstitial, whether impurity molecules are concentrated at the boundaries between blocks of the single-crystal lattice, or the solid solution is a mechanical mixture of the substances.

Below, we consider the possibility of using Raman effect to study the distribution of impurity molecules over the bulk of a Bridgman-grown single crystal. For this purpose, the data calculated by the scheme in [5] from the phase diagram are compared with the experimental data on Raman effect.

We studied a mixed *p*-dibromobenzene (p-$C_6H_4Br_2$)–*p*-dichlorobenzene (p-$C_6H_4Cl_2$) crystal, because its components are isomorphous and form solid solutions at any concentrations [6]. Paradibromobenzene and paradichlorobenzene (α-modification) crystallize in the centrosymmetric sp. gr. $P2_1/a$ with two molecules in the unit cell. These crystals were studied by the methods of X-ray diffraction [7], Raman effect [8], and nuclear quadrupole resonance [3]. We found no X-ray diffraction data on the mixed crystals studied in the present work.

For adequate comparison of experimental data, the same materials were used for the construction of the phase diagram and growth of single crystals. Pure-grade *p*-dibromobenzene (the measured melting point $t_m = 86.8 \pm 0.1°C$) and *p*-dichlorobenzene ($t_m = 53.0 \pm 0.1°C$) were used in the study. The materials used were additionally purified by zone melting (no decomposition was observed during melting).

The phase diagram was constructed by the method described in [9]. A test tube with a wire was filled with 1 g of the mixture with the given component ratio and was placed into a thermostat where the temperature was maintained constant within ±0.1°C. A crystal was formed at the wire end placed into the melt. The liquidus point was determined from the melting point of this crystal. The impurity concentration in the mixed crystals grown was determined using the Raman effect spectra recorded in the range of the lattice and intramolecular vibrations. The concentrations of the components were measured in molar units.

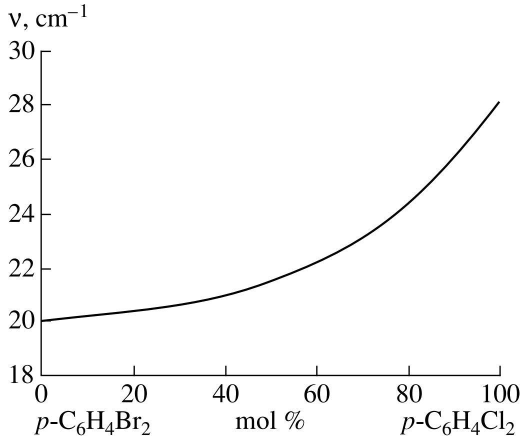

Fig. 1. Line frequency ν as a function of p-$C_6H_4Cl_2$ concentration in the mixed crystals.

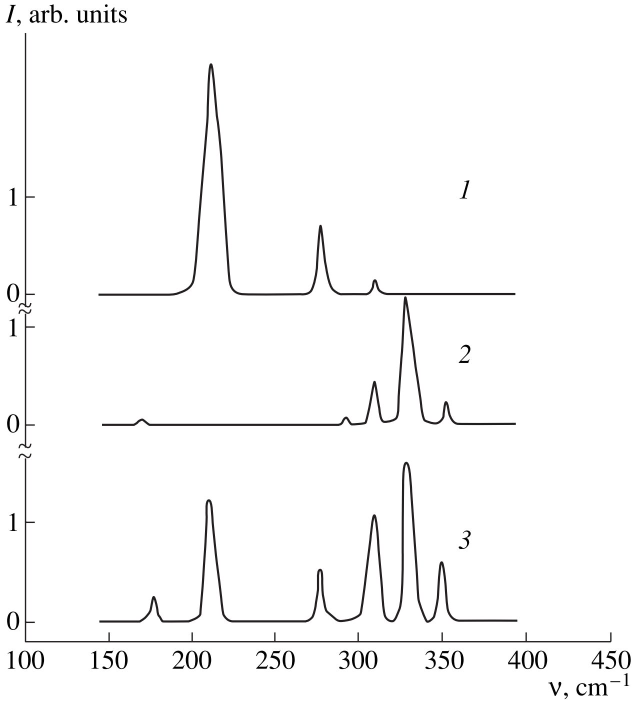

Fig. 2. Spectra of intramolecular vibrations of (*1*) p-$C_6H_4Br_2$, (*2*) p-$C_6H_4Cl_2$, and (*3*) the mixed crystal grown from these materials at a p-$C_6H_4Cl_2$ concentration of 60 mol % in the frequency range ν = 150–400 cm^{-1}.

First, we obtained the Raman spectra of the standard specimens with the specified p-$C_6H_4Br_2$ to p-$C_6H_4Cl_2$ ratio. The spectra of the lattice vibrations have a well-defined line at the frequency ν = 20.0 cm^{-1}. In the spectrum of a mixed crystal, ν changes monotonically with the component concentration (Fig. 1). This enables one to determine the impurity (p-dichlorobenzene) concentration in the solid solution using the frequency value. Frequencies were determined with an accuracy of ±0.07 cm^{-1}. If the spectrum of lattice vibrations contains a separate well-defined line, the impurity concentration can be determined by the above method. However, the lines in the spectrum are positioned in such a way that it is difficult to separate such a line. In this case, the impurity concentration can be determined from the relative intensity of the valence intramolecular vibrations. According to [10], the line in the Raman spectrum of p-$C_6H_4Br_2$ at ν = 212.0 cm^{-1} corresponds to the C–Br valence vibration; the line p-$C_6H_4Cl_2$ at ν = 327.0 cm^{-1}, to the C–Cl vibration. Figure 2 shows the spectra of intramolecular vibrations (in the range ν = 150–400 cm^{-1}) of (*1*) p-dibromobenzene, (*2*) p-dichlorobenzene, and (*3*) the mixed crystal with 60 mol % p-dichlorobenzene. It is evident that the spectrum of the mixed crystal is the superposition of the spectra of intramolecular vibrations of the components with due regard for their concentrations. The accuracy of the determination of the impurity concentration did not exceed 2%. Using this method, we determined the concentrations of the p-$C_6H_4Cl_2$ impurity in crystals grown in the thermostat. The points obtained allowed us to construct the solidus line. Figure 3 shows the p-$C_6H_4Br_2$–p-$C_6H_4Cl_2$ phase diagram constructed using the data obtained.

Then, the distributions of the component concentrations over the length and diameter of the Bridgman-grown single crystals were determined.

A single crystal was grown in a glass tube (diameter *d* = 1 cm and length *h* = 10 cm) with pulled end. The starting materials p-$C_6H_4Br_2$ and p-$C_6H_4Cl_2$ were placed into the tube in the required ratio, the air was pumped out, and the tube was sealed.

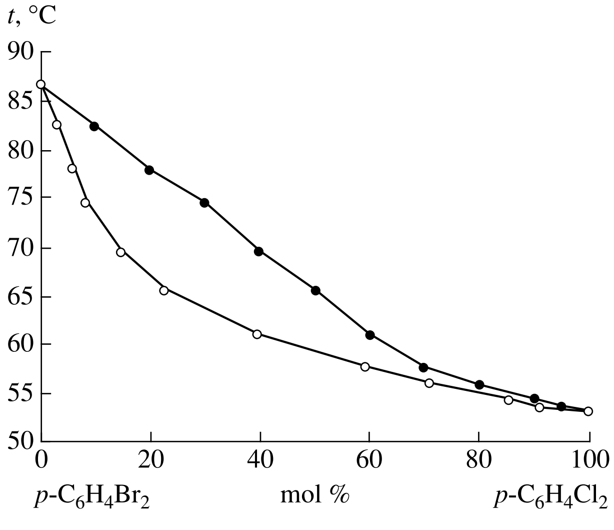

Fig. 3. Phase diagram of the p-dibromobenzene–p-dichlorobenzene binary system.

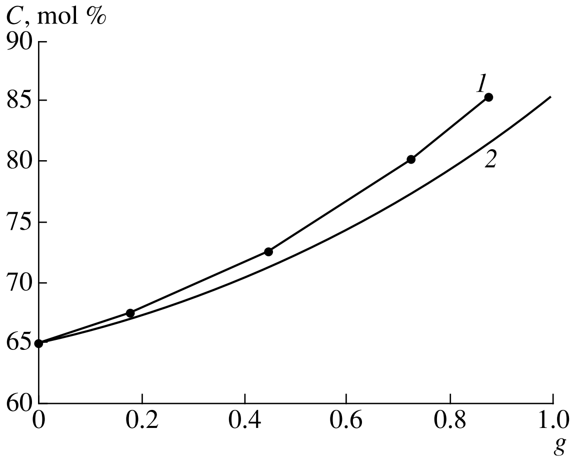

Fig. 4. Distributions of the p-$C_6H_4Cl_2$ impurity along the length of a single crystal of the p-dibromobenzene–p-dichlorobenzene solid solution (*1*) calculated from the data of phase diagram and (*2*) measured experimentally using Raman effect.

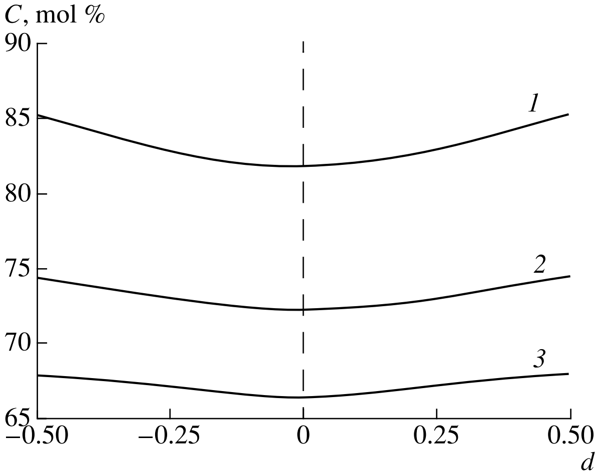

Fig. 5. Variation in the p-$C_6H_4Cl_2$ concentration along the diameter d of a single crystal of the p-dibromobenzene–p-dichlorobenzene solid solution in the cross sections (*1*) 0.9h, (*2*) 0.5h, and (*3*) 0.1h.

The ampule with the material was lowered from the hot to the cold zone of the furnace with the velocity $V = 8.3 \times 10^{-6}$ cm/s. The temperature gradient in the furnace was set by different winding of the heating coil and was equal to $dt/dl = 7.6$ K/cm.

The single crystal grown was cut into ~0.1-cm-thick tablets. In order to study the radial distribution of the impurity from the center to the periphery, several parallelepipeds (edge length 0.1–0.2 cm) were cut from these tablets. The single crystal state of the samples was checked on a polarizing microscope and then the Raman spectra of the samples were recorded. The Raman spectra allowed us to determine the concentration of the p-$C_6H_4Cl_2$ impurity in the samples and the variation in the component concentrations along the length and diameter of the single crystals.

The experimental data obtained are presented in Fig. 4. The concentration of the p-$C_6H_4Cl_2$ impurity C (in mol %) is shown as a function of the crystallized part g of the ingot. Curve *1* shows the equilibrium p-$C_6H_4Cl_2$ distribution along the length of the single crystal calculated from the data of the phase diagram (Fig. 3) using the scheme suggested in [5]. Curve *2* represents the experimental Raman effect data.

As is evident from Fig. 4, the experimental (*2*) and calculated (*1*) curves are in quite good agreement. The deviation from the p-$C_6H_4Cl_2$ concentration does not exceed 5%.

The study of the distribution of p-dichlorobenzene along the diameter of mixed crystals by Raman effect shows that the p-$C_6H_4Cl_2$ concentration increases in the direction from the center to the periphery of the plane normal to the axis of a single crystal. Figure 5 shows the distribution of p-dichlorobenzene along the diameter in different cross sections of the crystal.

Thus, our study shows that Raman effect can be used for studying the distribution of molecules of components in mixed organic single crystals.

REFERENCES

1. *New Physical Principles in Optical Processing of Information*, Ed. by S. A. Akhmanov and M. A. Vorontsov (Nauka, Moscow, 1990).
2. A. I. Kitaigorodsky and R. M. Myasnikova, Kristallografiya **5** (2), 247 (1960) [Sov. Phys. Crystallogr. **5**, 230 (1960)].
3. V. S. Grechishkin, *Nuclear Quadrupole Interactions in Solids* (Nauka, Moscow, 1973).
4. E. A. Krivandina and E. E. Kostyleva, Kristallografiya **18** (2), 247 (1973) [Sov. Phys. Crystallogr. **18**, 151 (1973)].
5. A. N. Kirgintsev, L. I. Isaenko, and V. A. Isaenko, *Distribution of Impurities during Directional Crystallization* (Nauka, Novosibirsk, 1977), App. 3, p. 209.
6. *Technical Encyclopedia: Handbook of Physical, Chemical, and Technological Quantities*, Ed. by B. M. Berkengeĭm (Sovetskaya Éntsiklopediya, Moscow, 1931), Vol. 6, p. 236.
7. A. I. Kitaigorodsky, *Organic Crystal Chemistry* (Akad. Nauk SSSR, Moscow, 1955).
8. V. F. Shabanov, V. P. Spiridonov, and M. A. Korshunov, Zh. Prikl. Spektrosk. **25** (4), 698 (1976).
9. A. I. Kitaigorodsky and V. M. Kozhin, Kristallografiya **4** (2), 209 (1959) [Sov. Phys. Crystallogr. **4**, 187 (1959)].
10. M. Suzuki and M. Ito, Spectrochim. Acta A **25** (5), 1017 (1969).

Translated by A. Zolot'ko

Crystallography Reports, Vol. 48, No. 3, 2003, pp. 483–485. Translated from Kristallografiya, Vol. 48, No. 3, 2003, pp. 528–530.
Original Russian Text Copyright © 2003 by Fedorov, Kuranova, Tyalin, Pluzhnikov.

On Microcrack Nucleation at Twin Vertices and Boundaries in bcc and fcc Metals

V. A. Fedorov, V. A. Kuranova, Yu. I. Tyalin, and S. N. Pluzhnikov
Tambov State University, ul. Internatsional'naya 33, Tambov, 392622 Russia
e-mail: feodorov@tsu.tmb.ru

Received March 4, 2002

Abstract—Nucleation of microcracks at the vertex and boundary of a decelerated twin is studied for a number of bcc and fcc metals. A twin and its boundary are represented as stepped pileups of twinning dislocations located in the neighboring glide planes. The formation of microcracks through the merging of head dislocations by the force and thermally-activated mechanisms is analyzed. Analytical expressions are obtained that describe the conditions necessary for microcrack nucleation at the vertices of stepped dislocation pileups. It is established that with an increase in the shear-modulus value, the critical parameters of microcrack nucleation by the two above mechanisms become closer in all the metals considered. *© 2003 MAIK "Nauka/Interperiodica".*

Studying the behavior of a loaded twin, one usually restricts the consideration to the model of a plane dislocation pileup [1, 2]. This simplification results in an overestimation of the stresses that provide fracture nucleation. The allowance for the real structure of dislocation pileups results in less rigid conditions of microcrack nucleation [3].

The boundaries of a real twin are built by twinning dislocations located in the neighboring atomic planes. The model taking into account this fact was considered elsewhere [4]. It was shown that the geometry of a twin boundary can considerably change the relation between the critical stresses of crack nucleation and the number of dislocations in the pileup. The same approach was considered in [5] and is also used in the present study to obtain the conditions of microcrack nucleation in the twin boundaries and at twin vertices in some bcc (Nb, V, W, Cr, Ta, α-Fe, Mo) and fcc (γ-Fe, Al, Cu, Pb, Ag, Ni) metals. This allowed us to establish the main factors that influence crack nucleation under the assumption of the absence of glide.

As in [4], a twin and its boundary were modeled by stepped pileups of rectilinear segments of twinning dislocations. To determine the x_i and y_i coordinates of the dislocations in the pileup, we solved the equations of their equilibrium distribution numerically by the method of successive approximations [6]. The equations of an equilibrium distribution of dislocations in a twin differ from the analogous equations for a single boundary in that it has an additional term that takes into account the interaction between the *i*th dislocation and the dislocations of the lower boundary [5]. The results of the computations performed for the twin and its boundary were compared with the results obtained for a plane dislocation pileup. We used the criteria of fracture nucleation by the force [7] and thermally activated [8] mechanisms of nucleation at the vertex of a decelerated dislocation pileup.

In the first case, head dislocations that approach one another to a distance of $d = 2.41h$, where h is the interplanar spacing, merge. The external stress τ providing the fulfillment of this condition is called the critical stress τ_{cr}.

In the case of thermally activated formation of a microcrack, one has to calculate the activation energy of its nucleation, which is fully determined by the energy of formation of a double kink at the second dislocation of the pileup [9], whose value is of the order of the sublimation energy $2Db^3$ (b is the Burgers vector of dislocations, $D = \dfrac{G}{2\pi(1-\nu)}$, G is the shear modulus, and ν is the Poisson ratio). For the metals considered here, this energy does not exceed 1 eV. The value thus calculated is then used as the critical value W_{cr} determining the distance between the head dislocations, for which the energy of the forming double kink is provided by thermal fluctuations. The expression for the energy of the double kink is given in [5].

Typical results of the two variants of computations for copper are illustrated by Fig. 1. It is seen that the dependence of d on τ is close to hyperbolic everywhere except for the small region $d < 4h$.

The critical stress depends on the number n of dislocations in the boundary (the same is also true for a twin). If one constructs the dependence $d = f(\tau)$ in arbitrary units, $d = f(\tau n/D)$, the points obtained correspond to different n values in Fig. 1 and can be well approximated by one curve. Being constructed in arbitrary units, these dependences do not depend on the lattice type any longer, which is explained by the fact that the ratios of the moduli of the Burgers vectors of twinning

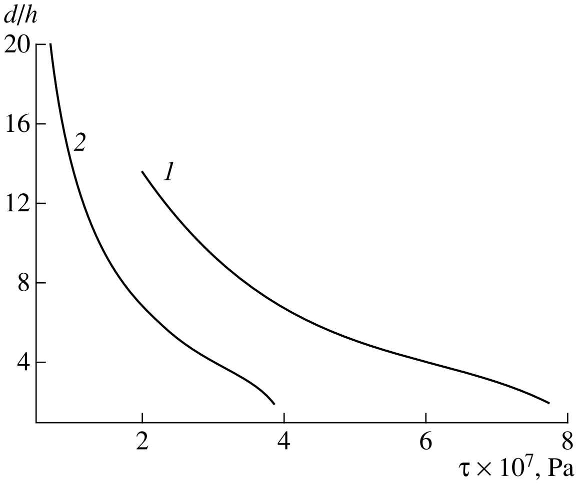

Fig. 1. Distance d between the head dislocations in a twin boundary as a function of the applied stress τ: (*1*) $n = 50$ and (*2*) $n = 100$.

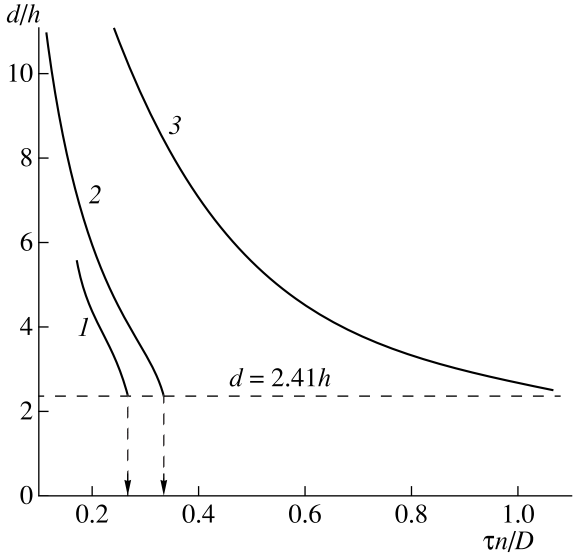

Fig. 2. The change in the distance between the head dislocations as a function of the applied stress and the determination of the critical stresses of microcrack nucleation: (*1*) twin, (*2*) twin boundary, (*3*) plane pileup.

dislocations to the interplanar spacings h in bcc and fcc lattices are the same. Indeed, the moduli of the Burgers vectors in these lattices are equal to $a\sqrt{3}/6$ and $a/\sqrt{6}$, respectively, whereas the interplanar spacings are equal to $a/\sqrt{6}$ and $a/\sqrt{3}$, respectively. Therefore, for each pileup type, the results can be represented by the same dependence irrespective of the material and the lattice type (Fig. 2). The minimum critical stresses of crack nucleation τ_{cr} correspond to a twin. If the other conditions are the same, the crack nucleation in a twin boundary containing the same number of dislocations can take place under stresses that are 1.5 times greater than those in the twin. For a plane pileup, the critical stresses are about five times higher than in the stepwise arrangement of dislocations in the neighboring glide planes.

Everywhere except for the region close to τ_{cr}, the dependences shown in Fig. 2 are approximated rather well by the following expression:

$$d/h = p(n\tau/D)^{-q}, \qquad (1)$$

where p and q are the constants. Their numerical values are $p = 0.29$ and $q = 1.85$ for a twin and $p = 0.50$ and $q = 1.53$ for a twin boundary. Assuming that $d = 2.41h$ in Eq. (1), we arrive at the following criterion of microcrack nucleation by the force mechanism:

$$n\tau = D(p/2.41)^{1/q}.$$

The critical stresses of crack nucleation by the thermally activated mechanism were determined from the intersection of the dependences $W = W(\tau)$ with the straight line $W_{\mathrm{cr}} = 1$ eV. In this case, we obtained a certain τ value and the corresponding $(d/h)_{W = W_{\mathrm{cr}}}$ ratio. Substituting this ratio into Eq. (1), we obtained the condition of microcrack nucleation by the thermally activated mechanism in the form

$$n\tau = D(p/(d/h)_{W = W_{\mathrm{cr}}})^{1/q}.$$

In the computations, the length l of the double kink was chosen to be the same for both lattices and corresponded to two translation periods along the $\langle 110\rangle$ directions coinciding with the direction of the dislocation line. In the range of the change of the kink length from $2\sqrt{2}l/a$ to $4\sqrt{2}l/a$, the energy of the double kink changes by not more than 15%.

Figure 3 shows the ratio of the critical stresses determined from the criteria of crack nucleation by the force and thermally activated mechanisms for metals under consideration as a function of the shear modulus G. It is seen that the critical stresses of microcrack nucleation by the force mechanism are higher than the stresses τ_{cr}^{th} corresponding to the thermally activated mechanism for all the materials. For all the fcc metals studied, the data obtained using both approaches differ only insignificantly (with the single exception of lead). In all the bcc metals considered, the crack nucleation by the mechanism of thermal activation is more probable. In this case, the critical stresses can be almost three times lower than in the case of the force mechanism of microcrack nucleation (e.g., in niobium and vanadium).

Thus, the conditions of microcrack nucleation by the force and thermally activated mechanisms of microcrack nucleation at the twin vertex and in twin boundaries have been analyzed and compared for a number of bcc and fcc metals under the assumption of the absence of glide. It is shown that, for all the metals considered,

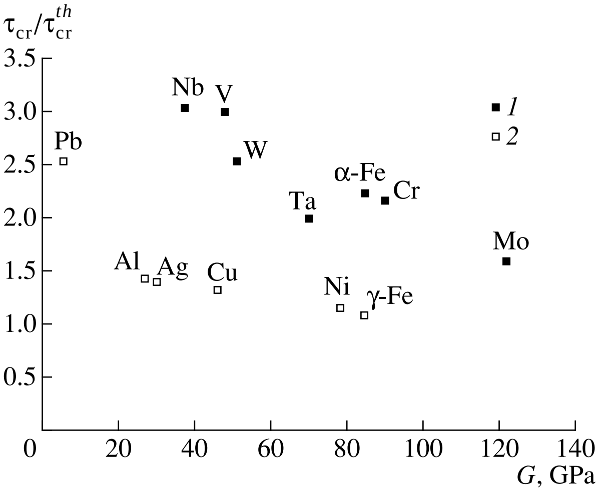

Fig. 3. Comparison of the critical stresses of microcrack nucleation in various metals with (*1*) bcc and (*2*) fcc lattices.

fracture nucleation is considerably facilitated during thermally activated merging of head dislocations. The role of thermal fluctuations is the most important in metals with low shear moduli for which the critical distance between head dislocations can attain a value of $d_{cr} \approx (7–20)b$.

With an increase in the shear-modulus value, the critical distances between the head dislocations determined for both mechanisms become closer in all the metals considered.

The analytical expressions for the conditions of microcrack nucleation in stepped pileups of dislocations are obtained. These expressions model both the twin boundary and the twin itself. It is shown that merging dislocations at the twin vertex occurs at lower stresses than in an isolated boundary.

ACKNOWLEDGMENTS

This study was supported by the Russian Foundation for Basic Research, project no. 02-01-01173.

REFERENCES

1. A. M. Kosevich, *Dislocations in Theory of Elasticity* (Naukova Dumka, Kiev, 1978).
2. A. M. Kosevich and V. S. Boĭko, Usp. Fiz. Nauk **104** (2), 201 (1971) [Sov. Phys. Usp. **14**, 286 (1971)].
3. V. V. Rybin and Sh. Kh. Khannanov, Fiz. Tverd. Tela (Leningrad) **11** (4), 1048 (1969) [Sov. Phys. Solid State **11**, 854 (1969)].
4. V. A. Fedorov and Yu. I. Tyalin, Kristallografiya **26** (4), 775 (1981) [Sov. Phys. Crystallogr. **26**, 439 (1981)].
5. V. A. Fedorov, V. M. Finkel', V. P. Plotnikov, *et al.*, Kristallografiya **33** (5), 1244 (1988) [Sov. Phys. Crystallogr. **33**, 737 (1988)].
6. J. Ortega and W. Rheinboldt, *Iterative Solution of Nonlinear Equations of Several Variables* (McGraw-Hill, New York, 1970; Mir, Moscow, 1975).
7. A. N. Stroh, Adv. Phys. **6** (24), 418 (1957).
8. V. I. Vladimirov, *Physical Nature of Fracture of Metals* (Metallurgiya, Moscow, 1984).
9. J. P. Hirth and J. Lothe, *Theory of Dislocations* (McGraw-Hill, New York, 1967; Atomizdat, Moscow, 1972).

Translated by L. Man

Crystallography Reports, Vol. 48, No. 3, 2003, pp. 486–490. Translated from Kristallografiya, Vol. 48, No. 3, 2003, pp. 531–535.
Original Russian Text Copyright © 2003 by Raevskiĭ, Reznichenko, Ivliev, Smotrakov, Eremkin, Malitskaya, Shilkina, Shevtsova, Borodin.

PHYSICAL PROPERTIES OF CRYSTALS

Growth and Study of Single Crystals of (Na, K)NbO_3 Solid Solutions

I. P. Raevskiĭ, L. A. Reznichenko, M. P. Ivliev, V. G. Smotrakov, V. V. Eremkin, M. A. Malitskaya, L. A. Shilkina, S. I. Shevtsova, and A. V. Borodin
Institute of Physics, Rostov State University, pr. Stachki 194, Rostov-on-Don, 344090 Russia

Received February 8, 2002; in final form, June 26, 2002

Abstract—(Na, K)NbO_3 crystals with a perovskite structure and a $KNbO_3$ content up to 40 mol % were grown from flux with the use of the solvent $NaBO_2$. The dielectric measurements of the crystals grown revealed phase transitions that had never been observed before in ceramic samples. © *2003 MAIK “Nauka/Interperiodica”.*

INTRODUCTION

The $Na_{1-x}K_xNbO_3$ (NKN) solid solutions of the $NaNbO_3$ antiferroelectric and $KNbO_3$ ferroelectric with a perovskite structure are widely used as ceramics [1, 2]. The number of phase transitions in the $NaNbO_3$ antiferroelectric is maximal among all the perovskites. At present, six phase transitions were recorded in $NaNbO_3$ [1, 3, 4], namely, $U(Pm3m) \longleftrightarrow T_2(P4/mbm) \longleftrightarrow T_1(Ccmm) \longleftrightarrow S(Pmmn) \longleftrightarrow R(Pmnm) \longleftrightarrow P(Pbma) \longleftrightarrow N(R3c)$, which makes the x–T phase diagram of the NKN solid solutions very complicated (Fig. 1a). Hereafter, we use the notation of the $NaNbO_3$ and NKN phases suggested in [3, 4]. Since some phase transitions in $NaNbO_3$ are accompanied by weak anomalies in the their structural, electrophysical, and optical parameters, the data on the x–T phase diagram of NKN solid solutions usually obtained on ceramic samples [1, 2, 4] are rather inconsistent. Although the synthesis of NKN single crystals was reported in a number of publications [5–8], only their structural and optical properties were studied, whereas no dielectric measurements were made at all. Moreover, the maximum x values for NKN single crystals did not exceed 0.25 [5–8]. The present study was undertaken to synthesize NKN single crystals over a wider range of x values and study their dielectric properties.

CRYSTAL GROWTH AND MEASUREMENT METHODS

NKN crystals were grown from flux with the use of the solvent $NaBO_2$ [9]. The starting charge in the form of the Na_2CO_3, K_2CO_3, Nb_2O_5, and B_2O_3 mixture was placed into a platinum crucible, heated for two to three hours at 1000–1060°C, was cooled at a rate of 6–7 K/h down to 930–870°C, and then the remaining melt was poured out. Unlike [5–8], where the NaF solvent was used and the grown crystals had yellow–brown color, we obtained colorless transparent plates 50–200 μm in thickness and several square millimeters in area and isometric crystals with edges of up to 3 mm. All the crystals were faceted by (001) planes of a perovskite basis and were twinned at room temperature.

For comparison, we also studied the $Na_{1-x}K_xNbO_3$ ceramic ($0 \le x \le 0.50$) obtained by two-stage solid-phase synthesis with subsequent sintering under a pressure of 19.6 MPa at 800–850°C with subsequent 40-min-hot pressing at 1100–1200°C.

The composition of crystals with mechanically treated surfaces was analyzed on a Camebax-Micro scanning microscope–microanalyzer. The standards were $NaNbO_3$ and $KNbO_3$ crystals. The error in the determination of the composition ranged within 0.5–4 at. % depending on the x value. The maximum K content attained 40 ± 4 at. %, i.e., was considerably higher than for the NKN crystals grown in [5–8].

The optical, dielectric, and X-ray studies were performed by methods described elsewhere [10].

EXPERIMENTAL RESULTS

X-ray diffraction studies showed that, at low x values, both NKN single crystals and ceramics contained, in addition to ferroelectric phase Q, the antiferroelectric phase P characteristic of $NaNbO_3$. However, unlike the ceramic, where a noticeable presence of the P phase was observed up to $x = 0.020$–0.025, the single crystals showed traces of the P phase at a concentration as low as $x \approx 0.01 \pm 0.005$.

Figure 2 illustrates the evolution of the temperature dependence of the dielectric constant ε of NKN crystals with an increase in the $KNbO_3$ content. The maximum of the $\varepsilon(T)$ curve increases with an increase in x, which correlates with the stabilization of the ferroelectric properties with an addition of potassium [1, 4]. In accordance with the data obtained earlier on ceramic samples [1, 2, 4, 5], a higher $KNbO_3$ content in NKN crystals gives rise, first, to a decrease in the temperature T_m

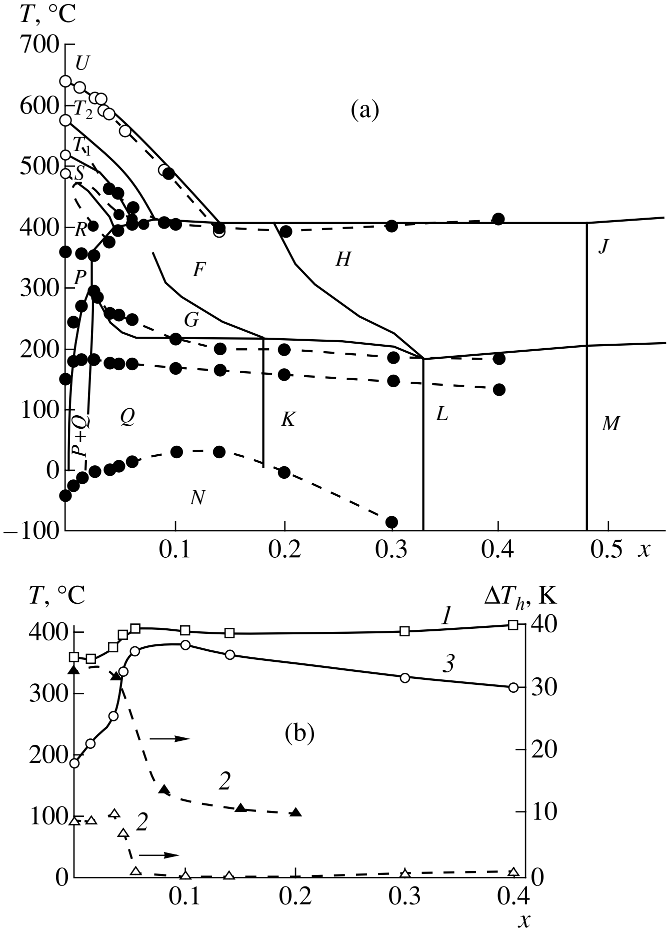

Fig. 1. (a) Phase x–T diagram of $\mathrm{Na}_{1-x}\mathrm{K}_x\mathrm{NbO}_3$ solid solutions and (b) concentration curves of (*1*) the temperature T_m measured on heating, (*2*) the temperature hysteresis ΔT_h of the maximum of ε(T), and (*3*) the Curie–Weiss temperature T_{CW} of $\mathrm{Na}_{1-x}\mathrm{K}_x\mathrm{NbO}_3$ single crystals (empty symbols) and ceramic (filled figures). Phase notation as in [2, 4, 7]. Solid lines are the lines of phase transitions for the ceramic according to [4]. Empty and filled circles indicate the temperatures of phase transitions determined in the present study from the data on dielectric and optical measurements of crystals, respectively. Dashed lines are the assumed lines of phase transitions.

of the maximum on the ε(T) curve and then to its increase, and, vice versa, the temperature of the step corresponding to the $N \longleftrightarrow P$ phase transition first increases and then decreases. Even the lowest potassium content ($x = 0.006 \pm 0.005$) results in the appearance of an additional step on the ε(T) curve in the vicinity of 280°C; with an increase in x, the temperature of this step gradually decreases to ~170°C at $x = 0.40 \pm 0.04$.

In crystals with low a x value which contain, according to the X-ray diffraction data, a small amount of P phase, the dielectric constant ε decreases in a jumpwise manner in the temperature range 40–70°C (Figs. 3b, 3c). These anomalies are characterized by a pronounced temperature hysteresis.

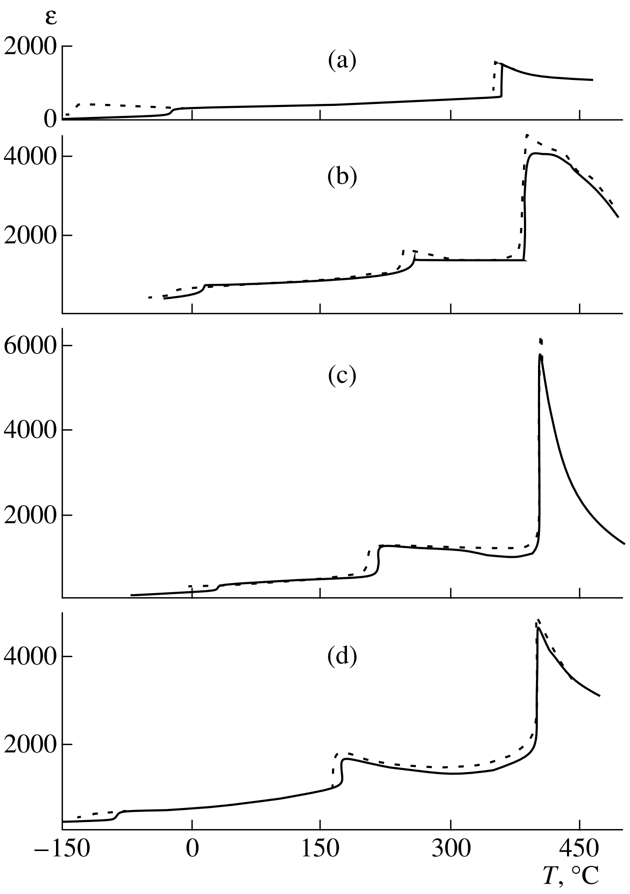

Fig. 2. Change of the ε(T) curves of $\mathrm{Na}_{1-x}\mathrm{K}_x\mathrm{NbO}_3$ crystals with an increase in x. Solid lines are obtained on heating; dashed lines, on cooling. Measurement frequency 100 kHz; x (a) 0, (b) 0.050 ± 0.005, (c) 0.090 ± 0.009, and (d) 0.30 ± 0.03.

The ε(T) dependence of crystals with $0.04 < x < 0.10$ shows kinks above T_m associated with the rotational phase transitions [4] (Figs. 2b, 4b).

Earlier, a small anomaly in ε(T) was observed in the vicinity of 150°C both in NaNbO_3 crystals and ceramics [11–14]; however, it was ignored because of its low value. As is seen from Figs. 2a and 4a, this anomaly is clearly seen only on an appropriate scale. In NKN crystals, this anomaly is also seen with an increase in x; the temperature of this anomaly, first, increases attaining ~185°C at $x = 0.010 \pm 0.005$ and then decreases to ~130°C at $x = 0.40 \pm 0.04$ (Fig. 4a).

The data on dielectric properties of NKN crystals obtained in this study are plotted onto the well-known x–T phase diagram of the (Na, K)NbO_3 system constructed mainly with the use of X-ray diffraction data for the ceramic [4] (Fig. 1a).

DISCUSSION

In general, the x–T phase diagram obtained in this study agrees with the well-known phase diagram. At

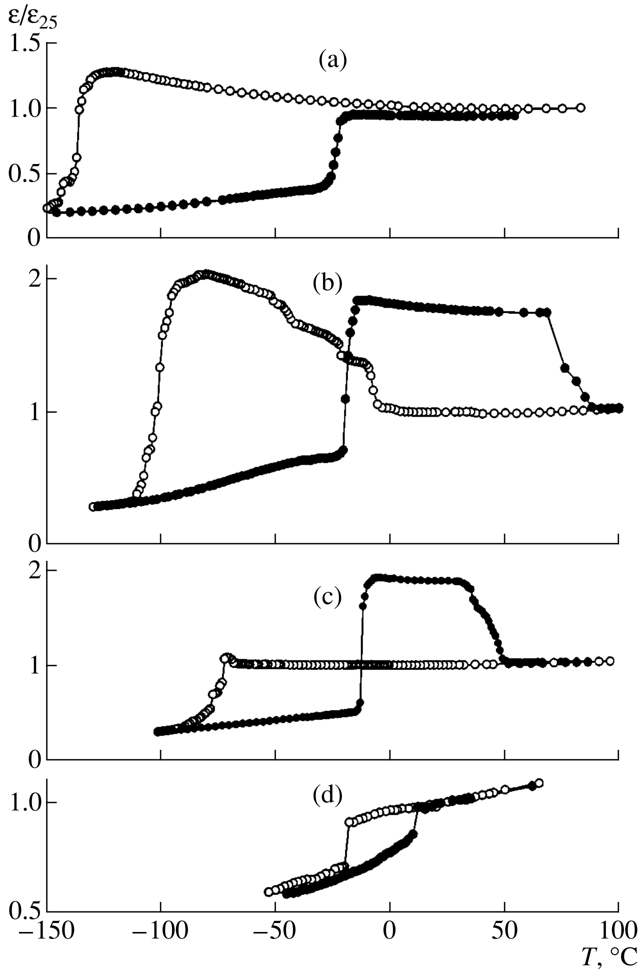

Fig. 3. Change of the low-temperature anomalies in ε(*T*) curves of $Na_{1-x}K_xNbO_3$ crystals with an increase in potassium content (ε_{25} is the ε value at 25°C). Measurement frequency, 100 kHz. Filled circles indicate the data obtained on heating; empty circles, on cooling; *x* (a) 0, (b) 0.006 ± 0.005, (c) 0.010 ± 0.005, and (d) 0.055 ± 0.005.

the same time, study of the dielectric properties of NKN crystals allowed us to reveal phase transitions and specific features of some properties that had never been observed before in the studies of ceramic samples.

According to [3], $NaNbO_3$ undergoes two phase transitions in the temperature range from –150 to 400°C, where the structural transformations $N \longleftrightarrow P$ and $P \longleftrightarrow R$ are observed. It was repeatedly indicated [1, 3, 15] that, since the difference in the structural parameters of the *N* and *P* phases in $NaNbO_3$ is quite pronounced, the phase transition $N \longleftrightarrow P$ is characterized by a very high temperature hysteresis. In real $NaNbO_3$ crystals, this transition as is seen from Fig. 3a does not proceed simultaneously in the whole volume, and, therefore, the ε(*T*) curve has jumps corresponding to the phase transitions undergone by individual parts of the crystal. Similar jumps are also observed in NKN crystals with a low potassium content (Figs. 3b, 3c).

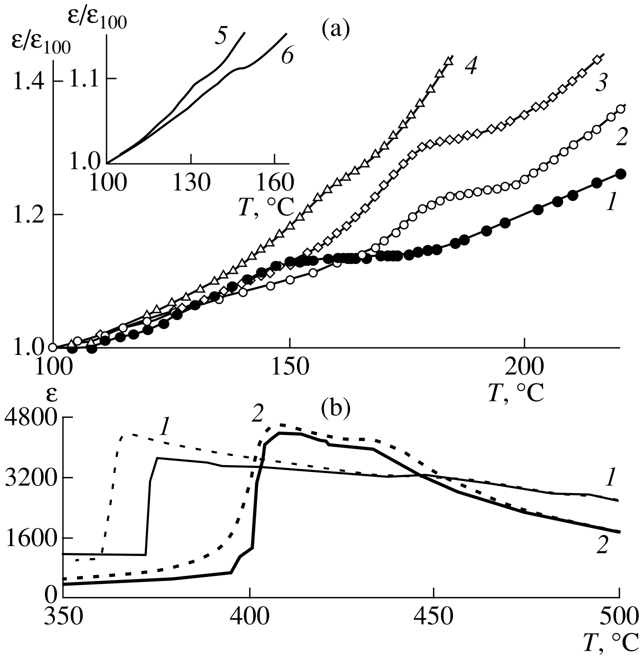

Fig. 4. (a) Change of the anomalies in ε(*T*) of $Na_{1-x}K_xNbO_3$ crystals observed with an increase in *x* in various temperature ranges. Measurement frequency 100 kHz; *x* (*1*) 0, (*2*) 0.006 ± 0.005, (*3*) 0.010 ± 0.005, (*4*) 0.130 ± 0.015, (*5*) 0.30 ± 0.03, and (*6*) 0.40 ± 0.04. (b) Measurements made in the heating mode (ε_{100} is the ε value at 100°C); *x* (*1*) 0.030 ± 0.005, (*2*) 0.055 ± 0.005. Solid lines correspond to heating; dashed lines, to cooling.

With an increase in *x*, the value of the step on ε(*T*) corresponding to the phase transition $N \longleftrightarrow P(Q, K, L, \ldots)$ and the value of its temperature hysteresis decrease; i.e., the structural parameters of the high- and low-temperature phases become closer.

Unlike other anomalies in ε(*T*) observed in all the crystals studied, the anomaly in the temperature range 40–80°C manifests itself only in crystals with $0.006 \le x \le 0.015$ containing the *P* and *Q* phases simultaneously. Earlier, the $NaNbO_3$ crystals containing, along with the *P* phase, the impurity *Q* phase showed anomalies in the temperature dependences of the lattice parameter in the temperature range 75–190°C, which were explained by the $P \longleftrightarrow Q$ [16] phase transition. These were first-order phase transitions, which, in particular, was confirmed by a pronounced temperature hysteresis ΔT_h. It seems that the anomalies in ε in the range 40–80°C in two-phase NKN crystals with a high ΔT_h value (Figs. 3b, 3c) are also explained by the $P \longleftrightarrow Q$ phase transition. This assumption is confirmed by the fact that, unlike other anomalies in ε(*T*), this anomaly is characterized by a decrease in ε at higher *T*. Indeed, the dielectric susceptibility in the ferroelectric phase is usually lower than in the antiferroelectric phase because of a high internal field and, therefore, one can expect a decrease in ε in the $P \longrightarrow Q$

transition, as in the case of the $P \longrightarrow N$ transition in $NaNbO_3$ (Figs. 2a, 3a).

A small anomaly in $\varepsilon(T)$ observed in the vicinity of 150°C for $NaNbO_3$ and in the range 130–185°C for NKN is accompanied by rather weak variations in the slope of the temperature curves of the unit-cell parameter [14]. Earlier, study of the dielectric properties [14] and Raman spectra [17] allowed one to draw the conclusion that this anomaly in $\varepsilon(T)$ in $NaNbO_3$ is caused by a phase transition. Our X-ray diffraction studies of $NaNbO_3$ crystals performed at various temperatures showed the formation of an incommensurate phase in the temperature range 135–165°C. The modulation period of this phase depends on the sample history and ranges within 35–50 nm. It seems that the diffuse $\varepsilon(T)$ anomaly observed in $NaNbO_3$ and NKN crystals in the temperature range 130–190°C is provided by two close phase transitions: initial phase $\longleftrightarrow$ incommensurate phase $\longleftrightarrow$ initial phase. This assumption is favored by the fact that the phase transition to the incommensurate phase in the $Sr_2Nb_2O_7$ and $Ca_2Nb_2O_7$ with a layer perovskite-like structures is also accompanied by low anomalies in $\varepsilon(T)$ [18].

One more anomaly not observed in ceramics is the kink on the dependence $\varepsilon(T)$ for a crystal with $x = 0.090 \pm 0.009$ in the vicinity of 300°C (Fig. 2c), which seems to correspond to the transition between the G and F phases. Earlier, this phase transition was recorded only in X-ray diffraction measurements [5]. The extrapolation of the structural data [4] allowed one to determine the coordinates of the triple point corresponding to the intersection of the $G \longleftrightarrow F$ and $F \longleftrightarrow T_1$ lines, namely, $x \approx 0.07$. At the same time, if one assumes that a small step on the dependence $\varepsilon(T)$ for a crystal with $x = 0.055 \pm 0.005$ preceding the maximum in ε (Fig. 4b, curve *2*) corresponds to the line of the $G \longrightarrow F$ transitions, then the coordinate of the triple point would be $x \approx 0.050$–0.055. This assumption is confirmed by the kink in the dependence $T_m(x)$ in the range of these x values and a dramatic decrease in the Curie–Weiss temperature at $x < 0.05$ (Fig. 1b).

Another characteristic feature of the dielectric properties of NKN crystals never observed earlier is a dramatic decrease in the temperature hysteresis ΔT_h of the maximum of $\varepsilon(T)$ at $x > 0.05$. In the $NaNbO_3$ and NKN crystals with $x < 0.04$, the temperature hysteresis equals ≈10 K, whereas at $x > 0.1$, it does not exceed 0.2–0.4 K. We also observed an analogous decrease in ΔT_h in the NKN ceramic in the region with $x \approx 0.05$ (Fig. 1b). At the same time, the ΔT_h value in the ceramic is much higher than in crystals, which seems to be associated with partial evaporation of Na_2O during sintering. Indeed, as we showed earlier [19], the ΔT_h values in the nonstoichiometric $Na_{1-x}NbO_{3-x/2}$ ceramic ($0 < x < 0.1$) increase with x. A similar increase in ΔT_h was also observed in $NaNbO_3$ crystals at a higher deficit in oxygen [20].

A decrease in ΔT_h for NKN crystals at $x > 0.05$ correlates with a dramatic decrease in the difference between T_m and the Curie–Weiss temperature T_{CW} (Fig. 1b) and also with a change in the shape of the maximum of ε approaching the shape typical of second-order phase transitions (Fig. 2c). At first glance, these changes are analogous to those observed in the $PbZrO_3$–$PbTiO_3$ system, where an addition of ≈6 mol % $PbZrO_3$ to the antiferroelectric $PbTiO_3$ phase results in the change of the first-order phase transition into the second-order transition [21]. However, analysis based on the phenomenological theory of phase transitions showed that, if an analogous situation had taken place in the $(Na_{1-x}, K_x)NbO_3$ system, in other words, at $x \approx 0.10$, the line of first-order phase transitions between the phases T_2 and F would have ended at a critical point and transformed into the line of second-order phase transitions. Then, in the vicinity of the latter phase transition there would have existed a phase with the symmetry *Pmc*. However, according to [4], the T_2 phase is adjacent to the F phase with the symmetry *P*2*mm*, which contradicts the assumption that a critical point exists in the $(Na_{1-x}, K_x)NbO_3$ system. According to the phenomenological model, a decrease in ΔT_h can be caused by a decrease in the section x = const of the region, where the paraelectric and ferroelectric phases coexist for the compositions with $x > 0.05$.

In conclusion, we would like to note that, strictly speaking, the solid solutions considered above are not equilibrium, because the experimental conditions (very weak diffusion, limited time, etc.) cannot guarantee their optimum compositions. However, the diffusion-free character of phase transitions and the absence of noticeable variations in the composition and properties within quite long time intervals (years) allow us to consider these solid solutions as quasi-equilibrium with negligible deviations from the equilibrium. Therefore, the concentration x may be considered as an external thermodynamic parameter without any loss of the generality of our study, and the results obtained (in particular the x–T phase diagrams) may be considered consistent with the Gibbs chemical thermodynamics of heterogeneous systems.

CONCLUSION

Thus, $(Na_{1-x}, K_x)NbO_3$ crystals with a considerably higher $KNbO_3$ content (up to 40 mol %) than before were grown from flux.

Like the ceramic, the real $(Na, K)NbO_3$ crystals at low x values show the coexistence of the antiferroelectric (P) and ferroelectric (Q) orthorhombic phases. The two-phase crystals show typical anomalies in $\varepsilon(T)$ with pronounced temperature hysteresis in the temperature range 40–80°C provided by the $P \longleftrightarrow Q$ phase transitions.

Small anomalies in $\varepsilon(T)$ for (Na, K)NbO_3 crystals in the temperature range 130–190°C seem to be caused by the formation of an incommensurate phase in this temperature range.

One of the possible explanations for the pronounced difference in the dielectric properties of (Na, K)NbO_3 single crystals and ceramics is the noncontrollable deficit in Na_2O (K_2O) in the ceramic.

ACKNOWLEDGMENTS

This study was supported by the Russian Foundation for Basic Research, project nos. 02-02-17781 and 01-03-33119.

REFERENCES

1. G. A. Smolenskiĭ, V. A. Bokov, V. A. Isupov, N. N. Kraĭnik, R. E. Pasynkov, A. I. Sokolov, and N. K. Yushin, *Physics of Ferroelectric Phenomena* (Nauka, Leningrad, 1985).
2. B. Jaffe, W. R. Cook, and H. Jaffe, *Piezoelectric Ceramics* (Academic, New York, 1971; Mir, Moscow, 1974).
3. H. D. Megaw, Ferroelectrics **7**, 87 (1974).
4. M. Ahtee and A. W. Hewat, Acta Crystallogr., Sect. A: Cryst. Phys., Diffr., Theor. Gen. Crystallogr. **34**, 309 (1978).
5. G. Shirane, R. Newnham, and R. Pepinsky, Phys. Rev. **96**, 581 (1954).
6. L. E. Cross, Nature **181**, 178 (1958).
7. M. Ahtee and A. M. Glazer, Acta Crystallogr., Sect. A: Cryst. Phys., Diffr., Theor. Gen. Crystallogr. **32**, 434 (1976).
8. M. Badurski and K. Stroz, J. Cryst. Growth **46**, 274 (1979).
9. O. A. Zhelnova, V. G. Smotrakov, I. P. Raevskiĭ, and E. G. Fesenko, Kristallografiya **28** (6), 1052 (1983) [Sov. Phys. Crystallogr. **28**, 623 (1983)].
10. I. P. Paevski, V. G. Smotrakov, V. V. Eremkin, *et al.*, Ferroelectrics **247**, 27 (2000).
11. N. N. Kraĭnik, Fiz. Tverd. Tela (Leningrad) **2**, 685 (1960) [Sov. Phys. Solid State **2**, 633 (1960)].
12. L. Pardo, P. Duran-Martin, J. P. Mercurio, *et al.*, J. Phys. Chem. Solids **58** (9), 1335 (1997).
13. K. Konieczny, Mater. Sci. Eng. B **60**, 124 (1999).
14. I. P. Raevskiĭ, L. A. Reznichenko, V. G. Smotrakov, *et al.*, Pis’ma Zh. Tekh. Fiz. **26** (16), 97 (2000) [Tech. Phys. Lett. **26**, 744 (2000)].
15. C. N. W. Darlington and H. D. Megaw, Acta Crystallogr., Sect. B: Struct. Crystallogr. Cryst. Chem. **29**, 2171 (1973).
16. I. Lefkowitz, K. Lukaszewicz, and H. D. Megaw, Acta Crystallogr. **20**, 670 (1966).
17. X. B. Wang, Z. X. Shen, Z. P. Hu, *et al.*, J. Mol. Struct. **385**, 1 (1996).
18. N. A. Zakharov, V. P. Orlovskiĭ, and V. A. Klyuev, Izv. Ross. Akad. Nauk, Ser. Fiz. **60**, 85 (1996).
19. S. O. Lisitsyna, I. P. Raevskiĭ, S. M. Maksimov, *et al.*, Izv. Akad. Nauk SSSR, Neorg. Mater. **21**, 997 (1985).
20. A. Molak, Solid State Commun. **62**, 413 (1987).
21. R. W. Whatmore, R. Clarke, and A. M. Glazer, J. Phys. C: Solid State Phys. **11**, 3089 (1978).

Translated by L. Man

Crystallography Reports, Vol. 48, No. 3, 2003, pp. 491–499. Translated from Kristallografiya, Vol. 48, No. 3, 2003, pp. 536–544.

Prediction of Piezoelectric Properties of Crystal–Ceramic Composites

S. V. Glushanin, V. Yu. Topolov, and A. V. Turik

Faculty of Physics, Rostov State University, ul. Zorge 5, Rostov-on-Don, 344090 Russia

e-mail: topolov@phys.rsu.ru

e-mail: turik@phys.rsu.ru

Received December 12, 2001; in final form, March 28, 2002

Abstract—In the framework of the model of a piezoelectrically active ferroelectric crystal–ceramic composite of the 0–3 type, the concentration dependences of the effective piezoelectric properties of this composite are determined. Two examples of such composites are discussed: the single-domain $PbTiO_3$ crystal $(Pb_{1-x}Ca_x)TiO_3$ ceramic and the polydomain $PbTiO_3$ crystal $(Pb_{1-x}Ca_x)TiO_3$ ceramic. Based on these examples, we analyzed the effect of the 90° domain structure, the form of crystalline inclusions, the remanent polarization of the ceramics, molar Ca concentration (x), and other factors of the effective piezoelectric coefficients e^*_{3j} and d^*_{3j} and their anisotropy. The relation between the piezoelectric polarization of the composite to single-domain inclusions and the anisotropy of its piezoelectric coefficients is also studied. © *2003 MAIK “Nauka/Interperiodica”.*

INTRODUCTION

Over the last few decades, the problems of manufacturing highly efficient piezoelectrics and the prediction and optimization of their properties have remained rather topical. Among the new materials, the crystal–ceramic composites with ferro- and piezoelectric activity (CCCFPA) are of special interest. The details of the synthesis of these materials based on $(Pb_{1-x}Ca_x)TiO_3$ perovskite-like solid solutions are described in [1] together with the results of the crystallo-optical study of the microstructure of $PbTiO_3$ crystal $(Pb_{1-x}Ca_x)TiO_3$ ceramic composites characterized by connectivity of the 0–3 type according to the Newnham classification [2]. Interest in the $PbTiO_3$ ferroelectric [3–5] and in the related solid solutions (for example, $PbTiO_3$–$Pb(Zn_{1/3}Nb_{2/3})O_3$ [6–8], $PbTiO_3$–$Pb(Mg_{1/3}Nb_{2/3})O_3$ [6, 9], $(Pb_{1-x}Ca_x)TiO_3$ [10, 11], $Pb(Zr_{1-y}Ti_y)O_3$ [6, 12–14], etc.), the potential components of crystal–ceramic composites with pronounced ferro- and piezoelectric activity, stems from their set of unique piezoelectric, dielectric, electrostriction, and other physical properties. In particular, the experimental studies of $PbTiO_3$ crystals [15, 16] and $PbTiO_3$-based polarized ferroelectric ceramics (PFC) [10, 17] stimulated interest in the physical nature of pronounced anisotropy of the piezoelectric moduli $d_{33}^{(FC)}/d_{31}^{(FC)}$ [18, 19] of these PFC[1] and the characteristics of the piezoelectric response of polydomain ferroelectric crystals [20, 21], PFC [22, 23], and PFC–polymer composites [24, 25]. At the same time, the effective parameter of the CCCFPA materials has not been studied as yet either theoretically or experimentally. Below, we report the results of the theoretical study of the piezoelectric characteristics of the $(Pb_{1-x}Ca_x)TiO_3$-based CCCFPA materials with the aim of interpreting the details of the electromechanical interactions of their components and the nontrivial behavior of the effective piezoelectric coefficients.

MODEL CONCEPTS AND THE AVERAGING PROCEDURES

In the course of manufacturing and experimental study of the $(Pb_{1-x}Ca_x)TiO_3$-based CCCFPA materials, it was noticed in [1] that the crystal–PFC interfaces have structural discontinuities. The relation of these discontinuities to the physical characteristics of these composite materials was also established. The study of the microstructure of the CCCFPA materials revealed the uniform distribution of the $PbTiO_3$ crystals that have the shape of a rectangular parallelepiped in the PFC matrix, the related displacement of the crystal–PFC boundaries, and the corresponding interaction of the crystal with the nearest crystallites in the PFC. Based on results reported in [1] and the experimental data [3–5, 10, 17, 19] on $PbTiO_3$-based PFC, we developed a model of the CCCFPA material that takes into account the discontinuities in the structure at the interfaces between a single-domain crystal and PFC or at the interfaces between a polydomain crystal and PFC. In

---

[1] Hereafter the superscripts FC and cr indicate the PFC and crystalline inclusions, respectively, and an asterisk denotes the physical parameters characterizing the CCCFPA materials.

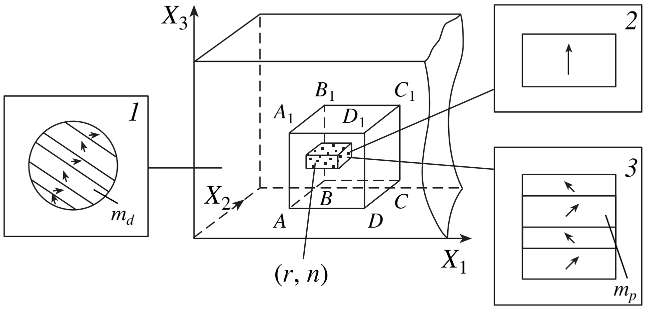

Fig. 1. Schematic representation of the structure of CCCFPA materials with the 0–3 type of connectivity. The inclusion in the shape of a rectangular parallelepiped with the square base indicated by dotted shading is characterized by the concentration parameters n and r, with n being the ratio of the parallelepiped height and the length of the $|AA_1|$ edge of the cube and r, the ratio of the base area of the parallelepiped to the area $|AB|^2$ of the cube face. Inset *1* shows the 90° domain structure of a crystallite in a PFC. Insets *2* and *3* show the fragments of single-domain and polydomain inclusions, respectively. The polarization vectors in the domains are indicated by arrows; $m = nr$ is the volume concentration of the inclusions; m_d is the volume concentration of the domains in the PFC crystallites, whose spontaneous-polarization vectors $\mathbf{P}_{dj}$ are inclined by a smaller angle to the OX_3 axis; m_p is the volume concentration of the inclusion domains that have positive projections of the spontaneous-polarization vectors $\mathbf{P}_{sk}$ onto the OX_1 axis.

this model, the CCCFPA material is represented as a cellular matrix (i.e., a system formed by the Banno cubic unit cells [26] in the sequence $ABCDA_1B_1C_1D_1$ uniformly filling the whole sample volume). The matrix is polarized along the OX_3 axis of the Cartesian coordinate system $(X_1X_2X_3)$ (see Fig. 1). The inclusions with $n \ll \sqrt{r}$ favor the pronounced relaxation of the internal mechanical stresses caused by the difference in the elastic moduli $c_{ab}^{(cr)}$ and $c_{ab}^{(FC)}$ components during hot pressing of the CCCFPA materials or the motion of the intercomponent boundaries of the composite [1]. The inclusions with $n \gg \sqrt{r}$ favor a significant decrease in the depolarization energy. In the simplest case, the orientation of spontaneous-polarization vectors in the inclusion domains is assumed to be fixed and is set in the coordinate system $(X_1X_2X_3)$ in the following way: $\mathbf{P}_s(0;\ 0;\ P_s)$ (Fig. 1, inset *2*) or $\mathbf{P}_{s1}(P_s/\sqrt{2};\ 0;\ P_s/\sqrt{2})$, $\mathbf{P}_{s2}(-P_s/\sqrt{2};\ 0;\ P_s/\sqrt{2})$ (Fig. 1, inset *3*). Here we have $|\mathbf{P}_{sk}| = |\mathbf{P}_s|$. The 180° domain reversals are assumed to be fully performed in the process of CCCFPA polarization, whereas the 90° domain structure of the crystallites in PFC (Fig. 1, inset *1*) and the inclusions with $\mathbf{P}_{sk}$ ($k = 1, 2$; Fig. 1, inset *3*) are characterized as layered (according to the experimental results [16, 28] on the ferroelectric $4mm$ phase of the $PbTiO_3$ crystals and of the $PbTiO_3$-based solid solutions). The 90° domain walls inside the inclusions and crystallites are assumed to be virtually motionless, as was established in experiments on tetragonal $PbTiO_3$-based PFC compounds [29]. According to [19], the vectors of spontaneous polarization $\mathbf{P}_{gr} = m_d\mathbf{P}_{d1} + (1 - m_d)\mathbf{P}_{d2}$ of crystallites in the polarized PFC are oriented in such a way that $0 \le \theta \le \theta_m$, where θ_m is the largest angle formed by $\mathbf{P}_{gr}$ and the poling field vector $\mathbf{E} \parallel OX_3$ with due regard for 180° and 90° domain reorientations in the $4mm$ phase, with $\theta_m = 45°$ in the case of crystallites divided into 90° domains [30]. Then, to describe the polarization process in PFC and to simplify the relationship [19, 30] between the effective electromechanical parameters and the remanent polarization $P_R^{(FC)}$ in PFC, we introduce the angle $\theta' = 180° - \theta$. The value of angle θ' increases from 0° to $180° - \theta_m$ with the poling electric field E, along with the growth of $P_R^{(FC)}$. The corresponding orientation dependence of the complete set of elastic compliances $s_{ab}^{(FC),\,E}(\theta')$, piezoelectric moduli $d_{ij}^{(FC)}(\theta')$, and dielectric constants $\varepsilon_{pp}^{(FC),\,\sigma}(\theta')$, denoted for brevity as $Y_{fg}^{(FC)}(\theta')$, characterizes the variation in the electromechanical parameters of PFC with a growth of $P_R^{(FC)}$. The electromechanical constant of the polydomain regions (Fig. 1, insets *1*, *3*) similar to $Y_{fg}^{(FC)}$ are determined as a result of the averaging procedure [31, 32] over the volume concentration of m_d or m_p. The obtained dependences on m_d are used in the averaging procedure in the framework of the effective medium method [18, 30]. As a result, we obtain a complete set of electromechanical constants of ferroelectric ceramics, $Y_{fg}^{(FC)} = Y_{fg}^{(cr)}(m_d)$. The electromechanical constants of a crystalline inclusion $Y_{fg}^{(cr)} = Y_{fg}^{(cr)}(m_p)$ (in the case of a single-domain inclusion shown in inset *2* of Fig. 1, $Y_{fg}^{(cr)}$ are independent of both m_p and θ') and of the PFC matrix $Y_{fg}^{(FC)} = Y_{fg}^{(FC)}(m_d, \theta')$ or $Y_{fg}^{(FC)} = Y_{fg}^{(FC)}(m_d, x)$ are used to determine the electromechanical parameters of the CCCFPA materials by the matrix method [25]. The calculations of $Y_{fg}^{(cr)}$ and $Y_{fg}^{(FC)}$ components of the composite and of Y_{fg}^{*} for the CCCFPA materials are performed using the elastic, piezoelectric, and dielectric constants of single-domain $PbTiO_3$ crystals [30] and $(Pb_{1-x}Ca_x)TiO_3$ $(0.1 \le x \le 0.3)$ at room temperature.

The constants of $(Pb_{1-x}Ca_x)TiO_3$ are evaluated by the method reported in [18] using the elastic, piezoelectric, and dielectric constants of single-domain of $PbTiO_3$ crystals, and the concentration dependences [10] of permittivity, remanent polarization, and the parameters of the perovskite unit cell of the $(Pb_{1-x}Ca_x)TiO_3$ PFC. According to our estimates, for example, at $x = 0.24$ (i.e., near $\max[d_{33}^{(FC)}/|d_{31}^{(FC)}|]$ of the

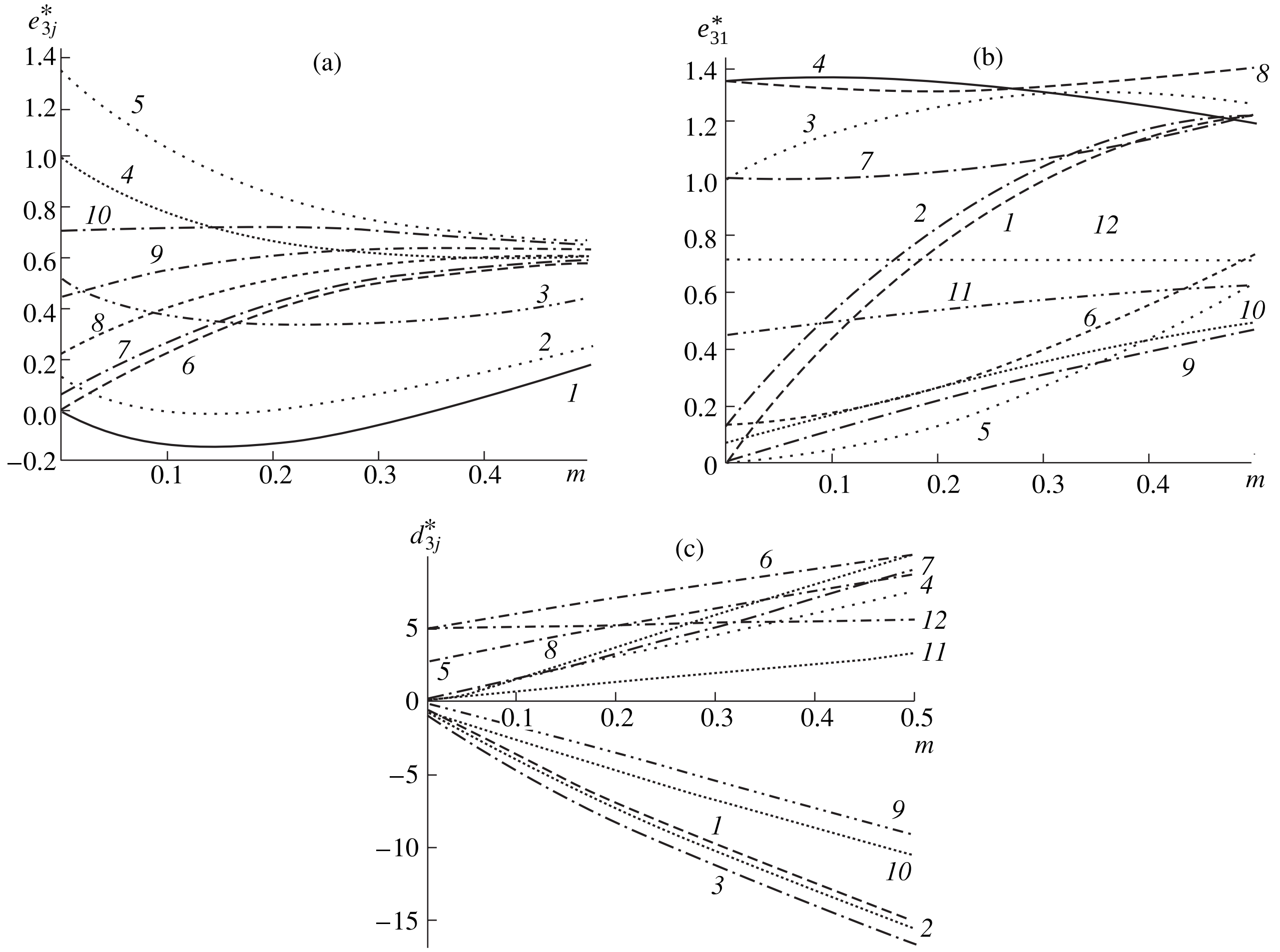

Fig. 2. Calculated curves demonstrating the behavior of the effective piezoelectric coefficients $e^*_{3j}(m, \theta')$ (in units of C/m^2) and $d^*_{3j}(m, \theta')$ (in units of pC/N) for (a, c) the CCCFPA single-domain $PbTiO_3$ crystal of cubic shape–$(Pb_{0.76}Ca_{0.24})TiO_3$ PFC (m_d = 0.5) and (b, c) the CCCFPA polydomain $PbTiO_3$ crystal of cubic shape (m_p = 0.5)–$(Pb_{0.76}Ca_{0.24})TiO_3$ PFC (m_d = 0.5). (a) e^*_{31} (angle θ' characterizing the remanent polarization takes the values 0°, 30°, 60°, 90°, and 135° (curves *1*, *2*, *3*, *4*, and *5*, respectively)), 10^{-1} e^*_{33} (θ' = 0°, 30°, 60°, 90°, and 135° (curves *6*, *7*, *8*, *9*, and *10*, respectively)); (b) e^*_{31} (θ' = 0°, 30°, 90°, and 135° (curves *1*, *2*, *3*, and *4* respectively)), e^*_{32} (θ' = 0°, 30°, 90°, and 135° (curves *5*, *6*, *7*, and *8*, respectively)), 10^{-1} e^*_{33} (θ' = 0°, 30°, 90°, and 135° (curves *9*, *10*, *11*, and *12*, respectively)); (c) d^*_{31} (θ' = 0°, 90°, and 135° (curves *1*, *2*, and *3*, respectively)), 10^{-1} d^*_{33} (θ' = 0°, 90°, and 135° (curves *4*, *5*, and *6*, respectively)) for the CCCFPA with single-domain inclusions; d^*_{31} (θ' = 0° and 135° (curves *7* and *8*, respectively)), d^*_{32} (θ' = 0° and 135° (curves *9*, and *10*, respectively)), 10^{-1} d^*_{33} (θ' = 0° and 135° (curves *11* and *12*, respectively)) for the CCCFPA with polydomain inclusions. The volume concentration of polycrystalline inclusions is assumed to be equal to $m = nr$.

corresponding PFC [10, 18]), the single-domain crystal is characterized by elastic compliances s^E_{11} = 7.09, s^E_{12} = –1.61, s^E_{13} = –6.85, s^E_{33} = 30.4, s^E_{44} = 12.8, and s_{66} = 7.60 (in units of 10^{-12} Pa^{-1}); piezoelectric moduli d_{33} = 188, d_{31} = –40.8, and d_{15} = 68.6 (in the units of pC/N); and the dielectric constants $\varepsilon^\sigma_{11}/\varepsilon_0$ = 213 and $\varepsilon^\sigma_{33}/\varepsilon_0$ = 198. Below, we discuss some features of the behavior of the effective piezoelectric coefficients d^*_{3j} and e^*_{3q} for such composites as single-domain $PbTiO_3$ crystal–$(Pb_{1-x}Ca_x)TiO_3$ PFC (point symmetry group 4*mm*) and polydomain $PbTiO_3$ crystal–$(Pb_{1-x}Ca_x)TiO_3$ PFC (point symmetry group *mm*2). In all the case analyzed, the volume concentration of inclusions is $m \leq 0.5$ (according to the experimental data reported in [1]).

ORIENTATION AND CONCENTRATION DEPENDENCE OF PIEZOELECTRIC COEFFICIENTS e^*_{3j} AND d^*_{3j}

The e^*_{3j} (m, θ') curves shown in Figs. 2a and 2b demonstrate a pronounced effect of the 90° domain structure of the PFC crystallites, inclusions, and remanent polarization of PFC on the piezoelectric coefficients e^*_{3j} of the CCCFPA materials. The $d^*_{3j}(m, \theta')$ curves (Fig. 2c) are strongly dependent on the 90° domain structure of inclusions. In particular, in the presence of polydomain inclusions (Fig. 1, inset *3*), the change in sign d^*_{31} is observed (Fig. 2c) because $d^{(cr)}_{31} > 0$ (this is characteristic of the polydomain $PbTiO_3$ crystal with $m_p = 0.5$ [30]). We also observed a fast variation of the anisotropy factors for the piezoelectric moduli of CCCFPA materials, $\zeta_{d,3j}^*(m, \theta') = d^*_{33}(m, \theta')/d^*_{3j}(m, \theta')$ ($j = 1; 2$, $\theta' = \text{const}$). The low values of $d^{(FC)}_{31}$ for PFC at $x = 0.24$ [10] and $0° < \theta' \le 135°$ [19] lead to the high anisotropy of d^*_{3j} at $m \le 0.1$ independent of the domain structure of inclusions (Fig. 1, insets *2*, *3*).

For different CCCFPA materials, it was found that their piezoelectric coefficients e^*_{3j} exhibit a nonmonotonic concentration dependence (see, for example, $e^*_{3j}(m, \theta')$ curves at $\theta' = \text{const}$ in Figs. 2a and 2b, $e^*_{3j}(r, n)$ surfaces in Figs. 3a, 3c, and $e^*_{3j}(m, x)$ curves at $x = \text{const}$ in Figs. 4a–4c). At the same time, the piezoelectric moduli $d^*_{3j}(m, \theta')$ at $\theta' = \text{const}$, $d^*_{3j}(r, n)$, and $d^*_{3j}(m, x)$ at $x = \text{const}$ vary monotonically (see Figs. 2c, 3d, 3f, 4b, 4d). From the relationships between the piezoelectric coefficients e^*_{3j} and d^*_{3j} [33], it follows that the nonmonotonic behavior of e^*_{3j} results from the concentration dependence of elastic compliances s^{*E}_{ab} obtained by averaging [25] of compliances $s^{(FC),E}_{ab}$ for the PFC matrix (∞mm symmetry) and $s^{(cr),E}_{ab}$ for the inclusions (point symmetry groups $4mm$ and $mm2$ for single- and polydomain crystals, respectively) with due regard for the electromechanical interactions between the components. In the wide range of (m, θ') or (m, x), the following relationships are valid for the CCCFPA materials with cubic polydomain inclusions:

$$e^*_{31}(m, \theta') \approx e^*_{32}(m, \theta'); \quad d^*_{31}(m, \theta') \approx -d^*_{32}(m, \theta') \quad (1)$$

(Figs. 2b, 2c) or

$$e^*_{31}(m, x) \approx e^*_{32}(m, x); \quad d^*_{31}(m, x) \approx -d^*_{32}(m, x) \quad (2)$$

(Figs. 4c, 4d). This is an additional indication of the important role of s^{*E}_{ab} in the formation of the characteristic features of e^*_{3j}. At fixed (θ', x), the following relationships are valid for the CCCFPA materials with polydomain inclusions in the form of a parallelepiped:

$$e^*_{31}(r, n) \approx e^*_{32}(r, n); \quad d^*_{31}(r, n) \approx -d^*_{32}(r, n) \quad (3)$$

(Figs. 3a, 3b, 3d, and 3e). Using the relationships from [33], we can find that the effective piezoelectric moduli for the corresponding CCCFPA materials as $d^*_{31} = e^*_{3j}s^{*E}_{j1} \approx e^*_{31}(s^{*E}_{11} + s^{*E}_{12} + \zeta^*_{e,31}s^{*E}_{13})$ and $d^*_{32} = e^*_{3j}s^{*E}_{j2} \approx e^*_{31}(s^{*E}_{12} + s^{*E}_{22} + \zeta^*_{e,31}s^{*E}_{23})$, where $\zeta^*_{e,31} = e^*_{33}/e^*_{31}$. Then, according to conditions (1)–(3), the following equality is fulfilled for elastic compliances s^{*E}_{ab} in the CCCFPA materials: $s^{*E}_{11} + 2s^{*E}_{12} + s^{*E}_{22} \approx -\zeta^*_{e,31}(s^{*E}_{13} + s^{*E}_{23})$. The resulting balance between the averaged compliances $s^{*E}_{kl} > 0$ and $s^{*E}_{pq} < 0$ ($kl = 11; 22$, $pq = 12; 13; 23$) eventually determines the characteristic features of the concentration dependence of e^*_{3j} and ensures the fulfillment of the conditions $e^*_{31} > 0$ and $e^*_{32} > 0$ in a wide range of values of (m, θ', x) and other parameters. Earlier, no cases were found where relationships of the type (1)–(3) were satisfied in the polydomain crystals or in the two-component composites (see, for example, [20, 21, 24, 25]).

The effect of the sample geometry on the piezoelectric properties of the CCCFPA materials is illustrated by the $e^*_{3j}(r, n)$ and $d^*_{3j}(r, n)$ plots in Fig. 3. Passing from the curves $e^*_{3j}(m, \theta')$ (Fig. 2b) to the sections of $e^*_{3j}(r, n)$ surfaces (Figs. 3a–3c) by the planes $r = \text{const}$ or $n = \text{const}$, one can see that there are only slight differences between the corresponding concentration dependences of e^*_{3j} for the polarized CCCFPA materials ($\theta' = 135°$) with polydomain cubic inclusions and similar CCCFPA with polydomain inclusions in the shape of rectangular parallelepipeds. The change in the shape of inclusions from a cube to a parallelepiped produces only an insignificant effect on the d^*_{3j} moduli in the CCCFPA materials. The relative changes in e^*_{3j} and d^*_{3j} caused by the variation of the volume content of 90° domains in crystallites ($0.5 < m_d < 1$; Fig. 1, inset *1*) do not exceed 5%. The e^*_{3j} and d^*_{3j} parameters remain almost constant because of the action of the following mechanisms. First, the change in the inclusion shape from a cube to a parallelepiped provides no significant redistribution of the electric and stress fields in the components of a composite that has comparable values of the parameters $s^{(cr),E}_{ab}$ and $s^{(FC),E}_{ab}$, $e^{(cr)}_{kl}$ and $e^{(FC)}_{kl}$, and $\varepsilon^{(cr),\sigma}_{pp}$ and $\varepsilon^{(FC),\sigma}_{pp}$. Second, the conditions $|d^{(cr)}_{3j}| \gg |d^{(FC)}_{31}|$ and $|d^{(cr)}_{3j}| \sim d^{(FC)}_{33}$ ($j = 1; 2$) valid for the components of the CCCFPA materials under study

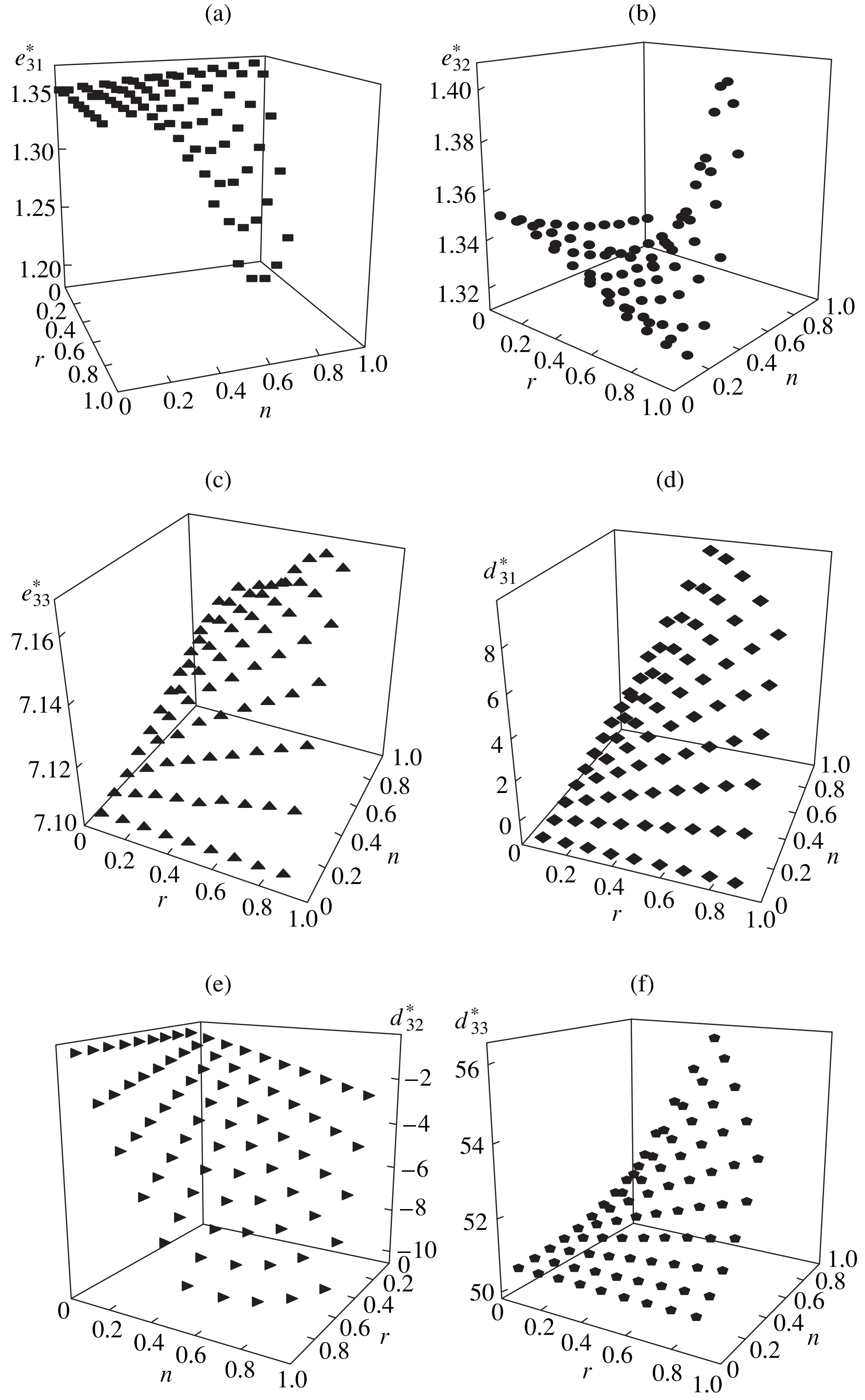

Fig. 3. The calculated concentration dependence for the effective piezoelectric coefficients e^*_{3j} (r, n) (in units of C/m^2) and d^*_{3j} (r, n) (in units of pC/N) for (a, c) the CCCFPA polydomain PbTiO$_3$ crystal (m_p = 0.5) of rectangular parallelepiped shape (Pb$_{0.76}$Ca$_{0.24}$)TiO$_3$ PFC (m_d = 0.5, θ' = 135°): (a) e^*_{31} (r, n); (b) e^*_{32} (r, n); (c) e^*_{33} (r, n); (d) d^*_{31} (r, n); (e) d^*_{32} (r, n); (f) d^*_{33} (r, n). The parameters (r, n) characterize the volume concentration of polycrystalline inclusions in the PFC matrix (Figs. 1, 2).

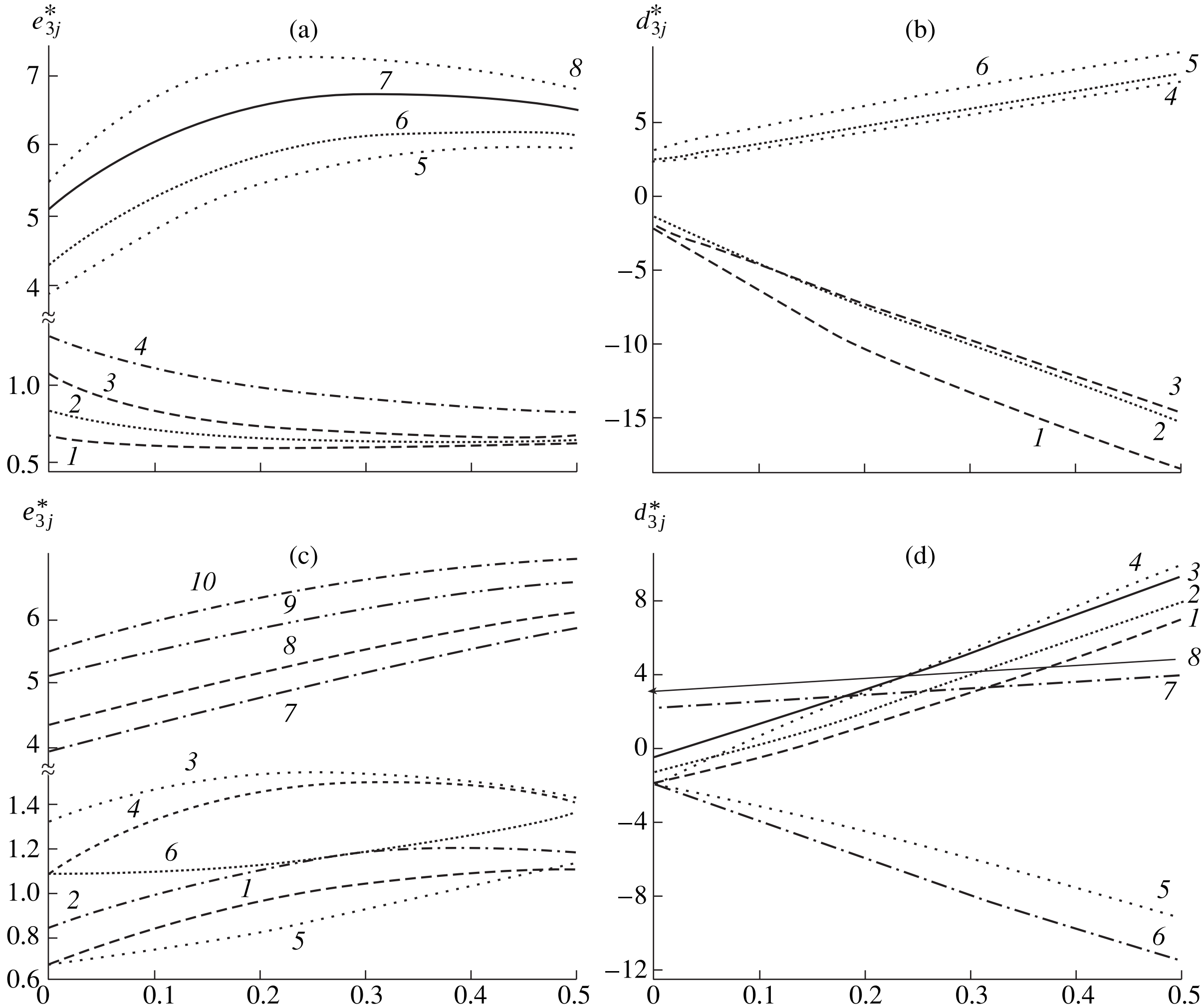

Fig. 4. Calculated concentration dependence of the effective piezoelectric coefficients e^*_{3j} (m, x) (in units of C/m^2) and d^*_{3j} (m, x) (in units of pC/N) for (a, b) the CCCFPA single-domain PbTiO$_3$ crystal of cubic shape–(Pb$_{1-x}$Ca$_x$)TiO$_3$ PFC ($m_d = 0.5$, θ' = 135°) and (c, d) the CCCFPA polydomain PbTiO$_3$ crystal of cubic shape ($m_p = 0.5$)–(Pb$_{1-x}$Ca$_x$)TiO$_3$ PFC ($m_d = 0.5$, θ' = 135°). (a) e^*_{31} (x = 0.10, 0.20, 0.25, and 0.30 for curves *1*, *2*, *3*, and *4* respectively), e^*_{33} (x = 0.10, 0.20, 0.25, and 0.30 for curves *5*, *6*, *7*, and *8*, respectively); (b) d^*_{31} (x = 0.10, 0.20, and 0.30 for curves *1*, *2*, and *3*, respectively), 10^{-1} d^*_{33} (x = 0.10, 0.20, and 0.30 for curves *4*, *5*, and *6*, respectively); (c) e^*_{31} (x = 0.10, 0.20, 0.25, and 0.30 for curves *1*, *2*, *3*, and *4* respectively), e^*_{32} (x = 0.10 and 0.30 for curves *5* and *6*, respectively), e^*_{33} (x = 0.10, 0.20, 0.25, and 0.30 for curves *7*, *8*, *9*, and *10* respectively); (d) d^*_{31} (x = 0.10, 0.20, 0.25, and 0.30 for curves *1*, *2*, *3*, and *4* respectively), d^*_{32} (x = 0.10 and 0.30 for curves *5* and *6*, respectively), 10^{-1} d^*_{33} (x = 0.10 and 0.30 for curves *7* and *8*, respectively).

favor the variations of piezoelectric moduli $d^*_{3j}(r, n)$ and $d^*_{3j}(m, m_d)$ only in narrow ranges.

The nonmonotonic behavior of the concentration dependences $e^{(FC)}_{31}(x)$ and $d^{(FC)}_{31}(x)$ [18] for the (Pb$_{1-x}$Ca$_x$)TiO$_3$ PFC at $0.10 \le x \le 0.33$ and $m_d = 0.5$ also affects the behavior of effective piezoelectric coefficients $e^*_{3j}(m, x)$ and $d^*_{3j}(m, x)$ of the CCCFPA materials. This is seen from the specific features in the sequence of $e^*_{31}(m)$ curves at x = const (Figs. 4a, 4c) and in the change in the slope of $d^*_{31}(m)$ caused by growth in x (Figs. 4b, 4d). These manifestations are pronounced most clearly in the vicinity of $x = 0.24$, which is associated with the established values of $\max e^{(FC)}_{31}(x)$ and $\max d^{(FC)}_{31}(x)$ [18] and high anisotropy of $d^{(FC)}_{33}/\left|d^{(FC)}_{31}\right| \gg 1$ [10].

PIEZOELECTRIC POLARIZATION AND ANISOTROPY OF PIEZOELECTRIC COEFFICIENTS e^*_{3j}

The discussed CCCFPA materials with single-domain inclusions have one more interesting feature: at $m \ll 1$ and $\theta \longrightarrow \theta_m$ and in the vicinity of $x = 0.24$, the factors characterizing the piezoelectric anisotropy are related by the inequality $0 < \zeta^*_{e,3j} < |\zeta^*_{d,3j}|$, where $j = 1; 2$. The high values of $|\zeta^*_{d,31}| \gg 1$ for the inverse piezoelectric effect ensure the piezoelectric strain of the CCCFPA sample in an applied field $\mathbf{E} \parallel OX_3$, $\xi^*_{3,p} \gg |\xi^*_{j,p}|$ ($j = 1; 2$). The effect of crystalline inclusions with $d^{(cr)}_{33}/|d^{(cr)}_{31}| \approx 5$–$6$ and $e^{(cr)}_{33}/e^{(cr)}_{31} \approx 6$–$7$ becomes more pronounced with a growth of m and eventually leads to the relationship $|\zeta^*_{d,31}| < \zeta^*_{e,31}$. The physical mechanisms underlying different factors characterizing the piezoelectric anisotropy of the $(Pb_{1-x}Ca_x)TiO_3$ $\zeta^{(FC)}_{d,31} = \zeta^*_{d,31}|_{m=0}$ and $\zeta^{(FC)}_{e,31} = \zeta^*_{e,31}|_{m=0}$ were discussed elsewhere [30]. Below, we consider the relation between the piezoelectric polarization $\mathbf{P}^*_p$ and the anisotropy $\zeta^*_{e,31}$ of the CCCFPA materials for the direct piezoelectric effect. If the CCCFPA sample (the orientation of $\mathbf{P}^*_s$ vectors in inclusions is shown in inset 2 in Fig. 1) is deformed along the OX_3 axis, the arising piezoelectric polarization corresponding to elastic strain ξ_3 can be written, in the linear approximation [33], as

$$P'_{3,p} = e^*_{33}\xi_3. \tag{4}$$

The strain ξ_3 caused by external sources, is accompanied by the strains ξ^*_1 and ξ^*_2 in the CCCFPA sample associated with its elastic properties [27]: $\xi^*_1 = \xi^*_2 = -\nu^*_{13}\xi_3$, where $\nu^*_{13} = -s^{*E}_{13}/s^{*E}_{33}$ is the Poisson ratio. If strains ξ^*_1 and ξ^*_2 are compensated with external strains $\xi_j = -\xi^*_j$ ($j = 1; 2$), the additional contribution to the piezoelectric polarization of the CCCFPA material is written as

$$P''_{3,p} = e^*_{3j}\xi_j = 2e^*_{31}\nu^*_{13}\xi_3. \tag{5}$$

The total piezoelectric polarization of the sample deformed only along the OX_3 axis (with due regard for Eqs. (4) and (5)) can be written as $P^*_{3,p} = P'_{3,p} + P''_{3,p} = e^*_{33}\xi_3\Psi^*_p$, where $\Psi^*_p = 1 + (2\nu^*_{13}/\zeta^*_{e,31})$ is the factor relating the elastic and piezoelectric constants of the CCCFPA material. According to our estimates, $\Psi^*_p \approx 1$ (see table) in a wide range of the parameters (m, θ', x), because the following condition is met:

$$2\nu^*_{13} \ll \zeta^*_{e,31}. \tag{6}$$

Thus, even if $\zeta^*_{e,31}$ in Eq. (6) is relatively small, we can neglect contribution (5) to the piezoelectric polarization $P^*_{3,p}$ of the $(Pb_{1-x}Ca_x)TiO_3$-based CCCFPA material. In other words, for the direct piezoelectric effect, we have $P^*_{3,p} \approx P'_{3,p}$ at any values of the strains ξ^*_1 and ξ^*_2 in the sample.

CONCLUSION

We performed a comprehensive study of the piezoelectric coefficients d^*_{3j} and e^*_{3j} in the composites with the 0–3 type of connectivity, namely, in a single-domain $PbTiO_3$ crystal–$(Pb_{1-x}Ca_x)TiO_3$ PFC and polydomain $PbTiO_3$ crystal–$(Pb_{1-x}Ca_x)TiO_3$ PFC. We also studied the dependence of these coefficients on the volume concentration m of inclusions and their geometry, the 90° domain structure of inclusions and crystallites in the PFC matrix, the remanent polarization of PFC $P^{(FC)}_R$ (angle θ'), and the molar concentration x. Because of the specific features of the electromechanical interactions between the components of the composite with the comparable values of the constants $Y^{(cr)}_{fg}$ and $Y^{(FC)}_{fg}$ at different parameters (θ', x), there exists two types of concentration dependence of the piezoelectric coefficients in the CCCFPA materials: monotonic ($d^*_{3j}(m)$ and some $e^*_{3j}(m)$) and nonmonotonic (most of $e^*_{3j}(m)$). The connecting links between d^*_{3j} and some e^*_{3j} are the elastic compliances s^{*E}_{ab}, which are highly sensitive to the changes both in m and the 90° domain structure of inclusions and crystallites in the PFC. Because of certain relationships between $Y^{(cr)}_{fg}$ and $Y^{(FC)}_{fg}$, the piezoelectric coefficients of the CCCFPA materials satisfy conditions (1)–(3). This can be useful for the practical application of these materials in piezoelectric, sensor, and microelectronic technologies.

For single-domain $PbTiO_3$ crystal–$(Pb_{1-x}Ca_x)TiO_3$ PFC composites with $0.2 \lesssim x \lesssim 0.3$, the most pronounced changes in the factors $\zeta^*_{d,31}(m)$ and $\zeta^*_{e,31}(m)$ characterizing the piezoelectric anisotropy were established. The effect of high anisotropy of piezoelectric coefficients $d^*_{3j}(m)$ and $e^*_{3j}(m)$ is characterized by the conditions $|\zeta^*_{d,31}| = |\zeta^*_{d,32}| \gg 1$ and (6), respectively, which is one more argument in favor of the important

Calculated values of the Ψ_p^* factor for composites formed by single-domain cubic $PbTiO_3$ crystals and $(Pb_{1-x}Ca_x)TiO_3$ PFC ($m_d = 0.5$)

m	x							
	0.24	0.24	0.24	0.24	0.24	0.10	0.20	0.30
	θ, deg							
	30	60	90	125	135	135	135	135
0	1.08	1.09	1.08	1.06	1.05	1.07	1.08	1.08
0.1	1.00	1.04	1.05	1.05	1.04	1.05	1.06	1.05
0.2	1.00	1.03	1.04	1.04	1.04	1.05	1.05	1.04
0.3	1.00	1.03	1.04	1.04	1.04	1.04	1.04	1.04
0.4	1.01	1.03	1.04	1.04	1.04	1.04	1.04	1.04
0.5	1.02	1.03	1.04	1.04	1.04	1.04	1.04	1.04

role of elastic compliances s_{ab}^{*E} in the formation of a nontrivial piezoelectric response of CCCFPA with single-domain inclusions. The established relations between $\zeta_{d,31}^*$, $\zeta_{e,31}^*$, and the Poisson ratio ν_{13}^* determine the characteristics of the piezoelectric polarization and piezoelectric strains in the CCCFPA both for the direct and inverse piezoelectric effect.

The prediction of effective piezoelectric properties of novel $(Pb_{1-x}Ca_x)TiO_3$-based composite materials allows one to indicate a number of specific features and advantages of the CCCFPA materials in comparison with those of their crystalline and PFC components. We have already mentioned conditions (1)–(3), which are encountered in these materials, the nontrivial piezoelectric response, and the unusual behavior of the factors characterizing the anisotropy of piezoelectric coefficients d_{3j}^* and e_{3j}^* of the CCCFPA materials. Such a combination of effective parameters was never observed earlier either in PFC or in piezoelectric crystals. The piezoelectric characteristics of the CCCFPA materials can be significantly changed by varying one of the parameters (for example, m or θ'). This is one of the advantages of these composite materials, which is useful for their application in sensors, antennas, etc. The orientation of the vectors $\mathbf{P}_s$ or $\mathbf{P}_{sk}$ in the crystalline inclusions favors the polarization of the CCCFPA in an electric field $\mathbf{E} \parallel OX_3$. It is an important crystallographic and technological factor that influences the piezoelectric activity of the CCCFPA materials. The above CCCFPA materials have another important advantage in comparison to their components. In manufacturing CCCFPA materials, it is possible to avoid, to some extent, the problem associated with the chemical purity of $PbTiO_3$ [3, 5, 29] (the possibility of self-destruction, the difficulties with polarization in field **E**, etc.) and also with the limited control of the piezoelectric parameters of $PbTiO_3$ crystals [16] by external factors. In general, the development of the high-quality CCCFPA materials opens up new possibilities for the control of the piezoelectric and other physical parameters of ferroelectrically active materials in comparison with single-domain and polydomain crystals and PFCs.

ACKNOWLEDGMENTS

We are grateful to E.S. Tsikhotskiĭ and V.V. Eremkin for their interest in our study and for useful discussion of the experimental aspects of the problem.

REFERENCES

1. V. G. Smotrakov, V. V. Eremkin, V. A. Aleshin, and E. S. Tsikhotskiĭ, Izv. Akad. Nauk, Ser. Fiz. **64** (6), 1220 (2000).
2. R. E. Newnham, MRS Bull. **22** (5), 20 (1997).
3. J.-H. Liao, S.-Y. Cheng, H.-C. Wang, and C.-M. Wang, Ferroelectrics **127** (1–4), 101 (1992).
4. K. Kakuta, T. Tsurumi, and O. Fukunaga, Jpn. J. Appl. Phys., Part 1 **34** (9B), 5341 (1995).
5. T. Ogawa, Jpn. J. Appl. Phys., Part 1 **39** (9B), 5538 (2000).
6. S.-E. Park and T. Shrout, Mater. Res. Innovations **1** (1), 20 (1997).
7. D.-S. Paik, S.-E. Park, S. Wada, *et al.*, J. Appl. Phys. **85** (2), 1080 (1999).
8. V. Yu. Topolov and A. V. Turik, Fiz. Tverd. Tela (St. Petersburg) **43** (6), 1080 (2001) [Phys. Solid State **43**, 1117 (2001)].
9. Yu Lu, D.-Y. Jeong, Z.-Y. Cheng, *et al.*, Appl. Phys. Lett. **78** (20), 3109 (2001).
10. N. Ichinose, Y. Fuse, Y. Yamada, and R. Sato, Jpn. J. Appl. Phys., Suppl. **28** (2), 87 (1989).
11. V. V. Eremkin, V. G. Smotrakov, L. E. Balyunis, *et al.*, Kristallografiya **39** (1), 155 (1994) [Crystallogr. Rep. **39**, 137 (1994)].
12. V. Yu. Topolov, Kristallografiya **43** (1), 75 (1998) [Crystallogr. Rep. **43**, 68 (1998)].
13. A. V. Sopit, A. G. Luchaninov, A. V. Shil'nikov, and A. I. Burkhanov, Izv. Akad. Nauk, Ser. Fiz. **64** (8), 1658 (2000).
14. L. Bellaiche, A. Garcia, and D. Vanderbildt, Phys. Rev. B **64** (6), 60103 (2001).
15. A. V. Turik, E. G. Fesenko, V. G. Gavrilyachenko, and G. I. Khasabova, Kristallografiya **19** (5), 1095 (1974) [Sov. Phys. Crystallogr. **19**, 677 (1974)].
16. E. G. Fesenko, V. G. Gavrilyachenko, and A. F. Semenchev, *Domain Structure of Multiaxial Ferroelectric Crystals* (Rostov. Univ., Rostov-on-Don, 1990).
17. D. Damjanovic, T. R. Gururaja, and L. E. Cross, Am. Ceram. Soc. Bull. **66** (4), 699 (1987).
18. V. Yu. Topolov, A. V. Turik, and A. I. Chernobabov, Kristallografiya **39** (5), 884 (1994) [Crystallogr. Rep. **39**, 805 (1994)].
19. A. V. Turik and V. Yu. Topolov, J. Phys. D **30** (11), 1541 (1997).
20. V. Yu. Topolov and A. V. Turik, Pis'ma Zh. Tekh. Fiz. **20** (15), 8 (1994) [Tech. Phys. Lett. **20**, 610 (1994)].

21. V. Yu. Topolov, J. Phys.: Condens. Matter **7** (37), 7405 (1995).
22. V. Yu. Topolov and A. V. Turik, Key Eng. Mater. **132–136**, 1044 (1997).
23. V. I. Aleshin and A. G. Luchaninov, J. Phys. D **34** (15), 2353 (2001).
24. V. Yu. Topolov and A. V. Turik, J. Appl. Phys. **85** (1), 372 (1999).
25. F. Levassort, V. Yu. Topolov, and M. Lethiecq, J. Phys. D **33** (16), 2064 (2000).
26. H. Banno, Ceram. Bull. **66** (9), 1332 (1987).
27. T. Mura, *Micromechanics of Defects in Solids* (Martins Nijhoff, Dordrecht, 1987).
28. L. A. Shuvalov, A. A. Urusovskaya, I. S. Zheludev, *et al.*, *Modern Crystallography*, Vol. 4: *Physical Properties of Crystals*, Ed. by B. K. Vainshtein, A. A. Chernov, and L. A. Shuvalov (Nauka, Moscow, 1981; Springer-Verlag, Berlin, 1988).
29. A. D. Feronov, V. V. Kuleshov, V. P. Dudkevich, and E. G. Fesenko, Zh. Tekh. Fiz. **50** (3), 621 (1980) [Sov. Phys. Tech. Phys. **25**, 372 (1980)].
30. A. V. Turik, V. Yu. Topolov, and V. I. Aleshin, J. Phys. D **33** (6), 738 (2000).
31. A. V. Turik, Fiz. Tverd. Tela (Leningrad) **12** (3), 892 (1970) [Sov. Phys. Solid State **12**, 688 (1970)].
32. E. Akcakaya and G. W. Farnell, J. Appl. Phys. **64** (9), 4469 (1988).
33. I. S. Zheludev, *Physics of Crystalline Dielectrics* (Nauka, Moscow, 1968; Plenum, New York, 1971).

Translated by K. Kugel

Crystallography Reports, Vol. 48, No. 3, 2003, pp. 500–503. Translated from Kristallografiya, Vol. 48, No. 3, 2003, pp. 545–548.
Original Russian Text Copyright © 2003 by Yatsenko.

Calculation of Effective Charges of Ions in Displacive-Type Ferroelectrics

A. V. Yatsenko
Taurida National University, Simferopol, Ukraine
e-mail: lab@ccssu.crimea.ua

Received April 18, 2002

Abstract—The procedure of calculating the effective charges of ions in *AB*O_3-type ferroelectrics is considered, which is based on the comparison of two experimentally determined quantities: spontaneous polarization in a crystal and the parameters of the tensor of an electric-field gradient at the quadrupolar nuclei of *A* ions calculated based on the classical electrostatic model. The determined effective charges of ions in an $LiNbO_3$ crystal are considered. *© 2003 MAIK "Nauka/Interperiodica".*

INTRODUCTION

Calculation of the electric field inside crystals is widely used to analyze the nature of the ferroelectric properties of crystals and to simulate their electric, dynamic, and structural characteristics [1, 2]. Generally, these calculations are performed based on the static ion model in which the ions are considered as material points possessing effective charges q_{eff} and electric dipole moments $\mathbf{p}$. In some cases, the electric moments of higher orders are also taken into account [3]. The accuracy of the results obtained depends on the accuracy of the values of q_{eff} and the electron polarizability of ions in the crystal.

It is commonly believed that the best method of determining the effective ion charge is *ab initio* calculations performed by the method of linear combination of atomic orbitals. Unfortunately, the accuracy of these calculations is rather low, and the q_{eff} values thus obtained are rather crude and require additional refinement.

At present, there exist rather reliable methods of determining electron polarizability of ions in optical uniaxial crystals which are based on both a pure quantum-mechanical approach [4] and analysis of the anisotropy of the optical properties of crystals [5]. The basic advantage of these methods is the possibility of determining the components of the tensor of electron polarizability of ions in the crystal, which considerably improves the accuracy of the computation of the local electric field at the ions in the crystal, with all the other conditions being the same.

COMPUTATION OF EFFECTIVE CHARGES

Spontaneous polarization $\mathbf{P}_s$ is one of the electric characteristics of ferroelectric crystals that can be determined experimentally. For a displacive-type ferroelectric, $\mathbf{P}_s$ is described as

$$\mathbf{P}_s = (\mathbf{P}_s)_{\text{ion}} + \sum_j^S N_j \mathbf{p}_j, \qquad (1)$$

where S is the number of the structurally nonequivalent ions in the unit cell, j is their serial number, N_j is the volume concentration of the structurally nonequivalent ions of the jth kind, $\mathbf{p}$ is the electric dipole moment of the ion of the jth kind, and $(\mathbf{P}_s)_{\text{ion}}$ is the ionic contribution to $\mathbf{P}_s$ because of the displacements of the cations with respect to the anion sublattice [1].

If the values of electron polarizability at all the ions in the crystal are determined with a sufficient accuracy, the q_{eff} values can be calculated without the invocation of any additional information. The calculation of q_{eff} is reduced to the following:

—the determination of the contribution of ions to the intensity of the local electric field ($\mathbf{E}_{\text{loc}}$) at all the structurally nonequivalent ions of the unit cell using either the q_{eff} values determined by the method of the linear combination of atomic orbitals or their arbitrarily values set under the requirement of the total electrical neutrality of the crystal;

—the calculation of the dipole contribution to $\mathbf{E}_{\text{loc}}$ by the iteration method [6] and the $\mathbf{p}_j$ values at all the structurally nonequivalent ions;

—the calculation of $\mathbf{P}_s$ values by Eq. (1) and the correction of the q_{eff} values; then the iteration procedure is repeated until the attainment of sufficient agreement between the calculated and the experimental $\mathbf{P}_s$ values.

The second alternative approach to the determination of q_{eff} is the analysis of the electric-field gradient (EFG) tensor at the quadrupole nuclei in the crystal. Practically all the *AB*O_3-type ferroelectrics, in particular, alkali and alkaline-earth tantalates and niobates, are

Table 1. Effective charges of ions in $LiNbO_3$ determined in *ab initio* calculations [12, 13]

Number of ions in cluster	q_{Li}, $\|e\|$	q_{Nb}, $\|e\|$	q_O, $\|e\|$	Reference
39	0.59	0.92	–0.84	[12]
67	0.69	1.26	–0.90	[12]
82	0.69	1.45	–0.88	[12]
	0.98	3.67	–1.55	[13]

characterized by the formation of a pure ionic bond between the mono- and bivalent *A* ions and the oxygen framework [1, 7]. As a result, q_{eff} of *A* ions is close to their formal charge, while the factor of the EFG antiscreening $(1 - \gamma_\infty)$ is close to the value determined for a free ion [8]. If the nucleus of the *A* ion has an electric quadrupole moment, the V_{jk} components of the EFG tensor at this nucleus can be determined experimentally by the NMR method, and then the true components of the EFG tensor can be calculated at the site of location of *A* ions as

$$(V^i_{jk} + V^m_{jk}) = V_{jk}(1-\gamma_\infty)^{-1}, \tag{2}$$

where V^i_{jk} and V^m_{jk} are the ionic and multipole contributions to the EFG, respectively, and $j, k = x, y, z$. Since V^i_{jk} directly and V^m_{jk} indirectly depend on the set of q_{eff} used in the calculation of the EFG from the structural data, the analysis of the EFG at the nuclei of alkali and alkaline-earth metals allows one to determine the effective charges of the ions in the lattice independently. The necessary condition for such a determination is also a high accuracy of the electron polarizability values of all the structurally nonequivalent ions in the crystal. The nonunique electron polarizability values of ions in calculation [9] or neglecting the multipole contribution to the EFG [10] hinders the accurate determination of q_{eff}.

The parallel use of both the above methods for determining q_{eff} provides additional verification of the initial data, in particular, the electron polarizabilities of ions in the crystal.

Calculation of Effective Charges of Ions in $LiNbO_3$

Now apply the above procedure to an $LiNbO_3$ crystal, which is extensively used in various optoelectronic and electroacoustic devices. It is a displacive-type ferroelectric with a high Curie temperature, sp. gr. $R3c$; the unit cell in a hexagonal setting contains six formula units. The parameters of the hexagonal unit cell at T = 293 K are c_H = 1.38581 nm and a_H = 0.51485 nm [11]; the polar **z** axis coincides with the threefold symmetry axis of the crystal.

Earlier q_{eff} values for a $LiNbO_3$ crystal were calculated by the method of the linear combination of atomic orbitals [12, 13] (Table 1). The results obtained in [12] demonstrate the shortcoming of the *ab initio* approach: the q_{eff} values strongly depend on the configuration of the cluster under consideration; also, despite the practically purely ionic character of $(Li^+ – O^{2–})$ bonds, the q_{eff} of Li^+ ions values obtained are obviously underestimated. The data obtained in [13] are more consistent with the interionic bonds in $LiNbO_3$, and, therefore, it is this set of q_{eff} values that was used as the basic one in all the subsequent calculations.

Analyzing the optical properties of $LiNbO_3$ crystals, we established [5] that the electron polarizability of $O^{2–}$ ions is anisotropic. Under the assumption of the axial symmetry of the tensor of electron polarizability of $O^{2–}$ ions (the main axis of the tensor coincides with the direction of the short Nb–O bond (0.1878 nm)), the dependences of the α_{33} and $\alpha_{22} = \alpha_{11}$ components of the tensor on electron polarizability of Nb^{5+} ions (α_{Nb}) were also obtained [5]. The electron polarizability of Li^+ (α_{Li}) was assumed to be isotropic and equal to $0.032 \times 10^{–24}$ cm^3 [14].

The calculations of the ionic contribution to $\mathbf{E}_{loc}$ were made by the transient-region method [15], which provides good accuracy and a fast convergence and also has a number of advantages over the widely used Ewald method. The dipole contribution to $\mathbf{E}_{loc}$ was calculated

Table 2. Sets of q_{eff} and the corresponding P_s for some α_{Nb} values

No.	α^*_{Nb}	α^*_{11}	α^*_{33}	q_{Li}, $\|e\|$	q_{Nb}, $\|e\|$	q_O, $\|e\|$	P_s, C m^{-2}
1	0	2.020	2.830	0.98	3.400	–1.460	0.711
2	0.025	1.995	2.845	0.98	3.376	–1.452	0.713
3	0.050	1.970	2.860	0.98	3.358	–1.446	0.710
4	0.075	1.945	2.875	0.98	3.340	–1.440	0.709
5	0.100	1.920	2.890	0.98	3.300	–1.427	0.712
6	0.125	1.895	2.905	0.98	3.260	–1.413	0.713
7	0.150	1.870	2.920	0.98	3.220	–1.400	0.714

* The values of the electron polarizability of ions (in 10^{-24} cm^{-3}) are taken from [5].

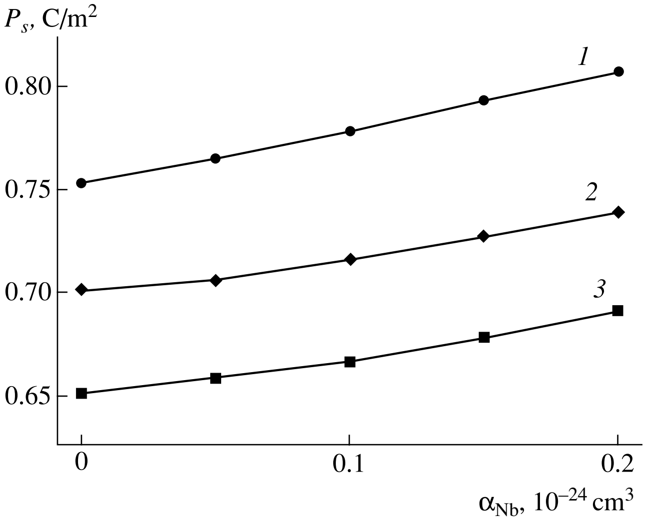

Fig. 1. P_s as functions of α_{Nb} in an LiNbO$_3$ crystal for the following sets of q_{eff}: (*1*) $q_{\mathrm{Li}} = 0.98$, $q_{\mathrm{Nb}} = 3.67$, $q_{\mathrm{O}} = -1.55|e|$; (*2*) $q_{\mathrm{Li}} = 0.98$, $q_{\mathrm{Nb}} = 3.34$, $q_{\mathrm{O}} = -1.44|e|$; (*3*) $q_{\mathrm{Li}} = 0.98$, $q_{\mathrm{Nb}} = 3.01$, $q_{\mathrm{O}} = -1.33|e|$.

with due regard for real mutual displacements of the charges forming the dipole moment of O^{2-} ions [5].

In an LiNbO$_3$ crystal, the direction of $\mathbf{P}_s$ coincides with the direction of the **z** axis, and the absolute value of $\mathbf{P}_s$ (P_s) can be calculated as

$$P_s = N[q_{\mathrm{Li}}\Delta_1 + q_{\mathrm{Nb}}\Delta_2 + 3p_z(\mathrm{O}) + p_z(\mathrm{Nb}) + p_z(\mathrm{Li})], \tag{3}$$

where N is the volume concentration of Li$^+$ ions, Δ_1 is the displacement of Li$^+$ ions with respect to the neighboring oxygen layer, Δ_2 is the displacement of Nb^{5+} ions from the centre of an NbO$_6$ octahedron, and p_z(Li), p_z(Nb), and p_z(O) are the z components of the electric dipole moments of the corresponding ions.

The calculated P_s for three sets of q_{eff} values are shown in Fig. 1. Analyzing the Li–O pairwise interactions in LiNbO$_3$ in the Born–Maier approximation, we come to the conclusion that the nonnegativity of z component of $\mathbf{E}_{\mathrm{loc}}$ (E_z) at Li$^+$ ions [5] is the necessary condition for the stability of Li$^+$ in the system. The dependences E_z (α_{Nb}) obtained for the same sets of q_{eff} are shown in Fig. 2. Thus, the range of the α_{Nb} values satisfying the condition of stability of Li$^+$ ions in the LiNb)$_3$ structure is (0–0.175) × 10^{-24} cm^3. The data presented in Fig. 1 allow one to determine the $P_s(q_{\mathrm{Nb}})$ dependences for the fixed α_{Nb} values and obtain the sets of q_{eff} values, for which P_s would correspond to the experimental value 0.71 C m^{-2} (Table 2).

The results obtained are not unambiguous because of the nonunique α_{Nb} value. Therefore, further refinement of q_{eff} requires additional analysis. Using the q_{eff} values from Table 2, one can readily calculate the main component V_{zz} of the EFG tensor at the ^{7}Li nuclei as a function of α_{Nb} using the conventional procedure (Fig. 3) [9]. In these calculations it was assumed that for ^{7}Li nuclei $(1 - \gamma_\infty) = 0.740$ [8]. It should be noted that the absolute values of V_{zz}^m are approximately twice as high as V_{zz}^i in the whole range of α_{Nb} variation. The experimental value of the quadrupole coupling constant C_z for the main position of ^{7}Li nuclei in LiNbO$_3$ is (55 ± 0.5) kHz [16, 17]; this corresponds to $V_{zz} = \pm 0.625 \times 10^{20}$ V m^{-2}, with the quadrupole moment of the ^{7}Li nuclei being $eQ = 0.036$ b [18]. Thus, the difference

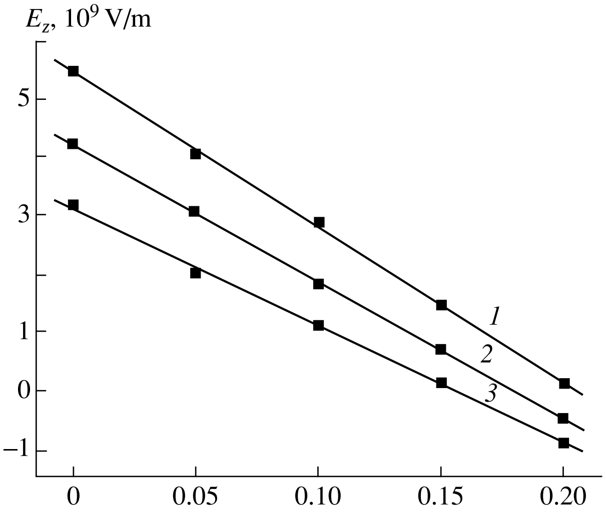

Fig. 2. z Component of $\mathbf{E}_{\mathrm{loc}}$ at Li$^+$ ions as a function of a_{Nb} for the sets of q_{eff} indicated in Fig. 1.

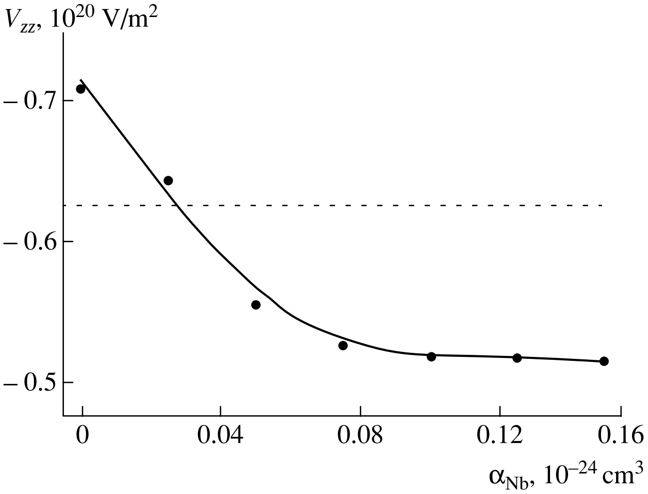

Fig. 3. V_{zz} at ^{7}Li nuclei in LiNbO$_3$ as a function of a_{Nb} calculated using the sets of q_{eff} indicated in Table 2. The experimental value of V_{zz} is shown by the dotted line.

between the experimental and calculated V_{zz} values does not exceed 18% in the whole range of possible values of α_{Nb}. This seems to be a very good result for calculations of the EFG by the static model [9].

The good agreement between the calculated and experimental V_{zz} values is also observed at $\alpha_{Nb} = 0.025 \times 10^{-24}$ cm^3. This corresponds to the conclusion drawn from the analysis of the repulsive potentials of the pairwise Li–O and Nb–O interactions according to which the probable value of α_{Nb} cannot exceed 0.05×10^{-24} cm^3 [5]. Therefore, the following set of effective charges of ions in $LiNbO_3$ seems to be the most reliable: $q_{Li} = 0.98$, $q_{Nb} = 3.376$, and $q_O = -1.452|e|$.

CONCLUSIONS

The electrostatic approach to the computation of effective charges based on the simultaneous calculation of the spontaneous polarization of a crystal and the EFG at the nuclei of alkali and alkali earth elements can be used for both ferroelectrics of the ABO_3 family and various nonpolar crystals. The necessary condition for the applicability of the method is the use of accurate values of electron polarizability of ions in the crystal.

REFERENCES

1. Yu. N. Venevtsev, E. D. Politova, and S. A. Ivanov, *Ferroelectrics and Antiferroelectrics of the Barium Titanate Family* (Khimiya, Moscow, 1985).
2. J. H. Calderwood, Philos. Trans. R. Soc. London, Ser. A **335**, 1 (1997).
3. R. Kirsch, A. Gérard, and M. Wautelet, J. Phys. C **7**, 3633 (1974).
4. D. Khatib, H. Chaib, and W. Kinase, Physica B (Amsterdam) **269**, 200 (1999).
5. A. V. Yatsenko, Fiz. Tverd. Tela (St. Petersburg) **42**, 1673 (2000) [Phys. Solid State **42**, 1722 (2000)].
6. V. M. Buznik, *Nuclear Magnetic Resonance in Ionic Crystals* (Nauka, Novosibirsk, 1981).
7. Yu. S. Kuz'minov, *Ferroelectric Crystals for Control of Laser Radiation* (Nauka, Moscow, 1982).
8. K. D. Sen, A. Weiss, and P. C. Schmidt, Hyperfine Interact. **30**, 253 (1986).
9. E. V. Charnaya, V. S. Kasperovich, and M. C. Shelyapina, Ferroelectrics **208–209**, 225 (1998).
10. G. E. Peterson, P. M. Bridenbaugh, and P. Green, J. Chem. Phys. **46**, 4009 (1967).
11. N. Iyi, K. Kitamura, F. Izumi, *et al.*, J. Solid State Chem. **101**, 340 (1992).
12. Th. Gog, P. Schotters, J. Falta, *et al.*, J. Phys.: Condens. Matter **7**, 6971 (1995).
13. W. Y. Ching, Z.-Q. Gu, and Y.-N. Xu, Phys. Rev. B **50**, 1992 (1994).
14. N. Ramesh and R. Ethiraj, J. Mater. Sci. Lett. **13**, 757 (1994).
15. A. V. Yatsenko, Kristallografiya **46**, 411 (2001) [Crystallogr. Rep. **46**, 361 (2001)].
16. A. V. Yatsenko and N. A. Sergeev, Ukr. Fiz. Zh. **30**, 118 (1985).
17. G. E. Peterson and P. M. Bridenbaugh, J. Chem. Phys. **48**, 3402 (1968).
18. J. W. Hennel and J. Klinowski, *Fundamentals of Nuclear Magnetic Resonance* (Longman, Harlow, 1993).

Translated by E. Shtykova

Crystallography Reports, Vol. 48, No. 3, 2003, pp. 504–508. Translated from Kristallografiya, Vol. 48, No. 3, 2003, pp. 549–553.
Original Russian Text Copyright © 2003 by Kurilkina, Shuba.

PHYSICAL PROPERTIES OF CRYSTALS

Enhancement of Magneto-Optical Kerr Rotation by Magnetoactive Dielectric Structures

S. N. Kurilkina and M. V. Shuba

Gomel State University, ul. Sovetskaya 104, Gomel, 246699 Belarus

e-mail: kurilkina@gsu.unibel.by

Received May 28, 2002

Abstract—The analytical expressions that describe the transformation of an arbitrarily polarized optical radiation in periodic magneto-optical structures are derived. It is established that the magnetic-field-induced splitting into two components of the frequency ranges of the resonance interaction of light with a magnetoactive structure corresponding to circularly polarized eigenwaves provides considerable enhancement of the rotation of the polarization plane of the reflected radiation. The expedience of using a dielectric mirror located behind the magnetoactive structure is shown. Such a mirror allows one not only to preserve the considerable enhancement of the rotation but also provides the total reflection of light. *© 2003 MAIK "Nauka/Interperiodica".*

The fact that dielectric layers enhance the magneto-optical Kerr effect (rotation of the polarization plane of the light reflected from the surface of a magnetized ferroelectric mirror) first established in [1] is widely used in magneto-optical memory units [2]. In recent years, various methods for the practical application of the so-called enhancement of the Kerr rotation were suggested, including the use of interference in a three-layer structure [3], short-period composites [4], and also various structures with defects [5, 6]. However, the enhancement of the Kerr rotation because of multiple light reflection is accompanied by a decrease in the reflection coefficient of a multilayer structure [1–7]. To overcome this shortcoming, periodic structures with an asymmetrically located defect layer are used [8]. This results in considerable enhancement of the Kerr rotation and simultaneously high reflection (up to 100%) at the frequency of the resonance transmission (defect mode) inside the photon band gap.

The interaction of light with multilayer magnetoactive structures was studied by various techniques including the matrix method [5–7] and the methods of an effective medium [4] and coupled waves [8].

Below, we give analytical expressions that describe the specific features of the light reflection from a magnetoactive periodic structure with a defect layer obtained by the method of Floquet–Bloch waves and demonstrate one more possibility of enhancing the Kerr rotation not only at the frequency of the defect mode but also at other frequencies of the resonance interaction of light with a medium.

PROPAGATION OF LIGHT WAVES IN A PERIODIC LAYER STRUCTURE

Let a plane monochromatic wave be incident from the medium *A* with the refractive index n_0 onto a periodic structure consisting of subsystems 1 and 2 separated by a transparent layer of thickness d of the material *B* with the refractive index n_d (Fig. 1). It is assumed that the structure is applied onto the substrate *C* with the refractive index n_3. Subsystems 1 (SS1) and 2 (SS2) are the periodic structures consisting of alternating layers with the refractive indices $n_1^{(i)}$ and $n_2^{(i)}$ and thicknesses $d_1^{(i)}$ and $d_2^{(i)}$ ($i = 1, 2$ is the sequential number of

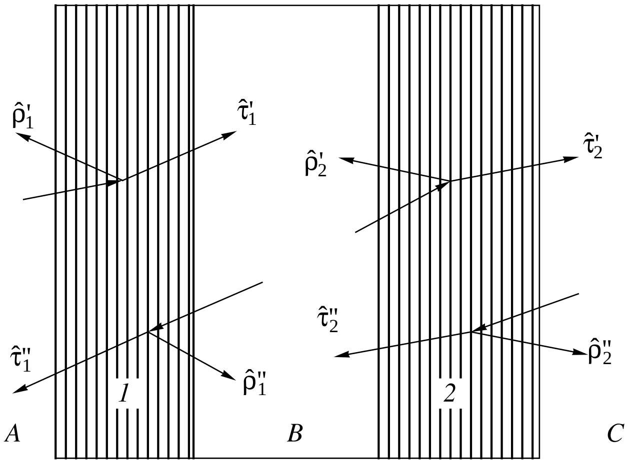

Fig. 1. Propagation of a wave in a plane-layer structure with a defect.

1063-7745/03/4803-0504$24.00 © 2003 MAIK "Nauka/Interperiodica"

the substructure). The numbers of periods in the first and second subsystems are N_1 and N_2, respectively.

The specific features of the radiation propagation in a medium are described by the reflection and transmission matrices, $\hat{\rho}$ and $\hat{\tau}$, respectively, which relate the components of the amplitudes of the electric-strength vectors of the transmitted, $\mathbf{E}^t$, reflected, $\mathbf{E}^r$, and incident, $\mathbf{E}^0$, waves:

$$\mathbf{E}^r = \hat{\rho}\mathbf{E}^0, \quad \mathbf{E}^t = \hat{\tau}\mathbf{E}^0. \tag{1}$$

If the reflection and transmission matrices of each of the subsystems in the forward ($\hat{\rho}_i'$ and $\hat{\tau}_i'$) and backward ($\hat{\rho}_i''$ and $\hat{\tau}_i''$) directions are known, as well as the transmission coefficient in the forward $\hat{\tau}_B'$ and backward $\hat{\tau}_B''$ directions of the layer B, then the superposition of all the reflected and transmitted waves transform the reflection and transmission matrices $\hat{\rho}$ and $\hat{\tau}$ of the whole structure into the form [9]

$$\hat{\rho} = \hat{\rho}_1' + \hat{\tau}_1''\hat{\tau}_B''\hat{\rho}_2'(\hat{I} - \hat{\tau}_B'\hat{\rho}_1''\hat{\tau}_B''\hat{\rho}_2')^{-1}\hat{\tau}_B'\hat{\tau}_1', \tag{2a}$$

$$\hat{\tau} = \hat{\tau}_2'(\hat{I} - \hat{\tau}_B'\hat{\rho}_1''\hat{\tau}_B''\hat{\rho}_2')^{-1}\hat{\tau}_B'\hat{\tau}_1', \tag{2b}$$

where $\hat{I}$ is the unit matrix. It should be emphasized that formulas (2) are also applicable to the case where SS2 is represented by a metal layer.

Using the method of Floquet–Bloch waves, we can determine the explicit form of the matrices $\hat{\rho}_i'$, $\hat{\tau}_i'$, $\hat{\rho}_i''$, and $\hat{\tau}_i''$. In this case, one has to take into account the fact that, for a two-layer periodic structure of isotropic layers, $\hat{\rho}_i' = \rho_i'\hat{I}$, $\hat{\tau}_i' = \tau_i'\hat{I}$, $\hat{\rho}_i'' = \rho_i''\hat{I}$, and $\hat{\tau}_i'' = \tau_i''\hat{I}$, where ρ_i', ρ_i'', τ_i', and τ_i'' are the reflection and transmission coefficients, respectively.

The electric field of the eigenwave propagating in a defect-free periodic structure occupying the region $0 < z < N\Lambda$ (the z axis is normal to the layer boundaries and N and $\Lambda = d_1 + d_2$ are the number of the layers and the structure period, respectively) can be represented by the superposition of the Floquet–Bloch waves [10]:

$$E(z) = C_1E_1(z) + C_2E_2(z), \tag{3}$$

where C_1 and C_2 are the constants. With due regard for the periodicity of the functions $E_{1,2}(z)$ for the first and second layer in Eq. (3), one can write

$$\begin{aligned} E_{1,2}(z) &= \exp[i\xi_{1,2}(N-1)] \\ &\times \sin\left(\theta_1[z-(N-1)\Lambda] - \frac{d_1\theta_1}{2} + \varphi_{1,2}\right), \end{aligned} \tag{4a}$$

$$\begin{aligned} E_{1,2}(z) &= \exp[i\xi_{1,2}(N-1)] \\ &\times \sin\left(\theta_2[z-d_1-(N-1)\Lambda] - \frac{d_2\theta_2}{2} + \psi_{1,2}\right). \end{aligned} \tag{4b}$$

Here, $\theta_i = n_ik_0$ and $k_0 = \omega/c$. Using the continuity condition for the functions $E_{1,2}(z)$ and their derivatives in the transition from one layer to another, we can determine the parameters entering Eq. (4) as

$$\begin{aligned} \xi_{1,2} &= \pm\arccos\left(\frac{1}{1-a^2}\cos\Omega - \frac{a^2}{1-a^2}\cos\Delta\right), \\ \varphi_{1,2} &= \pm\frac{1}{2}\arccos\left[\frac{a^{-1}\sin\Omega + a\sin\Delta}{2\sin(\theta_2d_2)}\right], \\ \psi_{1,2} &= \pm\frac{1}{2}\arccos\left[\frac{a^{-1}\sin\Omega + a\sin\Delta}{2\sin(\theta_1d_1)}\right]. \end{aligned} \tag{5}$$

Here, $a = \frac{n_2 - n_1}{n_2 + n_1}$ is the dielectric contrast, $\Omega = \theta_2d_2 + \theta_1d_1$, and $\Delta = \theta_2d_2 - \theta_1d_1$.

Now, represent the fields of an electromagnetic wave in the region $z \le 0$ in the form

$$\begin{aligned} E(z) &= (\exp(in_0k_0z) + \rho'\exp(-in_0k_0z)), \\ H(z) &= -in_0(\exp(in_0k_0z) - \rho'\exp(-in_0k_0z)), \end{aligned} \tag{6}$$

where $\rho'\exp(-in_0k_0z)$ is the reflected wave. For definiteness, we assume that in Eqs. (6) the incident light has a unit amplitude. In the region $z > N\Lambda$, the light wave can be described as

$$\begin{aligned} E(z) &= \tau'\exp(in_3k_0(z-N\Lambda)), \\ H(z) &= -in_3E(z) = -in_3\tau'\exp(in_3k_0(z-N\Lambda)). \end{aligned} \tag{7}$$

Using Eqs. (3)–(7) and the continuity condition for the vectors $\mathbf{E}$ and $\mathbf{H}$ at the boundaries $z = 0$ and $z = N\Lambda$, we arrive at the system of equations for the unknowns ρ', τ', C_1, and C_2:

$$\begin{aligned} 1 + \rho' &= \left(C_1\sin\left(-\frac{d_1\theta_1}{2} + \varphi_1\right) + C_2\sin\left(-\frac{d_1\theta_1}{2} - \varphi_1\right)\right), \\ &in_0(1-\rho') \\ &= n_1\left(C_1\cos\left(-\frac{d_1\theta_1}{2} + \varphi_1\right) + C_2\cos\left(-\frac{d_1\theta_1}{2} - \varphi_1\right)\right), \\ \tau' &= \left(C_1\exp(i\xi_1N)\sin\left(-\frac{d_1\theta_1}{2} + \varphi_1\right)\right. \\ &\quad \left. + C_2\exp(i\xi_2N)\sin\left(-\frac{d_1\theta_1}{2} - \varphi_1\right)\right), \\ in_3\tau' &= n_1\left(C_1\exp(i\xi_1N)\cos\left(-\frac{d_1\theta_1}{2} + \varphi_1\right)\right. \\ &\quad \left. + C_2\exp(i\xi_2N)\cos\left(-\frac{d_1\theta_1}{2} - \varphi_1\right)\right), \end{aligned} \tag{8}$$

whence it follows that

$$\rho' = \frac{-(n_1c_1 + in_0s_1)(is_2n_3 + n_1c_2)\exp(-i\xi N) + (n_1c_1 + in_0s_2)(n_1c_1 + in_3s_1)\exp(i\xi N)}{(in_0s_2 - n_1c_2)(n_1c_1 + in_3s_1)\exp(i\xi N) + (n_1c_1 - in_0s_1)(n_1c_2 + in_3s_2)\exp(-i\xi N)},$$
$$\tau' = \frac{2in_1n_0(s_2c_1 - s_1c_2)}{(in_0s_2 - n_1c_2)(n_1c_1 + in_3s_1)\exp(i\xi N) + (n_1c_1 - in_0s_1)(n_1c_2 + in_3s_2)\exp(-i\xi N)}, \tag{9}$$

where $s_{1,2} = \sin\left(\frac{1}{2}\theta_1 d_1 \mp \varphi\right)$ and $c_{1,2} = \cos\left(\frac{1}{2}\theta_1 d_1 \mp \varphi\right)$. Similar relationships for ρ'' and τ'' are determined from Eqs. (9) with due regard for the changes $d_{1,2} \longrightarrow d_{2,1}$, $n_{1,2} \longrightarrow n_{2,1}$, $n_{0,3} \longrightarrow n_{3,0}$, and $\varphi \longrightarrow -\varphi$. Rigorous analytical equations (9), which take into account the interference phenomena, allow one to determine the transmission and reflection coefficients of the defect-free periodic layer structure on the substrate with arbitrary dielectric contrast *a* and number of periods *N*.

Equations (9) yield the following expression relating the transmission, τ' and τ'', and reflection, ρ' and ρ'', coefficients:

$$\tau'\tau'' = -\frac{(1 - |\rho'\rho''|)}{|\rho'\rho''|}\rho'\rho''. \tag{10}$$

Now, consider the structure shown in Fig. 1. If SS1 is a two-layer periodic structure formed (like a defect) by isotropic materials, then Eqs. (10) and (2a) lead to an expression that allows one to establish the effect of the reflection coefficients of the substructures on the reflection coefficient of the whole structure:

$$\rho = \frac{\rho_1'(|\rho_1'\rho_1''| - \tau_B''\rho_2'\tau_B'\rho_1'')}{(1 - \tau_B'\rho_1''\tau_B''\rho_2')|\rho_1'\rho_1''|}. \tag{11}$$

Here τ_B' and τ_B'' are the transmission coefficients along the forward and backward directions in the defect layer *B*, which are introduced by the relationships $\hat{\tau}_B' = \tau_B'\hat{I}$ and $\hat{\tau}_B'' = \tau_B''\hat{I}$. Equation (11) considerably simplifies the calculation of the reflection coefficient of a layer structure.

In order to determine ρ_i' and ρ_i'' in Eq. (11), one has to use Eq. (9) with due regard for the fact that, for the *i*th structure, $n_1 = n_1^{(i)}$, $n_2 = n_2^{(i)}$, $d_1 = d_1^{(i)}$, $d_2 = d_2^{(i)}$, and $N = N_i$. For SS1, one also has to take into account the change $n_3 \Rightarrow n_d$, and, for the SS2, the change $n_0 \Rightarrow n_d$. It should also be noted that the transmission coefficients of the layer *B* in Eq. (11) are determined by the expression

$$\tau_B' = \tau_B'' = \exp(-in_dk_0d). \tag{12}$$

SPECIFIC FEATURES OF LIGHT PROPAGATION IN A MAGNETOACTIVE LAYER STRUCTURE

If a periodic structure is formed by layers of isotropic magnetoactive materials, the application of an external magnetic field along the periodicity axis gives rise to circular birefringence [11]: in each layer of the *i*th structure, the circularly polarized waves with the polarization vectors $\mathbf{e}_\pm = (\mathbf{e}_1 \pm i\mathbf{e}_2)/\sqrt{2}$ and the refractive indices

$$n_{j\pm}^{(i)} = n_j^{(i)} \pm \eta_j^{(i)}H/n_j^{(i)} \tag{13}$$

propagate along the direction $\mathbf{e}_\pm = (\mathbf{e}_1 \pm i\mathbf{e}_2)/\sqrt{2}$ ($\mathbf{e}_{1,2,3}$ are the unit vectors of the coordinate system used, with the *z* axis being normal to the interface between the layers), where $\eta_j^{(i)}$ is the parameter that characterizes the circular birefringence induced by a magnetic field *H*. The latter parameter is related to the Verdet constant $D_j^{(i)}$ by the relationship $D_j^{(i)} = \omega\eta_j^{(i)}/(cn_j^{(i)})$, where $j = 1, 2$ is the layer number. Hereafter, the plus and minus signs are taken for the waves with right- and left-hand circular polarizations, respectively. As is seen from analysis of the wave equation for the electric-strength vector, the propagation of each eigenwave through the structure should be considered independently. Then, in order to determine the reflection and transmission coefficients of the circularly polarized modes, one can use Eqs. (9) with due regard for the change $n_j \longrightarrow n_{j\pm}$. The transmission coefficients for the right- and left-hand circularly polarized waves in the magnetoactive layer *B* are determined by the expression

$$\tau_{B\pm}' = \tau_{B\pm}'' = \exp(-in_dk_0d \pm \Delta\varphi), \tag{14}$$

where $\Delta\varphi = D_BHd$ is the additional phase incursion due to the magnetic action and D_B is the Verdet constant of the layer *B*.

At the normal incidence of elliptically polarized optical radiation with an amplitude $\tilde{E}_0$, ellipticity τ_0, and polarization azimuth χ_0 (the angle formed by the major semiaxis of the ellipse and the *x* axis) onto the system of magnetoactive crystals (Fig. 1), the incident wave can be represented as the superposition of the circularly polarized waves:

$$\mathbf{E} = \tilde{E}[(1 + \tau_0)e^{-i\chi_0}\mathbf{e}_+ + (1 - \tau_0)e^{i\chi_0}\mathbf{e}_-]/\sqrt{2(1 + \tau_0^2)}$$
$$= E_+^0\mathbf{e}_+ + E_-^0\mathbf{e}_-. \tag{15}$$

Taking into account the independent propagation of these waves, we can obtain the reflection and transmission coefficients, $\rho_\pm$ and $\tau_\pm$, of the circularly polarized waves from Eq. (11) with due regard for Eqs. (13) and (14).

The polarization characteristics (polarization azimuth $\chi_{t,r}$ and ellipticity $\tau_{t,r}$) of the transmitted and reflected waves can be determined as

$$\chi_{t,r} = 0.5\arg(\beta_{t,r}), \quad \tau_{t,r} = \frac{|\beta_{t,r}| - 1}{|\beta_{t,r}| + 1}, \tag{16}$$

where $\beta_t = \dfrac{E_+^t}{E_-^t}$, $\beta_r = \dfrac{E_+^r}{E_-^r}$, and $E_\pm^r$ and $E_\pm^t$ are determined from the relationship

$$E_\pm^r = \rho_\pm E_\pm^0, \quad E_\pm^t = \tau_\pm E_\pm^0. \tag{17}$$

Equations (15)–(17) allow one to analyze the characteristics of the transformation of an arbitrarily polarized radiation during its propagation in a magnetoactive periodic structure. As follows from Eq. (11) with due regard for Eqs. (9), (13), and (14), the application of a magnetic field gives rise to a splitting of the interference transmission maxima of SS1 into two components corresponding to circularly polarized waves of opposite polarizations and their displacement with respect to one another, which, in turn, can give rise to a considerable phase difference of circularly polarized eigenwaves upon their exit from the structure and, thus, also to a considerable rotation of the polarization planes of the transmitted and reflected waves. The frequency range of the pronounced changes in the phases of the reflected waves is determined from the condition of the zero denominator in Eq. (11):

$$\tau'_B\rho''_1\tau''_B\rho'_2 \cong 1 \tag{18}$$

or

$$|\rho''_1||\rho'_2| \cong 1, \quad \arg(\tau'_B\rho''_1\tau''_B\rho'_2) = 2\pi m, \quad m = 0, 1, 2, 3\ldots. \tag{18a}$$

Substituting Eq. (14) into Eq. (11) and then Eq. (11) into Eq. (16) in the frequency range satisfying condition (18), one arrives at the analytical expression for the rotation angle of the polarization plane of the radiation reflected from the structure with one magnetoactive layer between two dielectric structures with the reflection coefficients ρ'_1 and ρ'_2:

$$\Psi(\Delta\varphi) = \arctan\left[\frac{|\rho'_2|(|\rho'_1|^2 - 1)\sin(2\Delta\varphi)}{|\rho'_1|(|\rho'_2|^2 + 1) - |\rho'_1|(|\rho'_1|^2 + 1)\cos(2\Delta\varphi)}\right]. \tag{19}$$

The estimates made with the use of Eq. (19) show that, under condition (18), the rotation angles of the polarization azimuth of the reflected light considerably exceed the corresponding angles for a homogeneous medium. Thus, enhancement of the Kerr rotation takes place. As follows from Eqs. (9), (11), (13), (14), and (19), an enhancement of the Kerr rotation is determined by the thickness and magneto-optical properties of the defect, the number of the layers in the structure, and also the strength of the controlling magnetic field. As the calculation shows (Fig. 2), the value of Ψ is limited and determined by the reflection coefficients ρ'_1 and ρ'_2 and the rotation angle $\Delta\varphi$ of the polarization plane of light transmitted once by the defect layer. Thus, at $\Delta\varphi < \pi/2$, the condition $\Psi < \pi$ is fulfilled. This fact is explained by the specific features of the formation of the interference transmission maxima of SS1 where enhancement of the Kerr rotation is observed: the phase difference of the waves with equal transmission coefficients but different frequencies does not exceed π for each maximum.

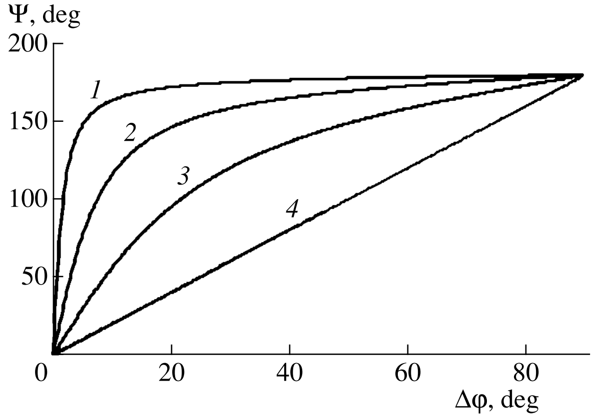

Fig. 2. Angle of rotation Ψ of the polarization plane of the radiation reflected from a periodic structure with a magnetoactive layer as a function of the rotation angle $\Delta\varphi$ of the polarization plane of light that has passed the magnetoactive layer once at different reflection efficiencies: (*1*) $|\hat{\rho}'_2| = 1$, $|\hat{\rho}''_1| = 9.5$; (*2*) $|\hat{\rho}''_1| = 0.8$; (*3*) $|\hat{\rho}''_1| = 0.5$, and (*4*) $\Psi(\Delta\varphi) = 2\Delta\varphi$.

It should be emphasized that the use of metal mirrors instead of SS2 even with extremely high reflection coefficients ($|\rho'_2| = 0.99$) is not expedient, because, as is seen from Eq. (11), the simultaneous fulfillment of conditions (18) and $|\rho| = 1$ is impossible, which results in low reflection from the structure at the frequencies that provide the enhancement of the Kerr rotation [1–4, 7]. For simultaneous enhancement of the Kerr rotation and high ($\rho \approx 1$) reflection from the structure, one has to use as SS2 those dielectric mirrors for which $|\rho'_2| \cong 1$. In this case, the materials of the dielectric layers of SS2 are selected in such a way that the frequency range of the nontransmission region of the given subsystem includes the forbidden gap of SS1. Then, as the calculation shows, one observes both enhancement of the Kerr rotation and the total reflection from the structure in the vicinity of the frequencies of the interference

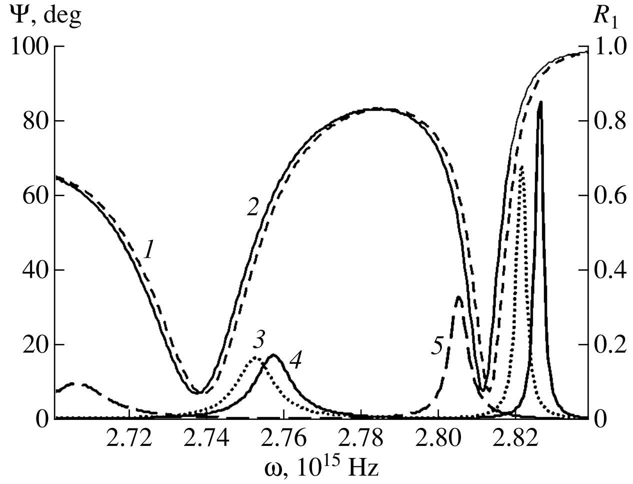

Fig. 3. Frequency dependence of the reflection coefficient R_1 of the circularly polarized waves with (*1*) right- and (*2*) left-hand polarizations from SS1 and (*3*–*5*) the angle of rotation of the polarization angle of the radiation reflected from the structure as a whole; (*3*) d = 105 nm, (*4*) d = 110 nm, and (*5*) d = 150 nm.

transmission maxima of SS1 located in the nontransmission region of SS2.

We illustrate the above with the example of a system with the parameters $n_1^{(1)} = n_1^{(2)} = n_3 = 1.5$, $n_2^{(1)} = 2.4$, $n_2^{(2)} = 3.4$, $n_d = 2$, $d_1^{(1)} = d_1^{(2)} = 60$ nm, $d_2^{(1)} = d_2^{(2)} = 83$ nm, $n_{1+}^{(1)} - n_{1-}^{(1)} = 7 \times 10^{-4}$, $n_{2+}^{(1)} - n_{2-}^{(1)} = 0$, $N_1 = 20$, and $N_2 = 7$. Figure 3 shows the frequency dependences of the energy reflection coefficient of SS1 $R_1 = |\rho_1'|^2$ and the rotation angle Ψ of the polarization azimuth of the radiation reflected from the structure as a whole constructed using Eqs. (9)–(16). It is seen (Fig. 3) that at frequencies of $\omega = 2.825 \times 10^{15}$ Hz and $\omega = 2.755 \times 10^{15}$ Hz, corresponding to the interference transmission maxima of the first subsystem, one observes rotation of the polarization plane by angles of 87° and 18° in the reflected light with a structure thickness of 4 μm. A decrease in the maximum rotation angle with distance from the nontransmission region of SS1 is explained by a broadening of the interference maxima with distance from the band gap and, thus, an increase in the relative displacement of the maxima of the circularly polarized eigenwaves with respect to one another induced by an applied magnetic field. It should be emphasized that the maxima of $\Psi(\omega)$ are somewhat displaced with respect to the maxima of $R_1(\omega)$, which is associated with an additional phase incursion of eigenwaves in the layer B between the subsystems SS1 and SS2. Figure 3 also shows the dependence $\Psi(\omega)$ at different thicknesses d of the B layer. The calculations show (Fig. 3) that the enhancement of the Kerr rotation is maximal at such d for which Eq. (18) is fulfilled most rigorously.

CONCLUSION

Thus, the magnetic-field induced splitting of the frequency ranges of the resonance interaction of light with a magnetoactive structure into two components corresponding to circularly polarized eigenwaves allows one to attain a considerably larger angle of rotation of the polarization azimuth of the reflected radiation. In this case, another structure (playing the role of a dielectric mirror) placed behind the magnetoactive structure allows one to attain the reflection coefficient of the whole system close to unity. The expressions obtained in our study can also be used in the design and optimization of the parameters of compact magneto-optical elements for optical systems used for information processing.

REFERENCES

1. M. M. Noskov, Dokl. Akad. Nauk SSSR **31** (2), 112 (1941).
2. A. K. Zvezdin and V. A. Kotov, *Magnetooptics of Thin Films* (Nauka, Moscow, 1988).
3. S. M. Zhou, M. Lu, H. Y. Zhang, and R. Zhai, J. Appl. Phys. **71** (8), 3950 (1992).
4. R. Sato, N. Saito, and T. Morishito, IEEE Trans. Magn. **24** (6), 2458 (1988).
5. S. Sakaguchi and N. Sugimoto, J. Lightwave Technol. **17** (6), 1087 (1999).
6. M. J. Steel, M. Levy, and R. M. Osgood, J. Lightwave Technol. **18** (9), 1297 (2000).
7. G. A. Bolotin, Fiz. Met. Metalloved., No. 6, 197 (1991).
8. M. J. Steel, M. Levy, and R. M. Osgood, J. Lightwave Technol. **18** (9), 1289 (2000).
9. O. V. Ivanov and D. I. Sementsov, Kristallografiya **45** (5), 899 (2000) [Crystallogr. Rep. **45**, 827 (2000)].
10. L. Brillouin, *Wave Propagation in Periodic Structures* (Dover, New York, 1953; Inostrannaya Literatura, Moscow, 1959).
11. F. I. Fedorov, *Theory of Gyrotropy* (Nauka i Tekhnika, Minsk, 1976).

Translated by L. Man

Crystallography Reports, Vol. 48, No. 3, 2003, pp. 509–511. Translated from Kristallografiya, Vol. 48, No. 3, 2003, pp. 554–557.
Original Russian Text Copyright © 2003 by Malkhasyan, Karakhanyan, Nazaryan, Shangmo Sang.

Electron Microscopy Study of the Microstructure of Nanosize MoO_3 Powders

R. T. Malkhasyan*, R. K. Karakhanyan*, M. N. Nazaryan*, and Shangmo Sang**
** Research and Production Enterprise Atom, Yerevan, Armenia*
e-mail: rmalkhas@aua.am
*** Center for Advanced Materials, Department of Chemical and Nuclear Engineering,*
University of Massachusetts, Lowell, Ma., 01854 USA

Received September 24, 2001; in final form, November 22, 2002

Abstract—Linear double-chain aggregates and orthogonal superlattices of nanoparticles are observed in nanosize MoO_3 powders treated by vibrationally excited hydrogen molecules. Coiled aggregates of MoO_3 nanoparticles are revealed which, under the action of intense electron irradiation, uncoil and form branched chains. *© 2003 MAIK “Nauka/Interperiodica”.*

Nanosize materials possessing unique physical and chemical properties are attracting ever-increasing attention among researchers [1, 2]. One of the important problems is the synthesis and study of new types of nanostructures of various materials. Below, we describe an electron microscopy study of the microstructure of nanosize MoO_3 powders and the processes occurring in these powders under the action of electron irradiation in an electron microscope. The studies were performed in a TESLA BS 500 electron microscope with an accelerating voltage of 90 kV. The samples were obtained by applying one or two drops of an MoO_3 suspension in hexane onto standard copper grids coated with carbon substrates produced by TED.PELLA, Inc. (USA).

Electron microscopy studies of nanosize MoO_3 powders treated with nonequilibrium hydrogen molecules vibrationally excited to the third quantum level [3] showed that these powders consist of agglomerates of nanoparticles with a size ranging from 0.4 to 16.0 μm. Under a low-intensity electron beam, these agglomerates are stable, but with an increase in the electron beam intensity up to 25 μA, some MoO_3 nanoparticles are ejected from the agglomerates. The nanoparticle size in the MoO_3 powder ranges from 5 to 30 nm.

After the ejection of some nanoparticles, the remaining parts of the agglomerates show a spatial organization of nanoparticles that was never before observed in nanomaterials. In particular, we observed the formation of an ordered network of long parallel chains of rounded MoO_3 nanoparticles with a minimum diameter of 20 nm (Fig. 1). The interchain distances vary from 0.4 to 1.0 μm, and the chain length is about 17 μm. It is seen from Fig. 2 (obtained at higher magnification) that the linear chain aggregates consist of two individual chains close to one another (double chains). Long double-chain aggregates of nanoparticles also have transverse branches, sometimes reaching the neighboring chains. These branches, in turn, have smaller branches.

After ejection of nanoparticles from the agglomerates treated with hydrogen molecules, we also observed orthogonal superlattices with the parameters $a = 60$ nm and $b = 80$ nm formed by chain aggregates of MoO_3 nanoparticles (Fig. 3). The microdiffraction patterns from the linear double-chain aggregates and orthogonal superlattices of MoO_3 particles proved that they are of polycrystalline nature (Fig. 4). Powder electron diffraction patterns were indexed based on the primitive orthorhombic unit cell with the lattice parameters $a =$

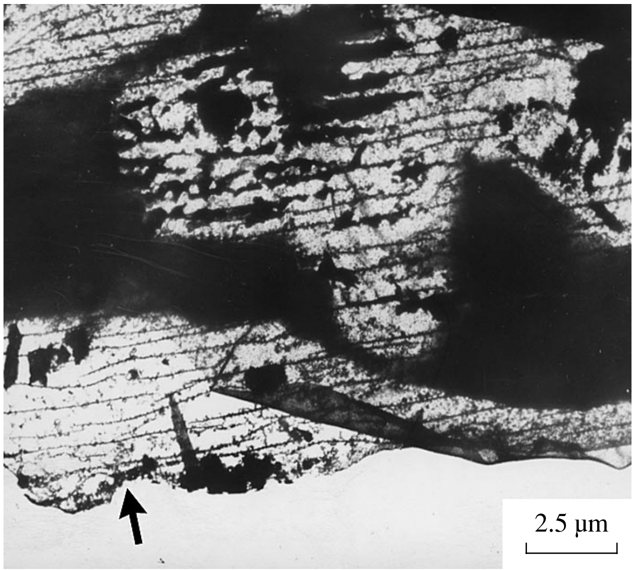

Fig. 1. Ordered network of linear chain aggregates of MoO_3 nanoparticles.

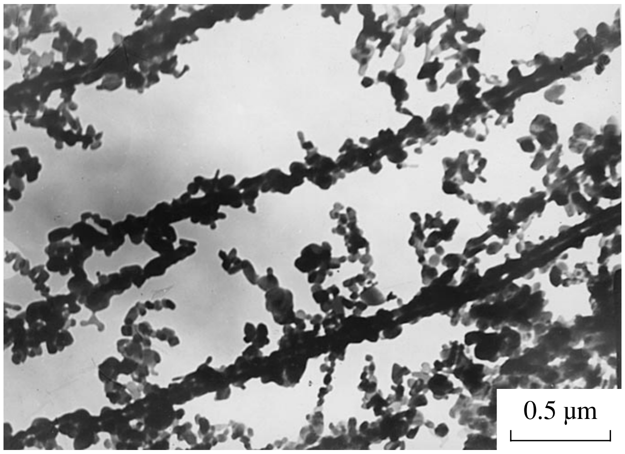

Fig. 2. Linear double-chain aggregates of MoO_3 nanoparticles.

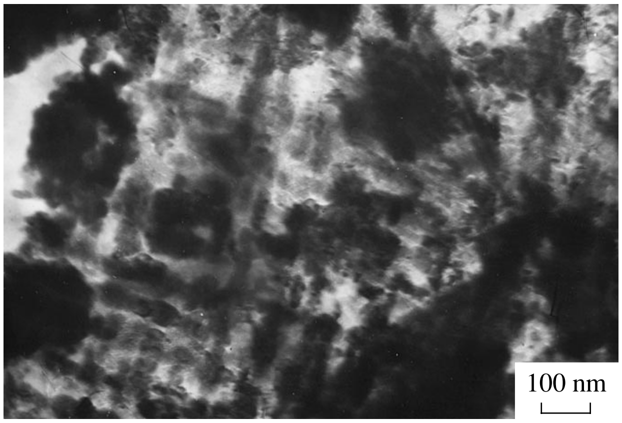

Fig. 3. Orthogonal superlattice of MoO_3 nanoparticles.

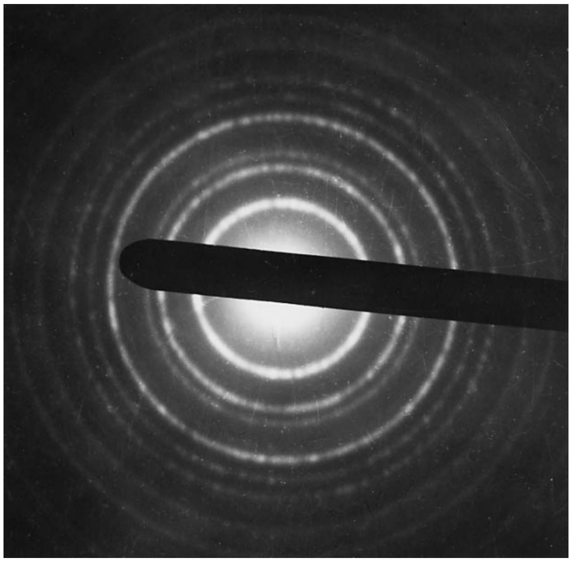

Fig. 4. Electron diffraction pattern from double-chain aggregates and orthogonal superlattices of MoO_3 nanoparticles.

3.961(1) Å, b = 13.845(3) Å, and c = 3.698(1) Å, which is consistent with the data obtained in [4] and the diffraction patterns from the initial nanosize MoO_3 powder and a standard MoO_3 sample.

Both the linear double-chain aggregates and orthogonal superlattices of MoO_3 nanoparticles are very stable against electron irradiation in an electron microscope. They also show high stability in the absence of a carbon substrate. Thus, the brighter background in the region indicated by an arrow in Fig. 1 corresponds to the region that has no carbon substrate. In [5], long single chains of Co nanoparticles were observed and their formation was attributed to ferromagnetism of cobalt. Our results indicate that the presence of ferromagnetic particles is not a necessary condition for the formation of long chain aggregates, because MoO_3 is not a ferromagnetic material.

Our studies also show that double-chain aggregates and superlattices of nanoparticles do not form in an electron microscope but can form in a reactor where nanosize MoO_3 powder is treated with excited hydrogen molecules [3]. The ejection of nanoparticles, which cover double-chain aggregates and superlattices in agglomerates, helps one to reveal these objects. Numerous attempts to obtain double-chain aggregates and orthogonal superlattices from nanosize MoO_3 powders that were not preliminarily treated with hydrogen molecules gave no positive results, although we always used the equivalent carbon substrates and nanoparticles with the same dimensions as MoO_3 nanoparticles treated with hydrogen molecules.

It is well known [6] that self-organizing systems are based, in particular, on hydrogen bonding. Since MoO_3 nanoparticles were treated with hydrogen molecules, it was obvious that the presence in the reactor of active hydrogen molecules provided hydrogen bonding between the MoO_3 nanoparticles. This process was also favored by the electronegative oxygen of MoO_3. Hydrogen bonds formed between MoO_3 nanoparticles do not change their crystal structure, which is confirmed by the electron diffraction pattern in Fig. 4. It is hydrogen bonds that promote the formation of chain aggregates of MoO_3 nanoparticles, i.e., a process similar to polymerization processes via hydrogen bonding. The formation of double-chain aggregates is also associated with hydrogen bonds formed between nanoparticles from two individual chains. Their high stability seems to be explained by the fact that neighboring nanoparticles in each double chain are related by the forces acting between the pairs of nanoparticles. In the final analysis, such pairwise contacts provide considerable total binding force between the nanoparticles and a high stability and rigidity of the linear double chains. The existence of linear double-chain aggregates and orthogonal superlattices is an indication of new forms of self-organizing nanostructures [7–9] and requires additional detailed experimental and theoretical study.

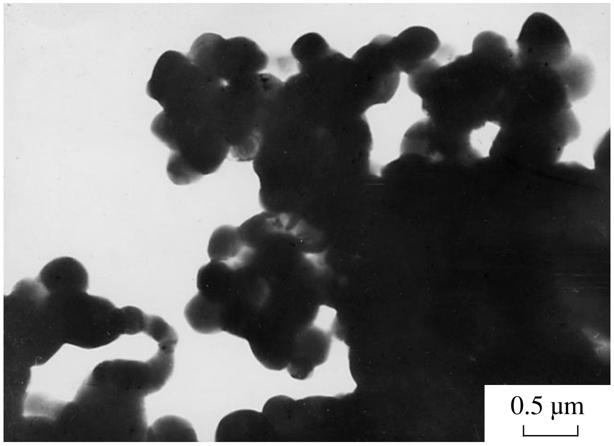

Fig. 5. Coiled chain aggregates of MoO_3 nanoparticles.

After the ejection of nanoparticles from MoO_3 agglomerates treated with hydrogen molecules, we also revealed the coiled chain aggregates of crystalline nanoparticles of these materials. As an example, Fig. 5 shows an electron micrograph of such aggregates of MoO_3 nanoparticles with a minimum size of 80 nm. If there had been no carbon substrate under some of the coiled chain aggregates (e.g., because of rupture of the film), then, with an increase in electron-beam intensity, we should have observed fast Brownian motion of these coiled aggregates. Despite the absence of a carbon substrate, the nanoparticles of the chain aggregates are kept together by cohesion forces which, in this case, exceed the gravitational forces. As a result of such motion, the coiled chain aggregates of nanoparticles uncoil and slightly straighten out. Chain aggregates start moving after the attainment of a certain equilibrium state, in which further electron irradiation by an electron beam of the given intensity produces no effect. In this case, the chain aggregates of MoO_3 nanoparticles form a branched disordered network. The microdiffraction patterns show that these chain aggregates also have a polycrystalline nature. In the absence of a carbon substrate, the chain aggregates of MoO_3 nanoparticles cannot move and straighten because of rather strong cohesion forces acting between these aggregates and the carbon substrate.

With a still further increase in the electron-beam intensity, we observed disintegration and coiling of the chain aggregates. The different behavior of coiled and linear double-chain aggregates may also be associated with the fact that a double chain is more stable than a single one and also with the different sizes of nanoparticles forming these chains.

We should like to emphasize that elongation of coiled chain aggregates of TiO_2 nanoparticles under the action of mechanical tensile stresses was also observed in [10]; during heating, these chain aggregates also tend to coil. According to [10], if one end of a chain aggregate of TiO_2 particles is free, this chain aggregate starts coiling. In our case, we observed stable (unshrinkable) branched networks of MoO_3 particles also in a situation where one of their ends was free.

Thus, the treatment of nanosize powders with vibrationally excited hydrogen molecules results in the formation of chain aggregates of nanoparticles which, depending on the local conditions, can form three different configurations: coiled chain aggregates, long linear double-chain aggregates, and superlattices of chain aggregates.

The coiled chain aggregates subjected to the action of an electron beam can elongate and form disordered branched networks. Unlike this process, linear double-chain aggregates and superlattices of nanoparticles are highly stable against intense electron irradiation. The formation of double-chain aggregates and superlattices of MoO_3 nanoparticles was observed only if the powders were preliminarily treated with vibrationally excited hydrogen molecules. This allows us to hope that such a treatment of nanosize powders may become one of the methods of obtaining long chains of inorganic materials with controllable properties.

ACKNOWLEDGMENTS

This study was supported by MNTTs, project no. A-139.

REFERENCES

1. Metastable Phase and Microstructures, Mater. Res. Soc. Symp. Proc. **400**, 368 (1995).
2. *Nanophase Materials*, Ed. by G. S. Hadjypanayis and R. W. Siegal (Kluwer Academic, Dordrecht, 1994).
3. R. T. Malkhasyan, Mater. Res. Soc. Symp. Proc. **400**, 77 (1995).
4. L. M. Utevskiĭ, *Diffraction Electron Microscopy in Metal Science* (Metallurgiya, Moscow, 1973).
5. A. R. Tholen, in *Nanophase Materials*, Ed. by G. S. Hadjypanayis and R. W. Siegal (Kluwer Academic, Dordrecht, 1994), p. 57.
6. W. M. Tolles, MRS Bull. **25**, 36 (2000).
7. Y. S. Lindsey, New J. Chem. **15**, 153 (1991).
8. G. M. Whitesides, I. P. Mathaires, and C. T. Seto, Science **2545**, 312 (1991).
9. I. M. Lehn, Angew. Chem. Int. Ed. Engl. **29**, 1304 (1999).
10. S. K. Friendlander, J. Nanopart. Res. **1**, 9 (1999).

Translated by L. Man

Crystallography Reports, Vol. 48, No. 3, 2003, pp. 512–514. Translated from Kristallografiya, Vol. 48, No. 3, 2003, pp. 558–561.
Original Russian Text Copyright © 2003 by Malkhasyan, Karakhanyan, Nazaryan, Changmo Sung.

NANOMATERIALS

In situ Electron Microscopy Study of Growth of WO_3 and MoO_3 Nanowhiskers

R. T. Malkhasyan*, R. K. Karakhanyan*, M. N. Nazaryan*, and Changmo Sung**
** Research and Production Enterprise Atom, Yerevan, Armenia*
e-mail: rmalkhas@aua.am
*** Center for Advanced Materials, Department of Chemical and Nuclear Engineering,*
University of Massachusetts, Lowell, Ma., 01854 USA

Received September 24, 2001

Abstract—WO_3 and MoO_3 nanowhiskers were grown from nanosize WO_3 and MoO_3 powders intensely irradiated with electrons in an electron microscope. Solid and hollow nanowhiskers of these materials were observed. A growth mechanism of nanowhiskers is suggested that is based on surface diffusion of WO_3 and MoO_3 molecules generated by the agglomerates of molecules under intense electron irradiation. © *2003 MAIK “Nauka/Interperiodica”.*

At present, the growth and study of various types of nanostructures possessing promising properties are among the most topical problems in the research of these properties [1]. One of the methods of growing various nanostructures [2–7], including diamond whiskers [8], is electron irradiation. Despite the fact that attention is focused mainly on carbon-based nanomaterials, it is important to obtain nanostructures of some other inorganic materials in order to reveal new features and properties of nanostructures. The present study was undertaken to grow WO_3 and MoO_3 nanowhiskers (several nanometers in width) by irradiation with electrons directly in an electron microscope and to consider the dynamical processes occurring in nanowhiskers in order to establish the conditions and mechanism of their growth. The experiments were made in a TESLA BS 500 transmission electron microscope under accelerating voltages of 60 and 90 kV. The samples for electron microscopy studies were prepared by applying one or two drops of suspensions of nanosize WO_3 and MoO_3 powders in hexane onto copper grids coated with amorphous carbon substrates. We used commercial nanosize WO_3 and MoO_3 powders and vibrationally excited hydrogen molecules (third quantum level) obtained as described elsewhere [9].

Electron microscopy studies showed that, for all types of nanosize WO_3 and MoO_3 powders irradiated with electron beams of conventional intensities, the agglomerates of these compounds preserved their initial state. With an increase in the electron-beam intensity (up to 30 μA), we observed very fast (several seconds) growth of a large number of WO_3 and MoO_3 nanowhiskers irrespective of the voltage and method of preparation of nanosize powders. It is seen from Fig. 1 that WO_3 nanowhiskers can be isolated and have arbitrary orientations or can form blocks of closely packed nanocrystals that have the same crystallographic orientation. The minimum width of WO_3 and MoO_3 nanowhiskers is about 8 nm; their maximum length is about 1 μm. In addition to conventional (solid) nanocrystals, we also observed hollow WO_3 and MoO_3 nanocrystals (indicated by arrows) (Fig. 2). The analysis of electron diffraction patterns from such crystals (for example, Fig. 3 shows the diffraction pattern of a WO_3 nanocrystal with the incident electron beam being close to the [010] axis of the sample) showed that both WO_3 and MoO_3 nanowhiskers grow along the [001] direction, which is provided by the close crystal structures of WO_3 and MoO_3 [10]. The first reflections along the [001] and [100] directions of WO_3 crystals (Fig. 3) have interplanar spacings of 3.831(1) and 3.641(1) Å, and

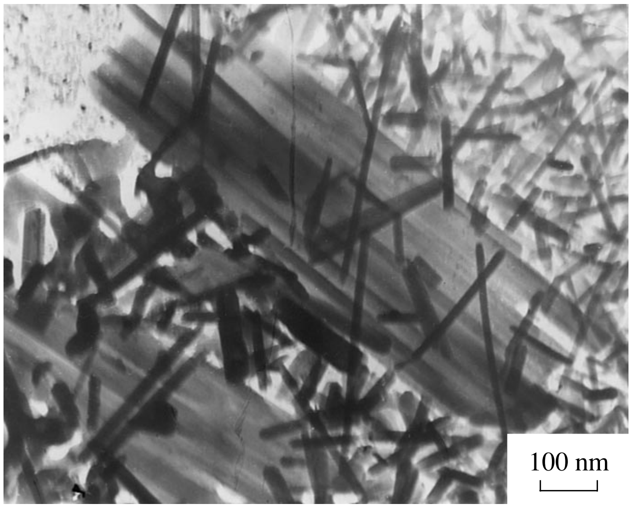

Fig. 1. WO_3 nanowhiskers.

those of MoO_3 crystals, 3.698(1) and 3.961(1) Å, which is consistent with the data in [10, 11]. It should be indicated that the MoO_3 crystals obtained by molybdenum heating in the oxygen flow took the form of plates with long edges parallel to the [001] direction [11, 12].

Since the growth of WO_3 and MoO_3 nanowhiskers proceeds almost instantaneously, it is very difficult to follow the process. Electron microscopy studies showed that nanowhiskers are formed on those segments of carbon substrates where the numbers of WO_3 and MoO_3 nanoparticles are relatively large. Indeed, it is seen from Fig. 4 that the regions with large numbers of long nanowhiskers are characterized by a considerable surface density of nanoparticles. With a decrease in the nanoparticle density along the boundary of the carbon film, the number and length of nanowhiskers decrease. Our studies show that if the number of nanoparticles is small, no nanowhiskers can form. Nanowhiskers can grow both on carbon substrates and on initial agglomerates and even in the absence of a carbon substrate.

With a further intensification of electron irradiation, the reverse process occurs—the WO_3 and MoO_3 nanowhiskers gradually disintegrate, with the process occurring slower than the growth, which allows one to record the disintegration process on micrographs. Figures 5 and 6 show WO_3 nanowhiskers at early and late stages of their disintegration. Electron irradiation allows one to distinguish individual nanoparticles in nanowhiskers. As was expected, the microdiffraction patterns from disintegrating nanocrystals fully corresponded to the electron diffraction patterns from the initial nanosize MoO_3 and WO_3 powders before the growth of nanocrystals. Still further irradiation with a more intense electron beam resulted in the complete disintegration and coiling of nanocrystals.

Based on our electron microscopy study, we can propose the following growth mechanism of WO_3 and MoO_3 nanowhiskers. At the first stage, it is necessary to have a sufficient number of individual nanoparticles that play the role of crystalline nuclei for the growth of nanowhiskers. Then, under the action of electron irradiation [13], the WO_3 and MoO_3 nanoparticles generate individual molecules of these substances. As a result of thermal motion and surface diffusion, WO_3 and MoO_3 molecules continuously migrate on the carbon substrate or on agglomerates. Diffusing molecules coming into contact with [001]-oriented crystalline nuclei (corresponding to the maximum growth rate) cause the formation of WO_3 and MoO_3 nanowhiskers. If nanowhiskers grow at the boundaries of the ruptured carbon film or at the agglomerate edges where no carbon substrate exists, molecular diffusion takes place on the surface of the already formed part of the nanowhisker. Taking into account the high rate of surface molecular diffusion, one can readily understand the very fast growth of WO_3 and MoO_3 nanowhiskers, which ceases with an increase

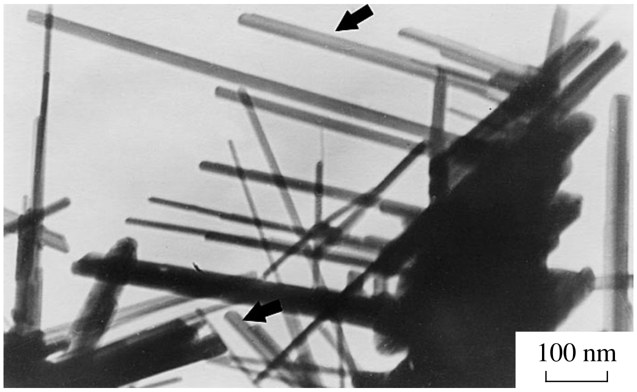

Fig. 2. Solid and hollow MoO_3 nanowhiskers.

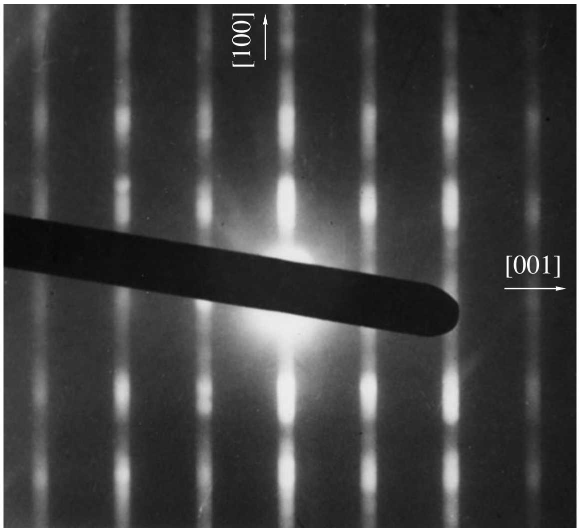

Fig. 3. Electron diffraction pattern from a WO_3 nanowhisker.

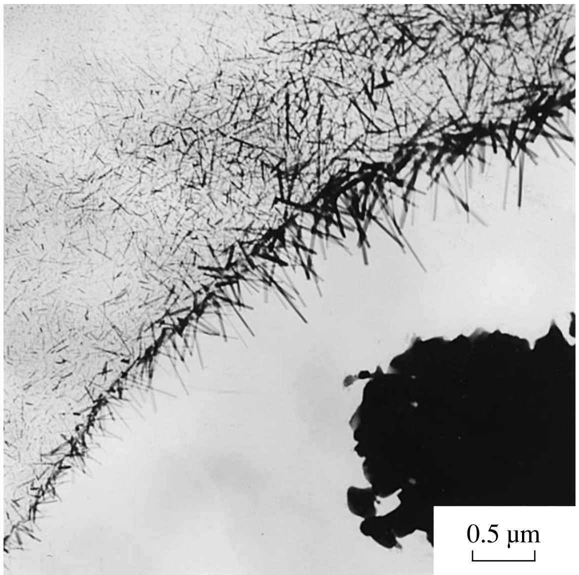

Fig. 4. WO_3 nanowhiskers at the boundary of a carbon substrate.

Fig. 5. WO_3 nanowhiskers at the early stage of their disintegration.

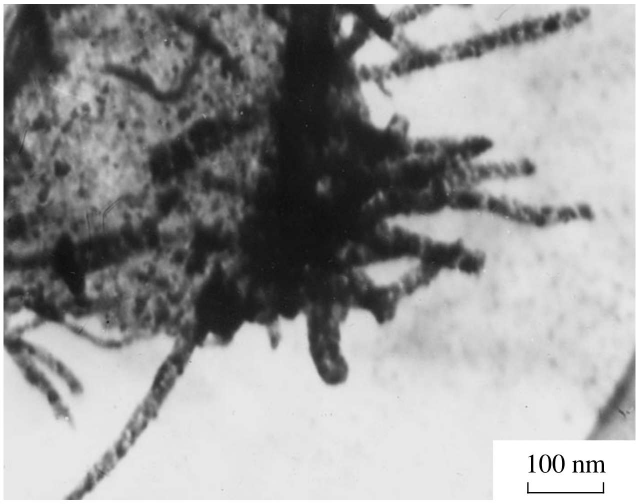

Fig. 6. WO_3 nanowhiskers at the late stage of their disintegration.

in the number of initial nanoparticles. If hollow nanowhiskers are formed, the initial crystalline nucleus has a circular shape because of the topology of the part of the film where this nucleus was formed. As a result of processes analogous to those observed in the growth of solid nanowhiskers, further growth of hollow nanowhiskers occurs.

Thus, one can draw the conclusion that if nanoparticles have a certain surface density, intense electron irradiation of nanosize WO_3 and MoO_3 powders results in fast growth of solid and hollow nanowhiskers of these materials. The results obtained allow us to state that WO_3 and MoO_3 powders should be added to the range of the well-known inorganic materials that can form hollow nanosize structures [14–18].

ACKNOWLEDGMENTS

This study was supported by MNTs, project no. A-139.

REFERENCES

1. S. M. Prokes and K. L. Wang, MRS Bull. **24**, 13 (1999).
2. D. Ugarte, Nature **359**, 707 (1992).
3. W. A. De Heer and D. Ugarte, Chem. Phys. Lett. **207**, 480 (1993).
4. Q. Ru, M. Okamoto, Y. Kondo, *et al.*, Chem. Phys. Lett. **259**, 425 (1996).
5. K. G. Mckay, H. W. Kroto, and D. I. Wales, J. Chem. Soc., Faraday Trans. **88**, 2815 (1992).
6. B. S. Xu and S.-I. Tanaka, in *Proceedings of Annual Meeting of the Scandinavian Society for Electron Microscopy, Espoo, Finland* (1997), p. 434.
7. T. Oku, T. Hirano, and K. Suganuma, J. Mater. Res. **14**, 4266 (1999).
8. V. D. Zamozhskiĭ and A. N. Luzin, Dokl. Akad. Nauk SSSR **224**, 369 (1975).
9. R. T. Malkhasyan, Mater. Res. Soc. Symp. Proc. **400**, 77 (1995).
10. K. Schubert, *Krystallstrukturen Zweikomponentiger Phasen* (Springer, Berlin, 1964).
11. L. M. Utevskiĭ, *Diffraction Electron Microscopy in Metal Science* (Metallurgiya, Moscow, 1973).
12. D. B. Williams and C. B. Carter, *Transmission Electron Microscopy. Basics* (Plenum, New York, 1996), Vol. 1.
13. L. W. Hobbs, in *Introduction to Analytical Electron Microscopy*, Ed. by J. J. Hren, J. I. Goldstein, and D. C. Joy (Plenum, New York, 1997).
14. S. Iijima, Nature **3545**, 56 (1991).
15. Y. Gogotsi, Y. A. Libera, N. Kalashnikov, *et al.*, Science **290**, 317 (2000).
16. E. I. W. Whittaker, Acta Crystallogr. **21**, 461 (1966).
17. Y. Gogotski, V. Yaroshenko, and F. Pozz, J. Mater. Sci. Lett. **11**, 308 (1992).
18. J. L. Gole, Z. R. Dai, J. D. Stout, and Z. L. Wang, in *Materials Research Society Fall Meeting* (Boston, MA, 2001), W.10.2, p. 464.

Translated by L. Man

Crystallography Reports, Vol. 48, No. 3, 2003, pp. 515–519. Translated from Kristallografiya, Vol. 48, No. 3, 2003, pp. 562–566.
Original Russian Text Copyright © 2003 by Kaminskiĭ, Akchurin, Alshits, Ueda, Takaichi, Lu, Uematsu, Musha, Shirikawa, Gabler, Eichler, Yagi, Yanagitani, Bagayev, Fernandez, Balda.

NANOMATERIALS

New Data on the Physical Properties of $Y_3Al_5O_{12}$-Based Nanocrystalline Laser Ceramics[1]

A. A. Kaminskiĭ*, M. Sh. Akchurin*, V. I. Alshits*, K. Ueda, K. Takaichi**, J. Lu**, T. Uematsu**, M. Musha**, A. Shirikawa**, V. Gabler***, H. J. Eichler***, H. Yagi****, T. Yanagitani****, S. N. Bagayev*****, J. Fernandez*****, and R. Balda********

** Shubnikov Institute of Crystallography, Russian Academy of Sciences,*
Leninskiĭ pr. 59, Moscow, 119333 Russia
e-mail: kamin.alex@mail.ru
*** Institute for Laser Science, University of Electro-Communications, 182-8585 Tokyo, Japan*
**** Optical Institute, Technical University, D-10623 Berlin, Germany*
***** Takuma Works, Konashima Chemical Co., 769-11 Kagawa, Japan*
****** Institute of Laser Physics, pr. Lavrent'eva 13/3, Novosibirsk, 630090 Russia*
******* Department of Applied Physics, Basque Country University, 48013 Bilbao, Spain*

Received December 11, 2002

Abstract—Microhardness and fracture toughness of highly transparent $Y_3Al_5O_{12}$- and $Y_3Al_5O_{12} : Nd^{3+}$-based nanocrystalline ceramics are measured for the first time. For the $Y_3Al_5O_{12} : Nd^{3+}$ laser ceramics, the use of a longitudinal scheme with a diode-laser pumping at a wavelength of 1.3186 μm ($^4F_{3/2} \longrightarrow {}^4I_{13/2}$ channel) enabled one to attain an output power of continuous-wave lasing of ~3.7 W with 35% efficiency. *© 2003 MAIK “Nauka/Interperiodica”.*

The highly transparent $Y_3Al_5O_{12} : Nd^{3+}$ ceramic produced by the modified methods of urea precipitation and vacuum sintering without application of external pressure [1, 2] is a representative of the new generation of active media, a rapidly developing field of contemporary laser materials science. This ceramic was used to design efficient diode-laser pumped continuous-wave (CW) lasers emitting at a wavelength of 1.06415 μm (main $^4F_{3/2} \longrightarrow {}^4I_{11/2}$ lasing channel of Nd^{3+} ions) with an output power of kilowatt level (from ~370 mW in the year 2000 [3] to ~1.5 kW in 2001 [13]; see also Fig. 1). These achievements show that the relatively cheap $Y_3Al_5O_{12} : Nd^{3+}$ ceramic with no size limitations may compete with $Y_3Al_5O_{12} : Nd^{3+}$ crystals, which are most widely used in quantum electronics and laser engineering.

This paper continues the series of our publications on lasing, nonlinear, and spectral properties of the $Y_3Al_5O_{12} : Nd^{3+}$ ceramic [3–16] and describes the first measurements of mechanical properties of this new active material and also new laser experiments with this material. In particular, we present new data on CW lasing in the 1.319-μm spectral range on the inter-Stark transition of the $^4F_{3/2} \longrightarrow {}^4I_{11/2}$ lasing channel of the Nd^{3+} activator ions. Preliminary data on measurements of microhardness and fracture toughness of the $Y_3Al_5O_{12}$ and $Y_3Al_5O_{12} : Nd^{3+}$ ceramics are presented. Let us review the initial stages of the study of laser ceramics obtained by sintering under high pressure. The first laser ceramics were the $CaF_2 : Dy^{2+}$-based fluoride ceramic [20] and the yttralox-Y_2O_3–$ThO_2 : Nd^{3+}$ oxide ceramic [21]. The same well-known technique was also used to obtain $Y_3Al_5O_{12} : Nd^{3+}$-based laser ceramics in the mid-1990s [17, 18]. However, like the first $CaF_2 : Dy^{2+}$ and Y_2O_3–$ThO_2 : Nd^{3+}$ ceramics, the latter ceramic had insufficient lasing characteristics (see Fig. 1).

Consider briefly the preparation of our highly transparent $Y_3Al_5O_{12} : Nd^{3+}$ laser ceramic. The process involved several steps. First, we mixed Al, Y, and Nb chloride solutions with ammonium carbonate NH_4HCO_3. Then, the mixture was filtered, and the product obtained was multiply washed with water and dried. Upon annealing of the product at ~1200°C, the oxide powder was obtained and ground with the corresponding solvents for 24 h. The suspension thus produced was placed into a gypsum mold and dried. Upon the removal of organic components by annealing, the material was finally sintered in vacuum at ~1750°C. The porosity of the highly transparent $Y_3Al_5O_{12} : Nd^{3+}$-

---

[1] The results of this study were presented at the International Quantum Electronics Conference IQEC-2002 (June 22–27, 2002, Moscow) and at the 204th meeting of the monthly Moscow Seminar on Physics and Spectroscopy of Lasing Crystals (December 26, 2000).

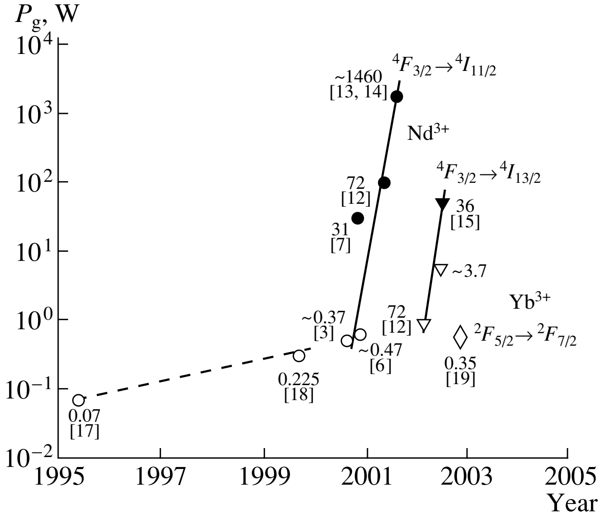

Fig. 1. Chronology of the studies of CW lasers based on the nanocrystalline $Y_3Al_5O_{12}$ ceramic doped with ions of trivalent lanthanides (Ln^{3+}). Open (circles, triangles, and rhombs) and solid (circles and triangles) symbols correspond to the output power of the ceramic neodymium (Nd^{3+}) lasers (at wavelengths of $^4F_{3/2} \longrightarrow {}^4I_{11/2}$ and $^4F_{3/2} \longrightarrow {}^4I_{13/2}$ lasing channels) and the ceramic ytterbium (Yb^{3+}) laser, obtained under longitudinal and transverse diode-laser pumping, respectively.

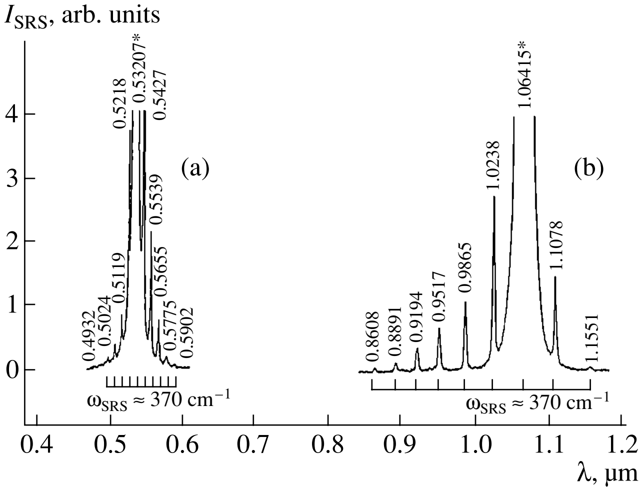

Fig. 2. The spectra of the steady-state SRS in the nanocrystalline $Y_3Al_5O_{12}$ ceramic recorded under excitation with pulses of a picosecond $Nd^{3+} : Y_3Al_5O_{12}$ laser [4, 5] in the (a) visible and (b) near IR ranges at 300 K (the pumping lines are marked with asterisks). The intensities were not corrected for the spectral sensitivity of the recording system. The relation between the Stokes and anti-Stokes components of the generation and the SRS-active vibrational mode of the $Y_3Al_5O_{12}$ ceramic with the frequency $\omega_{SRS} \approx 370$ cm^{-1} is shown in brackets.

based ceramics thus synthesized did not exceed 1 ppm (~10–4%); the thickness of the grain boundaries was less than 0.1 μm. The optical losses caused by scattering in the visible range in our $Y_3Al_5O_{12}$ and $Y_3Al_5O_{12} : Nd^{3+}$ ceramics were rather low (~0.009 cm^{-1}). The high quality of this optical and laser material is also confirmed by excitation of the high-order stimulated Raman scattering (SRS) [4, 5], which is well illustrated by two SRS spectra of our laser ceramics $Y_3Al_5O_{12} : Nd^{3+}$ shown in Fig. 2.

Mechanical properties of crystalline materials are usually studied by the indentation and sclerometry (scratching) methods. These methods allow one to estimate their strength characteristics—hardness (H) and brittleness. The latter characteristic is related to the fracture toughness (K_{1C}) and can be reliably determined from the measured linear dimensions of radial cracks (C) produced by an indenter as a function of the applied load P [22]. The measurements were made on 2 × 15 × 25 mm^3 plates of $Y_3Al_5O_{12}$ and $Y_3Al_5O_{12} : Nd^{3+}$ ($C_{Nd} \approx$ 1 at. %) ceramics and {100}-oriented $Y_3Al_5O_{12}$ single crystals with approximately the same dimensions. All the samples were polished to the 14th class of surface finish; some samples were also treated chemically in H_3PO_4 at $t \sim 320°C$ to remove the hardened layer. The experiments were made using a PMT-3 microhardness gauge with a diamond Vickers indenter and a Martens sclerometer. Microhardness was estimated using the well-known formula

$$H = k\frac{P}{d^2}, \qquad (1)$$

where P is the load applied to the indenter, k is the coefficient dependent on the indenter shape equal to 185 in our case, and d is the diagonal of the indentation (Fig. 3). The fracture toughness K_{1C} related to P and C values also depends on the indenter geometry and the properties of the material. In general, the fracture toughness is determined as [23]

$$K_{1C} = \psi_a\sqrt{P/C}. \qquad (2)$$

Since the parameter ψ_a is somewhat ambiguous, we used the formula for K_{1C} given in [24], which accounts for the elastic and strength characteristics of the material under study:

$$K_{1C} = 0.026\sqrt{\cot(\varphi/2)}\sqrt{E/H}\sqrt[3]{P/C}, \qquad (3)$$

where E is the Young's modulus and φ is the apex angle of the indenter. For the Vickers indenter used in this study, $\varphi/2 = 68°$, and Eq. (3) takes the form [25]

$$K_{1C} = 0.016\sqrt{E/H}\sqrt[3]{P/C}. \qquad (4)$$

The load applied to the indenter was chosen so as to provide indentations and radial cracks that could be measured. The experiments showed that the radial cracks in single crystals are well distinguished even at

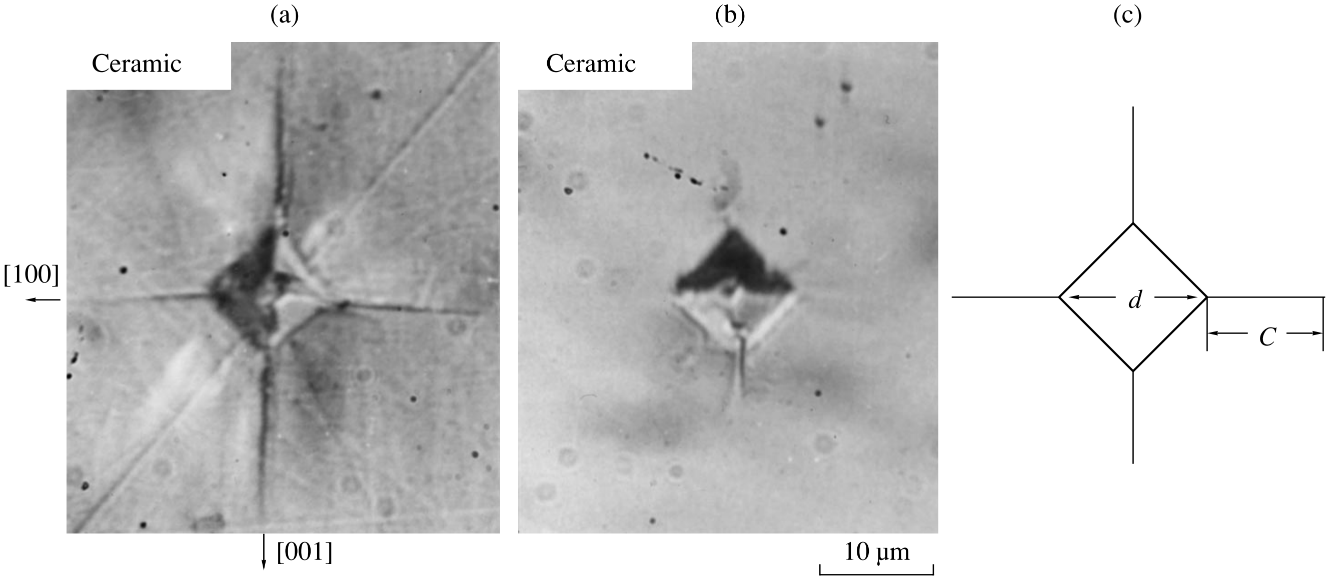

Fig. 3. Indentations on the {100} surface of (a) a $Y_3Al_5O_{12}$ single crystal, (b) a ceramic $Y_3Al_5O_{12}$ sample, and (c) a scheme illustrating the analysis of the indentation: d is the diagonal of the indentation and C is the crack length (for explanation see text). Scale: 10 μm in the figure corresponds to 15 mm.

loads as low as $P = 20$ g, while in ceramic samples, cracks are formed only at $P \geq 100$ g. Therefore, we measured the microhardness and the fracture toughness of both single crystals and the $Y_3Al_5O_{12}$-based ceramic at the same load, $P = 100$ g. The results of these experiments and their analysis are summarized in the table. In calculations, we used the Young's modulus along the [100] direction for $Y_3Al_5O_{12}$ single crystals ($E = 2.8 \times 10^{12}$ dyn cm^{-2}).

Our studies showed that, unlike $Y_3Al_5O_{12}$ single crystals [26], the samples of the $Y_3Al_5O_{12}$ and $Y_3Al_5O_{12} : Nd^{3+}$ ceramics (polished both mechanically and chemically) showed no anisotropy of hardness; but their microhardness is higher by 10–15% than the microhardness of the single crystals. The strength characteristics of the ceramic samples and single crystals are essentially different (see Fig. 3). As is seen from the table, the K_{1C} value of the ceramic samples is almost 5 times higher than that of the single crystals. This can play a decisive role when choosing the type of crystalline material for various applications (including those not related to lasers). As is seen from the table, the fracture hardness of the $Y_3Al_5O_{12} : Nd^{3+}$ laser ceramics is somewhat lower, which has not been explained as yet.

Both transverse and longitudinal schemes of diode-laser pumping of crystalline lasing media with Nd^{3+} ions (including ceramic media) have some advantages. For example, the transverse scheme provides a higher output power. In turn, it is easier to obtain single-mode lasing (which enables one to obtain a beam of laser radiation with extremely low divergence) with the use of a longitudinal (end) scheme of pumping.

The output power of the $Nd^{3+} : Y_3Al_5O_{12}$-ceramic CW laser operating on the inter-Stark transitions of the ${}^4F_{3/2} \longrightarrow {}^4I_{13/2}$ lasing channel under longitudinal pumping with a single 1-W AlGaAs laser diode attained in our earlier study [4] did not exceed 700 mW. In the present study, this parameter is substantially improved

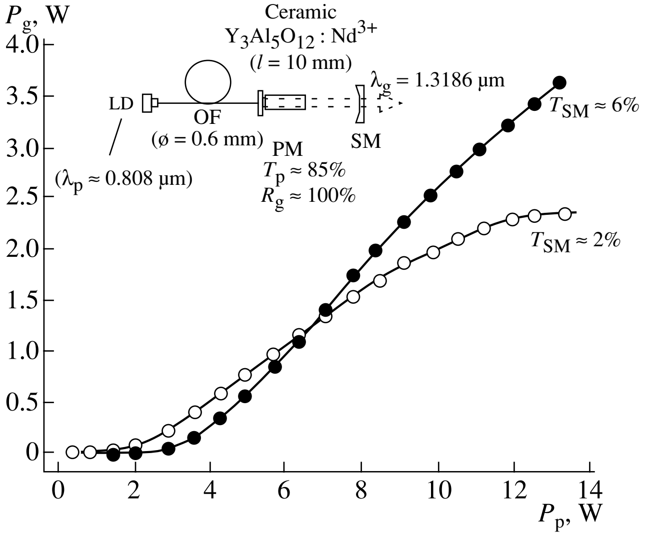

Fig. 4. The output power of the CW laser based on the nanocrystalline $Y_3Al_5O_{12} : Nd^{3+}$ ($C_{Nd} \approx 0.6$ at. %) ceramics as a function of the power of a laser-diode (LD) array for two values of optical transmission (T_{SM}) of the output spherical mirror (SM) of the laser cavity: OF is the optical fiber with 0.6-μm core diameter and PM is the plane mirror of the cavity with a high transmission of pumping radiation (T_p) and reflectivity (R_g) at a lasing wavelength of the ceramic of $\lambda_p = 1.3186$ μm.

Microhardness and fracture toughness of the nanocrystalline $Y_3Al_5O_{12}$ and $Y_3Al_5O_{12} : Nd^{3+}$ ceramics and the corresponding data for $Y_3Al_5O_{12}$ single crystals

Characteristic	Ceramics			$Y_3Al_5O_{12}$ crystal	
	$Y_3Al_5O_{12}$		$Y_3Al_5O_{12} : Nd^{3+}$		
H, GPa	16.0*	15.5**	15.0*	14.5*	14*
K_{1C}, MPa	8.7*	8.8**	5.2*	1.8*	1.86**

* Mechanical polishing of the surface.
** Chemical polishing of the surface.

with the use of the same longitudinal scheme of excitation but with considerably higher pumping power—the 16-W heterolaser AlGaAs array (λ_p = 0.808 μm) with an optical-fiber output.

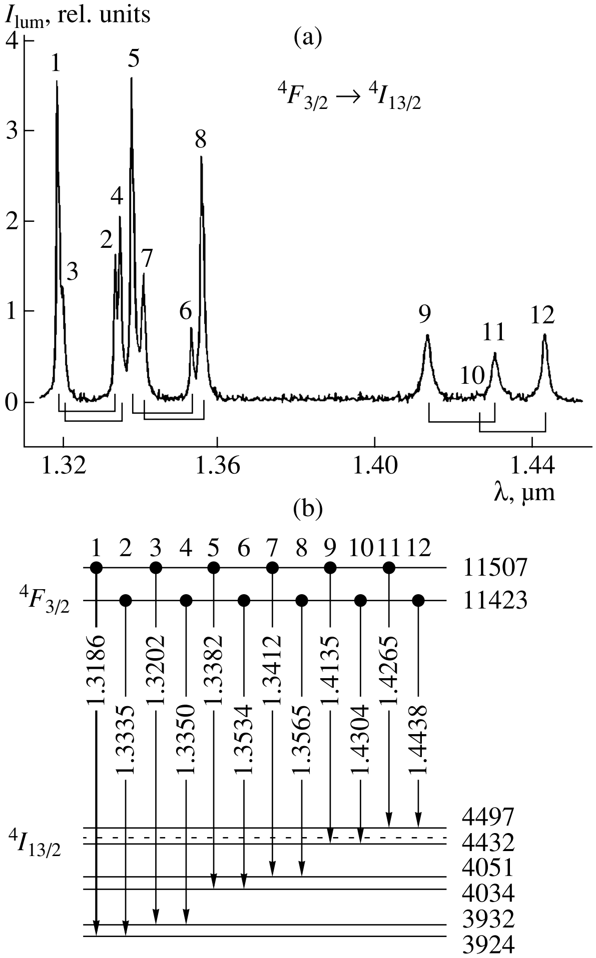

Fig. 5. (a) Luminescence spectrum ($^4F_{3/2} \longrightarrow {}^4I_{13/2}$ channel) and (b) scheme of the crystal-field splitting of the $^4F_{3/2}$ and $^4I_{13/2}$ multiplets of Nd^{3+} ions in the $Y_3Al_5O_{12}$ ceramic at 300 K. The brackets show the splitting of the initial laser state $^4F_{3/2}$. The energy of the Stark levels is given in cm^{-1}; the wavelength of the transitions between the levels, in μm. The bold arrow indicates a laser transition. The lines in the spectrum and the corresponding inter-Stark transitions are indicated by the same numerals. The dashed line indicates a possible position of one more level of the $^4I_{13/2}$ state.

The main experimental result is illustrated by Fig. 4 (the inset clarifies the components of the tested $Nd^{3+} : Y_3Al_5O_{12}$-ceramic laser and the parameters of its optical cavity). At a wavelength of 1.3187 μm of the 11507 cm^{-1} $^4F_{3/2} \longrightarrow {}^4I_{13/2}$ 3924 cm^{-1} low-threshold lasing transition (effective peak transverse cross-section $\sigma_{eff}^{p} = (0.8 \pm 0.2) \times 10^{-19}$ cm^2; for identification see Fig. 5), we managed to attain an output power of ~3.7 W with a rather high “slope” efficiency (~35%) for this lasing channel of the Nd^{3+} ions.

Thus, the studies performed with the $Y_3Al_5O_{12}$- and $Y_3Al_5O_{12} : Nd^{3+}$-based ceramics proved their high strength properties, which are important for various technical applications, and also confirmed their high laser potential. In addition, it is necessary to mention here a new $Y_3Al_5O_{12} : Yb^{3+}$ ceramic obtained in Konashima Chemical Co.; the lasing characteristics ($^2F_{5/2} \longrightarrow {}^2F_{7/2}$ channel) of this ceramic will soon be published [19].

ACKNOWLEDGMENTS

This work was supported by the Russian Foundation for Basic Research and the Ministry of Industry, Science, and Technology of the Russian Federation; INTAS, project no. 99-1366; the Ministry of Education, Science, Sport, and Culture of Japan; the Technical University of Berlin (Germany); and the Donostia International Physics Center of Spain. The authors also acknowledge their cooperation with the Joint Open Laboratory Laser Crystals and Precision Laser Systems.

REFERENCES

1. T. Yanagitani, Y. Yagi, and M. Ichirawa, Jpn. Patent No. 10-101, 333 (1998).
2. T. Yanagitani, Y. Yagi, and Y. Yamasaki, Jpn. Patent No. 10-101, 411 (1998).
3. J. Lu, M. Probhu, J. Song, *et al.*, Appl. Phys. B **71** (10), 469 (2000).
4. A. A. Kaminskii, H. J. Eichler, K. Ueda, *et al.*, Phys. Status Solidi A **181** (2), R19 (2000).
5. A. A. Kaminskiĭ, G. I. Eichler, and K. Ueda, Pis’ma Zh. Éksp. Teor. Fiz. **72** (10), 717 (2000) [JETP Lett. **72**, 499 (2000)].

6. J. Lu, M. Probnu, J. Xu, *et al.*, Appl. Phys. Lett. **77** (23), 3707 (2000).
7. J. Lu, J. Song, M. Probhu, *et al.*, Jpn. J. Appl. Phys. **39** (10B), L1048 (2000).
8. J. Lu, T. Murai, T. Uematsu, *et al.*, in *Advanced Solid State Lasers* (Optical Society of America, Washington, DC, 2001), p. 60.
9. J. Lu, M. Probnu, J. Song, *et al.*, Jpn. J. Appl. Phys. **40** (6A), L552 (2001).
10. Ju. Lu, Ji. Lu, A. Shirakawa, *et al.*, Phys. Status Solidi A **189** (2), R11 (2002).
11. J. Lu, T. Murai, T. Uematsu, *et al.*, Proc. SPIE **4267**, 61 (2001).
12. J. Lu, T. Murai, K. Takaichi, *et al.*, Appl. Phys. Lett. **78** (23), 3586 (2001).
13. J. Lu, M. Probhu, K. Ueda, *et al.*, Laser Phys. **11** (10), 1053 (2001).
14. J. Lu, K. Ueda, H. Yagi, *et al.*, J. Alloys Compd. **341** (1), 220 (2002).
15. Ju. Lu, Ji. Lu, T. Murai, *et al.*, Opt. Lett. **27** (13), 1120 (2002).
16. K. Takaichi, J. Lu, T. Murai, *et al.*, Jpn. J. Appl. Phys. **41** (2A), L96 (2002).
17. A. Ikesue, T. Kinoshita, K. Kamata, and K. Yoshida, J. Am. Ceram. Soc. **78** (4), 1033 (1995).
18. T. Taira, A. Ikesue, and K. Yoshida, in *Advanced Solid-State Lasers* (Optical Society of America, Washington, DC, 1998), p. 430.
19. K. Takaichi, J. Lu, T. Murai, *et al.*, Jpn. J. Appl. Phys. (2003) (in press).
20. E. Carnall, S. E. Yatch, and W. F. Parsons, in *Materials Science Research* (Plenum, New York, 1966), p. 165.
21. C. Greskovich and J. P. Chernoch, J. Appl. Phys. **44** (10), 4599 (1973).
22. A. Evans and A. Charler, J. Am. Ceram. Soc. **59** (3), 731 (1976).
23. M. H. Lewis, R. Fung, and D. M. R. Taplin, J. Mater. Sci. **16**, 3437 (1981).
24. B. R. Lawn, A. G. Evans, and D. B. Marshall, J. Am. Ceram. Soc. **63** (2), 576 (1980).
25. G. B. Anstis, P. Chantikul, B. R. Lawn, and D. B. Marshall, J. Am. Ceram. Soc. **64** (2), 533 (1981).
26. E. A. Stepantsov, M. Sh. Akchurin, and V. G. Govorkov, Kristallografiya **23** (4), 872 (1978) [Sov. Phys. Crystallogr. **23**, 492 (1978)].

Translated by A. Zolot'ko

Crystallography Reports, Vol. 48, No. 3, 2003, pp. 520–523. Translated from Kristallografiya, Vol. 48, No. 3, 2003, pp. 567–570.
Original Russian Text Copyright © 2003 by Borodin, Pet'kov, Frantsev.

Algorithm for Crystal-Profile Control in Automated Crystal Growth by the Czochralski Method

A. V. Borodin*, I. S. Pet'kov, and D. N. Frantsev*****

** Experimental Factory of Scientific Engineering, Russian Academy of Sciences, Chernogolovka, Moscow oblast, 142432 Russia*
e-mail: faramir@ezan.ac.ru
*** OOO ROSTOKS-N, Chernogolovka, Moscow oblast, 142432 Russia*
**** Institute of Solid State Physics, Russian Academy of Sciences, Chernogolovka, Moscow oblast, 142432 Russia*

Received October 2, 2001

Abstract—Growth setups of the new generation should provide crystal growth in the automated mode. One of the necessary conditions for growing quality crystals is the rigorous maintenance of the given boule profile. In the systems with weight control, the model weight is compared with the weight measured by the weight sensor. Below, we describe an algorithm for calculating the model weight based on the numerical solution of the Bardsley equation. The algorithm allows one to set the crystal profile either by a function or a point set. *© 2003 MAIK "Nauka/Interperiodica".*

INTRODUCTION

In order to grow high-quality crystals, one has to supply modern growth setups with automatic systems for the control of the growth process.

To a large extent, the quality of the crystals thus grown depends on the profiles of the expanding cone of the ingot, the ingot portion where the necessary diameter is attained, and the tapering-cone of the ingot. Therefore, at present, various automatic systems are designed to provide complete control of the crystal profile on all the stages of its growth.

For refractory oxides, the most widespread automatic control systems provide weight control of the crystal and variation of the HF-generator power (the so-called T channel).

Bardsley *et al.* [1] suggested the following equation to determine the weight recorded by the weight sensor:

$$\begin{gathered} W(t) = \rho_s g\pi\int_0^t R^2(t)V_c(t)dt + \rho_l g\pi R^2(t)h(R,\theta) \\ + \rho_l g\pi a^2 R(t)\cos\theta(t), \\ \theta(t) = \varepsilon + \alpha(t), \end{gathered} \tag{1}$$

where $W(t)$ is the weight recorded by the weight sensor, ρ_l and ρ_s are the densities of the crystal and the melt, R is the crystal radius, $R(t)$ is the crucible radius, a is the capillary constant, ε is the growth angle, $\alpha(t)$ is the surface tension coefficient of the melt, $\theta(t)$ is the tilt angle of the side surface of the meniscus, $V_c(t)$ is the crystallization rate, and $h(R, \theta)$ is the meniscus height. The first term in Eq. (1) corresponds to the crystal weight, whereas the second and third terms determine the weight of the meniscus of height h.

The meniscus height depends on the crystal radius and the growth angle and is determined from the Tsinskiĭ formula [2],

$$\begin{gathered} h(R,\theta) = a\left(1 - \sin\theta + \frac{a^2\cos^2\theta}{16R^2}\right)^{1/2} - \frac{a^2\cos\theta}{4R}, \\ a = \left(\frac{2\sigma_l}{\rho_l g}\right)^{1/2}, \end{gathered} \tag{2}$$

where σ_l is surface-tension coefficient of the melt.

The systems for growth control based on Eq. (1) are considered in a number of articles.

In [3], the automatic control of the radius of the growing crystal is implemented under the assumption that the crystal grows with a cylinder shape ($\alpha(t) = 0$). In order to determine the real crystal radius, Wilde and Feigelson [3] differentiate Eq. (1), ignore the terms that take into account the meniscus dynamics, and obtain an equation relating the weight recorded by the weight sensor and the crystal radius:

$$\dot{W}(t) = \rho_s g\pi R^2(t)V_c. \tag{3}$$

However this method of control cannot be used for crystals of a given shape with diverging and tapering cones.

The method of automatic control of growth of a crystal with a preset side-surface profile requires the comparison of the weight measured by the weight sensor with the calculated model weight.

In [4, 5], an iteration method for calculating the model weight based on Eq. (1) is proposed. The crystallization rate in this equation is represented by an analytical function. The crystal profile is given in the form of a polynomial or a smooth trigonometric function, whereas its change is determined by the selection of the appropriate coefficients.

Our study aimed to design an algorithm for automatic control of growth of crystals with a given profile such that the crystal shape used for calculating the model weight of the crystal can be given either numerically or as an analytical function.

CONTROL ALGORITHM

To grow a crystal with an arbitrary profile $R(l)$ we used a system of automatic control and a reference signal from the model weight of the crystal. The block diagram of the automatic control system is shown in Fig. 1. The reference weight is determined by the program based on Eq. (1). The weight value thus obtained is compared with the real weight recorded by the weight sensor. The difference between the reference signal and the signal from the weight sensor arrives at a PID-controller providing control along the T channel.

In order to use Eq. (1), one has to pass from the crystal radius varying along its length to the crystal radius varying with time, $R(l) \longrightarrow R(t)$.

The model length l of the crystal grown for time t can be considered as a sum of the distance passed by the rod with a velocity V_0 and the change in the melt in the crucible minus the meniscus height h. In the general case, the dependence of the length l of the grown crystal on time is nonlinear (Fig. 2):

$$l = V_0 t + \frac{\rho_s}{\rho_l R_c^2}\int_0^l R^2(l)dl - h(R(l), \theta(l)), \qquad (4)$$

where R_c is the crucible radius.

Now, determine the time necessary for the crystal to attain the length l at the constant pulling rate V_0 as

$$t(l, V_0) = \frac{1}{V_0}\left(l + h(R(l), \theta(l)) - \frac{\rho_s}{\rho_l R_c^2}\int_0^l R^2(l)dl\right). \qquad (5)$$

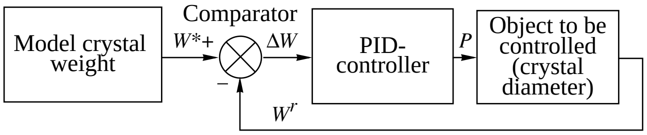

Fig. 1. Block diagram of the automatic control system for crystal growth.

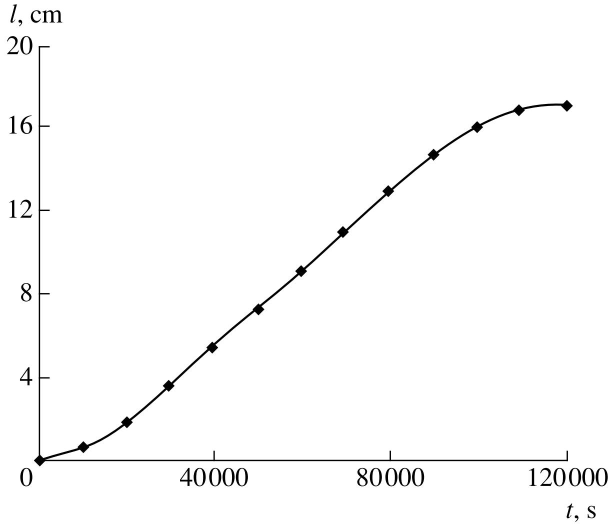

Fig. 2. Example of the change in the model crystal length with time at V_0 = 4 mm/h, R_c = 5 cm, and a = 0.6 mm.

When dividing the crystal into sufficiently small portions along its length, we can substitute the integral in Eq. (5) by a sum. Performing the integration by the trapezium method, we can rewrite Eq. (5) as

$$t_i(l_i, V_0) = \frac{1}{V_0}\left(l_i + h_i(R_i, \theta_i) - \frac{\rho_s}{\rho_l R_c^2}\frac{\Delta l}{2}\sum_{j=1}^{n(l_i)-1}(R_j^2 + R_{j-1}^2)\right), \qquad (6)$$

where

$$l_i = \frac{(i+1)}{N} l_{\max}, \quad i = 0\ldots N-1, \qquad (7)$$

with $l_{\max}$ being the maximum model length of the crystal and N being the number of the points of division along the model length of the crystal.

Now consider the main cycle of the control program (Fig. 3).

Before beginning the control cycle, the program creates a file whose cells are filled with the $R_i(l_i)$ and t_i values [t_i is the time necessary for the crystal to attain the length l_i at the constant pulling rate V_0 calculated by Eq. (6)]. The program is initiated by setting the initial values of the variables W^*, t^*, and l^* (the current control values).

The control cycle consists in questioning the computer timer and computing the time t^* passed from the moment of the process initiation. The computed time is used to search for such t_i and t_{i-1} values of the set t_i that $t_{i-1} < t^* < t_i$. The subscript i of the set determined in the course of the search is used for finding the tabulated l_{i-1}, l_i, R_{i-1}, R_i, h_{i-1}, and h_i values.

In the course of the crystal-growth control cycles, one can encounter a situation in which the time t^* passed from the beginning of the process lies in the

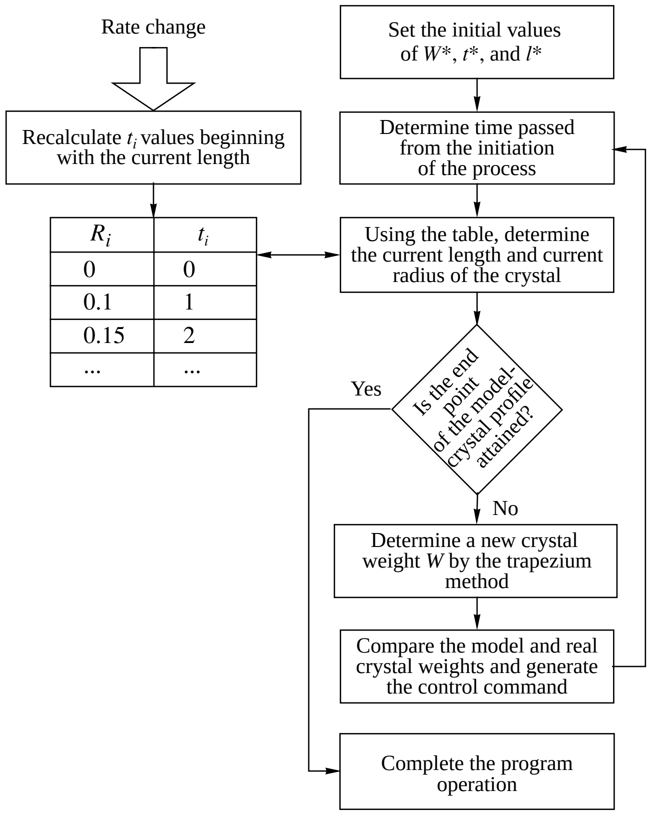

Fig. 3. Block diagram of the control algorithm.

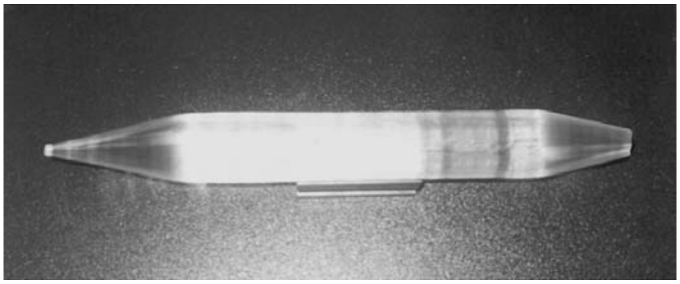

Fig. 4. Grown YAG crystal with the length of about 40 cm.

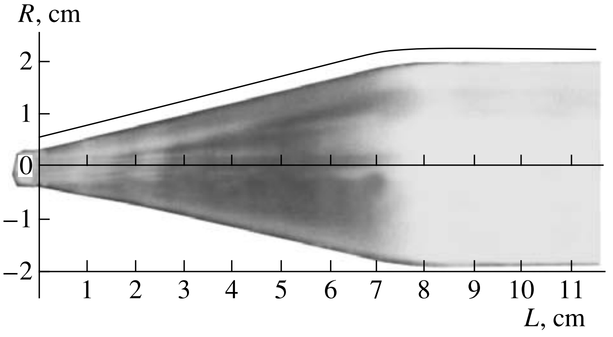

Fig. 5. Expanding cone of a YAG crystal and the corresponding profile.

same time interval $[t_{i-1}, t_i)$ as in the previous cycle. Therefore, to increase the accuracy of the computation of the model length l^*, radius R^*, and meniscus height h^*, one has to use a linear interpolation at the segment $[t_{i-1}, t_i)$,

$$l^* = \frac{l_i - l_{i-1}}{t_i - t_{i-1}}(t^* - t_{i-1}) + l_{i-1}, \tag{8}$$

$$R^* = \frac{R_i - R_{i-1}}{t_i - t_{i-1}}(t^* - t_{i-1}) + R_{i-1}, \tag{9}$$

$$h^* = \frac{h_i - h_{i-1}}{t_i - t_{i-1}}(t^* - t_{i-1}) + h_{i-1}. \tag{10}$$

In order to distinguish the real and model values at various cycles of growth control, introduce the cycle subscript t. Then, R_t^*, l_t^*, and h_t^* are the model quantities at the current control cycle, and R_{t-1}^*, l_{t-1}^*, and h_{t-1}^* are the quantities at the previous cycle. Using the formula for the volume of a truncated cone, we can calculate the model weight of the crystal as

$$\begin{aligned} W_t^* &= W_{t-1}^* \\ &+ \rho_s \frac{1}{3}\pi(l_t^* - l_{t-1}^*)((R_{t-1}^*)^2 + R_{t-1}^* R_t^* + (R_t^*)^2). \end{aligned} \tag{11}$$

Then, the weight signal W_t^* is supplied to a comparator that determines the difference between the model weight of the crystal and the weight signal recorded by the weight sensor. This difference signal ΔW from the comparator is supplied to the PID-controller that provides the control along the T channel:

$$\begin{aligned} P &= k_p \Delta\dot{W} + k_i \int_0^{t^*} \Delta\dot{W} dt + k_d \Delta\ddot{W} \\ &= k_p \Delta\dot{W} + k_i \Delta W + k_d \Delta\ddot{W}. \end{aligned} \tag{12}$$

In the case of variation of the model pulling rate V_0 by a certain law or its manual correction by an operator, the control system recalculates the t_i values beginning with the set element with the current subscript i:

$$\begin{aligned} t_i(l_i, V_0) &= t^* \\ &+ \frac{1}{V_0}\left((l_i - l^*) + h_i(R_i, \theta_i) - \frac{\rho_s}{\rho_l R_c^2}\frac{\Delta l}{2}\sum_{j=i}^{n(l_i)-1}(R_j^2 + R_{j-1}^2)\right). \end{aligned} \tag{13}$$

In order to visualize the growth process, the control program solves the inverse problem, i.e., calculates the real radius R^r of a growing crystal from the weight signal recorded by the weight sensor. The real radius is calculated under the assumption that the real radius changes linearly within a control cycle. Assuming that the model length l^* of the crystal equals the real length l^r and that the model weight of the meniscus equals its real weight, we arrive at the quadratic equation for determining R^r

$$R_t^{r^2} + R_{t-1}^r R_t^r + \left(R_{t-1}^{r^2} - \frac{3(W_t^r - W_t^* - W_{t-1}^r + W_{t-1}^*)}{\rho_s \pi (l_t^* - l_{t-1}^*)}\right) = 0, \qquad (14)$$

where W_t^* is the model weight of the meniscus at the current control cycle and W_t^r is the weight signal recorded by the weight sensor.

CONCLUSION

The algorithm for calculating the reference value of the crystal weight suggested above was used in the control program Nika-2000 designed for a Nika growth setup manufactured by the Experimental Factory of Scientific Engineering of the Russian Academy of Sciences.

The application of this algorithm allows one to grow the transient portions of the crystal in the automatic mode, calculate the real current radius of the crystal, and visualize the growth process (Fig. 4). It also allows one to switch to automatic-control mode of the crystallization process at any arbitrary point of the crystal profile. The growth program based on this algorithm allows one to change the pulling rate during the growth process.

Using the automatic control system based on Eq. (1), we managed to grow crystals of yttrium aluminum garnet (YAG), one of which is shown in Fig. 4.

The crystals grown with the use of the suggested algorithm were studied on a profilometer in order to determine the deviation of the real radius of the crystal from the given one. The deviation of the radius from its nominal value did not exceed ±0.5 mm. Figure 5 shows the corresponding photograph of the expanding cone of the crystal and its profile.

REFERENCES

1. W. Bardsley, D. T. Hurle, G. C. Joyce, and G. Wilson, J. Cryst. Growth **40** (1), 21 (1977).
2. S. V. Tsivinskiĭ, Inzh.–Fiz. Zh. **5** (9), 59 (1962).
3. J. P. Wilde and R. S. Feigelson, J. Cryst. Growth **113**, 337 (1991).
4. G. A. Satunkin, S. N. Rossolenko, V. H. Kurlov, *et al.*, Cryst. Res. Technol. **21** (9), 1125 (1986).
5. S. N. Rossolenko, Candidate's Dissertation (Chernogolovka, 1987).

Translated by L. Man

Crystallography Reports, Vol. 48, No. 3, 2003, pp. 524–529. Translated from Kristallografiya, Vol. 48, No. 3, 2003, pp. 571–575.

Structure Analysis by Reduced Data: V. New Approach to Refinement of Crystal Structures

A. P. Dudka

Shubnikov Institute of Crystallography, Russian Academy of Sciences,
Leninskiĭ pr. 59, Moscow, 119333 Russia

e-mail: dudka@ns.crys.ras.ru

Received November 14, 2001; in final form, September 12, 2002

Abstract—A new approach to refining crystal structures using reduced experimental data is considered. The data reduction, which requires the establishment of the common and different characteristics of the measured data, can be done using the method of interexperimental minimization. The method is used to analyze the thermal motion of atoms. The method can also be used for the detailed study of different groups of those model parameters that are especially important for each specific case. *© 2003 MAIK "Nauka/Interperiodica".*

Cognition comes through comparison…

INTRODUCTION

The concepts underlying diffraction analysis by reduced data and the method of interexperimental minimization (IEM) were first suggested in [1] and further developed in [2–4]. A systematical consideration of this new approach was begun in [5–8]. It was suggested that the accuracy of the results thus obtained be evaluated using the criteria of the relative accuracy, reproducibility, and physical reliability of the results [5] in this order of priority. It is assumed that the model of the crystal structure is known *a priori*. Thus, the problem consists in refining the parameters of this model.

In the traditional refinement, one searches for the parameter values that provide the minimum difference between the experimental and calculated structure factors, e.g., the minimum quadratic norm.

It was shown [7] that the quantities to be determined should also correspond to the minimum differences in the data measured in different experiments and reduced to the common scale, where these "interexperimental differences" are of a random nature. The introduction of this additional condition stabilizes the refinement process, decreases the influence of the systematic errors in the data and correlations between the parameters, and leads to a solution somewhat different from the traditional one.

If a researcher has several sets of experimental data obtained from different samples with almost equivalent structures, the refinement of their parameters allows one to establish both the differences in the experimental conditions and the individual characteristics of each sample [7]. If one possesses only one complete data set, the symmetrically related reflections are compared. The differences between the intensities of these reflections depend on the anisotropy of absorption, extinction, and some other effects. If no simultaneous reflections are recorded for such reflections, one can establish why they have different intensities and evaluate the above-mentioned effects. Comparing the reflection profiles for the small and large scattering angles, one can also evaluate the parameters of the phenomenon responsible for the reflection profile, i.e., the characteristics of thermal diffuse scattering (TDS) [4].

One can compare or average only the data reduced to the common scale, which, in turn, requires the reduction of the experimental data. Similar to the introduction of the correction for absorption or TDS into the integrated intensities, one can also introduce the corrections for extinction, the (energy) scale, thermal motion of atoms, etc. In our case, the parameters necessary for this procedure are not taken from reference books—they are determined as a result of an additional procedure of interexperimental minimization.

After eliminating from the measurements the effects whose study is beyond the scope of this work, the measurements can be averaged and then used for the refinement of the model parameters. This method of the refinement increases the relative accuracy of the results obtained and concentrates the attention on those model parameters that are the most important for the problem to be solved.

The suggested approach to the refinement of the structure model of a crystal requires the development of a formalized method for the reduction of experimental data and derivation of new goal functions of the refinement appropriate for interexperimental minimization.

1063-7745/03/4803-0524$24.00 © 2003 MAIK "Nauka/Interperiodica"

REDUCTION OF EXPERIMENTAL DATA

In [7], five methods for reducing experimental data were suggested. Initially, the data were reduced to the absolute scale within the kinematical theory of diffraction. The so-called computational method was developed [7] in which the reduction was based on the use of the relationship between the structure factors calculated with and without allowance for a certain phenomenon.

The traditional refinement of the model parameters is performed with simultaneous calculation of all the parameters from the experimental data. The contribution of each of the parameters is added to the total sum without any preliminary analysis, which does not allow one to take into account possible correlations. In the general case, the problem of reduction (expansion of the model in orthogonal functions) is rather complicated.

As is well known, the diffraction analysis is based on the formula for the structure factor F_{hkl} of the hkl reflection which relates the measured, $I_{hkl\,\text{obs}}$, and calculated, $I_{hkl\,\text{calcd}}$, intensities:

$$I_{hkl\,\text{obs}} = I_{hkl\,\text{calcd}} + \varepsilon_{hkl}$$
$$= A_{hkl}(Lp)_{hkl}\Big(1+\sum\alpha_{ihkl}\Big)ky_{hkl}|F_{hkl}|^2 + M_{hkl} + \varepsilon_{hkl},$$

where k is the scale factor, A is the absorption (transmission) correction, Lp is the correction for the Lorentz factor and radiation polarization, α_i is the correction for thermal diffuse scattering of the ith order, M is the correction for multiple diffraction, y is the correction for extinction, and ε are the correction for errors.

In diffraction analysis, only the *first-level reduction* is widely used, in which the contributions that come from the effects accompanying the Bragg scattering are excluded from the measured data. This requires knowledge of certain *a priori* information on the corresponding characteristics of the sample and the diffractometer. Thus, knowing the absorption coefficients and sample dimensions, one can take into account the radiation absorption. Omitting the *hkl* subscript and performing the first-level reduction, we obtain $I_{\text{obs}} = ky|F^2| + \varepsilon$. The reduction performed is favorable for the results—it increases their relative accuracy.

There are some methods for reducing data to the absolute scale and eliminating the extinction effect that are not included in the main process of the refinement. However, these methods are insufficiently accurate or are not of a general character. Therefore, further reduction is usually performed within the program of the refinement of the complete model, which enhances the interparametric correlations. The following alternative approach can be used.

Assume that we have a certain experimental data set $I_{\text{obs}1} = (k_1y_1)|F^2| + \varepsilon_1$ obtained under certain known conditions. Now, repeat this experiment under somewhat modified conditions such that the scale factor and the extinction parameters take different values: $I_{\text{obs}2} = (k_2y_2)|F^2| + \varepsilon_2$. If we deal with the same structure, then, within some errors, we have $|F^2| = I_{\text{obs}1}/(k_1y_1) = I_{\text{obs}2}/(k_2y_2)$. The values of the parameters can be obtained by minimizing the differences between the normalized measured data for the reflections with the same Miller indices $\sum[I_{\text{obs}1}/(k_1y_1) - I_{\text{obs}2}/(k_2y_2)] \longrightarrow$ min in the problem of a conditional extremum. If the y_m and k_m values at $m = 1, 2$ are determined correctly, the interexperimental scale factor (so-called *interfactor* K_w) should be close to unity. In fact, the interfactor is the criterion of the reduction quality. This method of reducing the experimental data to the absolute scale (state corresponding to the kinematical theory of diffraction) is called the *second-level reduction*. After this reduction, the measured data (or simply measurements) take the form $I_{\text{obs}} = |F|^2 + \varepsilon$.

The structure factor is the sum of the contributions that come from individual atoms. The contribution from each atom is represented by the product of three complex functions corresponding to scattering by an individual nonspherical atom F_f, coordinates of the atom F_x, and the thermal motion (displacements) F_T; namely, $F = \sum[F_fF_xF_T]$. In a similar way, one can also eliminate the contribution of any of these effects. Thus, the *third-level reduction* to the static state of atoms in the crystal (at 0 K) has the form $I_{\text{obs}} = \left|\sum[F_fF_x]\right|^2 + \varepsilon$. The separation of the partial structure factors can also be considered as the third-level reduction.

The most interesting result of the *fourth-level reduction* (any two of the three effects are eliminated) is the separation of the "experimental" scattering factors of individual atoms ($I_{\text{obs}} = \left|\sum[F_f]\right|^2 + \varepsilon$ or $I_{\text{obs}} = |F_f|^2 + \varepsilon$). The contribution of any effect is determined by many parameters. The separation of the "experimental atomic coordinates," scattering lengths of neutrons, coefficients of the tensors of the atomic-displacement parameters, the parameters of the wave functions, etc.; is considered as the *fifth-level reduction*.

The efficiencies of the different reduction methods and the appropriateness of the division of the models into general and particular parts are verified by a simple comparison of the alternative variants of minimization. The problem is solved in the general form and only by IEM methods. In principle, it is clear how one can fully formalize the procedure in order to avoid the use of any information on the model composition. One has to divide the model proceeding from the coefficients of the parameter correlation that are characteristic of the system under consideration.

METHOD OF INTEREXPERIMENTAL MINIMIZATION

The expression for the goal function in the IEM method was obtained in the search for the general solution of the minimization problem for several measured data sets [7]. In [8], these data were generalized for an arbitrary number of independent measurements. The simplest way of obtaining the corresponding formula is the solution of the problem of conditional minimization by the method of Lagrange multipliers

$$\Phi = \Phi_\alpha + \Phi_\delta + \Phi_{\text{cross}}$$

$$= \frac{1}{2N+1}\left\{\alpha \sum_{m=1}^{N}\sum_{hkl=1}^{n_{\text{cross}}} w_{hkl}\left(I^{m\ \text{norm}}_{hkl\ \text{obs}} - I^{m\ \text{base}}_{hkl\ \text{calcd}}\right)^2\right.$$

$$+ \delta \sum_{m=1}^{N}\sum_{hkl=1}^{n_{\text{cross}}} \frac{w_{hkl}}{w'_{hkl}}\left(I^{\text{norm}}_{hkl\ \text{cross}} - K^m_w I^{m\ \text{norm}}_{hkl\ \text{obs}}\right)^2 \qquad (1)$$

$$\left. + \gamma \sum_{hkl=1}^{n_{\text{cross}}} \frac{w_{hkl}}{w'_{hkl}}\left(I^{\text{norm}}_{hkl\ \text{cross}} - I^{\text{base}}_{hkl\ \text{calcd}}\right)^2\right\},$$

where n is the number of independent measurements; N is the number of repeated measurements (equivalent reflections); I_{obs}, I_{calcd}, w, and w' are the measured and calculated values, weights, and weight corrections; the superscript norm indicates that the experimental data are reduced to the common scale (are normalized), the subscript cross indicates averaging over N data; and α, γ, and δ are the Lagrange multipliers. Here, the δ-functional Φ_δ is written as the “average intensity-individual intensity” difference, an alternative to the difference between the repeated measurements of reflections with the same Miller indices [7, 8].

The problem of interexperimental minimization necessarily arises in attempts to use several measurements or data sets in one computational procedure. In order to pass from the LS to any other “parental method,” one has to change the expression for the δ-functional. The most natural method for such a change is the method of maximum entropy [9]:

$$H = \Phi_\delta$$

$$= -\sum_{m=1}^{N}\sum_{hkl=1}^{n_{\text{cross}}} \frac{w_{hkl}}{w'_{hkl}} I^{\text{norm}}_{hkl\ \text{cross}} \ln\left(I^{\text{norm}}_{hkl\ \text{cross}}/\left(K^m_w I^{m\ \text{norm}}_{hkl\ \text{obs}}\right)\right). \qquad (2)$$

The structure model is divided into two parts—the basic model (common to all the experiments) and the model perturbation. The basic model describes the invariant part of the mode, whereas the model perturbation defines the effects responsible for the differences in the measurements that should be reduced (or eliminated) from the experimental data. The existence of the second independent experiment allows one to apply the Bayes theorem in order to correct the *a priori* distribution of errors in the data. The normal distribution is used as the model one.

APPLICATION OF THE INTEREXPERIMENTAL MINIMIZATION TO A SINGLE DATA SET

Reduction of Anisotropic Effects (IEM-A)

Anisotropic effects (absorption, extinction, TDS) are responsible for the discrepancies between the intensities of symmetrically equivalent reflections. The reduction of the experimental data aimed at the elimination of the contributions that come from the anisotropic effects is based on the δ-functional in form (1) at $K_w \equiv 1$. The possibilities for correcting the weighting scheme here are rather limited.

Use of Data Subsets (IEM-S)

It is well known that the refined data should be independent of the experimental data subsets used. This signifies that the $|I_{hkl\ \text{calcd}}|$ sets obtained from different subsets should be rather close. Let us compose N data subsets in a random way that comprise from 50 to 90% of the complete data set. Now, write the δ functional for $|I_{hkl\ \text{calcd}}|$ with respect to the mean intensity

$$\Phi_\delta = \delta \sum_{m=1}^{N}\sum_{hkl=1}^{n_{\text{cross}}} w_{hkl}\left(I^{\text{norm}}_{hkl\ \text{cross}} - I^{m}_{hkl\ \text{calcd}}\right)^2 \longrightarrow \text{min.} \qquad (3)$$

In this case, no reduction of the experimental data is necessary at all, whereas the correction of the weights cannot be made because of their mutual dependence.

Consider a small perturbation in an ideal crystal, e.g., an impurity. As a rule, the difference in scattering from impurity and matrix atoms depends on the scattering angle θ. This fact underlies the low-order truncation (LOT) method [10], which allows one to overcome the difficulty associated with the correlations between the occupancies of the positions and the parameters of atomic displacements [11]. The LOT method consists in a number of refinements over data subsets that have different low-angle boundaries ($\sin\theta/\lambda$). The refinement conditions are selected in such a way that the results obtained coincide. Averaging the parameters yields the unknown occupancies of the positions with impurity atoms.

The IEM method is the logical continuation of the LOT method. We require that the parameters of the models obtained from data subsets with different low-angle boundaries with the aid of the δ-functional in form (3) coincide. For higher stabilization of the process of refinement, we also impose the requirement that the parameters P_m obtained using the mth subset only slightly differ from the mean P_{mean} values, $\|P_m - P_{\text{mean}}\| < \varepsilon$.

Reliability factors $R = \Sigma|Y_{obs} - Y_{calcd}|/\Sigma Y_{obs}$ for three variants of structure refinement

Experiment	Crystal	N_{par}	N_{refl}	R_{init}, %	Joint experiment	N_{refl}	$R(2)$, %	$R(3)$, %
1	CdTe (22°C)	10	209	0.915	+2	190		0.308
2	CdTe (218°C)	10	184	1.380	+3	150		0.248
3	CdTe (300°C)	10	151	1.486	+1	151		0.226
4	$Al_2BeO_4 : Cr^{3+}$	41	1303	1.157	+7	1270	0.729	0.516
5	$Al_2BeO_4 : Cr^{3+}$	41	1137	1.521	+6	789	0.807	0.647
6	$Al_2BeO_4 : Cr^{3+}$	41	972	1.040	+4	931	0.739	0.560
7	$Al_2BeO_4 : Cr^{3+}$	41	1596	0.990	+6	931	0.639	0.483

Note: R_{init} are the initial R factors obtained by the LS method; $R(2)$ and $R(3)$ are the reliability factors obtained by the IEM method for the second- and third-level reduction, N_{par} is the number of parameters, and N_{refl} is the number of measurements. Experiments 4–7 were made at room temperature.

The subsets can be selected proceeding from different principles. It is important that condition (3) imposed on the mutual correspondence of the model parameters obtained from different data sets can be used as the condition additional to (1).

RELATION BETWEEN CRYSTAL STRUCTURE AND PROPERTIES

Formula (1) is of a universal nature. It relates any processes having common parameters. Let two physical phenomena (functions or models) be dependent on a certain set of common parameters. Minimizing the δ-functional, one has to reduce the contribution of the parameters determining the differences between the corresponding measurements of different phenomena, average the data obtained, and refine the values of the common parameters using the cross functional. On the whole, the analytical expressions for I_{calcd1} and I_{calcd2} are the same if one compares different diffraction experiments, but they can be different if the data obtained in different experiments (e.g., diffraction and spectroscopy experiments) are jointly processed. Of course, one has also to take into account the possible difference in the volume and accuracy of the experimental data. Such an approach should yield physically reliable results [5, 7].

DISCUSSION

The general description of the corresponding program can be found elsewhere [8]. The program was tested in the mode of nonlinear LS refinement and using the variant of the second-level reduction based on the linear LS method for 17 experimental data sets [8].

The results discussed in the present article were obtained using the new version of the program with the algorithm that can be classified as the IEM method based on the adaptive nonlinear regularized LS method with the δ-functional in the form of the difference between the structure factors of the reflections with the same Miller indices taken from different experiments. The computations were performed in the following variant of interexperimental-minimization cycle: testing, the formation of a cross set and a weighting scheme, the refinement of the parameters of the model perturbation using the functional $\Phi = \Phi_\alpha + \Phi_\delta$, and the refinement of the parameters of the basic model using $\Phi = \Phi_{cross}$. Convergence was attained within two to three such cycles.

The table lists new results obtained after the reduction of the thermal motion (third-level reduction) for three alexandrite ($Al_2BeO_4 : Cr^{3+}$) crystals and one sphalerite-type CdTe crystal (for the latter crystal, the experimental data were obtained at different temperatures).

The use of the IEM method for the second-level reduction decreased the reliability factors [$R(2)$-factors] by 30–60% (see [5] and the table). The third-level reduction (at 0 K) considerably increases the *relative accuracy* in comparison with the accuracy of the initial data. A decrease in the reliability factors after the reduction of thermal motion reflects the well-known fact that positional parameters are determined with a much higher accuracy than parameters of atomic displacements.

The minimization of the functional $\Phi_\alpha + \Phi_\delta$ for highly symmetric CdTe crystals was, in fact, an attempt to determine such atomic displacements that would not displace all the atoms of the structure from the special positions. In other words, the values of the corresponding reliability factors, $R(3)$, reflect the experimental errors and the differences between the model spherical atoms and real nonspherical atoms. This fact explains the low values of the $R(3)$ factors. It should also be noted that, for these crystals, the second-level reduction has no sense.

In the $Al_2BeO_4 : Cr^{3+}$ structure, there are seven fixed positional parameters and 11 varying parameters, and the decrease in the $R(3)$ factor for this structure is much less. The $R(3)$ factor can be interpreted as the reliability factor calculated using the atomic coordinates and the characteristics of the electron-density distribution. It seems that, when reducing the thermal motion, one has to analyze the dynamics of the R factors rather than their absolute values.

The third-level reduction is performed under the following assumptions. First, scattering from a crystal with atoms at rest can be described by the formula for a structure factor with all the atomic displacements ($\left|\sum[F_fF_x]\right|^2$) being equal to zero. This extrapolation to the state at 0 K is rather crude, since it ignores both the quantum effects and the scattering by structural defects that should necessarily take place. The second assumption deals with the error that should be attributed to the experimental value reduced to 0 K. Both $\left|\sum[F_fF_xF_T]\right|^2$ and $\left|\sum[F_fF_x]\right|^2$ quantities are on the same scale, but, on the one hand, the value of the second one is always much higher, while on the other, it is well known that the measurements taken at low temperatures, with all the other conditions being the same, are usually more accurate. In the program, the reduced quantity is assigned the whole error of the experimental structure factor after its reduction to the absolute scale.

THE SOLUTION OF THE PROBLEMS OF INTEREXPERIMENTAL MINIMIZATION AND LEAST-SQUARES REFINEMENT

The solution of the problem of interexperimental minimization introduced into the LSM program with the initial experimental data and weights can give higher R factors than the initial LS refinement. This was always the case in the second-level reduction in our earlier studies. Thus, in this sense, we can state that the solution "diverges." The new program allows one, for the first time, to refine any parameters using the δ-functional. Now, modifying the weighting scheme in the third-level reduction, one can diminish the R factors calculated by the initial experimental structure factors ($R(3)$ factors calculated using cross sets are always lower). Thus, for the experiment on a CdTe crystal performed at 218°C, we obtained the initial R factor equal to 1.639% (see table), whereas the corresponding value calculated using the functional Φ_α is 1.564%, with the number of reflections and parameters being 191 and 10, respectively, in both cases. We believe that this fact is not of crucial importance because the only requirement here is that the solution of the interexperimental-minimization problem satisfy the criteria of the LS method.

CONCLUSION

Above, we considered and tested a new principle of data processing. We claim that the values of various parameters that describe the complete model of a phenomenon should be calculated using different "parts" of the initial measurements. The experimental structure factors of reflections allows one to single out a certain internal structure which corresponds to the division of the initial model into parts. We also considered a possible modification of the experimental data, which, however, can hardly be implemented in practice. The corresponding data correspond to a crystal at 0 K, i.e., to the absence of thermal motion of atoms.

The IEM method is an algorithm for regularizing the minimization problem in which the constraints are imposed onto the experimental data and not on the model parameters. The IEM algorithm searches for such a solution to which there correspond not only the minimum discrepancy between the experimental and calculated data, but also the maximum possible agreement of the reduced experimental data. One can state that the IEM algorithm implements the "difference refinement." The IEM algorithm is not used instead of the known minimization methods; it only extends these methods to the case of several independent measurements. This study uses a program that minimizes the quadratic functional. The expression for the IEM functional may also be written on another basis. We consider a IEM functional based on the method of maximum entropy.

The relative accuracy of the results obtained by the IEM method considerably increases and is higher, the more efficient the reduction of the data. The method is tested on crystals for which the relative accuracy of the data refined by the LS method is at a level of $R \approx 1\%$. It is shown that the values of the $R(2)$ factors refined by the IEM method are decreased by 30–60% (second-level reduction to the absolute scale). The specific reliability factors, $R(3)$, after the third-level reduction (thermal-motion-reduction) can have values from 0.2 to 0.6%.

The IEM method can be used in any field of research where the parameters of the theoretical model are refined by the experimental data. The corresponding programs are distributed free of charge.

ACKNOWLEDGMENTS

The author is grateful to M.Kh. Rabadanov for his help and B.M. Shchedrin for discussing problems associated with the processing of the experimental data.

REFERENCES

1. A. P. Dudka and A. A. Loshmanov, in *Proceedings of National Conference on Application of X-ray, Synchrotron Radiation, Neutrons, and Electrons to Study of Materials* (Dubna, 1997), Vol. 1.
2. A. P. Dudka, A. A. Loshmanov, and B. P. Sobolev, Kristallografiya **43** (4), 605 (1998) [Crystallogr. Rep. **43**, 557 (1998)].
3. A. P. Dudka, A. A. Loshmanov, and B. A. Maksimov, Kristallografiya **43** (4), 613 (1998) [Crystallogr. Rep. **43**, 565 (1998)].
4. A. P. Dudka, A. A. Loshmanov, and B. A. Maksimov, Poverkhnost, No. 2, 28 (2001).
5. A. P. Dudka and A. A. Loshmanov, Kristallografiya **46** (3), 565 (2001) [Crystallogr. Rep. **46**, 511 (2001)].
6. A. P. Dudka and A. A. Loshmanov, Kristallografiya **46** (6), 1135 (2001) [Crystallogr. Rep. **46**, 1049 (2001)].
7. A. P. Dudka, Kristallografiya **47** (1), 156 (2002) [Crystallogr. Rep. **47**, 145 (2002)].
8. A. P. Dudka, Kristallografiya **47** (1), 163 (2002) [Crystallogr. Rep. **47**, 152 (2002)].
9. D. M. Collins, Acta Crystallogr., Sect. A: Found. Crystallogr. **40**, 705 (1984).
10. H. Kroll, T. Lueder, H. Schlenz, *et al.*, Eur. J. Mineral. **9**, 705 (1997).
11. M. Heuer, J. Appl. Crystallogr. **34**, 271 (2001).

Translated by L. Man

Crystallography Reports, Vol. 48, No. 3, 2003, p. 530. Translated from Kristallografiya, Vol. 48, No. 3, 2003, p. 576.
Original Russian Text Copyright © 2003 by the Editorial Board.

INFORMATION

On the Fedorov Prize Competition Held by the Russian Academy of Sciences

The Department of Physical Sciences of the Russian Academy of Sciences announces that the Fedorov Prize Competition will be held in 2003.

The Fedorov Prize is awarded every three years for outstanding work in crystallography. The prize is awarded for a single published scientific work or a series of works on a common subject, as a rule, by one author. For collective studies, no more than three main authors should be proposed.

The right to propose candidates is granted to

(1) Academicians and Corresponding Members of the Russian Academy of Sciences;

(2) scientific institutions and institutes of higher education;

(3) scientific councils of the Russian Academy of Sciences and other departments working on fundamental scientific problems;

(4) scientific societies and technical societies of engineers;

(5) scientific and technical councils of State Committees, Ministries, and Departments, as well as technical councils of industrial enterprises and designer's offices.

The documents necessary to propose candidates for the Prize should be presented in triplicate to the Shubnikov Institute of Crystallography, Russian Academy of Sciences (Leninskiĭ pr. 59, Moscow, 119333 Russia) addressed "To the Fedorov Prize Competition." The following documents are required:

(1) a presentation justifying the nomination, including the scientific characteristics of the work and its importance for the development of science and the national economy;

(2) the scientific work (series of works) presented;

(3) data about the author (a list of main scientific works, discoveries, and inventions; affiliation and post; home address).

Works that have already been awarded State or name prizes are not accepted for the Fedorov Prize Competition.

The documents should be presented no later than September 22, 2003.

Department of Physical Sciences
Russian Academy of Sciences

Translated by I. Polyakova